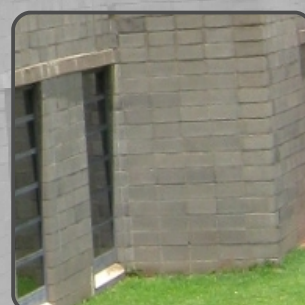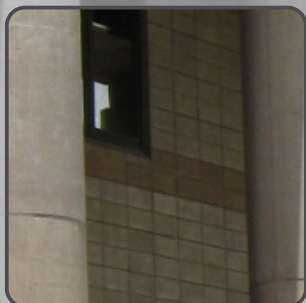# SAUPEC 2010

28 & 29 January

University of the
Witwatersrand
JOHANNESBURG

PROCEEDINGS OF THE NINETEENTH
SOUTHERN AFRICAN UNIVERSITIES
POWER ENGINEERING CONFERENCE

SAUPEC 2010

University of the Witwatersrand, Johannesburg

28 - 29 January 2010

Review: Authors were invited to submit full papers, and each full paper was then peer reviewed by at least two specialist reviewers, with final acceptance based on the value of the contribution and its scientific and engineering merit.

Disclaimer: Authors are responsible for the contents of the papers.

Acknowledgements

Foreword

Dear Colleagues

Welcome to the 19th Southern African Universities Power Engineering Conference, SAUPEC 2010, hosted by the School of Electrical and Information Engineering of the University of the Witwatersrand, Johannesburg.

SAUPEC conferences are primarily intended to provide a forum for post-graduate students and faculty from the region to present their research work in power related fields. The secondary but equally important goal is to provide a regional networking forum for researchers in the power engineering field.

The proceedings include all the panel reviewed and accepted papers. As in the past discussion papers that have not been subjected to the review process are also accepted for presentation and discussion at the conference. The discussion papers are not included in the printed proceedings, but are included on the CD-ROM.

We wish all the attendees to SAUPEC 2010 a wonderful stay in Johannesburg and a rewarding and enjoyable SAUPEC 2010.

SAUPEC 2010 Organising Committee

Table of Contents

Topic C: Power Systems   107

Topic D: Renewable and Alternative Energy   185

Topic A

Power Electronics

TOPIC A. POWER ELECTRONICS

Proceedings of the 19th Southern African Universities Power Engineering Conference
SAUPEC 2010, University of the Witwatersrand, Johannesburg

DISTRIBUTED CONTROL OF DC-DC CONVERTERS USING AUTONOMOUS AGENTS

Janos Hamar*/**

*   Budapest University of Technology and Economics, Department of Automation and Applied Informatics
       H-1111 Budapest, Goldmann Gyorgy ter 3, Hungary, European Union,
       Phone: +36 1 463-1165, Fax: +36 1 463-3163, E-mail: hamar@elektro.get.bme.hu
**   MFKK Invention and Research Center Services Co. Ltd., Budapest, Hungary

Abstract   The number of the consumer electric devices requiring low-voltage dc supply is increasing in the households and offices (e.g. DVD players, digital cameras, printers, mobile phones, shavers, electrical toothbrushes etc). The lack of the rigorous standardization implies that the necessary supply voltage levels of these consumers considerably vary in the range of approx. 2-20VDC. The existing distribution systems use multiple conversions of electrical energy from the mains grid to the final load (through often low quality ac/dc adapters) resulting in severe losses, poor efficiency and unreliable operation. The current project aims at design and implementing multi-channel dc-dc converter systems, customizing the output voltage and current ratings according to the requirements of the consumer. Distributed, multi-agent techniques will be applied for the control of the dc-dc converters.

Key Words   Electric power conversion, dc-dc converter, multiagent control

1. INTRODUCTION

The scheme that is currently and widely used for residential electrical energy distribution is simple. Access to a 230VAC/50Hz grid (3-phase, 400VAC) is needed, switches, and additional safety components (fuses, etc.) and simple outlets facilitates the supply of the consumers with fixed voltage and frequency. No consideration is given to the kind of load that will be attached, very limited flexibility and possibility for optimisation or for increasing efficiency. In the past, this scheme was not problematic because electrical-energy was almost exclusively applied for lighting and rotating fixed-speed motors. Today most loads do not directly use 230VAC/50Hz but they need other (often low dc voltages) for their operation. However, due to the traditional inflexible architecture, all conversions must be solved at the separate loads - one by one. This is an expensive and inefficient way of supplying electrical-energy. Moreover, the integration of renewable energy sources is also not efficient. Normally, almost none of these sources can be directly attached to the main grid and numerous conversion steps are required (dc-to-ac or ac-to-dc-to-ac).

The current research focuses on future intelligent, low-power residential electrical distribution systems with multi-channel dc-dc converters as shown in Fig. 1. The one input/multiple output converters, investigated in this paper, are supplied from a dc line, while the output voltage of each converter channel is automatically determined by the intelligence in the load. The agent-based control determines which converters are turned on and turned off in order to ensure the optimized power transfer. The aim of the optimization here will be the minimization of the power losses in the conversion system.
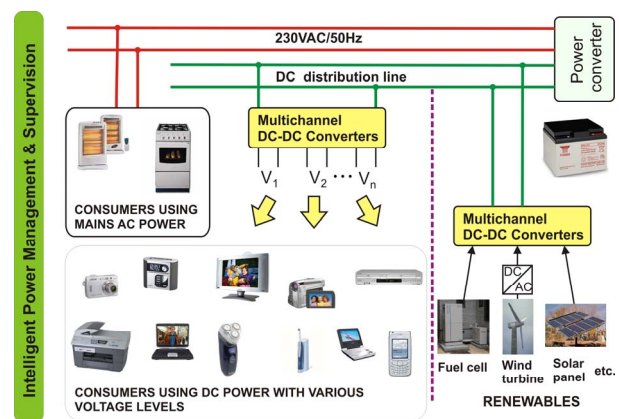
Fig. 1 Application of multichannel dc-dc converters in the local distribution

The converters facilitate the energy steering among the separate channels by running appropriate software control code.

2. TOPOLOGY

Digital control strategies, implemented in microcontrollers are considered at the switch-mode power converter units providing wide flexibility. The control scheme is presented for the buck (step-down) converter. The basic configuration of the proposed agent-based control is shown in Fig. 2a. The converters are assigned to control agents, while the output load is assigned to all consumer agents. The consumer agents have the same basic tasks: measuring the output voltage, and calculating the global current reference $I_{ref,total}$ by using the reference output voltage $V_{out,ref}$ and the measured output voltage V_{out}. A negotiation among the consumer agents is initiated after turning on the system, which results in the selection of the only active agent, while the other ones become passive, that is, they do not initiate any communication or make decisions, only accept the messages. During normal operation the same consumer agent will stay active until the next turn-on, however at

misoperation or failure the agents can redistribute this role among the working ones, increasing the failure-tolerance of the overall system. The implementation (Fig. 2b) facilitates the agent-based, fully distributed control of the parallel conversion units, focusing on the flexibly changeable structure, the quasi-optimal operation

and the increased error tolerance. In the proposed implementation the control agents are assigned to microcontrollers, while one consumer agent is also implemented in each microcontroller as shown in Fig. 2b.
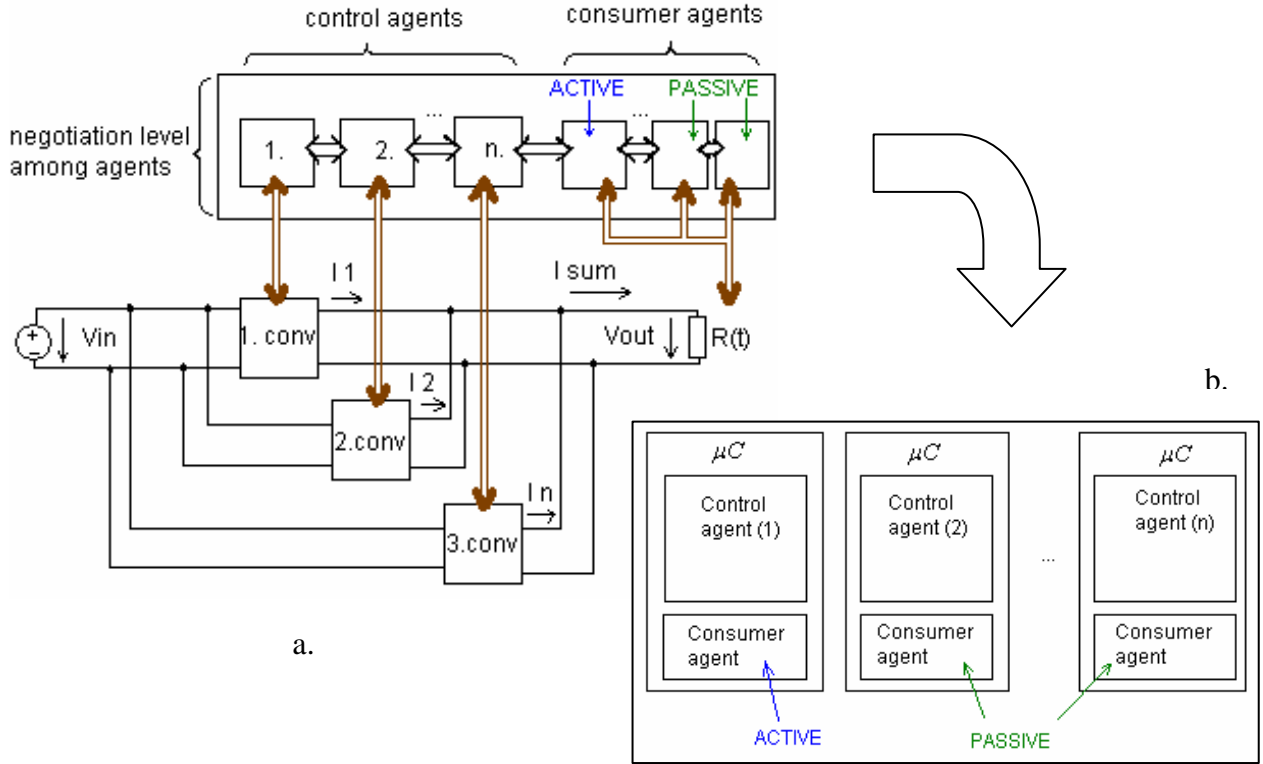
Fig. 2 Parallel conversion system with agent-based control (a), implementation of control and consumer agents (b)

Control agents have basically two important roles. First, every single agent makes its decision to optimally fulfill the overall control strategy. The control agent cares about the low-level control of the converter as shown in Fig. 3.

From the measured inductor current $I_{L,i}$, and the reference inductor current $I_{ref,i}$ the error amplifier and the PWM modulator produce the PWM signals to control the MOSFET switches. In contrast with Fig. 3 the practical implementation is an algorithm-based digital control. Second, the control agents negotiate with each other to optimally share the $I_{ref,total}$ current among the parallel converter units.

$$I_{ref,total} = I_{ref,1} + I_{ref,2} + ... + I_{ref,n} \qquad (1)$$

Where $I_{ref,i}$ is the reference current value of the i-th control agent, and n is the number of the control agents.

Its main advantage is that adding consumer agents requires only modification of the software running in the embedded microcontrollers, without further hardware-need, thus reducing the overall system costs. This kind of redundancy guarantees the fault tolerance if a microcontroller fails.

TOPIC A. POWER ELECTRONICS

Proceedings of the 19th Southern African Universities Power Engineering Conference
SAUPEC 2010, University of the Witwatersrand, Johannesburg
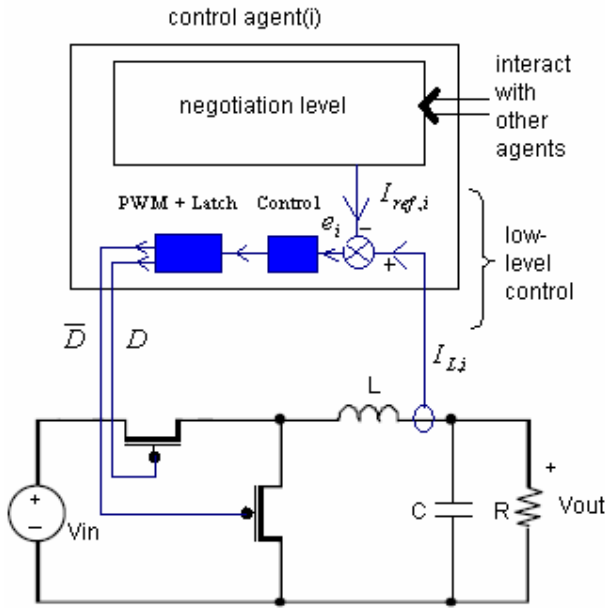
Fig. 3 A control agent and buck converter

3. CONTROL

In order to make the system operate smoothly, the following conditions and criteria are drawn up. The control strategy will be defined, taking into consideration these aspects:

1. All dc-dc converters work in Continuous Conduction Mode (CCM). This criterion gives a lower limit for the inductor currents:

$$I_{L,i} > \frac{DT_s}{2L}(V_{in} - V_{out}) = I_{L,\min} \tag{2}$$

where T_s is the PWM switching period, D is the duty ratio in steady-state and L is the inductance.
2. To avoid any damage in the semi-conductor switches (MOSFETs) an upper limit for the inductor currents is prescribed, $I_{L,i} < I_{L,\max}$
3. The power loss of each switching converter P_{loss} changes with the load current I_L. Power loss consists of two components: $P_{loss} = P_{switch} + P_{conduction}$. P_{switch} is the switching loss associated with the CMOS switching transition, and $P_{conduction}$ is the conduction loss from the CMOS on-resistance. The efficiency comes from this equation:

$$\eta = \frac{P_{out}}{P_{in}} = \frac{P_{out}}{P_{out} + P_{loss}} \tag{3}$$

The typical efficiency curves have a peak belonging to a certain current. Any alteration in the current value results in decreased converter efficiency. On the basis of the efficiency curves, every single converter has an optimal load current $I_{L,OPT}$, where η efficiency is maximal. From eq. (3):

$$\frac{P_{loss}}{P_{out}} = \frac{1}{\eta} - 1 \tag{4}$$

According to the efficiency curve, this equation has a minimum at $I_{L,OPT}$. When the converter is turned off, its power loss is nearly zero. A cost function, penalizing the power losses, is allocated to every single converter:

$$\mu(I_{L,i}) = \begin{cases} \dfrac{1}{\eta(I_{L,i})} - 1 \leftarrow if : I_{L,i} \neq 0 \\ 0 \leftarrow if : I_{L,i} = 0 \end{cases} \tag{5}$$

To define optimization strategies a cost function was created, which is minimized by the control agents. To demonstrate the viability of the control scheme the following simple function was selected:

$$f_{cost} = \min_{i_{L,1}...i_{L,n}} [W_1 * \sum_{i=1}^{n} \mu(I_{L,i})] \tag{6}$$

Control agents share their currents to minimize this cost function, while the following conditions are satisfied:

1. $I_{L,\min} < I_{L,i} < I_{L,\max}$ for all turned-on converters,
2. $I_{ref,total} = I_{ref,1} + I_{ref,2} + ... + I_{ref,n}$

The overall system has to provide the required output voltage in conjunction with the reference value. The composition of the individual reference currents is carried out in full agreement with the cost function minimization, keeping the requirements for the min and max currents.
n is the number of all paralleled converters, and m is the number of turned-on parallel converters. It must be noted here that many other cost functions can also be defined, e.g. aiming the maximization of the transmitted power, minimizing the voltage-ripples etc.

To decrease the system costs identical dc-dc converters are used, implying that the efficiency curves of the converters are also the same. To minimize the cost function, a possible solution for load current distribution can be that *m-1* dc-dc converters are operated in their optimal point (with maximum efficiency), while the mth converter provides the remaining current to exhibit $I_{sum} = (m\text{-}1)I_{opt} + I_m$ the total current required by the consumer. The research results pointed out that below a certain number of active paralleled converters $m_{threshold}$, using another approach can be more advantageous from the viewpoint of power losses. In this case the load current is distributed equally for all turned-on converters by the control agents to minimize the cost function. From now on this approach is discussed in details.

Each of the control agents decide about turning on or turning off their respective converter. At any load current value, an optimal number of turned-on

converters always exist, where the value of the cost function is minimal. Increasing or decreasing the number of the turned-on converters, that is, diverging from the optimal number, the cost function is monotonically increasing (Fig. 4).
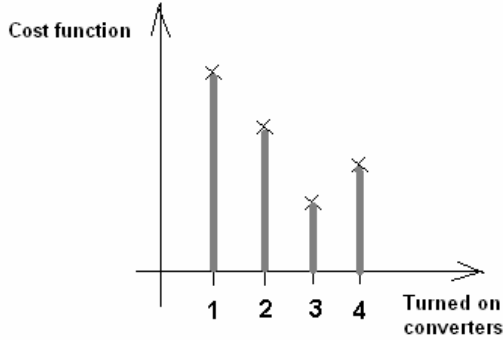
Fig. 4 Cost function values for different number of turned on converters

Let us assume that m is the number of the turned-on converters in a certain moment of the operation, and n is the number of all paralleled converters. The process to find the optimal number of turned on converters is presented in Fig. 5. This method guarantees that the control agents find the minimum of the cost function for every value of the load current. When more than one converter should be turned on or off due to a sudden significant change of the load current, the control agents can perform it in more consecutive steps. It means that the transients will appear consecutively in the load currents, and in the output voltage.
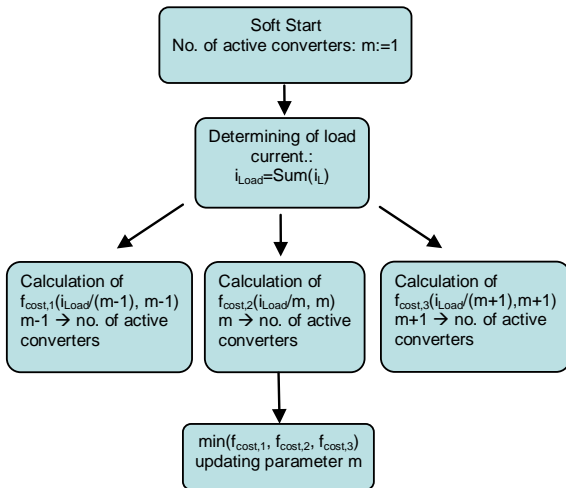
Fig. 5 Process leading to determine the optimal converter number

4. SIMULATION RESULTS

Four paralleled step-down converters were simulated by using Matlab/Simulink program package. The block diagram of the simulation can be seen in Fig. 6. The converters have the following parameters: $L = 39\,\mu H$, $C = 680\,\mu F$, $r_C = 20\,m\Omega$, $f_S = 400\,kHz$, where r_C is the series resistance of the capacitance, and f_s is the switching frequency. The input voltage $V_{IN} = 9V$, and the reference output voltage $V_{out,ref} = 5V$. The load resistance is decreased in a linear fashion.

During the simulation process, from V_{out} and $V_{out,ref}$ a PI (proportional–integral) control algorithm is calculated by the active consumer agent to obtain $I_{ref,total}$. Furthermore simple P (proportional) control algorithms are applied for the subordinated current control by each of the control agents.

The aim of the optimization here was the minimization of the power losses in the parallel converters. $W_I = 1$ was selected. The load resistance R_{Load} was changed according to the time function shown in Fig. 7. Its value is continuously decreasing in the range of 10-25msec from 5Ω to 1.25Ω. Initially the load current is 1A, only one converter is turned on. In order to maintain 5V at the output, the control has to increase the output current from 1A to 4A. It means that even if originally only one converter operates (with optimal current of 1A), but approaching to the end of the sequence while the load resistance is increasing, all the four converters must be turned on to facilitate the optimal power transfer.
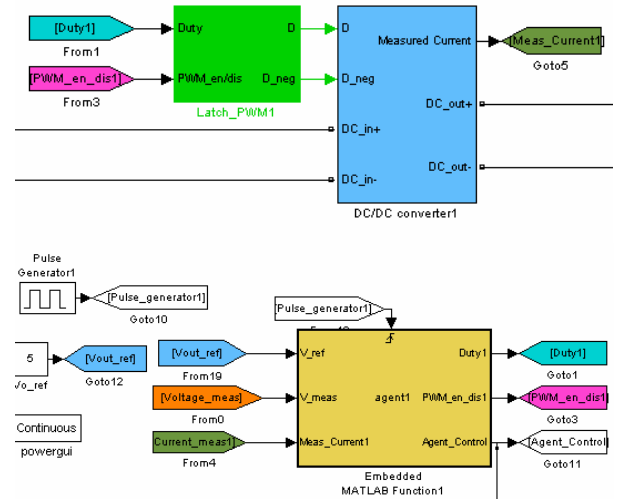
Fig. 6 Simulation block diagrams. Block of one dc-dc converter with the PWM generator (a), control agent (b)

TOPIC A. POWER ELECTRONICS

Proceedings of the 19th Southern African Universities Power Engineering Conference
SAUPEC 2010, University of the Witwatersrand, Johannesburg
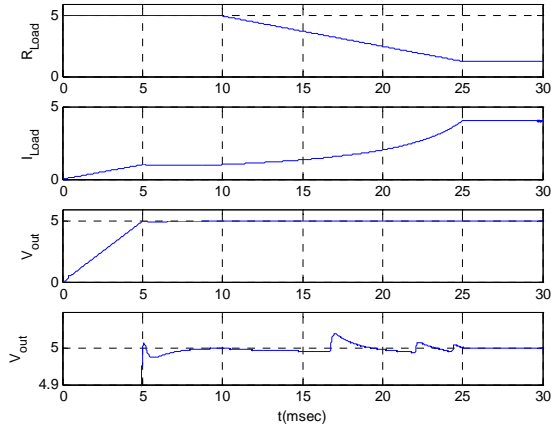
Fig. 7 Simulation results. $R_{Load}[\Omega]$: load resistance; $I_{Load}[A]$: measured load current; $V_{out}[V]$: measured output voltage

V_{out} indicates the output voltage in Fig. 7. The output voltage swings point out the effects of turning on of new converters. This value never exceeds 1% in the simulation. It is notable that the higher the number of the turned on converters, the smaller the disturbance in the control and in the output voltage. Its reason is that the ratio between the total current of the already turned on converters and the current provided by the additional converter is getting smaller by increasing the number of the converters. Fig. 8 shows the load currents of the converters. It is also true here, that by adding a new converter in the supply chain the effect of the current transients will be smaller as the total number of active parallel converters is increasing.
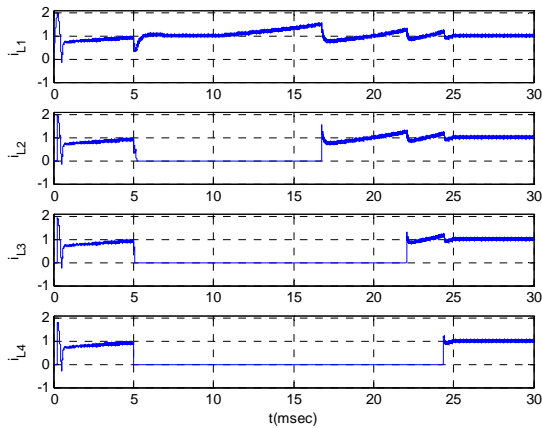
Fig. 8 Simulation results for power loss minimization strategy: Inductor currents of the converters

5. LABORATORY MEASUREMENT

For the laboratory measurements dsPICDEM™ SMPS Buck Development Board was used. A dsPIC30F2020 DSC controls two independent DC/DC synchronous buck converters, providing

closed-loop Proportional, Integral, Derivative (PID) control in software to maintain desired output voltage levels. The dsPIC DSC device provides the necessary memory and peripherals for A/D conversion, PWM generation and general purpose I/O, precluding the need to perform these functions in external circuitry. The used development board facilitates the agent-based control and investigation of parallel dc-dc converter units. In the laboratory measurement, two converters have been paralleled. The parameters of the converters are the same as the simulated ones. The PI voltage control algorithm and the inner P current control algorithms are also implemented with the same parameters. The paralleled converters are controlled by a microcontroller. The load resistance at the converters' output is 11Ω, constant. Another 5Ω load is attached to the output through a MOSFET that is controllable by the microcontroller too. Turning on this auxiliary MOSFET, that additional load resistance is connected in paralleled to the fixed one with 1sec time period. This measurement represents the sudden and periodical change of the load. The cost function is created so that the control agent turns off the 2nd converter when the load resistance is suddenly increased, and turns on the 2nd converter when the load resistance is suddenly decreased. During the laboratory measurement the 1st converter is always turned on.

The measured results are explained as follows. Fig. 9a shows the inductor currents of the converters. The current of the 1st converter is highlighted with yellow color, the 2nd one is highlighted with green. The sudden increase of load resistance $3.4375\Omega \rightarrow 11\Omega$ is indicated with the left side perpendicular dashed line. As depicted in the figure, both of the load currents are decreased in the same manner. The right side perpendicular dashed line shows the place where the 2nd converter is turned off. The time interval between the two dashed lines is 10.28msec. This dead time comes from microcontroller finite signal processing capacity, and the inner timing intervals. Fig. 9b shows the measured output voltage. The output voltage change caused by the sudden load change and the effect of the 2nd converter's turn off are completely separated in the figure. The first transient is caused by the sudden load change. Its overshoot is 320mV. Its settling time is 4msec.

The second transient is caused by the turn off of the 2nd converter. Its overshoot is 75mV. Its settling time is 3.44 msec. Fig. 9c shows when the load resistance decreases step-wise $11\Omega \rightarrow 3.4375\Omega$. The initially turned-off converter is now turning on and the output current is provided by the two working converters. The initial oscillations, which are in opposite phases in the two converters are damped quickly (271µsec).

Proceedings of the 19th Southern African Universities Power Engineering Conference
SAUPEC 2010, University of the Witwatersrand, Johannesburg

TOPIC A. POWER ELECTRONICS

Fig. 9 Measured results at sudden decrease of load current:
Inductor currents of the converters (a, c), Output voltage (b)

converters, while keeping power losses of the overall paralleled system at minimum. Simulation and experimental results confirmed the viability of the system.

ACKNOWLEDGEMENTS

REFERENCES

[1]   J. Hamar, I. Nagy, "Control Features of Dual Channel DC-DC Converters", IEEE Transactions on Industrial Electronics, 2002, pp.1293-1305.
[2]   Michael Wooldridge, "An Introduction to MultiAgent Systems", John Wiley & Sons; 1st edition, 2002, ISBN-10: 047149691X, ISBN-13: 978-0471496915
[3]   Fabio Luigi Bellifemine, Giovanni Caire, Dominic Greenwood, "Developing Multi-Agent Systems with JADE", Wiley, 2007, ISBN-10:0470057475, ISBN-13:978-0470057476
[4]   Stefan Huth "DC/DC Converters in Parallel Operation with Digital Load Distribution Control " Industrial Electronics, 1996. ISIE apos;96., Proceedings of the IEEE International Symposium on Volume 2, Issue , 17-20 Jun 1996 Page(s):808 - 813 vol.2
[5]   Matthew Reynolds "Calculation Losses and Junction Temperature for High-Power-Density Switching Converters" National Semiconductor: Power Designer No. 120.
[6]   V. Oleschuk, F. Blaabjerg, "Novel Simplifying Approach for Analysis and Synthesis of Space Vector PWM Algorithms", EPE'2003, Toulouse, France, 2003, ISBN: 90-75815-07-7.
[7]   Funato, H.; Kawamura, A.; Kamiyama, K., "Realization of negative inductance using variable active-passive reactance (VAPAR)", IEEE Transactions on Power Electronics, Volume 12, Issue 4, Jul 1997 pp. 589 – 596, Digital Object Identifier 10.1109/63.602553.
[8]   Y. Nishida, "A New Buck-And-Boost DC-DC Converter (Tokusada Converter)", EPE'2003, Toulouse, France, 2003.
[9]   K. Rigbers, S. Schroder, T. Durbaum, M. Wendt, R. W. De Doncker, "Integrated Method for Optimization of Power Electronic Circuits", 35th Annual IEEE Power Electronics Specialists Conference, PESC'2004, Aachen, Germany, June 20-25, 2004, pp. 4473-4478.
[10]   S. Iyasu, T. Shimizu, K. Ishii, "A Novel Iron Loss Calculation Method on Power Converters Based on Dynamic Minor Loop", International Conference EPE'2005, Dresden, Germany, September 11-14, 2005, ISBN: 90-75815-08-5 pp. P1-P10.
[11]   L. Benadero, R. Giral, A. El Aroudi and J. Calvente, "Stability Analysis of Single Inductor Dual Switching Dc-Dc Converter", 8th Int. Conference on Modeling and Simulation of Electric Machines, Converters and Systems (ELECTRIMACS'05), (Hammamet, Tunisia), Apr. 17-20, 2005. CD Rom ISBN:2-921145-51-0.
[12]   O Dranga, I Nagy, "Stability analysis of feedback controlled resonant DC-DC converter using Poincare map function", IEEE International Symposium on Industrial Electronics, 2001, ISIE 2001, Volume 3, 12-16 June 2001, pp. 2142 – 2147, Digital Object Identifier 10.1109/ISIE.2001.932048
[13]   Spartacus Gomaríz, Eduard Alarcón, Francisco Guinjoan, Enric Vidal-Idiarte, Luis Martinez-Salamero, Domingo Biel, "TSK-fuzzy controller design for a PWM boost DC-DC switching regulator operating at different steady state output voltages" ISCAS (5) 2004: 848-851

6.   CONCLUSION

Agent-based distributed control of parallel dc-dc converters was presented. Identical dc-dc converter units were applied in order to keep the system costs low, i.e. the large-scale production of the same converter units is possible. The converters were equipped with local intelligence. The control and consumer agents were implemented in microcontrollers. The control agents took care of the distribution of the load currents among the

Proceedings of the 19th Southern African Universities Power Engineering Conference
SAUPEC 2010, University of the Witwatersrand, Johannesburg
TOPIC A. POWER ELECTRONICS

DESIGN OF AN ISOLATED RESONANT SWITCH-MODE POWER-SUPPLY FOR A MODULAR SOLID STATE TRANSFORMER

P.S. Kemp, H. du T. Mouton, J.W. van der Merwe

Department of Electrical and Electronic Engineering, Stellenbosch University, Private Bag X1, Matieland, 7602, South Africa

Abstract. This paper documents the development of an isolated power supply to provide power to the control circuits of a modular series-input-parallel-output (SIPO) cell as used in a solid-state transformer (SST). A solution is suggested, analysed and its feasibility is verified through practical implementation. The primary focus of the paper is the so-called "series-string" multiple core isolation transformer, as this is the most critical – and most unconventional – aspect of the design.

Key Words. Resonant Conversion, Solid-State Transformer, Series-Input-Parallel-Output, Series-String Transformer, Multiple Core Transformer

1. INTRODUCTION

Recently, the development of a modular cascaded series-input-parallel-output (SIPO) solid-state transformer (SST) has been the subject of intensive research and development [1]–[3]. One of the design challenges is to provide power to the control circuits of every SST module, or cell.

Fig. 1 shows one phase of a modular cascaded SIPO SST. Every cell consists of two back-to-back converters, the first being a controlled rectifier and the second a DC to HF-AC inverter. The cells are connected in series to handle the high input voltage, which divides equally between the cells [1]. This series connection necessarily implies that all cells are at a different voltage potential relative to one another. The control circuitry of every cell therefore requires an isolated power supply. The number of series connected cells depends on the input voltage and the voltage handling capability of the power semiconductor devices used in each cell, but will typically be more than 10 for distribution voltage levels [4].
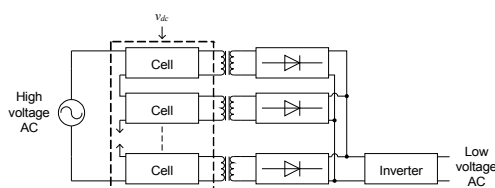
Fig. 1: One phase of a modular SIPO SST.

Fig. 2 illustrates the main components of a complete

power supply solution to power *n* cells per phase. The supply will source power from a 110 V voltage transformer, followed by a rectifier and filter, and a buck converter. The buck converter provides a bus voltage for three full-bridge resonant converters, connected in parallel. The supply voltage to every cell's control circuitry need not be regulated, as every cell will have on-board step-down regulators, and therefore it was decided to operate the resonant converters open-loop. However, a degree of control is still necessary to ensure reliable cell operation. The output of the buck converter will be controlled, thereby indirectly controlling all supply outputs to the cells. Control of the buck converter will be very slow, and its output voltage will only be adjusted if the output of the supplies exits a predefined tolerance band. The power supply should preferably be modular in order to ensure easy integration into the modular SST. Note that the scope of this paper does not cover the design of the input rectifier, filter and buck converter, as this is fairly straightforward to implement.

The supply needs to deliver a relatively high level of power to the cells. For example, if every cell requires 24 W under full load conditions, and 15 cells are to be powered, each phase will require $P_{perphase} = 24 \times 15 = 360$ W. For this reason it was decided to use a full-bridge switch topology for the resonant converters.

The most critical part of the design is the high frequency isolation transformer driven by the full-bridge

Fig. 2: Power supply implementation.
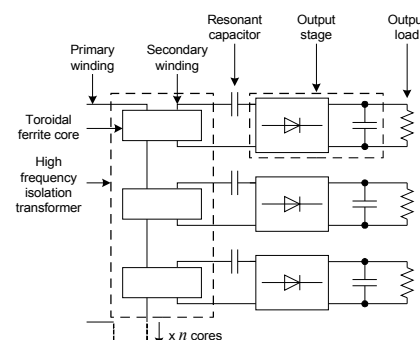
Fig. 3: Proposed high frequency isolation transformer and output stage.

Proceedings of the 19th Southern African Universities Power Engineering Conference
SAUPEC 2010, University of the Witwatersrand, Johannesburg

TOPIC A. POWER ELECTRONICS

switch network. See Fig. 3 for a proposed solution. The proposed transformer consists of a string of n cores, with a shared primary winding (of only one "turn") and separate secondary windings of multiple turns. Every secondary winding feeds into a series resonant capacitor and an output stage consisting of a full-wave rectifier and filter capacitor. This topology enables the implementation of a modular approach, whereby the number of supply outputs can be modified by simply adding or removing a core and output stage. A drawback of this transformer is that the primary winding will act as an antenna and cause severe EMI. It was therefore decided to implement resonant conversion, which will reduce the harmonic content of the current waveform in the primary winding.

2. INTRODUCTION TO THE SINUSOIDAL ANALYSIS OF RESONANT CONVERTERS

It has been shown that, using a fundamental approximation method, the equivalent circuit of a resonant converter can be modelled by the circuit in Fig. 4 [5].
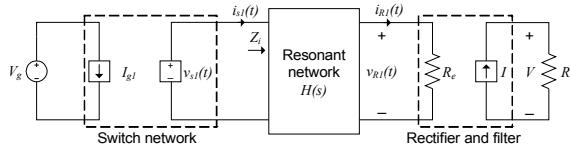
Fig. 4: Equivalent circuit of a resonant converter. (Source: [5])

The variables in Fig. 4 are given by:

$$I_{g1} = \frac{2I_{s1}}{\pi} \cos(\varphi_s) \quad (1)$$

$$v_{s1}(t) = \frac{4V_g}{\pi} \sin(\omega_s t) \quad (2)$$

$$i_{s1}(t) = I_{s1} \sin(\omega_s t - \varphi_s) \quad (3)$$

$$i_{R1}(t) = I_{R1} \sin(\omega_s t - \varphi_R) \quad (4)$$

$$v_{R1}(t) = V_{R1} \sin(\omega_s t - \varphi_R) \quad (5)$$

$$R_e = \frac{8}{\pi^2} R \quad (6)$$

$$I = \frac{2}{\pi} I_{R1} \quad (7)$$

$$V = \frac{\pi}{4} V_{R1} \quad (8)$$

In (3), I_{s1} and φ_s are the peak amplitude and phase of $i_{s1}(t)$, and similar for (4) and (5). The input DC bus voltage is denoted by V_g, and the output DC voltage and DC current are denoted by V and I, respectively.

The converter's voltage conversion ratio is given by

$$M = \frac{V}{V_g} = \|H(s)\|_{s=j\omega_s}. \quad (9)$$

With reference to Fig. 4, the switch network generates a square wave $v_s(t)$, with fundamental component $v_{s1}(t)$, that feeds a resonant tank network with transfer function $H(s)$. The tank network is followed by a full-wave rectifier and low-pass filter, which is followed by a DC load R. The output rectifier, filter and load can be represented by an equivalent resistance R_e. Because of the resonant tank, the output voltage is a function of both switching frequency f_s and resonant frequency f_0.

Several assumptions were made in the derivation of the equivalent model and these should be noted. It is assumed that the output of the switching network, and the input to the resonant tank, is a square wave with frequency f_s close to the resonant frequency f_0 of the tank network. It is also assumed that the frequency response of the resonant tank is of such a nature that harmonics of f_s are sufficiently attenuated. Furthermore, it is assumed that the cut-off frequency of the output low-pass filter is significantly lower than the switching frequency. Also, all components are assumed to be ideal. It is important to note that the approximation will only be accurate if the tank network has a high-Q resonance near f_s, and sufficient high frequency roll-off. However, in practice this is easily achievable.

3. EQUIVALENT CIRCUIT MODEL OF THE SERIES-STRING TRANSFORMER

It can be shown that the equivalent model of the multiple core transformer presented in Fig. 3, for n cores, is given by the circuit of Fig. 5 [6], if the following assumptions are made:

1) The cores identical and ideal.
2) Stray capacitances are negligible.
3) Winding resistances are negligible.
4) All secondary windings are identical, with N turns.
5) The primary winding only has one "turn".
6) All output loads are the same.

The variables in Fig. 5 are defined in Table 1.
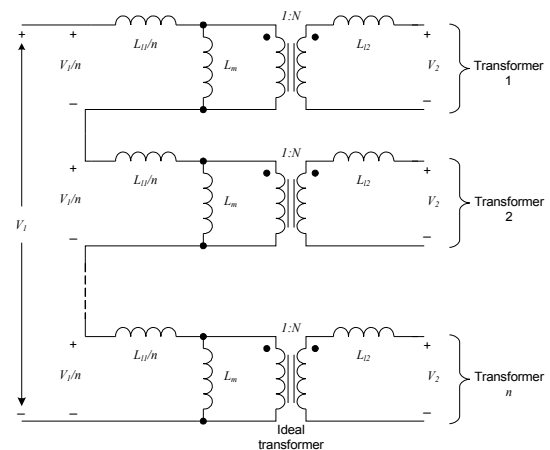
Fig. 5: A simplified equivalent model of a series-string transformer.

TOPIC A. POWER ELECTRONICS

Proceedings of the 19th Southern African Universities Power Engineering Conference
SAUPEC 2010, University of the Witwatersrand, Johannesburg

Table 1: Description of variables in Fig. 3.

Quantity	Description
V_1	Primary voltage
V_2	Secondary voltage, per core
N	Number of secondary winding turns
n	Number of transformer cores
L_{l1}	Total primary leakage inductance
L_{l2A}	Secondary leakage inductance, per core
L_m	Magnetising inductance, per core

Inspection of Fig. 5 shows that the series-string transformer is modelled as n conventional transformers, with their primary windings connected in series. When the output loads of all n transformers are the same, these individual transformers will be completely independent, each with a primary voltage of V_1/n and secondary voltage of V_2. This natural balancing is due to the inherent symmetry of the equivalent model and, of course, only holds true while symmetry is maintained. If different loads are connected to each output, symmetry will be lost and the above argument will not hold. However, for the rest of the paper symmetrical conditions will be assumed, unless stated otherwise. This assumption is based on the fact that all SST cells will be similar, and will hence present a similar load to the power supply. This greatly simplifies the design, because now only one core needs to be considered during most of the design.

It is interesting to note that the effective primary leakage inductance of the individual transformers decreases as n increases. Hence the transformers will become more ideal when more cores are added.

4. ANALYSIS OF THE RESONANT TANK

Normally, resonant conversion is primarily implemented to reduce switching losses in the switch network by means of zero-current- and/or zero-voltage switching. However, in this case the primary reason for resonant conversion is to reduce EMI generated by the transformer. Detailed switching characteristics are therefore not discussed in this paper.

The resonant tank network is created by adding a capacitive element to the inductances of the transformer. There are various resonant tank topologies, each with different characteristics. The most common tank networks are the series tank network, the parallel tank network and the LCC tank network [5], shown in Fig. 6.

It was decided to not implement a LCC tank network, as this network requires two capacitors and, where possible, component count should be minimised. Note that only a single inductance is shown in the circuits of Fig. 6. This is appropriate, because it will later be shown that the inductances of the transformer can be accurately approximated by a single inductance.

In order to decide on an appropriate tank topology, the series and parallel tank networks' transfer functions
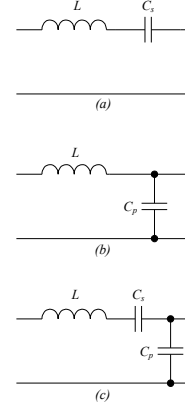
Fig. 6: Most common tank networks: (a) series, (b) parallel, (c) LCC. (Source: [5])

were calculated and the frequency response of both were investigated. For the purposes of the analysis, a damping resistance was added as load, based on the fact that the tank network's output load can be represented by an equivalent resistance R_e, as was shown in Section 2.

The circuits that were analysed are shown in Fig. 7. Table 2 summarises some results of the analysis. The voltage transfer function of the specific circuit is denoted by $H(s)$, while ω_0 and Q refers to its resonant frequency and quality factor, respectively.
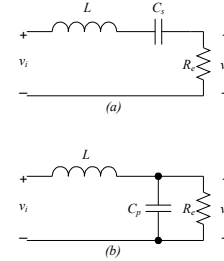
Fig. 7: Tank networks for analysis: (a) series damped, (b) parallel damped.

Table 2: Results of frequency analysis.

Parameter	Series Resonant	Parallel Resonant
$H(s)$	$\dfrac{s\frac{\omega_0}{Q}}{s^2+s\frac{\omega_0}{Q}+\omega_0^2}$	$\dfrac{\omega_0^2}{s^2+s\frac{\omega_0}{Q}+\omega_0^2}$
ω_0	$\dfrac{1}{\sqrt{LC_s}}$	$\dfrac{1}{C_p\sqrt{R_eL}}$
Q	$\dfrac{L}{R_e}\omega_0$	$\sqrt{\dfrac{R_e}{L}}$
HF roll-off	20 dB/decade	40 dB/decade

Inspection of Table 2 shows that the resonant frequency of the series resonant tank is independent of the equivalent load resistance R_e, which is a desirable result. Also, the Q of the series resonant tank increases as R_e decreases. This means that the sinusoidal approximation will be more accurate under heavy loading, which is desirable from a EMI perspective.

The frequency response of both transfer functions are

Proceedings of the 19th Southern African Universities Power Engineering Conference
SAUPEC 2010, University of the Witwatersrand, Johannesburg

TOPIC A. POWER ELECTRONICS

shown in Fig. 8 for different values of R_e. Values in Fig. 8 are normalised to unity, in other words $L = C_s = C_p$. In Fig 8 (a) $R_e = 1$. Note that the parallel resonant network has a high frequency roll-off of 40 dB/decade, while the series network only has a roll-off of 20 dB/decade. This is because the transfer function of the series resonant network contains a zero, as opposed to the parallel resonant network which does not contain any zeros. Fig. 8 (b) shows the effect on the frequency response when reducing the load resistance from $R_e = 1$ to $R_e = 0.1$. The Q of the series resonant network has increased tenfold, while the resonant frequency remains unchanged. In contrast, the Q of the parallel resonant network has decreased by about three times, and the resonant frequency shifted higher. In Fig. 8 (c) the load resistance is increased to $R_e = 10$ and, as expected, the results are the opposite of the case $R_e = 0.1$. This is in accordance with the information in Table 2. Also note that the gain at resonance remained unchanged for the series resonant network.

Although the parallel resonant tank has a steeper high frequency roll-off than the series tank, it was decided to implement a series tank network. This decision is based on the fact that the resonant frequency of the series resonant network is load independent and its Q increases with an increase in load, while the converse applies to the parallel network.
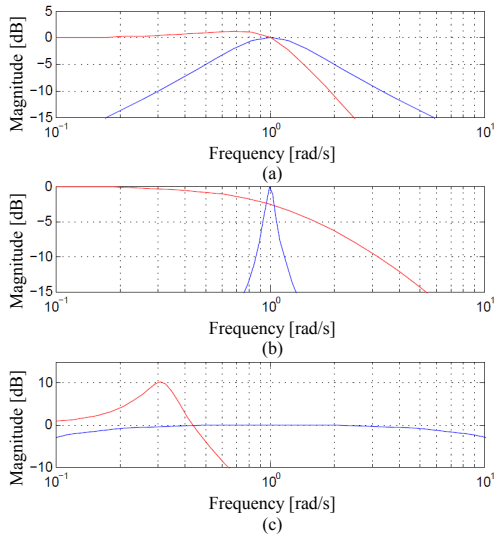
Fig. 8: Frequency response of series (blue) and parallel (red) resonant tanks for (a) $R_e = 1$, (b) $R_e = 0.1$ and (c) $R_e = 10$.

5. ANALYSIS OF THE SERIES-STRING TRANSFORMER WITH SERIES RESONANT CAPACITANCE

As stated earlier, only one individual transformer needs to be considered during most of the design. Fig. 9 shows the equivalent model of one individual transformer. The series resonant capacitor and equivalent load resistance, as explained in Section 2, are also shown. Note that all values are referred to the primary of the transformer.

Currents and voltages are approximated by their respective fundamental frequencies, and are indicated as in [5], with $v_{s1}(t)$ being the fundamental component of $v_s(t)$, $i_{s1}(t)$ the fundamental component of $i_s(t)$, etc.
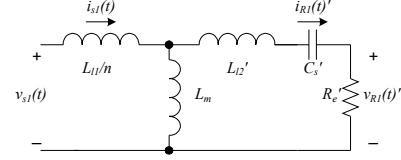
Fig. 9: Equivalent model of individual transformer and resonant capacitor, with load.

The transfer function $H(s)$ of the circuit in Fig. 9 can be approximated by

$$H(s) = \frac{V_{R1}(s)}{V_{s1}(s)} \qquad (10)$$

$$= N \frac{V_{R1}(s)'}{V_{s1}(s)} \qquad (11)$$

$$\approx N \frac{L_m}{L_{l1}/n + L_m} \left(\frac{s \frac{R_e'}{L_e}}{s^2 + s \frac{R_e'}{L_e} + \frac{1}{L_e C_s'}} \right), \qquad (12)$$

where

$$L_e = (L_{l1}/n) \parallel L_m + L_{l2}'. \qquad (13)$$

The transfer function of (12) is of the same form as the transfer function of the series resonant circuit as given in Table 2, with the only difference being a scaling factor. This suggests that the inductances of the transformer can be modelled as a single series inductance L_e and a voltage scaling factor. The transfer function of (12) can be expressed in terms of the quality factor Q and resonant frequency ω_0 as

$$H(s) = A \frac{s \frac{\omega_0}{Q}}{s^2 + s \frac{\omega_0}{Q} + \omega_0^2}, \qquad (14)$$

where:

$$Q = \frac{L_e}{R_e'} \omega_0 \qquad (15)$$

$$\omega_0 = \frac{1}{\sqrt{L_e C_s'}} \qquad (16)$$

$$A = N \frac{L_m}{L_{l1}/n + L_m} \qquad (17)$$

Note that A is the voltage gain of the resonant network at the resonant frequency. If V_o is the DC output voltage of each output stage and V_g is the converter's DC input bus voltage, the voltage conversion ratio M of the converter is given by [5] [6]

$$M = \frac{nV_o}{V_g} = \left\| H(s) \right\|_{s=j\omega_s}. \qquad (18)$$

TOPIC A. POWER ELECTRONICS

Proceedings of the 19th Southern African Universities Power Engineering Conference
SAUPEC 2010, University of the Witwatersrand, Johannesburg

Using Equation (14) and Equation (18), it can be shown that:

$$M = A \frac{\omega_s \frac{R'_e}{L_e}}{\sqrt{\left(\frac{1}{L_e C'_s} - \omega_s^2\right)^2 + \left(\omega_s \frac{R'_e}{L_e}\right)^2}} \qquad (19)$$

An important consideration in the design of a cored transformer is the core flux density. It can be shown that the peak magnetic core flux density in a transformer with a single primary winding turn, due to a sinusoidal primary voltage, is given by

$$B_{max} = \frac{V_m}{\pi f_s A_e}, \qquad (20)$$

where V_m is the peak value of the sinusoidal voltage across the magnetising inductance L_m, f_s is the frequency of the sinusoidal voltage, and A_e is the effective area of the core.

6. PRACTICAL IMPLEMENTATION

A converter was designed, simulated and built based on the preceding theory. The design methodology will be briefly outlined.

The series-string transformer's design contains a great many free parameters, and conventional optimisation techniques cannot be used. Therefore it was decided to choose an operating point, analyse the circuit at this operating point, and determine the feasibility of the chosen operating point.

Before the actual design commenced, a single core version of the transformer was wound and measured to obtain an idea of the magnitudes of the inductances involved. An Epcos N87 R25 toroidal core was chosen. The details of the transformer, and its measured parameters, is summarised in Table 3 [7]. Transformer parameters were measured by conducting a standard open-circuit and short-circuit test at 100 kHz [8].

It should be noted that this kind of test will not deliver accurate results, because the unconventional transformer topology employed is highly non-ideal. The primary winding of the transformer is very loosely coupled, and this will reduce the accuracy of the measured parameters. However, the purpose of the measurement was only to obtain a rough estimate of the transformer's parameters.

The parameters in Table 3 confirms the loosely coupled nature of the transformer, with the magnetising inductance being only about four times greater than the leakage inductance.

If a resonant frequency is chosen and the transformer inductances are known, the required capacitor value can be calculated using Equation 16. However, practically it is not so simple. The total transformer leakage inductance, which has a significant influence on the resonant frequency, is highly dependent on the area

Table 3: Parameters of single core transformer.

Parameter	Description	Value
N	Secondary winding turns	10
L_{l1}	Primary leakage inductance	643 nH
L'_{l2}	Secondary leakage inductance, referred to primary	643 nH
L_m	Magnetising inductance	2.737 μH
A_e	Effective core area	51.26×10^{-6} m^2
V_e	Core volume	3079×10^{-9} m^3
B_{sat}	Saturation flux density	390 mT
T_C	Curie temperature	210 °C

of the loop formed by the primary winding, which will vary as more cores are added. This makes it difficult to calculate the required capacitance value if more than one core is used. It was thus decided to determine the required capacitance experimentally. The resonant frequency can then be fine-tuned by manipulating the primary winding loop area or adding additional leakage inductance. However, one should keep in mind that, according to (17), a higher leakage inductance will result in a lower voltage conversion ratio.

Inspection of Fig. 8 (a) reveals that, if the converter is operated below resonance, harmonics of the switching frequency will be rejected less than when operating above resonance. It was therefore decided to operate the converter above resonance, ie. $f_s > f_0$. Operation above resonance also means that the switches used in the switch network will turn on at a zero current [9], improving overall converter efficiency.

Electrical insulation between the transformer's primary and secondary windings was provided by a PTFE (Teflon) mechanism that theoretically provides 69 kV of insulation. Providing power to an 11 kV SST means that at least $11 \times \sqrt{2} = 15.6$ kV of insulation is neccesary. Fig. 10 shows one transformer core, with windings and insulation.
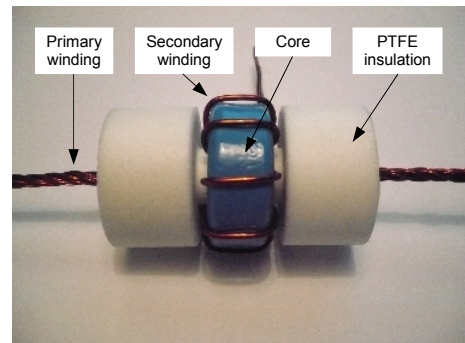
Fig. 10:   A single isolation transformer core, with windings and insulation.

7. MEASUREMENTS AND RESULTS

A converter with seven isolated output stages, and seven transformer cores, was built. Table 4 lists some of the converter's parameters.

Proceedings of the 19th Southern African Universities Power Engineering Conference
SAUPEC 2010, University of the Witwatersrand, Johannesburg

TOPIC A. POWER ELECTRONICS

Table 4: Parameters of resonant converter.

Parameter	Description	Value
n	Number of cores and outputs	7
N	Secondary winding turns per core	8
f_0	Resonant frequency	107.5 kHz
f_s	Switching frequency	120 kHz
V_g	Required input bus voltage at full load (measured)	24.5 V
V_o	Nominal output voltage, per output	24 V
I_i	Average input current at full load (measured)	8.065 A
I_o	Nominal full-load output current, per output	1 A
C_s	Resonant capacitor	220 nF
η	Efficiency at full load (measured)	85.6 %
% reg	Percentage load regulation	6.47 %

Fig. 12: Converter efficiency versus frequency versus output power.

Fig. 11 shows the current through the resonant capacitor when the converter is operating at resonance. The effect of resonant conversion is clearly visible in the approximately sinusoidal waveform. Note that Fig. 11 is also the transformer's secondary current. The primary current waveform is similar in shape, but larger in magnitude, than the current waveform of Fig. 11.

Fig. 11: Resonant capacitor current at resonance.

The converter's efficiency was measured at different values of frequency and output power. Fig. 12 shows a plot of this data. Note that the output power indicated in the graph refers to the output power per output (thus the total power output is seven times this value, for seven outputs). The efficiency rapidly decreases at lower frequencies. This is because of an increase in the magnetic flux density as frequency decreases. This causes greater hysteresis losses in the cores. At very light loads, the efficiency also falls rapidly. This is due to the relationship between the switching losses and the conduction losses in the converter, as a function of output current. This also explains the decrease in efficiency under heavy load conditions.

Based on Fig. 12, the switching frequency of the converter was chosen as $f_s = 120$ kHz. This gives an efficiency of 85.6 % under full load. Load regulation at the chosen operating point is 6.47 %, which is good considering the fact that the converter is operated in open-loop.

The converter that was built and tested is entirely feasible and can easily be expanded to provide more than 10 outputs.

8. CONCLUSION

In this paper the development of a power supply to provide power to the control circuitry of a SST was discussed. An unconventional resonant series-string transformer was analysed and theory was presented to provide insight into the operation of this transformer. A converter was designed, built and tested based on the underlying theory.

The converter performed remarkably well considering the loosely coupled nature of the transformer, and provides a feasible solution to the modular cascaded ISOP SST's power requirements.

REFERENCES

[1] W. van der Merwe and T. Mouton, "Natural balancing of the two-cell back-to-back multilevel converter with specific application to the solid-state transformer concept," in *Proceedings of the 4th IEEE Conference on Industrial Electronics and Applications*, May 2009.

[2] ——, "The solid-state transformer concept: A new era in power distribution," in *Conference Record of the 9th IEEE AFRICON*, Sept. 2009.

[3] E. Ronan, S. Sudhoff, S. Glover, and D. Galloway, "A power electronic-based distribution transformer," *Conference Record of the 9th IEEE AFRICON*, vol. 17, pp. 537–543, Apr. 2002.

[4] J.-S. Lai, "Designing the next generation distribution transformers: New power electronic-based hybrid and solid-state design approaches," in *Proceedings of the IASTED International Conference, Power and Energy Systems*, 2003, pp. 262–267.

[5] R. W. Erickson and D. Maksimovic, *Fundamentals of Power Electronics*, 2nd ed. New York USA: Springer Science, 2004.

[6] P. S. Kemp, "Switch-mode power supply for high voltage solid-state transformer," University of Stellenbosch, Stellenbosch, South Africa, Final year thesis, 2009.

[7] EPCOS. (2006, Sept.) Ferrites and accessories. r_25.pdf.

[8] A. V. der Bossche and V. C. Valchev, *Inductors and Transformers for Power Electronics*. United States of America: Taylor & Francis, 2005.

[9] N. Mohan, T. M. Undeland, and W. P. Robbins, *Power electronincs*, 3rd ed., B. Zobrist, Ed. United States of America: John Wiley and Sons, 2003.

MODULAR CELL CONTROLLER AND MEASUREMENT SYSTEM DESIGN FOR IMPLEMENTATION IN A SOLID-STATE TRANSFORMER

C.F. Breet,   H. du T. Mouton   and   J.W. van der Merwe

Stellenbosch University, Department of Electrical and Electronic Engineering, Private Bag X1, Matieland, Stellenbosch, 7602, South Africa.

Abstract.   This paper presents the measurement and control system designed to monitor and control the individual converter modules of a solid state transformer. Special consideration is given to the modularity of the design and the inherent advantages of such a system. Further information on the control and measurement circuitry is also provided, with particular reference to the central control and measurement systems.

Key Words.   Solid-State Transformer; Input-Series-Output-Parallel; Modular; Controller; Measurement.

1.   INTRODUCTION

With the ever-increasing demands placed on electricity distribution networks to conserve energy and to deliver reliable and especially more versatile energy options, it is increasingly necessary to develop a grid that facilitates these requirements. This resulted in the proposal of a smart grid model [1]. The model is aimed at establishing complete controllability and interconnectivity over a variety of distribution networks. With businesses, and even households, starting to produce their own electricity supplies, either as renewable or backup solutions, the central grid can be enhanced even further by selling excess power to the utility. With the improved information sharing capabilities of the smart grid, additional network controllability is gained, also referred to as cloud-based smart grid control [2]. This system suggests the use of web-based middleware to monitor and control interconnected networks, thus increasing the expansion capabilities of the network while minimizing the interruption of ongoing network operations. Although the system shows great promise, there is still a significant amount of research and development required to study the feasibility of these solutions.

With the smart grid in sight, the solid-state transformer (SST) aims to fit into this future network. The concept of the SST, also known as the intelligent universal transformer, was first introduced in 1980 with the objective of overcoming the various disadvantages of the line frequency transformer (LFT) [3], [4] and [5].

Fig. 1 illustrates the basic SST outline, which consists of three segments: converter(s) used to convert the incoming line frequency AC to the desired high frequency AC, a high frequency transformer used for galvanic isolation and lastly converter(s) to recreate the line frequency at the desired voltage [5].

The chosen SST topology, as discussed in [6], is shown in Fig. 2. An Input-Series-Output-Parallel (ISOP) configuration is used to overcome the problems caused by the high voltage side and to
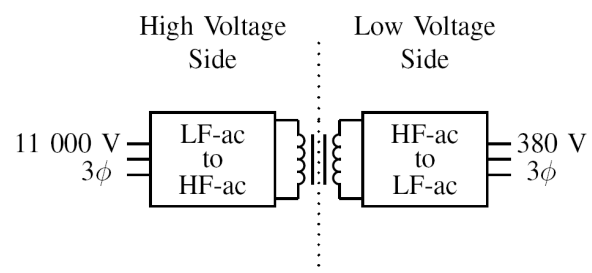
Fig. 1: Basic Solid-State Transformer Outline
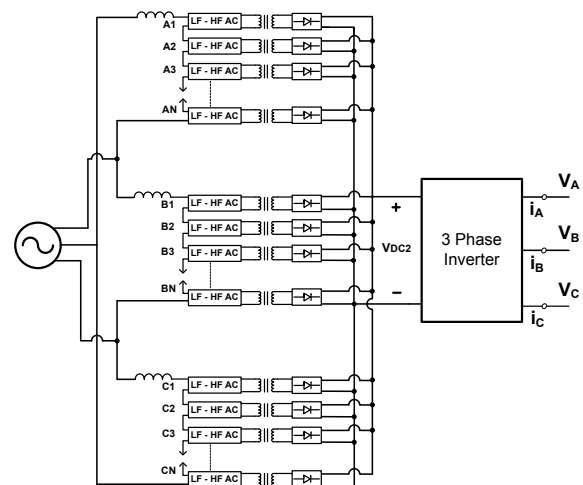
Fig. 2: SST Topology

achieve the required high to low voltage power conversion [5]. This is followed by a three phase inverter on the output stage of the SST.

Given the above mentioned SST configuration, illustrated in Fig. 2, it is required to develop a control strategy for this system. This paper will firstly discuss the desired modular system design parameters and the inherent advantages of increasing system modularity. Secondly, the measurement and control system that was developed to monitor and control the individual cells of the SST will be introduced followed by measurement results to validate the accuracy of the measurement acquisition system.

Proceedings of the 19th Southern African Universities Power Engineering Conference
SAUPEC 2010, University of the Witwatersrand, Johannesburg

TOPIC A. POWER ELECTRONICS

2. MODULAR CELL DESIGN

Functionality, complexity and cost are the most important factors to consider when designing a large and complex system like the SST. These parameters are often directly proportional to each other since, for example, an increase in functionality directly translates into an increase in complexity and cost. This section will discuss and elaborate on these factors, as well as present the chosen modular cell design and the advantages of a standardized system implementation.

Studies into the traditional implementation of ISOP stacked converter topologies have been under rigorous investigation in recent years [7], [8]. Various control techniques have been devised to achieve improved voltage balancing and current sharing between the modules [8], [9]. Considering the increased complexity of the solutions, a universal, more reliable and less complex solution is desired. Research on the natural balancing of similar converters in terms of duty cycle and transformer turns ratio mismatches showed promising results [10]. By switching the series connected cells in an interleaved pattern balance was obtained between the units.

A complete modular system design was desired to realize the SST. This would allow the SST to be as flexible as possible during its development and evaluation stages. It was thus decided to design standardized cells that would be stacked in a multilevel cascaded ISOP configuration to implement the SST (see Fig. 2). A generalized cell configuration was selected to increase the functionality of the cells. Each cell consists of two, back-to-back, full-bridge converters, as shown in Fig. 3 [11]. The first acts as an active rectifier, which is switched in a boost converter configuration and is used to control and maintain the desired inductor current of the SST as well as the DC-bus voltage of the cell [12]. This is followed by a DC-DC converter that transfers the power across the isolation barrier. The added benefit of this generalized configuration is the increase in its modularity, since it can be used in several other configurations.

Increasing the modularity of SST is especially important because it allows an increase in the redundancy, flexibility and thus functionality of the system. If all the cells are identical, a faulty cell can be isolated and simply replaced by another unit. By introducing redundant cells, the system can continue to function even if a cell fails, which also improves system reliability [5], [13]. Enhancing the controllability of each cell is thus also desired, since this will add to the isolation capabilities of the SST.

The designed SST control configuration, Fig. 4, consists of three main controllers, one per phase [14]. Each cell module has its own control and measurement system, which greatly reduces the control load of the main SST controllers and provides
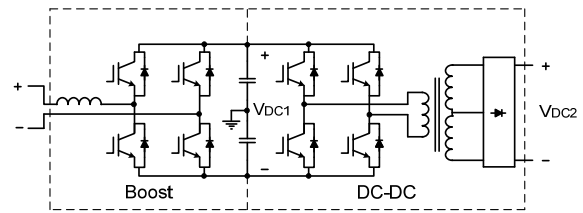
Fig. 3: Circuit Diagram of a Cell
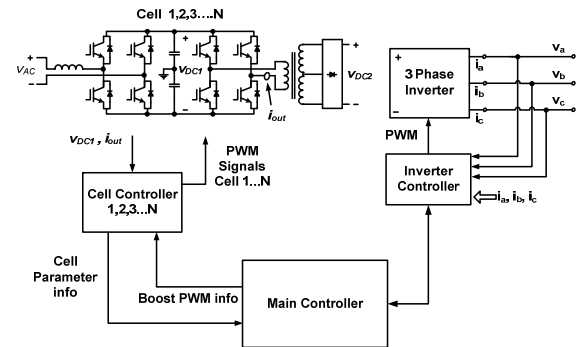
Fig. 4: SST Control Configuration

further monitoring capabilities. The main controllers will thus communicate with every cell controller and provide them with the necessary PWM information. Adding a dedicated controller for each cell also provides extra control lines, which enhances the functionality and reliability of the module. Additionally, this produces more accurate measurements, since the noise susceptibility of the measurement signals is significantly reduced due to the close proximity of the controller with relation to the measurement circuit.

A FPGA based control system was chosen because of its high-speed and parallel processing capabilities. By using such a controller, the various cell components can be managed almost simultaneously, with the only noteworthy delay being commands received from the main controller.

Due to the constant communication between the main controllers and their respective cells, additional isolation capabilities are also achieved. If communication with the main controller is lost, a cell can continue to function for a given period. If cell communication is not restored within a certain time frame, it can be shut down and isolated by its respective controller, and the utility informed to rectify the problem. This complete controllability of the cell can allow real-time data to be relayed to the utility, enabling increased monitoring capabilities for the SST.

As a result of this topology's completely modular nature the SST becomes fully scalable; this is particularly helpful during the development and experimentation stages of the SST. The additional application capabilities are an added benefit of the integrated cell, control and measurement module. The module can, for instance, be used as a standalone unit, or in various stacked topologies, such as ISOP and input-parallel-output-parallel (IPOP).

TOPIC A. POWER ELECTRONICS

Proceedings of the 19th Southern African Universities Power Engineering Conference
SAUPEC 2010, University of the Witwatersrand, Johannesburg

A significant limiting factor in respect of the design and development of the SST is cost. With the above mentioned modular cell design costs can be considerably reduced if the modules are created in sufficiently large enough quantities. Further integration of the cell's control circuitry, with the use of application-specific integrated circuits (ASICs), will greatly reduce the price and also increase the reliability of each module. Due to the high functionality of the design, it can be applied to various other operations, so it is not unreasonable to assume a significant decrease in cost, as soon as the technology has matured enough, which will result in an increase of the adoption rate of the module.

3.   MEASUREMENT SYSTEM

Given the universal design of each cell module, various measurements are needed to ensure the correct operation and controllability of the SST. This section will discuss the measurement circuits used and the design criteria that were followed to create a fully modular cell design.

The measurement system layout, used to monitor the cell, is show in Fig. 5. This system consists of three types of measurement circuits, i.e. current measurement, voltage measurement and temperature measurement circuits.

3.1 Central Measurement Circuits

The primary measurement circuits are used to measure the current and voltage values of a cell.

Taking into consideration the noisy environment within which the measurement system must function, appropriate signal conditioning techniques are required to maximize the accuracy of the measurements and to reduce or eliminate any noise that gathers along the measurement paths. Since the measurement path includes an IDC interface that connects the measurement and control system, special attention should be paid to noise that may accumulate on the interface cable. By using a differential measurement acquisition system, any noise accumulated on the common-mode (CM) voltage of the signals can be discarded by using a differential analog-to-digital converter (ADC). This characteristic creates a system that is extremely immune to noise and also improves the distortion performance obtained, since differential signals eliminate all even order harmonics [15].

3.1.1   Current Measurement Circuit

Fig. 6 illustrates the circuit used to measure the primary transformer current, i_{out} (on the output of the DC-DC converter), shown in Fig. 4. This circuit utilizes a current transducer to generate a single-ended voltage that represents the measured transformer current. This measurement is then converted into a differential signal pair by a fully differential amplifier, which also serves to buffer the measurement signal.
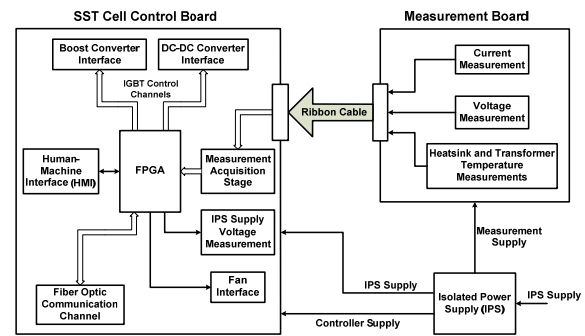
Fig. 5: Cell Control and Measurement System

To increase the accuracy and CM rejection of the measurement, an external, high accuracy reference chip is used to provide the required CM voltage. This reference voltage is applied to both the current transducer and op amp to decrease the deviations from the preferred reference voltage that cause unwanted offset errors on the measurement signal.

By adding a first-order differential low-pass filter (LPF), R5, R6 and C1 on the output of the measurement circuit, any unwanted high frequency noise can be eliminated. Care should be taken when driving capacitive loads with this circuit. The datasheet of the differential amplifier usually states the maximum capacitive load, or provides a diagram of the load resistance versus capacitive load, that can be connected to each of the outputs and still ensure accurate operation. R5 and R6 thus also serve to isolate the capacitive load from the loop gain path. By doing so the load is prevented from interacting with the output impedance of the differential amplifier, which could cause a phase shift in the loop gain. This phase shift, in turn, causes a reduction in the phase margin of the circuit, which results in oscillations on the output signals. (Overshoot, undershoot and ringing can also be expected when measuring a square-wave signal.) It is therefore advised to place the resistors as close as possible to the outputs of the op amp circuit.
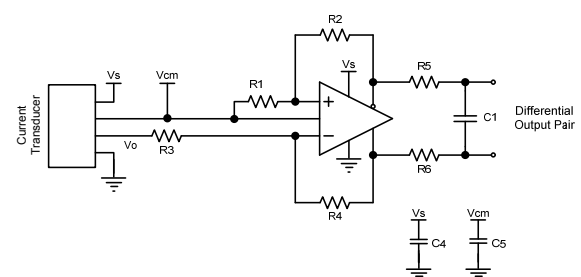
Fig. 6: Current Measurement Circuit

3.1.2   Voltage Measurement Circuit

Consider the circuit used to measure the DC-bus voltage of the cell shown in Fig. 7. Note that the ground used by the cell control and measurement system is situated in the centre of the DC-bus of the respective cell. Using this connection scheme enabled the differential measurement of the bus

Proceedings of the 19th Southern African Universities Power Engineering Conference
SAUPEC 2010, University of the Witwatersrand, Johannesburg

TOPIC A. POWER ELECTRONICS
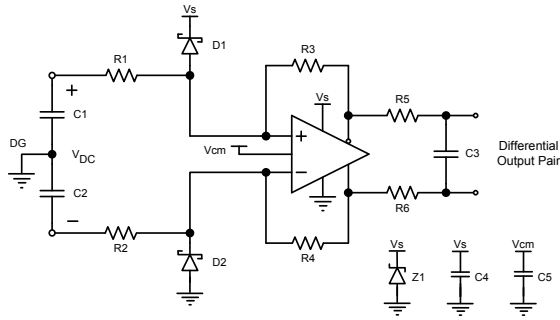
Fig. 7: Voltage Measurement Circuit

voltage. A fully differential amplifier is utilized to perform a differential-to-differential conversion which scales and level-shifts the measurement signals to the required values. The filter configuration implemented in this circuit is the same as discussed in section 3.1.1.

Various safeguards have been introduced to protect and ensure the safety of the measurement circuit. Schottky diodes, D1 and D2, have been placed to protect the op amp inputs against overvoltage fault conditions that may occur on the DC-bus side. A zener diode has also been placed to protect the measurement board's supply voltage, Vs, during possible faults.

3.2 Secondary Measurement Circuits

When considering the cell assembly, there are two temperature values that are of interest, namely the IGBT heatsink and high frequency transformer temperatures. These measurements only function as a safety measure and can be used to disable the SST if inadequate ventilation is present.

Fig. 8 shows the straightforward buffering circuit used to measure the desired temperatures of each cell. The circuit consists of an integrated-circuit (IC) temperature sensor, which provides a voltage value that is linearly proportional to the connected surface temperature. Since a cable is used to connect the sensor to the measurement board, three LPFs are used to filter the temperature sensor interface, and they are placed as close as possible to this interface.
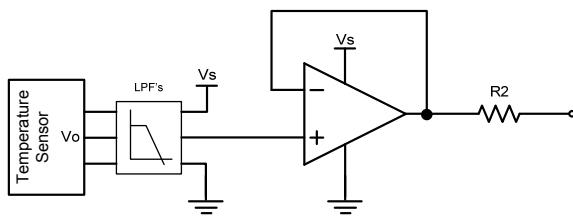
Fig. 8: Temperature Measurement Circuit

4. CELL CONTROL SYSTEM

The FPGA based control system that has been developed to monitor and control a cell is shown on the left hand side of Fig. 5. The majority of the components are self-explanatory. This section will provide supplementary information concerning the

main components of the measurement acquisition stage, the isolated power supply (IPS) monitoring system and the fiber optic communication channel.

4.1 Measurement Acquisition Stage

The measurement acquisition stage consists of a variety of ADCs to acquire the measurement data received from the measurement board. This subsection will discuss the signal conditioning required by the primary ADC configuration circuitry.

Consider the ADC configuration (see Fig. 9) that is used to acquire the primary measurements provided by the measurement system, as discussed in section 3.1. This circuit uses a fully differential amplifier to drive the inputs of a high speed, pipelined, ADC with parallel outputs. By using the CM voltage output of the ADC to drive the reference input of the op amp, which performs a differential-to-differential conversion, it is ensured that the correct DC voltage is used to bias the differential inputs of the respective ADC.

As the ADC input is capacitive by nature, it is advisable to include small series resistors, R5 and R6, to isolate the ADC from its source, as discussed in section 3.1.1. These resistors also reduce the transient currents caused by the ADC's switched capacitive front end. By introducing a shunt capacitor, C1, the final measurement is limited to the desired bandwidth before concluding the measurement acquisition stage. To reduce the sampling noise of the ADC inputs even further, additional capacitors, C2 and C3, are also added.

Appropriate biasing of reference voltages is always required. This ensures that the voltages stay stable and it minimizes clock feed-through. Low inductance 100nF capacitors, C4 and C5, are recommended and should be placed as close as possible to the corresponding reference pins.
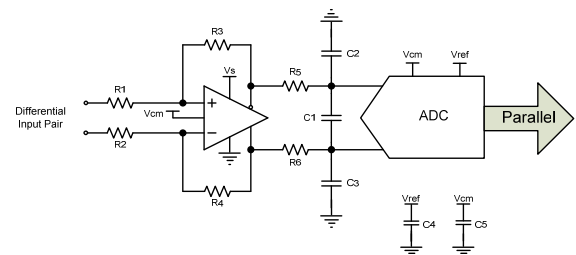
Fig. 9: Central ADC Configuration

4.2 Isolated Power Supply

Bearing in mind the series stacked configuration used to implement the SST, each cell module requires an IPS (see Fig. 5) [16]. As it is crucial for the cell module to be powered at all times, it was decided to implement a supervisory circuit for the supply's input voltage. The IPS supply measurement circuit utilizes an ADC to monitor the input voltage of the IPS. If the supply voltage drops below a certain threshold,

TOPIC A. POWER ELECTRONICS

Proceedings of the 19th Southern African Universities Power Engineering Conference
SAUPEC 2010, University of the Witwatersrand, Johannesburg

the main controller is notified to take corrective action.

4.3 Fiber Optic Communication Channel

The fiber optic channel is used for serial communication between the SST cells and their respective main controllers. This communication consists of PWM information concerning the boost converter, sent by the main controllers, and cell parameter information, sent by the individual cell controllers, as depicted in Fig. 4. Using fiber optics for data communication increases the reliability and safety of the system, since the main controllers are fully isolated from the core SST components.

PWM boost information is sent every switching period and consists of synchronization commands, used to synchronize the carrier signals of the controllers, and reference information, used to generate the IGBT gating signals.

Cell parameter information, in contrast, is sent multiple times every switching period, depending on the amount of information required, and consists of the requested measurement data and/or acknowledge commands to confirm instructions received from the main controller. Various error or warning messages are also sent if appropriate. The parameter information is then analyzed by the main controller and sent via a USB interface to a PC for data logging.

5. MEASUREMENTS

This section will present the measurement results, obtained from the primary measurement acquisition systems of a single cell module, as described in sections 3.1 and 4.1.

The following results were obtained by applying a DC voltage of 450V to the input of a cell, disabling the boost converter and switching the DC-DC converter of the module at a constant duty cycle.

Fig. 10 shows the DC-bus voltage, V_1, obtained with a high voltage differential probe, while Fig. 13 shows the primary transformer current, I_1, obtained with a DC coupled current probe. The corresponding measurements, obtained via the cell's primary measurement systems and extracted using the FPGA's Joint Test Action Group (JTAG) boundary-scan test (BST) interface, are shown in Fig. 11 and Fig. 14, respectively.

V_1 and V_2 both verify the bus voltage of 450V. Fig. 12 provides a comparison of V_1 and V_2. The voltage measurement, V_2, is extremely accurate since no additional peripheral devices were used to adapt the bus voltage to a lower, measureable value, with the only notable inaccuracies caused by the quantization noise of the ADC.

The current measurement, I_2 is relatively accurate when compared to I_1. Due to the lower bandwidth of the current transducer, I_2 does however display some

measurement mismatches at the positions where the current changes are too quick.
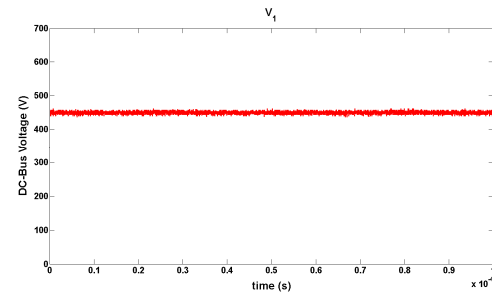
Fig. 10: DC-Bus Voltage, measured using Oscilloscope
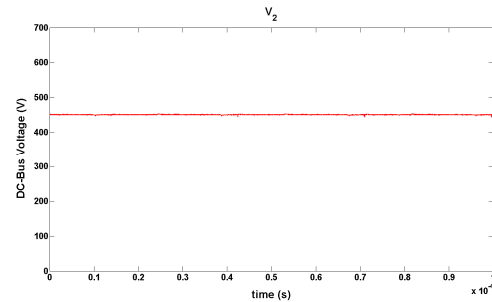
Fig. 11: DC-Bus Voltage, measured using measurement system
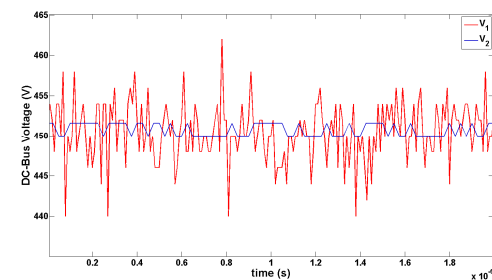
Fig. 12: DC-Bus voltage comparison
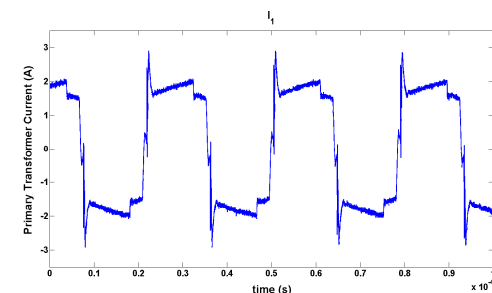
Fig. 13: Primary transformer current, measured using Oscilloscope
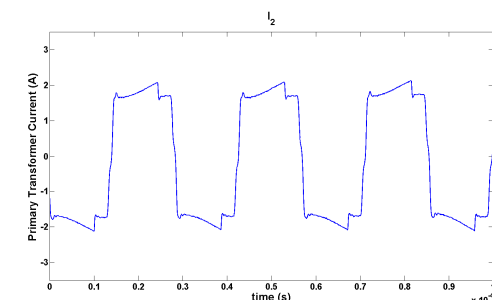
Fig. 14: Primary transformer current, measured using measurement system

Proceedings of the 19th Southern African Universities Power Engineering Conference
SAUPEC 2010, University of the Witwatersrand, Johannesburg

TOPIC A. POWER ELECTRONICS

CONCLUSION

The modularity of the series stacked configuration is of significant importance when assessing which topology should be used to realize the SST system, since the modularity greatly improves the maintainability and scalability of the SST [6]. By switching cells in an interleaving pattern, reliable natural balancing can be accomplished between the modules, which made it possible to design a modular SST system. This article discussed the modular cell design methodology which was followed, and the hardware development that was done, to implement a complete modular and reliable SST system. Further elaboration on the inherent advantages of such a universal system was also provided.

Measurement data of the designed measurement system illustrated the accuracy, noise resilience and thus reliability of the circuitry and signal conditioning techniques that were used. Further enhancements may involve increasing the bandwidth of the current measurement circuit, but this is not necessary at present.

ACKNOWLEDGEMENTS

REFERENCES

[1] S. M. Amin and B.F. Wollenberg, "Toward a Smart Grid", *IEEE Power and Energy Magazine*, Vol.3, No. 5, pp. 34-41, September/October 2005.

[2] A. Ipakchi and F. Albuyeh, "Grid of the future", *IEEE Power and Energy Magazine*, Vol. 7, No. 2, pp. 52-62, March/April 2009.

[3] J. Brooks, "Solid state transformer concept development," Naval Material Command, Civil Engineering Laboratory, Naval Construction Battalion Center, Port Hueneme, CA, Tech. Rep., 1980.

[4] J.S. Lai, "Designing the Next Generation Distribution Transformers: New Power Electronic Based Hybrid and Solid State Design Approaches", *in Proceedings of the IASTED International Conference*. Palm Springs, CA, USA, 24-26 Feb 2003.

[5] J.W. van der Merwe and H. du T. Mouton, "The Solid-State Transformer Concept: A New Era in Power Distribution", i*n Proceedings of the IEEE Africon Conference*, Nairobi, Kenya, 23-25 Sep 2009.

[6] J.W. van der Merwe and H. du T. Mouton, "Solid-State Transformer Topology Selection", in *Proceedings of the IEEE International Conference on Industrial Technology*, Gippsland, Australia, 10-13 Feb 2009.

[7] V. Vorpérian, "Synthesis of Medium voltage dc-to-dc Converters From low-voltage, High Frequency PWM Switching Converters", *IEEE Transactions on Power Electronics*, Vol. 22, No. 5, pp. 1619- 1635, 2007.

[8] X. Ruan, L. Cheng, and T. Zhang, "Control strategy for input-series output-paralleled converter," *in Conference Record of the 2006 IEEE 37th Power Electronics Specialists Conference*, 18-22 June 2006, pp. 1 – 8.

[9] J.-W. Kim, J.-S. You, and B. Cho, "Modeling, control, and design of input-series-output-parallel-connected converter for high speed train power system*," IEEE Transactions on Industrial Electronics*, Vol. 48, No. 3, pp. 536–544, June 2001.

[10] J.W. van der Merwe and H. du. T. Mouton, "Balancing of a 2-Cell Modular Input-Series-Output-Parallel Converter with Common Duty Ratio Control under Converter Mismatch", *in Proceedings of the South African Universities Power Engineering Conference (SAUPEC) Conference*, Stellenbosch, South Africa, 28-29 Jan 2009.

[11] M. Wolf, "Design and Implementation of a Modular Converter with Application to a Solid State Transformer", Master's thesis, Stellenbosch University, 2008.

[12] J.W. van der Merwe and H. du T. Mouton, "Natural Balancing of the Two-Cell Back-To-Back Multilevel Converter with Specific Application to the Solid-State Transformer Concept"*, in 4th IEEE Conference on Industrial Electronics and Applications*. Xi'an, China, 25-27 May 2009.

[13] E. Choudhary, V. Ledezma, R. Ayyanar, and R. Button, "Fault tolerant circuit topology and control method for input-series and ouput-parallel modular DC-DC converters", *IEEE Transactions on Power Electronics*, Vol. 23, No. 1, pp. 402–411, 2008.

[14] L.M. Schietekat and H. du T. Mouton, J.W. van der Merwe, "Design of a Cascaded Rectifier Control Strategy, Implemented in the Main Controller of a Solid-State Transformer", *Submitted for review for the SAUPEC conference*, 2010.

[15] S. Paterson, "Maximize performance when driving differential ADCs", *EDN Design Engineering Magazine Article*, June 2003. www.edn.com

[16] P.S. Kemp and H. du T. Mouton, J.W. van der Merwe, "Design of an Isolated Resonant Switch-Mode Power Supply for a Modular Solid-State Transformer", *Submitted for review for the SAUPEC conference*, 2010.

TOPIC A. POWER ELECTRONICS

Proceedings of the 19th Southern African Universities Power Engineering Conference
SAUPEC 2010, University of the Witwatersrand, Johannesburg

DESIGN OF A CASCADED ACTIVE-RECTIFIER CONTROL STRATEGY, IMPLEMENTED IN THE MAIN CONTROLLER OF A SOLID-STATE TRANSFORMER

L.M. Schietekat, H. du T. Mouton and J.W. van der Merwe

Department of Electrical and Electronic engineering, University of Stellenbosch, Private Bag X1, Matieland, 7602.

Abstract. This paper presents power-factor correction control applied to cascaded active-rectifiers. The control implements a double-loop strategy where the inner loop utilises average current mode control. The physical implementation of the control is discussed and the issues as well as the applied solutions thereof are presented. Emphasis is placed on the hardware computing power as well as the methods used to accomplish multisampling PWM.

Key Words. Power-Factor Correction Control, Multisampling PWM, Cascaded Active-Rectifiers.

1. INTRODUCTION

The line-frequency transformer (LFT) is the traditional method for transforming voltage levels in the power distribution grid. Due to the maturity of this technology, this method is both effective and cheap. However, as explained in [1], it introduces unwanted characteristics into the grid.

The solid-state transformer (SST) consists of three main sections, namely, a converter(s) section to create high-frequency AC from the input line-frequency AC, an isolation section with a high-frequency transformer, and lastly, another converter(s) section to create line-frequency AC output again. The SST, as an alternative to the LFT, addresses some of the distribution-system problems and all of the LFT problem areas. A few of the prominent advantages of the SST in comparison to the LFT, as stated in [1], are summarized below:

 (i) Output-voltage regulation: The output voltage is immune to input-voltage sags and dips and free of power frequency harmonics. The output voltage is also regulated throughout the load range.

 (ii) Input power-factor correction: The input current is controlled to be sinusoidal and in phase with the input voltage. The input of the SST is thus seen as a variable resistor.

(iii) Protection: The different controllers measure and have control over most operational parameters. This enables the SST to act as a fault barrier, between the input and output, able to make real time decisions regarding power flow during fault conditions.

(iv) Communication: The utility can be informed in the event of input faults such as voltage unbalancing or voltage sag, for corrective action. Certain SST outputs can be remotely controlled. Real-time and stored operational data can be available to the utility to be used for preventative maintenance.

The challenging aspects of the SST are the high-voltage (HV) side converter (because of the high voltage) and the high-frequency transformer (because of isolation and parasitic issues). Three well-known SST topologies are compared in [2]. These are the cascaded, diode-clamped and flying-capacitor converter topologies. It is concluded that the cascaded converter topology is the most feasible as a result of its cost and its modular nature.

This nature yields the implementation of the modular cell. In this paper the power-electronic configuration of the SST is briefly discussed as introduction to the controller-hardware configuration that enables all the added functionality of the SST. The hardware focus is on the main controller, whereas the software focus is on the active-rectifier control strategy.

2. POWER-ELECTRONIC CONFIGURATION

2.1 Three-phase SST topology

The three-phase SST, shown in Fig. 1, comprises three groups of N cascaded cells, one group per phase. The three-phase HV line-frequency AC input is connected in delta and the $3 \cdot N$ cell low-voltage (LV) DC outputs are connected in parallel. This is the LV bus voltage, V_{DC2}, of the three-phase inverter which, in turn, has a three-phase LV line-frequency AC output. As mentioned in [2], the modularity of this topology introduces scalability and improves maintainability.

2.2 Cell configuration

As mentioned, the cell consists of two back-to-back full-bridge converters. The front end converter is operated as an active-rectifier switched in a boost configuration. The active-rectifier ensures that the input current is sinusoidal and in phase with the input voltage and it also regulates the cell bus-voltage, V_{DC1}. This control is discussed in greater depth later in this paper. The second converter is a DC-DC converter that transfers the power across the isolation barrier. It consists of a full-bridge converter, an isolation transformer and a passive-rectifier. According to [3], the frequency of the DC-DC converter is limited by switching losses and parasitic inductances in the circuit. The cell configuration is shown in Fig. 2.

Proceedings of the 19th Southern African Universities Power Engineering Conference
SAUPEC 2010, University of the Witwatersrand, Johannesburg

TOPIC A. POWER ELECTRONICS
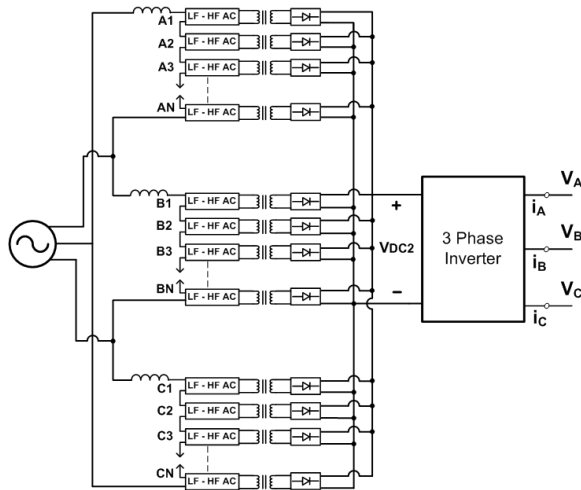
Fig. 1: Three-phase SST topology.
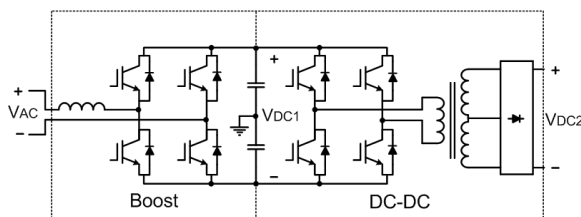
Fig. 2: Cell configuration.

3. CONTROL HARDWARE CONFIGURATION

There are three types of controllers present in the SST, namely, cell controllers (one for each cell), three main controllers (one for each phase) and an inverter controller.

3.1 Cell controller

The cell controller acts as the link between the main controller and each cell in the respective phase. The cell controller measures and monitors the operational parameters of the cell and sends regular status reports to the main controller. These reports indicate if the isolation-transformer input current and both the insulated gate bipolar transistors (IGBT) heat sink and transformer-core temperatures are within acceptable operating ranges. The report also relays the V_{DC1} measurement to the main controller, which is used in the active-rectifier control strategy. The cell controller also receives pulse width modulation (PWM) information from the main controller, which is used to generate duty cycles for the respective IGBTs.

3.2 Inverter controller

The inverter controller is responsible for one of the prominent advantages of the SST, namely the near perfect output voltage regulation. This is achieved with a double loop control strategy, for faster response. The strategy is developed in [3]. The inner loop controls the inductor current, whereas the outer loop controls the line-frequency AC load voltage. Communication is also available between one of the main controllers and the inverter controller.

3.3 Main controller

The main controller is the main hardware focus of this paper. It consists of five printed circuit boards (PCBs): The controller board, the fiber optic interface board and three measurement boards. The measurements taken by the latter are the input inductor current, I_L, at the front end of the cascaded cell group, the input voltage, V_{AC}, and the three-phase inverter bus voltage, V_{DC2}. The fiber optic interface PCB enables communication between the main controller and all the cell controllers in the respective phase and between the main controllers of each phase. Fiber optics are used because of immunity to system noise and to isolate the main controller from the cell controllers. As shown in Fig. 3, the controller PCB consists of a field programmable gate array (FPGA), three high-speed analog to digital converters (ADCs), flash memory, double data rate (DDR) memory, a real-time clock, a soft-start system interface and a USB interface.

The FPGA is configured using VHDL. This means that one actually creates logic, which has two very important advantages. The first is the ability to perform separate functions in a parallel fashion. For example, status reports can be received from multiple cell controllers at the same time, while a control strategy is implemented and while operational data is being stored etc. The second advantage is the speed at which operations can be executed. The high-speed FPGA together with the high-speed ADCs (53MSPS) enable the main controller to implement a high-speed control strategy (10MHz) to achieve multisampling PWM.

A Nios II embedded processor system is implemented to manage housekeeping on the main controller. As stated in [4], such a system can be implemented on a single Atera® chip; it includes a Nios II processor core, a set of on-chip peripherals, on-chip memory and off-chip memory interfaces. The DDR memory serves as an extension of the on-chip memory. Housekeeping involves, for example, the management of operational data and communication. The Nios II processor manages the
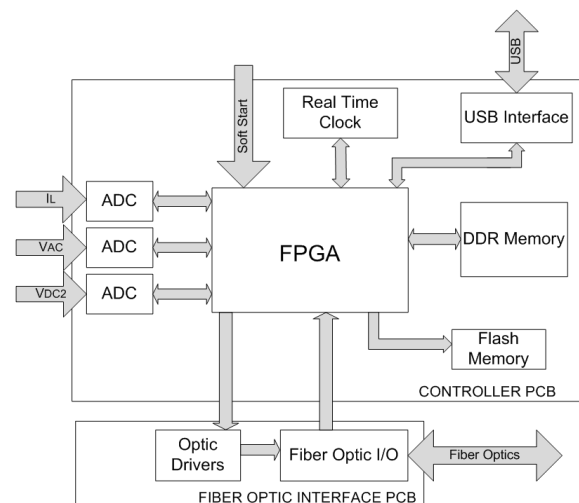
Fig. 3: Main controller block diagram.

Proceedings of the 19th Southern African Universities Power Engineering Conference
SAUPEC 2010, University of the Witwatersrand, Johannesburg

TOPIC A. POWER ELECTRONICS

communication interfaces between the FPGA, real-time clock, flash memory, DDR memory and USB interface device. The Nios II processor also gathers measurement data, uses the real-time clock to add time stamps and saves the data in flash memory. Using this combination of the FPGA and the Nios II processor thus yields the functionality to implement the fast, parallel input/output, control strategy, while still having the ease of use of a micro controller for housekeeping functions.

The soft-start system enables the SST to start up without damaging transition-stage currents.

The USB interface adds functionality as listed below:

 (i) Measurements from the measurement PCBs and the cell controllers can be sent to a PC for analysis during the SST design and testing phase.

 (ii) Operational data stored in flash memory can be downloaded to a laptop or any other data-capture device.

 (iii) A GSM or Bluetooth module can be included enabling remote control of the system as well as communication with the utility. The utility can thus be informed of the nature and extent of faults.

4. CASCADED ACTIVE-RECTIFIER CONTROL STRATEGY

This strategy is aimed at regulating the power flow by regulating the active rectifier output voltage, V_{DC1}, as well as the unity power factor, by ensuring that I_L is sinusoidal and in phase with V_{AC}. The control discussed in this section pertains solely to the front end of the cell, being the active-rectifier.

Average current mode control is implemented as opposed to peak current mode control and it incorporates a high gain integrator into the current loop. As discussed in [5], this control method enables the inductor current to track its reference with a high level of accuracy and also supplies the control system with a high level of noise immunity.

Fig. 4 is a block diagram of the power factor correction control strategy. As discussed in [6], the current loop is controlled by the input voltage, V_{AC}, so that the converter appears to be resistive. V_{DC1}, in contrast, is controlled by varying the current-reference amplitude. To maximize the power factor, the current reference must match V_{AC} as closely as possible. If the voltage-loop bandwidth is too large, it will try to keep V_{DC1} constant and thus distort I_L.
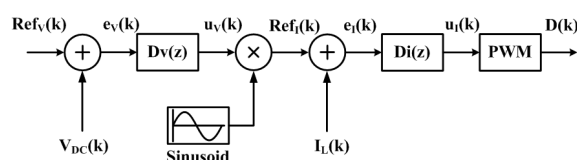
Conversely, the bandwidth should be as large as possible to minimize the output voltage transient response. The voltage-loop bandwidth is thus set to less than the input line frequency; however, the current loop needs a much larger bandwidth, as large as possible without causing system instability.

The only way to use this control strategy on a set of cascaded active-rectifiers is to have a single double loop system sending switching signals to all the active-rectifiers. As is explained in section 4.2 below, the active rectifier switching is interleaved. Fig. 5 shows the equivalent circuit of a group of cascaded active-rectifiers, for simulation purposes, and Fig. 6 shows the physical implementation of this control strategy.
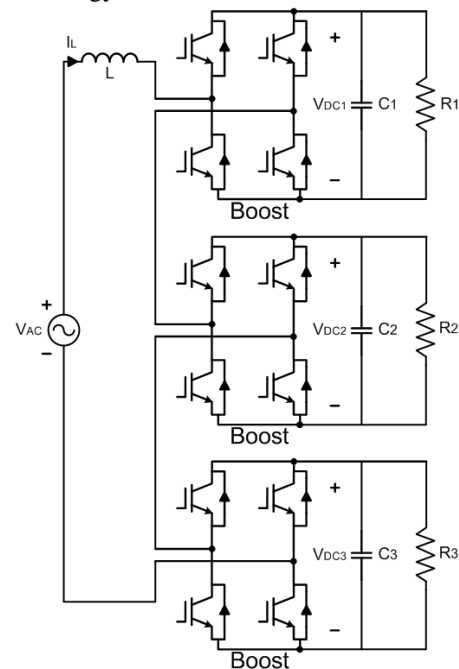
Fig. 5: Cascaded active rectifier circuit diagram.

4.1 Current loop

The inductor current, I_L, is measured, as an analog signal, with one of the three measurement channels. This channel consists of a LEM current transducer that converts the I_L measurement to a voltage. This voltage is then converted to a differential signal-pair, V_{ILdiff}, by the measurement PCB. It is carried to the controller PCB in differential mode because of its resistance to system noise. On the controller PCB, the signal is fed to one of the high-speed ADCs to be converted to a 12-bit digital signal.

This signal is compared to a current reference, Ref_I, and the error, e_I, is fed to the controller block $D_I(z)$. The controller block output, u_I, is the PWM reference. This signal is compared to two PWM carrier-signals per cell. The reference value, where the reference intercepts either of the carriers, is sent to the corresponding cell controller via the implemented serial communication interface (SCI) and the fiber optic interface PCB. The signal is thus converted from a digital signal to a serial optic signal.

Fig. 4: Power-factor correction control strategy.
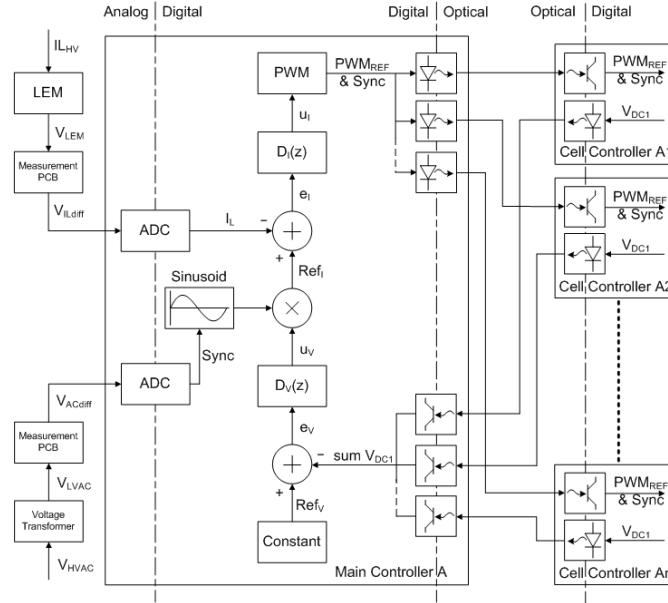
Fig. 6: Physical implementation of the active rectifier control strategy.

4.2 PWM generation

The active-rectifier switching frequency is 10 kHz, which means that the two carrier signals have a frequency of 10 kHz. There are two carrier signals because of the unipolar switching scheme. In this scheme, the two carrier signals are shifted 180° with respect to each other, which yields an effective active-rectifier switching frequency of 20 kHz. The respective cells in the phase group, however, are switched in an interleaved fashion, resulting in an effective phase group switching frequency of $N\cdot20$ kHz.

Saw-tooth PWM carriers are used, thus implementing asymmetrical PWM. The alternative would be to use triangular carriers and thus implementing symmetrical PWM. The saw-tooth carrier yields more harmonics, but these are acceptable, given the high effective switching frequency. Added advantages of asymmetrical PWM are that it simplifies the analysis of the system and makes the PWM less vulnerable to reference ripple. As indicated by [7], PWM reference ripple compensation is also simpler to implement with asymmetrical PWM. This ripple component is caused by the high bandwidth of the current loop, and the ripple amplitude is thus proportional to the current-loop gain, as discussed in [5].

Fig. 7 shows exactly how the PWM switching information is sent from the main controller, where the control is implemented, to the cell controller, where duty cycles are generated and sent to the respective IGBT drivers on the cell itself. The main controller sends two types of data packages, viz. a synchronize package and a reference package. The synchronize package is sent on the falling edge of the main controller's carrier1 signal, which triggers the cell controller to wait t_{delay1} seconds before resetting its carrier signals. The communication delay, caused by the respective buffers and fiber optic drivers and

receivers, is depicted as t_{delay2}. This results in the cell controller carrier signals being $t_{delay1} + t_{delay2}$ seconds behind the main controller carrier signals. The reference package is sent at the same time as a main controller reference-carrier-crossing, which results in a cell controller reference update with a delay of t_{delay2} seconds, well before a cell controller reference-carrier-crossing. Defining t_{delay1} ensures the continual implementation of multisampling PWM. The only difference between the reference-carrier-crossings of the two controllers is caused by aliasing effects in the main controller. It can clearly be seen how this communication method is less vulnerable to the reference ripple by effectively sampling exactly at a reference-carrier-crossing. An effective reference is thus created on the cell controller, as depicted by the dotted line in Fig. 7.
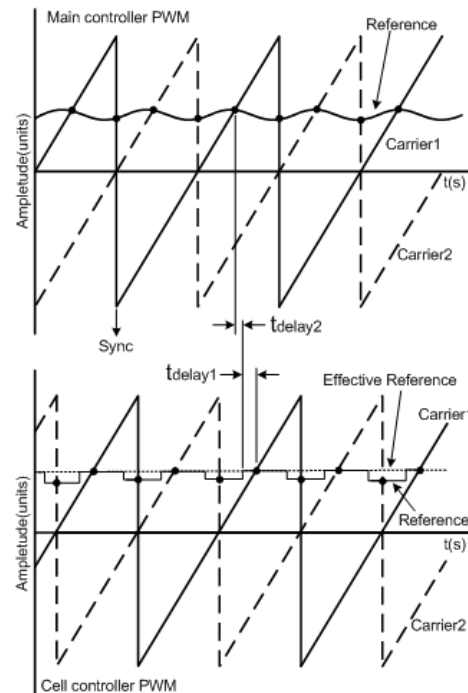
Fig. 7: PWM information communication protocol.

TOPIC A. POWER ELECTRONICS

Proceedings of the 19th Southern African Universities Power Engineering Conference
SAUPEC 2010, University of the Witwatersrand, Johannesburg

4.3 Voltage loop

The active-rectifier output voltages, V_{DC}, are measured as analog values and converted to digital signals by the respective cell controllers. The measurements are passed on to the main controller, once a switching period, via the implemented SCI interface and the fiber optic interface PCB. It is thus converted to a serial optic signal and then back to a 12-bit digital signal on the main controller.

The signals received from all the cell controllers, in the respective phase, are added together to represent the total output voltage, sum V_{DC}. This signal is compared to the constant voltage reference, Ref_V. The error, e_V, is fed to the controller block $D_V(z)$, and the controller block output, u_V, is multiplied with a unit amplitude sinusoid signal, synchronized with V_{AC} to generate the current reference of the current loop, Ref_I, in phase with V_{AC}.

This means that the current is always forced to follow a sinusoid, although the amplitude of this sinusoid is determined by the voltage loop, indirectly forcing the V_{DC} to follow a voltage reference.

5. SIMULATION RESULTS

The current and voltage loops are tested by means of time-domain simulations. Simplorer 8 from Ansoft LLC was used to simulate the interleaved switching of the cascaded active-rectifier circuit shown in Fig. 4 and the circuit parameters are listed in Table 1. I_L tracking Ref_I is shown in Fig. 8. The inductor current ripple is the sum of the ripples caused by each of the three active rectifiers and, as Fig. 9 indicates, the three separate ripples cancel out at certain time instances.

Fig. 8: Input inductor current tracking the current reference.
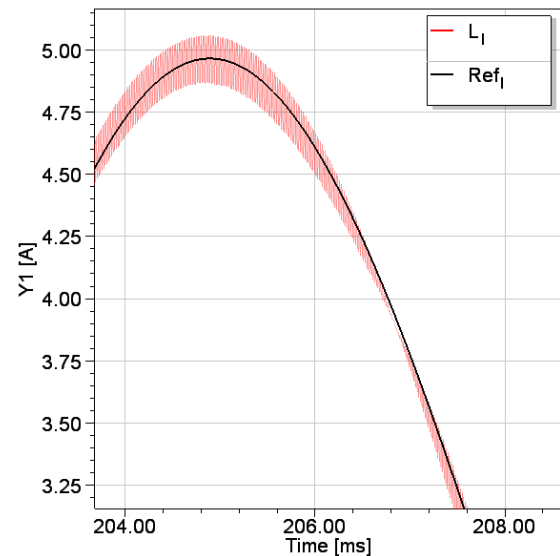
Fig. 9: Inductor current ripple and ripple cancelation.

Table 1: Simulation parameters.

V_{AC}	2.5kV	Pout	2kW
L	21.07mH	V_{DCA1-3}	1000V
C_{A1-3}	50μF	R_{A1-3}	500Ω

The V_{DC} ripple amplitude, however, is determined by the cell bus capacitor size and, as shown in Fig. 10, is 60V. This figure also indicates the V_{DC} settling time if the bus capacitors are charged to V_{DC} before switching begins. The settling time is determined by the gain component of controller block $D_V(z)$. As mentioned, there is a tradeoff between V_{DC} settling time and Ref_I distortion with regard to this gain component. Fig. 11 shows that the $D_V(z)$ output, u_V, is effectively not as constant as ideally required, and the gain component determines the ripple amplitude present on this signal. Because this ripple is multiplied with the unit-amplitude sinusoid, Ref_I is distorted. A sinusoid with the same amplitude as Ref_I is added in Fig. 11 to show clearly the slight Ref_I 3rd harmonic distortion created by a $D_V(z)$ gain of 1 unit.

Fig. 10: Bus voltage ripple and transient response.

The result of the natural voltage balancing mechanisms of cascaded active-rectifiers can be seen in Fig. 12, where a load-step is implemented in one

Proceedings of the 19th Southern African Universities Power Engineering Conference
SAUPEC 2010, University of the Witwatersrand, Johannesburg

TOPIC A. POWER ELECTRONICS

of the active-rectifiers. The load R_{A1} is stepped down from 500Ω to 250Ω at Time = 300ms and stepped back up to 500Ω at Time = 450ms. The two balancing mechanisms present are the strong balancing mechanism, determined by the load, and the weak balancing mechanism, determined by the filter components, as discussed in [8].
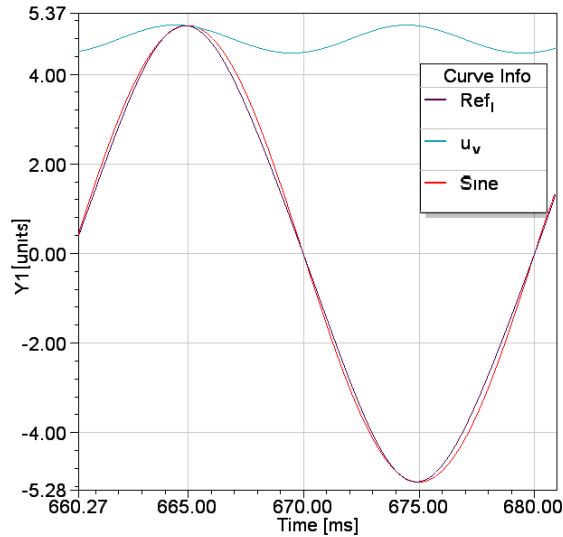
Fig. 11: Current reference 3rd harmonic distortion.
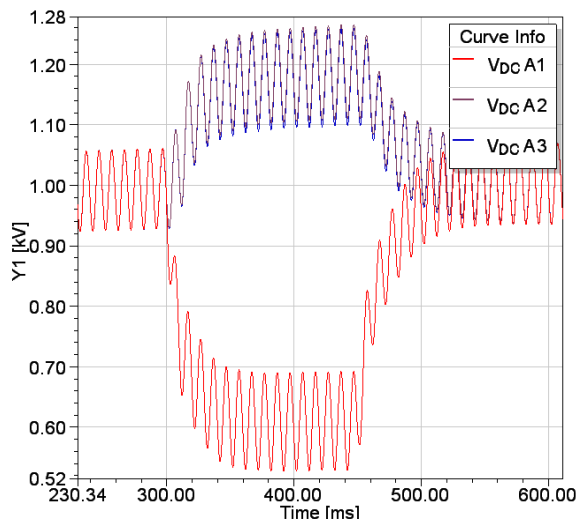
Fig. 12: Natural voltage balancing.

6. CONCLUSION

A power-factor correction control strategy, incorporating average current mode control, is applied to a set of cascaded active-rectifiers. The physical implementation of this control strategy is discussed with emphasis on the computing power that enables multisampling PWM. Simulation results are obtained to verify the functionality of this strategy and to confirm the presence of voltage balancing mechanisms introduced by interleaved switching.

ACKNOWLEDGEMENTS

REFERENCES

[1] van der Merwe, W. and Mouton, H du T.: The Solid-State Transformer Concept: A New Era in Power Distribution. In: *Proceedings of the IEEE Africon Conference*. Nairobi, Kenya, 23-25 Sep 2009.

[2] van der Merwe, W. and Mouton, H. du T.: The Solid-State Transformer Topology Selection. In: *Proceedings of the IEEE International Conference on Industrial Technology*. Churchill, Victoria 3842 Australia, 10-13 Feb 2009.

[3] Wolf, M.: *Design and implementation of a Modular Converter with Application to a Solid- State Transformer*. Master's thesis, Stellenbosch University, 2009.

[4] *Nios II Processor Reference Handbook*. Altera Corporation. Available at: http://www.altera.com. May 2004.

[5] Dixon, L.: Average Current Mode Control of Switching Power Supplies, Application note. Unitrode Application handbook, U-140.

[6] Todd, P. C.: Controlled Power Factor Correction Circuit Design, Application note. Unitrode Application handbook, U-134.

[7] Mouton, H. du T. and Putzeyz, B.: Digital Control of a PWM Switching Amplifier with Global Feedback. In: *Proceedings of the AES 37th international conference*. Hillerød, Denmark, 28-30 Aug 2009.

[8] van der Merwe, W. and Mouton, H du T.: An Investigation of Natural Balancing Mechanisms of Cascaded Active-Rectifiers. To be reviewed.

TOPIC A. POWER ELECTRONICS

Proceedings of the 19th Southern African Universities Power Engineering Conference
SAUPEC 2010, University of the Witwatersrand, Johannesburg

A COMPARATIVE STUDY OF VOLTAGE AND CURRENT MEASUREMENT SOLUTIONS IN POWER ELECTRONIC CONVERTERS

J F van Papendorp,   H J Beukes

Stellenbosch University, Department of Electrical and Electronic Engineering, Private Bag X1, Matieland, Stellenbosch, 7602,South Africa.

Abstract.   This paper provides a conclusive comparative study of numerous acquisition systems for two of the most predominant measurements made in switching converter systems, voltage and current. Both measurement- and digitization solutions are discussed. This paper determines the effectiveness and accuracy of these measurement solutions.

Key Words.   Voltage Measurement; Current Measurement; Digitization

1.   INTRODUCTION

Effective control of power-electronic converters (PECs) necessitate a controller capable of accurately regulating the output voltages and currents.

In the past, analog controllers were used to regulate the voltage and current in a PEC. These controllers were capable of achieving high control bandwidths and fast transient responses, but had the disadvantage of high cost when additional features needed to be incorporated [1]. Analog controllers are also notorious for their varying performance due to high tolerance in the component values of resistors, capacitors, etc. This is countered by the introduction of digital controllers.

Due to the characteristics of quantization and digital control strategies, digital controllers provide many advantages compared to analog controllers. These advantages include programmability, greater adaptability, improved flexibility and reduced susceptibility to environmental noise [2]. Consequently the use of digital controllers in PECs is increasing.

In the past, however, digital controllers had poor processing power. Control calculations required a large amount of computational time and the early controllers were unable to calculate the duty cycles before the start of the next modulation period. Fig. 1 shows a triangular carrier signal used in a PWM process and how the various processes are divided in the time available.
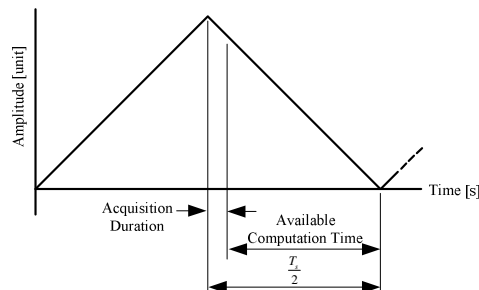
Fig. 1: Computation Limitation

Earlier analog-to-digital converters (ADC) required a large amount of time to acquire a measurement, because of the slow sampling rates, conversion- and acquisition times of the ADC. This reduced the time available for computation of the control calculations. Solutions proposed in [3] and [4] included the simultaneous use of DSPs and FPGAs.

In recent times great advancements have been made in microcontroller technology, increasing both DSP and FPGA processing capabilities. Digital controllers are now capable of completing all the required calculations before the next modulation period. As result of this, microcontrollers are no longer the main cause of steady-state tracking errors.

The ability of the controller to effectively regulate the output currents and voltages of PECs requires accurate measurements of these parameters [5]. Measurements are obtained by using analog circuitry to ensure that signals are compatible with ADCs. The resulting digital codes can then used by the controller.

This paper will focus on comparing various measurement circuits to determine the best solution for a specific application. Furthermore, an analysis is conducted on ADC architectures to determine which one is best suited for a specific measurement circuit.

2.   MEASUREMENT SOLUTIONS

It is important that the measurement circuit has the ability to give an accurate representation of the system's current or voltage values. As discussed in [5], some of the more typical measurements are the DC bus voltage, V_{DC}, load voltage, V_L, output currents like the inductor current, I_L, and load current, I_O.

To a large extent, power measurement equipment is designed under the assumption that a sinusoidal parameter is measured. This, however, is not the case for PECs due to their non-linear characteristics. The performance requirement of the measurement circuits is therefore much more demanding. Circuit specifications such as Gain-Bandwidth Product (GBW), Total Harmonic Distortion + Noise (THD+N), Signal to Noise ratio (SNR), Common-Mode Rejection Ratio (CMMR), amplitude error and phase error need to be considered when such systems are designed:

Proceedings of the 19th Southern African Universities Power Engineering Conference
SAUPEC 2010, University of the Witwatersrand, Johannesburg

TOPIC A. POWER ELECTRONICS

i. GBW: The non-linear behaviour of PECs produce output voltage and current signals containing multiple frequency components, some of which include:
- the desired output signal;
- ripple components caused by the switching behaviour of the converters; and
- feedback components caused by non-linear loads.

These additional high-frequency components are used in certain control algorithms, such as ripple compensation, consequently placing increased emphasis on the GBW of the measurement circuit to accurately produce the high frequency components without a drop in gain.

ii. THD+N: Even though the measurement of certain signal components are essential, care should be taken to prevent the injection of additional harmonic components on printed-circuit board level. Long measurement paths are susceptible to the induction of environmental noise. Digital clocks used by the microcontroller can also cause clock feed-through. It is important to draw the attention to the fact that the THD+N of both the system parameter and the measurement result should be similar. Any loss in frequency information may result in the degradation of controller performance.

iii. SNR: Common-mode instability and environmental noise can degrade the signal integrity of measurement signals. Unmistakably, the introduction of additional noise is undesired.

iv. CMRR: A high CMRR would guarantee that any signal introduced to the system that is common to the measurement circuit's input and its point of reference will be discarded. An insufficient CMRR degrades circuit precision by effectively introducing a voltage offset as a function of a DC level at the input [6]. However, this is rarely the case in power electronic applications where line voltage signals are used. It is also recommended in [6], that a complete differential-signal chain be used to achieve the benefits of differential signals, such as even-order harmonic cancellation and increased analog dynamic range.

v. Amplitude Error: As discussed in [8], this error occurs due to a non-linear impedance of the semiconductor switch. As a result, the half-bridge output amplitude applied to the power filter varies, effectively corrupting the system parameters.

vi. Phase Error: If the measurement result contains a phase error with respect to the measured parameter, the resulting digital code used by the controller would cause an inaccurate response. This could degrade the performance of the power electronic system.

The next sections compare systems that have a complete differential-signal chain and single-ended systems utilizing certain advantages of differential measurements.

2.1 System Setup

A voltage-source inverter (VSI) was used to obtain practical power-electronic system measurements. Fig. 2 shows the typical setup of such a system.
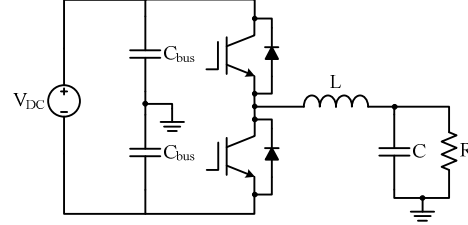
Fig. 2: VSI System

The specification of this system is given in Table 1:

Table 1: Inverter System Specifications

Parameter	Value
Bus Voltage	300V
Inductor	480μH
Capacitor	50μF
Switching Frequency	5kHz

The power filter parameters were chosen such that a sufficient ripple component can be observed on the output voltage and current. This will be discussed in greater detail in the following sections. It is also important to note that all measurements were done by a Tektronix TDS3014B digital oscilloscope with a bandwidth of 100MHz.

2.2 Voltage Measurement

Voltage measurements are used by the controller for numerous reasons. Some examples include power supply voltage error checks, as discussed in [3] and system state checks. A few measurement solutions are discussed:

2.2.1 Case I

As mentioned at the beginning of this section, it is highly recommended to utilize the CMRR properties of a differential solution. This has the added benefit that the measured voltage need not be measured with respect to the ground of the measurement circuit. This enables the system ground of the controller to be referenced to any point within the DC bus' upper or lower limits [3]. Even if the system ground of the controller is isolated from the high voltage power-electronic system, a large DC level can be observed due to ground differences. Consider the circuit proposed by [6] in Fig. 3, which depicts a high-voltage differential amplifier measurement solution.

Fig. 3: Case I Voltage Measurement Circuit

TOPIC A. POWER ELECTRONICS

Proceedings of the 19th Southern African Universities Power Engineering Conference
SAUPEC 2010, University of the Witwatersrand, Johannesburg
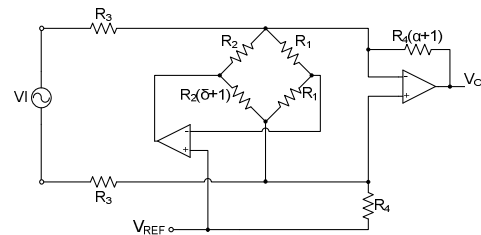
$$V_{O1} = \frac{-1}{R_3}\left\{\frac{(\delta+1)\left[R_1 R_3 R_4 \dfrac{\alpha+1}{\delta+2} + R_2 R_3 R_4 \dfrac{\alpha+1}{2}\right]}{R_1 R_3 R_4 + R_2 R_3 R_4 (\delta+1) + R_1 R_2 R_4 (\delta+1) + R_1 R_2 R_3 (\delta+1) - R_1 R_3 \dfrac{1}{\delta+2} - R_2 R_3 \dfrac{\delta+1}{2}}\right\} V_{CM} + \frac{-R_4(\alpha+1)}{R_3} V_{diff} \tag{1}$$

The circuit's high CMRR capability makes it a great option when high common-mode signals are experienced in the system. The transfer function for this circuit is given in (1), where V_{CM} is the common-mode noise component of the input signal and V_{diff} the differential component. This output voltage is then level shifted by V_{REF} for use by an ADC. Analysis of V_{CM}'s coefficient shows that it is an extremely small value. This corresponds with this circuit's characteristically high CMRR. The Wheatstone bridge in Fig. 3 has a high sensitivity and facilitates the active filtering of these common-mode components. Fig. 4 shows a signal of the converter being measured and the result of the measurement circuit in Case I.
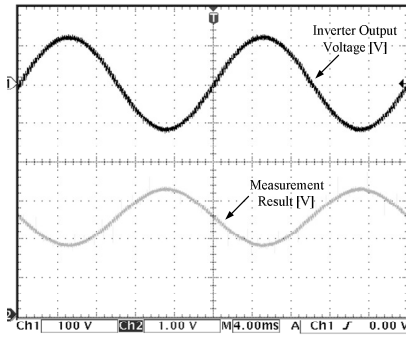
Fig. 4: Case I Voltage Measurement Results

It must be noted that the measurement result is an inverted representation of the inverter voltage which corresponds with the circuit's transfer function given by (1). Both contain a similar switching ripple as was chosen by the system discussed in section 2.1. Notwithstanding the inverted output, there is no additional phase error observed. This circuit has an increased common-mode input voltage range beyond the supply voltages and is highly capable of accurately represent the measured voltage. Simulations were done where a common-mode signal as large as 230 V_{RMS} was applied at the input and was effectively removed. Analysing the frequency response of this circuit, can be aided by looking at the Fast-Fourier-Transform (FFT) depicted in Fig. 5
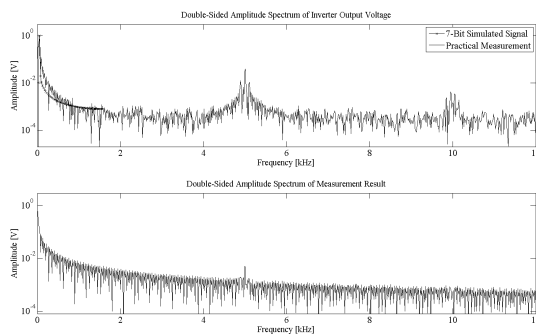
Fig. 5: Case I FFT of Inverter Voltage and Measurement

The increased harmonic distortion between the fundamental- and switching frequency is due to a low

resolution reference signal. A FFT of a sinusoidal signal which is digitized at a 7-bit resolution is also shown in Fig. 5. Notice the similarity between the FFT of the digital signal and the measured signal. Comparing the fundamental and switching frequencies between the input- and output signals points out the poor SNR and THD+N of this solution. A great deal of frequency information is lost, but will be irrelevant when using SAR-based acquisition solutions, since an averaging sampling scheme is used, which effectively disregards high frequency components. Conclusively, this solution is recommended to be used in conjunction with a SAR ADC.

2.2.2 Case II

The circuit in Fig. 6 was proposed by [9] and forms part of a complete differential-signal chain driving a full differential ADC.
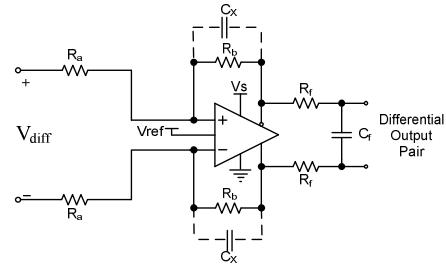
Fig. 6: Case II Voltage Measurement Circuit

It is common practice to place a LPF on the output signal to filter out high-frequency noise. This can be achieved by either using a RC network such as R_f and C_f or by including capacitors, C_X, in the feedback path. It is advisable to avoid the latter solution, since it results in the op amp driving a capacitive load. This results in a high-frequency oscillation on the output signal as can be seen in Fig. 7:
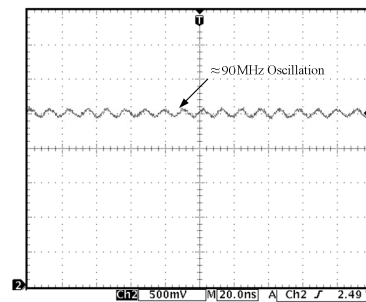
Fig. 7: Oscillation due to Capacitive Loading

The transfer function from the output of the amplifier to the input is given by equation (2):

$$V_O = \frac{R_b}{R_a} V_{diff} + \frac{0}{2R_a} V_{cm} \tag{2}$$

$$V_O = \frac{R_b}{R_a} V_{diff}$$

The resulting signal is then offset by V_{ref}. The circuit's performance can be investigated by looking

Proceedings of the 19th Southern African Universities Power Engineering Conference
SAUPEC 2010, University of the Witwatersrand, Johannesburg

TOPIC A. POWER ELECTRONICS

at Fig. 8, which shows both the voltage measured by the circuit and its corresponding output. Due to the differential format of the output, the signal has no DC offset, giving an accurately scaled representation of the measured signal with no amplitude- or phase error observed.
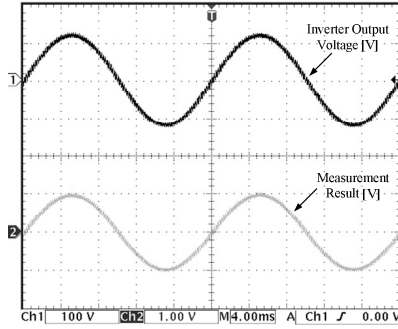
Fig. 8: Case II Measurement Results

The frequency performance can be seen by examining Fig. 9, which depicts the FFT of the signals shown in Fig. 8:
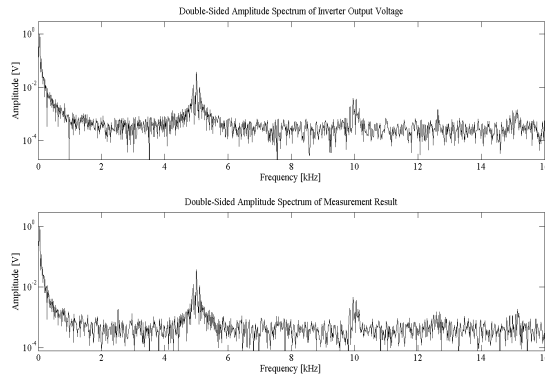
Fig. 9: Case II: FFT of Inverter Voltage and Measurement

Notice that the FFT of the signals compare excellently with each other. The ratio between the switching frequency and its harmonics to the fundamental frequency is nearly equal. The THD+N and SNR of this circuit are therefore very good.

2.3 Current Measurement

Numerous solutions exist in realizing current measurements in PEC systems. Some of these are discussed by [3]:
  i. Current Transformers (CT): This measurement method has the advantage of providing protection through galvanic isolation along with a scaled representation of the primary current, but has the drawback of being limited to AC measurements [3]. It furthermore has a limited spectrum of frequencies depending on the core material of the transformer [10].
  ii. Shunts: A current shunt circuit measures the small differential voltage across a resistive shunt. The switching of the converter, however, causes a large common-mode voltage and high slew rate. The result is highly corrupted measurement. As discussed in [11] the typical limiting factor is the self-heating of the shunts

due to I^2R losses. Temperature related errors however are not the primary contributor to overall errors. Other subtle errors such as current feed-point sensitivity, field coupling to the shunt, proximity of ferromagnetic materials and many others often dominate.
  iii. Hall-Effect Transducers: These provide excellent galvanic isolation and are not limited to AC signals. This component, nonetheless, has a limited measurement bandwidth, but with a range of 100-200 kHz, which is more than sufficient for most, if not all, power-electronic applications. Nevertheless, as pointed out in [12], the hall-effect sensor has a minor design problem in that it has a large gain at high frequencies, result in a highly distorted feedback signal in its closed loop circuitry.

2.3.1   Case I

The circuit shown in Fig. 10 is a simple solution utilizing a current transducer.
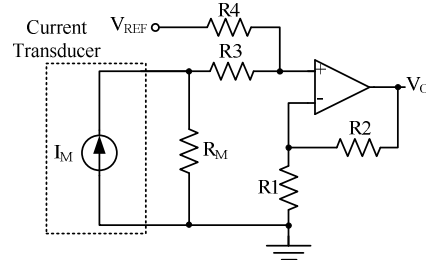
Fig. 10: Case I Current Measurement Circuit

The equation in (3) gives the transfer function for this circuit.

$$V_O = \left(1+\frac{R_2}{R_1}\right)\left(\frac{R_4}{R_3+R_4}V_{in}+\frac{R_3}{R_3+R_4}V_{ref}\right) \qquad (3)$$

where V_{in} is the voltage measured over resistor R_M. The current transducer provides a signal that is linearly proportional to the measured current. Consider Fig. 11 which show the output inductor current of the VSI discussed in Section 2.1.
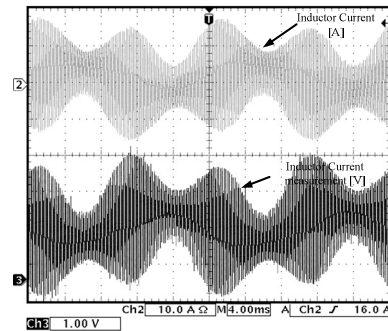
Fig. 11: Case I Current Measurement Results

The inductor current has this characteristic ripple as proven by [8] due to the value of the filter inductor according to equation (4) for a half-bridge topology:

$$\Delta i_L = \frac{V_d}{2L_{filt}f_c}\left(D-D^2\right) \qquad (4)$$

The circuit gives a good scaled representation of the

TOPIC A. POWER ELECTRONICS

Proceedings of the 19th Southern African Universities Power Engineering Conference
SAUPEC 2010, University of the Witwatersrand, Johannesburg

input current measurement. To analyse the THD+N and the SNR of this circuit, consider Fig. 12:
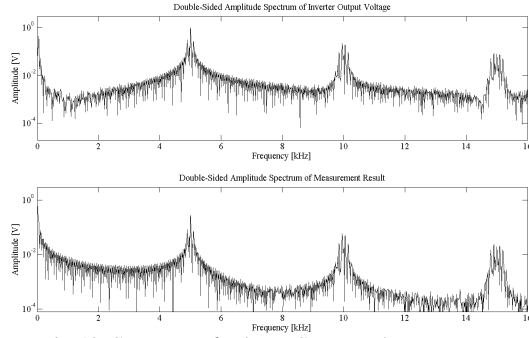
Fig. 12: Case I FFT of Inductor Current and Measurement

The noise floor is slightly distorted but the magnitudes of the fundamental and switching component compare excellently with one another.

2.3.2 Case II

Another current measurement solution is shown in Fig. 13:
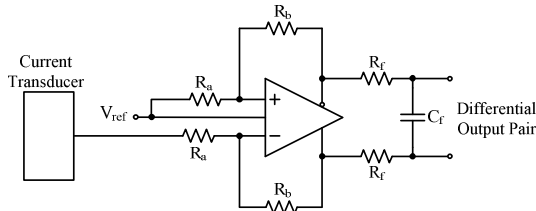
Fig. 13: Case II Current Measurement Circuit

This is a solution for a current measurement with a full-differential signal chain. The transfer function of this circuit is indicated by equation (5):

$$V_o = \frac{R_b}{2R_a}V_{ref} - \frac{R_b}{2R_a}V_{in} \qquad (5)$$

The response of this circuit can be seen in Fig. 14. The output signal in inverted as suggested by equation (6). No noticeable phase error occurs
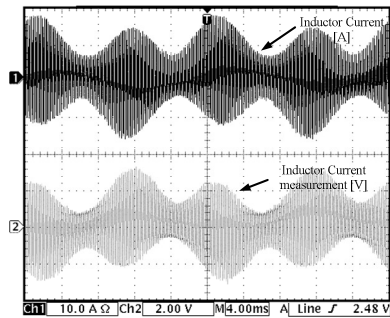
Fig. 14: Case II Current Measurement Results

The frequency response is shown in Fig. 15. Analysis of these FFTs shows a good correspondence between the input and output signals of this circuit. No significant amount of noise is added. Conclusively, the THD+N and SNR of this circuit are good.
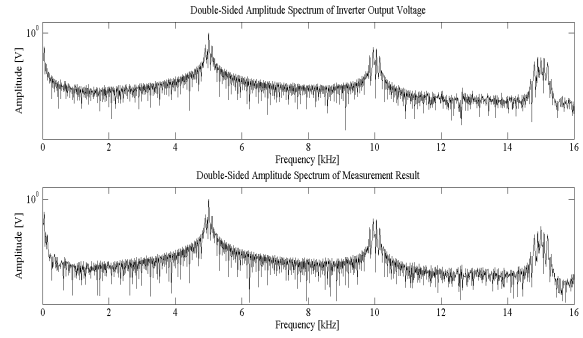
Fig. 15: Case II FFT of Inductor Current and Measurement

3. ACQUISITION SOLUTION

A brief discussion will be made on two of the most widely used ADC architectures in the industry. The successively approximated register (SAR) and the pipelined ADCs are very popular converters thanks to their relative high bit resolution and high sampling and conversion rates.

3.1 Referencing Realization

The ADC uses a reference voltage in its conversion process to produce the digital equivalent of the analog measurement. In the pursuit to remove common-mode noise on measurement results, this reference level needs to be as accurate as possible.
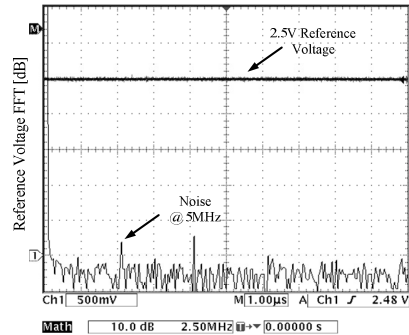
Fig. 16: Reference Voltage Measurement and FFT

Fig. 16 shows an oscilloscope screenshot of a 2.5 V reference voltage along with an FFT of the signal. Notice a large noise frequency component at 5 MHz. Such noise frequencies will not adversely affect measurement result, since it will be outside the frequency spectrum to which the measurement system has been designed. It is also a common practice to low-pass filter (LPF) the measurement results to eliminate such unwanted high frequency noise.

These noise components will, however, have a significant impact on the conversion results of the ADC. Even though the sampling rate of an ADC will be below these high frequency noise components, eg. 1 MSPS, the comparators used in the ADC operate at integer multiples of the sampling rate. Given that

$$1LSB = \frac{V_{range}}{2^{bit}} \qquad (7)$$

where LSB is a least significant bit, V_{range} refers to the analog dynamic range and bit being the resolution

Proceedings of the 19th Southern African Universities Power Engineering Conference
SAUPEC 2010, University of the Witwatersrand, Johannesburg

TOPIC A. POWER ELECTRONICS

of the ADC. Conclusively, any noise magnitude in the order of 1 LSB will corrupt the digital output code by one LSB. The noise will therefore directly affect the comparator results.

3.2 SAR

Descriptions in [13] and [14] show that a SAR functions by implementation of a binary search algorithm. A comparison is performed by determining if V_{IN} is greater or less than V_{REF}. A logic state is generated based on the result of this comparison, resulting in a digital equivalent of the analog signal. This can easily be understood by considering Fig. 17:
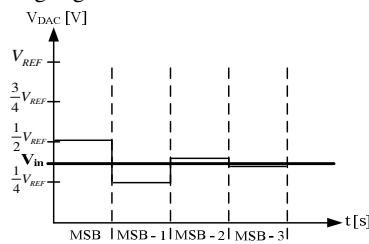
Fig. 17: SAR Architecture Functional Depiction

SAR ADCs are mostly used by doing a conversion every modulation period, resulting in a signal bandwidth limited to the modulation frequency. It is therefore recommended to use this architecture in conjunction with the circuit mentioned in section 2.2.1.

3.3 Pipelined

As explain in [15] and [16], this architecture utilizes parallel conversion, where the architecture is sub-divided into multiple stages with each converting a certain part of the analog input signal. Each stage consists of flash ADCs making it capable of achieving high sample- and throughput-rates. Thanks to these high rates, this architecture is best suited with measurement solutions that have great frequency performance. Such as the circuits in sections 2.2.2 and 2.3.2

4. CONCLUSION

A comparative study was done on two voltage measurement circuits and two current measurement circuits. Circuit accuracy and performances were discussed and compared. Furthermore, a brief discussion on popular ADC architecture and its application were done.
When an averaging scheme is used which disregards switching frequency components, it is recommended to use the *Case I* solutions along with a SAR ADC. If, however, high bandwidth control algorithms are used which are dependent on measurement data being acquired at very high sampling rates, the *Case II* solutions in conjunction with a high sampling Pipeline ADC is recommended.

REFERENCES

[1] L. T. Jakobsen, H. Schneider, and M. A. E. Andersen, "Comparison of State-of-the-Art Digital Control and Analogue Control for High Bandwidth Point of Load Converters," in *Applied Power Electronics Conference (APEC-08)*, 2008, pp. 1440-1445.

[2] L.-j. Hang, Z.-y. Lu, X.-w. Liu, and Z. Qian, "Comparison Research of Digital and Analog Control For Single-Stage Power Factor Correction AC/DC Converter," in *Industrial Electronics Conference (IECON-07)*, 2007, pp. 1466-1471.

[3] J. A. du Toit, "Development and Analysis of a Distributed Control Strategy for Power Electronic Converters," Stellenbosch University Thesis, 2002.

[4] J. A. du Toit, D. D. Bester, and J. H. R. Enslin, "A DSP based Controller for Back to Back Power Electronic Converters with FPGA Integration," *IEEE Applied Power Electronics Conference (APEC-97),*, vol. II, no. 12, pp. 699-705, 1997.

[5] S. Buso and P. Mattavelli, *Digital Control in Power Electronics*, 1st ed. Morgan & Claypool, 2006.

[6] P. Horowitz and W. Hill, *The Art of Electronics*, 2nd ed. Cambridge, 1989.

[7] S. Paterson. Maximize Performance when Driving Differential ADCs. EDN Design Engineering Magazine Article. [Online]. http://www.edn.com

[8] F. Koeslag, "A Detailed Analysis of the Imperfections of Pulsewidth Modulated Waveforms on the Output Stage of a Class D Audio Amplifier," PhD Thesis, Stellenbosch University, Stellenbosch, 2008.

[9] C. F. Breet, "Personal Communication," Stellenbosch University, 2009.

[10] D. W. Ackermann, "Current Transformer Measurements of Distorted Current Waveforms with Secondary Load Impedance," in *AFRICON*, 1999, pp. 765-768.

[11] D. E. Destefan and R. S. Stant, "AC and DC Shunts - Can You Believe Their Specs?," in *Instrumentation and Measurement Technology Conference (IMTC)*, 2003, pp. 1577-1582.

[12] J. Pankau, D. Leggate, D. W. Schlegel, R. J. Kerkman, and G. L. Skibiniski, "High-Frequency Modeling of Current Sensors," *IEEE Transaction on Industry Application*, vol. 35, no. 6, pp. 1374-1382, Nov. 1999.

[13] Maxim Integrated Products. Understanding SAR ADCs. Application Note.

[14] W. Kester. ADC Architectures II: Successive Approximation ADCs. Analog Devices.

[15] W. Kester. ADC Architectures V: Pipelined Subranging ADCs. Analog Devices.

[16] Maxim Integrated Products. Understanding Pipelined ADCs. Application Note.

TOPIC A. POWER ELECTRONICS

Proceedings of the 19th Southern African Universities Power Engineering Conference
SAUPEC 2010, University of the Witwatersrand, Johannesburg

INTRODUCING TAPPED TRANSFORMERS AND COUPLED INDUCTORS IN HIGH FREQUENCY ISOLATED POWER CONVERTERS WITH VARYING SOURCE VOLTAGE

D C Pentz* and A L J Joannou*

*University of Johannesburg, Industrial Electronics Technology Research Group, Auckland Park Campus, Johannesburg.

Abstract.   Tapped transformers are often used for voltage regulation in low frequency applications. Tapped secondary transformers are found in high frequency converters but usually only on the secondary windings to provide multiple isolated output voltages. This paper is aimed at investigating the use of multiple switched primary transformer taps in applications where the supply voltage varies over a wide range. A few of the standard converter topologies, modified to accommodate multiple primary taps, are shown and the principle is demonstrated on a push-pull topology.

Key Words. Tapped transformers, high frequency converters, varying source voltage.

1.   INTRODUCTION

Multiple secondary transformer taps are often used in isolated converters to provide various voltage levels while only using one set of switches [1]. In these cases it is possible to regulate the output of one of these secondary taps through feedback control by adjusting the pulse width of the converter driver signals.

Multi-tapped primary side windings are common in low frequency applications and are often used for voltage regulation. This practice has however not been considered widely in high frequency converter applications [2].

Power electronic converters are almost always designed with the assumption that the source voltage only varies to a limited degree and that the desired output voltage can be maintained through duty cycle control on the buck, boost or buck-boost converters used in these applications.

Renewable energy utilization has become an important field of research in recent years, one of the main factors being the affordability of the systems and components [4]. Cheap wind generators, designed for low power applications below 1kW, may not have variable pitch rotor blades. Field control may also not be an option because of the use of permanent magnets as opposed to wound field coils. The output voltage, which is simply a function of the wind speed for these generators, may then vary over a wide range. Duty cycle control of the converter output voltage then becomes limited and the efficiency of such a converter is also affected in the process. Generators required for higher power levels are more expensive and have added features which assist voltage regulation as a function of wind speed.

Multi-node converter concepts are currently being developed and if the interconnection of the secondary nodes can be automated, these converters should also be capable of handling variation in input voltage by reconfiguration of the output nodes. Time delays may however occur in the process and increased output capacitance will be required to compensate for these delays.

This work investigates the use of tapped high frequency transformer or coupled inductor windings to address the problem at hand. If the output voltage cannot be maintained accurately through duty cycle control any more, it is suggested here that the turns ratio of the transformer or coupled inductor is simply changed to allow the operating point to return to a position where fluctuations in the input voltage can be handled better.

The converters used in small installations below 1kW, have to be cheap and simple. Fly-back converters, buck-boost converters [3] and sepic converters are often used due to their low component count. A few of the simple isolated converters are listed here in an effort to show how the topologies may be adapted to accommodate multiple primary windings. It should be pointed out at that an added level of complexity should be expected. It is possible to obtain the same result by simply using multiple converters, each with its own switches and transformers or coupled inductors designed to operate optimally in a specific range of supply voltage and only one of them may then be operated at a time. The proposed solution is aimed at using the same magnetic component with multiple primary windings. A push-pull converter will be used to verify the concept and to point out the effect of the tapped windings in the transformer on the switch voltage ratings.

2.   CONVERTER TOPOLOGIES

2.1 Fly-back converter

Figure 1 shows the circuit diagram of a fly-back converter. The primary winding comprises a number of turns and the output voltage of the converter is

Proceedings of the 19th Southern African Universities Power Engineering Conference
SAUPEC 2010, University of the Witwatersrand, Johannesburg

TOPIC A. POWER ELECTRONICS

simply determined by equation (1) [6] where D is the duty cycle.

$$\frac{V_o}{V_d} = \frac{N_s}{N_p} \frac{D}{1-D} \qquad (1)$$

The open circuit switch voltage is given by equation (2) and it is evident that as the duty cycle increases the output voltage increases and the switch voltage decreases during the off intervals.

$$V_{sw} = V_d + \frac{N_1}{N_2} V_o = \frac{V_d}{1-D} \qquad (2)$$

For simplicity of the analysis a 50% duty cycle is chosen. The rated voltage of the fly-back converter switch should be at least twice the value of the supply voltage.
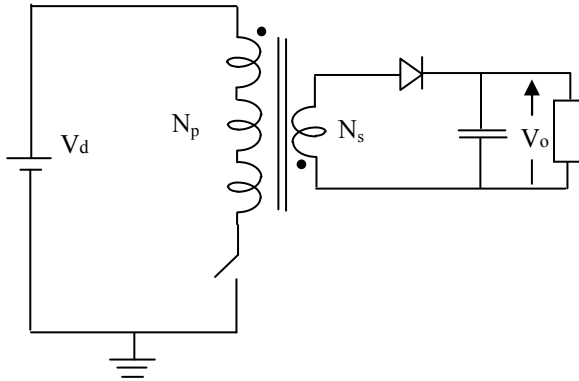
Fig. 1. Fly-back converter

Figure 2 illustrates the proposed strategy where the turn ratio of the coupled inductor is controlled with two additional switches. Only one of the switches will be modulated for a given range of supply voltage. The main concern is what effect the modulation of a specific switch has on its own open circuit voltage as well as that of the other switches in the circuit.

An analysis is performed for each of the possible combinations. Consider $N_{p1} = N_{p2} = N_{p3} = N_s$ for the moment. The duty cycle is still 50%. The values of the open circuit voltage for each switch are listed in table 1 for each of the cases where the switches S_1 through S_3 are operational. Keep in mind that V_d is not constant. The fact that the source voltage lowered in the first place necessitates S_1 and S_2 being modulated as opposed to the single switch fly-back converter. For this application the options for the turn ratio are 1:1, 2:1 and 3:1. With V_d equal to one third of the nominal source voltage V_{nom}, the turn ratio of 1:1 will be used, for $V_d = 2V_{nom}/3$ the 2:1 ratio and if the source voltage is equal to the initial design value the turn ratio will be 3:1. The worst case open circuit voltages are listed in the same table in terms of V_{nom} showing that for the chosen turns ratios the switches are not stressed more than usual.

Not all the equations used to obtain the results in table 1 are listed here. For the turns ratio 1:1, the equations (3), (4) and (5) are listed below.

$$V_{S1oc} = 2V_d \qquad (3)$$

$$V_{S2oc} = 2V_d + \frac{N_{p2}}{N_{p1}} V_d \qquad (4)$$

$$V_{S3oc} = 2V_d + \frac{N_{p2}}{N_{p1}} V_d + \frac{N_{p3}}{N_{p1}} V_d \qquad (5)$$

Table 1: Open circuit switch voltages

Operational switch	S_1	S_2	S_3
V_{S1oc}	$4.0V_d =$ $1.66V_{nom}$	$2.5V_d =$ $1.67V_{nom}$	$2.00V_d =$ $2.00V_{nom}$
V_{S2oc}	$3.0V_d =$ $0.99V_{nom}$	$2.0V_d =$ $1.33V_{nom}$	$1.67V_d$ $=1.66V_{nom}$
V_{S3oc}	$2.0V_d =$ $0.66V_{nom}$	$1.5V_d =$ $1.00V_{nom}$	$1.33V_d =$ $1.33V_{nom}$

These results were confirmed through simulation and experimental work. Conditions for different turns ratio's and duty cycles may be obtained in a similar way. The design method of the fly-back converter will probably have to be revised to make sure that it is still applicable in this case since the primary inductance changes with the addition of more primary turns.
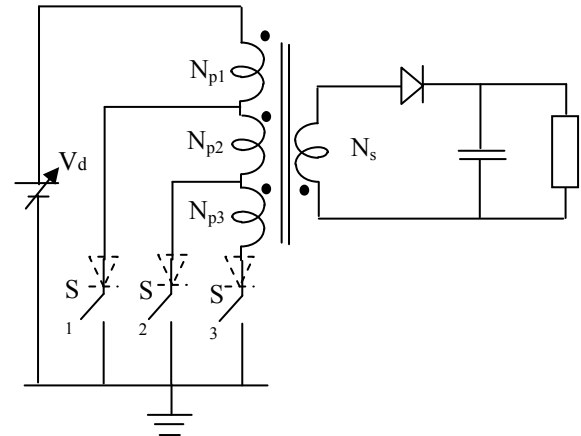
Fig. 2. Fly-back converter with tapped coupled inductor

Additional diodes need to be added in series with at least switches 2 and 3 of the shown topology. If S_1 is operated the voltage induced in primary windings N_{p2} and N_{p3} will forward bias the body diodes of the MOSFET switches S_2 and S_3 causing high short-circuit currents to flow through S_1.

2.2 Push-pull converter

A push-pull converter is shown in figure 3. This converter is also relatively simple since no high side drivers are needed. The symmetry of the driver signals needs to be maintained at all times to prevent core saturation. The open-circuit switch voltages are

TOPIC A. POWER ELECTRONICS

Proceedings of the 19th Southern African Universities Power Engineering Conference
SAUPEC 2010, University of the Witwatersrand, Johannesburg

the same as for the fly-back converter and have also been verified through simulation. The diodes in series with the switches prevent the problem described in the previous section. This converter is used in the experimental phase.
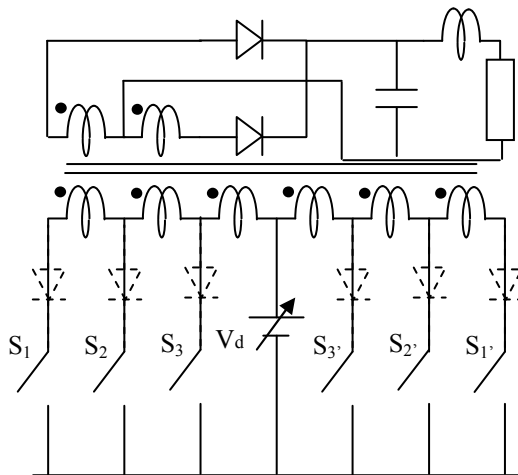
Fig.3. Push-pull converter with multiple primary transformer taps

2.3 Full-bridge converter

The full-bridge topology with added primary windings in figure 4 is shown but not analyzed in this work because they are suited for higher power applications than the application presently considered. The switches required to change the effective turn ratio of the transformer have to allow bi-directional current flow and they also need to be driven using isolated drivers, further complicating the practical implementation.
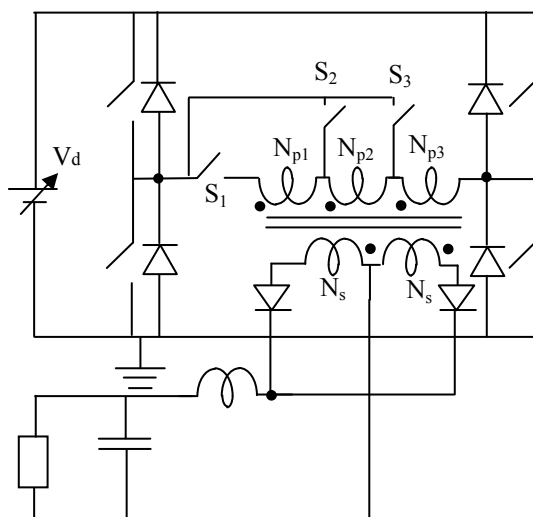
Fig.4. Full bridge converter

3. EXPERIMENTAL VERIFICATION

For experimental purposes a 30W push-pull converter is constructed. The transformer has three primary taps of three turns each and a 6 turn secondary, making turns ratios of 3:6, 6:6 and 9:6 possible. It should again be emphasized that the

leakage inductance of the transformer and any layout stray inductance should be minimized. Since the experimental setup is done on breadboard, the layout inductance is unavoidably high, the main reason for the limited power levels achieved in this experiment. Table 1 has shown that the outer switches experience open-circuit voltages four times the supply voltage with the 1:1 ratio and any overshoot on these switches are also multiplied by the same factor. The total number of primary turns is determined by the maximum input voltage and simply divided by three to form the different taps. The six primary windings are individually wrapped in copper foil conductors which in turn are arranged in a centre-tap configuration.

A block diagram of the experimental setup is shown in figure 5 and a photograph of the physical hardware with an insert of the low leakage inductance transformer is shown in figure 6.
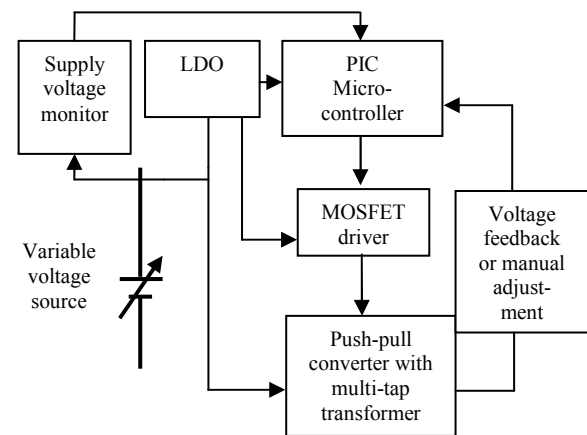
Fig. 5. Block diagram of experimental setup

During the experimental phase only one MOSFET driver is used and the desired operating switches are selected manually. In an actual application the cost of multiple drivers has to be weighed against a single driver with additional components required to route the driver current to the correct switches.
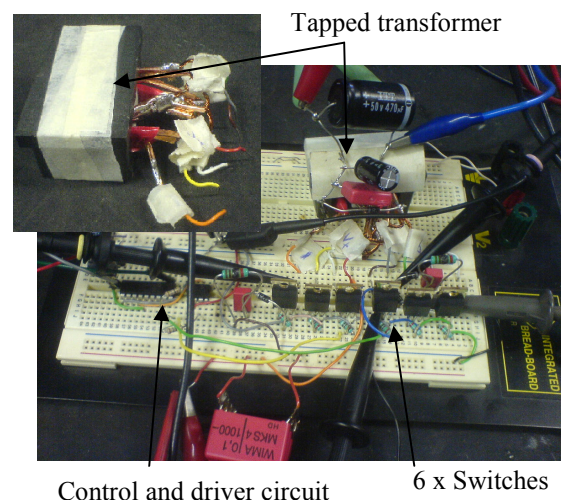
Fig. 6. Photograph of experimental setup

Proceedings of the 19th Southern African Universities Power Engineering Conference
SAUPEC 2010, University of the Witwatersrand, Johannesburg

TOPIC A. POWER ELECTRONICS

The output voltage is regulated at 11V whilst trying to adjust the input voltage between 5V and 30V. The trends for the full range of values are shown as a function of the input voltage in figure 7.
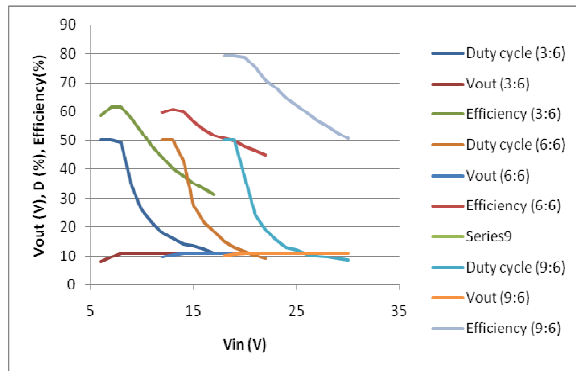
Fig. 7. Graphical representation of results

Running the converter at duty cycle values close to minimum and maximum values result in poor regulation with variation in load conditions and should be avoided. The efficiency of the converter also varies as a function of duty cycle. It is clear from the results that the tap changes are required to sufficiently cover the variation in the input voltage without sacrificing efficiency.

Table 2 shows the duty cycle range and efficiencies for the different turn ratios. The recommended ranges of input voltages listed in the same table are a result of the mentioned duty cycle limitations while trying to maintain the highest possible efficiency.

Table 2. Tap utilization

Turns ratio	Vd (V)	D (%)	Efficiency (%)
3:6	8-14	49-14	62-38
6:6	14-20	43-12	60-48
9:6	20-30	37-9	78-51

Figure 8 gives a graphical representation of the efficiency of the converter as a function of the duty cycle for the three different tap arrangements. The step-up tap selection displays the lowest overall efficiency because the primary transformer and switch currents are higher for the same output power. The step-down tap selection has the highest overall converter efficiency but cannot cover the full range of input voltage.

4. CONCLUSION

This work successfully illustrates the concept of using multiple switched transformer taps in a high frequency application. The wide range of variation of input voltage is compensated for by adjusting the turns ratio.

Voltage waveforms are not shown in the paper but the expected peak values for the different input voltage levels were obtained as discussed in table 1.
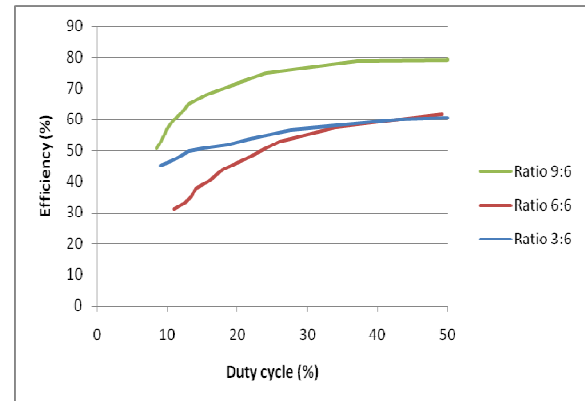
Fig. 8. Graphical representation of efficiency as a function of duty cycle.

The experimental results were obtained with snubbers in the switching circuits [7]. Snubbers obviously reduce the efficiency of the converter and work is currently being done to improve the layout and reduce transformer leakage inductance so as to avoid the necessity for snubbers at higher power levels.

The feedback loop still needs to be closed and the switch-over process should be automated once the desired duty cycle ranges are established.

The successes of this work justify further work being done on other converter topologies. Utilizing this concept is presently being investigated as a means of improving the power factor of high frequency power converters.

REFERENCES

[1] Rajapandian Ayyanar, Ned Mohan, "A Novel Full-Bridge DC–DC Converter for Battery Charging Using Secondary-Side Control Combines Soft Switching Over the Full Load Range and LowMagnetics Requirement", *IEEE Transactions on industry applications*, vol. 37, no. 2, March, 2001.

[2] V. Tarateeraseth, C. Tantisukarom, W. Khanngern, S. Nitta, " A Study of the EMI Characteristics of an Off-ine Single-Stage AC/DC Flyback converter with PFC-tapped Transformers.", *ICEMC*, Bangkok, 2002.

[3] J J Albrecht, J Joung, W A Peterson, "Boost-buck push-pull converter for very wide input range single stage power conversion.", *Proceedings of Applied power electronics conference and exposition*, APEC'95, part 1, vol.1, pp. 303-308, March 1995.

[4] M H Rashid, "Power Electronics for Alternative Energy Sources.", *11th IEEE International Power Electronics Congress*, CIEP 2008.

TOPIC A. POWER ELECTRONICS

Proceedings of the 19th Southern African Universities Power Engineering Conference
SAUPEC 2010, University of the Witwatersrand, Johannesburg

[5] N Mohan, T Underland, W Robbins, "Power Electronics-Converters, Applications and Design", Third Edition, John Wiley & Sons, INC.

[6] Xiaocheng Jing, Philip K.T. Mok and Ming Chak Lee, "A Wide-Load-Range Single-Inductor-Dual-Output Boost Regulator with Minimized Cross-Regulation by Constant-Charge-Auto-Hopping (CCAH) Control", *Proceedings IEEE Custom Intergrated Circuits Conference (CICC)*, 2009.

[7] M Brown, "Power Supply Cookbook", Second Edition, Boston Oxford Johannesburg.

Topic B

Machines

TOPIC B. MACHINES

Proceedings of the 19th Southern African Universities Power Engineering Conference
SAUPEC 2010, University of the Witwatersrand, Johannesburg

A finite-element-based optimization tool for linear generators

S. Gerber, J.M. Strauss

Stellenbosch University, Department of Electrical and Electronic Engineering, Stellenbosch, South Africa

Abstract. This paper discusses a finite-element-based optimization tool for short stroke tubular linear generators and illustrates it's use by means of an example. An overview of the finite-element code used as foundation for the tool is given and it's strengths and weaknesses are highlighted. The original code was modified to make it more suited to the simulation of short stroke linear machines. Additional code was written to improve the usability and to extend the functionality of the tool. The capabilities of the tool is discussed with specific focus on how it can be used to evaluate and optimize a given linear generator topology. The use of the tool is demonstrated by means of an example which illustrates that the tool is flexible and can make use of different optimization strategies. The final simulation results are validated by a comparison with results obtained using *Magnet 6*.

Key Words. linear generator, finite-element, optimization

1. INTRODUCTION

As the urgency of harnessing renewable sources of energy increases, research in energy conversion techniques has seen rapid growth. As a result, new challenges in generator design have arisen. For example, free piston Stirling engines hold numerous advantages when compared to their kinematic counterparts. These engines provide short stroke reciprocating movement ill-suited to rotary generators. In this case, the need for a short stroke linear generator arises. In the design of generators, it is desirable to optimize a specific topology so that the end product performs well and can be produced cost-effectively. To this end, a finite-element-based optimization tool for linear generators was developed using an existing finite-element code as foundation. Improvements were made to the original code to make it more usable and better suited to the analysis of short stroke linear generators. The tool, from here on referred to as SEMFEP (Stellenbosch Electrical Machines Finite-Element Program), was used to optimize a specific topology, making use of several different optimization methods. Finally the results obtained are validated by comparison with results obtained using *Magnet 6*.

2. OVERVIEW OF THE ORIGINAL FINITE-ELEMENT CODE

2.1 General overview

The finite-element code used as foundation is the Fortran implementation as presented by Wang et al. [1]. This code was used because of the following strengths:

- The code makes use of a Cartesian Air-Gap Element (CAGE) which is ideally suited to time-stepped simulations with motion because it avoids remeshing of the airgap and gives accurate results of the airgap field.
- The Fortran source code is directly accessible. This encourages a better understanding of the underlying calculations and allows greater flexibility in the use of the code.

- The code is fast – an important advantage due to the iterative nature of optimization algorithms.

Unfortunately, there were also a number of negative aspects to the implementation. The most important short comings were the following:

- The implementation was written in Fortran 77, an old standard upon which many improvements have been made in more recent years.
- The program performed many unnecessary file operations related to simulation inputs and outputs. This can be ascribed to the fact that the code was written in an era when memory usage was critical and had to be minimized. These specific operations are unnecessary on modern computers. Not only did these file operations have a negative impact on performance, but it also complicated the task of following the work flow of the program.
- The program was structured in such a way that the input describing a machine was split across multiple files which were very hard to interpret.
- Machines were drawn in the correct format for this code using a scripting approach. No graphical interface was available. This in itself was not a problem, however, drawing machines was a tedious process because of a lack of convenience functions. This was a major obstacle in making the tool easy to work with.
- The original code's graphical output capabilities were somewhat limited. This proved to be a major disadvantage.

In general, the program was poorly structured and although it was capable of producing good results, it was not very easy to work with and could make better use of the powerful tools available to modern programmers. Because of all the above mentioned difficulties it was decided to put the implementation through a complete clean-up process and make the changes that would allow the use of Fortran 95 instead of Fortran 77. The aim was to produce code that is more understandable and easier to work with and to improve performance.

Proceedings of the 19th Southern African Universities Power Engineering Conference
SAUPEC 2010, University of the Witwatersrand, Johannesburg

TOPIC B. MACHINES

2.2 Post-processing

This section describes some useful calculations that were already implemented in the original code. Only small modifications to these calculations were necessary.

The flux linkage, λ, of a coil can be obtained. The calculation involves integrating the magnetic vector potential over the surface area of the coil.

The magnetic force in the direction of movement on the translator, f_{mag}, can be obtained. Because the original implementation is targeted at rotary machines, the force was converted to a torque. A simple modification yields the force. The calculation is based on Maxwell's tensor. Details of this calculation are discussed by Abdel-Razek et al. [2].

3. OVERVIEW OF SEMFEP

3.1 Component description

The tool consists of a collection of components as illustrated in figure 1. The assembler draws the machine in the correct format for the mesher based on input provided by the user. The mesher generates a mesh and optimizes it by maximizing the smallest angle of all the triangles. The preprocessor performs CAGE related operations, sets up the boundary conditions and generates other data needed by the solver. The solver calculates the magnetic vector potential at every node. This step is repeated for a number of different positions of the translator. A new position is easily generated by modifying the CAGE. During the post-processing step the flux linkage, the magnetic force as well as all the outputs described in the next section are generated. SEMFEP offers the option to display the output – which can be quite comprehensive – graphically.

The components inside the dashed box represent a single simulation of a machine. For optimization purposes, a simulation is wrapped inside another program. This program repeatedly runs simulations with different values of the input parameters and finds the best design. Because it is often desirable to run different optimizers on the same problem, SEMFEP was designed so that it is easy to integrate a single simulation in different environments. An example illustrating how a simulation can be run from a Python environment is given in the next section. Running different optimization algorithms on the same problem allow results to be compared and the validity of optima to be verified.

Because the source code for all the components are available, it is possible to extend the tool by adding new functionality such as is recommended at the end of this paper.

3.2 Modifications to the original code

During the clean-up process, improvements were made to the code's structure and unnecessary file
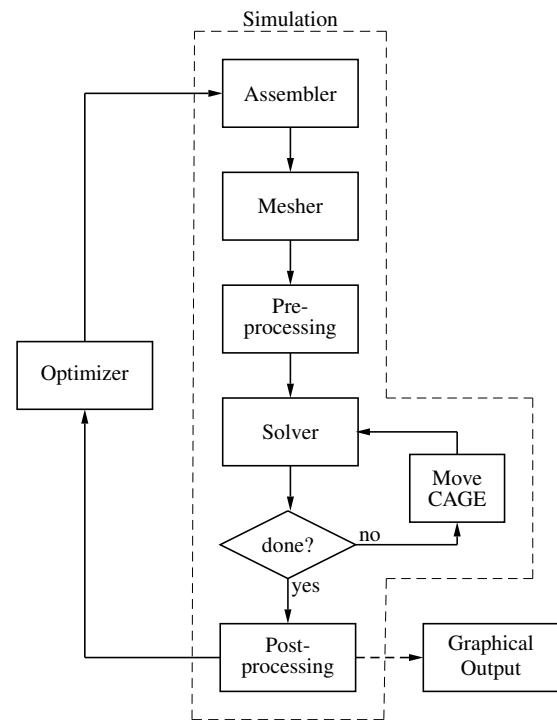
Fig. 1: Components of the tool

```
import semfep

input = [20e-3, 20e-3, 40e-3]
output = semfep.simulate(input)
```

Listing 1: Running a wrapped simulation in Python

operations were removed. This did have the desired effect of making the work flow of the program easier to follow. The option still exists to write all the generated data to files for the purpose of debugging, but the new implementation passes all data directly in memory from one component to the other. This had a positive effect on the performance of the code.

One goal of this project was to enable the use of Python, a powerful high-level open source scripting language, for optimization purposes. This was accomplished by wrapping an entire simulation with *f2py*, a tool that allows Fortran routines to be called directly from Python. Listing 1 shows just how simple it is to run a simulation from Python this way. The example in this paper was optimized using Fortran and Python optimizers.

Python, together with an extension called *matplotlib*, is also capable of producing high quality graphs. For this reason, all graphical output was done using Python.

The input mechanism of the implementation was completely restructured. A Fortran 95 module was used as a centralized point of input, eliminating the use of multiple files and ensuring that variables are not duplicated. Variables declared in this module can even be passed to Python functions, ensuring that no duplication occurs, even across different languages.

TOPIC B. MACHINES

Proceedings of the 19th Southern African Universities Power Engineering Conference
SAUPEC 2010, University of the Witwatersrand, Johannesburg

This allowed Python to be used for post-processing calculations as well.

The original implementation was primarily designed to simulate rotary axial flux permanent magnet machines. Typically only a section of a machine would be simulated and a periodic model would be used. This is not ideal for the type of linear generator under discussion because it is usually not possible to represent the machine with a periodic model or, in other words, to neglect the effects at the ends of the machine. For this reason, machines are drawn with an air box around them, sufficiently large so that fields at the extremities of the model are negligible.

Assembler

The assembler is the component responsible for drawing a machine in the correct format for the solver. As mentioned earlier, the original Fortran assembler was not very easy to work with. This problem was solved by completely reimplementing the assembler in Python. The new Python assembler is still based on the scripting approach – which is desirable for optimization purposes – but a multitude of convenience functions have been written to simplify the drawing of machines.

Constant time-stepping vs. constant displacement-stepping

Another important difference between rotary and short stroke linear machines is that the speed of the rotor is constant in the former case but the speed of the translator is sinusoidal in the latter case. This implies that either the displacement of the translator or the time steps have to vary sinusoidally in a time-stepped simulation. It was decided to implement a constant displacement of the translator at every time-step and to vary the time-steps sinusoidally. In this way, accurate flux linkage and force data is obtained over the entire range of translator displacements. However, when this data is plotted as a function of time, the data points are not evenly spaced, but further apart where the translator speed is low and closer together where the translator speed is high. For a half period simulation, the time at time-step n out of N is then given by

$$t(n) = \frac{1}{2\pi f} \arccos(1 - \frac{2n}{N}) \qquad (1)$$

where f is the frequency of oscillation.

Post-processing

The original post-processing code was applicable to three-phase machines and could not be used for the purposes of this tool. The calculations described in the next section were newly implemented, making use of Fortran and Python. The original implementation calculated derivatives using backward differences. Improvements which were made to this numerical
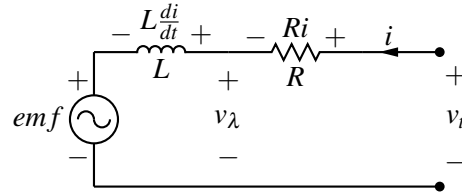
Fig. 2: Circuit model of the linear generator

differentiation technique is discussed in more detail in the next section.

4. SIMULATION OUTPUTS

4.1 Overview

This section describes the outputs of a simulation. All of the calculations in this section were implemented by the author. The circuit model used for the type of linear generator under discussion is shown in figure 2. Note that the current i is an input to the simulation and can be assumed to be sinusoidal (or any other waveform) for the case in which the generator is driven by a power electronic converter. This assumption was made for the purpose of this discussion. The current at time-step n out of N is given by

$$i(n) = I \cos\left(2\pi f t(n) - \phi\right) \qquad (2)$$

where I is the peak value of the current, ϕ is the phase shift of the current and $t(n)$ is given by (1).

The continuous derivatives and integrals that appear were first implemented by finite differences and trapezoidal integration respectively. Results obtained in this way were not sufficiently accurate however. Greater accuracy was achieved by using cubic-spline representations of the data which can be differentiated and integrated analytically. The use of Python greatly simplified these calculations because all the necessary functions are available in the *scipy* extension of Python. Figures 3 and 4 show a comparison between different numerical differentiation techniques where v_λ was calculated according to equation 7. It is clear that the spline technique performs much better in areas where points are not very closely spaced, as is emphasized in figure 4. With the sinusoidal time-stepping scheme discussed in section 3.2 generating unevenly spaced points, areas such as is illustrated in figure 4 will always occur. For this reason, a good differentiation technique is vitally important.

4.2 Resistance

The equivalent winding resistance of the machine is calculated as

$$R = \frac{N_p R_c}{N_{||}^2} \qquad (3)$$

where N_p is the number of coils and $N_{||}$ is the number of parallel circuits. R_c is the resistance of a single coil

Proceedings of the 19th Southern African Universities Power Engineering Conference
SAUPEC 2010, University of the Witwatersrand, Johannesburg

TOPIC B. MACHINES
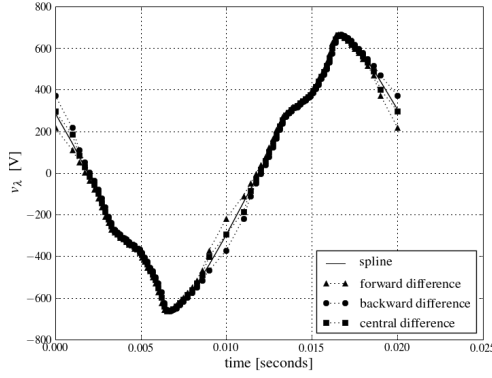
Fig. 3: Comparison of differentiation techniques
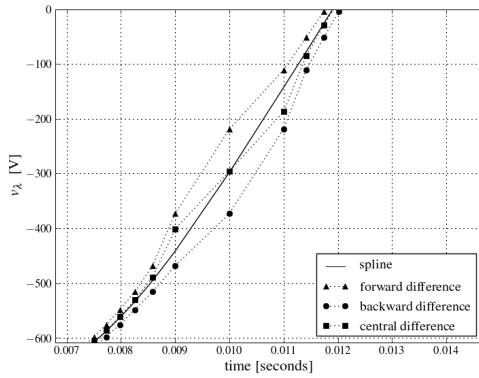
Fig. 4: Comparison of differentiation techniques: close-up

and is calculated as

$$R_c = \frac{l}{\sigma A} \qquad (4)$$

where l is the length of wire used in the coil, σ is electrical conductivity of the copper and A is the cross sectional area of the wire.

4.3 Inductance

The equivalent inductance is calculated as

$$L = \frac{N_p L_c}{N_{||}^2} \qquad (5)$$

where L_c is the inductance of a single coil. L_c is determined by a single dedicated simulation with all magnets "switched off" and a test current exciting a single coil. L_c is then calculated as

$$L_c = \frac{\lambda}{I_t} \qquad (6)$$

where λ is the flux linking the coil and I_t is the magnitude of the test current. In general, inductance is a function of both translator position and current. The aim of this calculation is to obtain a good average. This implies that the test current and, in some cases, the position of the translator have to be chosen carefully. SEMFEP is also capable of calculating the positional values of the inductance, but this is computationally more expensive. This can be used to validate the obtained average.

4.4 Electromotive force and terminal voltage

The voltage, v_λ, is calculated as the derivative of the flux linkage, namely

$$v_\lambda = \frac{d\lambda}{dt} \qquad (7)$$

With R known, the terminal voltage is calculated as

$$v_t = v_\lambda + Ri \qquad (8)$$

With L known, the emf can be calculated as

$$emf = v_\lambda - L\frac{di}{dt} \qquad (9)$$

The *emf* can also be obtained by running a simulation with the current, i, set to zero and taking the derivative of the flux linkage, i.e.

$$emf = \frac{d\lambda}{dt} \text{ with } i = 0 \qquad (10)$$

Calculating the *emf* using both methods should yield similar results if the calculated inductance is accurate. This is a good way to verify the accuracy of the calculated inductance.

4.5 Power and efficiency

The input power to the machine is calculated as

$$P_{in} = \frac{1}{T} \int_0^T f_{mag}(t)v(t)dt \qquad (11)$$

where T is the period of the oscillation, $f_{mag}(t)$ is the magnetic force exerted on the translator and $v(t)$ is the speed of the translator.

The input power can also be calculated as

$$P_{in} = \frac{1}{T} \int_0^T v_\lambda(t)i(t)dt \qquad (12)$$

Equations 11 and 12 should yield precisely the same results if the simulated flux linkage and force is exact, no numerical differentiation error is made when equation 7 is evaluated and no integration error is made during the evaluation of equations 11 and 12. In practice, small errors do occur. A notable decrease in these errors were observed after the spline differentiation and integration techniques were adopted. Comparison of P_{in} from equations 11 and 12 is one of the methods used to evaluate a simulation's accuracy.

The output power is calculated as

$$P_{out} = \frac{1}{T} \int_0^T v_t(t)i(t)dt \qquad (13)$$

The efficiency is then given as the ratio of the output and input power

$$\eta = \frac{P_{out}}{P_{in}} \qquad (14)$$

The simulation neglects hysteresis and eddy current losses.

TOPIC B. MACHINES

Proceedings of the 19th Southern African Universities Power Engineering Conference
SAUPEC 2010, University of the Witwatersrand, Johannesburg
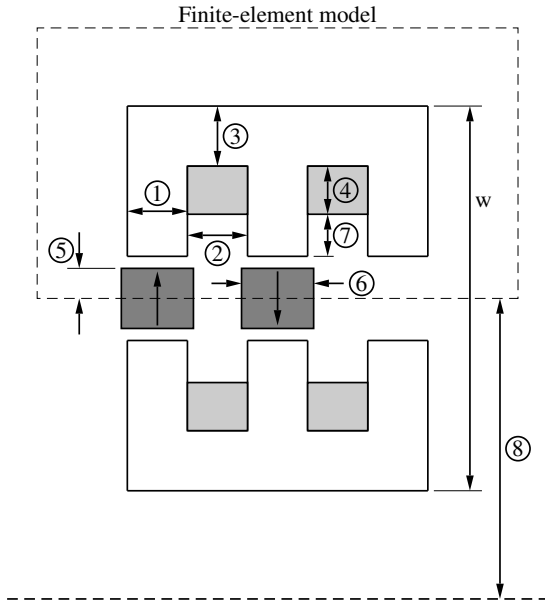
Fig. 5: An example of a short stroke linear generator

Method	MFD	SLP	SQP	PSO
m	35.1 kg	32.5 kg	33.0 kg	33.7 kg
P_{out}	9.98 kW	9.99 kW	10.0 kW	9.98 kW
η	97.8 %	96.8 %	96.7 %	96.8 %
B_{yoke}	1.60 T	1.59 T	1.57 T	1.60 T
B_{tooth}	1.60 T	1.60 T	1.60 T	1.60 T

Table 1: Optimization results: Objective function and constraint values

4.6 Other outputs

Two other outputs of the simulation are worth mentioning. The mass of a machine is available as output, the mass of the stator, translator and the total being reported. It is also possible to easily extract the peak flux density at a specific area in a machine. This is useful because it is usually desirable to constrain the peak flux density when optimizing a machine, especially since the simulation currently neglects hysteresis and eddy current losses.

5. APPLICATION EXAMPLE

The topology shown in figure 5 is presented as an example. Although this is an axisymmetric tubular machine, the machine was modelled as a flat machine for the purpose of this study. This was done because SEMFEP is currently limited to solving two-dimensional problems in cartesian coordinates. This approach does have the added advantage that only half the machine has to be simulated if the Neumann boundary condition ($\frac{dA}{dx} = 0$) is applied on the slice through the middle of the machine represented by the bottom edge of the dashed box in figure 5. The disadvantage of this method is that it is a poor approximation of a tubular machine when dimension 8 is not large compared to the width, w, of the tubular structure.

The dimensions 1 through 8 shown in figure 5 as well as the phase of the current i (see equation 2) were

Method		MFD	SLP	SQP	PSO
	1	18.6	13.3	13.0	14.0
	2	47.4	47.0	56.6	47.5
	3	17.9	13.2	13.1	13.8
Dimensions [mm]	**4**	25.3	32.7	30.4	30.4
	5	4.4	5.2	4.8	5.0
	6	46.1	36.6	43.2	36.0
	7	3.0	3.0	3.0	4.72
	8	10.0	10.0	10.0	11.8
ϕ [rad]		1.58	2.03	1.98	1.83

Table 2: Optimization results: Design variables

chosen as the design variables of the optimization problem. The goal of the optimization was to obtain a design which can meet required power and efficiency specifications while being as light as possible. With the outputs from the previous section available, the optimization problem was formulated as

$$\begin{aligned} \text{Minimize} \quad &: \quad F(X) = m \\ \text{Subject to} \quad &: \quad P_{out} > 10 \text{ kW} \\ &\quad \eta > 0.95 \\ &\quad B_{yoke} < 1.6 \text{ T} \\ &\quad B_{tooth} < 1.6 \text{ T} \end{aligned}$$

where X is the vector of design variables, m is the total mass of the machine, B_{yoke} is the peak flux density in the stator yoke and B_{tooth} is the peak flux density in a stator tooth. Reasonable upper and lower bounds were also placed on all of the design variables. This is necessary to ensure that the optimizer does not generate a set of design variables that will crash the simulation and cause the optimization process to terminate before completion. The rms current density in the coils was fixed at 4 A/mm^2 and the desired output voltage was set at 400 V for all simulations. The stroke of the machine was fixed at 40 mm.

The optimization problem was solved using four different optimization methods, namely the modified feasible directions method (MFD), sequential linear programming (SLP), sequential quadratic programming (SQP) and particle swarm optimization (PSO). The first three methods are part of *dot*, a commercial Fortran optimization program. These methods are all gradient-based. The fourth method is an implementation of the particle swarm algorithm as described by Vanderplaats [3] with a few additions by the author. The gradient-based optimizers have the advantage that an optimum is found using far less objective function evaluations. Global optimization algorithms, such as the particle swarm algorithm, are generally considered to be more robust than gradient-based algorithms.

The results for the objective function and constraint values are tabulated in table 1 and the corresponding design variables are tabulated in table 2. In this case, the different optimization algorithms report roughly the same optimum objective function value. Tables 1 and 2 show that the results from the SLP, SQP and PSO methods are especially similar. This suggests that the optimum results obtained with these methods are trustworthy.

Proceedings of the 19th Southern African Universities Power Engineering Conference
SAUPEC 2010, University of the Witwatersrand, Johannesburg

TOPIC B. MACHINES

	SEMFEP	Magnet 6
P_{out}	9.99 kW	10.3 kW
η	96.8 %	97.1 %
R	0.452 Ω	0.452 Ω
L	36.5 mH	35.4 mH
$V_{t,rms}$	398.7 V	410.9 V

Table 3: Comparison of results obtained from SEMFEP and Magnet 6
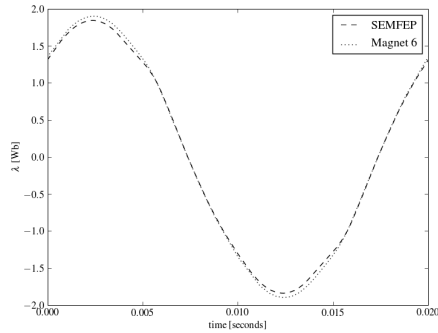
Fig. 6: Comparison of flux linkage

6. VALIDATION OF RESULTS

The SLP design from the previous section was chosen for comparison. The results obtained with SEMFEP were validated by running a complete model of this optimal design in *Magnet 6* as opposed to the half machine model used with SEMFEP. SEMFEP simulations were carried out over half the period of oscillation, but the simulation in *Magnet 6* was over a full period. In this way, the validity of the half period simulation is also verified. Table 3 shows that outputs are in good agreement. Furthermore, figures 6 and 7 show that the obtained flux linkage and force on the translator are almost identical.

7. CONCLUSIONS & RECOMMENDATIONS

A finite-element-based optimization tool for linear generators, SEMFEP, has been presented and it's use has been demonstrated. Results obtained from SEMFEP have been verified by comparison with results obtained using *Magnet 6*. The following recommendations regarding future work on the tool are made:
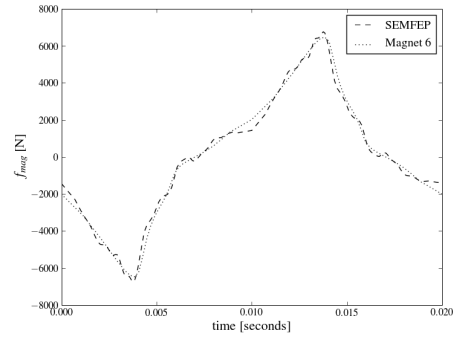
Fig. 7: Comparison of force on the translator

- SEMFEP can be extended to take core losses and winding eddy current losses into account. This will allow the tool to predict the efficiency of a machine much more accurately.
- The need exists for SEMFEP to have two-dimensional axisymmetric simulation capabilities in order to model tubular machines accurately. In this case, a full model of a machine would be simulated as opposed to the half model used in the present study. This would require, amongst other things, the use of two axisymmetric air-gap elements. An axisymmetric air-gap element model could be developed and two of these elements could be incorporated into the SEMFEP simulation.
- The gradient-based optimization algorithms can be sensitive to certain configuration parameters. Good guidelines for the setting of these parameters are required.
- SEMFEP can be extended to simulate the situation where the machine is connected to a predetermined impedance load. Nonlinear loads may also be considered.

REFERENCES

[1] R. Wang, H. Mohellebi, T. Flack, M. Kamper, J. Buys, and M. Feliachi, "Two-dimensional cartesian air-gap element (cage) for dynamic finite-element modeling of electrical machines with a flat air gap," *IEEE Trans. Magn.*, vol. 38, no. 2, pp. 1357–1360, Mar. 2002.

[2] A. Abdel-Razek, J. Coulomb, M. Feliachi, and J. Sabonnadiere, "The calculation of electromagnetic torque in saturated electric machines within combined numerical and analytical solutions of the field equations," *IEEE Trans. Magn.*, vol. 17, no. 6, pp. 3250–3252, November 1981.

[3] G. Vanderplaats, *Multidiscipline Design Optimization*, Vanderplaats Research & Development, Inc., 126 Bonifacio Place, Suite F, Monterey, CA 93940, 2007.

TOPIC B. MACHINES

Proceedings of the 19th Southern African Universities Power Engineering Conference
SAUPEC 2010, University of the Witwatersrand, Johannesburg

IMPLEMENTATION OF DOUBLE-FED INDUCTION MACHINE AS A NATIVE C-CODE S-FUNCTION SIMULINK MODEL

JC Bekker and HJ Vermeulen

University of Stellenbosch, Dept. of Electrical and Electronic Engineering, Stellenbosch, South Africa

Abstract. Wind energy is a very current topic, both locally and internationally. It follows that the analysis and prediction of the dynamic behaviour of the entire wind turbine system, i.e. from wind side to power grid side is also gaining in importance. Although the relevant model topologies are well established, obtaining or deriving appropriate parameter from first principles remains problematic. Some parameters are also dependent on operating conditions and are best determined from site measurements using system identification and parameter estimation methodologies. This paper discusses the modelling of a double-fed induction machine and implementation of this model as a native C-code S-function Simulink model for high-speed parameter estimation applications. The derivation of the DQ model of a double-fed or wound rotor induction machine is reviewed, followed by a discussion of the S-function functionality of MATLAB's Simulink platform and implementation of a C-code model as an S-function. The performance of the native C-code S-function is compared to the standard Simulink model to verify accuracy and simulation times. The model is used with Simulink's parameter estimation toolbox to estimate the machine parameters from simulated data. Finally, the next steps in developing models of the sub systems of the entire wind turbine system are discussed and some conclusions are presented.

Key words. Double-fed Induction Machine, Simulink, S-Function, Parameter estimation.

1. INTRODUCTION

WIND energy is a very current topic, both internationally and locally, especially in the Western Cape. The Western Cape Department of Environmental Affairs and Development Planning together with Deutsch Gesellschaft für Technische Zusammenarbeit in conjunction with Eskom consulted DIgSILENT GmbH to perform feasibility studies for wind generation in the Western Cape. The study showed that as much as 2800 MW of wind energy can be integrated into the Western Cape transmission grid [1].

The development of the local wind generation capacity creates a need to model and analyse wind turbine systems and power grid interactions in an efficient manner, both before and after installation [[2], [3]].

This paper discusses the modelling and implementation of a double-fed induction machine as a native C-code S-function MATLAB model. This model forms part of a larger project that envisages modelling of the entire wind generator system, i.e. from turbine to grid, in this manner. The double-fed induction machine has been chosen for the initial exercise because most manufacturers, for example De Wind, GE Wind Energy, Nordex and Vestas, produce wind turbines with double-fed induction machines as generators [4].

The complete project entails the implementation of native C-code MATLAB models for the dynamic modelling of the entire wind generation system shown in Figure 1, incorporating wind speed properties, turbine characteristics, gearbox, generator and the network.
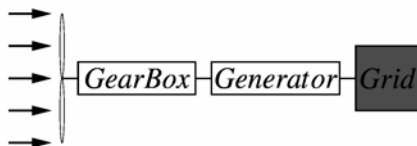
Figure 1: Wind Generation system

The main objective of the research is to develop a model implementation that is suitable for efficient use in deriving the model parameters from measured inputs and responses using the parameter estimation and optimization procedures available in the MATLAB environment.

Section 2 of this paper reviews the modelling of a double-fed induction machine in the DQ framework. Section 3 discusses implementation of such a model as C-code S-Function in Simulink, and highlights some of the problems encountered in this process. Section 4 presents results for the performance of the model and the parameter estimation implementation. The paper is concluded by presenting conclusions and recommendations for further work in section 5.

2. MODELLING OF THE DOUBLE-FED INDUCTION MACHINE

Figure 2 shows a simplified diagram of a three-phase wound rotor induction machine, also known as a double-fed induction machine [5].
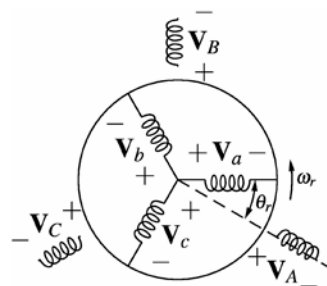
Figure 2: Simplified Three-phase machine

Neglecting saturation and losses in the core, and assuming a sinusoidal mmf, give rise to the basic dynamic equations given in [5]. These equations can be arranged in state-variable form to yield

$$\frac{d[I]}{dt} = [L]^{-1} \left\{ -[R] - \omega_r \frac{d[L]}{dt} \right\} [I] + [L]^{-1} [V] \quad (1)$$

where $[V]$ and $[I]$ contains the stator and rotor voltages and currents respectively, $[R]$ denotes the

Proceedings of the 19th Southern African Universities Power Engineering Conference
SAUPEC 2010, University of the Witwatersrand, Johannesburg

TOPIC B. MACHINES

resistance matrix and $[L]$ denotes the inductance matrix. As some of the terms of the inductance matrix are a function of the rotor position, these equations imply long simulation times due to the need to invert the time-varying inductance matrix at each simulation step [6]. The solution is to make use of DQ reference frame [[6], [7]] shown in Figure 3
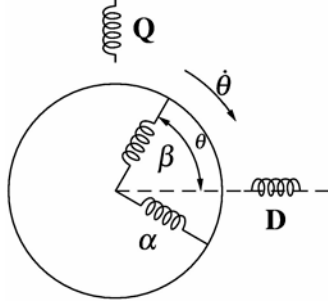
Figure 3: Two-phase machine

O'Kelly and Simmons derive the transformation current and voltage relationship between stationary three-phase (abc) and stationary two-phase systems (dq) in [7] as:

$$\left[i_{dq}\right]=[B]\left[i_{abc}\right], \ \left[i_{abc}\right]=[B]^{-1}\left[i_{dq}\right] \qquad (2)$$

$$\left[v_{dq}\right]=[B]\left[v_{abc}\right], \ \left[v_{abc}\right]=[B]^{-1}\left[v_{dq}\right] \qquad (3)$$

where $[B]=\sqrt{\dfrac{2}{3}}\begin{bmatrix} 1 & -\frac{1}{2} & -\frac{1}{2} \\ 0 & \frac{\sqrt{3}}{2} & -\frac{\sqrt{3}}{2} \\ \frac{1}{\sqrt{2}} & \frac{1}{\sqrt{2}} & \frac{1}{\sqrt{2}} \end{bmatrix}$ and $[B]^{-1}=[B]^{T}$.

Using this transformation, the stationary three-phase coils A, B and C of the stator from Figure 2 can be transformed to the stationary two-phase coils D and Q of Figure 3.

O'Kelly and Simmons also derive the transformation current and voltage relationship between rotating three-phase (abc) and pseudo-stationary two-phase systems (dq) in [7] as:

$$\left[i_{dq}\right]=[C]\left[i_{abc}\right], \ \left[i_{abc}\right]=[C]^{-1}\left[i_{dq}\right] \qquad (4)$$

$$\left[v_{dq}\right]=[C]\left[v_{abc}\right], \ \left[v_{abc}\right]=[C]^{-1}\left[v_{dq}\right] \qquad (5)$$

where $[C]^{-1}=[C]^{T}$ and $[C]$ is given as:

$$[C]=\sqrt{\frac{2}{3}}\begin{bmatrix} \cos\theta_{r} & \cos\left(\theta_{r}-\frac{2\pi}{3}\right) & \cos\left(\theta_{r}+\frac{2\pi}{3}\right) \\ -\sin\theta_{r} & -\sin\left(\theta_{r}-\frac{2\pi}{3}\right) & -\sin\left(\theta_{r}+\frac{2\pi}{3}\right) \\ \sqrt{\frac{1}{2}} & \sqrt{\frac{1}{2}} & \sqrt{\frac{1}{2}} \end{bmatrix}$$

Using this transformation the rotating coils of the rotor a, b and c can be transformed to the two-phase pseudo-stationary coils α and β.

Once these three-phase stator and rotor windings are transformed to a two-phase equivalent, as shown in Figure 3, the terminal voltages can be expressed as [8]:

$$v_{D}=R_{DD}i_{D}+p\left(L_{DD}i_{D}\right)+p\left(L_{DQ}i_{Q}\right)+p\left(L_{D\alpha}i_{\alpha}\right)+p\left(L_{D\beta}i_{\beta}\right)$$
$$v_{Q}=p\left(L_{QD}i_{D}\right)+R_{QQ}i_{Q}+p\left(L_{QQ}i_{Q}\right)+p\left(L_{Q\alpha}i_{\alpha}\right)+p\left(L_{Q\beta}i_{\beta}\right)$$
$$v_{\alpha}=p\left(L_{\alpha D}i_{D}\right)+p\left(L_{\alpha Q}i_{Q}\right)+R_{\alpha\alpha}i_{\alpha}+p\left(L_{\alpha\alpha}i_{\alpha}\right)+p\left(L_{\alpha\beta}i_{\beta}\right)$$
$$v_{\beta}=p\left(L_{\beta D}i_{D}\right)+p\left(L_{\beta Q}i_{Q}\right)+p\left(L_{\beta\alpha}i_{\alpha}\right)+R_{\beta\beta}i_{\beta}+p\left(L_{\beta\beta}i_{\beta}\right)$$
$$(6)$$

Where p is $\frac{d}{dt}$. Assuming that the windings are balanced and making use of the fact that no flux linkage occurs between windings that is 90° relative to each other, provides one with the following simplifications.

$$L_{\alpha\alpha}=L_{\beta\beta}=L_{r} , \quad R_{\alpha\alpha}=R_{\beta\beta}=R_{r} , \quad L_{DD}=L_{QQ}=L_{S} ,$$
$$R_{DD}=R_{QQ}=R_{S} , \ L_{\alpha\beta}=L_{\beta\alpha}=0 \ \text{and} \ L_{DQ}=L_{QD}=0$$

Substituting this into the equations for the terminal voltages one is left with:

$$v_{D}=R_{S}i_{D}+p\left(L_{S}i_{D}\right)+p\left(L_{D\alpha}i_{\alpha}\right)+p\left(L_{D\beta}i_{\beta}\right)$$
$$v_{Q}=R_{S}i_{Q}+p\left(L_{S}i_{Q}\right)+p\left(L_{Q\alpha}i_{\alpha}\right)+p\left(L_{Q\beta}i_{\beta}\right)$$
$$v_{\alpha}=p\left(L_{\alpha D}i_{D}\right)+p\left(L_{\alpha Q}i_{Q}\right)+R_{r}i_{\alpha}+p\left(L_{r}i_{\alpha}\right) \qquad (7)$$
$$v_{\beta}=p\left(L_{\beta D}i_{D}\right)+p\left(L_{\beta Q}i_{Q}\right)+R_{r}i_{\beta}+p\left(L_{r}i_{\beta}\right)$$

All the inductance left in this equations are a function of θ and thus a function of time. Assuming that the air-gap is uniform and that the inductance change sinusoidally with θ , the inductances can therefore be written as:

$$L_{\alpha D}=L_{D\alpha}=M\cos\theta , \ L_{\beta D}=L_{D\beta}=M\sin\theta ,$$
$$L_{\alpha Q}=L_{Q\alpha}=-M\sin\theta \ \text{and} \ L_{\beta Q}=L_{Q\beta}=M\cos\theta$$

Substituting this into the equations for v_{D} and v_{Q} provides one with:

$$v_{D}=R_{S}i_{D}+L_{S}pi_{D}+Mp\left(\cos\theta i_{\alpha}+\sin\theta i_{\beta}\right)$$
$$v_{Q}=R_{S}i_{Q}+L_{S}pi_{Q}+Mp\left(-\sin\theta i_{\alpha}+\cos\theta i_{\beta}\right) \qquad (8)$$

Introducing four new variables i_{d} , i_{q} , v_{d} and v_{q} , with relations as shown in equations (9) and (10).

$$\begin{bmatrix} i_{d} \\ i_{q} \end{bmatrix}=\begin{bmatrix} \cos\theta & \sin\theta \\ -\sin\theta & \cos\theta \end{bmatrix}\begin{bmatrix} i_{\alpha} \\ i_{\beta} \end{bmatrix} \qquad (9)$$

$$\begin{bmatrix} v_{d} \\ v_{q} \end{bmatrix}=\begin{bmatrix} \cos\theta & \sin\theta \\ -\sin\theta & \cos\theta \end{bmatrix}\begin{bmatrix} v_{\alpha} \\ v_{\beta} \end{bmatrix} \qquad (10)$$

Applying the relation and inverse relation of equations (9) and (10) to equations (7) and (8) the expressions for v_{D} , v_{Q} , v_{d} and v_{q} can be expressed as equation (11) in matrix format or as equation (12) in state-variable format:

$$\left[v_{DQdq}\right]=[H]\left[i_{DQdq}\right]+[L]\left[\dot{i}_{DQdq}\right]. \qquad (11)$$

Proceedings of the 19th Southern African Universities Power Engineering Conference
SAUPEC 2010, University of the Witwatersrand, Johannesburg

TOPIC B. MACHINES

$$\left[\overset{\bullet}{i}_{DQdq} \right] = -[L]^{-1}[H]\left[i_{DQdq} \right] + [L]^{-1}\left[v_{DQdq} \right]. \quad (12)$$

$$\text{where} \quad [R] = \begin{bmatrix} R_S & 0 & 0 & 0 \\ 0 & R_S & 0 & 0 \\ 0 & -\overset{\bullet}{\theta}M & R_r & -\overset{\bullet}{\theta}L_r \\ \overset{\bullet}{\theta}M & 0 & \overset{\bullet}{\theta}L_r & R_r \end{bmatrix} \quad \text{and}$$

$$[L] = \begin{bmatrix} L_S & 0 & M & 0 \\ 0 & L_S & 0 & M \\ M & 0 & L_r & 0 \\ 0 & M & 0 & L_r \end{bmatrix}$$

3. IMPLEMENTATION OF THE NATIVE C-CODE S-FUNCTION IN MATLAB

Dynamic simulations combined with numerical optimisation routines induces high processor loads and results in long simulation times. Simulink makes provision for implementing C-code models with its S-Function block. This functionality can be used to reduce the overall model computation times, thereby reducing simulation times dramatically, especially for parameter estimation applications.

The S-Function can be coded in C, Fortran, Ada or M [9]. This code needs to be coded in a specific format and compiled as a MEX-file, using the *mex* utility in the MATLAB command window. Figure 4 shows a flow diagram of the main function blocks associated with the S-Function C-code. The functionality of these blocks can be summarized as follows:

- Function *mdlCheckParameters* verifies that the parameters entered in the S-Function's parameter dialog box is within the required boundaries. This can be accomplished by using function calls like: mxGetPr(PARAM*x*(S)), mxGetNumberOfElements(PARAM*x*(S)) and IS_PARAM_DOUBLE(PARAM*x*(S)). This function call is performed each time any parameter in the dialog box is changed.
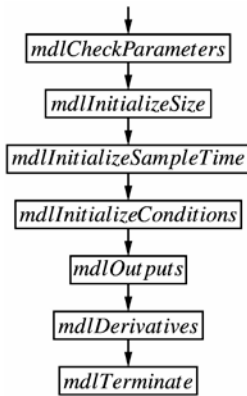
Figure 4: Flow diagram of the main functional components of C-code S-Function

- Function *mdlInitializeSize* structures the input and output ports of the Simulink block, e.g. the number and dimension of the ports. The number of expected parameters, as well as the relevant

states are also set in this function. If an input contributes an output, a direct feed needs to be implemented here.

- Functions *mdlInitializeSampleTime* and *mdlInitiallizeConditions* set the sample time and the initial conditions of the states. For this application the sample time is designated as continuous and the initial conditions are set through a value entered via the parameter dialog box.

- Functions *mdlOutputs* and *mdlDerivatives* implement the code to solve the differential equation and to calculate the output at every time step. The state space formulation given in (13), where *x* denote the states, *y* denotes outputs and *u* denotes inputs, gives rise to the code shown in (14) and (15) for *mdlDerivatives* and *mdlOutputs* respectively.

$$\begin{bmatrix} \dot{x}_1 \\ \dot{x}_2 \end{bmatrix} = \begin{bmatrix} a_{11} & a_{12} \\ a_{21} & a_{22} \end{bmatrix}\begin{bmatrix} x_1 \\ x_2 \end{bmatrix}$$
$$\begin{bmatrix} y_1 \\ y_2 \end{bmatrix} = \begin{bmatrix} b_{11} & b_{12} \\ b_{21} & b_{22} \end{bmatrix}\begin{bmatrix} x_1 \\ x_2 \end{bmatrix} + \begin{bmatrix} c_{11} & c_{12} \\ c_{21} & c_{22} \end{bmatrix}\begin{bmatrix} u_1 \\ u_2 \end{bmatrix} \quad (13)$$

$$dx[0] = a_{11}x[0] + a_{12}x[1]$$
$$dx[1] = a_{21}x[0] + a_{22}x[1] \quad (14)$$

$$y[0] = b_{11}x[0] + b_{12}x[1] + c_{11}u(0) + c_{12}u(1)$$
$$y[1] = b_{21}x[0] + b_{22}x[1] + c_{21}u(0) + c_{22}u(1) \quad (15)$$

- Function *mdlTerminate* represents a mandatory task, which provides the S-Function with an opportunity to perform some tasks at the end of the simulation.

Some practical considerations of importance in coding S-Functions include ensuring that the correct working directory is used when compiling the MEX file, ensuring that the function has a unique name and ensuring that the states are initialised as uninitialised states leads to random behaviour of the S-Function. Standard C-code precautions apply, e.g. ensuring that the dimensioning of variables take cognisance of the arithmetic rules, etc.

4. SIMULATION AND ESTIMATION

4.1 Simulation

In order to verify that the model was implemented correctly, the output torque of the S-Function model was simulated over a range of rotor speeds and compared to the values generated by the model of the Wind Turbine Blockset developed by Aalborg University. The machine was operated as an induction machine; i.e. with an applied voltage of 0V for the rotor windings. Table 1 summarises the parameter values used for the simulation. The results of the Torque-Speed curve for the S-Function model and the Wind Turbine Blockset are shown in Figure 5, and excellent correlation is achieved. The torque goes to zero at 1500 rpm as expected for a 4 pole induction machine.

Table 1: Parameters of Induction machine

Parameter	Symbol	Value
Stator resistance [Ω]	R_s	0.115
Stator leakage inductance [mH]	$L_{s\lambda}$	1.65
Rotor resistance [Ω]	R_r	0.184
Rotor leakage inductance [mH]	$L_{r\lambda}$	1.68
Magnetising inductance [mH]	L_m	46.6
Number of poles	p	4
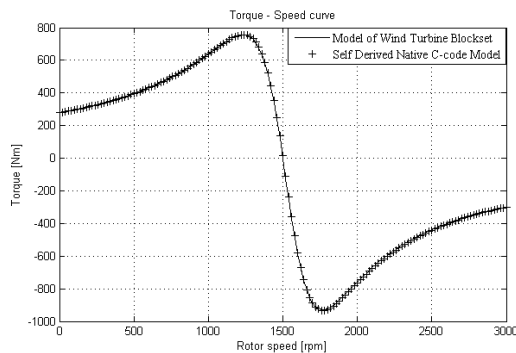
Figure 5: Torque- Speed curves for derived model and Wind Turbine Blockset Model

For the same parameter values and a rotor speed of 1910 rpm, the S-Function model yields a simulation time of approximately 1 second compared to approximately 7 seconds for the Simulink ABC model from the Wind Turbine Blockset. The simulation time is improved by a factor of 7, which validates the approach of using the C-code S-Function and the DQ transformation instead of the ABC Simulink block model for the parameter estimation exercise to implement in the project.

4.2 Estimation

A number of input/output datasets were generated with the C-code S-Function model using the parameter values shown in Table 1. These datasets were then used to estimate the parameters of the model for comparison with the original parameters. All the parameters were estimated except for the number of poles, since this is always known.

The first dataset reflects the machine running at a constant speed while the second set involves a step in the rotor speed. The initial values for the parameters were taken as 1mΩ for the stator and rotor resistance and 0.1mH for the rotor and stator leakage inductance, as well as the magnetising inductance.

For the dataset with the constant rotor speed, the parameters were estimated with an average accuracy of 95.7%, with the accuracy of all of the individual parameters above 90%. The stator and rotor leakage inductances yielded the lowest accuracy.

For the dataset with the step in rotor speed, the average accuracy increased to 96.7%, with a lowest individual accuracy of 94.8%. The accuracy of the

rotor and stator leakage inductance improved as expected, because of the transient nature of the response.

From these results it is clear that the parameters of the model can be estimated with good accuracy, using Simulink's Parameter Estimation capabilities.

5.   CONCLUSIONS AND FURTHER WORK

The DQ model for the double-fed induction machine was successfully implemented as a native C-code S-Function in Simulink. It was found that the DQ S-Function model simulates about 7 times faster compared to the ABC Simulink model. This gives rise to the conclusion that the use of the native DQ C-code S-Function model will result in a significant improvement in execution time when estimating the parameters of the entire wind turbine system.

Models must also be implemented for the wind model, turbine model, gearbox and power converter. Modelling of the gearbox is currently in progress. A two-mass gearbox model will be used, as shown in Figure 6, where an equivalent stiffness and damping factor is used for the system. The moments of inertia for the shaft and gearbox wheels are neglected, because it is small relative to the moment of inertia of the generator and the wind turbine.
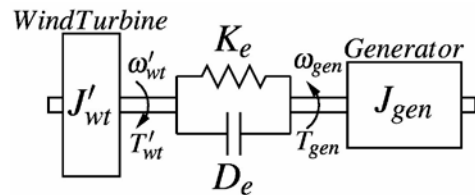
Figure 6: Representation of a 2-mass Gearbox Model transformed to generator side

Once the entire system from wind to power grid has been developed, some of the blocks will be refined to include effects such as deep-bar effects, saturation and iron losses in the generator.

REFERENCES

[1] *Pöller, M., Grid Integration of Wind Energy in the Western Cape – Results of Feasibility Studies.* Gomaringen: DIgSILENT GmbH, 2009.
[2] Hansen, A.D., Sorensen, P., Blaabjerg, F., Becho, J., *Dynamic modelling of wind farm grid intgeraction.* Wind Engineering Volume 26, No. 4, pp 191-208, 2002.
[3] Sorensen, A., Hansen, A.D., Janosi, L., Bech, J., Bak-Jensen, B., *Simulation of Interaction between Wind Farm and Power System.* Roskilde: Riso National Laboratory, 2001.
[4] Petersson, A., *Analysis, modelling and Control of Double-Fed Induction Generators for Wind Turbines.* Göteborg: Chalmers University of Technology, 2003.
[5] Iov, F., Hansen, A.D., Sorensen, P., Blaabjerg, F., *Wind Turbine Blockset in Matlab/Simulink.* Aalborg: Aalborg University, Inc., 2004.
[6] Pillay, P., Levin, V., *Mathematical Models For Induction Machines.* 0-7803-3008-0/95 $4.00 © 1995, pp 606-616.
[7] O'Kelly, Simmons, *Introduction to generalized electrical machine theory.* New York : McGraw-Hill, 1968. ISBN 978-0070940505
[8] Hancock, N.N., *Matrix analysis of electrical machinery.* Oxford :Pergamon Press, 1964.
[9] The MathWorks, *Simulink 7 – Writing S-Functions.* Natick: The MathWorks, 2008

TOPIC B. MACHINES

Proceedings of the 19th Southern African Universities Power Engineering Conference
SAUPEC 2010, University of the Witwatersrand, Johannesburg

THE ELECTROMAGNETIC AND MECHANICAL DESIGN OF A RELUCTANCE SYNCHRONOUS MACHINE ROTOR USING THE FINITE ELEMENT METHOD

J.G. Wright and W.A. Cronje

University of the Witwatersrand, School of Electrical and Information Engineering, Johannesburg, South Africa,
e-mail: jgwright@ieee.org

Abstract. A 4-pole Reluctance Synchronous Machine (RSM) electromagnetic and mechanical design is presented using commercially available Finite Element Method (FEM) software packages - FLUX 10.2 and ANSYS 12. User def ned functionality is obtained via Python and the embedded PyFLUX command language in FLUX 10.2. The electromagnetic design focuses on maximum mean torque and minimum torque ripple. Several geometric parameters are varied consecutively and once the choice of a geometric parameter is made where maximum mean torque and minimum torque ripple occurs the next geometric parameter is varied. The f nal electromagnetic design is used in mechanical FEM analyses in ANSYS. In the mechanical FEM analyses, the mechanical strutting parameter values are chosen (tangential webs and radial ribs). The design decision for the values of these parameters is based purely on a mechanical safety factor.

Key Words. Reluctance Synchronous Machine, design, electromagnetic FEM, FLUX 10.2, mechanical FEM, ANSYS 12

1. INTRODUCTION AND BACKGROUND

THE Reluctance Synchronous Machine (RSM) belongs to the family of brushless AC machines including the induction machine, synchronous machine and permanent magnet synchronous machine. It has a typical three-phase AC stator winding and salient rotor which develops reluctance torque via the difference in inductance on the f ctitous D and Q axes. The RSM has several advantages including easy control, synchronous speed, cold rotor, high speed operation and robustness [1]. Improved, low-cost power electronics has allowed the RSM to become a viable option in industry where variable synchronous speed, cool operation and an eff cient overall process is required.

A transversally laminated (TL) 4-pole RSM is shown in Figure 3 with the relevant geometric parameters and D and Q axes shown. The simplif ed equivalent circuits of the RSM (ignoring core losses) are shown in Figures 1(a) and 1(b). Also, shown in Figure 2 is a simplif ed steady state phasor diagram of the RSM (also ignoring core losses). The well known equation for torque in the RSM is:

$$T_{el} = \frac{3P}{2}(L_{dm} - L_{qm})i_{ds}i_{qs} \qquad (1)$$

where

L_{dm} = D-axis magnetising inductance
L_{qm} = Q-axis magnetising inductance
T_{el} = Electromagnetic torque
P = Number of pole pairs
i_{ds} = D-axis terminal current
i_{qs} = Q-axis terminal current

The inductance difference is known as the torque index ζ:

$$\zeta = L_{dm} - L_{qm} \qquad (2)$$

Equation 1 can now be expressed as:

$$T_{el} = \frac{3P}{2}\zeta i_{ds}i_{qs} \qquad (3)$$

and alternatively, using simple trigonometry as:

$$T_{el} = \frac{3P}{4}\zeta i_{dqs}^2 sin(2\theta_i) \qquad (4)$$

where

i_{dqs} = Terminal current space vector
θ_i = Current space vector angle from the D-axis
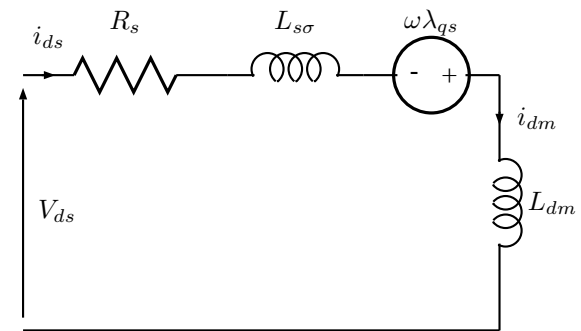
(a) D-axis model of RSM
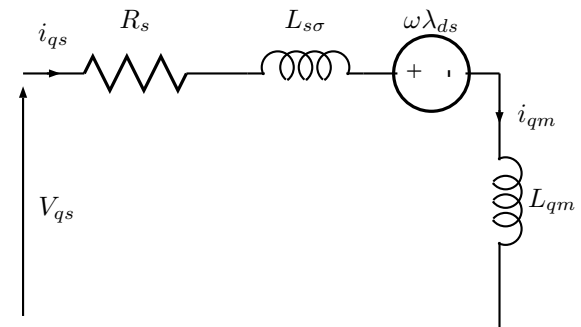
(b) Q-axis model of RSM

Figure 1. D and Q axis models of RSM

Proceedings of the 19th Southern African Universities Power Engineering Conference
SAUPEC 2010, University of the Witwatersrand, Johannesburg

TOPIC B. MACHINES
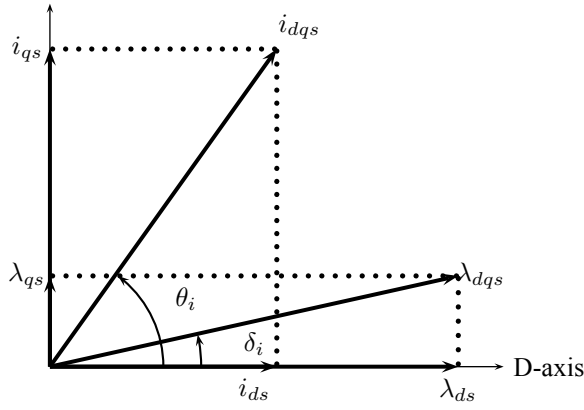
Figure 2.   Vector diagram of RSM excluding iron losses
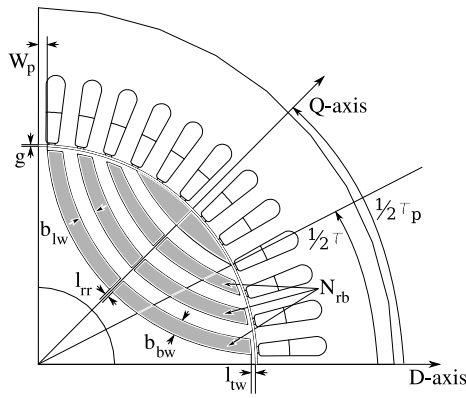
Figure 3.   Example of a 4 pole transversally laminated RSM rotor

It can be seen from equations 1 - 4 that if a constant current i_{dqs} with associated constant current angle θ_i driving the RSM, the only parameter defining the torque capability is the torque index ζ. The higher the value of ζ the higher the torque capability of the RSM. Also, once the machine has been designed (torque index is inherent in the machine), the main parameter in the control of the RSM is the current vector angle θ_i. The best way to control the RSM if maximum torque is a performance requirement is Maximum Torque Control (MTC). As can be seen from equation 4, this ideally requires a current vector angle of $\theta_i = 45^o$ but when taking into account core losses and saturation can approach higher values closer to $\theta_i = 60^o$ [2].

In this paper, the electromagnetic design procedure for a 4-pole TL RSM is presented. This is followed by the implementation of this design in FLUX 10.2 utilising the built-in PyFLUX command language. The resultant electromagnetic design is used to do mechanical FEM case studies to investigate the mechanical integrity of the newly designed RSM rotor. This is followed by some suggestions for future work and a concluding section.

2. ELECTROMAGNETIC DESIGN

2.1 Overall Design Approach

In order to design the RSM rotor, the most important performance criteria for the application should be prioritised. In this design, the application is an underground shuttle vehicle traction motor. Thus, the prioritised performance criteria should be torque density [3]. The torque requirement should not only be the maximisation of average torque but should also include the minimisation of torque ripple. Torque ripple can be visualised as the direct result of the discontinuity of reluctance between the rotor barriers and stator slots [4].

The desirable design outcome is to have maximum mean torque and minimum torque ripple to allow for minimal vibrations, acoustic noise and possible mechanical resonances. In this design procedure, the rotor is rotated through a predefined angle with a constant chosen current vector angle of $\theta_i = 60^o$. The mean electromagnetic torque and torque ripple are then defined as:

$$T_{mean} = \frac{\sum_{a=0}^{N} T_{ea}}{N} \qquad (5)$$

$$T_{ripple} = \frac{T_{max} - T_{min}}{T_{mean}} \times 100\% \qquad (6)$$

where

T_{mean} = Mean of torque waveform
a = a_{th} element in torque waveform
N = Total number of elements in torque waveform
T_{max} = Maximum torque in waveform
T_{min} = Minimum torque in waveform
T_{ripple} = Calculated torque ripple

In the design, a 4-pole induction machine stator identical to the stator shown in Figure 3 is utilised with a TL RSM rotor topology. A brief description of the geometric parameters that are changed during the electromagnetic design (shown in Figure 3) are listed in Table I.

Table I
PARAMETERS TO BE CHANGED DURING DESIGN PROCEDURE.

Parameter	Description
N_{rb}	Number of rotor barriers
$\beta = \dfrac{b_{bw}}{b_{bw} + b_{lw}}$	Insulation ratio
W_p	Position of first rotor barrier
$\alpha = \dfrac{\tau}{\tau_p}$	Pole pitch to pole span ratio
g	Airgap length

TOPIC B. MACHINES

Proceedings of the 19th Southern African Universities Power Engineering Conference
SAUPEC 2010, University of the Witwatersrand, Johannesburg

The electromagnetic design procedure follows the flow diagram in Figure 4. It investigates the geometric parameters effect on torque production in a linear progression. Thus, it is noted that this is not an optimum global multi-variable design but merely a first pass design to investigate the effects that the parameters listed in Table I have on average torque and torque ripple. In the design, one parameter is varied and the torque waveform analysed over the defined rotor angle with a defined current angle. The mean torque and torque ripple are then extracted using equations 5 and 6. Thereafter, the parameter value which results in maximum average torque and minimum torque ripple is chosen. This value of the relevant parameter is then utilised for the rest of the design procedure that follows where the process is repeated until all paramaeters have been varied accordingly. The order in which the design proceeds is N_{rb} and β together, W_p, α and g. Intuitively, l_{tw} and l_{rr} should be zero for optimum electromagnetic performance (to maximise saliency). However, this is contradictory to mechanical requirements as the rotor would disintegrate. Thus, l_{tw} and l_{rr} are changed purely for investigative purposes in the electromagnetic design procedure. The mechanical design will determine the appropriate widths of these supports.

START

Develop overall 2-D model

Set relevant geometric values

Parametrise a geometric value $(N_{rb}, \beta, W_p, \alpha, g)$

Parametrise rotor movement

Solve

Choose value of parameter with:
$\max(T_{mean})$
$\min(T_{ripple})$

More parameters to optimise?

No   Yes

FINISH
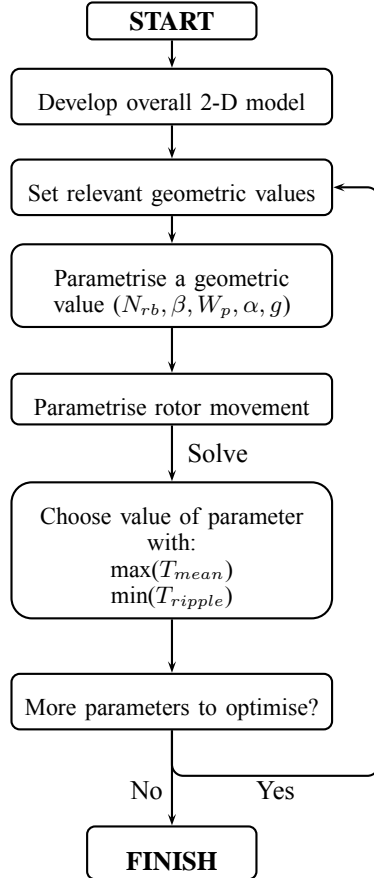
Figure 4.   Linear progression approach for design procedure

2.2 Electromagnetic design implementation in FLUX

The design procedure is implemented in FLUX 10.2 using Python scripts incorporating generic Python and the built in PyFLUX command language

in FLUX 10.2 [5]. The FLUX 3-D beta solver allows all required model development, solving and post-processing to be incorporated into one integrated development environment. This also allows for insight into the relevant PyFLUX commands required for solving and post-processing. The geometry of the RSM is developed parametrically to allow for quick changes in the geometry when required. The three stator windings have two parallel paths each assigned as stranded coil conductors with imposed currents defined by three I/O parameters as follows:

$$I_a = I_p \sin((2\theta + \theta_i)\frac{\pi}{180}) \qquad (7)$$

$$I_b = I_p \sin((2\theta + \theta_i)\frac{\pi}{180} + \frac{2\pi}{3}) \qquad (8)$$

$$I_c = I_p \sin((2\theta + \theta_i)\frac{\pi}{180} - \frac{2\pi}{3}) \qquad (9)$$

where

I_{rated} = Rated current of original induction machine
I_p = Peak current = $\dfrac{I_{rated}}{2}\sqrt{2}$
θ = Angular position of the rotor

The rated current $I_{rated} = 93\ A$ (the rated current of the original 55 kW induction machine). Seperate FLUX 10.2 projects are created for each design step (each geometric parameter) and Python files utilised to change the parameter during the design as shown in Figure 5. A distinct modular approach to these files allows reuse of the Python file structure with only slight modifications required.

3. MECHANICAL DESIGN

Following the electromagnetic design of the RSM, there are two geometric design parameters that are not optimised electromagnetically (l_{tw} and l_{rr}). There is a clear offset between electromagnetic and mechanical requirements for these two parameters. Ideally, they should be zero to maximise saliency but for mechanical support, they need to be non-zero. To investigate the necessary widths of l_{tw} and l_{rr}, mechanical FEM analysis (in ANSYS 12) is performed on the resultant electromagnetic design presented in section 4.1. The original values of $l_{tw} = 2$ mm and $l_{rr} = 2$ mm chosen in the electromagnetic design were merely chosen as a multiple of the lamination thickness and in this case were four times the lamination thickness of 0.5 mm.

3.1 Types of mechanical analyses

The scalar von Mises stress plot is used to analyse the mechanical strength of the RSM rotor. It is traditionally used to predict yielding of materials and is

Proceedings of the 19th Southern African Universities Power Engineering Conference
SAUPEC 2010, University of the Witwatersrand, Johannesburg

TOPIC B. MACHINES

START

Delete Mesh

Set relevant geometric values

Define rotor position:
Resolution (1°)
Range ($0 - 30^o$)

Define scenario name relevant to parameter being changed

Define scenario settings: rotor movement, accuracy settings

Define array of values for relevant geometric parameter

Anymore values in array?

Yes → Delete mesh

No → Save project → FINISH

Set relevant geometric value from array of values

Mesh lines and faces

Solve scenario

Extract torque vs rotor angle waveform

Write torque vs rotor angle waveform to *.txt file

Perform *.txt file editing for easy interpretation in Octave

Figure 5. Modular structure of Python file for variation of required geometric parameter

thus quite applicable for this analysis. There are three analyses performed in the mechanical FEM analysis:

- Case I: Analysis of the original electromagnetic designed RSM rotor.
- Case II: Analysis of the RSM rotor with rounded barrier edges.
- Case III: Analysis of the RSM rotor with rounded barrier edges and wider l_{tw} and l_{rr} .

The mechanical properties of the material (M400-50A steel) are a Poissons ratio of $\nu = 0.29$ and a Youngs modulus of $E = 200 \ GPa$.

3.2 Types of loads

The mechanical loads chosen for the rotor were mechanical angular velocity and angular acceleration inertia loads. The angular velocity chosen was $\omega = 100\pi$ rad/s and $\omega = 50\pi$ rad/s. These

are equivalent to 3000 rpm (twice the rated speed) and 1500 rpm (rated speed) respectively. The angular acceleration load is chosen so as to simulate a mechanical torque requirement on the rotor. It is based on an approximation of the rated output torque of the RSM ($\approx$ 400 N.m) and a moment of inertia ($\approx$ 0.4 kg.m^2). From these values, the angular acceleration load was approximated as 2000 rad/s^2. In any case, it has been shown that the resultant mechanical stresses and strains as a result of the angular acceleration load alone are a few orders of magnitude lower than the stresses and strains that result from the angular velocity load.

4. DESIGN RESULTS AND ANALYSIS

4.1 Electromagnetic results

4.1.1 Variation of N_{rb} and β: Mean torque and torque ripple versus β plots for a range of rotor barriers are shown in Figure 6. Maximum mean torque occurs around $\beta = 0.3$ for rotor barrier numbers higher than five. Minimum torque ripple occurs between $\beta = 0.1$ to $\beta = 0.3$. A value of $\beta = 0.3$ is chosen along with $N_{rb} = 6$ to allow for ease of manufacturing and mechanical strength of the rotor.
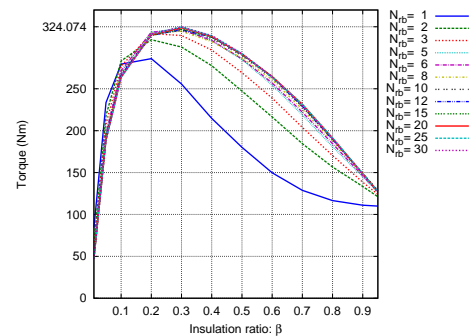
(a) Mean torque
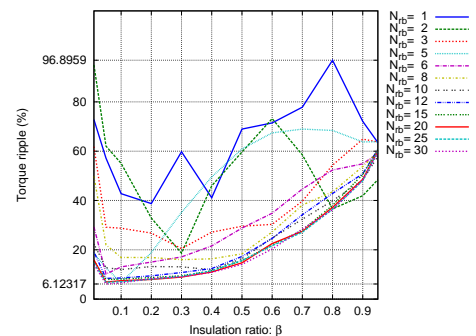
(b) Torque ripple

Figure 6. Mean torque and torque ripple versus beta for a range of rotor barriers

4.1.2 Variation of W_p: Torque versus rotor barrier position W_p is shown in Figure 7. As W_p increases there is an initial increase in mean torque but thereafter as the the rotor barriers move towards the Q-axis torque decreases. This is due to less flux being linked with the high permeance D-axis as the rotor barriers

TOPIC B. MACHINES

Proceedings of the 19th Southern African Universities Power Engineering Conference
SAUPEC 2010, University of the Witwatersrand, Johannesburg

move away from the D-axis and towards the Q-axis. Maximum mean torque occurs around $W_p = 20$ mm and minimum torque ripple at $W_p = 25$ mm. A value of $W_p = 20$ mm is chosen.
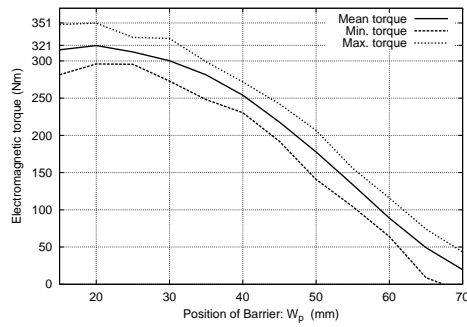
Figure 7. Torque versus position of rotor barrier

4.1.3 Variation of α: Torque versus rotor cutout is shown in Fig. 8. A rotor cutout should significantly increase the reluctance in the Q-axis while leaving the D-axis reluctance relatively constant. As seen in Figure 8 maximum mean torque as well as minimum torque ripple occur around $\alpha = 0.85$. A value of $\alpha = 0.85$ is chosen.
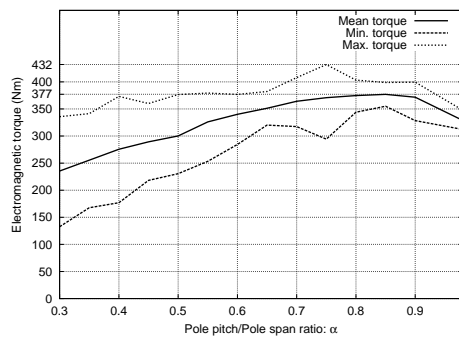
Figure 8. Torque versus pole pitch to pole span ratio

4.1.4 Variation of g: Torque versus airgap length is shown in Figure 9. Mean torque increases significantly as the airgap length decreases. However, torque ripple also increases as the airgap length decreases as a result of the interaction between the stator slots and rotor barriers as they approach one another (as g decreases). Also, consideration needs to be given to whether a significantly smaller airgap of 0.4 mm is obtainable considering manufacturing tolerances. The airgap is left at the nominal airgap value of 0.8 mm.

4.1.5 Variation of l_{tw} and l_{rr}: Purely for investigative purposes, torque versus l_{tw} and l_{rr} plots are shown in Fig. 10 to reveal the expected results. Mean torque decreases as l_{tw} and l_{rr} increase. An interesting result is how torque ripple increases when l_{tw} is close to zero as a result of an increased magnetic reaction between the stator slots and rotor barriers. Traditionally, RSM designers have chosen the length of l_{tw} and l_{rr} to be a multiple of the lamination thickness [6, 7]. Initial electromagnetic design choices of $l_{tw} = 2$ mm and $l_{rr} = 2$ mm (4x lamination thickness) are chosen.
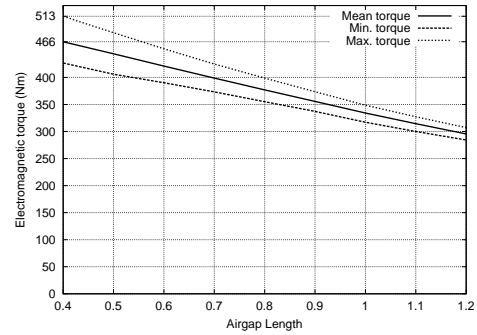
Figure 9. Torque versus airgap width
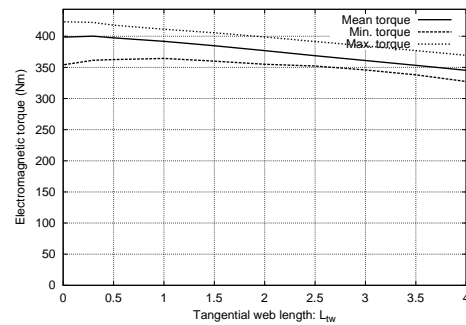
(a) Torque vs length of tangential web width
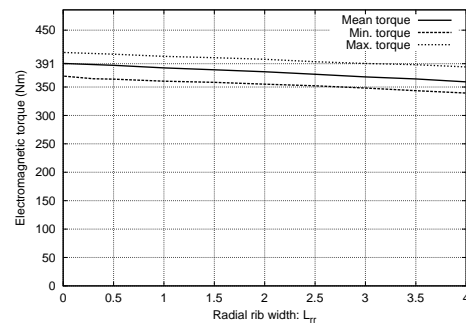
(b) Torque vs length of radial rib length

Figure 10. Torque vs lengths of rotor supports

The cross section of the final electromagnetic design is shown in Figure 11.

4.2 Mechanical results

It has been found that the highest mechanical stresses in the rotor occur on the innermost radial rib. This is expected as a result of this radial rib being required to hold in the largest mass of the rotor while rotating at speed and undergoing transient torque changes. In the next sections the results from the three case studies are revealed.

4.2.1 Case I: The von Mises stress plot is shown in Figure 12. As expected, the stresses in the rotor are pronounced around the straight edges of the rotor barriers. Clearly, the straight edged rotor barriers are a problem mechanically.

4.2.2 Case II: The original electromagnetic RSM rotor geometry is adjusted so that the rotor has rounded

Proceedings of the 19th Southern African Universities Power Engineering Conference
SAUPEC 2010, University of the Witwatersrand, Johannesburg

TOPIC B. MACHINES
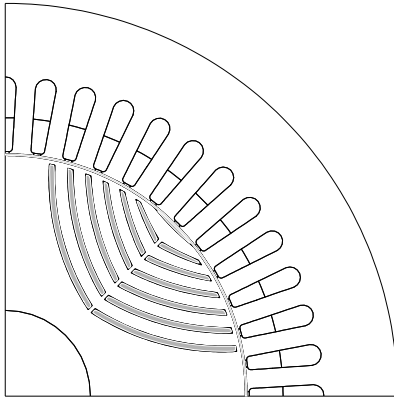
Figure 11.   Electromagnetic design of RSM rotor
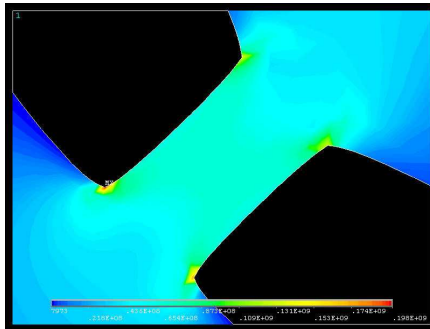
Figure 12.   von Mises stress plot of RSM with straight barrier edges

barrier edges. It is expected that the stress in the rotor should decrease substantially with the removal of the straight edges. The stress contour plot for the new rounded barrier edge rotor is shown in Figure 13. As expected, the stresses on the inner most barrier of the rotor have reduced quite substantially when compared to Case I (they have more than halved). This is a very promising result even though the mechanical safety factor is still below the accepted value of ten in a demanding environment like an underground mine.
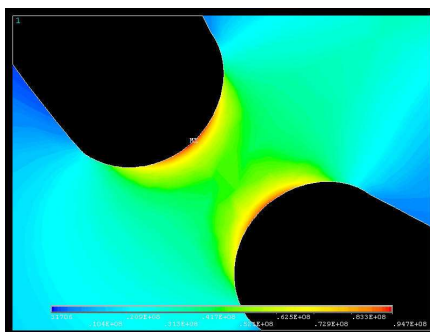
Figure 13.   von Mises stress plot of RSM with rounded barrier edges

4.2.3 Case III: The geometry in this analysis is based on the geometry in Case II but with wider tangential webs and radial ribs. These lengths have been increased to 4 mm. The stress contour plot is shown in Figure 14. Again, the stresses have reduced signif cantly when compared to Case II (37% lower). Yet the stresses in the rotor are still not below

the required safety factor of ten. However, they are approaching the required value and the results so far seem promising. It is interesting to note how the stress distribution between the rotor barriers has decreased signif cantly. This is very important as these areas will be stressed the most during operation.
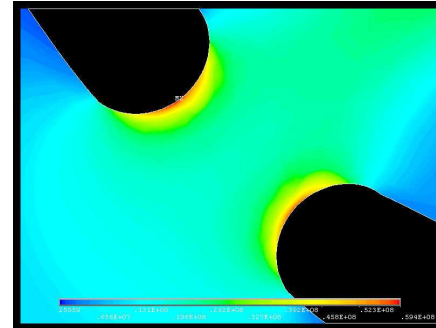
Figure 14.   von Mises stress plot of RSM with straight barrier edges and wider mechanical supports

4.2.4 Discussion of mechanical FEM results: The material used for the rotor (M400-50A steel) has a yield strength of 320 MPa. If a safety factor of ten is required (a reasonable assumption for a mining application) then the maximum stress that should be present in the rotor should be 32 MPa. Based on the operating stresses revealed in the mechanical FEM investigations (Cases I-III) Table II details the safety factors for each analysis. As can be seen, a safety factor of 5.39 is the highest safety factor attained when at twice rated speed. This may seem disheartening but consideration must be given to the mechanical loads imposed on the RSM rotor. An angular velocity inertia load of twice the expected rated speed has been imposed. This case will not always occur and it is more likely that this is a special case and on average the machine will more than likely operate at a lower speed. Simulations of Cases I-III with a more likely angular velocity of rated speed $\omega = 50\pi$ (1500 rpm) has been performed with interesting results as shown in Table II. As can be seen, the mechanical safety factor is larger than ten for Cases II and III where rounded barrier edges are used. After consultation with the motor manufacturer, a RSM rotor with rounded barrier edges is chosen and mechanical supports $l_{tw} = 4$ mm and $l_{rr} = 4$ mm. The cross section of the f nal RSM rotor design is shown in Figure 15.

.

5. FUTURE WORK

A few of the many possible future improvements could include:

- A prototype of the f nal RSM should be built and tested in a laboratory environment for veri-f cation of performance.
- In the design procedure presented, a f rst pass design has been presented where a linear pro-

TOPIC B. MACHINES

Proceedings of the 19th Southern African Universities Power Engineering Conference
SAUPEC 2010, University of the Witwatersrand, Johannesburg
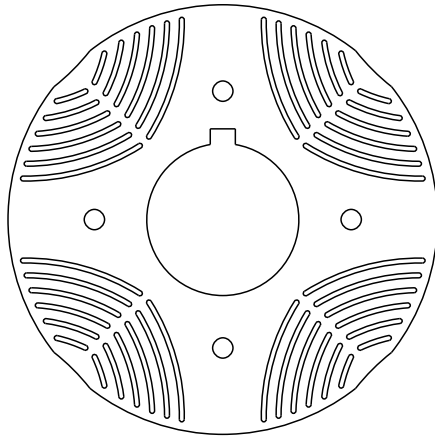
Figure 15. Final RSM rotor after electromagnetic design and mechanical case studies

Table II
STRESSES AND SAFETY FACTOR FOR THREE MECHANICAL
FEM INVESTIGATIONS

$\omega = 100\pi$ **rad/s** $\alpha = 2000$ **rad/s**^{2}	**Goal value**	**Case I**	**Case II**	**Case III**
s_{yield} (MPa)	320	320	320	320
s_{op} (MPa)	32	198	94.7	59.4
n_{op}	10	1.62	3.38	5.39
$\omega = 50\pi$ rad/s $\alpha = 2000$ rad/s^2				
s_{yield} (MPa)	320	320	320	320
s_{op} (MPa)	32	54.7	24.8	16
n_{op}	10	5.85	12.9	20

gression through all the relevant geometric parameters has been made. A global multi-variable design procedure which accounts for the mutual effect of different parameters could be performed. The work by Kamper in [8] is a feasible solution where an algorithm chooses the direction of the geometric parameter choice and FEM is used directly in the design.

- The use of permanent magnets in the rotor barriers as performed in [6, 9, 10] would result in increased performance especially with regards to power factor, eff ciency, torque and enhanced f eld weakening ability.

6. CONCLUSIONS

A RSM design is developed using PyFLUX and generic Python in FLUX 10.2. The linear progression approach to the electromagnetic design is outlined and the overall structure of each Python f le presented, revealing a modular reusable approach. Geometric parameter values are chosen based on where maximum mean torque and minimum torque ripple occurs. After choosing a rotor barrier number of 6 and insulation ratio of 0.3, the f rst barrier position of 20 mm is chosen. A rotor cutout value of $\alpha = 0.85$ is then chosen. A smaller airgap allows for more torque to be generated but with more torque ripple and owing to manufacturing constraints the nominal airgap length of 0.8 mm is maintained. The choice of the values

of the tangential webs (l_{tw}) and radial ribs (l_{rr}) were made after the electromagnetic design. The choice of these values was based on mechanical FEM case studies performed in ANSYS. The mechanical FEM studies were performed for different rotor barrier edge shapes and mechanical support widths with different mechanical loads imposed. The f nal values of $l_{tw} = 4$ mm and $l_{rr} = 4$ mm were chosen to allow for a mechanical safety factor much higher than ten.

REFERENCES

[1] R. Betz, R. Lagerquist, M. Jovanovic, T. Miller, and R. Middleton, "Control of synchronous reluctance machines," *IEEE transactions on industry applications*, vol. 29, pp. 1110–1122, Nov./Dec. 1993.

[2] X. Bomela and M. Kamper, "Effect of machine design on performance of reluctance synchronous machine," *Conference Record of the 2000 IEEE Industry Applications Conference*, vol. 1, pp. 515–522, 2000.

[3] J. Germishuizen, F. Van der Merwe, K. Van der Westhuizen, and M. Kamper, "Performance comparison of reluctance synchronous and induction traction drives for electrical multiple units," *Conference Record of the 2000 IEEE Industry Applications Conference*, vol. 1, pp. 316–323, 2000.

[4] M. Sanada, K. Hiramoto, S. Morimoto, and Y. Takeda, "Torque ripple improvement for synchronous reluctance motor using asymmetric f ux barier arrangement," *IEEE transactions on industry applications*, vol. 40, pp. 1076–1082, 2004.

[5] www.cedrat.com, *FLUX users guide*, Cedrat.

[6] P. Niazi, "Permanent magnet assisited synchronous reluctance motor design and performance improvement," Ph.D. dissertation, School of Electrical Engineering, Texas A&M University, 2005.

[7] J. Haataja, "A comparative performance study of four-pole induction motors and synchronous reluctance motors in variable speed drives," Ph.D. dissertation, Lappeenranta University of Technology, Lappeenranta, Finland, June 2003.

[8] M. Kamper, F. Van der Merwe, and S. Williamson, "Direct f nite element design optimisation of the cageless reluctance synchronous machine," *IEEE transaction on energy conversion*, vol. 11, pp. 547–555, Sep. 1996.

[9] M. de Kock, H.W. Kamper, "Dynamic control of the permanent magnet-assisted reluctance synchronous machine," *IET Electric Power Applications*, vol. 1, pp. 153 – 160, Mar. 2007.

[10] S. Sibande, M. Kamper, R. Wang, and E. Rakgati, "Optimal design of a pm-assisted rotor of a 110 kw reluctance synchronous machine," in *Proc. 7th AFRICON Conference in Africa AFRICON*, vol. 2, 2004, pp. 793–797 Vol.2.

Proceedings of the 19th Southern African Universities Power Engineering Conference
SAUPEC 2010, University of the Witwatersrand, Johannesburg

TOPIC B. MACHINES

MAGNETOSTATIC FEM SIMULATIONS OF A DOUBLE SIDED TUBULAR LINEAR PERMANENT-MAGNET GENERATOR FOR WAVE ENERGY EXTRACTION

Rael Schmulian and **W. A. Cronje**

School of Electrical and Information Engineering, University of the Witwatersrand, Johannesburg

Abstract. Due to growing environmental awareness and an increasing energy demand, the search for an alternative, renewable energy resource has intensified. Most traditional devices use a method of pumping hydraulic fluid through a hydraulic motor coupled to a rotating generator to generate electricity. This method is less efficient and needs more regular maintenance. This paper presents the simulation results of a double sided tubular linear permanent magnet generator to address these issues. Simulations were done using the ANSYS FEM package, forces acting on the translator were recorded for a set number of positions. The graphs show an agreement with previous results.

Key Words. Renewable Energy, Ocean Power, Finite Elements Method

1. INTRODUCTION

Growing environmental concerns and an increasing demand for energy has accelerated the research into renewable energy sources. One such source, wave energy, has the potential over all other renewable energy technologies to compete with traditional power generation systems such as coal or nuclear. Estimates account for power levels of 1 TW to 10 TW that can potentially be extracted from ocean waves [1].

Wave energy is essentially a concentrated form of solar energy. The sun heats up the earth unevenly, this causes differential pressures which causes winds to blow. As the wind blows over the ocean water surface it transfers some of the energy into the water creating waves. The waves can travel for thousands of kilometres with little energy loss. South Africa is located in a fortunate position, experiencing wave-fronts with up to 50 kW per meter wave-crest [2].

Methods of harnessing energy from ocean waves have been studied since the 1970's [1]. Interest was lost due to a low oil price and high capital investment required to commercialise such a system. Most existing devices operate on the principle of pumping hydraulic fluid through a hydraulic motor coupled to a traditional rotating generator. These devices can be deployed relatively quickly because it is based on existing technology, however, the added energy conversion stages and moving parts make it less efficient and in need of more regular maintenance.

A possible alternative is to directly couple the heaving motion of the ocean water to a linear generator using a device such as a buoy. By directly coupling the generator to a buoy, extra unnessesary energy conversion stateges are eliminated and with a proper design, the machine

has the potential to be maintanance free [3]. A double sided tubular linear permanent magnet generator for such an application will be simulated in this paper. The following sections of the paper will contain: a description of the machine, the set-up for the simulation, the simulation results and future work.

2. MACHINE SPECIFICATIONS

D. Joseph's novel design combines two different designs to create the double sided coaxial machine [4]. A flat double sided design increases the air gap surface area linking more flux than single sided machines. Tubular designs encapsulate the magnetic field, reducing the end effects prevalent in flat machines. The two air gaps in the double sided coaxial design allows for an increase in force density without a proportional increase in volume. An example of this can be found in [4] where the design is compared to the linear generator found in the Archimedes Wave Swing(AWS), for a similar force capability the double sided coaxial machine has a magnetic material footprint of 63.5% of that of the AWS's linear generator.

A scaled down version has been designed primarily for lab testing, Figure 1 shows a cross sectional cut-out of the machine. The simulations in this paper is done using this design. The design specifications of the machine are listed in Table 1.

The ratio between the pole-pitch and the magnet-pitch, $\alpha_m = 0.8$, is chosen to minimise cogging forces. Cogging (or reluctance) forces are as a result of the interaction between the permanent magnets and the stator teeth, the attracting forces constantly tries to align the permanent magnets and teeth [5] [6]. In an environment where maintenance becomes difficult such as the ocean,

TOPIC B. MACHINES

Proceedings of the 19th Southern African Universities Power Engineering Conference
SAUPEC 2010, University of the Witwatersrand, Johannesburg
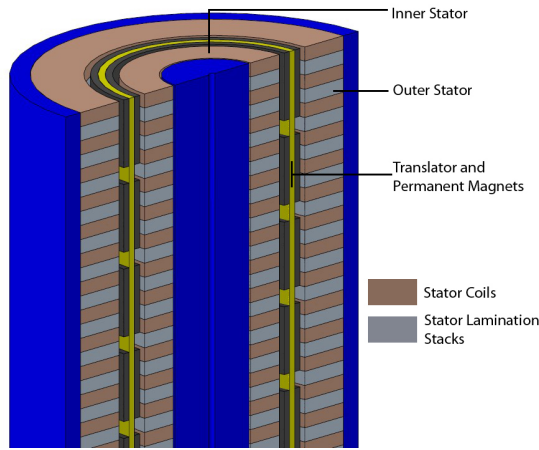
Figure 1: Cut-Out of Stator and Translator Sections.

Table 1: Design Specifications of the Scaled Down Machine.

Parameter Name	Value
Stator Length	0.36 m
Translator Length	1 m
Pole-Pitch	0.06 m
Magnet-Pitch	0.048 m
Air Gap Length	0.0045 m
Magnet Thickness	0.005 m
Stroke	0.6 m
Number of Phases	3
Inner Stator Turns Per Slot	80
Outer Stator Turns Per Slot	14
Slots/Pole/Phase	1

excessive cogging forces are undesirable as this would create vibrations potentially damaging the permanent magnets and stator.

Determining α_m is essentially an optimisation problem with many researchers using the brute force approach, α_m is varied while the total force ripple (TFR) is minimised. The TFR is calculated using equation 1 [4]:

$$TFR = \frac{\sqrt{\sum_{v=2} F_v^2}}{F1} \qquad (1)$$

Where F_v is the force component of the vth harmonic.

3. SIMULATION MODEL

Finite elements modelling (FEM) packages have revolutionised the way in which machines are designed today. Seemingly impossible problems can now be solved in a matter of days, hours and even minutes. FEM is still just a tool and it is up to the designer to apply his/her skills and knowledge to interpret the results and to make sure that it is reasonable.
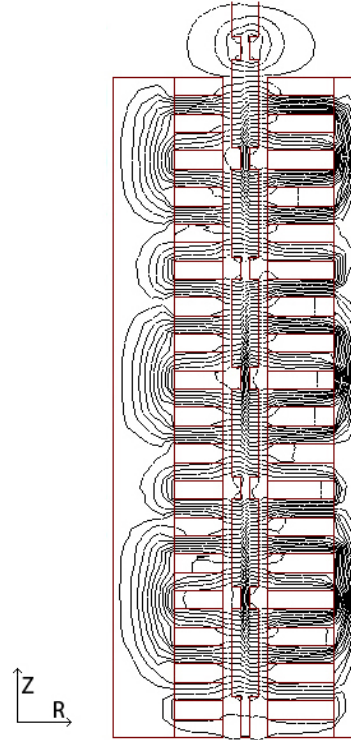
Figure 2: Starting Position of the Translator and Magnetic Flux Lines.
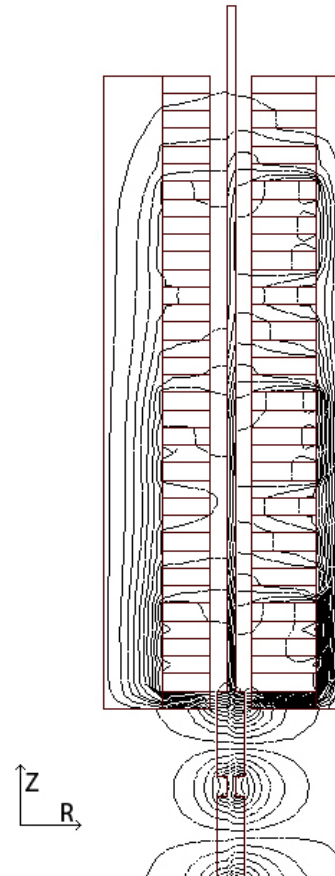
Figure 3: End Position of the Translator and Magnetic Flux Lines.

From D. Joseph's results it was known what the magnitude of the total force with respect to

Proceedings of the 19th Southern African Universities Power Engineering Conference
SAUPEC 2010, University of the Witwatersrand, Johannesburg

TOPIC B. MACHINES

translator displacement should be, this 'target' was used to develop the model and change aspects such as element size and number of sample points. ANSYS [7] was used as the FEM package and the model was set up as a 2D axisymmetric simulation. The geometry modelling phase is done in 2D, but the solution is done by rotating the planar geometry around an axis of symmetry, namely the centre of the machine.

The forces acting on the translator were calculated by the built in Maxwell stress tensor method. The translator was moved through one stroke starting with bottom aligned with the stator (see Figure 2), for each iteration the translator was moved by 0.0015 m resulting in 400 sample points. The last position is shown in Figure 3.
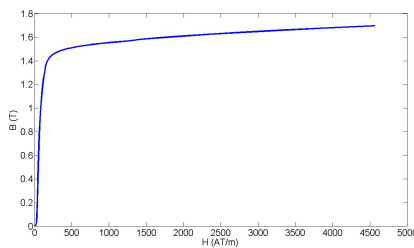
Figure 4: B-H curve Used for the Simulation.

The B-H curve was modelled using data from the 'US Steel Type 2-S 0.018 inch thickness' library in the FEMM package (Figure 4). In order to simulate a 'snapshot' in time, the stator coils were excited by DC currents. This replicates the instance in time where phase A is at a peak value and the return current splits through phases B and C. This was used in order to calculate the total force on the translator, the stator coils were left unexcited to calculate the reluctance forces.

4. SIMULATION RESULTS

The forces acting on the translator were recorded for each iteration. Figure 6 shows the combination of reluctance and lorenz forces, the Lorenz force having a period of 2 pole pitches. The larger the degree of magnetic coupling between the magnets and stator coils, the larger the Lorenz force component will be. This is illustrated by the amplitude of the force decreasing as the permanent magnets are no longer in the air gaps (Figure 3).

Assuming the B-H relationship does not go into saturation, the Lorenz forces were extrapolated

by subtracting the reluctance force from the total force. The three forces are plotted across two pole pairs and shown in figure 5. This illustrates that if the reluctance forces are eliminated the resulting force wil be 'smooth' and would reduce wear on the components.
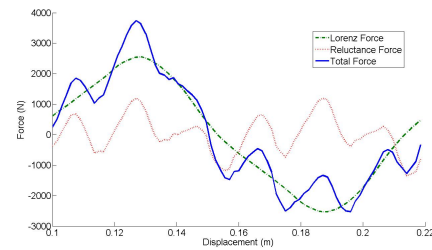
Figure 5: Total, Lorenz and Reluctance Force

A FFT was operated on the data to produce the results in Figure 7. The fundamental sits at 8.33 Hz which corresponds to a repetition of the fundamental every 0.12 m which is correct. The harmonics can be attributed to the harmonics in the permanent magnet flux distribution. Each of these harmonics interact with the stator teeth to produce a force. The DC offset is as a result of the unbalance in force when the magnet array starts to move outside the stator stack, a reluctance force tries to pull the stator back in one direction.
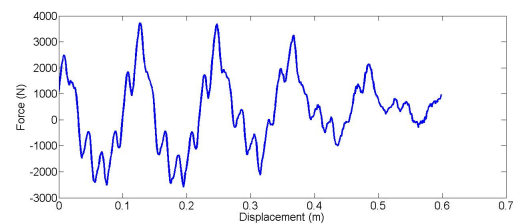
Figure 6: Force vs. translator displacement.
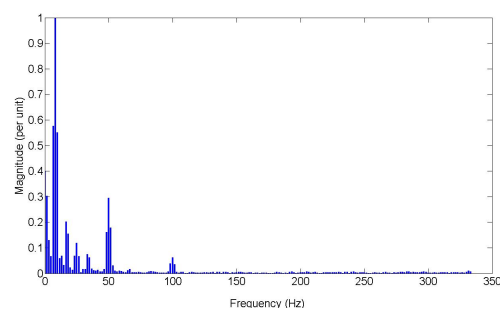
Figure 7: Frequency Spectrum of Translator forces.

TOPIC B. MACHINES

Proceedings of the 19th Southern African Universities Power Engineering Conference
SAUPEC 2010, University of the Witwatersrand, Johannesburg

5. FUTURE WORK

The magnetostatic simulations gives important feedback in validating the magnetic circuit design. This does not give any information on transients and the dynamic performance. Further work will include a dynamic simulation by connecting a resistive load and applying a force to the translator inducing currents. Aspects such as efficiency, regulation and the power factor will be analysed and improved.

Mechanical optimisations need to be looked at in more depth, ANSYS has functionality for mechanical simulations. A possible mechanical-electromagnetic coupled analysis can be implemented depending on computational resources and flexibility. This would give a good indication of the overall system performance.

After satisfactory simulation results are obtained, a new scaled down model will be built for lab testing. The model will mechanically actuated to simulate wave motion. Possible mechanisms are being considered at the time of writing.

6. CONCLUSION

Magneto-static simulations of a double sided tubular linear generator have been done to validate the force production. The resulting force vs. displacement graph indicates a good agreement with previous results. A frequency spectrum of the forces illustrates the forces due to the harmonics of the permanent magnet magnetic flux distribution. Future work needs to be done on dynamic simulations as well as mechanical simulations and optimisations.

REFERENCES

[1] R. Boud, "Status and research and development proroties, wave and marine current energy," International Energy Agency, Tech. Rep., 2003.

[2] The resource - pelamis wave power. Pelamis Wave Power. Last Accessed: 2 October 2009. [Online]. Available: http://www.pelamiswave.com/content.php?id=155

[3] M. Mueller, "Wave energy: linear versus hydraulic generators for energy conversion," Department of Trade and Industry, Tech. Rep., 2002.

[4] D. M. Joseph and W. A. Cronje, "Design of a double-sided tubular permanent-magnet linear synchronous generator for wave-energy conversion," *COMPEL*, vol. 27, pp. 154–169, 2008.

[5] N. M. Kimoulakis, A. G. Kladas, and J. A. Tegopoulos, "Cogging force minimization in a coupled permanent magnet linear generator for sea wave energy extraction applications," *IEEE TRANSACTIONS ON MAGNETICS,*, vol. 45, pp. 1246–1249, 2009.

[6] K.-C. Lim, J.-K. Woo, G.-H. Kang, J.-P. Hong, and G.-T. Kim, "Detent force minimization techniques in permanent magnet linear synchronous motors," *IEEE TRANSACTIONS ON MAGNETICS*, vol. 38, pp. 1157–1160, 2002.

[7] ANSYS, Inc. Last Accessed: 27 November 2009. [Online]. Available: http://www.ansys.com/

Proceedings of the 19th Southern African Universities Power Engineering Conference
SAUPEC 2010, University of the Witwatersrand, Johannesburg

TOPIC B. MACHINES

A 1-D THERMAL MODEL FOR A HIGH SPEED PERMANENT MAGNET SYNCHRONOUS MACHINE STATOR

A.J. Grobler, S.R. Holm and G. van Schoor*

* *Department of Electrical Engineering, North-West University, Potchefstroom, 2520, South Africa.*
E-mail: andre.grobler@nwu.ac.za

Abstract: Thermal modelling of small electric machines is becoming more important, especially in high power density and high speed machines. This paper presents a simple, lumped parameter based thermal model of the stator of such a machine. The model is verified using a finite element method model and good correlation is achieved. The stator's themal model will form part of a final coupled model.

Key words: Permanent magnet synchronous machine, thermal modelling, lumped parameter.

1. INTRODUCTION

The work presented in this paper forms part of a reseach project that aims to develop a coupled thermal and electromagnetic model for high speed permanet magnet synchronous machines.

Coupled models are used when the interaction between two domains needs to be taken into account, in this case the thermal and electromagnetic domains. These two domains are connected through losses and material properties. The electromagnetic loss changes the machine's temperature. Since a material's properties e.g. conduction, are temperature dependent, this temperature change influences the electromagnetic domain. Traditionally, the machine was designed to be optimal in terms of electromagnetics. Thermal effects were only included as limits, for example limiting the current density in the windings based on the designer's experience or empirical data. By using coupled models, the electromagnetic and thermal domains can be solved simultaneously, thus taking into account the interaction between these two domains.

In a coupled model, the electromagnetic part predicts the losses and their location in the machine. The losses found in a PMSM can be grouped into mechanical, conduction and magnetization losses. Conduction losses occur when current flows in a material. The voltage source can be the supply (e.g. I^2R losses in the stator windings) or an induced emf (e.g. eddy currents flowing in the shielding cylinder). Magnetization losses are found in ferromagnetic materials when the direction of the magnetic domains is changed by a magnetic field. Hysteresis loss in the stator laminations is an example of magnetization loss. In different areas in an electric machine, one or more of these loss types can cause distributed heat generation.

Thermal methods can be used to determine the effect of the various losses on the temperature distribution inside an electric machine. Heat flow occurs through three modes: conduction (in the solid parts of the machine), convection (between the solid and fluid found in and around the machine) and radiation (between non-contacting parts). The temperature distribution can be determined for a transient or steady state. Coupled thermal and electromagnetic design methods are becoming more important because:

- The thermal and electromagnetic worlds are coupled thus coupled models are a better approximation of reality.

- A good thermal design is also important when considering reliability. Winding insulation decay is influenced by the winding temperature and can cause machine failure.

- Various new machine structures are being proposed which have high power densities, making thermal modelling absolutely necessary. These machines are physically smaller thus reducing the heat extraction surface.

- Using a coupled model can result in a more electrically efficient machine thus reducing running costs. Manufacturing costs can also be lowered by using the optimum material volume.

- Permanent magnet (PM) machines are also increasingly used because of their good electric efficiency, dynamic response, brushless operation and power density. Unfortunately PMs can demagnetize when heated above the material's Curie temperature [1].

It can be concluded that reliability, efficiency and cost are the main reasons for coupled thermal and electromagnetic modelling.

1.1 LP motivation

Solving the temperature distribution is mostly done using lumped parameters (LPs) and finite element method (FEM) techniques. Lumped parameters are based on the analogy that can be drawn between the thermal and electrical domains. The relations are: Voltage difference to

TOPIC B. MACHINES

Proceedings of the 19th Southern African Universities Power Engineering Conference
SAUPEC 2010, University of the Witwatersrand, Johannesburg

temperature difference, electric current to heat transfer rate, electric capacitance to thermal capacitance and electric resistance to thermal resistance. Machine designers with an electrical engineering background can thus easily understand LP thermal models.

LP models can be solved using less computational resources than other techniques. This makes LPs very well suited for use in machine optimization and "what if" analyses.

It is easier to anticipate the effect a parameter or variable has on the whole model when using LPs. Numerical methods like FEM have a "black box" feel since the user usually has no knowledge of the solution process. The user also does not understand the modelled process as well as when using LPs.

1.2 Previous work

Most electric machine thermal modelling in literature is based on induction motors since these machines are the most widely used [2]. Small machines have also not received much attention, due to smaller return on investment than large machines. The high speed machines found in literature are mostly cooled using a water jacket because high power density results in a smaller cooling surface than in low speed machines. Using a shielding cylinder to decrease rotor losses in high speed PMSMs has been analyzed in the electromagnetic domain [3]. Thermal analysis of the shielding cylinder has not been published.

Even though thermal models using lumped parameters (LPs) have been used for many years, there are still unresolved issues. Calculating the values of especially convection and contact resistances remains a challenge.

1.3 Test platform: TWINS

The McTronX research group of the North-West University developed a high speed PMSM testing platform in 2008. This system consists of two identical, 4kW 30 000 r/min PMSMs with directly connected axes, and is called the TWINS. Figure 1 shows the TWINS mounted on a vertical base plate in the high speed test chamber. A Neodymium-Iron-Boron (Nd-Fe-B) magnet, sintered into a cylindrical form supplies the rotor magnetic field. The PM is retained with an Inconel shielding cylinder to ensure that the rotor withstands the centrifugal forces at 30 000 r/min.

This platform will be used to compare various control strategies for PMSMs and is also suited for thermal analysis since it is equipped with strategically placed temperature sensors. The influence of the shielding cylinder on the machine performace and temperature can thus be analyzed with this test platform. The machines can be operated in motoring or generating mode, thus one machine can variably load the other. The experimental setup will be discussed in more detail in section 5.
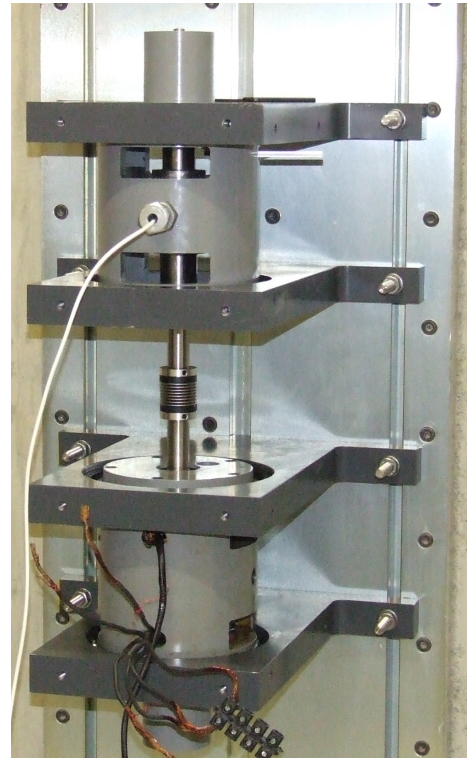
Figure 1: TWINS photograph

1.4 In this paper

The final goal is to derive a coupled thermal and electromagnetic model for a high speed permanet magnet synchronous machine (PMSM). In this paper the development of a one dimensional (1-D) model for the stator is presented. The proposed model is based on LPs and will be verified using a commercial finite element method (FEM) package. Since all the material properties are temperature dependent, a variable resistor is used to model the convection thermal resistance. Most thermal models are based on previous experience and experimental results. This paper aims to derive an accurate yet simple thermal model based on first principles.

The results shown in this paper are based on the geometry of the TWINS. The following assumptions have been made to simplify the stator model:

- Only radial heat flow is included. In the final model axial and radial heat flow will be included.

- Constant copper winding losses are assumed, thus only heat generation inside the stator winding is included in this preliminary model. All the other types of losses mentioned earlier will be included later in the final model.

- The contact between parts of the machine is not perfect, a phenomenon that can be modelled using contact resistances. In this model contact resistance

Proceedings of the 19th Southern African Universities Power Engineering Conference
SAUPEC 2010, University of the Witwatersrand, Johannesburg

TOPIC B. MACHINES

is not included, thus it is assumed different parts are in perfect contact.

- Radiation heat transfer is not included in the model presented in this paper. It will be taken into account in the final model.

The work presented in this article is only a part of the final coupled model. A thermal model for the rotor as well as an electromagnetic model for the whole machine must still be completed. In this paper the focus is on the stator's thermal model and thus not the exact size and location of the losses.

2. THERMAL MODELLING: AN OVERVIEW

2.1 Heat transport modes: Conduction

Conduction occurs in a solid or a fluid. If a temperature difference exists in a medium, a heat flux will result in order to eradicate this temperature difference. The conduction heat transfer rate (q_{cond}), in watts, can be described using Fourier's law. In one dimension it is written as:

$$q_{cond} = -kA\frac{dT}{dx}, \tag{1}$$

where k is the thermal conductivity, A is the cross-sectional area and $\frac{dT}{dx}$ is the temperature gradient in the medium [4]. Thermal conductivity is a material property similar to electric conductivity. Another important equation is the conduction equation. In one dimension it is

$$\frac{\partial}{\partial x}\left(k\frac{\partial T}{\partial x}\right) + \dot{q} = \rho c\frac{\partial T}{\partial t}, \tag{2}$$

where $\dot{q}$ is the heat generated internally, ρ is the density and c is the specific heat. The first term of (2) gives the longitudinal conduction, the second the internal heat generation and the last the thermal inertia.

Conduction forms the basis of all thermal modelling of electric machines and has thus been researched extensively. Current research topics in conduction include: interface gaps between components, stator winding models, material data and bearing heat transfer [5].

2.2 Heat transport modes: Convection

Convection is the heat transport mechanism found between a solid surface and a moving fluid. This heat transport mode can be categorized into two groups (forced and natural) according to the cause of the fluid movement. In forced convection, the fluid movement is caused by an external force like a fan. In natural convection, the fluid movement is caused by buoyancy forces resulting from a change in fluid density when a change in temperature

occurs. Conduction heat flow is still present between a solid and a fluid, but to a lesser extent. The Nusselt number is a dimensionless number that indicates the heat transfer rate due to convection (q_{conv}) versus that due to conduction (q_{cond}):

$$Nu = \frac{q_{conv}}{q_{cond}}. \tag{3}$$

This means that a large Nusselt number indicates a large amount of the heat transfer is due to convection, compared to conduction. The heat transfer rate caused by convection (q_{conv}) can be described by :

$$q_{conv} = hA(T_s - T_\infty), \tag{4}$$

where T_s is the surface temperature, T_∞ is the surrounding fluid temperature and h is the convection coefficient. The convection coefficient is a function of the fluid speed and thermal properties. In the case of natural convection, the air speed and thus the convection coefficient is dependent on the surface temperature.

Convection heat flow occurs inside and outside the electric machine. The air movement resulting from the rotor movement causes convection heat flow between the rotor and the stator. Convection heat transfer also occurs between the stator outside and the surrounding medium (usually air). Both of these areas have received attention in recent years, with most of the work done on induction machines with shaft mounted fans and stator fins. [6]

2.3 Heat transport modes: Radiation

Radiation occurs between two surfaces through electromagnetic waves, where no intervening medium is present as in convection situations. Radiation is thus the only heat transfer mode found between different objects in vacuum situations. The radiation heat transfer rate (q_{rad}) can be described using

$$q_{rad} = \varepsilon\sigma A(T_s^4 - T_{sur}^4), \tag{5}$$

where σ is the Boltzmann constant, ε is the emissivity, T_s is the surface temperature and T_{sur} is the room surface temperature.

To separate the heat flow caused by convection and radiation is difficult since radiation is always present to an extent. Radiation and natural convection heat transfer are in the same order of magnitude when no external fan is present in industrial induction motors [7]. A small amount of experimental work has been done in this field.

Proceedings of the 19th Southern African Universities Power Engineering Conference
SAUPEC 2010, University of the Witwatersrand, Johannesburg

TOPIC B. MACHINES

3. 1-D STATOR MODEL

3.1 Model geometry

Since the stator of the TWINS is symmetrical around the center, an axisymmetrical approach can be taken. This means that the cylindrical machine can be modelled in two dimensions in FEM and using cylindrical lumped parameter (LP) resistances. Figure 2 shows a simple cut view of the TWINS machine and highlights the area that will be modelled in this paper. The winding is wound inside the coil former, which in turn slides into the slotless laminations. The stator laminations are stacked inside the stator housing and kept in place with a circlip. In this 1-D model the heat will only flow radially outward from the windings to the surrounding air.

3.2 Lumped parameter model

This section introduces a 1-D LP model for the TWINS stator. Figure 3 shows the lumped parameters used for each section of the stator. Only copper conduction losses are included in this model, thus only one loss source (q_L) is included in the centre of the windings. The sections where conduction heat flow occurs were modelled using an equivalent thermal resistance:

$$R_{cyl} = \frac{\ln\left(\frac{r_2}{r_1}\right)}{2\pi Lk}, \quad (6)$$

where r_1 and r_2 is the inner and outer radii of the cylinder respectively, L is the axial length and k is the thermal conductivity of the material. Sections where only conduction occurs, are: the coil former first part (R_{cf1}), winding first part (R_{wm1}), winding second part (R_{wm2}), coil former second part (R_{cf2}), lamination (R_l) and stator housing (R_s).

Where the machine comes into contact with the surrounding air, an equivalent resistance can also be used to model the convection heat transfer. The TWINS has natural convection heat flow on the outside and the convection resistance (h) is dependent on the surface temperature (T_s). The convection constant can be determined using:

$$h = \frac{0.59k}{L}\left(\frac{g\beta L^3 \text{Pr}(T_s - T_\infty)}{\nu\alpha}\right)^{1/4}, \quad (7)$$

where g is the gravitational acceleration, β is the volume expansivity, Pr is the Prandtl number, ν is the kinematic viscosity and α is the thermal diffusivity. The derivation of (7) is reported in Appendix A. The Prandtl number is also a dimensionless number, given by

$$\text{Pr} = \frac{\nu}{\alpha}, \quad (8)$$
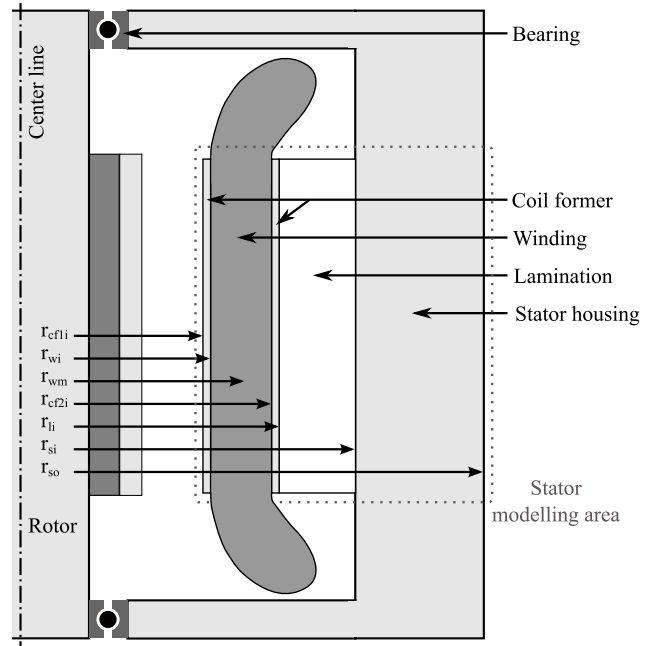
Figure 2: Model geometry
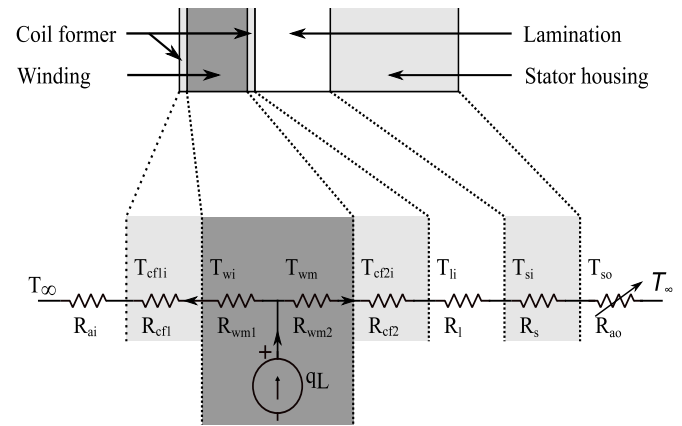
Figure 3: LP model

thus giving the ratio of momentum diffusivity and thermal diffusivity.

The convection resistance R_{conv} can be calculated using

$$R_{conv} = \frac{1}{hA}, \quad (9)$$

where A is the cross sectional area and h is the heat transfer coefficient or convection coefficient. The temperature dependence of h results in R_{ao} (the outside convection resistance) being a variable resistance, as shown in Figure 3. The LP model were implemented in MATLAB® Simulink®. The variable resistor was modelled using a variable current source, as shown in Figure 4. The temperature at node 1 represents T_{so} and the temperature at node 2, T_∞. The difference between these temperatures is used to calculate the Rayleigh number, which is used

Proceedings of the 19th Southern African Universities Power Engineering Conference
SAUPEC 2010, University of the Witwatersrand, Johannesburg

TOPIC B. MACHINES
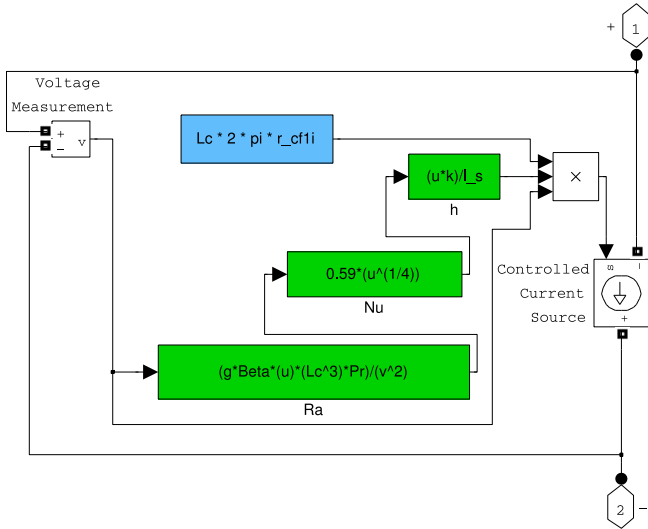
Figure 4: h implementation in Simulink®
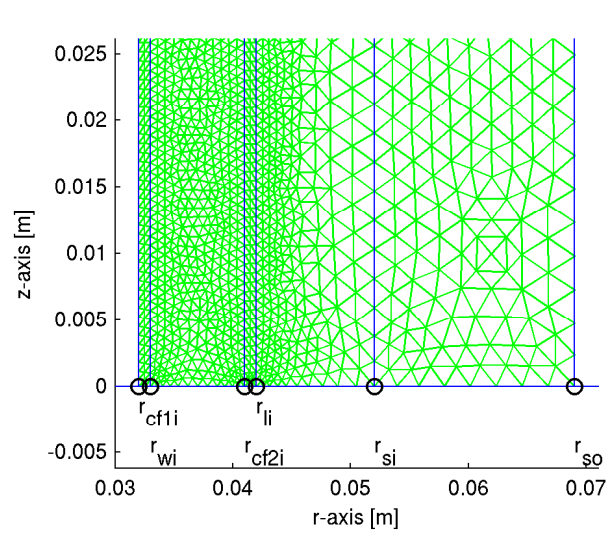
Figure 5: FEM mesh

to calculate the Nusselt number. This is then used to calculate h, which, multiplied by the voltage (temperature) difference and surface area, gives the heat transfer rate q.

Radiation heat transfer can be included into the LP model by placing another variable resistor in parallel with R_{ao}. Since only the stator model is presented in this paper, the inner convection resistance (R_{ai}) is assigned a large value to act as a thermal insulation. When adding the rotor to the model, this will be changed.

3.3 FEM model

The heat transfer module of the commercial FEM package COMSOL® was used to verify the LP model. The same material properties were used in both the LP and FEM models. COMSOL® also uses a formula simular to (7) to determine h. Figure 5 shows the mesh of the FEM model. At the right boundary convection heat flow is modelled and the rest of the outer boundaries are modelled as thermal insulation.

4. COMPARISON BETWEEN LP AND FEM MODELS

4.1 h sensitivity analysis

All the material properties found in (7) are dependent on the average fluid temperature (T_f), which can be determined using

$$T_f = \frac{T_s - T_{inf}}{2}. \qquad (10)$$

Including all the material properties as temperature dependent functions into (7) will further complicate the LP model. The goal of this section is to determine the modelling error resulting by assuming the material properties are constant.

Assume the surface temperature (T_s) has a range of [293 - 413] K and T_∞ = 293 K, then T_f will have a range of [293 - 353] K. The sensitivity of h, and thus the convection heat flow, is shown in Table 1. All the properties except Pr has a significant influence on h. Care should be taken to use the correct value of these properties for the corresponding average fluid temperature. As shown in the last line of Table 1, combining the variation results in a 5% deviation in h.

The fluid temperature is not known when solving the model the first time since T_s is still unknown at this stage. It is proposed that the LP model be solved iteratively to ensure the correct fluid properties are used:

- First iteration - Assume $T_f = T_{inf}$ and use this to determine the fluid properties. Solve the LP model to determine a preliminary T_s.

- Other iterations - Now use the preliminary T_s to calculate a new T_f. Use the new T_f to calculate the fluid properties and solve the LP model again, thus finding a new T_s.

Figure 6 shows the results of the first, second and third iterations of the PM model compared with the FEM results. It is clear that the LP model correlates much better with the FEM results after the second iteration.

Table 1: h temperature sensitivity

Property	Lower temp [293 K]	Upper temp [353K]	$\%\Delta h_{conv}$
β	3.413e-3	2.83e-3	4.72%
ν	15.16e-6	20.96e-6	16.72%
k	0.02514	0.02953	15.63%
Pr	0.7309	0.7154	0.53%
Combined			5.377%

TOPIC B. MACHINES

Proceedings of the 19th Southern African Universities Power Engineering Conference
SAUPEC 2010, University of the Witwatersrand, Johannesburg
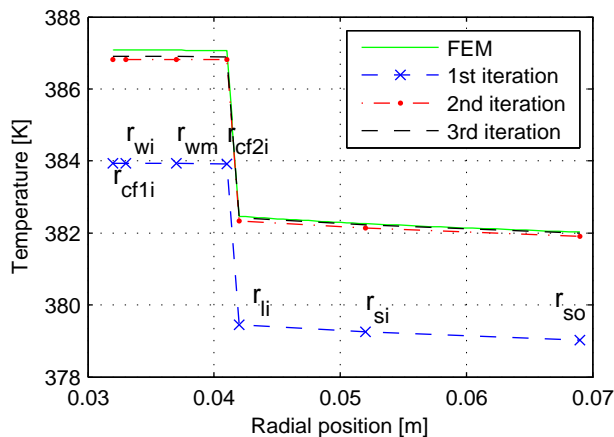
Figure 6: 1st, 2nd and 3rd iteration results versus FEM results
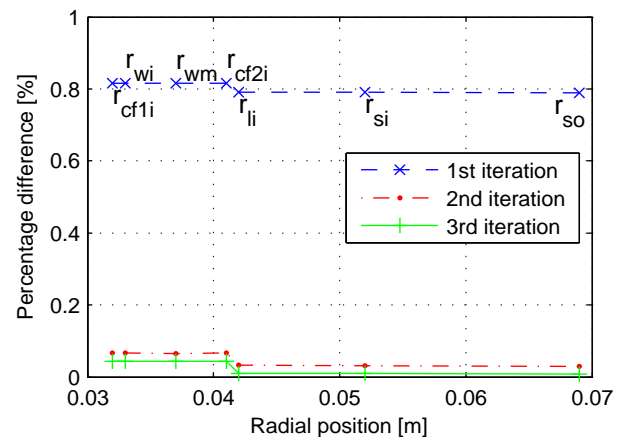
Figure 7: 1st, 2nd and 3rd iteration results versus FEM, percentage difference

4.2   Comparing the two models

The correlation between the LP model and FEM can be summarized by calculating the percentage difference of the iterations as shown in Figure 7. After the third iteration, the difference is less than 0.05 %. When taking into account the accuracy of temperature measurements, it can be concluded that the LP model of 1-D is accurate enough after two iterations.

5.   PROPOSED EXPERIMENTAL SETUP

The next step is to verify the LP model using measured results. Since the stators of the TWINS are manufactured in house, temperature sensors can be placed throughout the stator. Figure 8 shows the proposed locations of the temperature sensors in the upper half, and a block diagram of the rest of the components in the lower half. The power electronics converts power from the three phase supply to the required stator currents. A three phase inverter, implemented with SEMIKRON stacks, powers each of the three phase machines from a common DC bus. The DC bus is realized by rectifying a three phase isolated 220 VAC supply. The phase voltages and currents are also measured.

The interface board isolates the controller from the power electronics, powers the sensors and conditions the sensor signals. All the control and signal sensors connect through the interface board to the controller (dSPACE®). The controller is a stand alone system and is programmed using a fiber optic connection from a personal computer. The control software is compiled in MATLAB® and all signals can be displayed in a LabVIEW™ experiment. The data can also be stored on the personal computer.

6.   CONCLUSION AND FUTURE WORK

This paper introduced a 1-D lumped parameter thermal model for the stator of a high speed PMSM. The proposed model showed good correlation with FEM results. A variable resistor, dependent on the surface temperature,
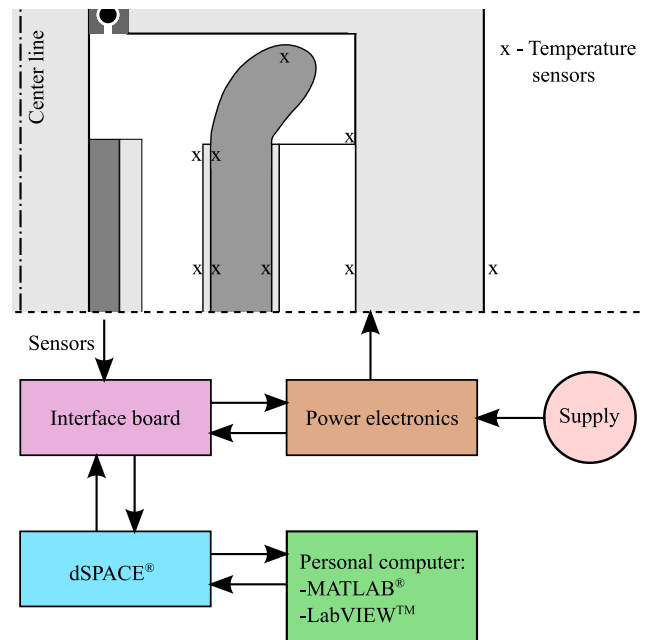
Figure 8: Thermal experimental setup

was used to model the convection heat transfer between the machine outer surface and the surrounding air.

The model still needs to be verified using the experimental setup. The next step is to derive a 2-D stator model. Multiple loss sources must be included when taking into account the stator and rotor losses caused by the rotating stator field. This will lead to a coupled thermal and electromagnetic model. The rotor movement must also be included to complete the model.

APPENDIX A

The derivation of (7) is presented in this appendix. The dimensionless Rayleigh number (Ra) is given by

Proceedings of the 19th Southern African Universities Power Engineering Conference
SAUPEC 2010, University of the Witwatersrand, Johannesburg

TOPIC B. MACHINES

$$\mathrm{Ra} = \frac{g\beta(T_s - T_\infty)L^3\mathrm{Pr}}{\nu\alpha}, \qquad (11)$$

where g is the gravitational acceleration, β is the volume expansivity, Pr is the Prandtl number, T_s is the surface temperature, T_∞ is the surrounding fluid temperature, L is the axial length, ν is the kinematic viscosity and α is the thermal diffusivity. The Nusselt number can be calculated using

$$\mathrm{Nu} = 0.59\mathrm{Ra}^{1/4}. \qquad (12)$$

The convection coefficient h is given by

$$h = \frac{\mathrm{Nu}k}{L}. \qquad (13)$$

Substituting (11) and (12) into (13) gives (7).

REFERENCES

[1] D. G. Dorrell, "Combined thermal and electromagnetic analysis of permanent-magnet and induction machines to aid calculation," *IEEE Transactions on Industrial Electronics*, vol. 55, no. 10, pp. 3566 – 3574, 2008.

[2] D. Staton, A. Boglietti, and A. Cavagnino, "Solving the more difficult aspects of electric motor thermal analysis in small and medium size industrial induction motors," *IEEE Transactions on Energy Conversion*, vol. 20, no. 3, pp. 620 – 628, 2005.

[3] H. Polinder and M. J. Hoeijmakers, "Effect of a shielding cylinder on the rotor losses in a rectifier-loaded PM machine," in *Conference Record of the 2000 IEEE Industry Applications Conference*, 2000, pp. 163–170.

[4] F. P. Incropera, D. P. DeWitt, T. L. Bergman, and A. S. Lavine, *Fundamentals of heat and mass transfer*, 6th ed., V. Vargas, Ed. John Wiley and sons, 2007.

[5] A. Boglietti, A. Cavagnino, and D. Staton, "Determination of critical parameters in electrical machine thermal models," *IEEE Transactions on Industry Applications*, vol. 44, no. 4, pp. 1150–1159, 2008.

[6] D. Staton and A. Cavagnino, "Convection heat transfer and flow calculations suitable for analytical modelling of electric machines," in *IEEE IECON*, Paris, France, November 2006, pp. 4841–4846.

[7] A. Boglietti, A. Cavagnino, M. Parvis, and A. Vallan, "Evaluation of radiation thermal resistances in industrial motors," *IEEE Transactions on Industry Applications*, vol. 42, no. 3, pp. 688 – 693, 2006.

TOPIC B. MACHINES

Proceedings of the 19th Southern African Universities Power Engineering Conference
SAUPEC 2010, University of the Witwatersrand, Johannesburg

A NON-LINEAR SIMULATION MODEL OF AN ACTIVE MAGNETIC BEARING SUPPORTED ROTOR SYSTEM

S. Myburgh*, G. van Schoor*

School of Electrical, Electronic and Computer Engineering, North-West University, Potchefstroom Campus

Abstract: Nowadays active magnetic bearings (AMBs) are utilised in a wide range of applications including high-speed flywheel energy storage devices. This paper aims at reporting on the modelling and simulation of a flywheel energy storage system supported by AMBs. Firstly the non-linear AMB model is discussed that comprises the power amplifiers, displacement sensors, anti-aliasing filters and controller. The results of the non-linear AMB model are compared to conventional linear AMB models. Secondly the rotor model is discussed. The rotor model was implemented by means of the finite element method and the simulated results compared to a commercial rotor-dynamic software package. The rotor model is then integrated with the AMB models and the system is simulated under step disturbance inputs at the bearing positions as well as a run-up test to determine the unbalance response of the rotor.

Key Words: active magnetic bearings, rotor-dynamic simulation, flywheel energy storage system

1. INTRODUCTION

Active magnetic bearings (AMBs) have come of age in the past two decades since the first International Symposium on Magnetic Bearings held in 1988 [1]. Nowadays AMBs are routinely utilised in applications such as turbomachinery, centrifuges, vacuum machinery, machine tool spindles, medical devices, robotics, high-speed drives, spacecraft equipment, contactless actuators and vibration isolation [2]. AMBs are also used in flywheel energy storage applications where the flywheel is operated inside a vacuum chamber in order to reduce windage losses. Conventional rolling element bearings usually fail inside vacuum environments due to poor lubrication [3].

In 2007 the McTronX research group at the North-West University successfully developed such a flywheel energy storage system hereinafter referred to as the Fly-Ups system. The Fly-Ups system is capable of running at speeds of up to 30,000 r/min and delivering 2 kW of power to a load for a time of 15 minutes. The flywheel rotor is fully suspended in 5-axes by AMBs, is powered by a 2 kW permanent magnet synchronous machine (PMSM) and is operated in a vacuum housing [4].

Upon completion of the Fly-Ups project initial tests showed that the AMBs could not stably support the rotor up to the operating speed of 30,000 r/min due to large unbalance residing on the flywheel rotor. The AMBs could also not perform at their design stiffness and damping due to noise effects within the control enclosure given that the noise is amplified by the differentiator of the PD-controller. This fact lead to a significant reduction in bearing damping capabilities of the radial AMBs since the derivative gain of the PD-controller had to be reduced in order to stably suspend the flywheel rotor [5].

In order for the McTronX research group to further their research into AMB systems and to analyse current issues with the experimental AMB systems, an integrated rotor-AMB simulation platform needed to be developed. The simulation platform may be used to simulate the response of a complex rotor-AMB system including critical frequency analysis of the rotor, mode shapes, rotor unbalance response, AMB response due to disturbance inputs, cross-coupling effects, controller performance and AMB performance analysis under operating conditions. The simulation platform may also be used for the testing of advanced control algorithms and vibration suppression schemes employed in AMBs.

2. ACTIVE MAGNETIC BEARINGS

2.1 Basic operating principle

Magnetic bearings utilise magnetic forces to support the moving machinery without physical contact. Stable operation of the magnetic bearing system is only possible by making use of feedback control since magnetic bearings are open-loop unstable. Typically an AMB system comprises a rotor, an electromagnetic actuator, power amplifiers, position sensor and a digital controller. Figure 1 shows the functional diagram of an AMB system.
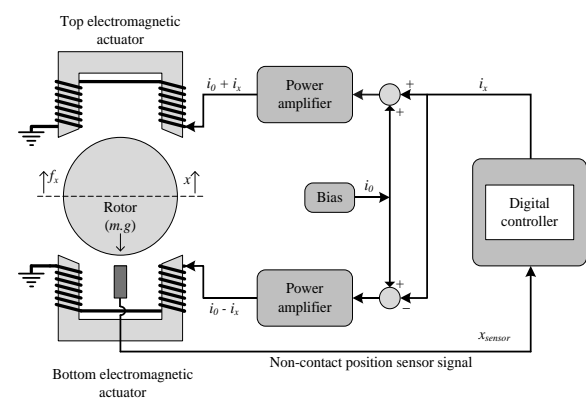

Figure 1: Functional diagram of an AMB system

The non-contact position sensor is used to measure the position (x_{sensor}) of the rotor and this signal is used by the controller to generate the control signal (i_x) which is fed to the power amplifier, which in turn

Proceedings of the 19th Southern African Universities Power Engineering Conference
SAUPEC 2010, University of the Witwatersrand, Johannesburg

TOPIC B. MACHINES

supplies the required currents (i_0+i_x) to the actuator coil. The actuator exerts a force (f_x) on the rotor keeping it in its reference position. The air gap between the rotor and the actuator is denoted by x.

2.2 Non-linearities inherent to AMBs

As shown in Figure 1 magnetic bearing systems typically comprise a rotor, magnetic actuators, displacement sensors, power amplifiers and a digital controller all of which are characterised by non-linear behaviour. This in turn suggests that the entire magnetic bearing system is characterised by highly non-linear behaviour. The main non-linearities inherent to AMB systems include [2]:

(i) Non-linear force-current and force-displacement relationship of the electromagnetic actuators

(ii) Saturation effect of the ferromagnetic core material and the non-linearity of the actuator coil inductance

(iii) Hysteresis of the magnetic core material

(iv) Saturation of the power amplifiers and the limitation on control current caused by physical limitations of the power amplifiers

(v) Geometric coupling between the electromagnets which results in coupling between different orthogonal coordinate directions

(vi) Time delays in the feedback loop caused by processing time of the digital controller and A/D- and D/A conversion time

(vii) Non-linearity of the sensor system and noise effects in the sensor system

Other effects include eddy current- and leakage- and fringing effects.

The non-linear force-current and force-displacement relationship of an 8 pole heteropolar radial AMB is shown in (1) where k_m denotes the electromagnetic constant, i_0 denotes the bias current in the actuator, i_x denotes the control current, x_0 denotes the rotor nominal position, x denotes the rotor displacement from the nominal position and α denotes the angle of the pole with the geometric coordinate axis.

$$f_x = k_m \left[\frac{(i_0+i_x)^2}{(x_0-x)^2} - \frac{(i_0-i_x)^2}{(x_0+x)^2} \right] \cos(\alpha) \qquad (1)$$

The traditional approach of characterising the AMB is to linearise (1) about the operating point where $i_x = i_0$ and $x = x_0$ which translates to the linear force-current force-displacement relationship shown in (2) where k_i is the current gain and k_s is the negative position stiffness.

$$f_x = k_i i + k_s x \qquad (2)$$

The linear force relationship shown in (2) holds true only for small rotor deflections and small control currents about the operating point. If the rotor deflection exceeds half the air gap, the net magnetic force of the opposite pair of electromagnets differs by more than 44% from its linear approximation [6]. This leads to rapid deterioration of performance of the AMB when operation deviates from the nominal position. This fact leads to the need for non-linear dynamic analysis of magnetic bearing systems since the dynamic behaviour of AMB may be totally different from the predicted linear model [2].

2.3 AMB model

Table 1 shows the characteristics of the magnetic bearings developed for the Fly-Ups system. The rotor-dynamic analysis of the flywheel rotor yielded a maximum load of the radial AMBs of 150 N with bearing stiffness of 500,000 N/m and bearing damping of 2500 N.s/m. An air gap of 0.5 mm was specified together with a maximum flux density of 1 T in order for the magnetic bearing to operate in the linear region of the magnetic material. The maximum current flowing in the AMB coils was specified as 5 A due to power amplifier limitations. This together with the slew rate requirements yielded the maximum power amplifier bus voltage of 54 V.

Figure 2 shows the developed Simulink® model of the radial AMB. This model represents the rotor as a point mass for verification purposes. The model includes a PID controller, power amplifier models, non-linear force-current, force-displacement relationship in (1), anti-aliasing filter, eddy current displacement sensor model and a noise generator.

The AMB is controlled by a discrete PID controller operating at a sampling rate of 10 kHz. The input of the controller is the actual displacement of the rotor whereas the controller output is a current reference to the power amplifiers. The current bias of 2.5 A is added to the top- and bottom control current reference.

Table 1: AMB properties [5]

Bearing parameter	Parameter value
Maximum load capacity	F_{max} = 150 N
Bearing stiffness	k_{eq} = 500,000 N/m
Bearing damping	b_{eq} = 2500 N.s/m
Air gap	g_0 = 0.5 mm
Saturation flux density	B_{sat} = 1 T
Number of turns per coil	N = 80
Maximum current	I_{max} = 5 A
Bias current	I_{bias} = 2.5 A
Power amplifier bus	V_{max} = 54 V

TOPIC B. MACHINES

Proceedings of the 19th Southern African Universities Power Engineering Conference
SAUPEC 2010, University of the Witwatersrand, Johannesburg
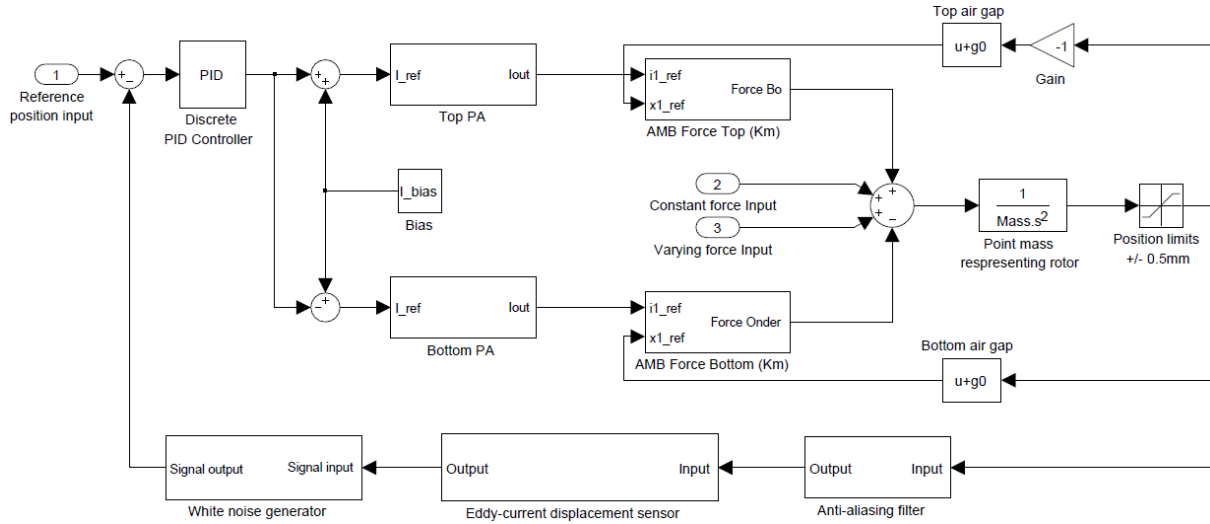
Figure 2: AMB model including the various subcomponents

The power amplifiers are modelled as current feedback power amplifiers with a PI controller determining the duty cycle. The power amplifier models also contain the resistance and inductance characteristics of the AMB coils. The current is determined by varying the duty cycle of the applied bus voltage to the transfer function of the AMB coils and the power amplifier has a bandwidth of 2.5 kHz.

The current output of the power amplifier together with the actual position of the rotor serves as input to the force calculation block which contains the non-linear force characteristic in (1). The output force is applied to the rotor (in this case only a point mass) and is integrated twice to obtain the position of the mass.

In order to scale the output voltage of the eddy current displacement sensor to +/- 10 V in the actual system, a signal conditioning circuit is added with a zener diode and a low pass filter at the Nyquist frequency (f_N) of 5 kHz in order to reduce anti-aliasing effects. The transfer function of the low pass filter is given by (3).

$$G_f(s) = \frac{2\pi f_N}{s + 2\pi f_N} \tag{3}$$

The eddy current displacement sensor was modelled as a low pass transfer function of second order with the two parameters being the bandwidth ω_s and the dimensionless damping ζ_s of the sensor as shown in (4) where K_{sens} is the sensor gain [7].

$$G_S(s) = K_{sens} \frac{\omega_s^2}{s^2 + 2\zeta_s\omega_s + \omega_s^2} \tag{4}$$

A white noise generator is also included in the model in order to simulate the actual noise present in the Fly-Ups system. The white noise is scaled to be comparable in amplitude to the actual high frequency noise present within the Fly-Ups system.

2.4 AMB model verification

In order to get a measure of how well the AMB model corresponds with the actual specifications of the Fly-Ups AMBs, the stiffness and damping properties of the AMB model has to be verified. Since the AMB system can be seen as a second order system close to its working point, a step response can be employed to determine the stiffness and damping properties [5].

The non-linear AMB model was connected to a mass of 13.22 kg and a step disturbance input of 10 μm was introduced after 0.5 seconds as can be seen in Figure 3. The model was also compared with a linear AMB model that makes use of equation (2) to determine the force exerted on the mass.

$$k_{eq} = \frac{\omega_n^2}{m} \quad ; \quad b_{eq} = 2\zeta\sqrt{k_{eq}m} \tag{5}$$

Graphically the percentage overshoot, settling time and final value are determined and used to determine the natural frequency and damping ratio.

Figure 3: Step response of linear- and non-linear AMB models

Proceedings of the 19th Southern African Universities Power Engineering Conference
SAUPEC 2010, University of the Witwatersrand, Johannesburg

TOPIC B. MACHINES

Using (5) the equivalent stiffness of the AMB is determined to be 500851 N/m and the damping is determined to be 2531 N.s/m. The stiffness values compares to within 0.2 % and the damping values compares to within 1.24 % of the design values listed in Table 1 [5]. The AMB model thus shows good correlation to the design values.

3. FLYWHEEL ROTOR

3.1 Rotor-dynamics

According to the ISO definition, a rotor is a body suspended through a set of cylindrical hinges or bearings that allows it to rotate freely about an axis fixed in space. Rotor-dynamics in turn is the study of the dynamic behaviour of rotors [8]. In high-speed machinery the dynamic behaviour of rotors needs to be analysed to ensure the desired operational performance is achieved. To analyse the dynamic behaviour of a rotor, an accurate model of the rotor has to be developed. The most common modelling methods employed in rotor-dynamic analysis today can be subdivided into two wide classes, the *lumped parameter methods* an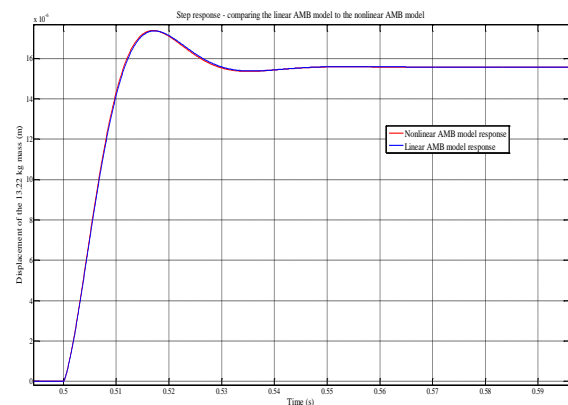d the *finite element methods* (FEM) [3]. For the purpose of this study the finite element method was selected to develop the rotor model since it is numerically more stable [3].

Rotor models can be further divided in rigid- and flexible rotor models. Rigid rotor models operate under the assumption that the rotor is uniformly symmetric and rigid, and bearing- and sensor locations are scaled to a distance from the centre of gravity (CG). The displacement of the rotor is only described in terms of translational and angular motion about the CG [8]. This in turn suggests that the rigid rotor model is only capable of predicting the rigid body modes of the rotor i.e. cylindrical and the conical modes.

In flexible rotor models in turn, the rotor is divided into several beam elements characterised by numbers n (n = 1, 2, 3, …, N). Each beam element n is described by length l_n, bending stiffness EJ_n, mass per unit length μ_n, mass eccentricity e_n, angle of eccentricity γ_n and further parameters describing internal and external damping as well as additional rotational inertia and gyroscopic effects. The system matrix is then determined for each element. This includes a mass-, stiffness-, damping- and forcing matrix for each element which is then integrated into the equation of motion of the flexible rotor as shown in (6). Theoretically the number of natural frequencies that can be calculated is equal to the number of elements in the flexible rotor model [9]. Flexible rotor models can thus predict critical frequencies above the 1st and 2nd rigid modes.

In high speed machines, it is vital to know where in the frequency spectrum the critical speeds are located since operation at these critical speeds may be harmful to the machine. In order to determine the critical speeds of a rotor the natural frequency has to be determined first.

Natural- or fundamental frequency: Every system encounters resonance at a particular number of frequencies. At these resonance frequencies a small disturbance can cause the system to vibrate [9].

Critical Speed: The critical speed of a rotor is defined as the speed at which the rotating shaft imbalance coincides with the natural frequency of that shaft. If a rotor is operated at or near a critical speed, it will exhibit high vibration levels, and is likely to be damaged [9]. Operation between critical speeds ensures that the vibration levels are kept to a minimum thus ensuring safe operation and a longer machine lifetime [8].

Gyroscopic effects have an influence on the critical speeds of a rotor and they are significant in long rigid rotors as well as flywheel rotors that are supported by flexible bearings. Gyroscopic effects cause the critical speeds of the rotor to be dependent on the rotational speed of the rotor [8]. However, with increasing speed, each pair of identical eigen-frequencies splits up into one set of ascending eigenvalues and another set of descending eigenvalues. The eigenmodes that relate to the increasing eigenvalues are the so-called forward modes, since their motions have the same sense of rotation as the rotational speed itself [8].

Correspondingly, all eigenmodes with decreasing eigenvalue dependency are the so-called backward modes [9]. This can be seen when the eigenvalues are plotted against the rotational speed of the rotor which is also known as a Campbell diagram [9]. A typical illustration of the well known Campbell diagram is shown in Figure 4 together with the corresponding modes of the rotor.

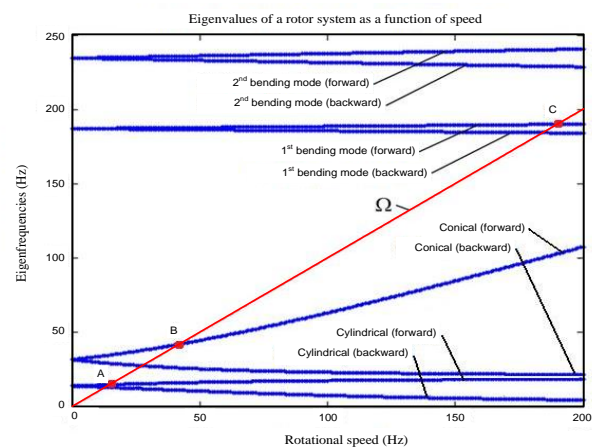**Figure 4: Campbell diagram of rotor with gyroscopic effect**

When the eigen-frequencies of the rotor are known, they indicate the gyroscopic effect of splitting the eigen-frequencies or critical speeds into forward whirl and backward whirl [8].

TOPIC B. MACHINES

Proceedings of the 19th Southern African Universities Power Engineering Conference
SAUPEC 2010, University of the Witwatersrand, Johannesburg

This is because the two radial directions (x and y) are coupled by gyroscopy which causes the system to experience a critical frequency in the x and y directions at different speeds. The critical speeds of the rotor can also be determined from Figure 4. Critical speeds occur where the diagonal Ω line intersects any of the forward or backward whirl mode lines as seen at point A, B and C in Figure 4. In practice critical speeds are rarely experienced at the intersection of the diagonal Ω line with the backward whirl lines. Backward whirl modes are usually damped but may occur when the rotor is non-symmetric or the bearings are anisotropic in the x- and y directions [1].

3.2 Flywheel rotor

The flexible rotor model of the flywheel is based on the equation of motion shown in (6) where M, D, G, K, ω denotes the mass-, damping-, gyroscopic effect-, stiffness-, speed of rotation of the element respectively. The unbalance quantity is denoted by me and u denotes the external forces applied to that element as defined in the rotor model template.

$$M_x \ddot{x} + (D_x + \omega G_x)\dot{x} + K_x x = me\omega^2 \cos(\omega t) + u_x$$
$$M_y \ddot{y} + (D_y + \omega G_y)\dot{y} + K_y y = me\omega^2 \sin(\omega t) + u_y \quad (6)$$

Making use of a FEM package written by Dr. Izhak Bucher called RotFE, a MATLAB® model of the Fly-Ups rotor can be derived which is governed by (6). The model can then be used to determine critical frequencies, mode shapes, unbalance response, displacements at various speeds and Campbell diagrams.

In the development phase of the Fly-Ups system a rotor-dynamic analysis was done on the flywheel rotor using a software package called DyRoBeS® [4]. In order to compare the results from DyRoBeS® with the results from RotFE an exact copy of the DyRoBeS® rotor was implemented in RotFE and is shown in Figure 5.
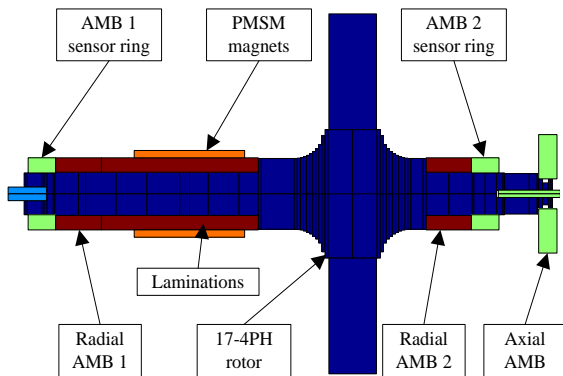
Figure 5: MATLAB® representation of the Fly-Ups rotor

Table 2: Critical frequency comparison

Mode shape	DyRoBeS®	RotFE
1st rigid mode	35.43 Hz	35.55 Hz
2nd rigid mode	143.94 Hz	147.45 Hz
1st bending mode	519.89 Hz	516.23 Hz

From Table 2 it can be seen that there is a good correlation between the two implementations of the Fly-Ups rotor model. The results show a maximum deviation of 3.01 % at the 2nd rigid mode which is due to modelling differences in the two software packages.

3.3 INTEGRATED ROTOR-AMB MODEL

Upon completion of the AMB model and the rotor model respectively the rotor model was implemented in Simulink® by means of an S-function. This was done in order to derive a new rotor model for each time-step of the simulation since the rotor model is speed dependent as seen in (6). The output of the rotor model is the rotor position whereas the input to the rotor model is force. The force input (denoted by u in (6)) was specified to be applied at the bearing locations and the position output was specified at the sensor positions on the rotor. The force output of the AMB model then connects to the rotor force input and the position output of the rotor connected to the position input of the AMB as shown in Figure 5. This was done for both radial AMBs in the X- and Y-directions to support the rotor in 4-axis of freedom.

4. RESULTS

The integrated rotor-AMB model was employed to determine the response of the system to a step disturbance input of 10 µm. The maximum attainable damping (k_d of the PD-controller) is however significantly lower in the actual Fly-Ups systems due to noise in the sensor system. Since the rotor is asymmetric the response of AMB 1 differs from the response of AMB 2 (refer to Figure 5). The equivalent mass of the rotor at AMB 1 scaled from the CG was determined to be 5.38 kg and the response of the system is shown in Figure 6. At AMB 2 the equivalent mass was determined to be 13.22 kg and the system displays more overshoot as seen in Figure 7. This is because of the inertia of the rotor and since the AMBs only have a load capacity of 150 N. When actuation of the right part of the rotor occurs the inertia of the rotor causes the rotor position to overshoot several times before stabilising. The overshoot is also caused by the lower damping capability of the AMB due to the noise.

Figure 8 shows the rotor response due to the actual unbalance residing on the Fly-Ups rotor during a run-up test simulation. The rotor is accelerated from 0- to 33,000 r/min in 100 seconds. It can be seen that the

Proceedings of the 19th Southern African Universities Power Engineering Conference
SAUPEC 2010, University of the Witwatersrand, Johannesburg

TOPIC B. MACHINES

rotor is stably suspended throughout the run-up test to well below 250 μm where the backup bearings are located.
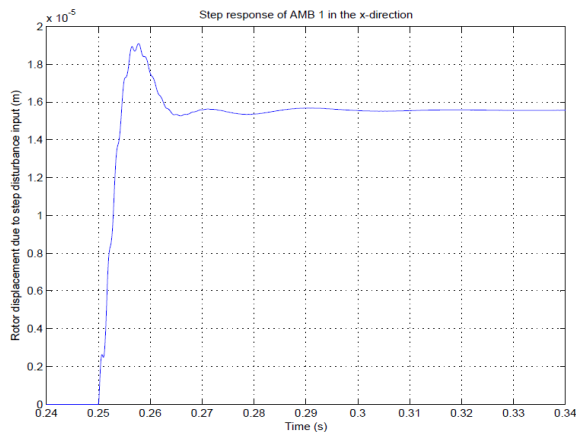
Figure 6: AMB 1 response due to 10μm step disturbance
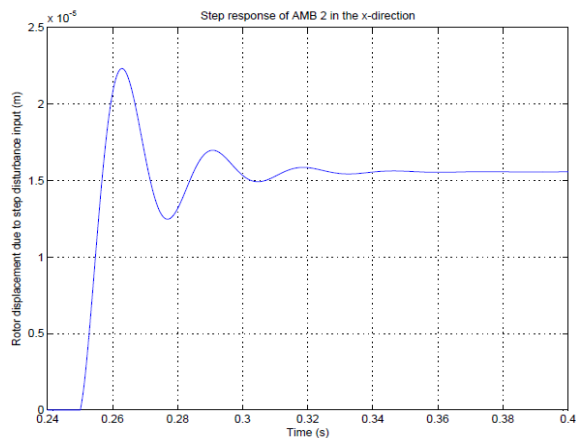
Figure 7: AMB 2 response due to 10μm step disturbance
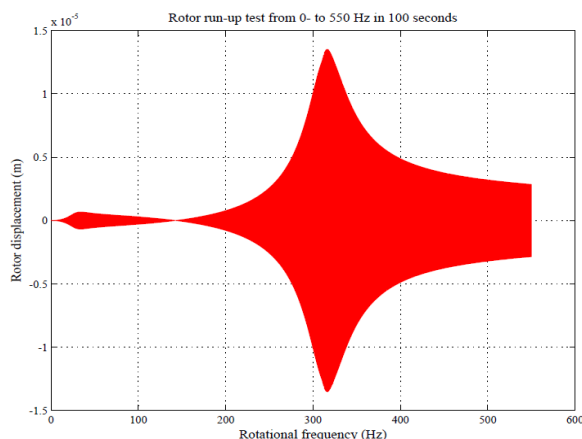
Figure 8: Rotor run-up unbalance response

5.   CONCLUSIONS

A simulation model has been developed in order to investigate the dynamic effects associated with magnetic bearings in high-speed rotating machines. The simulation model was developed to simulate the response of the Fly-Ups system which features a 5-axes suspended flywheel rotor used to store electric energy.

The simulation model includes models of the actual AMB actuators used in the Fly-Ups system including models of the power amplifiers, eddy current displacement probes, anti-aliasing filters and the non-linear force-current, force-displacement relationship inherent to AMBs. A rotor model of the Fly-Ups flywheel rotor was also developed and verified against a rotor-dynamic software package showing a maximum deviation of 3.01%.

The rotor model was integrated with the AMB models in order to realise a model of the Fly-Ups rotor-AMB system. Results show that the AMBs can suspend the rotor in the presence of a step disturbance inputs as well as during a run-up test.

Further work has to be done to compare the simulated results with the actual operation of the Fly-Ups system. The model was not yet validated against the actual Fly-Ups system since there were issues regarding the balancing of a rotor fitted with permanent magnets. The Fly-Ups rotor has since been balanced and the system will be recommissioned in early 2010.

The AMB model will also be expanded to include time delays in the control loop, non-linear coil inductance effects as well as leakage- and fringing effects. This will enable the simulation platform to be used as a design verification tool in future rotor-AMB projects within the McTronX research group.

REFERENCES

[1] G. Schweitzer and E.H. Maslen, Magnetic Bearings: Theory, Design, and Application to Rotating Machinery.: Springer Verlag, 2009.

[2] JC Ji, C.H. Hansen, and A.C. Zander, "Nonlinear Dynamics of Magnetic Bearing Systems," Journal of Intelligent Material Systems and Structures, vol. 19, p. 1471, 2008.

[3] G. Li, Z. Lin, P.E. Allaire, and J. Luo, "Modeling of a High Speed Rotor Test Rig With Active Magnetic Bearings," *Journal of Vibration and Acoustics*, vol. 128, p. 269, 2006.

[4] J.J. Janse van, *Development of a Flywheel Energy Storage System: Uninterrupted Power Supply (FLY-UPS).*: North-West University, Potchefstroom Campus, 2007.

[5] Stefan Myburgh, "The development of a fully suspended AMB system for a high-speed flywheel application," 2007.

[6] N. Skricka and R. Markert, "Improvements in the integration of active magnetic bearings," *Control Engineering Practice*, vol. 10, pp. 917-922, 2002.

[7] B. Aeschlimann, "Control aspects of high speed precision active magnetic bearings," 2002.

[8] G. Genta, *Dynamics of rotating systems*.: Springer, 2005.

[9] J.S. Rao, *Rotor dynamics*.: New Age Publishers, 1996.

TOPIC B. MACHINES

Proceedings of the 19th Southern African Universities Power Engineering Conference
SAUPEC 2010, University of the Witwatersrand, Johannesburg

EFFECTS OF VARIATIONS IN MATHEMATICAL MODELLING OF SYNCHRONOUS MACHINE SATURATION ON SMALL-SIGNAL STABILITY ANALYSIS

DS Mudau *, KA Folly ** and K Awodele ***

Department of Electrical Engineering, University of Cape Town, Rondebosch, South Africa, MudauDS@eskom.co.za
**Department of Electrical Engineering, University of Cape Town, Komla.Folly@uct.ac.za*
***Department of Electrical Engineering, University of Cape Town, Kehinde.Awodele@uct.ac.za*

Abstract – The complexity and size of power systems require digital simulation tools for efficient planning, analysis and control. Adequate synchronous machine modelling is important for reliable analysis results. However, different simulation tools make use of different synchronous saturation models that can affect the simulation results. This paper covers synchronous machine saturation modelling and its effect on the small-signal stability results.. Two power system simulation tools, MatNetEig and PacDyn 8.1.1 are selected for comparison. It is shown that PacDyn eigenvalue results matched the results from MatNetEig simulation tool in all test cases when saturation was neglected. However, when saturation is included, the variations in mathematical saturation models in the different simulation tools resulted in differences in numerical eigenanalysis results. It was found that the effects of saturation modeling are very small on frequency and slightly bigger on damping ratios. On a well-damped system, the effects of saturation are small enough to be ignored in all simulation tools. However, the effects are higher when the system is marginally damped.

Key Words: Eigenvalues, power system stability, PacDyn, MatNetEig, synchronous machine saturation.

1. INTRODUCTION

The power system is a complex and by far the largest human-made system on earth with many generators, transmission lines and loads. This makes it difficult to predict the dynamic behaviour of such a big system. The overall system becomes difficult to analyse without the use of digital computer simulations [1 – 3].

Computer simulation tools assist in modelling and analysis for efficient planning, operation and control. Adequate synchronous machine modelling is important for reliable analysis results. However, different simulation tools make use of different mathematical models when modelling and calculating synchronous machine saturation [1]. It is important to investigate the synchronous machine saturation modelling in the different tools and understand the reasons for the differences.

In this paper synchronous machine saturation modelling and their effect on the small signal stability results are investigated. Two power system simulation tools, MatNetEig and PacDyn 8.1.1. are used for comparison. Eigenvalue analysis on the "Two-area, four-machine" power system show similar results from both PacDyn and MatNetEig when saturation is neglected. However, when saturation is included, the variations in mathematical saturation models in the different simulation tools resulted in differences in numerical eigen-analysis results. It was found that the effects of saturation modeling are very small on frequency and slightly bigger on damping ratios [4 – 7].

2. SIMULATION TOOLS

In the following subsection, some of the features of the two power system simulation tools (i.e., MatNetEig and PacDyn 8.1.1.) that were selected for comparison are discussed.

2.1. PacDyn 8.1.1

PacDyn is a comprehensive small-signal stability analysis package developed by CEPEL [8 – 10]. Input data formats supported include PSS/E, ANAREDE, binary and PacDyn data file formats. PacDyn has built-in as well as user defined models. It requires converged electrical network data and comes with editors for different data formats as well as user-defined models for unlimited dynamic models [10]. PacDyn has easy-to-use disturbance tools.

2.2. MatNetEig

MatNetEig is a Matlab based simulation tool and uses classes called net_c for network model structures [11, 12]. MatNetEig supports data file formats in PST V2, PSS/E and IEEE common data file formats. Analysis can be done in either command line or via the graphical user interface. It has limited disturbance tools.

PacDyn and MatNetEig tools give eigenvalues, mode shapes and participation factors. PacDyn tool provides mode shapes in polar, histograms and lists while MatNetEig gives these results in list formats only. These tools can also give time domain plots.

3. POWER SYSTEM STABILITY

Power system stability is the ability of a power system to remain in a state of equilibrium under normal operating conditions and to regain acceptable state of equilibrium after being subjected to a disturbance [3]. It is subdivided into voltage and rotor angle stability. Rotor angle stability is further divided into small-signal and transient stability [13].

Rotor angle stability is the ability of interconnected synchronous machines to remain in synchronism. Analysis is done using time domain and eigenanalysis methods [13].

Proceedings of the 19th Southern African Universities Power Engineering Conference
SAUPEC 2010, University of the Witwatersrand, Johannesburg

TOPIC B. MACHINES

Small-signal stability is the ability of a power system to maintain synchronism under small-disturbances such as small changes in loads and generation. The disturbance is termed "small" if equations governing the dynamics of the system can be linearized around an operating equilibrium point [13, 14].

Oscillatory modes is a term used for the complex eigenvalues, the imaginary part of the eigenvalue gives the oscillatory frequency. The oscillatory modes are classified into four categories based on the frequency range and the location of dominant state variables [1, 11 – 13]. These modes are local area plant mode, inter-area mode, control mode and torsional mode. Only the local area and inter-area modes are covered in this paper.

3.1. State space equations and eigenvalues

State space equations and eigenvalue analysis techniques give the dynamic behaviour of a power system modelled by a set of non-linear differential and algebraic equations (1) linearized around an equilibrium operating condition [13].

$$\dot{x} = f(x, u, t)$$
$$y = g(x, u, t) \quad (1)$$

where
x – State variables of dimension n x 1
f – Non-linear functions of size n x 1
u – Input variables of size rx1
y – Output variables of dimension m x 1
g – Non-linear functions of size m x 1
t – Time
n – Order of the power system model.

The linearized equations above are commonly given as follows [12, 15 – 17]:

$$\dot{x} = Ax + Bu$$
$$y = Cx + Du \quad (2)$$

where
A – is an n x n state matrix
B – is an n x r input matrix
C – is an m x n output matrix
D – is an m x r feed-forward matrix

Matrices **A**, **B**, **C** and **D** are matrices of partial derivatives of non-linear functions *f* and *g* with respect to time. Eigenvalues of the system can be computed by solving the characteristic equation (3).

$$\det(A - \lambda I) = 0 \quad (3)$$

Where λ are the eigenvalues and **I** is a diagonal square dimensional identity matrix. Each eigenvalue of the system can be represented as (4)

$$\lambda = \sigma \pm j\omega \quad (4)$$

Where σ is the real part and ω is the imaginary part of the eigenvalue in question.

These eigenvalues give the dynamic performance of the system as follows [1, 10, 13, 17, 18] without the need to experiment with the actual power system:

- Real eigenvalues indicate non-oscillatory modes.
- Oscillatory modes are given by complex conjugate pairs.
- The real part of the eigenvalue gives the damping while the imaginary part gives the frequency of oscillation.
- The system is stable if all real parts are negative and unstable if at least one real part is positive.
- The damping ratio (ζ) determines the rate of decay of the amplitude and is given by (5).

$$\zeta = \frac{-\sigma}{\sqrt{\sigma^2 + \omega^2}} \quad (5)$$

Eigenvectors and participation factors are closely related. Participation factors are the product of left and right eigenvector components of the selected eigenvalue. Participation factors give the relative participation of state variable to a mode while eigenvectors describe the activity of the state variables in a mode given. Participation factors are given by (6) [17].

$$P_{ki} = \Phi_{ik} \Psi_{ki} \quad (6)$$

Where P_{ki} is the participation, Ψ_{ki} and Φ_{ik} are the left and right eigenvector components respectively.

4. COMPONENT MODELLING

Power system stability analysis results can only be accurate and reliable if all individual components are modelled to closely reflect the steady-state and dynamic behaviour of the actual power system. For this reason, it is important to understand different power system components and how they are modelled and interconnected [1, 13, 14].

4.1. SYNCHRONOUS MACHINES

Small-signal stability of a power system is about keeping all interconnected synchronous machines in synchronism. The modelling of this machine is therefore important for reliable power system stability analysis results [13].

There are many synchronous machine models ranging from simple classical machine (2nd order) models to detailed higher order machines with magnetic saturation. The order indicates the number of states associated with the generator. For the purpose of this paper, only the 6th order synchronous machine model is discussed [13, 18 – 20].

The coupled direct (d-) axis and quadrature (q-) axis circuits define the complete synchronous machine model and is widely used in simulation tools. The d-axis in Fig. 1 and axis q-axis in Fig. 2 are for the 6th order machine model [1, 13, 20].

TOPIC B. MACHINES

Proceedings of the 19th Southern African Universities Power Engineering Conference
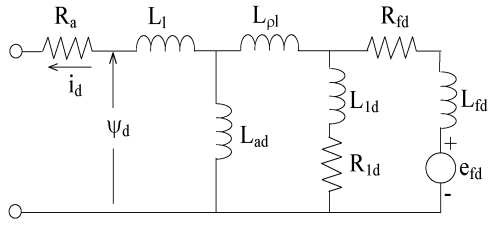SAUPEC 2010, University of the Witwatersrand, Johannesburg

Figure 1: Direct axis machine circuit [1]
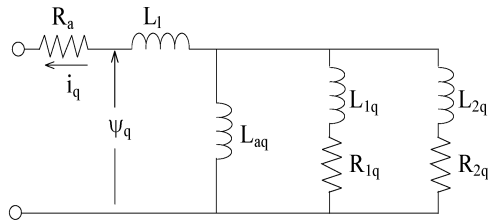
Figure 2: Quadrature axis machine circuit [1]

Saturation in d- and q-axis is generally specified using the total saturation model given by the exponential equation (7)

$$I_{fd}(\psi) = S_\psi = Ae^{B[\psi(t)-C]}$$
$$C = \psi_{T_1} \tag{7}$$

where Ψ is the flux linkage or the terminal voltage; A, B and C are the constants defining the nonlinear open-circuit saturation curve in Fig. 3 [13, 20].
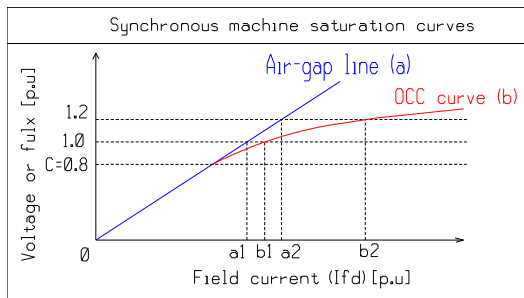
Figure 3: Generator saturation curves

Equation (7) is used to calculate values $S_{1.0}$ and $S_{1.2}$ that are used by the different simulation tools. Parameters $S_{1.0}$ and $S_{1.2}$ (not shown in Fig. 3) are calculated from the air-gap line (a) and OCC curve (b) using a_1, a_2, b_1 and b_2 as indicated in Fig. 3, where a_1 is the field current required to produce 1.0 p.u flux on the air-gap line and a_2 is the field current required to produce 1.2 p.u flux [13].

Different simulation tools make use of different mathematical models when modelling and calculating synchronous machine saturation [1, 10]. This section covers mathematical descriptions of the saturation moles used in PacDyn and MatNetEig.

4.1.1. PacDyn saturation model

PacDyn has two saturation models as follows for different synchronous machines [10]. In this paper,

only the exponential saturation model in equation (8) below used to model 5th and 6th order models is discussed.

$$SAT = A_{sat}e^{B_{sat}(|E'|-C)} \tag{8}$$

The saturation data in PacDyn is specified using A_{sat}, B_{sat} and C that are internally used to calculate machine saturation (SAT) in d- and q- axis. Given the OCC curve, the user can calculate both $S_{1.0}$ and $S_{1.2}$ as follows in PacDyn [10]:

$$S_{1.0} = \frac{b_1 - a_1}{a_1} = \frac{b_1}{a_1} - 1$$
$$S_{1.2} = \frac{b_2 - a_2}{a_2} = \frac{b_2}{a_2} - 1 \tag{9}$$

Where a_1, a_2, b_1 and b_2 are the field current values. Manipulating equations (9) results in equations (10) for b_1 and b_2 respectively.

$$b_1 = 1 + a_1(S_{1.0})$$
$$b_2 = 1 + a_2(S_{1.2}) \tag{10}$$

Equations (10) will be used when comparing PacDyn and MatNetEig saturation models.

4.1.2. MatNetEig saturation model

MatNetEig simulation tool has three saturation models. The round rotor synchronous machine given by "type 21 and 31" uses saturation models modelled by equations (11) as defined in m-file program [11].

$$I_{fd}(\psi) = \psi_a + A_{sat}e^{B_{sat}(\psi_a-0.8)} - A_{sat}$$
$$B_{sat} = 5.0\log\left(\frac{1.2S_{1.2}}{S_{1.0}}\right)$$
$$A_{sat} = S_{1.0}e^{-0.2B_{sat}} \tag{11}$$

The equations above indicate that this mathematical model is different from PacDyn OCC curve models. There is an additional term given by $\Psi_a - A_{sat}$, the value of C in (7) is fixed at 0.8 per unit and MatNetEig uses the flux as opposed to voltage.

In MatNetEig tool, the synchronous machine saturation data is specified using $S_{1.0}$ and $S_{1.2}$ as follows [11]:

$$S_{1.0} = \frac{b_1 - a_1}{a_1}$$
$$S_{1.2} = \frac{b_2 - a_2}{a_2} \tag{12}$$

Solving for b1 and b2 from (12), taking into consideration equation (11) results in the above re-written as follows for MatNetEig:

$$b_1 = (1 - A_{sat}) + [1 + a_1(S_{1.0})]$$
$$b_2 = (1.88 - 1.2A_{sat}) + [1 + (a_2)^2(S_{1.2})] \tag{13}$$

Proceedings of the 19th Southern African Universities Power Engineering Conference
SAUPEC 2010, University of the Witwatersrand, Johannesburg

TOPIC B. MACHINES

Equations (13) indicate that there are two fundamental differences between models in MatNetEig and PacDyn as follows:

- MatNetEig has additional terms $(1-A_{sat})$ and $(1.88-1.2A_{sat})$ for b_1 and b_2 respectively.
- In MatNetEig, b_2 is proportional to $(a_2)^2$ compared to a_2 in PacDyn.

The mathematical models used in PacDyn and MatNetEig simulation tools are all different as indicated in this section. The simulation results from these two tools are therefore expected to be different following these variations in magnetic saturation.

4.2. AVR EXCITATION SYSTEM

The main function of the automatic voltage regulator (AVR) excitation system is to provide direct current (DC) field voltage to control the generator terminal voltage. Many types of excitation system models have been developed over the years including rotating DC, rotating AC and static thyristor AVR exciters [1, 11 – 13].

4.3. POWER SYSTEM STABILIZERS (PSS)

PSS systems are used to damp power system oscillations and to enhance stability of a power system following a disturbance using auxiliary speed, frequency or voltage signals. Figure 4 shows a PSS block diagram [12, 13].
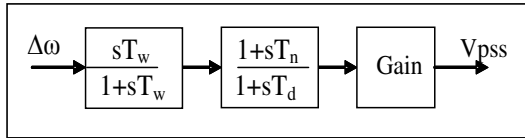

Figure 4: A generic PSS block diagram

Figure 4 above is composed of the washout circuit (1st block), lead-lag circuit (2nd block) and gain circuit (3rd block). The lead-lag circuits can be more than one. The input used was the change in speed while the output is V_{pss} to the AVR exciter.

5. ANALYSIS METHOD

Two-area four-generator (2A4M) power system models was selected for small-signal stability analysis. The system was modelled and results were then compared using eigenvalues, mode shapes, participation factors and time domain simulations.

6. RESULTS AND DISCUSSIONS

The eigenvectors and participation factors from the simulation tools were used to identify the inter-area and different local area modes in the 2A4M model.

6.1. 2A4M SYSTEM MODEL RESULTS

6.1.1. SYSTEM ON MANUAL CONTROL

Table 1 shows the inter-area and local area oscillatory modes using eigenvalues, oscillatory frequencies and damping ratios for both MatNetEig and PacDyn simulation tools.

Table 1: Eigenvalues: System on manual control

Case description			MatNetEig	PacDyn	Difference
Manual Control	Saturation not considered	Inter-area	λ = -0.0921±j3.4265 f = 0.5453 Hz ζ = 2.6869 %	λ = -0.0921±j3.4265 f = 0.5453 Hz ζ = 2.6872 %	0.0000 Hz -0.0003 %
		Local area 1	λ = -0.5726±j6.8115 f = 1.0841 Hz ζ = 8.3768 %	λ = -0.5726±j6.8115 f = 1.0841 Hz ζ = 8.3768 %	0.0000 Hz 0.0000 %
		Local area 2	λ = -0.5742±j7.0355 f = 1.1197 Hz ζ = 8.1344 %	λ = -0.5742±j7.0355 f = 1.1197 Hz ζ = 8.1344 %	0.0000 Hz 0.0000 %
	Saturation considered	Inter-area	λ = -0.086±j3.4307 f = 0.546 Hz ζ = 2.506 %	λ = -0.0956±j3.4238 f = 0.5449 Hz ζ = 2.7923 %	0.0011 Hz -0.2863 %
		Local area 1	λ = -0.4537±j6.8832 f = 1.0955 Hz ζ = 6.5771 %	λ = -0.549±j6.809 f = 1.0837 Hz ζ = 8.0368 %	0.0118 Hz -1.4597 %
		Local area 2	λ = -0.4604±j7.105 f = 1.1308 Hz ζ = 6.4664 %	λ = -0.5527±j7.0328 f = 1.1193 Hz ζ = 7.8347 %	0.0115 Hz -1.3683 %

Both tools gave a stable system and similar results on system modelled without saturation on the generator models. The inclusion of saturation resulted in a stable system with different simulation results as expected on these different saturation models.

Table 2 shows the effects of saturation on oscillatory frequencies and damping ratios as compared to when the saturation is neglected. The effects were calculated using the equation (14).

$$\Delta Freq = F_{sc} - F_{sn}$$
$$\Delta \zeta = \zeta_{sc} - \zeta_{sn} \tag{14}$$

where subscripts "sc" and "sn" indicate "saturation considered" and "saturation not considered" respectively on frequency and damping ratios.

Table 2: Effects of saturation on modal solution

Deviation effect		MatNetEig	PacDyn
Inter-area	ΔFreq	0.0007 Hz	-0.0004 Hz
	Δζ	-0.1809 %	0.1051 %
Local area 1	ΔFreq	0.0114 Hz	-0.0004 Hz
	Δζ	-1.7997 %	-0.34 %
Local area 2	ΔFreq	0.0111 Hz	-0.0004 Hz
	Δζ	-1.668 %	-0.2997 %

Saturation effects indicated very small differences in frequency and damping ratios between PacDyn and MatNetEig tools. Although the effects are different on the two tools, they are negligible on frequency and slightly higher on damping ratios.

A step change in mechanical power input was made and the time domain plots rotor speed in Fig. 5 was plotted to check the effects of saturation in PacDyn.
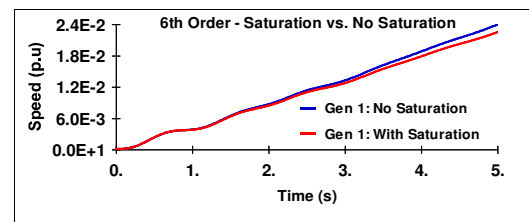

Figure 5: Speed response saturation effects for PacDyn

TOPIC B. MACHINES

Proceedings of the 19th Southern African Universities Power Engineering Conference
SAUPEC 2010, University of the Witwatersrand, Johannesburg

PacDyn and MatNetEig showed similar and consistent response in both eigenvalue analysis and time domain simulations results over 5 seconds.

6.1.2. AVR EXCITATION WITHOUT A PSS

The eigenvalues in table 3 below indicate the modal solution of 6th order machine models controlled by an AVR with high transient gain on all four generators. It can be seen that both tools gave unstable system modal solutions. The two tools gave identical results when neglecting generator saturation.

Table 3: Eigenvalues – AVR excitation only

Case description			MatNetEig	PacDyn	Difference	
AVR excitation only	Saturation not considered	Inter-area	λ = 0.0151±j3.8493 f = 0.6126 Hz ζ = -0.3923 %	λ = 0.015±j3.8491 f = 0.6126 Hz ζ = -0.39 %	0.0000 -0.0023	Hz %
		Local area 1	λ = -0.6594±j7.1859 f = 1.1437 Hz ζ = 9.1379 %	λ = -0.6594±j7.1858 f = 1.1437 Hz ζ = 9.138 %	0.0000 -0.0001	Hz %
		Local area 2	λ = -0.6572±j7.4092 f = 1.1792 Hz ζ = 8.8354 %	λ = -0.6572±j7.4092 f = 1.1792 Hz ζ = 8.8354 %	0.0000 0.0000	Hz %
	Saturation considered	Inter-area	λ = 0.0157±j3.8184 f = 0.6077 Hz ζ = -0.4112 %	λ = 0.0422±j3.8492 f = 0.6126 Hz ζ = -1.0968 %	-0.0049 0.6856	Hz %
		Local area 1	λ = -0.5158±j7.1448 f = 1.1371 Hz ζ = 7.2005 %	λ = -0.6011±j7.1557 f = 1.1389 Hz ζ = 8.3708 %	-0.0018 -1.1703	Hz %
		Local area 2	λ = -0.5222±j7.3693 f = 1.1729 Hz ζ = 7.0684 %	λ = -0.6039±j7.3765 f = 1.174 Hz ζ = 8.1595 %	-0.0011 -1.0911	Hz %

Table 4 below shows the effects of saturation on oscillatory frequencies and damping ratios as compared to when the saturation is neglected. The results were calculated from table 3 above using the equation (15) to analyze the effects of saturation for the system controlled by AVR only.

$$\Delta Freq = F_{sc(AVR)} - F_{sn(AVR)}$$
$$\Delta \zeta = \zeta_{sc(AVR)} - \zeta_{sn(AVR)} \tag{15}$$

where subscripts "sc(AVR)" and "sn(AVR)" indicate "saturation considered" and "saturation not considered" respectively on frequency and damping ratios when the generators were on AVR excitation.

Table 4: AVR excitation - Effects of saturation

Deviation effect		MatNetEig		PacDyn	
Inter-area	ΔFreq	-0.0049	Hz	0	Hz
	Δζ	-0.0189	%	-0.7068	%
Local area 1	ΔFreq	-0.0066	Hz	-0.0048	Hz
	Δζ	-1.9374	%	-0.7672	%
Local area 2	ΔFreq	-0.0063	Hz	-0.0052	Hz
	Δζ	-1.767	%	-0.6759	%

Saturation increased both the frequency and damping ratios in all tools. The effects are significant on the damping ratios with the increase of up to 1.9374 % in MatNetEig and 0.7672 % in PacDyn respectively on the local area mode. The AVR exciters had increased frequency and reduced damping ratios in all tools.

6.1.3. AVR EXCITATION AND A PSS

Table 5 shows eigenvalues of the system modeled with AVR and PSS excitation in all two tools. A simple static thyristor AVR excitation system with high transient gain was used.

Table 5: Eigenvalues – AVR and PSS

Case description			MatNetEig	PacDyn	Difference	
AVR and PSS	Saturation not considered	Inter-area	λ = -0.7167±j3.8156 f = 0.6073 Hz ζ = 18.4606 %	λ = -0.7167±j3.8154 f = 0.6072 Hz ζ = 18.4615 %	0.0001 -0.0009	Hz %
		Local area 1	λ = -2.1602±j8.2668 f = 1.3157 Hz ζ = 25.2821 %	λ = -2.1602±j8.2667 f = 1.3157 Hz ζ = 25.2824 %	0.0000 -0.0003	Hz %
		Local area 2	λ = -2.2423±j8.6237 f = 1.3725 Hz ζ = 25.1648 %	λ = -2.2428±j8.6236 f = 1.3725 Hz ζ = 25.1704 %	0.0000 -0.0056	Hz %
	Saturation considered	Inter-area	λ = -0.6345±j3.7587 f = 0.5982 Hz ζ = 16.6453 %	λ = -0.6937±j3.8623 f = 0.6147 Hz ζ = 17.6779 %	-0.0165 -1.0326	Hz %
		Local area 1	λ = -1.9066±j7.7802 f = 1.2383 Hz ζ = 23.8015 %	λ = -2.01±j8.2694 f = 1.3161 Hz ζ = 23.6188 %	-0.0778 0.1827	Hz %
		Local area 2	λ = -2.0335±j8.1285 f = 1.2937 Hz ζ = 24.269 %	λ = -2.0985±j8.6114 f = 1.3705 Hz ζ = 23.676 %	-0.0768 0.5930	Hz %

Results in table 5 above shows that except for the rounding errors in MatNetEig, the two tools gave similar results for the system modelled without saturation. The system is stable in all tools whether saturation is considered or not. The effects of saturation on modal solution are shown in table 6 below.

Table 6: Saturation effects – AVR and PSS

Deviation effect		MatNetEig		PacDyn	
Inter-area	ΔFreq	-0.0091	Hz	0.0075	Hz
	Δζ	-1.8153	%	-0.7836	%
Local area 1	ΔFreq	-0.0774	Hz	0.0004	Hz
	Δζ	-1.4806	%	-1.6636	%
Local area 2	ΔFreq	-0.0788	Hz	-0.002	Hz
	Δζ	-0.8958	%	-1.4944	%

The results indicate that the effects are different in frequency as indicated; these are still small and negligible. There are significant increases in damping ratios in all modes as given by all tools. The effects are higher in PacDyn's local area modes while higher in MatNetEig's inter-area mode. Figure 6 shows time domain simulation results for PacDyn.
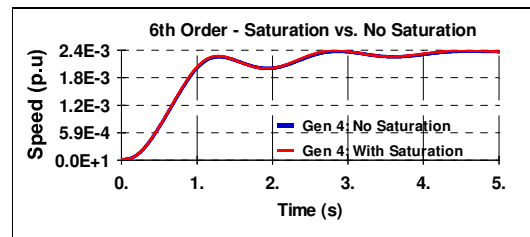

Figure 6: PacDyn speed response – AVR and PSS

The rotor speed oscillations were damped after three seconds. Figure 7 below shows MatNetEig tool's time domain simulation results.
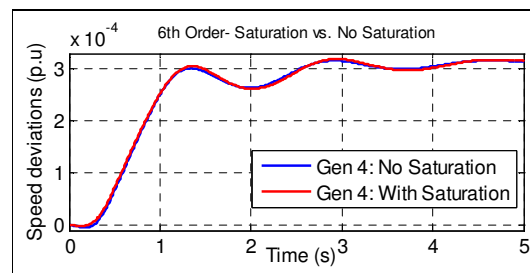

Figure 7: MatNetEig rotor speed response – AVR and PSS

Proceedings of the 19th Southern African Universities Power Engineering Conference
SAUPEC 2010, University of the Witwatersrand, Johannesburg

TOPIC B. MACHINES

The results in Fig.7 are similar to those given by PacDyn tool as shown in Fig.6. The effects of saturation are insignificant and negligible in small-signal stability analysis for well damped systems.

7. CONCLUSSIONS

Variations exist in mathematical saturation models between simulation tools. The effects of saturation are small and negligible on numerical results for small-signal stability analysis. However, the effects of saturation are different due to the mathematical models used in these two simulation tools. Time domain simulations analysis confirmed and matched the dynamic response as predicted using modal analysis in PacDyn and MatNetEig tools. PacDyn is more advanced and recommended.

APPENDIX

A: 2A4M power system model and data
A.1: Two-area, four-machine (2A4M) model
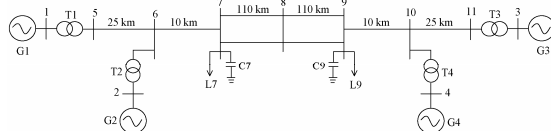
A.1.1: 2A4M power system model data

The complete power system model data is tabled in table A.1 on 100 MVA, 20 kV 60 Hz system base.

Table A.1: 2A4M power system model data

	X'd	X'q	Xd	Xq	T'd0	T'q0	X"d	X"q	T"d0	T"q0
Machine Data	0.30	0.55	1.80	1.70	8.0	0.40	0.25	0.25	0.03	0.05
	H	Kd	Ra	Xl	A_sat	B_sat	C=Ψ_Ti	Freq	MVA	kV
	***	0	0.0025	0.20	0.015	9.6	0.9	60	900	20
AVR Data	Ka	Tr			**PSS Data**	Gw	Tw	T1	T2	T3	T4
	200	0.01				20.0	10.0	0.05	0.02	3	5.4

*** Generators 1 and 2: H=6.5, G3 and 4: H=6.175

REFERENCES

[1].   KK. Kaberere, *Variations in modelling and algorithmic factors impacting on small-signal stability results: assessment of five industrial-grade power system simulation tools*, PhD, University of Cape Town, 2006.

[2].   JD. Glover and MS. Sarma, *Power system analysis and design*, 2nd edition, PWS Publishing, 1994.

[3].   N. Martins, "Efficient eigenvalue and frequency response methods applied to power system small-signal stability studies", *IEEE Transactions on Power Systems*, USA, v. PWRS-1, n. 1, pp. 217-226, 1986.

[4].   KK. Kaberere, M. Ntombela, KA. Folly and AI. Petroianu, "Comparison of industrial-grade analytical tools used in small-signal stability assessment," *AUPEC* 2005, pp. 147-152, University of Tasmania, 25-28 2005.

[5].   BP. Chuco, *Electrical software tools overview: Centro de Investigaciones*

Eléctricas Electrónicas del Perú – CIEEP, http://eurostag.regimov.net/files/doc2.pdf

[6].   W. Gua, F. Milano, P. Jiang and J. Zheng, "Improving large-disturbance stability through optimal bifurcation control and time domain simulations", *Electric Power Systems Research*, vol. 78, Issue 3, pp. 337-345, 2008.

[7].   RD. Rangel, S. Gomes JR, CHC. Guimaraes, N. Martins, A de Castro, HJ. Pinto, and AR. Carvalho, "Recent Developments in Anatem - A Comprehensive Program for the Analysis of Eletromechanical Stability of Large Power Systems", i*n: VII SEPOPE, 2000, Curitiba proceedings of VII SEPOPE*, 2000, Brazil. http://www.nelsonmartins.com/pdf/apresentac oes/ 2000_VII_SEPOPE_ANATEM.pdf.

[8].   DS. Mudau, KA. Folly, "Effect of initial angle estimate on the convergence of Newton-Raphson method used for load flow studies", *Discussion paper, SAUPEC*, University of Stellenbosch, Stellenbosch, South Africa, 2009.

[9].   Nelson Martins, *Overview of numerical algorithms for small-signal stability analysis and control design*, Draft technical report CEPEL/DSE – 167/2004.

[10]. CEPEL, *PacDyn 8.1.1 user manual*, 2008

[11]. Graham Rogers, Cherry Tree Farm, *MatNetEig User manual documentation.*

[12]. M. Ntombela, *An investigation into the capabilities of three simulation tools for small-signal stability analysis*, Msc. thesis report, University of Cape Town, 2007.

[13]. P. Kundur, *Power system stability and control*, McGraw-Hill, 1994

[14]. Mariesa Crow, *Computational methods for Electric power systems*, CRC Pres, 2003.

[15]. Vincent Del Toro, *Electric Power Systems*, Prentice Hall, 1992.

[16]. JH. Chow, FF. Wu and JH. Momoh, *Applied mathematics for restructured electric power systems: Optimization, Control, and Computational Intelligence*, Springer, 2004.

[17]. N. Martins and LTG. Lima, "Eigenvalue and Frequency Domain Analysis of Small-Signal Electromechanical Stability Problems", *In: IEEE Symposium on Application of Eigenanalysis and Frequency Domain Method for System Dynamic Performance*, pp. 17-33, 1989

[18]. GT. Heydt, *Computer analysis methods for power systems*, Stars in a circle, 1996.

[19]. O Ruhle, *Eigenvalue analysis – All information on power system oscillation behaviour rapidly analyzed, Siemens Newsletter*, issue 99, Siemense PTI Software solutions. Available online: http://www.siemens.com/power-technologies.

[20]. IEEE Standards, *IEEE guide for synchronous generator modelling practices and application in power system stability analyses*, IEEE, New York, 2003.

TOPIC B. MACHINES

Proceedings of the 19th Southern African Universities Power Engineering Conference
SAUPEC 2010, University of the Witwatersrand, Johannesburg

DEVELOPMENT OF A SHUTTER TYPE MAGNETIC GEAR

L Brönn, R-J Wang and M J Kamper

University of Stellenbosch, Department of Electrical & Electronic Engineering, Private Bag X1, Matieland 7602.

Abstract. Magnetic gears offer significant advantages over traditional mechanical gears, such as the ability to increase as well as decrease the input speed, contactless power transfer, high gear ratios, oil free operation, inherent overload protection, high torque density, potential for high efficiency and little or no maintenance. This paper reports the design, construction and experimental evaluation of a shutter-type magnetic gear. The experimental results show that the gear could be an alternative to mechanical gears especially in applications where the advantages of magnetic gears are essential.

Key Words. Permanent magnet; gear; finite element method; torque density; magnetic design.

1. INTRODUCTION

It is usually more cost and size effective to use a high speed electrical machine together with a mechanical gearbox to achieve the required load torque and speed. The downside of using a mechanical gear is that the gear lubrication and cooling are often required, while noise, vibration and reliability can also be significant issues. In renewable energy generation it is often necessary to increase the speed of the input with a gear system, which implies an oversized mechanical gearbox to handle up-speed power flow. Magnetic gear is an attractive alternative technology, which offers significant advantages over conventional mechanical gear such as bi-directional and contactless power transfer, oil-free operation, inherent overload protection, high torque density, potential for high efficiency and little or no maintenance. Despite these advantages, magnetic gears have received little attention from both research institutions and industry, due to the relative complexity of magnetic gears and the shortcomings of earlier permanent magnet (PM).

The basic concept of magnetic gearing can be tracked down to the beginning of the 20th century. An early U.S. patent [1] described the electromagnetic gear consisting of two rotational shafts with salient steel poles. The two shafts are magnetically connected with stationary electromagnetic poles. Even though the idea in the patent seemed quite effective, apparently nothing was done to utilize the idea in commercial applications. Another interesting patent [2] described two discs with different diameters and different number of PMs on the two disks. The gearing topology proposed in the patent was also weak in the utilisation of PMs as only one magnet on each disk contributes to torque transfer. In the mid 1900s only ferrite magnets were available, which is only about one tenth of the field strength of modern neodymium magnets. This limited the force transfer capabilities of magnetic gearing and also the development and progress of the magnetic gearing technology.

There are a few publications where magnetic spur gears were considered [3]. Spur-like magnetic gears could work very well in applications where contactless power transfer is necessary, where space is not a problem and where relatively simple designs are essential. The main disadvantage is that only a limited amount of magnets transfer torque at any given mo-ment, which lowers the maximum torque per volume (or torque density) that can be transferred. These simple magnetic gears are feasible but they have poor torque density and lower gear ratios, which makes them ineffective.

Another interesting topology is shown in Fig. 1, in which two rotating discs are coupled with magnets axially. The advantages of using axially placed magnets rather than radially placed magnets are that the two shafts can be separate from each other and the gap between two discs can be more easily observed; also two or more high speed output or input shafts can be used. These discs are relatively easy to manufacture and the torque density is relatively high when compared to spur-like magnetic gears.
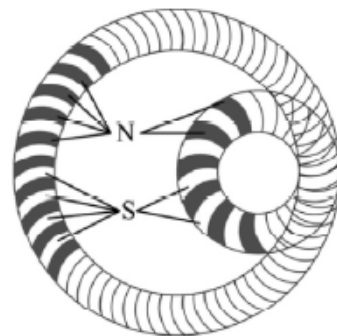
Fig. 1: Magnetic disk gear schematic.

The magnetic worm gear was proposed in [4], the topology of which is illustrated in Fig. 2. The gearbox is of a gear ratio of 1:33, with a maximum torque of 11.5 Nm and an approximate torque density of 0.1 kNm/m³. This example illustrates that magnetic worm gears have very low torque densities but relatively high gear ratios. This topology could be used in applications where the worm configuration is necessary.

Fig. 2: Magnetic worm gear schematic [4]

Proceedings of the 19th Southern African Universities Power Engineering Conference
SAUPEC 2010, University of the Witwatersrand, Johannesburg

TOPIC B. MACHINES

Literature [5] reported the development of a magnetic planetary gearbox and an illustration can be seen in Fig. 3. The advantage of using a planetary gearbox is that it has three transmission modes and a high gear ratio. The gearbox exhibited a torque density of nearly 100 kNm/m³ and a gear ratio of 3:1. By adding more planet gears the transmission torque can be increased, but adding more planet gears also increases the cogging torque. The magnetic planetary gear exhibits a relatively high torque density and a high gear ratio, but the planet arrangement makes it unnecessarily complicated.
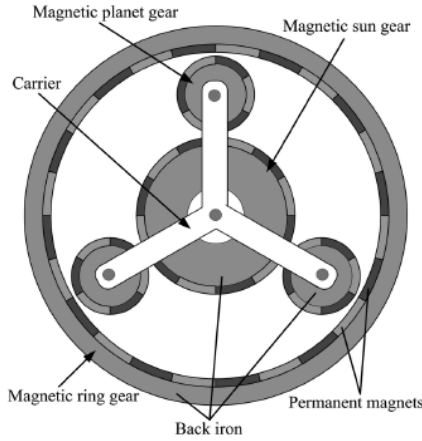
Fig. 3: Magnetic planetary gear schematic [5]

In [6] a novel magnetic gear configuration was introduced, which is relatively simple in design. The gear consists of a high speed inner rotor, a low speed outer rotor and stationary pole pieces (see Fig. 4). The gear topology is known as a shutter-type magnetic gear. The shutter magnetic gear may attain a torque density exceeding 100 kNm/m³, which is comparable to that of two- to three-stage helical gearboxes (50-150 kNm/m³). Normally the pole pieces are kept stationary and the high speed rotor and low speed rotor are rotated. However, alternative configuration may also be used; for example, the high speed rotor and the pole pieces rotate while the low speed rotor (outer rotor) is stationary. This arrangement is sometimes preferred as it simplifies the mechanical design. The main advantage that the shutter-type gear has over the other above described magnetic gear topologies is that almost all the magnets are involved in transmitting torque at a given moment, which greatly increases its torque density.

There are also more complex topologies for example the cycloid magnetic gear [7]. The cycloid magnetic gear works on the same principle as a mechanical harmonic gear. Andersen et al [7] designed and built an experimental cycloid gear with two gear sets to balance the unbalanced magnetic force, which is able to reach a maximum torque of 33 Nm, a gear ratio of 1:22 and a torque density of 183 kNm/m³. The problem with this type of gearbox is that it needs 12 needle roller bearings just to counter the cycloid motion. But with all these extra complications they still measured an efficiency of 94% at 500 rpm.
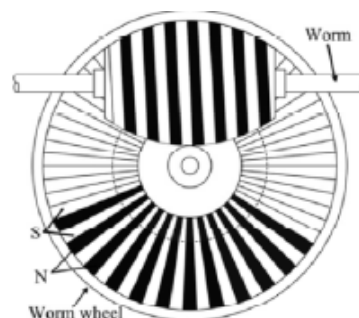
For this specific study, the shutter-type magnetic gear is selected as the suitable topology for a prototype. The shutter-type topology shows potential for high torque density, high gearing ratios and it is relatively simple in design. In this paper the shutter-type magnetic gear is examined. The first step is to complete the magnetic and mechanical designs. Next the construction and assembly of the prototype are discussed. The testing and performance evaluation are then looked at and finally the recommendations and conclusion are considered.

2. PRINCIPLE OF OPERATION

The coupling between magnets is a function of several variables including the number of poles, the material properties, dimensions and separation.

Fundamental to the operation of a magnetic shutter gear is the magnetic fields produced by the PMs on either the high- or low-speed rotors modulated by the steel pole pieces, which results in space harmonics having the same number of poles as the related magnet rotor. Fig. 4 illustrates the schematic of a shutter-type magnetic gear. It has been showed in [8] that the number of pole pairs in the space harmonic flux density distribution produced by either the high or low speed rotor PMs is given by:

$$p_{m,k} = \left| mp + kn_s \right|$$
$$m = 1, 3, 5, \cdots, \infty \tag{1}$$
$$k = 0, \pm 1, \pm 2, \pm 3, \cdots, \pm \infty$$

where p is the number of pole-pairs on the PM rotor and n_s the number of stationary pole-pieces. Furthermore, the gear ratio is given as:
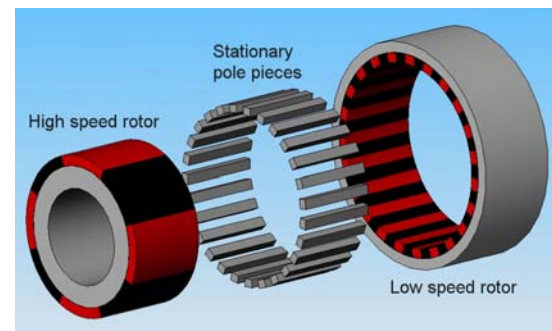
$$G_r = \frac{n_s - p}{p} \tag{2}$$

Fig. 4: Magnetic shutter gear schematic

Keeping the outer rotor stationary may be a preferred operating arrangement since it may simplify the overall mechanical design. The torque will then be transmitted to the pole pieces instead of the outer rotor, the gear ratio then becomes:

$$G_r = \frac{n_s}{p} \tag{3}$$

TOPIC B. MACHINES

Proceedings of the 19th Southern African Universities Power Engineering Conference
SAUPEC 2010, University of the Witwatersrand, Johannesburg

3. DESIGN OF THE PROTOTYPE

The design of the magnetic gear involves both magnetic and mechanical design.

3.1 Magnetic Design

Similar to PM machine design, one has to pay attention to the torque quality when designing a magnetic gear. To minimize the cogging torque a cogging factor defined in [9] is used for selecting suitable PM poles and modulator pole-pieces combinations, i.e.

$$f_c = \frac{2pn_s}{N_c} \quad (4)$$

where N_c is the smallest common multiple between the number of poles on one of the PM rotors (p) and the number of stator pole-pieces (n_s). The factor gives a good estimate of the severity of the cogging torque. The lower the cogging torque factor the lower the cogging torque is likely to be. From the cogging torque factor it is clear that the larger the smallest common multiple and the lower the number of poles, the smaller the cogging torque factor will be and thus the cogging torque. To keep a reasonable number of total magnets, the number of pole-pairs on the high speed rotor was chosen to be two ($p_h=2$). Figure 5 shows the number of pole-pieces and number of PM poles on the low speed rotor against the gear ratio. The graph also shows the cogging torque factors. To obtain the lowest cogging torque the cogging torque factor was chosen as one ($f_c=1$). With a cogging torque factor of one, from the graph, gear ratios of 1.5 to 11.5 could be selected. A gear ratio of 10.5 ($G_r=10.5$) was chosen to simplify calculations and to demonstrate the high gear ratios obtainable by magnetic gears. With this the rest of the parameters can be calculated as $n_s=23$ and $p_l=21$ by using Eqns (1) and (2).
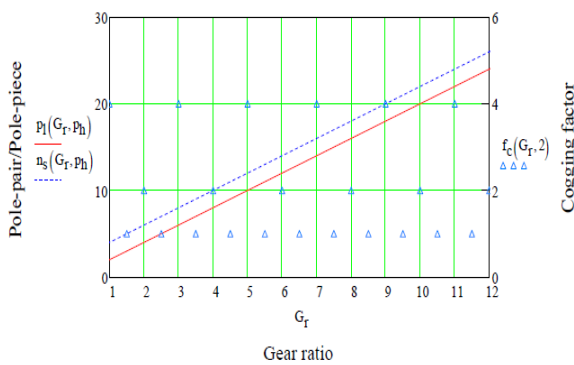
Fig. 5: Cogging torque vs. gear ratio graph.

3.1.1 Simulation Studies

Two-dimensional (2D) finite element (FE) analysis method was used for the simulation studies, the program used was Maxwell 2D. Fig. 6 shows the 2D FE model of the magnetic gear. Since there is no magnetic symmetry, the whole device has to be modeled. To minimize the iron losses the stationary pole-pieces were chosen to be laminated steel. These small parts make the mechanical design very difficult. It was proposed in [6] that the stator pole-pieces may

be connected by a very thin steel strip at the outer diameter and after all the laminations were stacked together the outer ring would then be machined away leaving just the small squares (or pole-pieces). To simplify the mechanical design even further it was realized that the pole pieces could be connected at the inner radius rather than the outer radius by thin steel strip. It has been shown that the presence of the thin steel strip makes relatively little impact on the performance of the gear and strengthens the already weak structure of the stator laminations significantly.
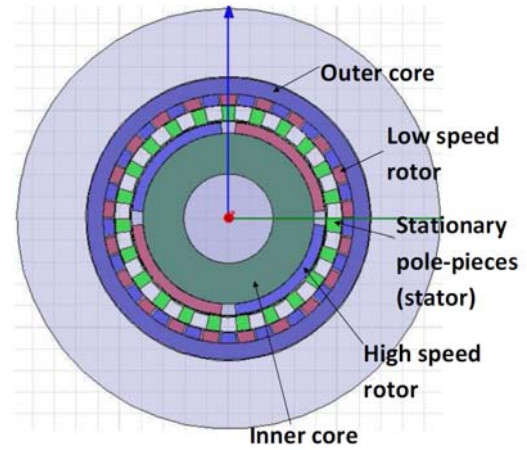
Fig. 6: 2D finite element model of shutter-type magnetic gear.
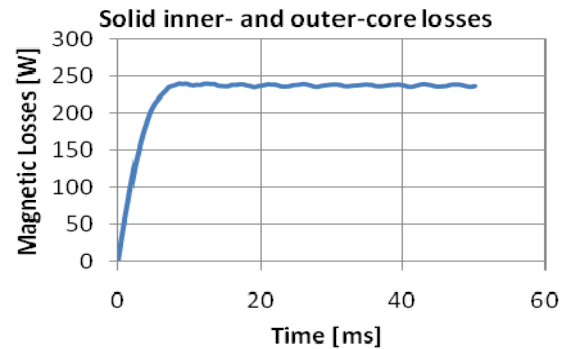
Fig. 7: Maxwell 2D transient analysis of solid inner- and outer-yoke magnetic losses

To minimize core losses the yoke of rotating PM rotors would normally need to be laminated steel. Analyses are carried out to determine if the inner- or outer- yoke could be solid- or needs to be laminated-steel. Fig. 7 shows an FE transient analysis of core losses when both the inner- and outer-yoke are solid steel. It can be seen that almost 250 W of energy is lost if both the inner- and outer-yokes are made of solid steel.

The next graph (Fig. 8) shows the losses when both the inner- and outer-yokes are laminated steel, the losses is only about 500 mW, which is much lower than the case when both yokes are solid-steel. Fig. 9 shows the losses where the inner yoke is solid steel and the outer-yoke laminated steel. The losses from Fig. 9 is about 3 W, which is a lot better than when both yokes are solid-steel and comparable with when both yokes were laminated-steel. From these results it is clear that the outer-yoke must be made of lami-

Proceedings of the 19th Southern African Universities Power Engineering Conference
SAUPEC 2010, University of the Witwatersrand, Johannesburg

TOPIC B. MACHINES

nated steel and the inner yoke can be solid steel without causing major core losses. The final parameters for the magnetic shutter gear are given in Table 1.

Fig. 8: Maxwell 2D transient analysis of laminated inner- and outer-yoke magnetic losses

Fig. 9: Maxwell 2D transient analysis of solid inner yoke and laminated outer yoke magnetic losses

Table 1: Final Parameters for Magnetic Gear Prototype

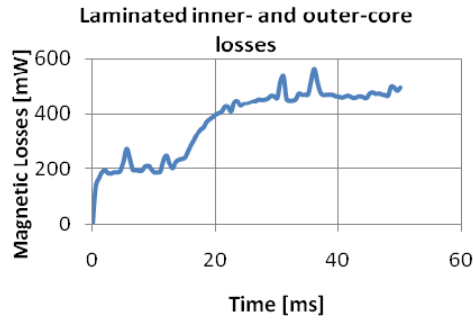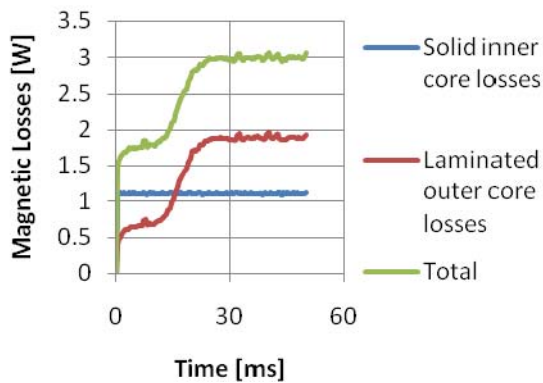| Pole pairs on high speed rotor (p_h)	2
Pole pairs on low speed rotor (p_l)	21
Number of stator segments or pole-pieces (n_s)	23
Outer radius of low speed yoke, mm	57.5
Inner radius of low speed yoke, mm	52.5
Outer radius of stator segments, mm	52
Inner radius of stator segments, mm	45
Outer radius of the high speed rotor, mm	44.3
Stack length, mm	39.3
Permanent magnet thickness, mm	5
Permanent magnet length, mm	40
Permanent magnet grade	N35

3.2 Mechanical Design

In the magnetic design the main dimensions are determined and can be seen in Table 1. One of the biggest difficulties in the design was the small clearances between the inner- and outer-rotors and the stationary pole-pieces. The air gaps between the inner rotor and the stationary pole pieces and between the pole pieces and the outer rotor are 0.7 mm and 0.5 mm respectively. The design was further complicated by the fact that the stationary pole-pieces and the outer-rotor's yoke needs to be laminated steel to minimize magnetic losses. The housing of the gearbox was also carefully designed to minimize magnetic losses from the moving PMs in the rotors. Another difficulty was how to support the two rotating rotors without compromising the structural integrity of the stationary pole-pieces in between them. In most mechanical machines the shafts of the machine (or rotors) are supported by two bearings at each end of the shaft, in the case of the magnetic gearbox this is not practical because the two rotors are on different shafts and the stationary pole-pieces also needs to be supported. Figs. 10 and 11 show the finished low speed rotor assembly and the high speed rotor assembly respectively.

Fig. 10: Finished low speed rotor assembly
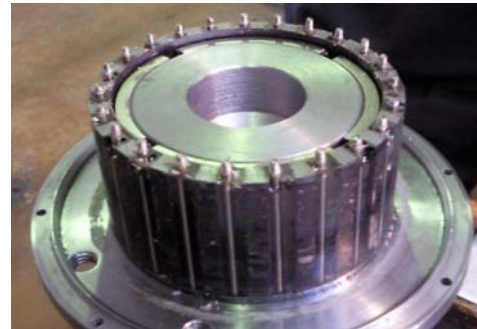
Fig. 11: Finished high speed rotor assembly

4. TESTING AND PERFORMANCE EVALUATION

To evaluate the performance of the gearbox a test bench needs to be setup. The test bench consists of an induction machine to drive the gearbox, a direct-drive low speed PM generator to act as a load to the gearbox, two torque sensors to measure the input and output torque of the gearbox, a stand and fittings to connect all the parts involved.

The first test conducted was a no-load test. This test was done to determine the losses of the gearbox at different speeds. The test was done by starting the induction machine at a low speed and measuring the torque and losses of the gearbox at speed increments of around 50 rpm. Fig. 12 shows a graph of the results from the no-load test. It can be seen that at the design speed of 1000 rpm, the losses are almost 70 watts, which is far greater than the predicted losses which were only about 3 watts. From this test it is clear that the magnetic gearbox has additional losses that the analytical model did not account for. Next a load test was done where the load resistors, connected to the PM generator, were incrementally changed to keep the load at a constant of 20 Nm; this was to determine if the efficiency will change at different speeds. The constant load of 20 Nm was chosen as 20 Nm is near the maximum load before the

TOPIC B. MACHINES

Proceedings of the 19th Southern African Universities Power Engineering Conference
SAUPEC 2010, University of the Witwatersrand, Johannesburg

gearbox starts to slip. The results of the constant load-test are shown in Fig. 13. From this test it can be seen that the efficiency decreases when the speed increases. At a speed of 1000 rpm the efficiency is just above 70 %.
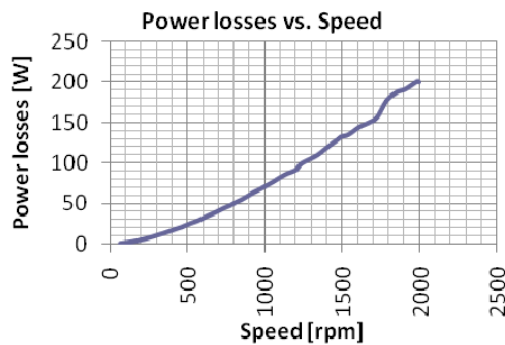
Fig. 12: Experimental results of the no-load test
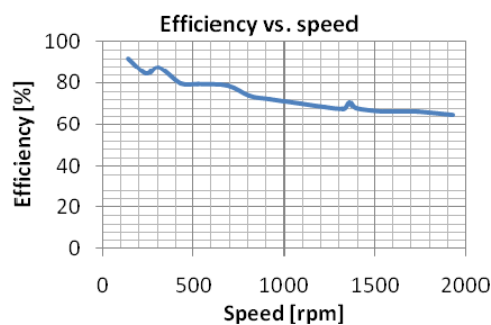
Fig. 13: Experimental results of the constant load test

Table 2 shows a comparison of the magnetic gear that was developed against different mechanical gear topologies. All comparisons are done at 1000 rpm input speed. As can be seen from the table the magnetic gear is comparable to the mechanical gears in most parameters. The magnetic gear's efficiency is not as good as the mechanical gears, but the magnetic gear is still in the beginning phase of development. With continuous research and development the construction difficulties of the magnetic gear can be overcome and the performance can be further improved.

Table 2: Gearbox Comparison

Manufacturer	Rino	Rino	Iron horse	PGC	Magnetic gear
Gear type	Single stage spur gear	Bevel gear	Worm gear	Planetary gear	Shutter gear
Gear ratio	7:1	12:1	10:1	10:1	10.5:1 or 1:10.5
Torque, Nm	25.1	19.1	58.195	35	33
Efficiency, %	93	88	88	90	70
Volume, m³	0.00237	0.00085	-	-	0.00358
Weight, kg	5.5	-	10.43	1.4	9.552

5. CONCLUSION

This paper describes the development and testing of a shutter-type magnetic gear. A topology is chosen from literature to investigate. The parameters of the gearbox are optimised using two dimensional finite element modelling. A prototype was constructed and tested. The results showed that the magnetic gearbox is comparable with its mechanical counterparts, but it still lacked in areas especially efficiency. The unique advantages of the magnetic gear compared to mechanical gears are very beneficial especially in renewable energy applications. Further studies will be focusing on improving the efficiency, the mechanical design and the investigation of other topologies.

ACKNOWLEDGEMENTS

REFERENCES

[1] AH Neuland, "Apparatus for transmitting power," Patent No: 1171351, Feb. 1916.

[2] HT Faus, "Magnetic gearing," Patent No: 2243555, May 1941.

[3] G Lemarquand and JF Charpentier, "Mechanical behavior of axially magnetized permanent-magnet gears," *IEEE Transactions on Magnetics*, vol. 37, no. 3, pp. 1110-1117, May 2001.

[4] K Tsurumoto and S Kikuchi, "Design and characteristics of a new magnetic worm gear using permanent magnet," *IEEE Transactions on magnetics*, Vol. 30, No. 6, pp. 2923-2925, November 1993.

[5] MC Tsai, GD Dorrel, BJ Lin and CC Haung, "Development of a magnetic planetary gearbox," *IEEE Trabsactions on Magnetics*, Vol. 44, No. 3, pp. 403-412, 2008.

[6] SD Calverly, D Howe and K Atallah, "High performance magnetic gears," *Journal of magnetism and magnetic materials*, pp. 272-262, 2004.

[7] TO Andersen, PO Rasmussen and FT Joergensen, "The cycloid permanent magnetic gear," *IEEE Industial Applications Conference*, Vol. 1, pp. 373 - 378, 2006.

[8] D Howe and K Atallah, "A noval high-performance magneti gear," *IEEE Transactions on magnetics*, Vol. 37, No. 4, pp. 2844-2846, July 2001.

[9] D Howe and ZQ Zhu, "Influence of design parameters on cogging torque in permanent magnet machines," *IEEE Transactions on magnetics*, pp. 407-412, 2000.

Proceedings of the 19th Southern African Universities Power Engineering Conference
SAUPEC 2010, University of the Witwatersrand, Johannesburg

TOPIC B. MACHINES

NON-INTRUSIVE EFFICIENCY ESTIMATION OF INDUCTION MACHINES

B. Herndler, P. Barendse, M.A Khan

Department of Electrical Engineering, University of Cape Town, Rondebosch 7701
Email: barbara.herndler@uct.ac.za, paul.barendse@uct.ac.za

Abstract. The induction machine is the most commonly used machine in industry, due to its cost effectiveness and robust nature. These electromechanical workhorses ensure optimal functionality of most plant processes in industrial applications and serve as a driving force in a country's economy. In light of the global energy crisis, much interest has been taken in exploring method to assess and improve energy consumption. Since motors are industries largest energy consumers the need to determine the operating efficiency has become highly topical. In particular, to be able to measure the efficiency in-situ without the use of highly intrusive and costly equipment is fast becoming mandatory in industrial applications. The non intrusive air gap torque method (NAGT) owes its non intrusiveness to the estimation of stator resistance, rotor speed, no load losses and stray load losses. The accuracy of this technique, therefore, is affected by the accuracy of the estimation techniques. This paper provides an evaluation of stray load loss estimation and its effect on using the NAGT as a method of determining the efficiency of a motor in field applications.

Key Words. Efficiency, Air- Gap Torque, Non-intrusive, IEEE 112 Standard, IEC 34-2-1 Standard, Stray Load Losses

1. INTRODUCTION

Induction machines have provided industry with the ability to convert energy from electrical to mechanical form reliably and cost-effectively for over a hundred years. These machines provide the driving force to various equipments such as conveyors, fans and pumps and are necessary for numerous processes in production and manufacturing plants. Motorised loads account for two thirds of the total energy consumed in industry today [1]. The impact of green house gas emissions has catalysed the sudden increase in awareness to conserve energy and has encouraged industry to identify possible areas of energy savings. Since motors are the prime consumers, they provide industry with huge saving potentials.

The need to measure the efficiency is to be able to identify whether the machine is operating in such a way so as to maximize production output with minimised resources. The motor may be worn out or out of date, thus analysis of the motor efficiency will assist in the decision to either replace or repair an existing motor. Efficiency measurement provides industry with the ability to perform energy audits of its plants in order to assist with cost analysis. Another reason to be able to measure efficiency exists in the event of receiving a rewound machine. Traditionally the efficiency of a motor is measured in a laboratory using advanced instrumentation that is accurate, precisely calibrated and makes use of dynamometers. Under laboratory conditions the efficiency is obtained under balanced, rated voltage and stable load. These tests are highly intrusive because they require a no load test, reduced voltage and unpowered stator resistance measurements [2]. These are factors that are often undesirable in the field environment.

In contrast, the machine, when place in the field, is subjected to many non-ideal situations. For instance, the power supply may not be perfectly balanced or may contain a certain degree of harmonics [1]. These factors affect the efficiency of the machine and thus it may not meet the capabilities proposed by the manufactures. Due to the high intrusion levels of the tests required for efficiency evaluations, they can only be conducted during plant outages and maintenance. Also, the equipment required to perform advanced testing is often inaccessible and very costly to be implemented in the field environment.

The need for non intrusive efficiency estimators has become mandatory in many industrial applications. The main aim of these methods are to avoid the use of high cost equipment and to reduce the amount of intrusion while still maintaining a high level of accuracy. If the method is too intrusive it may result in unwanted and unnecessary down time of processes and includes high level coordination of complex procedures in order to decouple the machine or remove it from its supply. These factors are highly undesirable and are costly to the user.

Many non intrusive efficiency methods have been developed. In particular, the non-intrusive air gap torque (NAGT) method developed by [3], allows for the efficiency of machines to be calculated by measuring the instantaneous voltage and current, which is easily accessible from the motor control centre. The method owes its non intrusiveness, as an improvement to the original air gap torque method, to estimation of stator resistance, rotor speed and loss estimation.

This paper, therefore, will focus on the loss estimation aspect of the NAGT and aims to validate its accuracy when

TOPIC B. MACHINES

Proceedings of the 19th Southern African Universities Power Engineering Conference
SAUPEC 2010, University of the Witwatersrand, Johannesburg

the NAGT method is used to determine the efficiency of an induction machine.

2. EFFICIENCY OF INDUCTION MACHINES

Efficiency can broadly be defined as the ratio of mechanical energy output to electrical energy input [4]. The efficiency can be calculated using the direct method or indirect method (which accounts for the machine losses) as show in equation (1) and (2) respectively

$$\eta = \frac{P_{out}}{P_{in}} = \frac{P_{mechanical}}{P_{electrical}} \qquad (1)$$

$$\eta = \frac{P_{in} - P_{losses}}{P_{in}} = 1 - \frac{P_{losses}}{P_{in}} \qquad (2)$$

The operating efficiency can be defined as the efficiency of a machine running at a particular moment in time [5]. In contrast the rated or nameplate efficiency value is specified by the manufacturer and is obtained by conducting various tests performed according to a specific standard.

There are many factors that can affect the efficiency of a machine. These factors should be closely monitored and maintained within suitable levels such that the efficiency of the machine is realistically represented. Factors affecting the efficiency of the machine include the following:

- *Losses*

The losses associated in an induction machine is the main determining factor when calculating the efficiency of a machine. Thus it is vital that they are taken into account as accurately as possible. The losses of a machine can be broadly categorised into load dependant losses and load independent losses [6]. Table I shows the type of losses and loss distribution for a typical 4-pole induction machine [4, 6]

TABLE I
TYPES OF LOSS AND LOSS DISTRIBUTION IN AN INDUCTION MACHINE

Type of Loss	% of Total Loss	Load Dependent/ Independent
Stator Losses	25-40	Dependent
Rotor Losses	15-25	Dependent
Core Losses	15-20	Independent
Stray Load Losses	10-15	Dependent
Friction and Windage	5-15	Independent
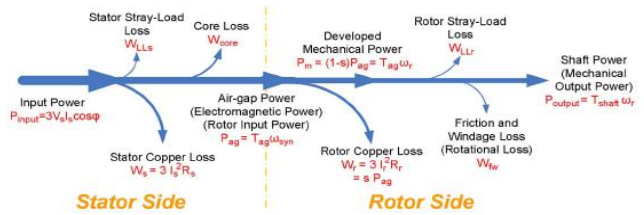
Figure 1 Power flow through a typical motor [3]

Figure 1 shows the power flow through a typical machine in motor mode and accounts for the type of losses developed under typical operating condition.

- *Unbalanced supply and harmonics*

The effects of supply unbalance are known to greatly affect the efficiency of a machine. If the supply is unbalanced, negative sequence currents will become prominent and cause a reduction in overall efficiency. Low voltage levels may also cause the machine to operate at levels of lower efficiency as well as cause an increase in operating current levels [7]. If the machine is operated at over voltage. an increase in magnetising current will result and eventually saturation will occur, leading to decreased efficiency.

- *Loading*

On average, industrial motors operate at 60% of rated load [3]. As seen on a typical efficiency curve, the efficiency does not vary drastically above 60% loading [7], however, operators should ensure that the correct loading be sustained such that the motor operates at an acceptable efficiency level and that the loading conditions is not harmful to the machine. Under low-loaded operating conditions the machine is seen to be less efficient operation while overloading the machine may result in a significant increase in temperature and hence a significant drop in efficiency [8].

- *Condition Monitoring and Maintenance*

Machine misalignment, physical looseness and other imbalances can have an impact of the machines efficiency as well as its lifespan. Improper lubrication can cause increased friction resulting in increased losses. Unwanted vibrations may result if the machine is not properly mounted or correctly aligned which also decreases the efficiency. It is imperative that sufficient condition monitoring and maintenance procedures be implemented in order to assess the state of the machine. The installation of fans or other cooling methods will assist in the dissipation of excess heat and reduction of excessive losses and thus improving the efficiency.

Proceedings of the 19th Southern African Universities Power Engineering Conference
SAUPEC 2010, University of the Witwatersrand, Johannesburg

TOPIC B. MACHINES

3. OVERVIEW OF EFFICIENCY EVALUATION METHODS

Over the years there has been much development of efficiency evaluation methods. The authors of [1] and [10] have conducted a critical survey of the various methods. These methods can be assessed in terms of accuracy, level of intrusion, cost and use of equipment and ease of implementation.

3.1 Name Plate Method

As the name describes, the method identifies the motor efficiency to be constant and equal to the value seen on its nameplate. This method is the least intrusive of all methods, however, is describes as being the least accurate. There are three main reasons contributing to the lack of accuracy. Firstly, the machines may be tested according to different standards. These methods have different methodologies are not entirely in agreement with each other This may result in the motor being stamped with different efficiencies making it difficult for the user to make reasonable judgement for motor purchasing. Secondly, the field environment in which the machine is operating may not have been accurately reflected when the nameplate value was obtained. The field environment contains voltage unbalances and harmonics of which affects the value of the operating efficiency. Lastly, the machine may have been rewound and thus the nameplate value is no longer valid.

3.2 Slip Method

The slip method makes use of the motor speed measurement and is considered to be a simple method to implement. This method exploits the fact that the percentage of the load is presumed to be proportional to the ratio of the measured slip to the full-load slip as described by

$$\eta = \frac{slip}{slip_{rated}} \cdot \frac{P_{output,rated}}{P_{input}} \qquad (3)$$

The method has a relatively low intrusion level if the speed is measured using an optical tachometer and the input power measured non-intrusively. Although this method provides an improvement on the nameplate method it is still not deemed as accurate. Since National Electrical Manufacturers Association (NEMA) allows the motor speed to be deviate within the 20% of nameplate speed, the resulting efficiency value will also deflect by 20% and thus provide inaccurate efficiency values. The authors of [9] explored modifications to the standard slip methods. These included the *Ontario Hydro Modified Slip Method* which attempts to improve the standard slip method by incorporating a voltage correction technique and the *Upper Bound Slip Method* which sets an upper bound efficiency limit and accounts for stator losses.

3.3 Current Method

The current method makes use of current measurements and nameplate values to estimate efficiency. It presumes that the percentage of load is closely proportional to the percentage of the ratio of measured current to full load current, as described in

$$\eta = \frac{I}{I_{rated}} \cdot \frac{P_{output,rated}}{P_{input}} \qquad (4)$$

This method does provide improved accuracy when compared to the slip method however it is still dependant on nameplate values. Its main advantage is its simplicity since it can be easily implemented.

3.4 Equivalent Circuit Method

The efficiency of a motor can be obtained by the derivation of an equivalent circuit. The method is deemed as highly intrusive since it requires impedance, no load, variable voltage, removed rotor and reverse rotation test. This method is thus impractical to implement in the field. The main advantages of these methods are their accuracy and that they can provide the efficiency of a machine at values other than those at which measurements are made [9].

3.5 Segregated Loss Methods

The segregated loss method estimates the magnitudes of the losses of the machines. The efficiency is then obtained since the shaft power is merely the input power minus the losses. These methods are accurate but can be highly intrusive due to the need for a no load, variable-voltage, removed-rotor and reverse- rotation test. Some methods are dependant on empirical values making them less dependable. A variation to this method in order to lower the level of intrusion is to allow the friction and windage and core losses to be lumped together as no load losses and then estimated using rated empirical values. Likewise the values of the stray load losses (SLL) are similarly estimated to be a percentage of rated output power.

3.6 Air gap Torque Method

The air gap torque method uses the product of air gap torque and rotor speed as mechanical power to calculate the efficiency [10] as shown in

$$\eta = \frac{T_{ag} \cdot \omega_r - P_{noload} - P_{SLL}}{P_{in}} \qquad (5)$$

TOPIC B. MACHINES

Proceedings of the 19th Southern African Universities Power Engineering Conference
SAUPEC 2010, University of the Witwatersrand, Johannesburg

The air gap torque equation makes use of the motor instantaneous input line voltages and currents which can be calculated using

$$T_{ag} = [(i_A - i_B) \int [v_{CA} - R(i_C - i_A)]dt$$
$$- (i_C - i_A) \int [v_{AB} - R(i_A - i_C)]dt \quad (6)$$

This method is considered to be highly accurate and can be used in conjunction with condition monitoring techniques. The need for a no load test is a major pitfall of this method and makes it highly intrusive [9].

3.7 Shaft Torque Method

The shaft torque method measures the shaft torque directly (using a torque transducer) and the rotor speed to calculated the shaft power. This method is highly accurate and simple since the need to calculate losses is no longer necessary. Despite its attractiveness, this method is highly intrusive and costly, due to the need for a torque transducer, making it an unacceptable method for industrial applications.

4. COMPARISON OF STANDARDS AND STRAY LOAD LOSS ESTIMATION

Testing standards have been developed to standardise the way in which efficiency is determined. These testing standards have set procedures and methods which may vary according to the standard. In terms of motor efficiency, the direct or indirect method can be applied. The main difference between various testing standards is evident in the treatment of the losses[4]. The three most important standards that exist globally are the IEEE standard 112 [12], the IEC 34-2 [13] and the JEC. Stray load losses are known to be highly complex and difficult to model. These losses are not fully understood and thus it is important that the effects of these losses are not ignored. For instance, a small percentage of stray load loss may have an effect on the efficiency of the machine and therefore it is important that these effects be quantified. Since this paper only focuses on the stray load loss estimation, the JEC standard will be neglected because it does not account for stray load losses when determining motor efficiency [14, 15]. Due to the different strategies associated with the testing procedures, the efficiencies obtained for a given motor may differ significantly [16].

SLLs are a result of space harmonics in the stator and rotor and are produced by the leakage flux near the end windings. SLLs are considered to be difficult to model and quantify [17] and have therefore sparked a highly topical area for research and analysis. The stray load loss (SLL) can be defined as all the losses not otherwise accounted for.

In terms of international standards, the SLL can be determined directly using the IEEE Std 112 method E, F and E/F or indirectly using IEEE Std 112 method B, B1, C and C/F with different degrees of accuracy. The SLL can be calculated indirectly using

$$P_{SLL} = (P_{in} - P_{out}) - (P_{Fe} + P_{Stator} + P_{Rotor} + P_{Fr,W}) \quad (7)$$

The IEC 34-2-1 Standard follows a similar method to the IEEE Std 112 method B and also determines the additional losses indirectly. The following sections describe the methods of obtaining SLLs for the IEEE Std 112 and IEC Std 34-2-1in more detail.

5.1 IEEE Standard 112

The IEEE Std 112 consists of five basic methods to measure efficiency. Method B is most commonly used and is considered as the baseline for laboratory testing of induction motors due to its high accuracy [19] and particular attention is given to this method in this paper.

The stray load losses at different loads are obtained using (7). In order to correct these values and reduce the influence of measurement error [15], the stray load losses are smoothed, using linear regression techniques, by expressing the stray load loss as

$$P_{stray} = AT_{shaft}^2 + B \quad (8)$$

A correlation value is used to determine whether the results are satisfactory. A good measurement is seen to have a correlation of higher than 0.9. [15]. The stray load loss can also be estimated relative to the size of the machine. Table II shows the assumed values of stray load loss at rated load as a percentage of rated output power. For other than rated load conditions, the stray load loss can be assumed to be proportional to the square of the rotor current and is calculated using

$$P_{SLL} = P_{SLL,rated} (\frac{I_2}{I_2'})^2 \quad (9)$$

Where
$P_{SLL,\ rated}$ is obtained from Table II
I_2 is the rotor current at the load where the stray load loss is to be determined
I_2' is the rotor current at rated load

The rotor current can be obtained according to

$$I_2 = \sqrt{I^2 - I_0^2} \quad (10)$$

Where

I is the stator line current
I_0 is the value of the no load current

Proceedings of the 19th Southern African Universities Power Engineering Conference
SAUPEC 2010, University of the Witwatersrand, Johannesburg

TOPIC B. MACHINES

TABLE II
ASSUMED VALUES FOR STRAY LOAD LOSS IN IEEE
STANDARD 112

Machine Rating	Stray-Load Loss Percent of Rated Output Power
0-90 kW	1.8%
91-375 kW	1.5%
376-1850 kW	1.2%
>1851 kW	0.9%

5.2 IEC Standard 34-2-1

The IEC Standard 34-2 uses the segregation of loss method to calculate the efficiency of a machine. However, the standard does not measure the SLLs directly, instead it estimates it to be equivalent to 0.5% of the full load input power. The new IEC Standard IEC 34-2-1 (2007) [13] is comparable to the IEEE Std 112 since its testing methodologies are very similar. The SLL component can either be calculated as with IEEE Std 112 method B or it can be estimated by relating a fixed amount from a predefined curve based on the power rating of the machine [13]. The curve can be seen in figure 2 and the governing equations for the graph are shown in Table III where P_1 is the input power and P_2 is the rated output power.
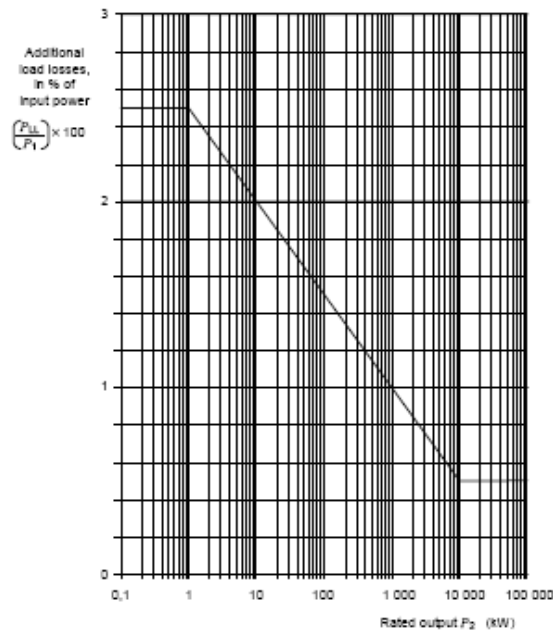

Figure 2 Assigned allowance for additional load loss

TABLE III
EQUATIONS OF STRAY LOAD LOSS FOR THE IEC 34 2-1
STANDARD

Machine Rating	Equation
$P_2 < 1$ kW	$P_{sll} = P_1 \times 0.025$
1kW $< P_2 <$ 10 000kW	$P_{sll} = P_1 \times [0.025 - 0.005\log_{10}(P_2/1kW)]$
$P_2 >$ 10 000 kW	$P_{sll} = P_1 \times 0.005$

5.   THE NON INTRUSIVE AIR GAP TORQUE METHOD

The Air Gap Torque Method in its original form (as described in section 3) although highly accurate, it is highly intrusive. In order to overcome this pitfall, the authors of [3] have proposed a technique which allows the Air Gap Torque method to be used non-intrusively. As seen in equations (5) and (6) the method requires the line voltage, line current, stator resistance, rotor speed, no load loses and stray load losses to be measured. The non intrusive approach to the air gap torque (NAGT) method addresses the components that contribute to high intrusiveness, namely stator resistance, rotor speed, the no load losses and stray load losses. In order to avoid the traditional un-powered test used to measure the dc resistance of the stator winding, an online stator winding resistance technique can be incorporated as shown in [3]. This is performed by injecting a dc signal into the motor using a MOSFET-controlled circuit. The speed of the motor can be estimated using sensorless rotor speed estimation techniques. In [3] a method using the harmonic frequency of the rotor and dynamic eccentricities, of which can be related to the rotor speed, is used. To avoid the intrusive nature of a no load test, the no load losses need to be estimated using empirical values. The no load losses, consisting of core losses and friction and windage losses are presumed to be equivalent to 3.5% of rated output power [3], with the friction and windage losses amounting to 1.2% of the rated output power. Likewise, the stray load losses can be also estimated according to IEEE Standard 112 relative to the size of the motor [13].

Since the NAGT relies on the estimation of various parameters, there is room for improving accuracy through further investigation. In [3], the authors estimate the stray load loss according to Table II. This assumes the stray load loss is constant and not dependant on load. However, this method is preferred since the technique of using equation (9) is dependant on the no load current, which is unacceptable under non intrusive conditions. However, there is a significant difference between the values of SLLs at varying loads. Also, the use of the IEC 34-2-1 SLL estimation as noted in Table III was not considered as a possible candidate. This paper, therefore, will explore the effects of different SLL estimating techniques on efficiency estimation when using the NAGT method.

6.   EXPERIMENTAL VALIDATION

6.1 Experimental Setup

The experimental procedure is conducted on a 4 pole, 3 kW induction machine. The machine is connected to a dynamometer fixed to a test rig at the University of Cape Town (UCT). A WT1600 Yokogawa Digital Power Meter is used to capture the instantaneous line voltages and currents. The data is then passed through a model developed in MATLAB-Simulink® in order to obtain the

TOPIC B. MACHINES

Proceedings of the 19th Southern African Universities Power Engineering Conference
SAUPEC 2010, University of the Witwatersrand, Johannesburg

efficiency using the air gap torque method. The accuracy of the NAGT method was tested using four methodologies of testing. Firstly, using the SLL obtained from the IEEE Std 112 method B was applied to the NAGT method. Secondly, using the SLLs at rated value for all loads as estimated in [3] using Table II. Thirdly, using equation (9) which is load dependant since current is related to load, and lastly using the IEC 34-2-1 equation found in Table III. For comparison purposes the IEEE Std 112 method B was conducted according to [12] and served as the base case. The machine is loaded accordingly to values ranging from 25-150 % and data is captured at each loading point. The power analyser is set to capture data at a sampling rate of 10 kHz.

6.2 Comparison of Stray Load Losses

According to Table II, the IEEE Std 112 assumption for a 3 kW machine translates to SLLs of 54 W at rated load. To compare the values of SLL at each load as estimated by each of the techniques, the results are shown in figure 3. From the graph it is evident that there is a discrepancy between the four techniques. When comparing the IEEE Std 112 SLL and IEC 34-2-1 SLL values obtained from Table III it can be seen that the assumed values of SLL of the IEC 34-2-1 technique estimates a higher value of SLLs than the IEEE Std 112. This discrepancy will have an effect on the accuracy of the efficiency when using the NAGT method. The difference may result in over estimation of motor efficiency which may lead to incorrect decision making of whether to repair or replace a motor as well as incorrect energy evaluation of a plant. The efficiency curves of the NAGT and IEEE 112 method B are shown in figure 4. From the graph it can be seen that the curves are closely related at higher loads. For less than rated load, the efficiency of the IEEE Std 112 load dependant SLL estimation technique (method 3) is higher, thus showing an overestimation of efficiency. The efficiencies of methods 2 and 4 appear to coincide with the IEEE Std 112 method B at 60% of rated load.
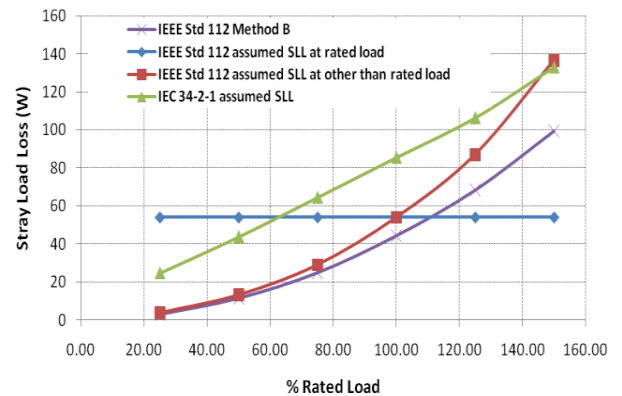
Figure 3 Comparison of SLLs
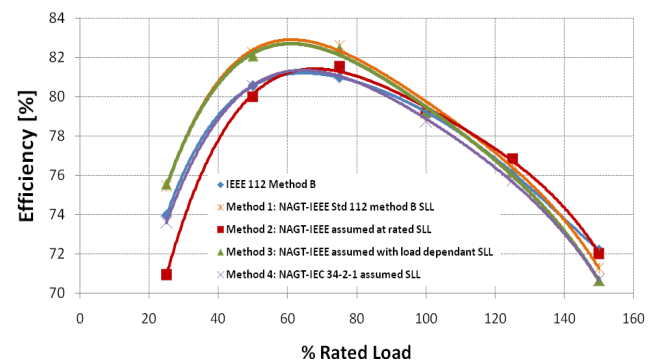
Figure 4 Comparison of efficiency using different SLL estimations

The exact efficiency of each of the methods at each load is shown in Table IV. Ideally method 1 should reflect the values of method B; however, the validity of the NAGT method is part of current research and needs to be further investigated. It can be seen that the efficiency using the IEEE assumed SLL (method 2) at rated technique is within 0.75% barring a deviation at 25% load. The efficiency using the IEEE assumed load dependant SLL (method 3) is within 1.6% and is notably within 0.01% at rated load. The efficiency using the IEC 34-2-1 SLL (method 4) estimation is within 0.5%, with a deviation of 1.52% at 150% loading. Overall the efficiencies are within range for higher values of loading. However, the differences become evident at lower levels of loading.

TABLE IV
EFFICENCY RESULTS OBTAINED USING EACH SLL ESTIMATION TECHNIQUE

% Load	IEEE 112 Method B (Dynamometer)	Method 1: IEEE Std 112 (Method B SLLs)	Method 2: IEEE Standard 112 (at Rated Load)	Method 3: IEEE Standard 112 (Load Dependant)	Method 4: IEC 34-2-1
150	72.21	71.27	72.03	70.64	70.68
125	76.15	76.56	76.86	76.16	75.75
100	79.22	79.47	79.21	79.21	78.75
75	80.97	82.61	81.56	82.44	81.20
50	80.55	82.24	80.01	82.08	80.52
25	73.98	75.46	70.96	75.55	73.62

Proceedings of the 19th Southern African Universities Power Engineering Conference
SAUPEC 2010, University of the Witwatersrand, Johannesburg

TOPIC B. MACHINES

TABLE V
MEASURED AND ESTIMATED NO LOAD LOSSES

Loss Type	Estimated [W]	Measured [W]
Core Loss	69	140.21
Friction and Windage	36	22
Total No Load Loss	105	162.22

6.3 Comparison of No Load Losses

The total combined no load losses are estimated as described in section 5 sums to 105W for a 3kW machine. The friction and windage loss as estimated at 1.2% of rated output power is 36 W. Table V shows a comparison of the estimated values to that obtained for the measured values obtained using the IEEE Std 112 method B.

Based on these results one can see that there is a discrepancy between the values with a maximum difference of 57.22 W between the total no load losses.

7. CONCLUSIONS

The IEC 34-2-1 estimation of SLL is a better reflection of the true SLL since these losses are dependant on load. Thus the IEC 34-2-1 is more accurate (within 0.5%) than the IEEE Std 112 method of estimation (both load dependant and independent) when is comes to estimating the values of the stray load loss. It is observed that using the fixed, IEEE Std 112 load independent value of SLL produced more accurate efficiency results than that of the load dependant IEEE Std 112 technique. This is somewhat questionable and should be verified by more testing. The IEC 34-2-1 method is not only more accurate, but also non intrusive since it only requires the input power to measured. This can be exploited when used in conjunction with the proposed NAGT method as proposed by [3] since the input power is easily measured. The estimation of the no load losses proved to deviate from the actual loss measured during the no-load test. Thus the empirical estimation of the no-load losses could somewhat be improved in order to enhance the level of accuracy of the NAGT method. Overall, the NAGT method has proved to be accurate and easy to implement, thus providing industry with a low cost solution to efficiency estimation of induction machine while they are in operation.

8. FUTURE WORK AND RECOMMENDATIONS

The above conclusions will be validated by testing on 5 kW, 7.5 kW, and 15 kW machines.

The incorporation of online rotor speed and stator resistance estimation techniques will be researched, developed and implemented to ensure full non intrusiveness of the NAGT method. Furthermore, an error analysis should be performed in order to account for the level of accuracy. The instrumentation errors associated with experiment should also be accounted for when providing accuracy statistics of the NAGT.

REFERENCES

[1] J. Hsu, J Kueck, M Olszewski, D. Casada, P Otaduy, LTolbert, 'Comparison of Induction Motor Field Efficiency Evaluation Methods' *IEEE Transaction on Industry Applications*', Vol. 34, No 1, January/February, 1998

[2] E. Agamloh, A.Wallace, A. Jouanne, K. Anderson, J. Rooks, 'Assessment of Nonintrusive Motor Efficiency Estimators', *IEEE Trans. on Industry Applications*, Vol 41, No.1, January/February 2005

[3] B. Lu, T. Habetler, R Harley, 'A Nonintrusive and In-service Motor-Efficiency Estimation Method Using Air-Gap Torque With Consideration of Condition Monitoring', *IEEE Trans. on Industry Applications*, Vol 44, No 6, November/December, 2008

[4] S. Corino, E Romero, LF. Mantilla, 'How the Efficiency of Induction Machine is Measured?', Department of Electrical Engineering and Energy, Universidad de Cantabria. Cited at: http://www.icrepq.com/icrepq-08/352-mantilla.pdf

[5] E. Wiedenbrug, 'Measurement, analysis and efficiency of three phase induction machines using instantaneous electrical quantities' PhD Dissertation, September 1998, Cited at: http://ir.library.oregonstate.edu/jspui/bitstream/1957/8890/1/Wiedenbrug_Ernestro_J_1998.pdf

[6] Reliable Solutions Today, 'Understanding Energy Efficient Motors'. Cited at: http://www.easa.com/indus/ee_399.pdf

[7] A. Bonnett, 'Understanding Efficiency in Squirrel Cage Induction Motors', *IEEE Trans. on Industry Applications*, Vol. IA-16, No. 4, July/August 1980

[8] Control Engineering Europe, 'Motor Condition Monitoring: Efficiency does Matter'. 30 December 2008, Cited at http://www.controlengeurope.com/article.aspx?ArticleID=21440

[9] B. Lu, T. Habetler, R Harley, 'A Survey of Efficiency-Estimation Methods for In-Service Induction Motors '*IEEE Trans. on Industry Applications*, Vol 42, No 4, July/August, 2006

[10] J Kueck, P Otaduy, J Hsu 'Evaluation of Methods for Estimating Motor Efficiency Without Removing Motor from Service' 1996

[11] P .Pillay, V. Levin, P. Otaduy, J. Kueck. 'In- Situ Motor Efficiency Determination Using the Genetic Algorithm', *IEEE Trans. on Energy Conversion*, Vol. 13. No. 4, December, 1998

[12] IEEE *'Standard Test Procedure for Polyphase Induction Motors and Generators'*, 2004

[13] IEC International Standard 60034-2-1, 2007

[14] H. Mzungu, A. Sebitosi, M Khan, 'Comparison of Standards for Determining Losses and Efficiency of Three-Phase Induction Motors', *IEEE PES Power Africa 2007 Conference and Exposition*, July 2007

[15] B. Renier, K. Hameyer, R. Belmans, 'Comparison of Standards for Determining Efficiency of Three Phase Induction Motors', *IEEE Trans. on Energy Conversion*, Vol 14, No. 3, September 1999

[16] A. de Almeida, F Ferreira, J. Busch, P. Angers, 'Comparative Analysis of IEEE 112B and IEC 34-2 Efficiency Testing Standards Using Stray Load Losses in Low-Voltage Three-Phase Cage Induction Motors' *IEEE Trans. on Industry Application*, Vol. 38, No. 2, March/April 2002

[17] A. Boglietti, A. Cavagnino, M Lazzari, M. Pastorelli, 'International Standards for the Induction Motor Efficiency Evaluation: A critical Analysis of the Stray- Load Loss Determination', *IEEE Trans. on Industry Application;* Vol.4, No.5, September /October 2004

[18] A. Wallace, E. Wiedenbrug, 'Motor Efficiency Determination: From Testing Laboratory to Plant Installation' Cited at: http://www.whitelegg.com/products/files/Motor_Efficiency_Testing.pdf

TOPIC B. MACHINES

Proceedings of the 19th Southern African Universities Power Engineering Conference
SAUPEC 2010, University of the Witwatersrand, Johannesburg

EFFECT OF SUPPLY VOLTAGE UNBALANCE ON ENERGY EFFICIENT INDUCTION MOTOR

A.L. Van Wyk, A. Muller, M.A. Khan and P.S. Barendse

University of Cape Town, Dept. of Electrical Engineering, Cape Town, South Africa

Abstract: This paper presents some of the effects of voltage unbalanced supplies on induction motors with particular focus on energy-efficient general purpose induction motors. Several key design differences between energy efficient and standard motors are outlined. Furthermore, it will be shown that energy efficient motors draw higher unbalanced currents. The test results for that of two 7.5kW motors showed that the temperature rise increase for the energy efficient motor were higher than that of the standard motor for a 4.5% voltage unbalance.

Key Words: Voltage unbalance, energy efficient induction motors, current unbalance

1. INTRODUCTION

The first energy efficient (EE) motors were introduced in 1970 but no significant penetration was established prior to the Energy Act of 1992 [1]. The main reasons for this were the relatively cheap electricity and incremental capital cost of EE motors.

With the recent energy crisis experienced in South Africa, electricity cost is expected to escalade sharply. This as well as the lack of supply capacity and hence the need for demand side management (DSM) makes EE motors more attractive as a means of energy conservation.

Often life cycle costing (LCC) of electrical motors is based on the catalogue or "name plate" efficiency of the motor. Replacing a failed motor with an EE motor rather than rewinding it, can be justified using LCC techniques. However, the catalogue efficiencies are measured under near perfectly balanced voltage supply (>0.5% Voltage Unbalance) conditions. Also, the mean time between failures (MTBF) of a motor is greatly affected by the voltage unbalance. Thus, the estimated cost does not reflect the real cost of the motors that operates in practise.

In almost all three-phase networks a certain degree of voltage unbalance exists and is particularly large in weak networks and networks with many single phase loads [2,3]. A study done in the USA estimated the voltage unbalance in 66% of the distribution systems is less than 1%. Furthermore, 98% of distribution systems is less than 3% and the remaining 2 % is greater than 3% [2,3]. Similar figures are expected for the South African distribution network.

Induction motors are designed to operate under balanced conditions, but even a small degree of voltage unbalance can cause the motor to draw large unbalanced currents and can eventually lead to premature failure [4]. An unbalanced supply induction motor increases the losses and hence temperature rise of the motor. This result in a reduced developed torque and efficiency [3]. Operation of motors under voltage unbalance conditions can lead to premature failure of the motor if not derated appropriately.

The paper begins with a brief description of some design differences between standard and EE motors before mentioning some effects of voltage unbalance on these motors. Finally, some results will be presented.

2. STANDARD AND EE MOTOR DESIGN DIFFERENCES

Generally EE motor designs vary from manufacturer to manufacturer based on a variety of design techniques. It is impossible for the designer to optimise all the design parameter like efficiency, power factor, winding life and starting currents etc. simultaneously [1]. For example; improving the efficiency might reduce the power factor of the motor. Designers and manufacturers typically utilise some of the following methods to lower the losses of motors:

- Standard motors use lower cost annealed steel, which is more susceptible to temperature and environmental conditions. Newer magnetic steels are capable of operating at higher flux densities [5]. The magnetizing flux needs to be

Proceedings of the 19th Southern African Universities Power Engineering Conference
SAUPEC 2010, University of the Witwatersrand, Johannesburg

TOPIC B. MACHINES

small to minimize the core loss [6]. By increasing the length of the core the flux density in the stator teeth can be reduced.

- The largest loss in induction motors is due to the finite resistance of the stator and rotor winding for a given current that produces heat. This loss can be reduced by increasing the cross sectional area of the copper by either increasing the slot fill or by using larger slots in the stator core [5].

- Smaller cooling fans can be used to reduce the windage loss, since EE motors produce less heat than their standard counterparts [7]. Bearings and seals are often kept unchanged to maintain the same mechanical loading and ingress protection.

- Other ways to improve the efficiency are by implementing more accurate manufacturing tolerances and tighter quality control, which will reduce the stray load losses. Often designers increase the airgap of the motor to reduce the stray load loss, but that may result in lower power factors.

3. SYMMETRICAL COMPONENTS

Symmetrical components can be used in order to analyse an unbalanced supplied induction motor on a per phase basis. The symmetrical components theory was developed in 1918 by Charles L. Fortescue [8], which essentially converts any poly-phase unbalanced system into symmetrical independent systems. As depicted in figure 1, three-phase unbalanced networks can be resolved into two balanced sources and a zero sequence component. These components are known as the positive, V_{pos} and negative sequence, V_{neg} components. The zero sequence components are equal in magnitude and have no phase displacement. However, it can be eliminated since induction motors are typically connected in delta or ungrounded star hence, no zero sequence currents will flow [9,10].
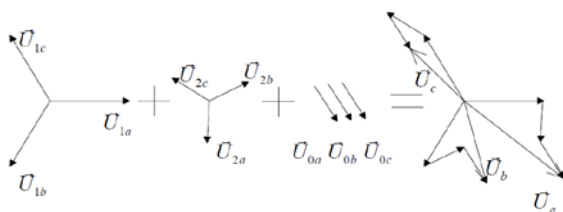

Figure 1. Decompositioned unbalanced system into three sequence components [11]

The analysis of induction motors subjected to unbalanced voltages is greatly simplified by applying the balanced positive and negative components independently to the models in figure 2 and adding the two to obtain the total effect.

4. DEFINITIONS OF VOLTAGE UNBALANCE

In a three-phase system, voltage unbalance is caused by an inequality in the rms values of the (fundamental) phase voltages, which causes an inequality in the line voltages [12]. The degree of voltage unbalance is not uniquely defined, but the following definitions are most commonly used:

The National Manufacturers Association (NEMA) in Standards Publication no. MG 1-1993 [13] definition calculates voltage unbalance as follows:

$$VU = \frac{\Delta V_{max}}{V_{avg}} \times 100\% \qquad (1)$$

Where V_{avg} is the average line voltage and ΔV_{max} is the maximum deviation from the average line voltage. The IEEE defines voltage unbalance in a similar way, but uses phase voltages instead. These definitions are straight forward to use since it only needs magnitudes and is widely used for commercial and industrial installations.

The International Electrotechnical Commission (IEC) uses symmetrical components described in section 3 to define the voltage unbalance factor, (VUF) as,

$$VUF = \frac{V_{neg}}{V_{pos}} \times 100\% \qquad (2)$$

The IEC definition is considered more accurate than the NEMA definition to analyse the effects of voltage unbalance on motors and will be referred to in this paper.

5. INDUCTION MOTOR MODELLING

An unbalanced three-phase voltage supply connected to a motor causes the motor to draw unbalanced currents of multiple times the voltage unbalance. The rule of thumb is that for every one percent of voltage unbalance, a standard motor will draw about five to six times as much current unbalance. The degree of current unbalance for a given voltage unbalance varies a great deal, because of the variations in design and manufacturing techniques of EE motors. According to [15], the current unbalance can be as high as nine times the voltage unbalance for some small EE motors.

The positive and negative sequence equivalent circuits of induction motors in figure 2 are used to explain this further.
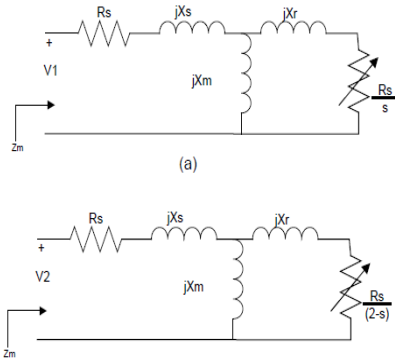
TOPIC B. MACHINES

Proceedings of the 19th Southern African Universities Power Engineering Conference
SAUPEC 2010, University of the Witwatersrand, Johannesburg

Figure 2. Positive and negative sequence equavalent circuit

Due to the positive and negative sequence circuits, the induction motor behaves as two machines operating in opposite directions, one with voltage V_{pos} and slip s, and another with voltage V_{neg} and slip (2-s) [16]. The effect of the reduction in negative sequence impedance in EE motors is an increase in negative sequence current under unbalanced voltage conditions. This can result in additional heating of the rotor and vibration of twice the supply frequency. In addition to that, EE motors operate at slightly higher speeds, and may result in increased power delivered to the load causing further overheating [17]. Current unbalance can be defined by equation 3 below:

$$CUF = \frac{I_{neg}}{I_{pos}} \times 100\% \qquad (3)$$

Where *CUF* is the percentage current unbalance and I_{pos} and I_{neg} is the positive and negative sequence current respectively.

As can be seen from the equivalent circuits in figure 2, the positive and negative sequence currents are proportional to the following:

$$I_{pos} \; \alpha \; \frac{s}{R'_{rot(pos)}} \qquad (4)$$

$$I_{neg} \; \alpha \; \frac{2-s}{R'_{rot(neg)}} \qquad (5)$$

Using the equation in 4 and 5 and combining it into the current unbalance equation in 3, the following proportionality expression can be made:

$$CUF \; \alpha \; \frac{2-s}{s} \qquad (6)$$

Therefore, since EE motors operate at lower slip speeds, the current unbalance generated for a specific voltage unbalance is higher than standard motors. An example of this can be seen in the two 7.5kW motors that were studied in section 6. At

100% load, the standard motor operates at a slip of 0.034 while the EE motor operates at a slip of 0.028. Thus, using the expression in (6), for the standard motor: (2-s)/s = 57.8, and for the EE motor: (2-s)/s = 70.4, for this reason current unbalance will be more severe in EE motors than it will be for standard motors. The same reasoning applies to why current unbalance is worse at no load than it is at full load. At full load, the slip is greater than at no load, therefore at full load (2-s)/s will be less than at no load and current unbalance will not be as high.

The effect of a negative sequence current flowing is a reduced resultant torque, T_m and hence power P_m as can be seen from equations 7 and 8 respectively.

$$T_m = I^2{}'_{rp} \cdot R'_{rp} \cdot \left(\frac{1}{s \cdot \omega_o}\right) - I^2{}'_{rn} \cdot R'_{rn} \cdot \left(\frac{1}{(2-s) \cdot \omega_o}\right) \qquad (7)$$

$$P_m = I^2{}'_{rp} \cdot R'_{rp} \cdot \left(\frac{1-s}{s}\right) - I^2{}'_{rn} \cdot R'_{rn} \cdot \left(\frac{1-s}{2-s}\right) \qquad (8)$$

As depicted in figure 3, the negative sequence current causes a torque in the opposite direction of the torque developed by the positive sequence current. The effective torque delivered by the motor is the summation of the two, which is less than the positive torque.
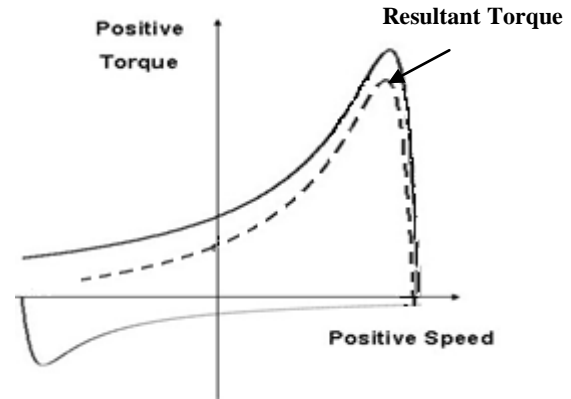
Figure 3. Pos., neg. and resultant developed torque of voltage unbalanced supplied induction motor

Since EE motors draw higher negative sequence currents for a particular voltage unbalance, the percentage reduction of the developed torque is higher than the same size standard motor. Subsequently the percentage increase in slip for EE motors is more, leading to a higher temperature rise increase. This phenomenon is illustrated in section 6. Motors that are continuously operating under unbalanced conditions will experience a decrease in efficiency due to the increase in the current and winding resistance [4].

6. CURRENT UNBALANCE TEST RESULTS

Proceedings of the 19th Southern African Universities Power Engineering Conference
SAUPEC 2010, University of the Witwatersrand, Johannesburg

TOPIC B. MACHINES

Laboratory tests were done on a 7.5kW standard and EE motor. Voltage unbalances were introduced at four loading points ranging between no-load and 150% of full load. The current unbalance measured is depicted in figures 4 and 5. A comparison of the two motors at full load is illustrated in figure 6.
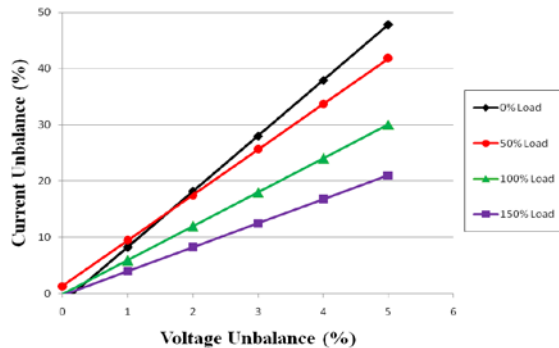

Figure 4. EE Motor current unbalance as a result of voltage unbalance

Both motors revealed similar trends as shown in figure 4 and 5. However, the EE motor is more susceptible to voltage unbalance as can be seen in figure 6. At all loading points, the trend line gradient is steeper in the case of the EE motor. This can be explained due to the fact that the EE motor operates at a lower slip when compared to the standard efficiency motor.
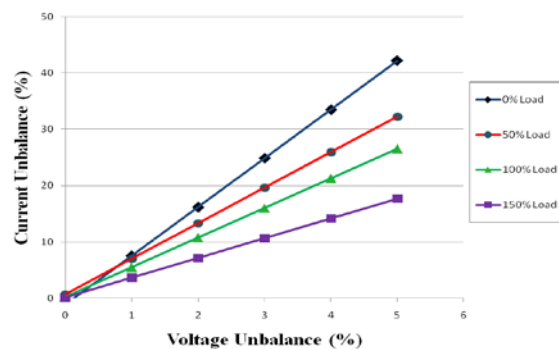

Figure 5. Standard Motor current unbalance as a result of voltage unbalance
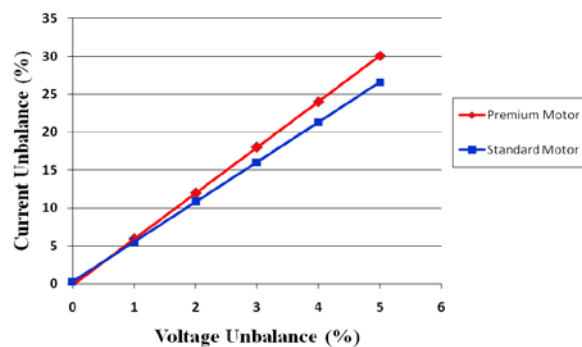

Figure 6. EE motor vs Standard motor current unbalance at full load

7. TEMPERATURE RISE TEST RESULTS

These tests involved the same motors as in section 6 to attain the temperature rise increase when subjected to an unbalance supply condition. Both motors were subjected to the same unbalance supply condition. Three K- type thermocouples were installed on the stator drive-end-side end winding of each motor. The motors were supplied with balanced voltages and than a 4.5 % voltage unbalance always starting the test at room temperature. In each case the motor was loaded to 75% of its full load and allowed to stabilise at its operating temperature according to [18] and [19].
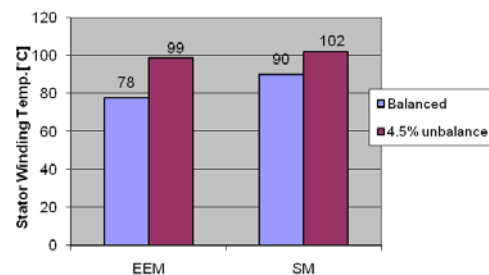

Figure 7. Stabilised temperature at 75% of FL

Figure 7 shows the temperatures at which the motors stabilized for the two conditions. The standard motor and EE motor temperature increase measured is 13.3% and 26.9% respectively. Since EE motors have lower losses in general than standard motors, they run even cooler under voltage unbalance conditions. Thus, although the effect of voltage unbalance might be more on energy efficient motors, the temperature rise (which is the most detrimental) will be less [20].

8. CONCLUSION

This paper addresses the effect that unbalanced supplies have on energy efficient motors. Several design differences have also been summarised. Apart from using more material in energy efficient motors, higher quality materials and better machining tolerances are the main differences between the two motor classes. Energy efficient motors draw more unbalanced currents due to their lower negative sequence impedances. This leads to greater percentage reduction in the developed torque and slip.

REFERENCES

[1]   A. H. Bonnet, "Reliability Comparison between Standard and Energy Efficient motors", *IEEE Transactions on Industry Applications, Vol. 33, No 1. Jan/Feb 1997*

[2]   A. von Jouanne, B. Banerjee, "Assessment of Voltage Unbalance" *IEEE Transactions on Power Delivery, Vol. 16, No 4. Oct. 2001.*

TOPIC B. MACHINES

Proceedings of the 19th Southern African Universities Power Engineering Conference
SAUPEC 2010, University of the Witwatersrand, Johannesburg

[3]   J. Faiz, H. Ebrahimpour, "Precise Derating of three phase induction motors with unbalanced voltages", *Energy Conversion and Management, 2007 (Avail. Online at www.sciencedirect.com).*

[4]   L. Refoufi, H. Bentarzi, F. Z. Dekandji, "Voltage Unbalance Effects on Induction Motor Performance", *6th WSEAS International Conference on Simulation, Modelling and Optimization, Lisbon, Portugal, Sept 2006.*

[5]   D.G. Walters, I.J. Williams, D.C. Jackson, B. Hansen "The case for a new generation of high efficiency motors – Some problems and solutions*", Electrical Machines and Drives,11-13 Sept. 1995, Conference Publication No. 412, IEE 1995.*

[6]   A.H. Bonnett, "Understanding Efficiency in Squirel-Cage Induction Motors", *IEEE Transactions on Industry Applications, Vol IA-16, No.4, July/August 1980.*

[7]   E. Chiricozzi, F. Parasiliti, M. Villani, "New Materials and Innovative Technologies to Improve the Efficiency of Three-phase Induction Motors – A Case Study," *International Conference on Electrical Machines (ICEM), 2004*.

[8]   G.C. Paap, "Symmetrical Components in the Time Domain and Their Application to Power Network Calculations", *IEEE Transactions On Power Systems, Vol. 15, No. 2, May 2000*.

[9]   M.M. Berndt and N.L. Schmitz," Derating of Polyphase Induction Motors Operated with Unbalanced Line Voltages", *AIEE Trans. Power Apparatus and Systems*, Vol. 81, pp. 680-686, Feb. 1963

[10]   W.H. Kersting and H. Phillips," Phase Frame analysis of the Effects of Voltage unbalance on Induction Machines", *IEEE Trans. on Industry Applications*, Vol. 33, No. 2, March/April 1997.

[11]   W. Du Deprez, "Energy Efficiency of induction Machines; A Critical Assessment", *PHD thesis, Katholieke Universiteit Leuven, Dec. 2008.*

[12]   M. Manyage, P. Pillay, "Operation of induction Machines from Unbalanced Supplies", SAUPEC, Dec 2001

[13]   "Motors and Generators", *NEMA Standards Publication no. MG 1-1993.*

[14]   P.C. Sen, " Principle of Electric of Machines and Power Electrical" *John Wiley & Son, 1997*

[15]   Parasiliti F., Villani M., Paris C., Walti O., Songini G., Novello A., Rossi T., "Three-Phase Induction Motor Efficiency Improvements With Die-Cast Copper Rotor Cage And Premium Steel", *Proceedings of SPEEDAM'04 Symposium, Capri, Italy, 16-18 June 2004*.

[16]   P. Pillay, P. Hofmann, "Derating of Induction Motors Operating with a Combination of Unbalanced Voltages and Over- or Undervoltages", *IEEE Trans. on Industry Applications*, 2001.

[17]   Kueck J.D.,Casada D.A., Otaduy P.J.,"A Comparison of Two Energy Efficient Motors", *IEEE Trans. on Energy Conversion, Vol. 13, No. 2, June 1998*

[18]   "IEEE Standard Test Procedure for Polyphase Induction Motors and Generators*", IEEE Standard 112-2004.*

[19]   "Standard methods for Determining losses and efficiency from tests (excluding machines for traction vehicles)", IEC 60034-2-1, 2007.

[20]   "Power Quality and performance Issues with Energy-Efficient motors" EPRI, Commentary Number 2, November 1998

Proceedings of the 19th Southern African Universities Power Engineering Conference
SAUPEC 2010, University of the Witwatersrand, Johannesburg

TOPIC B. MACHINES

DISCRETE LOGIC CURRENT CONTROLLED BRUSHLESS DC MOTOR DRIVE

M D Britten*, J Tapson*, I D de Vries**

* Department of Electrical Engineering, University of Cape Town
** Department of Electrical Engineering, Cape Peninsula University of Technology

Abstract. Multiple function discrete logic gates were used to implement the control electronics for a one kilowatt current regulated BLDC motor controller. The design was carried out in modules so as to be simple, robust and efficient. A two quadrant motor controller was successfully built and tested on an electric bicycle, and a four quadrant controller was simulated. Overcurrents during the commutation process were avoided using the proposed topology. The recovery of braking energy revealed the need for a better energy storage system.

Key Words. PMDC, Brushless, SPICE

1. INTRODUCTION

Brushless direct current (BLDC) motors using permanent magnet (PM) Neodymium-Iron-Boron (NdFeB) rare earth magnets have simple drive requirements and are power dense in both per unit volume and per unit weight.

Many methods exist for controlling the power semiconductor switches in BLDC inverter drives, such as μPs (microprocessors), digital signal processors (DSPs), field programmable gate arrays (FPGAs) and application specific integrated circuits (ASICs), [3], [5], [6]. These methods, especially the sensorless types outlined by Acarnely and Watson [1], usually result in a system beyond the comprehension of the owner of an electric vehicle (EV) where such a drive may be present. Furthermore, there are more strict operation limits and more complex equipment is required for analysis.

The elementary nature of BLDC control logic is efficiently handled by multiple function gates which use little power, reduce cost and improve reliability. The potential for flash memory failure [2] is eliminated by using fixed function logic devices.

Small EVs are becoming more popular and therefore so are small electric drives. The high efficiency of BLDC motors makes it worth while to recover energy regeneratively during slowing down or braking.

2. PM MACHINE OVERVIEW

The BLDC machine can behave as a generator as easily as it can behave as a motor. However there are limitations to this dual nature. The torque-speed characteristic in Fig. 1 shows that along with motoring and generating operation, there is another situation: active braking. In these areas, power and energy are injected into the machine from both mechanical and electrical sources. A machine with lower overall resistance, mechanical and/or electrical, has smaller active braking regions and is more efficient at both motoring and regenerating electricity.

In the active braking zones shown in Fig. 1, V_m, the machine terminal voltage, has to be of opposite polarity to ω, angular velocity. Thus a controller with
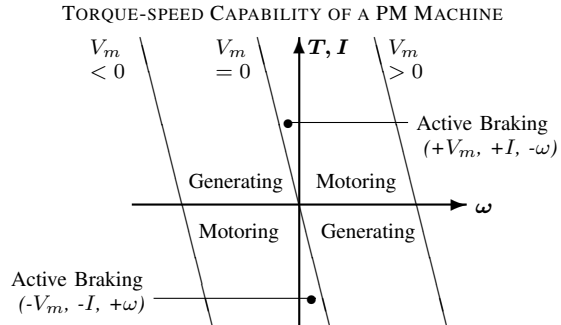

Fig. 1: The torque-speed ($\boldsymbol{T}$-$\boldsymbol{\omega}$) capability of a DC machine. The resistances in the machine cause "Active Braking" zones where both electrical and mechanical energy are dissipated within the machine. V_m and I are the effective terminal voltage and armature current of the machine, respectively.

only the ability to create $V_m > 0$ would be unable to achieve zero speed with reverse torque.

The maximum ω for a BLDC machine is governed by the maximum supply voltage and imitates the $V_m > 0$ line, which resembles a shunt direct current (DC) machine torque-speed characteristic.

3. PROPOSED SOLUTION

Torque control is a primary design goal for this drive because it is intended for use in an EV, where the operator would expect output torque to be related to throttle input.

The operation of a BLDC machine is separated into two basic requirements, commutation of phases and control of instantaneous current. Fig. 2 shows this graphically. The current controller operates independently to the position of the machine and aims to control the output torque by increasing or decreasing the current flowing through the phase switcher block.

The phase switcher is designed for a three phase BLDC machine. Three digital Hall effect sensors, angularly displaced by 120° in electrical terms, are used to determine the angular position of the machine rotor. The information from the sensors is correlated to the required switching pattern in Table 1. The logic function that relates a specific switch to the Hall sensors' state is derived in Equation 1.

TOPIC B. MACHINES

Proceedings of the 19th Southern African Universities Power Engineering Conference
SAUPEC 2010, University of the Witwatersrand, Johannesburg
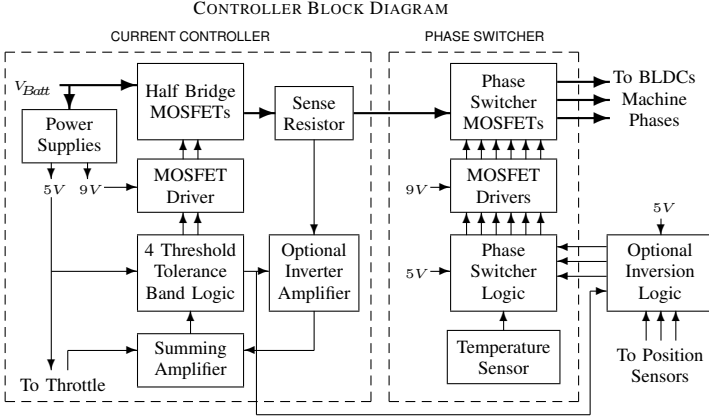
CONTROLLER BLOCK DIAGRAM

Fig. 2: Four quadrant BLDC motor controller block diagram. The optional inversion amplifier and logic blocks enable operation in the active braking zones. V_{Batt} refers to the source and sink of power, the battery.

Table 1: Gate Drive Signal Truth Table

Inputs			Gate Driver Logic Input Signals					
			Phase A		Phase B		Phase C	
H_A	H_B	H_C	Q_1	Q_2	Q_3	Q_4	Q_5	Q_6
0	0	1	1	0	0	1	0	0
0	1	1	0	0	0	1	1	0
0	1	0	0	1	0	0	1	0
1	1	0	0	1	1	0	0	0
1	0	0	0	0	1	0	0	1
1	0	1	1	0	0	0	0	1
Unused Combinations of H_A, H_B, H_C								
0	0	0	0	0	0	0	0	0
1	1	1	0	0	0	0	0	0

$$
\begin{aligned}
A_{low} &= \overline{H_A} \bullet H_B \bullet \overline{H_C} + H_A \bullet H_B \bullet \overline{H_C} \\
&= (\overline{H_A} + H_A) \bullet H_B \bullet \overline{H_C} \\
&= H_B \bullet \overline{H_C}
\end{aligned} \tag{1}
$$

All the switches in the phase switcher have the exact same logic function relating their state to the Hall sensors. Furthermore, this particular function is easily created using the multiple function gate (MFG). Fig. 3 shows the how the 74LVC1G58 MFG is set up to provide the function required by the phase switcher. An advantage to this implementation of the phase switcher logic is that when all Hall sensor signals are logic high or logic low, all the switches are forced to the off state.

The Hall sensors are open collector and use a pull up resistor to enable logic high output. The temperature cut out simply forces the Hall sensor signals to zero when an overtemperature condition is detected. This forces the switches in the phase switcher to turn off, disabling the controller.

The physical layout of current controller and phase switcher switches shown in Fig. 4 ensures the current flowing in R_SENSE represents the effective armature current in the BLDC machine. Kavanagh *et al.* [6] used the same location for a current sense element with a bipolar switching scheme. The current controller monitors the current in R_SENSE, assuming it is directly related to the machine output torque, which
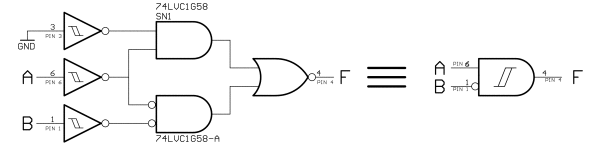
MFG CONFIGURATION

Fig. 3: The internal logic of a MFG is shown on the left, configured to provide the function shown on the right. A and B could be any two of H_A, H_B and H_C. F then represents the desired state for a particular phase switcher MOSFET.
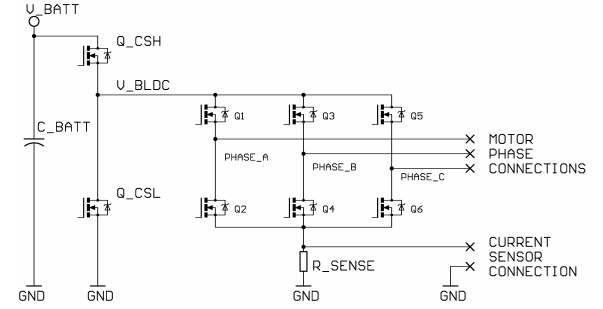
POWER SWITCH ARRANGEMENT

Fig. 4: The phase switcher is represented by MOSFETs, Q_1 to Q_6. The current controller uses Q_{CSH} and Q_{CSL} to control V_BLDC. The current source is connected to the phase switcher as above, forcing the effective motor current, I, to flow in R_SENSE.

is true except during some commutation events. The BLDC machine has one phase with zero current in it during the time between commutations, which simplifies current measurement compared with other three phase machine types investigated by Green and Williams [4]. Space vector PWM schemes [7] and [8] have been specially designed to reduce the amount of switching in an inverter and circumvent the mechanism by which a phase current leaves the tolerance band during commutation.

The current controller uses tolerance band current control. The current controller together with the phase switcher are designed to implement a unipolar switching scheme for controlling the BLDC machine current. Four thresholds are used to accomplish this.
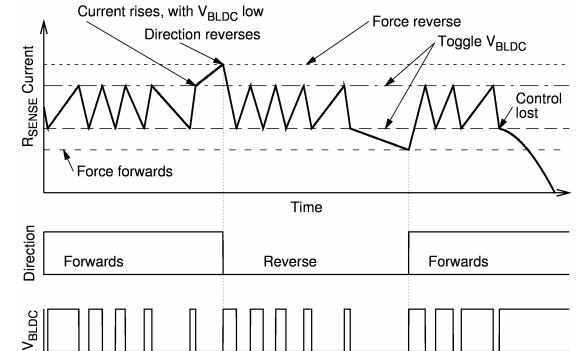
CURRENT CONTROLLER TIMING DIAGRAM

Fig. 5: The sense resistor current is compared continuously to the four thresholds labelled in the top graph. In forwards mode, a high V_BLDC pulse makes V_m positive and a a low pulse makes $V_m = 0$. In reverse a high V_BLDC pulse makes V_m negative.

Proceedings of the 19th Southern African Universities Power Engineering Conference
SAUPEC 2010, University of the Witwatersrand, Johannesburg

TOPIC B. MACHINES

The two inner thresholds are used to determine the state of the voltage at V_BLDC, shown in Fig 4. The outer thresholds in Fig. 5 control the polarity of V_m.

The direction of applied voltage to the machine is automatically changed by simply commanding the optional inverter components to change the polarity of all the Hall sensor signals and the sensed current signal simultaneously. The current controller can then resume operation within the tolerance band in exactly the same way as before. The current cannot be controlled when the supply voltage is incapable of overcoming the generated voltage of the BLDC machine.

4. RESULTS

The experiments were conducted with a two quadrant version of the Discrete Logic BLDC Motor Drive. The four quadrant version has been simulated and is to be tested in future work.

Fig. 6 shows the equipment configuration for testing the BLDC motor drive. The induction machine was supplied from an inverter with the ability to source and sink power, enabling testing of motoring and regenerating modes. The power flow between the battery and the BLDC controller was measured along with the phase switcher current and mechanical system speed.
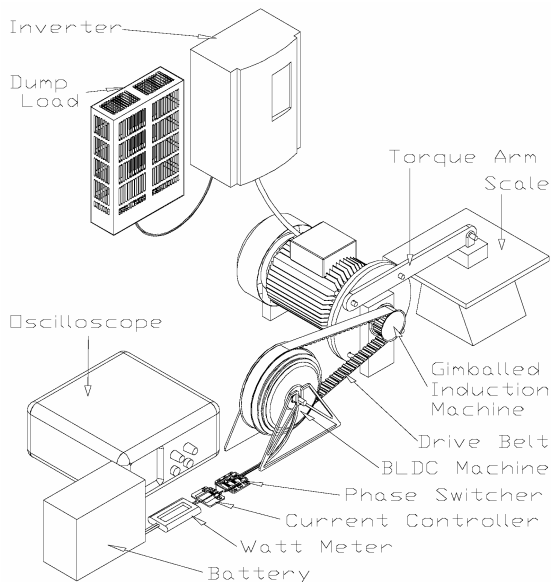

Fig. 6: Experimental setup for BLDC controller.

4.1 Motoring mode

The torque is assumed to be directly related to the current in the machine. Fig. 7 plots the current against BLDC machine speed for several cases where the current or torque signal is set to a constant level. The controller manages to keep a constant torque from zero speed until the point where the battery voltage cannot overcome the generated voltage and resistance
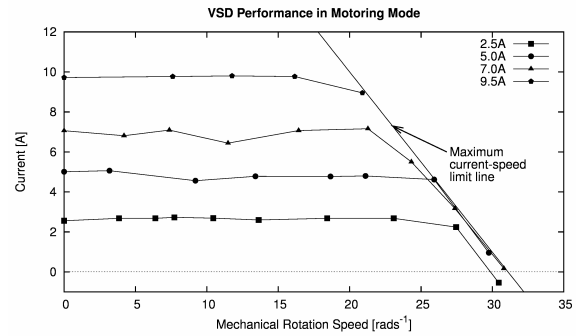

Fig. 7: The motoring test results confirm operation within the window shown in Fig. 1, especially with regard to the maximum speed obtained at a particular current or torque level.
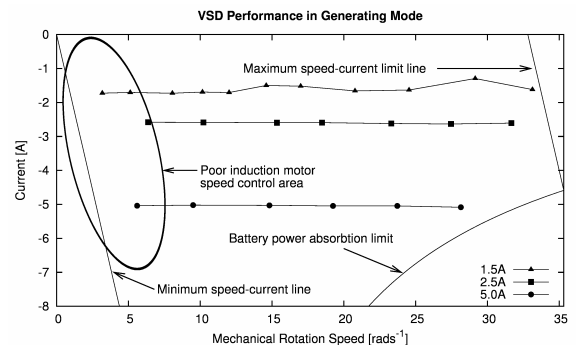

Fig. 8: The BLDC controller is good at maintaining a constant current in this mode but is limited by several physical factors. The most evident are the resistance of the machine and the power acceptance rate of the battery.
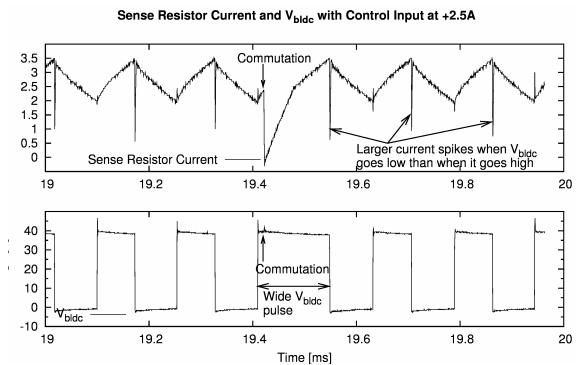
Fig. 9: V_BLDC and the sense resistor current are captured above for a commutation event while motoring. The current controller lengthens the V_BLDC pulse to speed up the current rise in the newly commutated phase.

of the machine. This agrees with the predictions of performance in Fig. 1.

4.2 Generating mode

The direction of rotation was maintained and tests performed for negative constant current levels that caused the BLDC machine to regenerate electrical energy and return it to the battery, shown in Fig. 8. In these tests some further practical limitations were experienced. The induction machine had poor speed control at low speeds. The battery could not absorb

Proceedings of the 19th Southern African Universities Power Engineering Conference
SAUPEC 2010, University of the Witwatersrand, Johannesburg

TOPIC B. MACHINES

Fig. 10: BLDC controller, battery and BLDC motor fitted to a bicycle.

SIMULATED CURRENT-SPEED PERFORMANCE

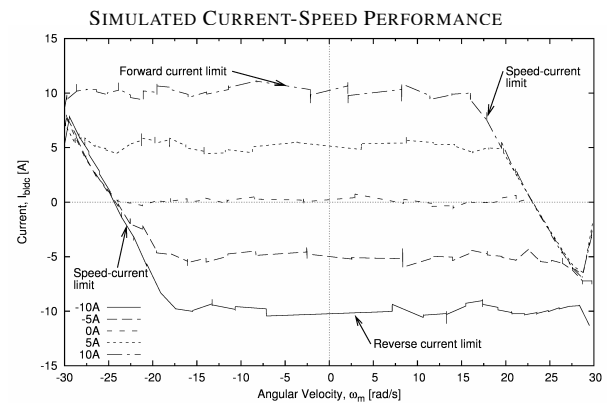Fig. 11: Simulated testing with constant I for different I levels. The limits of the results agree with Fig. 1 and the practical results obtained.

energy fast enough to test up to the maximum speed current line.

4.3 Commutation

Fig. 9 shows the phase switcher current and the V_BLDC signal during a commutation event in motoring mode. The controller tries to keep the current in R_SENSE constant by applying a longer positive voltage pulse to V_BLDC. This works well at low speeds where the battery voltage is much larger than the sum of the generated voltage and resistive drops in the machine. As the machine spins faster the rise of current can be much slower and cause torque ripple in the machine. This is not a big problem for the EV case, since at higher speed the stored energy in the vehicle absorbs the torque ripple better.

4.4 Electric Bicycle Test

The two quadrant controller was tested in an electric bicycle which only required unidirectional rotation of the BLDC machine. Fig. 10 shows the test bicycle with the battery pack mounted in the middle of the frame and the BLDC machine installed in the back wheel. The current controller was held inside the case of the battery and the phase switcher was mounted under the battery case. The electrified bicycle or E-bike was able to use the regenerative mode of operation of the controller to slow down without using the friction brakes.

4.5 Simulation results

The four quadrant controller is essentially the same as the two quadrant controller with the ability to apply reverse voltages to the machine and thus achieve a wider operating range. Fig. 11 was generated using SPICE 3f5 from Berkeley and shows the capabilities of the four quadrant controller in terms of currents and speeds achievable. The desired level of current was set in the simulation code as a constant, but the variation of current in a switching cycle caused some fluctuation in the points selected for plotting.

Fig. 1 is effectively the same shape as Fig. 11, which shows that the simulation was successful at reaching the desired operating limits.

5. CONCLUSION

A simple, effective BLDC motor drive was presented based on discrete logic MFG.

The internal resistance of BLDC machines necessitates a four quadrant controller for operation at zero speed with positive and negative torque.

The commutation process can be well managed with simple hardware and control but there is still room for improvement.

The battery used in the tests proved to be one of the more limiting aspects of the motor drive system. In the future this could be augmented with a more powerful technology such as supercapacitors.

ACKNOWLEDGMENT

REFERENCES

[1] Acarnley, P.P., Watson, J.F., *Review of Position-Sensorless Operation of Brushless Permanent-Magnet Machines*, IEEE Transactions on Industrial Electronics, Vol. 53, No. 2, pp. 352 – 362, April 2006.

[2] Cappelletti, P., *Flash Memory Reliability*, Microelectronics Reliability, Vol. 38, No. 2, pp. 185 – 188, 1998.

[3] Dixon, J.W., Leal, I.A., *Current Control Strategy for Brushless DC Motors Based on a Common DC Signal*, IEEE Transactions on Power Electronics, Vol. 17, No. 2, pp. 232 – 240, March 2002.

[4] Green, T.C., Williams, B.W., *Derivation of motor line-current waveforms from the DC-link current of an inverter*, IEE Proceedings B, Vol. 136, No. 4, pp. 196 – 204, July 1989.

[5] Kang, S., Sul, S., *Direct Torque Control of Brushless DC Motor with Nonideal Trapezoidal Back EMF*, IEEE Transactions on Power Electronics, Vol. 10, No. 6, pp. 796 – 802, November 1995.

[6] Kavanagh, R.C., Murphy, J.M.D., Egan, M.G., *Innovative Current Sensing for Brushless DC Drives*, Third International Conference on Power Electronics and Variable Speed Drives, No. 291, pp. 354 – 357. July 1988.

[7] Narayanan, G.,Krishnamurthy, H.K., Zhao, D., Ayyanar, R., *Advanced Bus-Clamping PWM Techniques Based on Space Vector Approach*, IEEE Transactions on Power Electronics, Vol. 21, No. 4, pp. 974 – 984, July 2006.

[8] Trzynadlowski A.M. and Legowski, S., *Minimum-Loss Vector PWM Strategy for Three-Phase Inverters*, IEEE Transactions on Power Electronics, Vol. 9, No. 1, pp. 26 – 34, January 1994.

TOPIC B. MACHINES

Proceedings of the 19th Southern African Universities Power Engineering Conference
SAUPEC 2010, University of the Witwatersrand, Johannesburg

MULTIVARIABLE H_∞ CONTROL FOR AN LTI ACTIVE MAGNETIC BEARING FLYWHEEL SYSTEM

S J M Steyn*,   P A van Vuuren* and G van Schoor*

*North-West University, School of Electrical, Electronic and Computer Engineering, Private Bag x6001, Potchefstroom, 2520

Abstract. A multivariable robust H_∞ controller for an active magnetic bearing energy storage flywheel system (Fly-UPS) is developed. The six block problem weighting scheme is explained and used for H_∞ controller synthesis. Furthermore, the additive uncertainties between the nominal (20 000 r/min) and varied rotational speed (15 000 r/min and 25 000 r/min) models are characterised. Stability robustness to additive uncertainties is verified via the closed-loop μ-analysis stability robustness test. The performance robustness (disturbance attenuation) is analysed by assessing model sensitivity with the ISO/CD 14839-3 sensitivity standard.

Key Words. H_∞ control; multivariable; active magnetic bearing; flywheel; robust control.

1. INTRODUCTION

Conventional ball-bearings in rotational applications can potentially be replaced by active magnetic bearings (AMBs) [2]. AMBs levitate the rotor via contact-free, actively controlled, electromagnetic force. The basic functioning of an AMB is shown in Fig. 1 and it operates as follows [3]: sensors are used to measure the air gap between the rotor and the bearing. This measurement is sent to the controller to regulate the current in the actuator using the power amplifier. The current in the actuator manipulates the magnetic force on the rotor, keeping it in suspension.

In modern high-tech systems, flywheels are used as energy storage batteries [8]. In this particular case AMBs are applied to a flywheel uninterrupted power supply (Fly-UPS) system [4]. The disc shape of a flywheel makes the axial moment of inertia greater than that of an elongated rotor of the same mass, making a flywheel the more effective energy storage method [8]. The energy is supplied to the flywheel via an electric motor, and can be recovered using the same motor as a generator. By utilizing AMBs for the Fly-UPS, a contact- and lubrication-free ideal vacuum environment is achieved [5]. Alas, the inherently unstable nature and complexity of AMBs necessitates sophisticated feedback control [6].

By introducing multivariable H_∞ control to the AMBs of the Fly-UPS, robust control can be realized [7]. The aim of H_∞ control is to compute a controller K such that the effects of modelling uncertainties, noise and disturbances are minimized according to predefined performance requirements at low frequencies and robustness requirements at high frequencies [9-10]. H_∞ control synthesis allows frequency-dependent bounds to be specified, ensuring that the above mentioned effects remain within permissible levels [9].

H_∞ control has successfully been applied to AMBs in [1, 2, 7, 9], and provide promising results. However, in [7], H_∞ control was found lacking in position deviation regulation when compared to optimal LQR control. But when compared to LQR or PID control, H_∞ control showed reduced control current and provided greater stability robustness with varying rota-
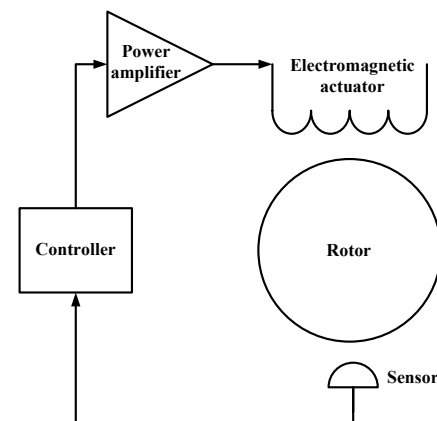

Fig. 1: Basic AMB functioning.

tional speed. It should be noted that in most cases the weighting functions used within H_∞ control are chosen on a trial and error basis, which makes it difficult to form a generalised perception of H_∞ control.

In this paper a multivariable robust H_∞ controller for an active magnetic bearing flywheel system is developed for comparison with presently used PD control. Because the Fly-UPS design is subject to various uncertainties as well as gyroscopic effects at varying rotational speeds, stability robustness and disturbance attenuation (performance robustness) are the primary feedback requirements.

2. FLY-UPS MODEL

This section will use analytical methods to develop and describe the five degrees of freedom (5-DOF) AMB Fly-UPS. The 5-DOF are the top AMB ('b') and bottom AMB ('a') radial x and y directions and the axial direction z (Fig. 2). The model will be able to represent the dynamic behaviour of the system within small deviations from the nominal values. The rotor displacement, gyroscopic coupling, coil currents, power amplifier bandwidth as well as sensor bandwidth are all represented within this model [5]. Some effects such as rotor touchdown during a power failure as well as rotor whirls are not represented due to their highly nonlinear nature [1].
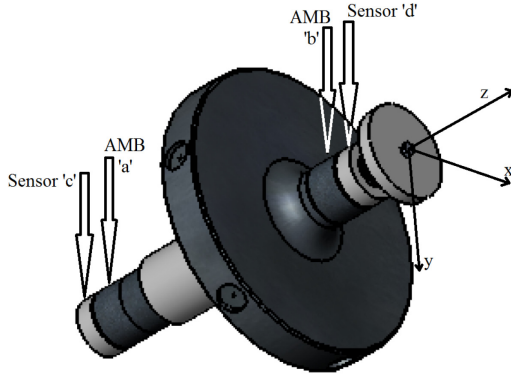
Proceedings of the 19th Southern African Universities Power Engineering Conference
SAUPEC 2010, University of the Witwatersrand, Johannesburg

TOPIC B. MACHINES

Fig. 2: Fly-UPS Rotor [14].

2.1 State-Space Model

A linear time invariant (LTI) state-space model of the rigid-rotor Fly-UPS plant is developed using parameters from the existing Fly-UPS system. This model is linearised around a nominal working point, or set-point. This makes the model valid for small deviations from its set-point values. A detailed approach to the Lagrange analysis as well as obtaining the state-space equations can be found in [5, 8, 9] and [13].

The state-space state vector $\mathbf{x}$ represents the rotor displacements and their time derivates. The linearised state-space equation can be derived by using Newton's second law of motion with equation (1),

$$F = ma = k_s x + k_i i \qquad (1)$$

where F is the force on the rotor, m the rotor mass, a the acceleration, x the displacement, i the current, k_s the force-displacement constant and k_i the force-current constant. The input to the model is current (i) and the output is displacement (x_a, x_b, y_a, y_b). The sensor measurements of the rotor are realised by representing the rotor dynamics in the bearing coordinate system ($\mathbf{z}_B^T = \begin{bmatrix} x_a & y_a & x_b & y_b \end{bmatrix}$) instead of the Euler coordinate system ($\mathbf{z}^T = \begin{bmatrix} x & \beta & y & \alpha \end{bmatrix}$) which represents displacement (x, y) and inclination (β, α) about the centre of mass [13]. Furthermore, the state vector, input vector, and output vector are defined as follows:

$$\mathbf{x}^T = \begin{bmatrix} \mathbf{z}_B^T & \dot{\mathbf{z}}_B^T \end{bmatrix},$$

$$\mathbf{u}^T = \begin{bmatrix} i_{ax} & i_{ay} & i_{bx} & i_{by} \end{bmatrix} \text{ and } \mathbf{y}^T = \begin{bmatrix} x_a & y_a & x_b & y_b \end{bmatrix}.$$

The state-space model of the two radial AMBs is

$$\dot{\mathbf{x}} = \mathbf{A}\mathbf{x} + \mathbf{B}\mathbf{u} \qquad (2)$$

$$\mathbf{y} = \mathbf{C}\mathbf{x} \qquad (3)$$

with state-space matrices

$$\mathbf{A} = \begin{bmatrix} \mathbf{0} & \mathbf{I} \\ \mathbf{M}_B^{-1}\mathbf{K}_s & -\mathbf{M}_B^{-1}\mathbf{G}_B \end{bmatrix},$$

$$\mathbf{B} = \begin{bmatrix} \mathbf{0} \\ \mathbf{M}_B^{-1}\mathbf{K}_i \end{bmatrix}, \quad \mathbf{C} = \begin{bmatrix} \mathbf{I} & \mathbf{0} \end{bmatrix}$$

The matrices $\mathbf{M}_B$ and $\mathbf{G}_B$ are the mass and gyroscopic matrices, $\mathbf{M}$ and $\mathbf{G}$, transformed to bearing positions, with

$$\mathbf{M}_B = \mathbf{T}_B^{-1}\mathbf{M}\mathbf{T}_B \qquad \mathbf{G}_B = \mathbf{T}_B^{-1}\mathbf{G}\mathbf{T}_B$$

where

$$\mathbf{M} = \begin{bmatrix} m & 0 & 0 & 0 \\ 0 & I_y & 0 & 0 \\ 0 & 0 & m & 0 \\ 0 & 0 & 0 & I_x \end{bmatrix} \quad \mathbf{G} = \Omega \begin{bmatrix} 0 & 0 & 0 & 0 \\ 0 & 0 & 0 & I_z \\ 0 & 0 & 0 & 0 \\ 0 & -I_z & 0 & 0 \end{bmatrix}$$

$$\mathbf{T}_B = \frac{1}{l_b - l_a} \begin{bmatrix} l_b & -l_a & 0 & 0 \\ -1 & 1 & 0 & 0 \\ 0 & 0 & l_b & -l_a \\ 0 & 0 & -1 & 1 \end{bmatrix}$$

Variable Ω (rad/s) represents the rotational speed of the flywheel and matrices, $\mathbf{K}_s$ and $\mathbf{K}_i$ are simply diagonal matrices of the previously mentioned, k_s and k_i constants. The distance of the bearing positions from the centre of mass is represented by l_a and l_b and the distance of the sensor positions from the centre of mass is represented by l_c and l_d.

The final state-space system is referenced to the sensor coordinate system by transforming the state matrices $\mathbf{A}$ and $\mathbf{B}$ to

$$\mathbf{A}_S = \mathbf{T}_S \mathbf{A} \mathbf{T}_S^{-1} \qquad \mathbf{B}_S = \mathbf{T}_S \mathbf{B}$$

with

$$\mathbf{T}_S = \begin{bmatrix} \begin{bmatrix} 1 & l_c & 0 & 0 \\ 1 & l_d & 0 & 0 \\ 0 & 0 & 1 & l_c \\ 0 & 0 & 1 & l_d \end{bmatrix} \mathbf{T}_B & \mathbf{0} \\ \mathbf{0} & \begin{bmatrix} 1 & l_c & 0 & 0 \\ 1 & l_d & 0 & 0 \\ 0 & 0 & 1 & l_c \\ 0 & 0 & 1 & l_d \end{bmatrix} \mathbf{T}_B \end{bmatrix}$$

The axial (z axis) AMB state-space model with

$$\mathbf{A}_z = \begin{bmatrix} 0 & 1 \\ \dfrac{k_{sz}}{m} & 0 \end{bmatrix}, \quad \mathbf{B}_z = \begin{bmatrix} 0 \\ \dfrac{k_{iz}}{m} \end{bmatrix}, \quad \mathbf{C}_z = \mathbf{I}$$

is simply appended to the above radial AMB state-space model.

The variables used for this model were experimentally measured: $m = 17.65$ kg is the rotor mass, $I_x = I_y = 1.16\times10^{-1}$ kg·m^2 are moments of inertia about the x and y axes, $I_z = 1.07\times10^{-1}$ kg·m^2 is the z axis moment of inertia, $k_s = 154.84\times10^3$ N/m and $k_i = 30.5$ N/A are the radial AMB force-displacement and force-current constants, $k_{sz} = 922\times10^3$ N/m and $k_{iz} = 260$ N/A are the axial force-displacement and force-current constants, finally lengths from the centre of mass are: $l_a = -160\times10^{-3}$ m, $l_b = 65\times10^{-3}$ m, $l_c = -190\times10^{-3}$ m and $l_d = 95\times10^{-3}$ m.

TOPIC B. MACHINES

Proceedings of the 19th Southern African Universities Power Engineering Conference
SAUPEC 2010, University of the Witwatersrand, Johannesburg

The sensor electronics are modelled as a second order low-pass transfer function (bandwidth of 10 kHz) and connected to the output of the AMB model [1]:

$$T_{sens} = \frac{\omega_s^2}{s^2 + \zeta\omega_s s + \omega_s^2} \qquad (4)$$

with damping $\zeta = 0.707$ and bandwidth $\omega = 2\pi10000$.

The power amplifier model consists of a closed loop PI controlled system with a bandwidth of 2.5 kHz,

$$T_{PA} = \frac{2V_{bus}(K_i + K_p s)}{Ls^2 + (2K_p V_{bus} + R)s + 2K_i V_{bus}} \qquad (5)$$

where [4]: V_{bus} = 51 V is the bus voltage, R = 0.152 Ω is the coil resistance, L = 6.494 mH is the coil inductance, K_p = 1 is the proportional constant and K_i = 0.1 is the integral constant. The PA model is connected to the input of the AMB model.

2.2 Uncertainty

The maximum rotational speed of the Fly-UPS is 25 000 r/min [4]. However, when the stored power is being drained from the flywheel, the rotational speed gradually reduces to 15 000 r/min [4]. Thus it is necessary to synthesise a controller for the plant that maintains stability robustness and performance robustness within this range. Developing a controller for the plant at 20 000 r/min ensures the speed variation is 5000 r/min upwards and 5000 r/min downwards. Therefore, in order to ensure robustness, the additive normalised uncertainty ($\|\Delta\|\leq1$) bound between a 25 000 r/min model and a 15 000 r/min model must be obtained.

Denote the frequency response of the maximum rotational speed model as $H_{25k}(j\omega)$ and the drained rotational speed model as $H_{15k}(j\omega)$. The additive model error frequency response function (FRF) can be determined experimentally [9], and is defined as:

$$|W_\Delta(j\omega)| \geq |H_{25k}(j\omega) - H_{15k}(j\omega)| \qquad (6)$$

The upper bound (maximum) of the difference between the two models is taken as the uncertainty bound, W_Δ. W_Δ describes the frequency characteristics of the uncertainty and defines the model variation around the 20 000 r/min model [10].

Including modelling uncertainties in the mathematical model is the key to successful robust H_∞ control design [12]. Fig 3 shows the model with bounded additive uncertainty ($G + \Delta\times W_\Delta$) and fig. 4 shows the 4th order uncertainty bound $\mathbf{W_\Delta}$, up to 5 kHz with transfer function,
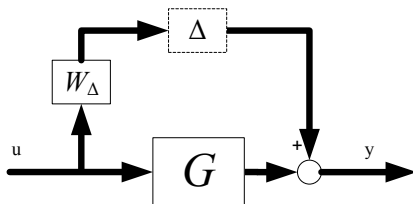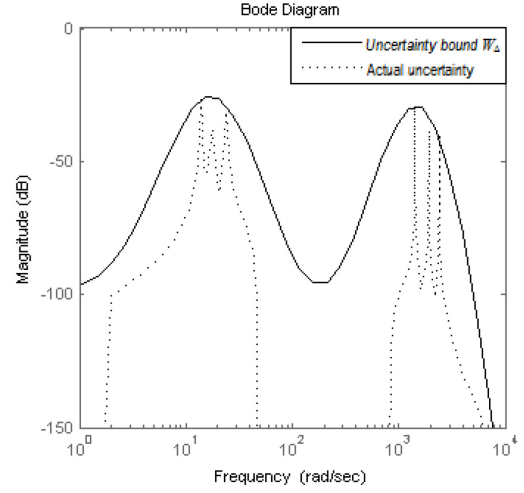

Fig. 3: Additive uncertainty.

Fig. 4: Uncertainty bound W_Δ.

$$W_\Delta = \frac{-4.1s^3 - 2570s^2 + 4.74\times10^5 s - 9.1\times10^5}{s^4 + 82.75s^3 + 2.15\times10^6 s^2 + 6.6\times10^6 s + 6.3\times10^8}$$

3. CONTROL

The two basic design approaches in H_∞ control are open-loop transfer function loop shaping and closed-loop transfer function loop shaping [11]. In loop shaping, the required shape of a transfer function is defined in the frequency domain using singular values, and a controller is designed to shape the system transfer function into that required shape [2].

For open-loop shaping, the classical $L=GK$ loop shaping is transposed to MIMO systems by using the singular values of the loop transfer functions as the loop gains [14]. One such open-loop transfer function loop shaping is the Glover-McFarlane H_∞ loop shaping method [2, 10]. Alternatively, closed-loop transfer function shaping aims to shape the sensitivity function, $S = (I + GK)^{-1}$ and the complementary sensitivity function (closed-loop transfer function) $T = GK(I + GK)^{-1} = I - S$ [11]. This leads to classic mixed sensitivity H_∞ control synthesis.

By adhering to open-loop design objectives, it is relatively easy to estimate the closed-loop requirements over specific frequencies [11]. But, because the Fly-UPS AMBs are open-loop unstable, specifying an open-loop shape is relatively difficult. Consequently, closed-loop transfer function design using mixed sensitivity H_∞ control synthesis will be the primary focus [2]. This allows robust stability by including uncertainties in the model as well as providing robust performance by minimizing the H_∞ norm via weighting [15].

3.1 H_∞ Control Design

The standard mixed sensitivity control scheme uses three weights (or bounds [16]) in the following mixed sensitivity cost minimisation problem,

Proceedings of the 19th Southern African Universities Power Engineering Conference
SAUPEC 2010, University of the Witwatersrand, Johannesburg

TOPIC B. MACHINES

$$\min_K \left\| \begin{matrix} W_e S \\ W_u R \\ W_y T \end{matrix} \right\|_\infty \tag{7}$$

where K is a stabilising controller [11].

The weights are applied to the control error, e, to shape the sensitivity, S_o; to the control signal, u, to shape the input sensitivity, KS_o; and to the plant output, y, to shape the complimentary sensitivity, T_o. The weighting functions must be proper to be solvable, and stable, since they are not in the loop to be stabilised by the controller [1]. The weighting functions are used to shape, or penalise, the above signals into their desired shapes.

However, mixed sensitivity control has one serious drawback: pole-zero cancellation. It aims to cancel poorly damped stable poles of the system with controller zeros, making the poorly damped poles unobservable and uncontrollable [12, 16]. Furthermore, the controller designed using this method, contains the inverse of the plant, causing complications if the plant is non-invertible [1]. In order to bypass these problems another weighting scheme is applied, namely the *six block problem* weighting scheme [2]. This scheme includes the plant in the weighting of the sensitivity, preventing the inclusion of the inverted plant within the controller. In addition to weighting the standard S_o, KS_o and T_o signals, the input disturbance sensitivity function (GS_i), and closed-loop transfer function from the plant input to the plant output (T_i) are also shaped. Thus a term involving GS_i is included in the standard mixed sensitivity minimisation problem as given in (8) below [2, 8-9].

$$\min_K \left\| \begin{matrix} W_e S_o W_r & -W_e GS_i W_d \\ W_u KS_o W_r & -W_u T_i W_d \\ W_y T_o W_r & W_y GS_i W_d \end{matrix} \right\|_\infty \tag{8}$$

As can be seen in (8), the standard weights W_e, W_u and W_y are present with the addition of two new weights, W_r and W_d. W_r shapes the reference input to the system, and W_d shapes (attenuates) the input disturbances. W_d is important in preventing pole-zero cancelation [16]. The structure of the augmented (weighted) plant is shown in Fig. 5, where the inputs are $\mathbf{w} = [r, d]$ and $\mathbf{u} = [i_{ax}, i_{ay}, i_{ax}, i_{by}]$, and the outputs are $\mathbf{z} = [z_1, z_2, z_3]$ and $\mathbf{v} = [x_a, y_a, x_b, y_b]$.
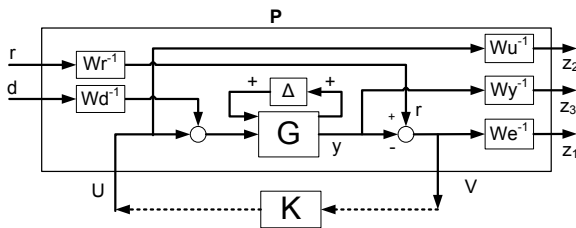

Fig. 5: Augmented control formulation.

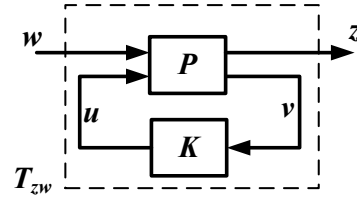The augmented system in Fig. 5 is then reformulated into a system T_{zw} (Fig. 6).

Fig. 6: Control configuration for system T_{zw}.

The H_∞ control design for T_{zw} is now:

- Find a controller K that stabilizes system T_{zw}.

- The controller must minimise the H_∞ norm; $\left\| T_{zw} \right\|_\infty < \gamma$. ($\gamma$ is the ratio between the maximum and minimum singular values.)

In order to solve the above minimization problem, the solutions to two Riccati equations are required. MATLAB®'s Robust Control Toolbox is used to solve these Riccati equations and synthesise the H_∞ controller [15].

3.2 Weighting function selection

There are five weighting functions to be selected in the *six block problem* weighting scheme, namely W_e, W_u, W_r, W_y and W_d. Each weighting function is created according to predefined specifications and requirements of the AMB Fly-UPS system. As stated in section 1, the weighting functions are mostly selected on a trial and error basis [1-2, 7-9, 16]. Furthermore, once the required weighting function shape is designed, the inverse is supplied for controller synthesis [1-2, 7-11]. This is done in order to 'guide' the minimisation weight of the H_∞ norm [7-11]. Fig. 7 shows the singular value plots of the designed weighting functions.

Weight W_r plays a part in shaping the sensitivity (S_o) and controller gain (KS_o). In order to simplify the weighting selection, W_r will be a constant, 1.

The error weight, W_e, shapes the sensitivity function (S_o). According to the ISO/CD 14839-3 standard, the sensitivity for newly commissioned machines should be below 8 dB. Furthermore, the two critical rigid modes of the Fly-UPS are at 33.91 Hz (2 034 r/min) and 175.52 Hz (10 531 r/min). Thus it would be ade-
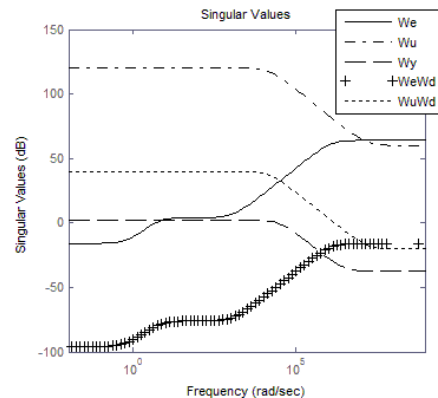

Fig. 7: Singular value plots of designed weighting functions.

TOPIC B. MACHINES

Proceedings of the 19th Southern African Universities Power Engineering Conference
SAUPEC 2010, University of the Witwatersrand, Johannesburg

quate to select the weighting function as a first order high-pass transfer function with a bandwidth of 200 Hz, and a stop-band gain of 4 dB. In order to obtain an integration effect, the magnitude of the error weight at frequencies lower than 1 Hz should be small.

Weight W_u represents the controller gain (KS_o). In the Fly-UPS, an absolute maximum of 1 A per 1 μm displacement error should be realised. Thus the weight W_u is chosen with a gain of 1×10^6 and a controller roll-off bandwidth of 2.5 kHz.

Transfer function W_y, shapes the complimentary sensitivity T_o. In order to keep the closed loop gain close to unity, W_y is selected as a first order low-pass transfer function with a 5 kHz bandwidth and a 2.5 dB pass-band gain.

Finally, $W_d \times W_e$ shapes the input disturbance signal (GS_i), and $W_d \times W_u$ shapes the closed-loop transfer function (T_i). In order to obtain good input disturbance rejection, the weight W_d is chosen as a small constant of 100×10^{-6}. Therefore, the combined weight $W_d W_e$ bounds the displacement to 160 μm for an input disturbance of 1 A, and the combined weight $W_d W_u$ bounds T_i to a gain of 40 dB.

The γ value achieved with the selected weighting functions during control synthesis is 0.92. If $\gamma < 1$, it means that the synthesised controller is able to comply with the required specifications (bounds) provided by the weighting functions.

Using the explained method, a controller is synthesised. However, the 5-DOF controller has an order greater than 260. This is impractical in most applications, and thus the order of the controller is reduced using the multiplicative error bound Hankel singular value order reduction method [10, 15]. The controller order is successfully reduced to a 24th order controller with a multiplicative error bound of less than 2%.

4. SIMULATION RESULTS

The synthesized H_∞ controller is implemented on the mathematical (LTI) model of the Fly-UPS. From this simulation, certain theoretical predictions concerning the system response, closed-loop system stability and sensitivity functions of the physical system can be made.

According to MATLAB®'s stability robustness analysis (μ-analysis algorithm), the controller can tolerate up to 165% of the modelled additive uncertainty. Fig. 8 shows the radial 10 μm step response of the plant at 15 000 r/min, 20 000 r/min and 25 000 r/min. It can be seen that the controller maintains stability throughout the variation of rotational speed. The integration effect, by reducing steady-state error, can also be seen. Furthermore, a similar step response with a PD controller (used to control the actual Fly-UPS system) is included in Fig. 9 for comparison with H_∞ control. The PD controller has a proportional gain of 14 213 and a derivative gain of 20. The H_∞ controlled plant shows a faster settling

time and superior speed variation robustness when compared to the PD controlled plant.

The performance robustness is evaluated via the sensitivity function. The sensitivity function is obtained by feeding a sinusoidal reference into each separate rotor input over a predefined frequency range [17]. The magnitude of the response of the rotor due to the signal provides the sensitivity function. The sensitivity, S, and the sensitivity weight, W_e, for the closed–loop model at 15 000 r/min and 25 000 r/min are shown in Fig. 10 and Fig. 11 respectively. As can be seen, the sensitivity of both models remain below the bound placed by the weight, W_e. It also remains below the 8 dB limit imposed by the ISO/CD 14839-3 sensitivity standard.
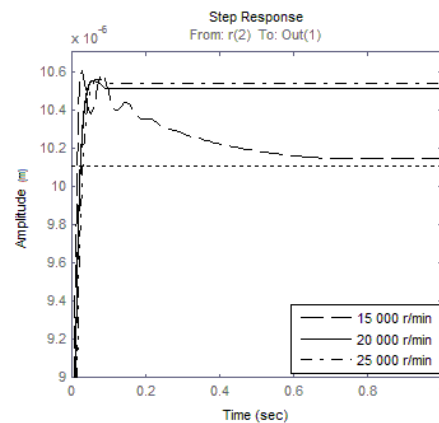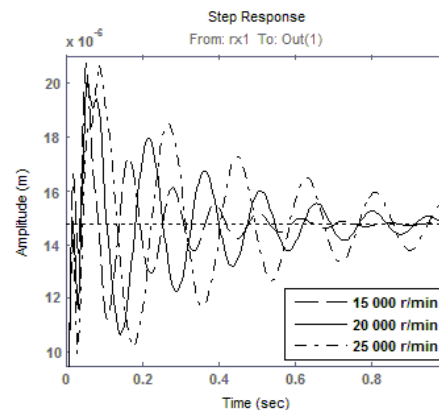

Fig. 8: H_∞ controlled 10 µm step response.

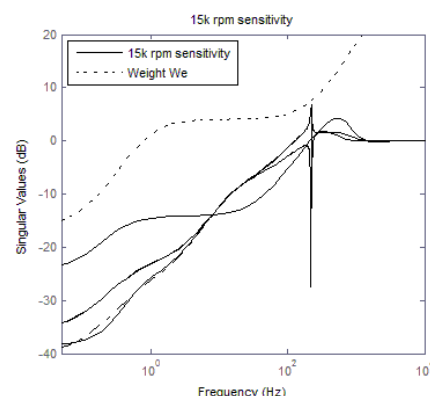Fig. 9: PD controlled 10 µm step response.

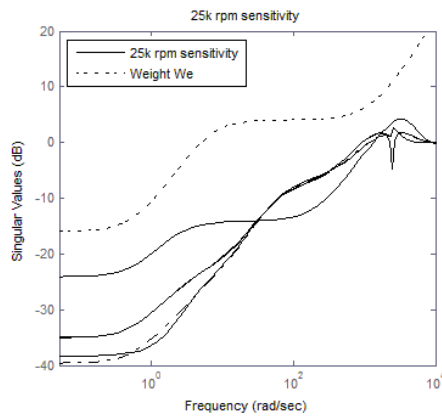Fig. 10: Sensitivity plot at 15 000 r/min.

Fig. 11: Sensitivity plot at 25 000 r/min.

5.   CONCLUSION

In this paper a multivariable robust H_∞ controller for an active magnetic bearing flywheel system (Fly-UPS) is developed. The Fly-UPS design is subject to various gyroscopic effects at varying rotational speed. Thus stability robustness and performance robustness (disturbance attenuation) are the primary feedback requirements.

A linear time invariant (LTI) model of the Fly-UPS system is successfully developed for use in H_∞ control synthesis. The additive model uncertainties between the operational speed variation of 15 000 r/min and 25 000 r/min are characterised. Furthermore, the *six block problem* weighting scheme for H_∞ control synthesis is implemented. Each weighting function used in the controller synthesis is fully characterised and designed. Finally a H_∞ controller is synthesised and implemented. The synthesised controller proves stability robustness against rotational speed variation by providing stable system responses at 15 000 r/min and 25 000 r/min. It also robustly tolerates (via μ-analysis) up to 165% of the modelled additive uncertainty. Furthermore, the controller performance is evaluated according to the ISO/CD 14839-3 sensitivity standard. However, one of the setbacks of H_∞ control is that the weighting functions are chosen on a trial and error basis. This makes it difficult, when compared to PD control, in designing a controller.

ACKNOWLEDGEMENTS

REFERENCES

[1] B. Aeschlimann, "Control Aspects of High Precision Active Magnetic Bearings," Ph.D. Thesis, Dept. Elect./Electron. Eng., EPFL, Lausanne, 2002.

[2] G. Li, "Robust Stabilization of rotor- active magnetic bearings systems," Ph.D. Thesis, Dept. Mech./Aero. Eng., Virginia Univ., Virginia, 2007.

[3] E. O. Ranft, "The Development of a Flexible Rotor Active Magnetic Bearing System," M.Eng. Dissertation, Dept. Elect./Electron. Eng., North-West Univ., 2005.

[4] S. Myburgh, "The Development of a fully suspended AMB system for a high speed flywheel system," M.Eng. Dissertation, Dept. Elect./Electron. Eng., North-West Univ., 2007.

[5] S. J. M. Steyn, "The development of MIMO LQG control for an AMB energy storage flywheel system," Mini-Dissertation, Dept. Elect./Electron. Eng., North-West Univ., 2008.

[6] R. Larsonneur, "Design and Control of Active Magnetic Bearing Systems for High Speed Rotation," Ph.D. Thesis, Dept. Mech./Aero. Eng., Georgia Inst. of Tech., Zurich, 1990.

[7] N.-C. Tsai, C.-H. Kuo, and R.-M. Lee, "Regulation on radial position deviation for vertical AMB systems," Mechanical Systems and Signal Processing, vol. 21, no. 7, pp. 2777-2793, 2007.

[8] B. C. D. Wilson, "Control designs for low-loss active magnetic bearings: Theory and Implementation," Ph.D. Thesis, Dept. Elect./Electron. Eng., Georgia Inst. of Tech., Georgia, 2004.

[9] N. S. Gibson, " H_∞ Control of Active Magnetic Bearings: An Intelligent Uncertainty Modeling Approach," Ph.D. Thesis, Dept. Mech./Aero. Eng., North Carolina State Univ., North Carolina, 2004.

[10] K. Zhou, J. C. Doyle, and K. Glover, Robust and Optimal Control. Upper Saddle River, NJ: Prentice Hall, 1996.

[11] S. Skogestad and I. Postlethwaite, Multivariable Feedback Control Analysis and Design. West Sussex, England: John Wiley & Sons Ltd., 2005.

[12] R. S. Sànchez-Pena and M. Sznaier, Robust Systems Theory and Applications. NY: John Wiley and Sons, Inc., 1998.

[13] G. Schweitzer, H. Bleuler, and A. Traxler, Active Magnetic Bearings, Basics, Properties and applications of Active Magnetic Bearings. Zürich: Authors Working Group, 2003.

[14] J. J. Janse van Rensburg, "Development of a flywheel energy storage system – uninterrupted power supply (FLY-UPS)," M.S. dissertation, Dept. Elect./Electron. Eng., North-West Univ., South-Africa, 2007.

[15] MATLAB®. (2004). The language for Technical Computing. The MathWorks, Inc. [DVD].

[16] K. A. Folly, "On the prevention of pole-zero cancellation in H∞ power system controller design: A comparison," South African Institute of Electrical Engineers, vol. 99, no. 4, pp. 103-113, 2008

[17] ISO-TC108/SC2/WG7, "Active magnetic bearing - evaluation of stability margin," ISO CD148393-3, Oct. 2003.

Topic C

Power Systems

TOPIC C. POWER SYSTEMS

Proceedings of the 19th Southern African Universities Power Engineering Conference
SAUPEC 2010, University of the Witwatersrand, Johannesburg

LOAD MODELING FOR RELIABILITY AND CUSTOMER INTERRUPTION COSTS EVALUATION

Nicolas F. S. Ip Cho*, Kehinde Awodele**, S Chowdhury*** and S P Chowdhury****

University of Cape Town, Department of Electrical Engineering, Cape Town, South Africa.

*nicolasipcho@gmail.com **Kehinde.awodele@uct.ac.za ***sunetra.chowdhury@uct.ac.za****sp.chowdhury@uct.ac.za*

Abstract. This paper presents the study of load modeling for reliability and customer interruption costs (CIC) evaluation. In this paper, several approaches used in the assessment of reliability and/or customer interruption costs have been identified. For each approach, the load is modeled differently and varies in accuracy and level of difficulty. Based on the data available from existing surveys on South African customers, two approaches were chosen for comparison using the time sequential Monte Carlo Simulation (MCS) techniques. The paper demonstrates the impact of different load modeling approaches on reliability and customer interruption costs assessment.

1. INTRODUCTION

When the restructuring of power industry is concerned, service reliability has emerged as a major issue in recent years [1]. As part of their requirements, energy utilities have to guarantee that the reliability of the energy supply to their customers matches to the importance of reliability needed and so the quantification of the impacts of outages is needed and sought by energy providers and regulators [2]. Similarly to reliability assessment, customer interruption costs (CIC) evaluation has significant importance in power system planning and operation for a power utility industry and this is due to the growing interests and consideration to customer costs of power outages [3, 4]. As utility industries continue in the path of deregulation, higher reliability levels are likely to be critical for different existing customer sectors [5]. While customers wish for improved reliability, reduced electricity prices are also one of their priorities and thus it is important to understand and consider the nature of this trade-off, which may vary for various customer categories[6,7].

Fig. 1 shows the relationship between the reliability costs and the reliability worth.
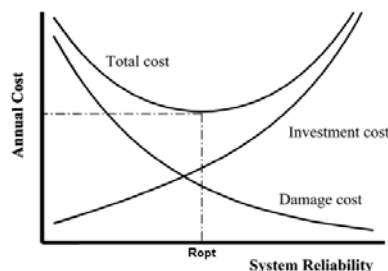

Fig. 1: Reliability Cost and Reliability Worth Concept [8].

The vertical line crossing the point R_{opt} and the total cost curve depicts the point where the total cost is a minimum on the total cost curve [1]. Thus, the point where the line intersects the curves can be seen as the optimum point where the utility customer will receive the least cost service and the reliability cost is minimized for the utility [2]. Using different load models, the paper reports on investigating the impacts on reliability and CIC evaluations by comparing reliability indices and interruption costs of different customer sectors for different approaches. In the study, seven approaches have been identified for reliability and CIC evaluations, but only two of these approaches were used in the time sequential Monte Carlo Simulations for comparison.

2. LOAD MODELING FOR RELIABILITY AND CUSTOMER INTERRUPTION COSTS EVALUATION

Load can be modeled for reliability and/or CIC assessment from various information such as the load demand (average load and/or peak load), load profiles and load duration curves for different customer sectors, the variability with time (time of the day, day of the week), the duration of outage [9, 10], and the outdoor temperature (seasons) [10].

2.1 Approximate Methods for CIC Evaluation

The approximate methods used in [9] are based on using customer data sets and the outage cost estimates are compared with a set of base methods results. The magnitude of the outage cost associated with a specific delivery point depends on many factors which include the load curtailed, the type of customers involved and the duration of the outage [9]. Also reference [9] uses variability in time where time of the day, day of the week and week/month of the year will have an influence on the magnitude of the interruption costs [9]. The data sets used in [9] include customer data, load data and cost data.

Base Methods

Using average load with peak load and the load factor relationship as the load model, the base methods also comprises a cost weight factor that uses information on customer damage functions, system reliability indices such as the expected energy not supplied (EENS), the interrupted energy assessment rate (IEAR) and the expected interruption cost (ECOST) to determine the interruption costs [9].

Expected Un-served Energy

As an alternative to the base methods, reference [9] offers the sector-by-sector demand approach and modifies it by simplifying the calculation process and reducing the effort required to estimate the customer interruption costs. Two simplified techniques are represented in [9] and the first approach is the sector-by-sector expected un-served energy (EUE) approach. In this approach the time varying load and cost models are formed separately and then combined to create a time varying cost weighted load model [9]. This new model is then used in conjunction with a transformed feeder sector customer damage function (SCDF) to estimate the interruption cost for a specific event [9]. The results obtained in [9]

Proceedings of the 19th Southern African Universities Power Engineering Conference
SAUPEC 2010, University of the Witwatersrand, Johannesburg

TOPIC C. POWER SYSTEMS

showed that the expected interruption costs (ECOST) for the EUE approach were reasonably comparable to the base method values while the sector-by-sector demand approach showed more accurate results. However, the results obtained using the EUE approach were still very close and the approach is much simpler with relatively little error ranging from -0.024 % to +1.870 % relative to the base method values for outage duration between 15 minutes and 8 hours [9].

Annual Energy Approach

The second simplified technique called the Annual Energy Approach, is extended from the sector-by-sector EUE approach and has in objective to reduce the effort required to approximate the customer interruption costs [9]. The annual energy consumption for each customer sector is a data set which is usually available in practical application and therefore the percentage of energy consumption for each customer sector in the system can be calculated [9]. Then the EENS for a given outage situation can be obtained by rough calculation based on metering experience [9].

A formula for the Interrupted Energy Assessment Rate (IEAR) is available in [9] and using both the results for IEAR and EENS, the ECOST can be obtained. The results obtained in [9] showed that during the day, those obtained from the annual energy approach are reasonably comparable to those of the base methods while at night time; the annual energy approach overestimates the actual costs of the outages. The main reason for this error is the use of annual energy consumption percentages in the calculation and the assumption is that the percentages used are assumed to be constant values throughout the year [9]. However, in practical situations, the percentages of energy consumption during the night time are quite different [9].

2.2 Time Varying Load Model for Customer Interruption Costs Evaluation

In reference [11], a time sequential Monte Carlo simulation technique is used for evaluating customer unreliability costs in distribution systems and the results are compared with those from average load and cost models. Annual chronological load models for different individual customer sectors are developed and used for analysis and random load fluctuations are combined with time varying load models to identify the residual uncertainty associated with system load [11]. A time varying load (TVLM) and cost model (TVCM) are used in [11] for seven customer sectors to show that different load and cost models result in different interruption costs which can lead to different planning and operating decisions.

The customer damage functions for different customer sectors are used to find the interruption costs for specific time durations [11]. The TVCM is described in [11] and the TVLM provides an accurate representation of the actual load by incorporating the load on an hourly basis. The TVLM uses detailed customer load profiles which vary with customer type, location and time of the day, day of the week and week of the year [11]. Then the TVCM and TVLM are used in conjunction with the load point and system reliability indices to find the interruption costs and ECOST and these are compared with values available when average load model is used [11].

Fig. 2 shows the ECOST results for time varying load model and average load model for different load points (representing different customer sectors) [11].
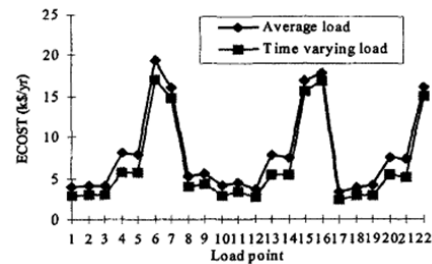

Fig. 2: Load Point ECOST for time varying and average load models [11].

It can be seen that for all the load points, the ECOST for the time varying load model is smaller than for average load [11]. Thus time varying load model provides a more accurate representation of the load demand and for the interruption costs incurred during a power outage [11]. This suggest that the load model used has an impact on the evaluation of customer interruption costs.

2.3 Probabilistic Model for Reliability and CIC Evaluation

The probabilistic approach consists of a probabilistic reliability assessment (PRA) which is available for more details in [12], a probabilistic cost model (PCM) available in [13] and a probabilistic load model which is discussed in [14] and [15]. The probabilistic reliability evaluation in [14, 15] uses a load duration curve model in simulations to calculate the un-served energy costs for a total load served by a distribution system. Simulations are run a different system load levels (100%, 80%, 70%, etc) and the annual un-served energy cost are calculated by weighting the results of each simulation by the percent of the year that each load level is present [15]. The five step load model used in [15] is represented in Table 1.

Table 1: Five-Step Load Duration Curve Approximation [15]

Load Level	100% (PEAK)	80%-90%	70%-80%	60%-70%	<60%
Probability	0.001	0.025	0.040	0.097	0.837

From a load duration curve, each of the load levels shown in Table 1 are represented by a probability distribution and the sum of each of the probability assigned to the load levels is equal to one.

2.4 Fuzzy Logic Techniques for Reliability and CIC Evaluation

The fuzzy set theory can be used to deal with the imprecision of practical systems and by incorporating human experiences and preferences by using membership function and fuzzy rules [16]. The fuzzy logic techniques include fuzzy logic based reliability assessment available in [17], a fuzzy cost model which can be obtained in [13] and a fuzzy load model [18]. The fuzzy load model is represented in Fig. 3 below [18].
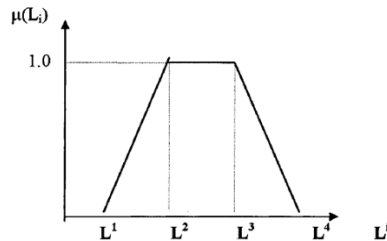

Fig. 3: Load Possibility Distribution [18].

The possibility distribution will have a value of 1 for the load values that are highly possible and will drop as the possibility decreases [18]. A zero possibility is assigned to the values that are rather impossible to occur, which are located beyond the two extremes [18].

2.5 Combined Fuzzy and Probabilistic Approach for Reliability Assessment

This method combines the fuzzy load model for a peak load with a probability distribution for a load curve and the system component outages can be modeled using a traditional Monte Carlo or enumeration technique [14].

In the combined fuzzy and probabilistic approach, the fuzzy load model uses the most probable peak load with high and low bounds with a specific confidence grade as shown in Fig. 4 [14].
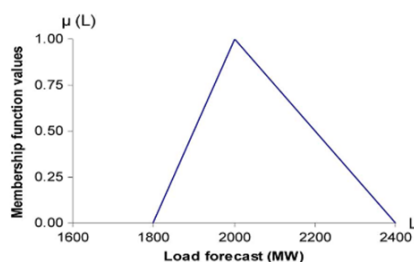

Fig. 4: Membership Function of Peak Load Forecast [14].

In general, the high and low bounds are not in the same distance from the most probable peal, and therefore, the triangle membership function is not a symmetrical one [14].

The probabilistic load model uses a discrete probability distribution for a load curve and the annual load curve reflects the load levels at different time points during one year [14]. The annual load duration curve can be created using historical hourly load records, and then a probability distribution can be obtained to represent the load duration curve [14].

In this model, each load level is a percentage with respect to the peak with a probability and is mathematically expressed as [14]:

$$p(Load=L_i) = p_i \,(i=1,...,n)$$

Where L_i is the load level (% of the peak), p_i is the probability of L_i and n is the number of load levels in the annual load duration [14].

The combined fuzzy and probabilistic load model are then used in reliability evaluation for a composite generation and transmission system and the following indices are obtained: the expected energy not supplied (EENS in MWh/year), the expected number of load curtailment (ENLC in failures/year) and the average duration of load curtailment (ADLC in hours/failure) [14]. The results obtained show a wider insight into impacts of load uncertainty on uncertainties of reliability indices in such evaluations [14].

2.6 Hybrid Neurofuzzy System for CIC Evaluation

The hybrid neurofuzzy system introduces an Artificial Intelligence technique to determine the cost assessment throughout the analytical process of customer outage costs [19]. Data is collected fro surveys to built the customer damage function (CDF) and the interrupted energy assessment rate (IEAR) is determined using the CCDF and other variables such as the number and duration of interruptions, and load loss [19]. The method integrates the computational paradigms of expert systems and neural systems by using the strength of both systems to expand over their individual applications [19].

The learning algorithm in the hybrid neurofuzzy system uses recurring neural network (RNN) architecture for online learning and fuzzy rules are used for customer outage costs onto various customer sectors and a variety of outage durations [19]. Thus past information on the system is reused for other assessments and the new results are updated in the database and allow tracking of the system reliability conditions [19]. In this manner, results can be compared to historical data and provide analysis in future interruption costs or reliability aspects [19].

2.7 Methodology

Using the time varying load and average load models with the time sequential Monte Carlo Simulation techniques, a simulation procedure is created to determine the interruption costs of each load points of a distribution system using the data on different customer sectors such as their customer damage functions CDF and load profiles. A failure mode and effect analysis (FMEA) is also required for the distribution system being tested. The average load model is chosen as the base method and is compared to the time varying load model to show the accuracy between the two methods using the results for the interruption costs of different customer sectors. The aim is to design a program that implements the conditions for both load models separately and compare their interruption costs. The average load model is chosen as the base method as it uses a constant load and thus allows an easier implementation in the simulation program. The time varying load model is chosen for comparison with

Proceedings of the 19th Southern African Universities Power Engineering Conference
SAUPEC 2010, University of the Witwatersrand, Johannesburg

TOPIC C. POWER SYSTEMS

the base method as the time varying nature of the load can be used to compare several parameters such as the effect of time of time of occurrence, weather or type of customers on the interruption costs. The time varying load model was also used as the data required for this procedure is available for South Africa.

3. TIME SEQUENTIAL MONTE CARLO SIMULATION TECHNIQUES

The Monte Carlo simulation (MCS) approach can be used for reliability assessment of a distribution system and it provides the opportunity to develop an appreciation of the variability associated with the annual indices [20]. Reference [20] offers a full description of the basic principles used in the Monte Carlo Simulation techniques and the application to distribution system reliability evaluation. The technique basically uses up and down times, including the number of failures, times to failures, restoration times, etc [20]. A failure mode and effect analysis (FMEA) can be used to determine which components in the distribution system that fails affect a particular load point which represents a customer sector [10, 21]. The MCS technique is used to design the simulation procedure for the program and implements the conditions for the average and time varying load models in separate procedures.

3.1 Simulation Procedure

The simulation procedure combines and follows the steps detailed in references [20] and [21] where only the time to failure was considered and repair and switching time were neglected. Time sequential simulation was used to assess the reliability of the network by obtaining the relevant reliability indices [10, 21]. These steps were then modified in order to write the Monte Carlo simulation program in MATLAB. The step by step procedure is shown below:

Simulation Procedure for Time Varying Load

Step1: Generate a random number for each component in the system and convert these random numbers into time to failure (TTF) using the appropriate component failure probability distributions.

Step 2: Generate another random number and scale it to a 24 hours period (i.e. random number*24) and call it TOD (Time of Day). This 24 hours period represent the time of outage a failure occurring in any day of a year.

Step 3: Repeat step 1-2 for the desired simulation period. Period *n* must be in the appropriate range to capture the outage events considered.

Step 4: Repeat step 1-3 for the desired number of simulated period *N* years.

Step 5: Consider the simulated period lasting *n* years.

Step 6: Consider the components and obtain the load points affected by their failure using FMEA.

Step 7: Depending the load profiles, assign load demand values to a specific TOD interval. Then create conditions in the code and if the TOD conditions are present, set the current load demand to a particular value calculated using load profiles.

Step 8: If the TTF conditions are met, cumulate the number of failures for n years, and determine the outage duration using the FMEA and the corresponding interruption costs from the SCDF and cumulate these parameters for n years respectively. Also cumulate values of load loss using the value obtained in step 7 for n times.

Step 9: Find the load point indices and system performance indices for each load point. Also calculate the mean value for the load loss for each load point by taking the cumulate load loss value and dividing by n years and tabulate the results.

Simulation Procedure for Average Load

The procedure is very similar to the time varying load model. The procedure for the average load is much simpler and does not consider the TOD parameter and since the load is constant, there is no need for a load profile.

3.2 Simulation Program

The simulation program is written in MATLAB using the simulation procedure described above. The program is divided into six parts, two for each of the load points LP1, LP2 and LP3 shown in Fig. 5. The two parts for each of the load points consist of changing only the load model, one for average load and the other for time varying load model. All other parameters were left unchanged and the load point indices such as the outage duration, failure rate and the average annual outage time were calculated for the system. The interruption costs as well as the system reliability indices (SAIFI, SAIDI and ENS) were also calculated and used in the Swedish Cost Model taken from [21] to obtain the ECOST of the test system. A flowchart for the simulation program for the time varying load model is shown in Fig. 5 below.
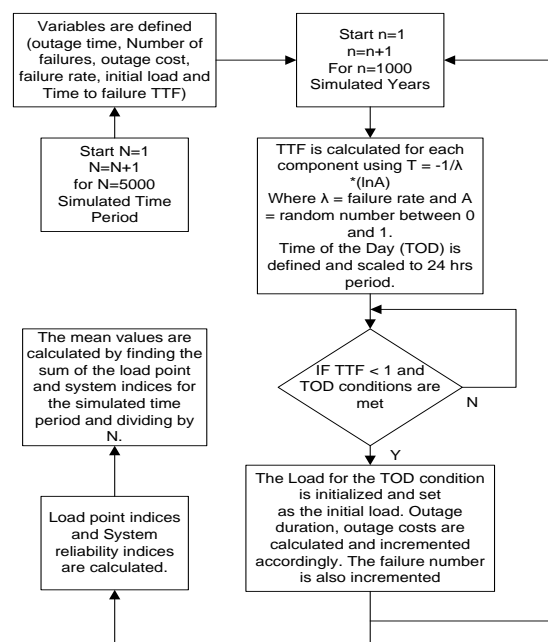

Fig. 5: Flow Chart for the Time Varying Load Model.

TOPIC C. POWER SYSTEMS

Proceedings of the 19th Southern African Universities Power Engineering Conference
SAUPEC 2010, University of the Witwatersrand, Johannesburg

The flow chart for the average load model will be similar except for the time of the day conditions.
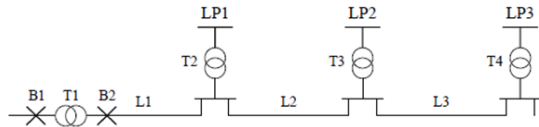
4.   SYSTEM ANALYSIS

Fig. 6: Distribution System used a Test System [10].

Fig. 6 shows a test system which is a distribution network taken from reference [10] consisting of 3 load points, 2 circuit breakers, 4 transformers and 3 overhead lines of different length. The test system from [10] has been modified where it was initially used as a rural distribution system with all load points as residential customers. In this case, due to time constraints and so as to differentiate the interruption costs for different customer categories, a simple distribution network [10] was used and the load point information (customer type, number of customers, etc) were changed and taken from [21]. LP1 and LP3 were unchanged as for the customer type (Residential) but the number of customers and load demand were changed while LP2 was assigned different customer sector (Commercial), number of customers and load demand.

5.   RESULTS

The calculations for the system reliability indices, SAIFI, SAIDI and ENS can be obtained from [20, 21] and have been implemented in the simulation codes for faster calculation. The following tables show the results for load point and system reliability indices and the interruption costs for both models.

5.1 Results for Average Load Model

Table 2: Load Point and System Reliability Indices

Load Points	λ	r	U	SAIFI	SAIDI	ENS
LP1	0.16	6.29	1.01	0.06	0.4	132.66
LP2	0.43	5.06	2.17	0.07	0.37	132.67
LP3	0.8	4.55	3.66	0.34	1.57	442.35

Where λ in failures/yr, r in hrs/failure, U in hrs/yr, SAIFI in failures/yr, SAIDI in hrs/yr and ENS in kWh.

5.2 Results for Time Varying Load Model

Table 3: Load Point Reliability Indices

Load Points	λ	r	U	SAIFI	SAIDI	ENS
LP1	0.16	6.23	0.97	0.06	0.39	126.64
LP2	0.38	4.68	1.79	0.07	0.31	106.23
LP3	0.61	3.86	2.36	0.26	1.01	284.64

Where λ in failures/yr, r in hrs/failure, U in hrs/yr, SAIFI in failures/yr, SAIDI in hrs/yr and ENS in kWh.

5.3 Application of the Load Models in the Swedish CIC Model

Table 4: Interruption Costs per Load points for Average and Time Varying Load Models

Load Points	Avg Load		Time Var. Load	
	(kR/kWh) $(C_{e,i,j})$	(kR/kW) $(C_{p,i,j})$	(kR/kWh) $(C_{e,i,j})$	(kR/kW) $(C_{p,i,j})$
LP1	0.08	159.55	0.08	157.88
LP2	334.3	720482.6	317	683068.1
LP3	0.1	207.26	0.09	191.92

The following equations were used from the Swedish customer interruption costs model [21]:

$$IC_e = \sum_{i,j}(SAIDI_j \ x \ P_i \ x \ c_{e,i,j})$$

$$IC_p = \sum_{i,j}(SAIFI_j \ x \ P_i \ x \ c_{p,i,j})$$

$$IC_{Sw} = IC_e + IC_p$$

Table 5: Outage cost using the Swedish CIC model with Average Load

Load Points	Average Load(kW)	ICe(kR/yr)	ICp(kR/yr)	ICs(kR/yr)
LP1	132	4.1	1344.8	1348.9
LP2	61	7700	3242400	3250100
LP3	121	19	8628.7	8647.7
System Interruption Costs (kR/yr) =				3260096.6

Table 6: Outage cost using the Swedish CIC model with Time Varying Load

Load Points	Average Load (kW)	ICe (kR/yr)	ICp (kR/yr)	ICs (kR/yr)
LP1	130.45	3.9	1284	1288
LP2	59.4	5800	2657500	2663300
LP3	120.42	11.3	6072	6083.3
System Interruption Costs (kR/yr) =				2670671.3

Table 7: ECOST comparisons between Average and Time Varying Load Models.

Load Points	ECOST (kR/Year) Average Load Model	ECOST (kR/Year) Time Varying Load Model
LP1	1348.90	1288
LP2	3250100	2663300
LP3	8647.70	6083.3
System	3260095.7	2670671.3

Proceedings of the 19th Southern African Universities Power Engineering Conference
SAUPEC 2010, University of the Witwatersrand, Johannesburg

TOPIC C. POWER SYSTEMS

It can be seen from Table 7 that while keeping the reliability and cost model constant during the simulations, the ECOST (in kR/year) is smaller for the load points and overall system when the time varying load model is used. This is because time varying load model considers the time varying nature of load demand for different customer categories. Fig. 7 shows the ECOST (yearly expected interruption costs) in R/year for LP 1 and LP3 and in kR/year for LP2 and the test system.
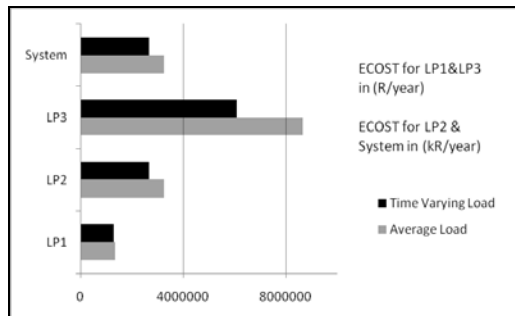

Fig. 7: ECOST for Load Points and System [10].

LP1 and LP3 represent residential customers while LP2 represents a commercial customer. It can be seen from the values in Table 7 that the interruption costs for commercial customer are far higher and hence an accurate representation of the load is necessary in order to provide an accurate evaluation. Thus the type of load modelling used in a CIC evaluation is crucial.

6. CONCLUSION

It has been observed that customer interruption/outage costs evaluation can be modelled using various approaches. These approaches rely on various factors such as the customer information, the load information and the cost information. The method used to evaluate CIC will also determine other parameters that are required, such as time dependencies, outdoor temperature, season, etc.

CIC evaluation as seen from the Swedish model in [21] also requires a reliability, load and cost model. In the interest of determining the impact of load models on interruption costs, a program was written in MATLAB using the time sequential Monte Carlo Simulation technique. The average and time varying load models were used and the results obtained were tabulated and compared. While some of the load models explained previously offer accurate results, required data were unavailable for some, while others are new development and have limited information on the methodology available.

Based on the results obtained from the simulations, it can be concluded that the type of load modelling used in a CIC evaluation impacts on the accuracy of the interruption costs obtained. Some load models require more information than others, but in the case of commercial customers, it is necessary to use accurate load modelling as the interruption costs are scaled to billions of rand. While time varying load model may be necessary for commercial customers,

average load model can be used in the absence of adequate information as the interruption costs are relatively lower.

REFERENCES

[1] Navjot Kaur, S. Gurdip, M.S. Bedi, and Tejpal Bhatti, "Evaluation of Customer Interruption Cost for Reliability Planning of Power Systems in Developing Economies", *8th International Conference on Probabilistic Methods Applied to Power Systems, Iowa State University*, Ames, Iowa, Sept. 2004.

[2] A.A. Chowdhury, T. C. Mielnik, L. E. Lawton, M. J. Sullivan and A. Katz, "System Reliability Worth Assessment at a Midwest Utility – Survey Results for Industrial, Commercial and Institutional Customers", *8th International Conference on Probabilistic Methods Applied to Power Systems, Iowa State University*, Ames, Iowa, Sept. 2004.

[3] G.Tollefson, R. Billington and G. Wacke, "Comprehensive Bibliography on Reliability Worth and Electrical Service Interruption Costs: 1980-1990", *IEEE Transactions on Power Systems*, vol. 6, Nov.1991, pp. 1508-1514.

[4] D.W. Caves, J.A. Herriges and R.J. Windle, "Customer Demand for Service Reliability in the Electric Power Industry: A Synthesis of the Outage Cost Literature", *Bulletin of Economic research*, vol. 42, April 1990, pp. 79-119.

[5] M.J. Sullivan and B.N. Suddeth, "Interruption Costs, Customer Satisfaction and Expectations of Service Reliability", *IEEE Transactions on Power Systems*, vol. 11, Nov. 1996, pp. 989-995.

[6] A.A Chowdhury and D.O. Koval, "Value-Based System Reliability Planning", IEEE Transactions on Industry Applications, vol. 35, March/April 1999, pp. 305-311.

[7] K.H. Tiedemann, "Estimating the Value of Reliability for Business Customers", *8th International Conference on Probabilistic Methods Applied to Power Systems, Iowa State University*, Ames, Iowa, Sept. 2004.

[8] R. Billinton and W. Zhang, "Cost Related Reliability Evaluation of Bulk Power Systems", *Electrical Power and Energy Systems*, Vol. 23, 2001, pp. 99-112.

[9] R. Billinton and W. Wangdee, "Approximate Methods for Event-Based Customer Interruption Cost Evaluation", *IEEE Transactions on Power Systems*, Vol. 20, No. 2, May 2005.

[10] Karin Alvehag, "Impact of Dependencies in Risks Assessment of Power Distribution Systems", *Thesis Report, Royal Institute of Technology, School of Electrical Engineering, Electric Power Systems*, Stockholm, Sweden, September 2008.

[11] Peng Wang and Roy Billinton, "Time Sequential Distribution System Reliability Worth Analysis: Considering Time Varying Load and Cost Models", *IEEE Transactions on Power Delivery*, Vol. 14, No. 3, pp. 1046-1051, July 1999.

[12] Pei Zhang, Stephen T. Lee and Dejan Sobajic, "Moving Towards Probabilistic Reliability Assessment Methods", *8th International Conference on Probabilistic Methods Applied to Power Systems*, Iowa State University, Ames, Iowa, September 2004.

[13] Diego Midence and Alberto Vargas, "Customer Outage Cost Models-Comparison", *19th International Confernece on Electricity Distribution, Vienna*, May 2007.

[14] Wenyuan Li, Jiaqi Zhou, Jiping Lu, and Wei Yan, "Incorporating a Combined Fuzzy and Probabilistic Load Model in Power System Reliability Assessment", *IEEE Transactions on Power Systems*, Vol. 22, No. 3, August 2007.

[15] A. A. Chowdhury and D. E. Custer, "A Value-Based Probabilistic Approach to Designing Urban Distribution Systems", *8th International Conference on Probabilistic Methods Applied to Power Systems, Iowa State University*, Ames, Iowa, Sept. 2004.

[16] *Tutorial on Fuzzy Logic Applications in Power Systems. Prepared for the IEEE-Power Eng. Soc. Winter Meeting in Singapore*, January 2000.

[17] J. Nahman, "Fuzzy Logic Based Network Reliability Evaluation", *Microelectron. Reliab*. , Vol. 37, No. 8, pp. 1161-1164, 1997.

[18] Ajit K. Verma and H. M. Ravi Kumar, "A Fuzzy Logic Approach to Security-based Bulk Power System Reliability Evaluation", Electric Machines and Power Systems, Vol. 28, pp. 45-54, 2000.

[19] T. Sangpetch, "Assessment of Customer Outage Costs with a Hybrid Neurfuzzy System", *System Planning Division, Electricity Authority of Thailand, Thailand, February 2007.*

[20] R. Billinton and P. Wang, 'Teaching Distribution System Reliability Evaluation", IEEE Transactions on Power Systems,Vol.14, No.2, May 1999.

[21] Michael Dijerenge, "Comparison of Customer Outage Cost Models in Quality Regulation of Electricity Distribution using Monte Carlo Simulations", Thesis Report, University of Cape Town, Department of Electrical Engineering, May 2009.

[22] "Power System reliability", available at:

http://www.docstoc.com/docs/DownloadDoc.aspx?doc_id=9960451
obtained [13:30 21 September 2009].

TOPIC C. POWER SYSTEMS

Proceedings of the 19th Southern African Universities Power Engineering Conference
SAUPEC 2010, University of the Witwatersrand, Johannesburg

THE DEVELOPMENT OF A PROBABILISTIC RELIABILITY ASSESSMENT PROCESS FOR DECISION-MAKING IN SOUTH AFRICA USING CIC SURVEYS

R Herman*, C.T. Gaunt*, M Edimu* and O Dzobo*

*Electrical Engineering Department University of Cape Town.

Abstract.   This paper proposes a method of predicting the probability of interruptions to customers connected to a given network and at a given time of day, weekday or week-end and season. From CIC (Customer Interruption Cost) surveys a method of scaling these costs is proposed for different sizes of customer. The result of the whole approach is the probabilistic financial impact assessment of interruptions, which provides an appropriate basis for decision-making.

Key Words. Customer Interruption Costs, probabilistic reliability evaluation

1. INTRODUCTION

There are a wide variety of issues that contribute to the complexity of assessing the impact of electricity supply interruptions.   To tackle this problem, analytical methods to predict the reliability of networks using simulation techniques, the measurement of individual customer costs and the interpretation of their combined effects in terms of the supply performance are constantly being developed. Adequacy of supply is a criterion that influences decisions for both the utility and the Regulator.

The goals of our current research programme in South Africa are to:

- Develop a probabilistic time-specific assessment tool for deriving interruption indices for particular local networks.
- Derive appropriate CIC values for various categories of customers in the South African context.
- Develop methods to combine interruption indices with CIC to derive probabilistic interruption costs for the particular network.
- Provide the utility and regulator with probabilistic monetary values so that, together with defined levels of risk, they may be used in decision-making.

While these problems have been addressed in a variety of ways in other countries [1,2,3], local conditions require specific local approaches. In this paper we describe some of the milestones reached so far in achieving the listed goals.

2. PROBABILISTIC APPROACH TO RELIABILITY

The standard method of expressing network reliability is to use average annual values of frequency and duration of failure occurrences. These are:

- SAIFI: System Average Interruption Frequency Index (Average Interruptions per year)

- SAIDI: System Average Interruption Duration Index (Average Interrupted hours per year)

Monte Carlo simulation methods are used extensively to predict system failure [4]. Billinton and Wangdee showed that the resultant reliability indices from these simulations are probabilistically distributed and are often skew [5]. Analyses of the probability distributions of this type were investigated by Cross [7] suggesting that the Beta pdf is a suitable statistical description. In recent work, using Monte Carlo simulations on the RBTS (see fig 1), we have shown that the Beta pdf is appropriate for describing the resultant outputs [8].
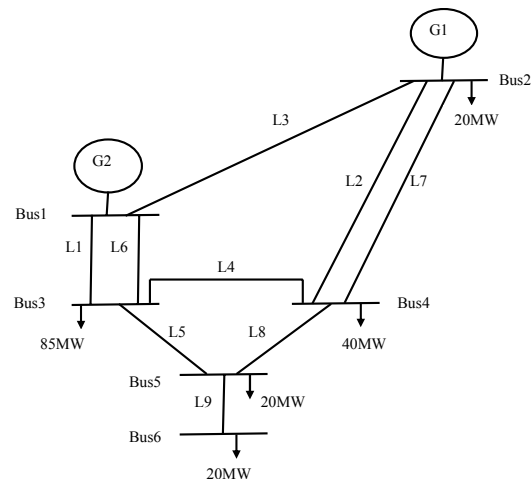

Fig. 1: Roy Billinton Test System (RBTS)

This analytical approach provides the basis for probabilistically assessing the interruption frequencies and durations for predetermined time intervals. The outputs from the Monte Carlo simulations are the statistical parameters of the frequency and duration of interruptions rather than average values. This process is partially described in the flow diagram shown in figure 2.

3. INTERRUPTIONS CAN BE TIME-DEPENDENT

Both SAIFI and SAIDI are expressed as average values per annum. However, many interruptions have specific time dependence. For example,

lightning activity in South Africa is more likely to occur on summer afternoons. This suggests that, besides the statistical description of duration and frequency, the description should be enhanced to include when the interruption may occur. Wangdee

and Billinton recognize this phenomenon and use weighting factors for different times of the day [6]. In our approach the variability within different time intervals will be treated in the following way:
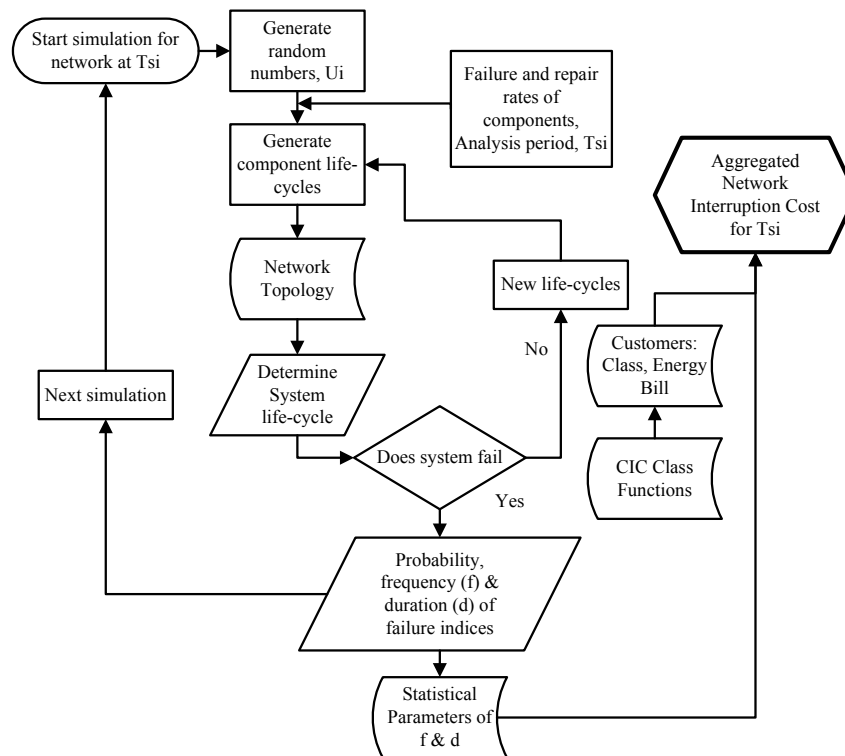

Fig. 2: Flow diagram for reliability assessment process

3.1 Time-dependent characterization

Both duration and frequency indices should be associated with seasonal and time-of-day intervals, T_{si}. A possible arrangement is shown by the 4 by 4 matrix represented in Table I. The seasons need not coincide with the natural yearly seasons, nor be of equal duration, but should rather be categorized according to their vulnerability to interruptions. The time periods during the day also can be variable, but are shown here as equal. Instead of using average values for the duration and frequency indices, it is proposed that the statistical parameters be used to represent these values. These could be mean and variance, as shown in Table I, or possibly Beta pdf parameters [9]

Table 1 Interruption Intervals for duration and frequency

S/I	00 - 06	06 - 12	12 - 18	18 – 24
Season 1	$\mu_{11};\ \sigma_{11}$	$\mu_{12};\ \sigma_{12}$	$\mu_{13};\ \sigma_{13}$	$\mu_{14};\ \sigma_{14}$
Season 2	$\mu_{21};\ \sigma_{21}$	$\mu_{22};\ \sigma_{22}$	$\mu_{23};\ \sigma_{23}$	$\mu_{24};\ \sigma_{24}$
Season 3	$\mu_{31};\ \sigma_{31}$	$\mu_{32};\ \sigma_{32}$	$\mu_{33};\ \sigma_{33}$	$\mu_{34};\ \sigma_{34}$
Season 4	$\mu_{41};\ \sigma_{41}$	$\mu_{42};\ \sigma_{42}$	$\mu_{43};\ \sigma_{43}$	$\mu_{44};\ \sigma_{44}$

3.2 Types of Interruption

Interruptions are typified by the following descriptions [10].

- *Momentary interruptions*: These are characterized by flicker, dips, sags caused by switching actions such as auto-reclosers and the switching of large loads. They usually manifest themselves at HL2 and HL3. While these interruptions are often ignored in broader reliability assessments, they can in some cases represent more than 60% of the total outages [11]. Consequently they can significantly affect the performance of delivery systems.

- *Sporadic interruptions*: These are mainly found in developed countries with robust delivery systems. In these situations the interruptions are often caused by severe weather conditions and occur mainly at HL2 and HL3. Most CIC surveys in developed countries measure sporadic interruptions.

- *Chronic interruptions*: The interruptions that occur more regularly are generally due to load shedding necessitated by a shortfall in generation (HL1) or severe ageing, lack of maintenance or overloading of the delivery systems (HL2 and HL3). This type of interruption is typical of developing countries where the load growth outstrips the supply and reinforcement requires substantial capital investment and lead time. This type may also occur in developed countries when

TOPIC C. POWER SYSTEMS

Proceedings of the 19th Southern African Universities Power Engineering Conference
SAUPEC 2010, University of the Witwatersrand, Johannesburg

a particular fuel source such as hydro suffers from a drought condition (HL0). In reliability terms the System Average Interruption Duration Index (SAIDI) values are usually significantly higher in developing than in developed countries. Similarly the interruption of supply associated with regular load shedding will have higher frequency of occurrence (SAIFI) than that experienced in developed countries.

4. CIC SURVEYS

4.1 CIC Survey 2009

During the previous surveys it became evident that CIC is significantly affected by the type of process engaged by the customer. Questions relating to the relative activity intervals during the day, week and season were also included.

4.2 Classification of Commercial and Industrial Customers

An obvious basis for classifying industrial and commercial customers is use the SIC (Standard Industrial Classification) codes, as used by Billinton and Wangdee [6]. They emphasize that the classification process may differ from country to country and it also depends on recent South African survey, the customers were classified according to the process of the business. To keep the total number of classes within manageable limits only twelve classes were chosen and are shown in Table 2.

Table 2 Interruption Intervals for Duration and Frequency

1. Bakeries, food processing	7. Metal and Engineering industries
2. Chemical industries	8. Foundries, glass, ceramics
3. Retail shops, food, non-food	9. Service stations, workshops
4. Professional practices	10. Warehousing, distribution, transport
5. Commercial & government offices	11. Agriculture, livestock
6. Clothing, textile, furnishing	12. Hotels and restaurants

4.3 Activity level

Respondents were asked to indicate the activity level of their business for six designated periods of the day for weekdays, Fridays, Saturdays and Sundays. They were further asked if this varied in the beginning, middle or end of the month. A similar question related to each month of the year.

4.3 Interruption occurences and estimated cost

The respondents were requested to consider 1, 2, 4 and 8 hour interruptions. In order to investigate the effects of time-of-interruption on CIC, the respondents were divided into groups and each group was asked to consider these interruption intervals for summer and winter scenarios, on weekdays and weekends and including mornings and evenings. The outages experienced during 2008 caused many customers to procure additional generating equipment ranging from uninterrupted power supplies to installed diesel generators. Questions were included in the 2009 survey to include these facilities in the costing of outages.

5. RESULTS OF SURVEYS

Some survey results pertaining to the suggested assessment process are shown here. These measurements are aimed at deriving CIC values that can be time-tagged according to Table I and scaled by type. The resultant time-dependent CIC for a number of customers of similar class, connected to a given network, can then be derived. In the survey it was found that CIC can be reasonably well correlated with the customer's average monthly electricity bill. Figure 3 shows the measured CIC values for a 1-hour outage on a summer weekday morning for category 6 (clothing, textile, furniture).

The figure shows a correlation of $R^2 = 0.937$ for a linear regression model for summer weekday morning interruption of 1-hour is given by:

$$CIC = 1.56\ W_M + 1203 \quad (1)$$

The units in (1) are Rands and W_M is the average monthly electricity cost for this type of customer.
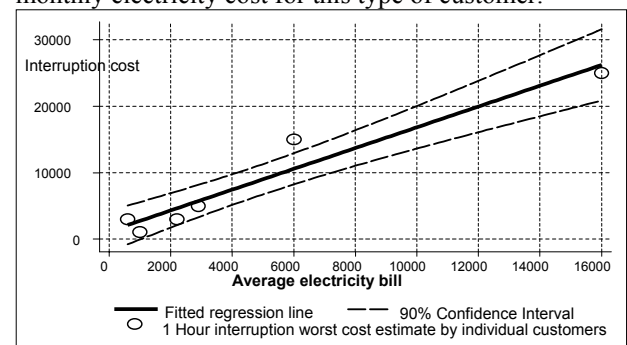

Fig 3 Customer Category 6: Correlation between CIC and Average Monthly Electricity cost (including 90-percentile envelope), for a One-hour outage on a Summer Weekday Morning
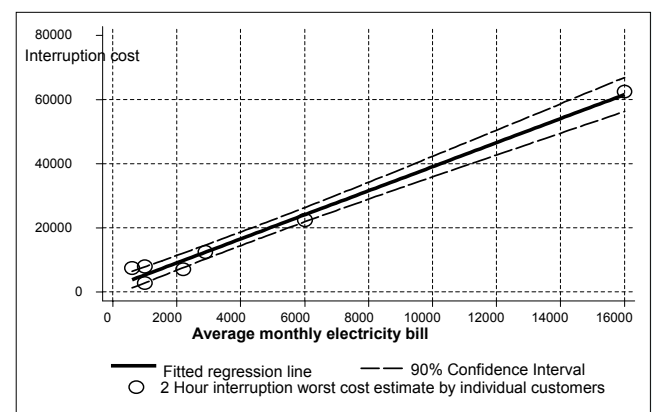

Fig 4 Customer Category 6: Correlation between CIC and Average Monthly Electricity cost (including 90-percentile envelope), for a 2-hour outage on a Summer Morning

Figure 4 shows an identical scenario with the exception that the interruption interval is 2 hours. In this case the correlation, $R^2 = 0.985$ and the linear regression function is given by:

$$CIC = 3.75W_M + 1622 \quad (2)$$

The analyses were repeated for other customer categories and for various predictor variables including: average daily operational hours, average electricity costs and number of employees. These correlations showed that scaling the CIC with electricity costs gave good estimates. Monthly electricity costs for customers are reasonably easy to obtain and so scaling the CIC values according to monthly electricity cost is recommended for future applications.

6. RELIABILITY ASSESSMENT PROCESS

For the purpose of this discussion refer to the flow diagram in fig 2. Suppose that a CIC assessment is to be performed on a given network for a given time of day, day of week and season, T_{si}. The evaluation must produce results for making engineering decisions. The following procedures are proposed.

6.1 Perform a probabilistic reliability study of the network

We next use probable failure rates of the individual T_{si} intervals and the given network structure to perform Monte Carlo simulations. From these we derive the statistical elements of the interruption time-table. These would be μ_{si} and σ_{si} in Gaussian statistics. The simulations can be performed in one of two ways. One way would be to analyze all the probabilities of when (i.e. at which T_{si}) interruptions may occur. The other way would be to determine the probability of occurrence for a designated T_{si}.

6.2 Assign customer types to the network

From geographical and technical data of the network, determine how many customers are connected. These are assigned to the network at the major load busses as percentages. Lower voltage customers will be fed from a feeder connected to a major bus. Larger customers requiring more secure supplies could be ring-fed, which will be reflected in the reliability simulations. For all the non-residential customers the information should include the:

- Number of connected customers
- Classification of each customer
- Cost of energy per month for each customer

The number of residential customers should also be counted but may be treated in a simpler fashion. Their CIC rates could be presented probabilistically as reported in [8].

6.3 Derive the probable cost of the outage

At this point we should know what the probability of occurrence for an interruption for the identified network would be for a chosen interval, T_{si}. For this T_{si} we have the estimated CIC in the form of linear expressions with respect to cost of energy. These values were obtained for the various classes and interruption durations for various T_{si} scenarios. It is

thus possible to estimate the individual CIC values for the given conditions.

The final step is to aggregate the individual CIC values to determine the total cost for a predicted outage occurring at interval T_{si}. Simple addition is possible because the individual CICs are in monetary units.

In practice the process starts by considering a specific part of the power system. With a priori knowledge of the conditions that are likely to cause supply failure (e.g. wet coal at HL0, lightning storms at HL2 and HL3 or essential maintenance outages) we then perform a reliability analysis using Monte Carlo simulation. The results of the simulation are in the form of a probability distribution whose parameters may be determined. Using the same conditions of time, day and season we can determine the CIC regression function for the various customer categories. Knowing how many customers within each class are connected to the specified load point and their individual monthly electricity costs we can aggregate the total interruption cost for the network. We envisage this process to be repeated for a number of probable scenarios. This assessment process will provide a tangible result for decision-making.

7. CONCLUSIONS

The work described in this paper is still in progress. The Monte Carlo simulation procedure was developed and tested on the Roy Billinton Test System (RBTS) using Matlab™. It is proposed to further develop the analytical procedure using more appropriate software to include larger systems such as those within the South African context. The CIC measurement should also be extended and refined. With these enhancements it will be possible to perform reliability assessments for a variety of probable scenarios.

Appropriate decisions relating to the planning and operation of the electricity supply industry are vital to the economy of the country. Often these decisions are made by executives who are not adequately skilled in interpreting the complicated technical problems that are endemic to the operation and regulation of the electricity supply industry. The outputs from the proposed process should simplify the criteria for decision-making, as they will relate delivery adequacy to the costs associated with levels of risk.

ACKNOWLEDGEMENTS

REFERENCES

[1] R. Billinton (convenor), "Methods to consider customer interruption costs in power system analysis", Cigré Task Force 38.06.01, Paris, 2001.

[2] G. Wacker, E. Wojcznski, & R. Billinton, "Interruption cost methodology and results – Canadian residential survey", *IEEE T-PAS*, vol. PAS-102, 1983.

[3] K.H. Tiedemann, "Estimating the value of reliability for business customers", PMAPS04, Iowa, September 2004.

[4] R. Billinton & R.N. Allen, Reliability Evaluation of Engineering Systems, Concepts and Techniques, New York, Plenum Press (1992)

[5] R. Billinton & W. Wangdee, "Delivery Point Reliability Indices of a Bulk Electric System Using Sequential Monte Carlo Simulation", *IEEE T-PWD* vol. 21, 2006.

[6] R. Billinton & W. Wangdee, "Approximate Methods for Event-Based Customer Interruption Cost Evaluation", *IEEE TRANS on POWER SYSTEMS*, vol. 20, MAY 2005

[7] N. Cross, R. Herman & C.T. Gaunt, "Investigating the usefulness of the Beta pdf to describe Parameters in Reliability Analyses", PMAPS06, Stockholm, July 2006

[8] R Herman & CT Gaunt, "Direct and Indirect Measurement of Residential and Commercial CIC: Preliminary findings from South African Surveys", PMAPS08, Puerto Rico, Jun 2008.

[9] M. Edimu, "Evaluation Of Reliability Indices Of A Composite Power System Using Probability Distribution Function", MSc Thesis, UCT, 2009.

[10] C.T. Gaunt, R.Herman & B. Bekker, "Probabilistic Methods for Renewable Energy Sources and Associated Electrical Loads for Southern African Distribution Systems", CIGRÉ & IEEE-PES International Symposium, Calgary, Jul 2009.

[11] K.H. La Commare & J.H. Eto, "Cost of Power Interruptions to Electricity Consumers in the United States (U.S.)", DOE, 2005, LBNL-58164

A REVIEW OF CUSTOMER INTERRUPTION COST MODELLING FOR REGULATORY DECISION MAKING

K. O. Awodele, C.T. Gaunt, R. Herman

University of Cape Town, Department of Electrical Engineering, Private bag X3 Rondebosch 7701, CapeTtown

Abstract.   The monopoly nature of the electricity distribution network business has made regulation necessary. Some minimum standards of frequency and duration of interruptions used for regulation are inappropriate in regulating continuity of supply performance, as there is no incentive for a utility to improve performance in networks where minimum standards are already being met . If customer-interruption-cost (CIC) is used to regulate performance, the utility always has an incentive to provide the optimal quality level. The stochastic and uncertain nature of some of the parameters such system reliability, loads and costs, though researched to some extent, have not been incorporated in the existing models used for regulation. This is necessary in order to have probabilistic models and therefore know the confidence/risk levels of CIC values being used for regulatory decision making. This paper reviews CIC in regulatory decision making in the context of South Africa and identifies a suitable process for developing models for regulation.

Key Words.   Electricity Distribution, Regulation, Customer interruption Cost, Decision making

1. INTRODUCTION

Although competition has been introduced in some parts of electricity supply industry in some countries as a result of deregulation, the network businesses - transmission and distribution - have remained monopolies because of the huge investment involved. South Africa is similar although restructuring has not occurred.

Adequate maintenance as well as capital investment is necessary to maintain a given level of reliability. As distribution equipment ages, the reliability reduces and the aging equipment also needs to be replaced. South Africa exhibits many features of equipment deterioration and interruption of supply. The publication of South Africa's Regulators' forum of December 2005 points out the following about the electricity distribution industry in South Africa [1]:

"The National Energy Regulator (NER) is concerned with the large number and severity of power interruptions caused by the poor state of electricity distribution infrastructure in the country."

A number of surveys conducted by NER (now NERSA) to assess the experience of electricity users and evaluate their interactions with the utilities revealed that an increasing number of customers were not happy with their supply due mainly to the level of reliability and availability; more than 53 % of respondents were dissatisfied with the interruption frequency and durations. A survey of distribution licensees revealed among other things that there was no common yardstick for measuring performance [5].

However, South Africa is not the only country where supply reliability is important, and issues arise in

many countries where regulators identify fall in reliability standards.

The cost incurred in maintaining and improving reliability is passed to the customer through increased tariffs. Some questions arise in this regard. What is optimal reliability? How much reliability is the customer willing to pay for? Economic regulation was

introduced for cost efficiency but as distribution companies cut cost in order to make enough profit, the danger of quality deterioration became apparent.

2.   CIC VERSUS MINIMUM STANDARDS

Minimum standards, as shown in figure 1, used for other aspects of power quality such as voltage magnitude, are considered to be inappropriate in regulating continuity of supply performance, as there is no incentive for a utility to improve performance in networks where minimum standards are already being met [3]. If the incentive is set on the basis of customer interruption costs (CIC), the utility always has an incentive to provide the optimal quality level [4]. CIC is the 'cost of unreliability' used to represent the 'worth of reliability' which is rather difficult to measure. CIC is also used to evaluate investments for cost/benefit analysis in value-based reliability planning [5],.
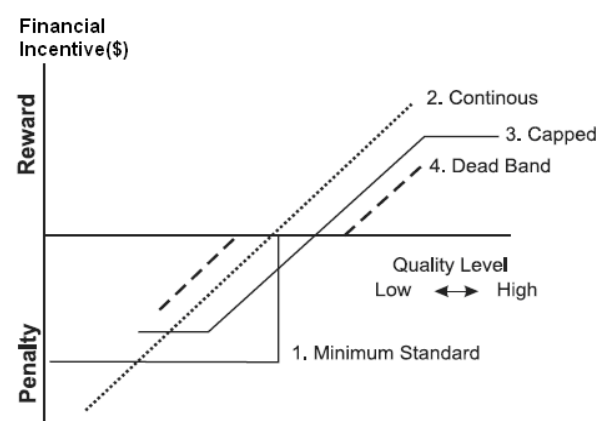

Figure 1: Reward and penalty versus minimum standard [4]

The unreliability costs decrease as the level of reliability increases but increased reliability is obtained with increased utility costs as shown in figure 2. The sum of the utility cost versus reliability curve and the CIC versus reliability curve gives a third curve which is the total societal cost versus reliability curve. The optimal reliability is the reliability corresponding to the

TOPIC C. POWER SYSTEMS

Proceedings of the 19th Southern African Universities Power Engineering Conference
SAUPEC 2010, University of the Witwatersrand, Johannesburg

minimum total cost. An investment at point A or point B is suboptimal. At point A there is over-investment and the cost would be passed to the customer which is typical of Rate-of-return (ROR) regulation, while at point B there is under-investment and therefore insufficient reliability which is typical of price-capped regulation.
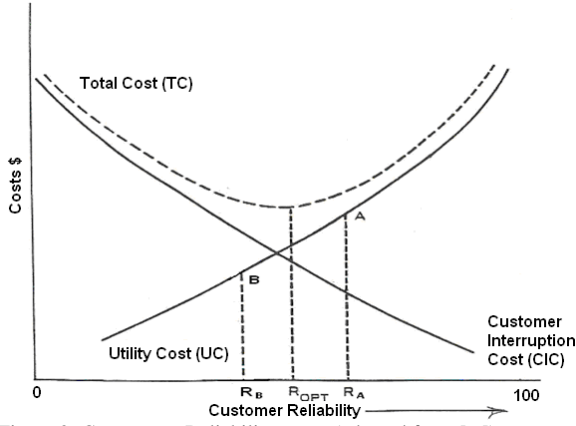

Figure 2: Cost versus Reliability curve (adapted from [6]).

From figure 2, $TC_{op} < TC_A$, TC_B ; $TC_A = TC_B$

$$At \ R_A, \frac{\Delta(TC)}{\Delta R} = +ve, \Delta CIC < \Delta UC \ \text{-------(1)}$$

Equation (1) is undesirable, as the excess cost will be passed to customers. This occurs under Rate of Return (ROR) regulation.

$$At \ R_B, \frac{\Delta(TC)}{\Delta R} = -ve, \Delta CIC > \Delta UC \ \text{----(2)}$$

Equation (2) is also undesirable, there is insufficient reliability. It occurs under price cap regulation.

$$At \ R_{Opt}, \frac{\Delta(TC)}{\Delta R} = 0, \Delta CIC = \Delta UC \ \text{----(3)}$$

Equation (3) represents optimal reliability which is the goal of quality regulation.

For performance evaluation, a target value of CIC is therefore determined for each utility and the actual CIC is compared to the *target*. Deviations from the target would lead to penalty or reward depending on whether the actual CIC is more or less than the target as illustrated in figure1 above.

3. CUSTOMER INTERRUPTION COST MODEL ACCURACY

In figure 1 above, it is assumed that the utility costs and the customer interruption costs have been measured accurately to obtain the given curves used to arrive at the optimal reliability. Utility costs can be easily determined but it is not that easy to determine the costs related to customer reliability. There will be a range, or an envelope of uncertainty. An under-estimation (CIC_A) or over-estimation (CIC_B) of CIC will inadvertently lead to the "optimal" reliability

corresponding to points R_A or R_B on the reliability axis respectively as shown in figure 3.
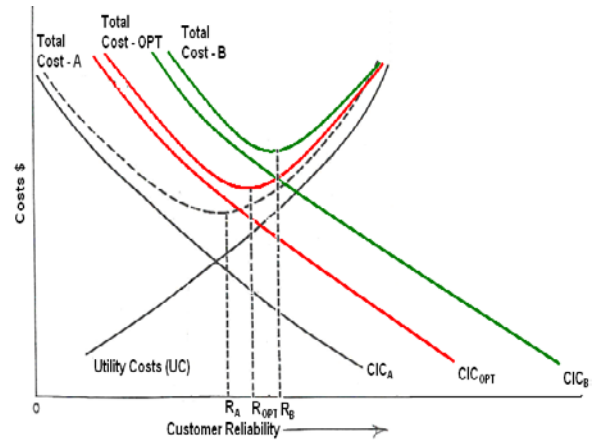

Figure 3 : Effect of different CIC models on the determination of optimal reliability.

In figure 3 ,

$$\frac{\Delta(TC_A)}{\Delta R} = \frac{\Delta(TC_B)}{\Delta R} = \frac{\Delta(TC_{Opt})}{\Delta R} = 0, \Delta CIC = \Delta UC$$

but R_A and R_B are sub-optimal because CIC is not well modelled.

An accurate measurement of CIC is therefore crucial for effective determination of the optimal reliability and the attendant level of utility investment.

Several factors affect CIC. They include duration, frequency and time of interruption; whether advanced notice is given, the type of activity interrupted in the different customer categories and the degree of dependence on electricity, season of the year, day of the week, time of the day and passage of time[7]. It is believed that CIC is less in the night, but the penetration of electric vehicles whose batteries may be charged mostly at night might change this in future. The penetration of more electricity-dependent appliances will also affect CIC in future.

Different methods have been used for the determination of CIC as shown in figure 4. These methods vary in their cost of execution, accuracy of results and amount of information acquired. Earlier researches tried to equate CIC to the cost of unsold energy [8], some use the analytical method, which divides the GNP of a country by the electrical energy consumed [9]. None of these capture the actual customer cost of interruption that depends on the process or activity that is interrupted. Kariuki and Allan [10] state that reliability, from the perspective of the customer, is influenced by the number of interruptions experienced, the duration of the interruptions and the cost incurred as a result of the interruptions.

In South Africa [11],[12] and other countries [13], the survey method has been most widely accepted as the customer is believed to be in the best position to estimate the impact of an interruption.

Proceedings of the 19th Southern African Universities Power Engineering Conference
SAUPEC 2010, University of the Witwatersrand, Johannesburg
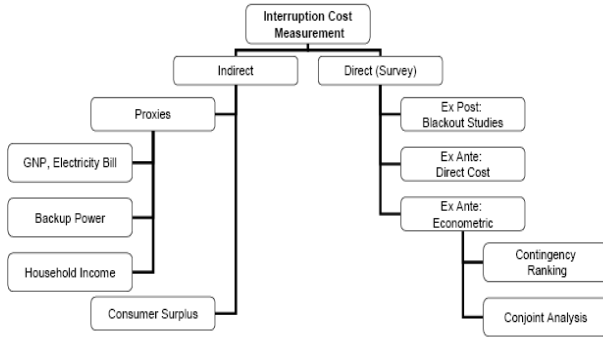
TOPIC C. POWER SYSTEMS

Figure 4: Overview of customer interruption cost measurement techniques [7].

In areas with higher reliability, it is possible that the last experience of interruption before the survey is so remote that hypothetical scenarios of interruption are used to estimate costs. The costs obtained from places with more frequent interruptions are therefore expected to be more accurate [10],[11], [12].

A cross comparison of interruption costs obtained from different countries shows a very large variation [4]. Reasons attributed to such variation include differences in country, region and economic development. The costs obtained are largely a function of the method used and the location. *CIC values obtained in one country may not be readily applicable to another country and should therefore be determined for each country where they are to be used either for planning purposes by the utility or for regulatory decision making.*

The need for an accurate model of CIC for quality regulation has been established. CIC application in quality regulation provides a good link between performance and investment. Models have been developed by some countries. The question is how appropriate are the existing models for application in a country such as South Africa.

4. TYPICAL CIC MODELS

Typical CIC models in literature, used for regulation, are functions of cost, load and reliability e.g. Swedish, Norwegian and Canadian models [5],[14].

Swedish

$$IC = \sum_i \sum_a \left[\left(SAIDI \; x \; C_{Eia} \; x \; \frac{E_a}{8760} \right) + \left(SAIFI \; x \; C_{Cia} \; x \; \frac{E_a}{8760} \right) \right]$$

C_E (R/kWh) and C_C(R/kW) are the costs associated with energy and capacity respectively. E_a is the energy consumption in area *a* within the reference grid, i indicates unplanned interruption when i = 1; or planned interruption when i = 2.

This is a two part model with a duration dependent component and a frequency dependent component. Sweden since 2003 uses a reference network, the Network performance assessment model (NPAM) in which quality is regulated separately with a CIC model that is a function of SAIDI and SAIFI [14]. Solver [14]

examined the incentive features in the regulation to see what incentives for grid investments and maintenance the regulated distribution companies are given through the regulatory framework in general and the quality regulation in particular, and how the future reliability and availability in the distribution system will be affected. The applicability of the same quality regulation model to all distribution companies being regulated was questioned since they may not all be comparable. He also compared the quality regulation models of Sweden, Norway, Netherlands and Spain and concluded that in comparing different countries the circumstances under which the different distribution companies operate; the differences in customer densities and in geography must be considered. Furthermore, Wallnerström and Bertling [15] have investigated the robustness of the NPAM and concluded that it is sensitive to small changes in input data; the response of the model to small changes is unpredictable, differing among the different systems analyzed.

Norwegian

$$CENS = \sum_i \sum_c C_{ic} \; x \; ENS_{ic} = \sum_i \sum_c C_{ic} \; x \; D_{ic} \; x \; \frac{E_c}{8760}$$

where i indicates whether the interruption is planned or not and c is the customer categories, 1-5, D is the total interruption duration and E is the energy consumption for each separate customer category.

This model is mainly duration and average load dependent. In the Norwegian regulation scheme cost of energy not supplied (CENS) which was implemented in 2001, the Network companies' revenue caps are adjusted depending on the customer interruption costs [16].

Canadian

$$CIC = \lambda_j \; x \; L_p \; x \; C_{(rj, \; p)}$$

Where λ_j is the failure rate of section *j*, L_p is the average load connected at load point *p* and $C_{(rj,p)}$ is the cost of interruption (R/*/kW*).

This model is a function of the failure rate of system components and average load.

While Sweden has a penalty system, Netherland has both a penalty and reward system without a dead band [19]. Finland, which has been using outage duration as a quality parameter in the efficiency regulation model, has decided to change to CIC as the quality parameter because the earlier parameter did not give the expected directing signals to the distribution companies [14], [17], [18].

5. CUSTOMER INTERRUPTION COST MODELLING

In evaluating reliability and decision making in the transport sector, Husdal [19] stated that all decision making has a degree of uncertainty, ranging from a predictable, deterministic situation to an uncertain situation. He further stated that in some situations,

TOPIC C. POWER SYSTEMS

Proceedings of the 19th Southern African Universities Power Engineering Conference
SAUPEC 2010, University of the Witwatersrand, Johannesburg

decision making involves the risk or some uncertainty of making a "wrong" decision, because the information acquired is insufficient or the approach used is inappropriate. In the end, it is the decision maker who determines the criteria, the factors, the constraints, the individual weighting and the decision rules [19]. These comments apply equally in reliability studies in power systems and some approaches, key criteria, factors, constraints and weightings in CIC modelling are examined below.

The independent variables (cost, load and reliability) in the CIC model have to be modelled separately. Data needed for cost and load modelling can be obtained from surveys.

5.1 Cost Estimation and Modelling

The cost of planned interruptions has been estimated to be about half that of unplanned interruptions, while the costs of momentary interruptions and dips are estimated to be about the same or more than the cost of planned interruptions [17], [18].

The costing methods in customer surveys are classified into direct costs and indirect costs. Direct approach attempts to measure the impacts of actual interruption events subsequent to their occurrence. The indirect approach is based on hypothetical scenarios suggested in the questionnaires to the customers [11]. Direct costs are more applicable to non-residential customers while indirect costs such as willingness-to-pay (WTP), willingness-to-accept (WTA) and preparatory action method (PAM) are usually used for residential customers where the impacts are largely intangible [11],[20]. A combination of the methods is used sometimes to detect strategic responses from those surveyed [12], [17].

Cost estimates obtained using different methods have been observed to be different. Direct cost methods have given values higher than willingness-to-pay, an indirect approach, and the values have large variance [11]. In a survey carried out in Norway, the two were averaged [16]. Herman and Gaunt [12] suggest that scaling of the CIC measurement may be done more comprehensively when both direct and indirect approaches are used. Averaging of cost obtained from direct and indirect approaches may not give the best estimate. Apart from averaging, other methods of combining these costs such as fuzzy logic and fuzzy arithmetic have not been proposed in literature.

Development of cost functions

Various methods are used to transform the data obtained from surveys which are costs per interruption into a cost function. A commonly used cost function, the customer damage function (CDF) which is cost as a function of duration, is obtained by averaging or aggregating the cost data [21]. The aggregating method gives a lower cost value because it reduces the effect of customers with relatively low consumption but high interruption cost estimates (e.g. computer users) [21]. The obtained data is usually normalised using peak demand, average demand or energy consumed. Equivalent CDF for each load point is created to represent the specific mix of customers connected to specific part of the system [21]. Sector customer damage functions (SCDF) and Composite customer damage functions are obtained using the CDF, the customer mix at load points and the proportion of system energy consumed by each sector [20].

Wojczynski and Billinton in [22] found that the use of average outage duration to calculate CIC can, in a significant number of cases; result in large errors as compared with using the entire duration distribution especially when there is a large variance. Although some researches have been done to develop fuzzy and probabilistic cost functions, as well as include time/seasonal dependencies of costs [12],[23],[24], the existing CIC models used for regulation as seen in the literature seem to have used average values of costs.

Extreme cost estimates

Different methods have been proposed to deal with outliers in the cost data collected in surveys. Kivikko et al [18] have applied some elimination techniques. They have applied 5 % reduction of the highest and lowest values but have suggested that customers with unusually high CICs be treated separately. Herman and Gaunt [12] have pointed out the need to understand, and use correctly the values of 'outliers'.

5.2 Load Modelling

Average load models that were approximations of the actual loads were used in earlier researches on CIC [24]. Wang et al [24] developed a time varying chronological load model that incorporates the load for each hour. Alvehag [23], proposed a time varying load model in which outdoor temperature that affects loads is modelled to be stochastic. A probabilistic residential load model was developed by Heunis and Herman [25]. Li et al [26] identified two types of uncertainties, randomness and fuzziness in power systems and developed a combined fuzzy and probabilistic load model in which the fuzzy model is for the peak load and the probability distribution is for the load curve. The existing CIC models used for regulation seem not to have used probabilistic load models or fuzzy load models to capture the variability and uncertainties in the loads.

5.3 Reliability Modelling

Reliability can be modelled from historical frequency and duration of interruption data kept by the utilities or predictive reliability of the system can be evaluated using the failure rates, restoration times, switching times of the different system components, and the system configuration. The choice of load and reliability models is dependent on the available data as well as the goal of the regulation [14].

Reliability indicators/parameters are customer based e.g. System Average Interruption Duration Index SAIDI; load based e.g. Average System Interruption Duration Index ASIDI; component based e.g. λ, r, U or energy based e.g. Expected Energy Not Supplied

Proceedings of the 19th Southern African Universities Power Engineering Conference
SAUPEC 2010, University of the Witwatersrand, Johannesburg

TOPIC C. POWER SYSTEMS

EENS. Solver pointed out that customer oriented indices tend to give priority to load points with more customers even when the load is not much [14]. These average indices do not however capture the variability of the duration and frequency of interruptions and are not adequate for decision making.

To account for the variability of the reliability of the system, the failure rates are represented by probability density functions. Components with constant failure rates are usually represented by exponential distribution and the time to repair is represented by log-normal distribution [14]. Some researches have suggested the use of the probability distribution of SAIDI and SAIFI instead of the mean to capture the variability of these indices [27].

System probability of failure, frequency of failure and duration of failure pdfs have been presented by Edimu [28], and fuzzy arithmetic and fuzzy logic have been used in reliability analysis of power systems [29]. Nahman et al [29] have also researched on using fuzzy logic to account for data uncertainty in distribution system performance evaluation.

Probability distribution of the frequencies and durations of interruptions, giving the System Interruption Frequency (SIF) beta pdf and System Interruption Duration (SID) beta pdf respectively, had been obtained using Monte Carlo simulations and fitting beta pdfs to the histograms [30]. Such pdfs can be used in developing a probabilistic CIC model.

There is need to have a model that can be used to predict future outage costs for planning and regulation purposes. It is necessary to be able to relate a predictive reliability level with the customer interruption costs associated with that reliability level [31].
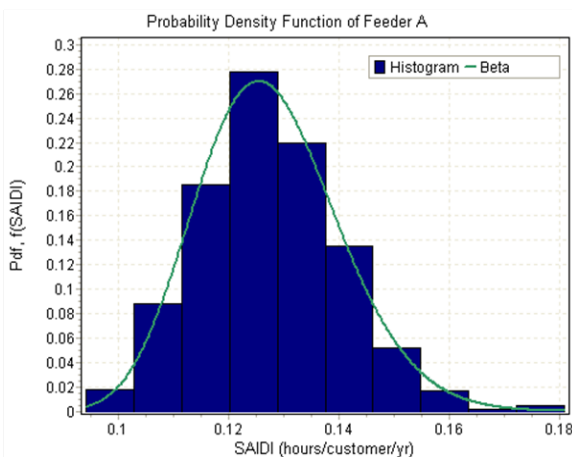
Figure 5: SAIDI distribution of Feeder A in Philippi network, Cape Town [30]

5.4 Analysis Methods

Various methods have been used in literature to carry out the reliability analysis of systems. Analytical methods are sufficient for less complex systems but as the complexity increases simulation methods become more appropriate. The method used should however accommodate distributions of some kind.

Monte Carlo simulation methods have been used extensively not only for complex systems but to capture the stochastic nature of the costs, the reliability and the loads. Different variants of the Monte Carlo simulation methods have been proposed, they include the sequential, non-sequential and the pseudo chronological methods, and tests have been carried out on reliability test systems such as the Roy Billinton Test System and the IEEE test system [14],[22],[23]. Typical national systems are also used, e.g. the test distribution system used by Alvehag [23] is assumed to be located in the Gothenburg area of Sweden where high wind events are deemed to be a larger threat to system reliability than for example lightning, icing and snow; and had to be considered in the modelling.

5.5 CIC Target & Reward/Penalty structure

Setting the quality target can be considered as consisting of two parts: setting the initial target and adjusting the target over time to reflect the improvement in quality performance achieved by the utility [4].

The determination of the target or expected CIC usually takes into cognisance the historical performance of the different utilities e.g. in Norway, the quality target differs per firm. Two sources of information are used to establish the quality target. First, a regression analysis is performed to calculate the expected ENS (energy not supplied) per firm taking into account factors such as network type, number of transformers, and some climatic and geographical factors. Secondly the historical performance levels of the distribution firms are considered. The quality target for each firm is set equal to the average of the predicted and the actual quality level, measured in kWh non supplied energy [4]. The target can also be the historical average reliability index [32].

Feng [32] proposed that the width of the deadband should be related to the standard deviation of the historical or predictive data and the remaining parameters of the reward penalty structure should be related to the incentive philosophy of the regulatory authority[32] i.e. the input parameters define the nature of the output of the model.

6. CONCLUSION

Based on this review, it is evident that the existing models of Customer interruption cost used for regulation do not capture the probabilistic nature of the relevant parameters of the model. It is important to consider the variability of the reliability, load and cost in the CIC model for regulatory decision making since the input parameters define the outputs of the model.

7. AKNOWLEDGEMENT

TOPIC C. POWER SYSTEMS

Proceedings of the 19th Southern African Universities Power Engineering Conference
SAUPEC 2010, University of the Witwatersrand, Johannesburg

REFERENCES

[1] SARF (2005) South Africa's Regulator's forum Newsletter, December

[2] Kessides I N, Bogetic Z and Maurer L (2007), "Current and Forthcoming Issues in the South African Electricity Sector", World Bank Policy Research Working Paper 419.

[3] Carter-Brown C, Cameron M and du Preez M (2007), "Determining a relationship between Eskom Distribution network performance and capital investment", Eskom Distribution, Cape Town.

[4] Ajodhia V S (2005), "Regulation Beyond Price: Integrated Price-Quality Regulation for Electricity Distribution Networks", PhD thesis, Department of Electrical Engineering, technical University, Delft, Netherlands

[5] Chen R, Allen K and Billinton R (1995), "Value-based distribution reliability assessment and planning", IEEE Transactions on Power Delivery, Volume 10, No 1, pp. 421 – 429

[6] Hambata J. (2009) "Customer Interrution Cost Evaluation: Industrial customers" B.SC thesis, Dept of electrical Engineering, UCT, Cape Town, South Africa.

[7] M. Sullivan and M. Sheehan (2000), " Observed changes in Residential and Commercial Customer interruption Costs in the Pacific Northwest Between 1989 and 1999", IEEE Power Engineering Society summer meeting, Volume 4, pp. 2290 – 2293

[8] Kariuki K. K. and Allan R. N. (1996), "Factors affecting customer outage costs due to electric service interruptions", IEE Proceedings, Generation, Transmission and Distribution, Volume 143, no 6, pp. 521 –528.

[9] Choi S.B., Kim D.K., Jeong S.H. and Ryu H.S.(2002), "Evaluation of the Customer Interruption Costs taking into consideration Macro Economic approach in Korea", International Power System Technology Conference Proceedings, Powercon 2002, Volume 4 , pp. 2358 – 2362

[10] Kariuki K.K. and Allan R.N.(1996), "Evaluation of Reliability Worth and Value of lost Load", IEE proceedings, Generation, Transmission and Distribution, Volume 143, no 2,pp. 171 –180.

[11] Herman R, Gaunt T, Minaar U. and Koch R. (2007), "Direct and Indirect estimation of domestic customer interruption costs: considerations and preliminary results", CIGRE SC-C6 (COLL 2007) Working Group C6-13, Malaysia.

[12] Herman R. and Gaunt C.T. (2008), "Direct and Indirect Measurement of Residential and Commercial CIC: Preliminary findings from South African Surveys" Proceedings of Probabilistic Methods Applied to Power Systems (PMAPS).

[13] Billinton R. (Convenor) (2001), "Methods to consider customer interruption costs in power system analysis", Cigré task Force 38.06.01, Paris.

[14] Solver T.(2005), "Reliability in Performance-based regulation", Licentiate thesis, Electrical power systems, Department of Electrical Systems, Royal Institute of Technology, Sweden.

[15] WallnerstrÖm C.J. and Bertling L(2008, "Investigation of the Robustness of the Swedish Network Performance

[16]Kjølle G.H, Samdal K, Singh B and Kvitastein O.A.(2008), "Customer costs related to Interruptions and voltage problems: Methodology and results", IEEE transactions on power systems, Volume 23, No 3, pp. 1030-1038.

[17] Lassila J, Honkapuro S and Partanen J (2005), "Economic Analysis of outage costs parameters and their implications on investment decisions", IEEE Power Engineering Society General Meeting, Volume 3, pp 2165 - 2172 .

[18] Kivikko K, Mäkinen A, Verho P, Järventausa P, Lassila J,Viljainen S, Honkapuro S and. Partanen J(2005), "Outage Cost Modelling for Reliability Based Network Planning and Regulation of Distribution Companies", Eighth IEE International Conference on Developments in Power-System Protection, Volume 2, pp.607 – 610

[19] Husdal J. (2004), "Reliability and Vulnerability versus Costs and Benefits" European Transportation Conference, Strasbourg, France

[20] Kariuki K. K and Allan R.N. (1996), "Factors affecting customer outage costs due to electric service interruptions", IEE Proceedings, Generation, Transmission and Distribution, Volume 143, no 6, pp. 521 –528.

[21] Bozic Z (2000), "Customer Interruption Cost Calculation for Reliability Economics: Practical Considerations" International Conference on Power System Technology, Vol. 2, pp 1095 – 1100.

[22] Wojczynski E. and Billinton R. (1985), "Effects of distribution system reliability index distributions upon interruption cost/reliability worth estimates", IEEE Transactions on Power Apparatus and Systems., PAS Volume 104, pp 3229–3235.

[23] Alvehag K.(2008), "Impact of Dependencies in Risk Assessments of Power Distribution Systems" Licentiate thesis, Department of Electrical Systems, Royal Institute of Technology, Sweden.

[24]Wang P and Billinton R(1999), "Time Sequential Distribution System Reliability Worth Analysis Considering Time varying load and Cost Models" IEEE Transactions on Power Delivery, Volume 14, No 3,pp. 1046 – 1051

[25] Heunis S.W and Herman R (2002), "A probabilistic Model for residential Consumer loads", IEEE Transactions on power systems, Volume 17, No 3, pp. 1386 –1388.

[26] Li W, Zhou J, Lu J and Yan W(2007), "Incorporating a combined Fuzzy and Probabilistic Load model in Power System reliability assessment", IEEE Transactions on power systems, Volume 22, No 3, pp. 1386 –1388.

[27] Billinton R (2006), "Probabilistic Applications In Power Systems Planning", Seminar paper, University of Saskatchewan, Canada.

[28] Edimu M (2009), " Evaluation of Reliability Indices of a Composite Power System Using Probability Distribution Functions" M.Sc thesis, , Department of Electrical Engineering, University of Cape Town, Cape Town, South Africa.

Proceedings of the 19th Southern African Universities Power Engineering Conference
SAUPEC 2010, University of the Witwatersrand, Johannesburg

TOPIC C. POWER SYSTEMS

[29] Nahman J (1997), "Fuzzy logic based network reliability evaluation", Micro-electron. Reliability, Volume 37, No 8, pp. 1161 – 1164

[30] Shavuka S. (2009) "Application of Predictive Reliability Techniques to distribution systems" B.SC thesis, Dept of electrical Engineering, UCT, Cape Town, South Africa.

[31] CEER (2005), "Third benchmarking report on quality of electricity supply", Quality of Supply task force C05-QOS-01-03, Technical Report.

[32] Feng Z (2006), "Electric Distribution System Risk Assessment using Actual Utility Reliability Data", M.Sc thesis, College of Graduate Studies and Research, Department of Electrical Engineering, University of Saskatchewan, Saskatoon, Saskatchewan, Canada.

TOPIC C. POWER SYSTEMS

Proceedings of the 19th Southern African Universities Power Engineering Conference
SAUPEC 2010, University of the Witwatersrand, Johannesburg

THE IMPACT OF TRANSMISSION NETWORK CONSTRAINTS ON MARKET STRATEGIES

J Yan*

University of Cape Town, Department of Electrical Engineering, Private Bag, Rondebosch 7701

Abstract. In this paper, the impact of transmission network constraints on market strategies is investigated. Three market strategies, which include Dynamic Shadow Pricing, Nash-Cournot, Dynamic Shadow Pricing together with Nash-Cournot, have been investigated. Perfect competition is also included in the simulations and is served as a comparison model. A three-bus network is used to illustrate how market strategies are influenced by the network constraints. Profit maximization is the driving force in the market for all market participants. In this paper, the market participants refer to the Independent Power Producers (IPPs). Three market strategies plus perfect competition and three transmission constraint limits are included in the simulations. For each transmission limit, the market price and IPPs' net profits are compared to determine which market strategy they may adopt in real-time. The results from the simulations show that IPPs will change market strategies according to the change of transmission limits. IPPs obtain significant profits through their strategic behaviours.

1. INTRODUCTION

In a regulated electricity industry, network constraints may exist due to the transmission capacity limits. In a vertically integrated utility (centralized dispatcher control) the power stations do not have any capability for gaming. In contrast, in a competitive and restructured electricity market, market participants are free to adopt any strategies to maximize their profits.

Through gaming, market participants could obtain excessive profits from the market. It is found that there is a need to investigate whether there is a coupling between network constraints and market strategies. A number of papers [5, 8, 9, and 10] have already investigated the strategic behavior of market participants in a congested network.

Most of the researchers are trying to formulate the conditions for market equilibriums. They assume that each market participant could have more than one strategy. However, there is not enough research with regard to determining which market strategies will be adopted by market participants with different transmission network constraints.

Many researchers [5, 9, and 10] have studied different cases of Nash-Cournot competition in a congested power network. Nash-Cournot game strategy has been used extensively to study the electricity market, especially in the presence of network constraints.

These researchers have mainly focused on how to determine the optimal strategies for Independent Power Producers (IPPs). But how to predict the change of market strategies adopted by the market participants has not yet been investigated.

2. CASE STUDY

A three-bus network is presented in this paper. There are three IPPs supplying one load. The load is at the same bus with most expensive IPP.

The profit maximization problem has the following constraints:

- Load demand should be satisfied
- Power flows should be confined to the transmission capacity limits.

In the simulations, the time scale is one year. The type of market is a real-time market with locational marginal pricing mechanism. The data of each generator and the load are shown as follows.

Table 1: Generators' capacity and cost

	Pmin (MW)	Pmax (MW)	Marginal cost (R/MWh)
IPP1	150	400	100
IPP2	100	300	150
IPP3	50	200	200

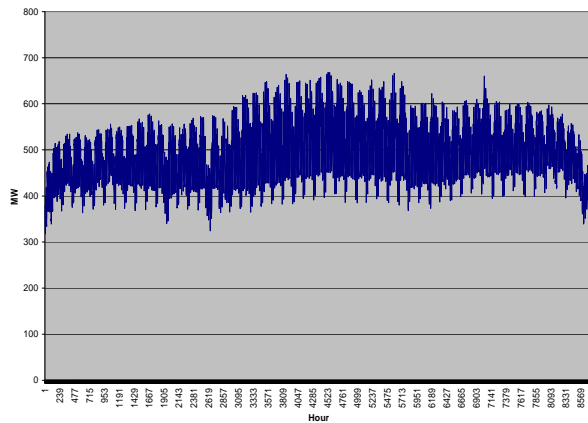The load curve is shown as follows.

Fig. 1. Load demand curve for 3-bus network.

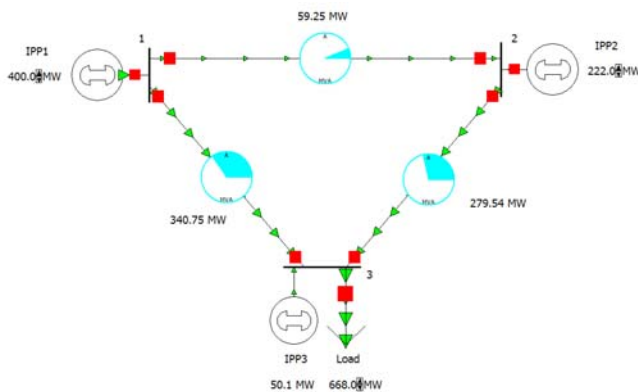When the load is at its peak with 668MWh, the load flow of the network is shown as follows.

Fig. 2. 3-bus network with peak load at 668MWh.

When the load reaches its peak, the power that is sent through the transmission line between bus1 and bus 3 (L1-3) is 340.75MWh.

To investigate the effect of transmission constraints on the market strategies, three transmission limits are applied to L1-3:

- Limit 1: 300MW
- Limit 2: 275MW
- Limit 3: 250MW

With each limit, we simulate three market strategies:

- Dynamic Shadow Pricing (DSP)
- Nash-Cournot (NC)
- DSP together with NC

Perfect competition model is also included in the simulation for comparison. Perfect competition and DSP are simulated at short-term basis NC and NC together with DSP are simulated at medium-term basis. A price cap of R500/MWh is applied to all simulations.

3. SIMULATION RESULTS

To illustrate the results from the simulations, the following market indices are used for discussion.

- Market price
- IPPs' net profits

When the line limit of 300MW is applied to L1-3, the market price and IPPs' net profits are shown as follows.
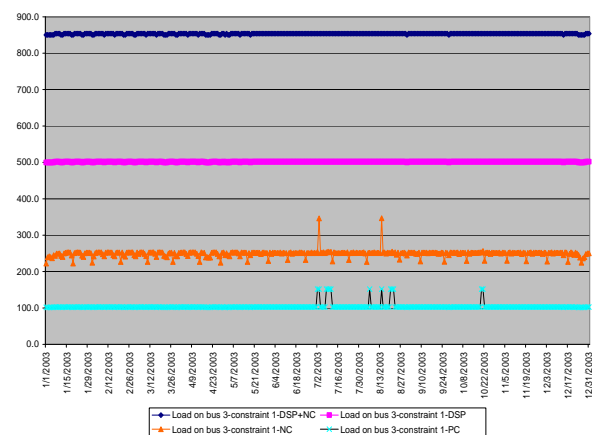
Fig. 3. Market price with limit 1 on L1-3 at 300MW.
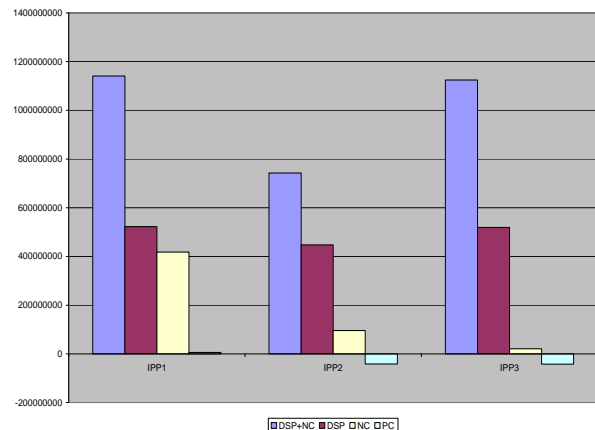
Fig. 4. IPPs' net profits with limit 1 on L1-3 at 300MW.

Figure 3 shows that the DSP together with NC is the optimal strategy, which gives the highest net profits to all IPPs.

Proceedings of the 19th Southern African Universities Power Engineering Conference
SAUPEC 2010, University of the Witwatersrand, Johannesburg
TOPIC C. POWER SYSTEMS

For a market to reach equilibrium, all rational IPPs should follow the same strategy. If one of these three IPPs changes its strategy, its profit will decrease. When the line limit of 275MW is applied to L-3, the market price and IPPs' net profits are shown as follows.
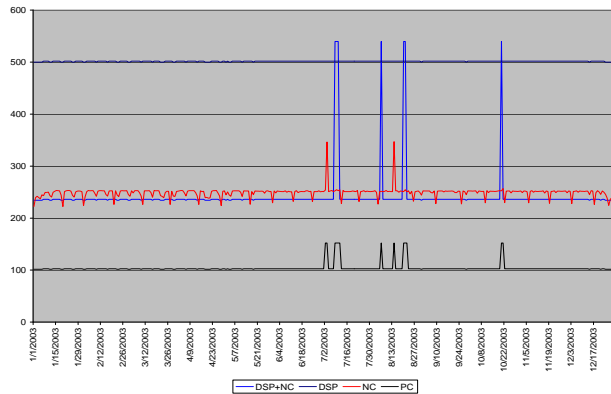
Fig. 5. Market price with limit 2 on L1-3 at 275MW.
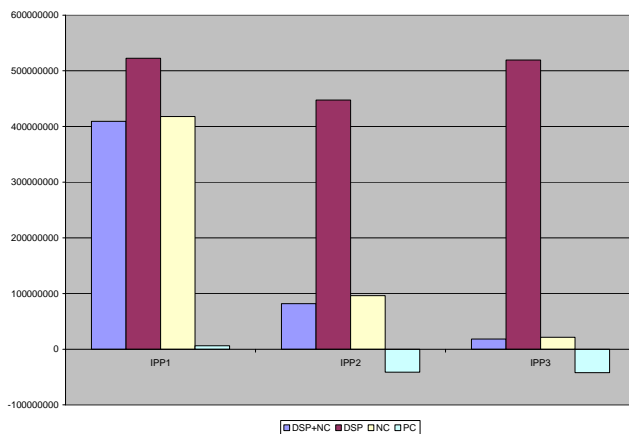
Fig. 6. IPPs' net profits with limit 2 on L1-3 at 275MW.
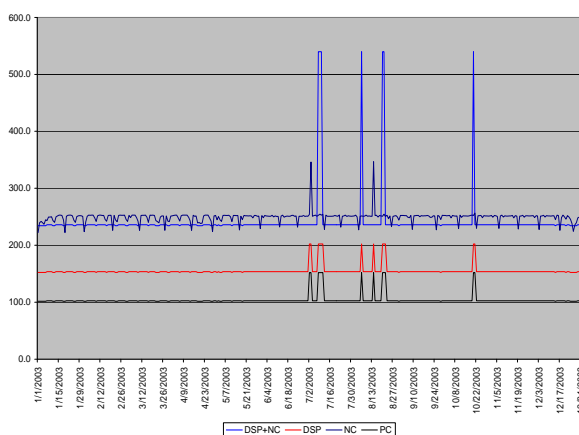
Fig. 7. Market price with limit 3 on L1-3 at 250MW.
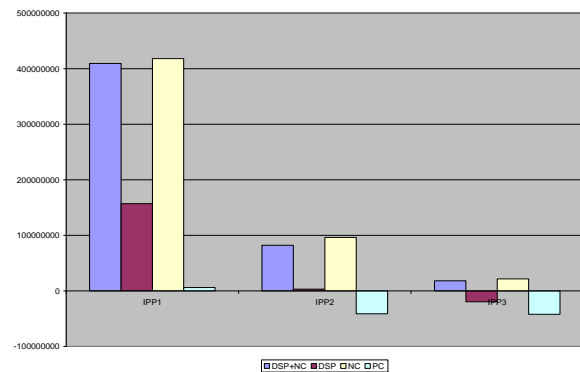
Fig. 8. IPPs' net profits with limit 3 on L1-3 at 250MW.

Figure 6 shows that DSP is the optimal strategy for profit maximization for all IPPs. When the line limit of 250MW is applied to L1-3, the market price and IPPs' net profits are shown as follows.

In figure 8, NC strategy gives the most profits to all IPPs. According to the figures 3 to 8, there is a similar pattern of the relationship between total profits and market price. When a certain market strategy brings the maximum profits to the IPPs, the related market price is always the highest.

This is due to one of the assumptions that the load demand has to be satisfied fully. This is different from the case in which the load is flexible (price dependent) by bidding a demand curve. In that case, load is deciding how much to take according to the market price. This gives the opportunity for the IPPs to withhold the total generation to push up the price.

When the load is not flexible (price independent), the generation withhold is among the IPPs themselves. It means that some IPPs will reduce their output, but this part of generation reduction has to be covered by other IPPs. More possibly, the cheaper generator will withhold capacity, and the more expensive generator will be dispatched for more power. As a result, market price rises in this case. However, this is subject to the transmission constraints.

The above simulation results show that IPPs may apply different market strategies at different transmission limits. With limit of 300MW, IPP has the incentive to apply both DSP and NC strategies. This maybe due to the fact that when line has less opportunities of congestion, there is more room for IPPs to play games. However, when the line L1-3's limit has decreased to 275MW, DSP has become the optimal strategy. In this case, market price reaches the price cap level.

Proceedings of the 19th Southern African Universities Power Engineering Conference
SAUPEC 2010, University of the Witwatersrand, Johannesburg

TOPIC C. POWER SYSTEMS

When the line L1-3's limit becomes 250MW, the optimal strategy is NC. This is because that IPP3 withholds capacity at its minimum stable level. And IPP3's net profit becomes negative if it chooses DSP strategy. This is also due to the generation withholding by IPP3 which has significantly reduced the effect of price increase in DSP strategy.

4. CONCLUSIONS

In this paper, the impact of transmission network constraints on the market strategies has been analyzed. In this study, real-time market is assumed to be operated with locational marginal pricing mechanism. It is important to mention that load satisfaction is one of the basic conditions. The results from the above cases have proved the expectation that, when network congestion is becoming more possible, the most expensive IPP will withhold its generation rather than raise its bid towards the price cap.

As a rational market participant, the cheapest IPP prefers to increase its bid rather than withholding its generation in the presence of transmission constraints. This is because when the load has to be fully covered, generation withhold is very risky. The results from the first two transmission limits have shown that DSP or DSP together with NC are the best choices for the IPPs. However, when the transmission limit has become very low, as the third transmission limit, generation withhold has become more effective in the market. This is actually the main threat to the load demand.

The main application of this study is to provide a possible judgment method to the system and market operators to identify and distinguish the possible gaming behaviors in a network with potential constraints. However, this study is based on the assumption that only one market strategy is adopted in one simulation each time. It means that it does not allow the IPPs to change strategies during the year of simulation. It requires all IPPs to adopt the same strategy simultaneously. The future research may focus on the dynamic change of market strategies for each IPP at different stages.

5. ACKNOWLEDGEMENTS

REFERENCES

[1] A. K. David and F. Wen, "*Market power in electricity market*", IEEE Transactions on Energy Conversion., Vol. 16, No. 4, December 2001, pp. 352-360

[2] L. Geerli, L. Chen and R. Yokoyama, "*Pricing and operation in deregulated electricity market by noncooperative game*", Electric Power System Research., 57, 2001, pp. 133-139

[3] D.J. Kang, J. Hur, Y.H. Moon, K.H. Chung and B.H.Kim, "*Bidding Strategy Determination by Defining Strategic Vector*", International Conference on Electrical Engineering., 2002, pp. 384-388,

[4] L. L. Lai (editor), "*Power System Restructuring and Deregulation,*". John Wiley & Sons. 2001.

[5] S. Oren, "*Economic Inefficiency of Passive Transmission Rights in Congested Electricity Systems with Competitive Generation*", The energy Journal 18 (1)., 1997, pp. 63-84

[6] G. Rothwell and Gómez, "*Electricity Economics: Regulation and Deregulation,*" Wiley-Interscience., 2003

[7] M. Shahidehpour and M. Alomoush, "*Restructured Electrical Power Systems: Operation, Trading, and Volatility,*" Marcel Dekker., Inc., 2001.

[8] H. Singh, "*Market Power Mitigation in Electricity Market*", Game theory applications in electric power markets, IEEE catalog number: 99TR136-0, IEEE power engineering society winter meeting., 1999, pp. 3-6

[9] S. Stoft, "*Using Game Theory to Study Market Power in Simple Networks*", Game theory applications in electric power markets, IEEE catalog number: 99TR136-0, IEEE power engineering society winter meeting., 1999, pp. 33-40

[10] B. Willems, "*Modeling Cournot Competition in an Electricity Market with Transmission Constraints*", The Energy Journal., Vol. 23, No 3, IAEE, 2002, pp. 95-125

Proceedings of the 19th Southern African Universities Power Engineering Conference
SAUPEC 2010, University of the Witwatersrand, Johannesburg

TOPIC C. POWER SYSTEMS

HVDC HARMONIC ANALYSIS USING TIME DOMAIN SOFTWARE

J Smith, WC Stemmet & G Atkinson-Hope

Cape Peninsula University of Technology

Abstract. The research work in this paper focuses on the evaluation and application of PSCAD time domain software for conducting harmonic analysis on integrated HVAC/HVDC power systems. Typically frequency domain software is used for conducting such studies. They however do not take the dynamic behaviour of the system components into account, only giving steady-state results. To overcome this problem time domain software is used. The PSCAD software was found to have shortcomings in its library tools in that established harmonic analysis indices are not directly generated. Where such shortcomings were found adaptive tools were developed, namely, "Compact Distortion Index Tool", "Compact Harmonic Component Power Calculation Tool" and "Apparent Power and True Power Factor Tool". These tools were applied in a case study using the CIGRE HVDC Benchmark system. Results were generated and it was found that the developed tools were effective for conducting harmonic analysis using time domain software.

Key Words: Time domain software, harmonic analysis, model development

1   INTRODUCTION

The non-linear behaviour of HVDC converters cause distorted voltage and current waveforms in the HVAC network to which it is connected. These drawbacks make it imperative to study the effect of harmonics as well as apply suitable mitigation solutions. Harmonics is a steady-state concept [1]. An integrated HVAC/HVDC system is however a time varying system and therefore traditional harmonic analysis software tools are not adequate for taking into account the dynamic behaviour of the different elements in such networks. A time domain software package is needed to conduct such studies.

Currently there is very little published on the study of the impact of harmonics in power systems which include HVDC systems. There is thus a need to research how to conduct harmonic analysis in the time domain.   The time domain software package that is used for this study is PSCAD/EMTDC. Tools are available in the library of this package for conducting studies but how to combine them so that established indices for analysis can be generated and simultaneously visualized is needed.

No individual and total harmonic distortion indices as well as *RMS* quantities for voltage and current are available as a single tool. Also no compact tool for generating results for individual and total powers for harmonics are present. Further there is no combined tool for the measurement of apparent power when harmonics are present and there is no single compact tool to give the true power factor.

To achieve these results harmonic analysis tools in the library were utilized and combined to develop adaptive tools to obtain established index results. Thus the contribution of this paper is the development of adaptive tools to simplify harmonic analysis procedures.

2   RESEARCH STATEMENT

The objective of this project is to design and develop compact tools and procedures for the purpose of conducting harmonic analysis that includes both harmonic penetration and resonance studies.

3   PSCAD SOFTWARE TOOLS

The time domain software package PSCAD/EMTDC version 4.2.1 has the following tools in its library [2].

3.1 Measuring Devices

To be able to conduct harmonic analysis, the voltages and currents in a network must be known [3]. PSCAD comes equipped with devices to measure the voltage, current, real and reactive power.

The first measuring device is the multimeter. This meter can measure instantaneous voltage and current as well as *RMS* voltage (V_{RMS}) [4]:

$$V_{RMS} = \sqrt{\sum_{h=1}^{h_{max}} (V_h)^2} \qquad (1)$$

It does not measure *RMS* current (I_{RMS}). This meter can be used both for single and three-phase and for measuring real and reactive power when harmonics are present. It can also be used to measure DC voltage and current.

The meter is connected in series at the point where the measurement is required. The meter is shown in Figure 1.

Fig. 1: Multimeter Measuring Device

This software also has dedicated meters for individual quantities (amps and volts). It comes equipped with an ammeter, line-to-line voltmeter and a phase-to-ground voltmeter. These are used as inputs to all the different harmonic analysis tools and are shown in Figure 2.
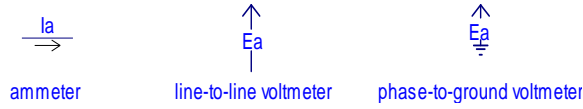
Fig. 2: Dedicated Measuring Devices

3.2 Fast Fourier Transform (FFT) Tool

To obtain the magnitudes and phase angles of the fundamental and harmonics of a waveform, the Fast Fourier Transform (FFT) tool is used.

This Fast Fourier Transform (FFT) can determine the harmonic magnitude and phase angle of the input signal as a function of time. The input signals are first sampled before they are decomposed into harmonic components. The main purpose of this tool is the decomposition of distorted waveforms (time domain into harmonic domain) to obtain individual harmonic components ($V_h \angle \theta_h °$ and $I_h \angle \delta_h °$).

The FFT tool requires an input from a measuring device and produces data outputs. In order to display the results it is necessary to combine the FFT with output channels one for each component. This tool is shown in Figure 3.
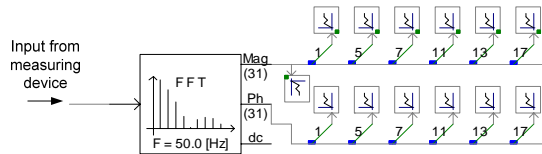
Fig 3: FFT Tool

3.3 Root-Mean-Square Index Tools
3.3.1 RMS Calculator Tool

To overcome the deficiency that the multimeter (Figure 1) is inadequate to measure I_{RMS}:

$$I_{RMS} = \sqrt{\sum_{h=1}^{h_{max}} (I_h)^2} \qquad (2)$$

A combination of tools is required to obtain I_{RMS}.
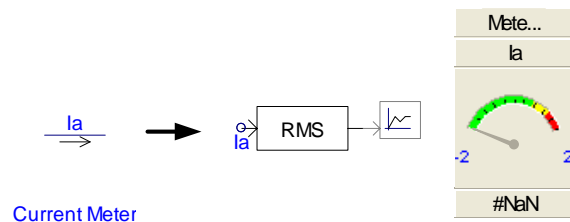
Fig 4: RMS Current Meter Tool

This tool will be called an *RMS* Current Meter Tool. The tool is made up of an ammeter (*Ia*) and a calculator (*RMS* calculator tool) together with an output channel and a control panel to display the results. This tool can also be applied for voltage measurement.

3.4 Harmonic Distortion Tool

For evaluating harmonic penetration the total (V_{THD} and I_{THD}) and individual harmonic distortion indices (V_{HD} and I_{HD}) of an input signal needs to be measured. The *THD* is a measure of the effective value of the harmonic components of a distorted waveform. It is the potential heating value of the harmonics relative to the fundamental and calculated by the following indices [4]:

$$\%V_{THD} = \frac{\sqrt{\sum_{h=2}^{h_{max}} (V_h)^2}}{V_1} \qquad (3)$$

$$\%I_{THD} = \frac{\sqrt{\sum_{h=2}^{h_{max}} (I_h)^2}}{I_1} \qquad (4)$$

The contribution to distortion by individual components is evaluated by the *HD* index:

$$\%V_{HD} = \frac{V_h}{V_1} \times 100\% \qquad (h>1) \qquad (5)$$

$$\%I_{HD} = \frac{I_h}{I_1} \times 100\% \qquad (h>1) \qquad (6)$$

To simultaneously measure these indices a combined tool is needed and will be called a Harmonic Distortion Calculator Tool. The main component of this combined tool is the harmonic distortion calculator and is shown in Figure 5.
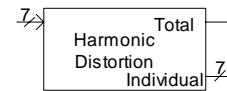

Fig 5: Harmonic Distortion Calculator

On its own it cannot be applied. Before the harmonic distortion can be quantified for a specific waveform (current or voltage) the waveform must first be put through a FFT tool and the output data is then fed to the harmonic distortion calculator. The outputs (total and individual) are then displayed on an output channel or on a bar graph (PolyMeter, Figure 12).

The developed harmonic distortion calculator is shown in Figure 6.
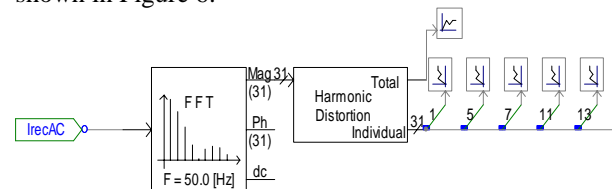

Fig 6: Harmonic Distortion Calculator Tool

TOPIC C. POWER SYSTEMS

Proceedings of the 19th Southern African Universities Power Engineering Conference
SAUPEC 2010, University of the Witwatersrand, Johannesburg

Also required for harmonic penetration studies is the measurement of V_{RMS} and I_{RMS}. Instead of individual methods being used (Figure 1 and 4) it was found that a more complete tool which can do all the indices simultaneously. Thus such a tool was developed and it makes analysis more compact and this saves screen display space on a PSCAD page. This tool can provide complex wave decomposition and provides the magnitudes as well as the phase angles of the various individual components. It can also calculate the individual as well as the total harmonic distortion indices and finally produce the *RMS* values for the input signal.

This developed tool is shown in Figure 7 and is for a current input (similarly for a voltage input).
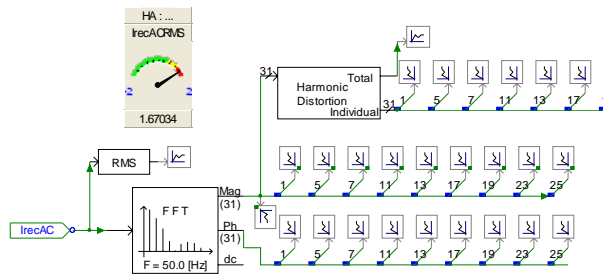
Fig 7: Compact Distortion Index Tool

3.5 Power Indices
A multimeter measures real and reactive power. These are calculated as follows [5]:

Total active power P_T (W).

$$P_T = \sum_{h=1}^{\infty} P(h) \qquad (7)$$

Total reactive power Q_T (var)

$$Q_T = \sum_{h=1}^{\infty} Q(h) \qquad (8)$$

A shortcoming of a multimeter is that it does not measure powers and phase angles per harmonic order nor does it give apparent power, displacement or true power factor quantities (*DPF* and *PF*).

To obtain these outputs (except *PF*) it was necessary to develop a compact tool for this purpose, specifically the power components and power factors per harmonic order.

The developed compact tool is shown in Figure 8. This is for fundamental frequency only. The same compact tool can be applied for all harmonic orders.
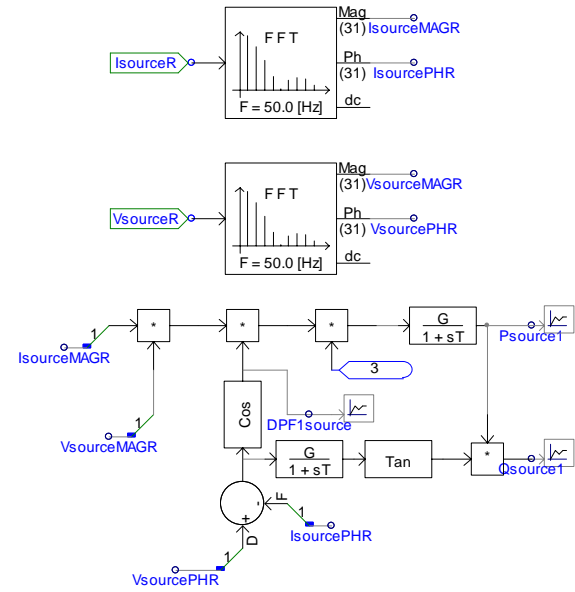
Fig 8: Compact Harmonic Component Power Calculator Tool

The voltage and current at the specific point are broken up into individual harmonic components by means of a FFT tool and are given in terms of magnitudes and phase angles. The tool applies (1) and (2) but the reactive power can also be obtained in terms of real power by means of (9) and this feature is added to the tool:

$$Q(h) = P(h)\tan(\phi_h) \qquad (9)$$

Current and voltage magnitudes are multiplied with each other as well as with the cosine of the difference between the current and voltage phase angles (which is φ_h). The multiplication of these elements produces the per-phase real power and needs to be multiplied by three to produce the total individual harmonic real power. This is fed to an integrator to eliminate ripple due to the time domain nature of the package.

The output from the integrator will produce the individual real power for the specified harmonic order. This real power is then multiplied with the tangent of φ_h to produce the individual reactive power for the specified harmonic.

When the cosine of φ_h is taken the *DPF* for the fundamental and power factor per harmonic order, $\cos(\varphi_h)$ for the rest of the frequencies are obtained. Thus the tool developed can produce individual power results for both real and reactive power as well as the *DPF* and $\cos(\varphi_h)$ power factors (Figure 8).

The multimeter produces total real and reactive results but no total apparent power nor true power factor.

Proceedings of the 19th Southern African Universities Power Engineering Conference
SAUPEC 2010, University of the Witwatersrand, Johannesburg

TOPIC C. POWER SYSTEMS

To measure these outputs the following equations are used to develop another compact tool (Figure 9):

$$S_T = V_{rms} \cdot I_{rms} \qquad (10)$$

$$PF = \frac{P_T}{S_T} \qquad (11)$$

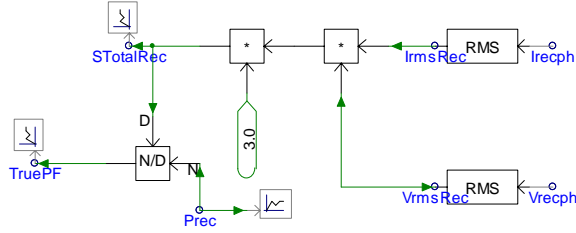This tool uses STotalRec and TruePF for total apparent power and true power factor, respectively, namely:

Fig 9: Apparent Power and True Power Factor Tool

3.6 Three-Phase to SLD Electrical Wire (Breakout) Tool

An essential requirement for harmonic penetration studies is that the analysis needs to be conducted on a per-phase basis. The node where the analysis needs to be conducted on the one-line-diagram must be separated into single-phases with the use of a "Three-Phase to single-line-diagram (SLD) Electrical Wire (Breakout) Tool" as shown in Figure 10.
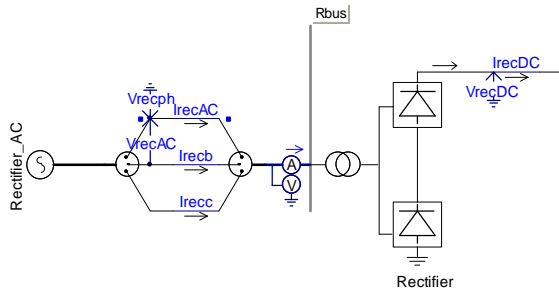
Fig 10: Three phases split into single-phase paths

This is an essential configuration for harmonic studies as all the developed tools are fed there from.

3.7 Impedance Scan Tool

To conduct harmonic resonance studies PSCAD comes equipped with an impedance scan tool, which allows the user to perform a frequency sweep at nodes in a system.

Its shortcoming is that the output data comes in the form of a text file. To obtain a sweep and see resonance points an additional tool is needed such as an external graphical analysis program (e.g. LiveWire). The application is shown in the case study.

4   CASE STUDY

The tools described in Section 3 are applied to the integrated HVAC/HVDC CIGRE Benchmark system [6], [7]. An ammeter and voltmeter are inserted in each path to measure the respective quantities and these are used as inputs to all the different harmonic analysis tools. The case study is conducted with the harmonic filters and reactive compensation installed.
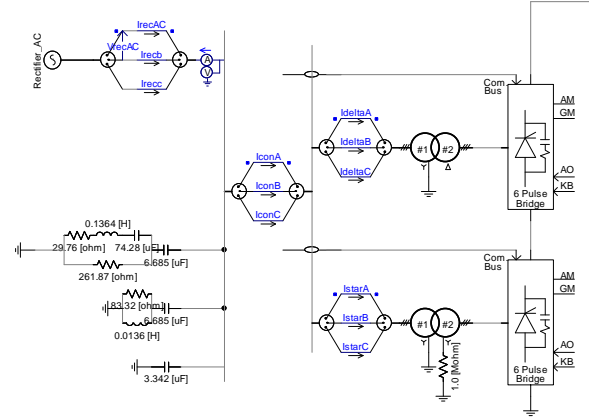
Fig 11: Case study diagram

Figure 11 shows the rectifier side. Four breakout tools are utilized to demonstrate the harmonic mitigation techniques. The 12-pulse configuration (two 6-pulse converters in series) uses a star-star and star-delta transformer configuration, harmonic filters and reactive compensation and the overall system is supplied from an AC source. The results of the harmonic analysis on the rectifier side are given for the four breakouts.
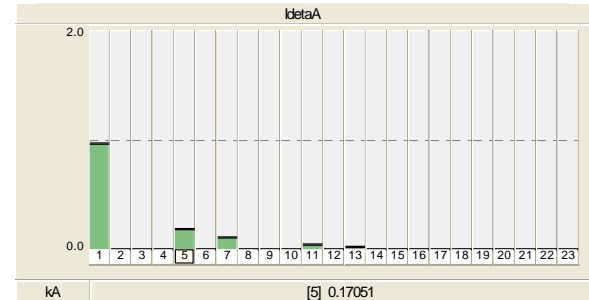

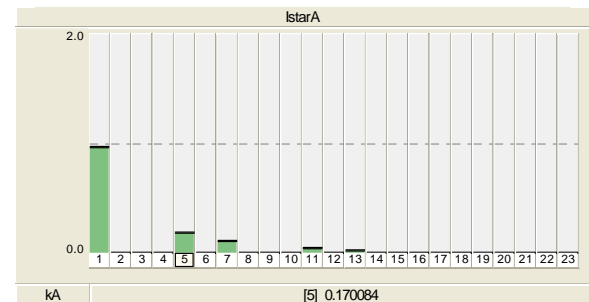Fig 12: Harmonic analysis on the primary of the Star-Delta transformer.

Fig 13: Harmonic analysis on the primary of the Star-Star transformer.

TOPIC C. POWER SYSTEMS

Proceedings of the 19th Southern African Universities Power Engineering Conference
SAUPEC 2010, University of the Witwatersrand, Johannesburg
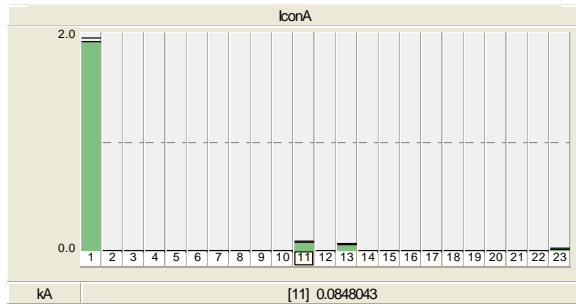
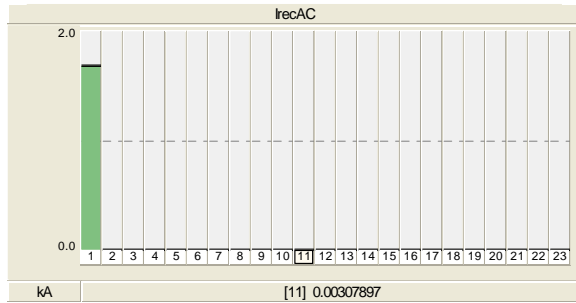Fig 14: Harmonic analysis on the AC input side of the HVDC system.

Fig 15: Harmonic analysis in the AC source path

From Figures 12 & 13 it can be seen that the converters each inject 5th, 7th, 11th and 13th harmonics. Figure 14 shows that the 5th and 7th harmonics are cancelled out by the combination of transformer configurations leaving 12th and 13th which is summed up. Figure 15 shows the analysis in the AC source path showing the importance of the harmonic filters which eliminates all the harmonics.

To further demonstrate harmonic analysis, only the AC source path breakout point is reported on. Four different categories for the analysis are used, they are:

a) Current harmonics (AC Fourier analysis including I_{HD}, I_{THD} and I_{RMS})

b) Voltage harmonics (AC Fourier analysis including V_{HD}, V_{THD} and V_{RMS})

c) Power components (individual and total powers).

d) Impedance scans (AC busbar).

4.1 Current Harmonics
The current harmonics are measured. The harmonic magnitudes and phase angles are noted and the individual and total harmonic distortion is calculated using the tools and checking by hand. Only one phase is examined. The output from the ammeter (IrecAC, Figure 11) is used as an input to the "Compact Distortion Index Tool" (Figure 7) which provides all the different indices required. The "FFT Tool" that is present in the developed tool provides the magnitudes and phase angles of the fundamental frequency and its harmonics. The FFT produces both magnitude and phase angle results and this can also be displayed on output channels as shown in Figure 16.
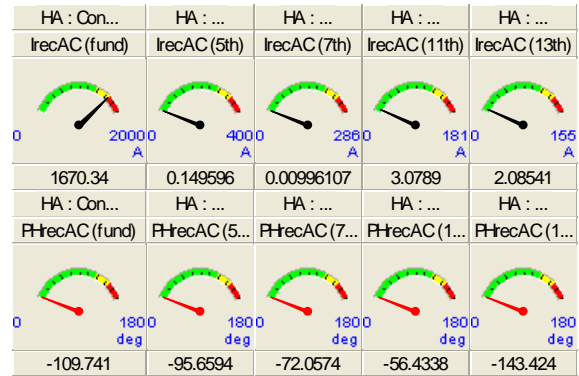

Fig 16: Rectifier AC current harmonic magnitudes

The harmonics are negligible and only the fundamental has a significant value due to harmonic filtering. The "Compact Distortion Index Tool" (Figure 7) is used to obtain the total and individual harmonic distortion indices. To prove the effectiveness of the developed tool these different indices are checked using a MathCAD supported hand calculation method.

Table 1: Rectifier current distortion results

Harmonic index results	PSCAD	Hand calculation
I_{HD11}	0.18433%	0.1843%
I_{HD13}	0.12485%	0.1248%
I_{HD23}	0.04300%	0.0430%
I_{HD25}	0.03439%	0.0344%
I_{THD}	0.26255%	0.2293%
I_{RMS}	1.6703 kA	1.6703 kA

The individual current distortion and I_{RMS} is identical for both the hand calculation and the PSCAD results. Small discrepancies exist for the total current harmonic distortion due to the fact that the hand calculation only considered the characteristics harmonics whereas PSCAD includes the non-characteristic harmonics (small quantities).

4.2 Voltage Harmonics
The same approach to that of the current harmonics is followed. The harmonic magnitudes and phase angles are examined and the individual, total voltage harmonic distortion and RMS voltage are calculated. The results obtained from the developed tool (Figure 7) when applied to voltage harmonics on the rectifier side as well as the results from hand calculations are shown in Table 2.

Table 2: Rectifier voltage distortion results

Harmonic index results	PSCAD	Hand calculation
v_{HD11}	0.773926%	0.7739%
v_{HD13}	0.615185%	0.6152%
v_{HD23}	0.34933%	0.3493%
v_{HD25}	0.298717%	0.2987%
v_{THD}	1.09209%	1.0903%
v_{RMS}	347.536 kV	347.54 kV

Proceedings of the 19th Southern African Universities Power Engineering Conference
SAUPEC 2010, University of the Witwatersrand, Johannesburg

TOPIC C. POWER SYSTEMS

4.3 Power Indices

Here individual and total powers (real and reactive) as well as the total apparent power are measured. A multimeter is inserted to measure the total real and reactive power (Figure 11). The developed "Compact Harmonic Component Power Calculator Tool" (Figure 8) for individual harmonic measurements is used and the power for each frequency is obtained. The results from the developed tool are shown in Figure 17.
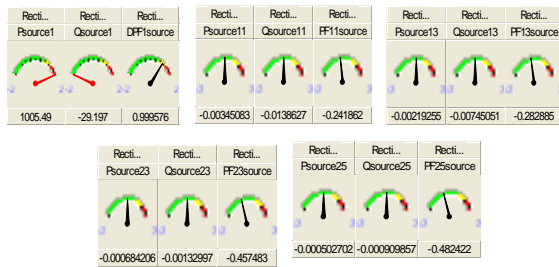
Fig 17: Rectifier individual harmonic results

To evaluate the power results obtained from the multimeter, (7) and (8) are applied using the individual harmonic components shown in Figure 17. They are summed together and compared to the multimeter as shown in Figure 18.
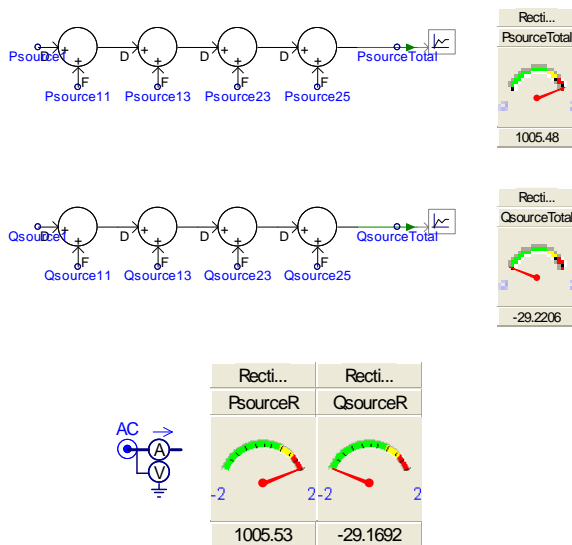
Fig 18: Comparison of multimeter results

Figure 18 show that the developed tool gives the same results to that of the multimeter. This proves that the multimeter is measuring complex power.

4.4 Impedance Scan

An impedance scan is performed at the rectifier AC bus as shown in Figure 19. The Zscan only provides a text file output and this is a disadvantage of PSCAD as no frequency sweep plot is directly obtained.
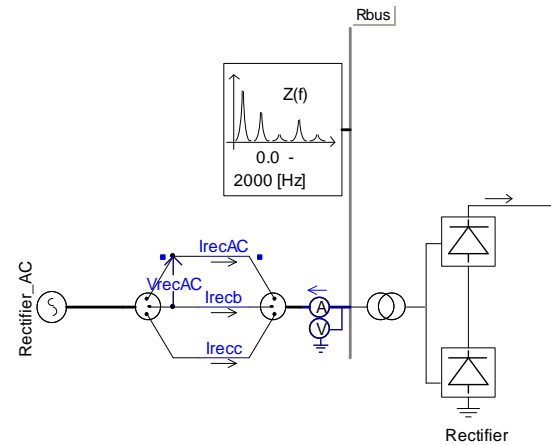
Fig 19: Impedance scan performed

An external graphic output program called "LiveWire" is needed to obtain a sweep. The "LiveWire sweep" result for the rectifier is shown in Figure 20.
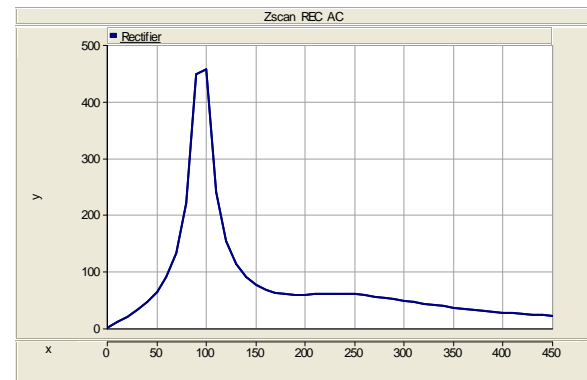

Fig 20: Impedance scan performed (Rectifier bus)

The results obtained for the AC source path of inverter side are as follows:

Table 3: Inverter current distortion results

Harmonic index results	PSCAD	Hand calculation
I_{HD11}	0.23089%	0.2342%
I_{HD13}	0.18087%	0.1809%
I_{HD23}	0.05341%	0.0534%
I_{HD25}	0.04244%	0.0425%
I_{THD}	0.43876%	0.3037%
I_{RMS}	2.4298 kA	2.4295 kA

Again almost similar results are obtained.

The voltage harmonic results for the inverter side are tabulated in Table 4.

Table 4: Inverter voltage distortion results

Harmonic index results	PSCAD	Hand calculation
v_{HD11}	0.616412%	0.6164%
v_{HD13}	0.452116%	0.4521%
v_{HD23}	0.352654%	0.3527%
v_{HD25}	0.271904%	0.2719%
v_{THD}	0.907167%	0.8847%
v_{RMS}	226.356 kV	226.38 kV

Proceedings of the 19th Southern African Universities Power Engineering Conference
SAUPEC 2010, University of the Witwatersrand, Johannesburg

TOPIC C. POWER SYSTEMS

When a scan study is conducted on the inverter side and plotted by "LiveWire" a similar response to the rectifier side (94 Hz) is obtained and shown in Figure 21.
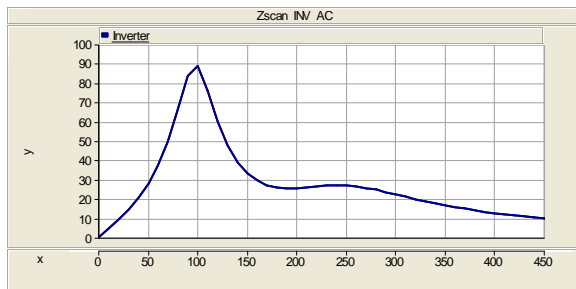

Fig 21: Impedance scan performed (Inverter bus)

5 CONCLUSIONS

When conducting harmonic analysis on integrated HVAC/HVDC power systems time domain rather than frequency domain software is found to be more suitable as it takes into account the dynamic behaviour of its components. It is also required to use established indices to assess the impact of harmonics on such a system. The toolbox in the PSCAD library was evaluated to ascertain if there are any tools available for directly generating these indices. The following measuring devices (multimeter, ammeter and voltmeter), FFT, Harmonic distortion, RMS calculator and Zscan tools were found.

When evaluating these tools it was found necessary to develop combined tools to directly generate established indices making harmonic analysis more user-friendly and effective. It was found that the following tools needed to be developed.

Firstly, a "Compact Distortion Index Tool" was developed. Its advantage is that instead of individual methods being used which clutter the work space a more complete tool which can do all of the indices in on go was more beneficial. It makes analysis more compact and easier to be accommodated on a work space. This tool can provide complex wave decomposition and provide the magnitude as well as the phase angle of the different individual components. It can also calculate the individual as well as the total harmonic distortion indices and finally produce the RMS values for an input signal.

This was followed by the "Compact Harmonic Component Power Calculation Tool". This tool produces the total individual harmonic real powers as well as the individual reactive powers for the specified harmonics. Next, the "Apparent Power and True Power Factor Tool" was developed combining these indices making these measurements visible.

A case study was conducted and the application of the tools has been demonstrated. The HVDC CIGRE Benchmark network was used for the case study and harmonic analysis results were obtained on the rectifier and inverter sides. The tools were also very effective for demonstrating the harmonic mitigation techniques applied to HVDC systems.

The results were similar to hand calculation results, thus proving their effectiveness of the modelling and simulation studies.

An important factor is the establishment of resonance in a HVDC system. For this purpose the Zscan tool was evaluated. It was found that it only provides a text output file and no graphical representation of a frequency sweep versus impedance. It was further found that an external graphic program (LiveWire) can be used to generate the desired plot.

These developed tools are innovative and recommended for use when conducting harmonic analysis on integrated HVAC/HVDC power systems.

REFERENCES

[1] S. J. Ranade (Chairman, Editor), "Modelling and Simulation of the Propagation of Harmonics in Electric Power Networks, Part I: Concepts, Models and Simulation Techniques", IEEE Transactions on Power Delivery, Vol.11, No.1, January 1996, pp. 452-465.

[2] Manitoba HVDC Research Centre. 2005. "PSCAD User's Guide" v.4.21. Winnipeg Canada.

[3] J. Arrillaga and N.R. Watson, "Power System Harmonics", 2nd Edition, pp. 2, 2003. ISBN: 0-470-85129-5.

[4] R.C Dugan, M.F. McGranaghan, S. Santoso and H.W. Beaty," Electrical power systems quality, MacGraw-Hill, 2nd Edition, pp.175-185, 2002, ISBN: 0-07-138622-X.

[5] J. Arrillaga, B. Smith, R. H. Watson & A. R. Alan, ".Power System Harmonic Analysis" pp 134-137, 1997. ISBN: 0 471 97548 6.

[6] M.Szechtman, T. Wess and C.V.Thio, "First benchmark model for HVDC control", Electra, No. 135, pp.55-73, 1991.

[7] M.Szechtman, T. Wess and C.V.Thio, "A benchmark for HVDC studies", International conference on AC and DC power transmission, pp.374-378, 1991. ISBN:0-85296-517-6.

BIOGRAPHIES

- **Johan Smith**
  E-mail: smithj@cput.ac.za
- **Willem Stemmet**
  E-mail: stemmetw@cput.ac.za
- **Prof. G. Atkinson-Hope**
  E-mail: atkinsonhopeg@cput.ac.za

Proceedings of the 19th Southern African Universities Power Engineering Conference
SAUPEC 2010, University of the Witwatersrand, Johannesburg

TOPIC C. POWER SYSTEMS

DEVELOPMENT OF SOFTWARE TOOLS FOR OPTIMAL PLACEMENT PHASOR MEASUREMENT UNITS IN ELECTRICITY NETWORKS

M Shilubane*, S Chowdhury* and S P Chowdhury*

*University of Cape Town, Electrical Engineering Department,Cape Town, South Africa.

Abstract. For reliable and secure operation of power utilities, especially with distributed generation, it is essential to know the state or condition of the system. For this purpose, phasor measurement units (PMUs) are used in electricity networks to achieve complete system observability by obtaining time synchronised measurements of voltage and current phasors at substation buses. The availability and accuracy of these measurements are of key importance for wide area monitoring, protection and control (WAMPAC) applications. It is however not economical to place a PMU at every bus of a in the network. Therefore they must be optimally placed at strategic locations to maximise system observability with minimum PMUs. Thus PMU placement takes the form of an optimization problem which can be solved by several optimization algorithms with different levels of performance. In this paper, the authors develop relevant software and compare the performance of two optimization techniques for PMU placement, viz. Genetic Algorithm (GA) which is an evolutionary technique and Binary Integer Linear Programming (BILP) which is a numerical technique. Both software are tested for a 4-bus hypothetical system and two IEEE test systems. Results indicate the superiority of GA over BILP in optimally placing the PMUs in the most cost-effective way.

Key Words. Phasor Measurement Unit, optimal placement, optimization techniques, Genetic Algorithm, Binary Integer Linear Programming.

1. INTRODUCTION

The ideal state of operation of a power system implies that it is operating normally with all electrical quantities, specially voltage, frequency, active power and reactive power within specified values. However, power systems may deviate from their ideal operating condition due to disturbances such as faults, loss of generation, loss of bulk load, etc. In that case, the disturbance event should be detected and dealt with such that ideal state of operation of the system is restored. Hence, the system should be continuously monitored for any devitation in the electrical quantities, operating states identified and necessary preventive actions initiated [1]. This requires a 'well designed and coordinated protection and control strategy' [4] for maintaining the normal operating state of the system and hence complete global vision of the power system. Since the development of Global Positioning System (GPS), Phasor Measurement Units (PMUs) have been utilized to obtain time synchronized measurements of voltage and current phasors from geographically distant locations to get a real-time snapshot of the wide area network [2]. Currently, with more dispersed generation coming into the utility grids, the concept of wide area monitoring protection and control (WAMPAC) with time synchronized phasor measurement is gaining importance gradually in power utilities.

A PMU is basically a measurement unit that submits AC voltage and current phasors up to 50/60 Hz [6]. These phasors are synchronized through a GPS. A Fast Fourier Transform is performed on two or more different signals from respective substations, which are then displayed on the same phasor diagram. It takes in both analogue and binary inputs but gives out binary outputs. PMUs have trigger functions for: (i) Abnormal frequency, (ii) Overcurrent and (iii) under voltage. They are designed to comply with the IEEE standard 1344-1995, which is the synchrophasor data format [6]. It is stated by Decker et al. [5] that PMUs complement the data acquisition functions of traditional protection components such as protective relays, fault recorders and the Supervisory Control and Data Acquisition (SCADA) systems.

PMUs have several applications as listed below: [1,7-15]:
(a) Real-time monitoring and control
(b) Post-Disturbance analysis
(c) Inter-area oscillation monitoring, analysis and control
(d) State estimation and Improving Observability
(e) Power plant monitoring and integration
(f) Bad data detection
(g) Real-time monitoring and control
State estimation and real time monitoring and control are especially important as they enable the operator to view the power system in real-time and then determine the state of the system from the measurements obtained from the PMUs. This consequently helps to identify impending system abnormalities in due time and enable the operators to take preventative action against faults and voltage collapse conditions.

For observing a system, these units could be placed on every bus at a substation, but then the implementation becomes uneconomic [3]. For cost-effective implementation, the number of PMUs to be placed in a power system should be minimized

TOPIC C. POWER SYSTEMS

Proceedings of the 19th Southern African Universities Power Engineering Conference
SAUPEC 2010, University of the Witwatersrand, Johannesburg

for optimizing the cost of their deployment. Thus PMU placement problem can be formulated as a constrained optimization problem where objective is to achieve complete system observability with minimum number of PMUs placed at some strategic locations. In this paper, the authors discuss the importance of PMUs in power system applications, survey different PMU placement techniques in use, develop software tools for PMU placement using two different methods and compare the performance of these two methods in placing PMUs in a test system and two IEEE test systems.

However, the problem of PMU placement is broad. The PMUs can be placed for complete observability for the following scenarios: (a) placement without conventional measurements, (b) placement with power injections and flow measurements and (c) placement with loss of PMU. In this paper, the authors consider scenario (a) only while scenarios (b) and (c) would be undertaken as future work. The authors also assume that the test systems have no existing PMUs.

2. REVIEW OF PMU PLACEMENT TECHNIQUES

Several optimal PMU placement techniques have been reported in existing research literature. Some of these are discussed in this section.

2.1 Binary Search Algorithm

Binary search algorithm in used in reference [12] for obtaining the locations for the minimum number of PMUs. The algorithm is exhaustive as it all the possible combinations through a binary search. While searching, the algorithm increments the number of PMUs by one if the system is found to be unobservable and decrements it by one if the contrary occurs. This ensures that only the minimum number of PMUs is found as a solution. Under 'Observability under single branch outage' condition, the already available PMU location candidates are examined for each single branch outage. A branch is disconnected one at a time and if the system remains observable the PMU combination is labelled as a candidate or solution [12]. In [19] an event detection method is used for branch outage or line outage. This is done using the PMU, transmission line and transformer data.

2.2 Binary Integer Linear Programming (BILP)

References [13], [16] and [17] report on the application of BILP for optimal PMU placement. In [16] the method is applied to the IEEE 14 system for finding the PMU placement locations. Results indicate that by knowing the voltage and branch currents at the nodes with the PMUs and by using Ohm's law and Kirchhoff's law, the state of the entire bus system can be determined. Constrained problem formulation with this method for three cases, viz., non-conventional power flow, conventional power flow and with injection measurements is detailed in [13], [16] and [17].

2.3 Genetic Algorithm (GA) and Immunity Genetic Algorithm (IGA)

Reference [18] reports on the applications of GA and IGA for optimal PMU placement. IGA is a modification of the well-documented GA method. GA has two operators, mutation and crossover, which ensure the optimization of a particular individual. This analogy evolves from the fact that when a species breeds, a formulation of new genetics takes place from generation to generation. This results in the transformation of the species [18]. Unfortunately, these operators can cause degeneracy hence the modification to IGA is required.

IGA problem is formulated by introducing two operators to the GA, viz., the vaccination and the immunity operators. This comes from the analogy of the natural immune system which defends the body against germs. In the same way, a vaccinated body is better able to resist bacteria or it results in the modification of genes of an individual to obtain higher fitness [18]. Thus the IGA is able to restrict the operators of the GA from transforming the individuals beyond their original characteristics. The Vaccines are as follows:

(i) Vaccine 1: The buses with one line incident to them should not have any PMU. This is in accordance with the fact that a PMU at a bus reveals not only information about that particular bus but also of the branches incident to the PMU bus and any other buses the branch might be connected to. So in order to find the optimal number of PMUs, they must be placed at those buses that have more than one branch incident to them. This is illustrated in reference [18].

(ii) Vaccine 2: A PMU can be installed on the other side of the bus with only one line incident to it provided the bus has zero-injection measurements.

(iii) Vaccine 3: A PMU should not be placed at a zero-injection bus although sometimes the topology of a system might dictate that placing a PMU at a zero-injection bus would result in an optimal solution.

2.4 Topology Method

Most conventional power networks today are provided with traditional measurement and protection systems. Thus, if new PMUs are installed in that system, their functions are merely

to enhance the state, visualization and control of the power system or to complement the SCADA system. The topology method may be more effective where there are existing measurements and where a few observable islands can be formed within the system [15,16]. This method strategically places PMUs by merging observable islands. In this method, only buses on the boundary of the island are eligible for a PMU installation. This process of optimization involves two steps: (i) performing a numerical observability analysis to determine the observable islands and (ii) determining the boundary buses where the PMU can be placed. Reference [16] suggests that desirable location might be the bus that is connected to a maximum number of other islands.

2.5   Tree Search Technique

The concept of incomplete observability is explored in reference [20]. Reference [20] describes this as 'the depth of incomplete observability'. Here the states of all the buses are not necessarily known as there are insufficient PMUs to make the system completely observable. The credibility of this concept lies in the findings that less PMUs are required but also that the unobservable buses can be estimated from the observable and the calculated buses. Therefore in reference [12], a PMU placement technique is developed for this purpose. To achieve placement, a spanning tree and search tree technique is used. It is applied in such a way that a certain depth of unobservability is achieved. In the Fig.1 below [20], buses B and F are observable while A, C, E and G are calculated buses. However bus D is unobservable. This illustrates a depth of one unobservability.
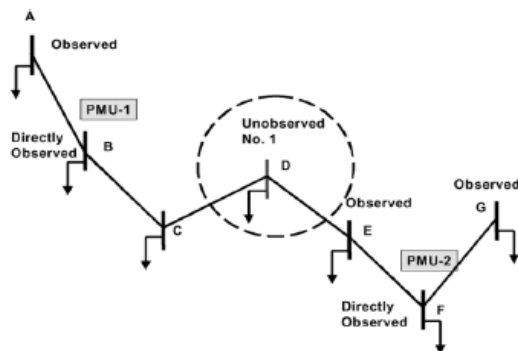
Fig.1: Depth of one observability [20]

This search technique involves 'walking' along the branches of a spanning tree. The search for PMU locations is terminated only when all the possible tree links have been traversed and the route has led back to the root node.

2.6   Comparison of Different PMU Placement Techniques

Table-1 summarises the comparative advantages and disadvantages of different PMU placement techniques. It is evident from Table-1 that the PMU placement techniques are not without disadvantages. It is argued by a number of researchers [8,12,17] that integer programming is mathematically challenging owing its non-linear equations. This technique however takes less computation time to perform the optimization. It is argued in [18] that evolutionary techniques such as Simulated Annealing (SA) may require much greater time to reach a near global minimum and for large power systems. It is a real disadvantage for large power systems. However its advantage is that it eliminates the problem of local minima. Binary search technique is computationally simple and guarantees a timely solution, though the method is exhaustive.

Table-1 : Summary of Advantages and Disadvantages of PMU Placement Techniques [8,12,16,17,18]

Technique	Advantages	Disadvantages
Binary Integer programming	Less computational time[8]	Constraints are non-linear[16]
		Can be trapped in the local minima [8]
Binary search	Exhaustive search	May be time consuming
Topology method	Simple logic and PMU implementation	Suitable only for power systems already equipped with a few observable islands
Evolutionary techniques		
Genetic algorithm	Local minima not a problem	For large power systems, SA is computationally burdensome and may consume a lot of time before reaching a global minimum [17] Robust Adaptable, applicable to various modelling problems [21]
Simulated Annealing	Constraints are mathematically simpler [8]	Careful tuning of free parameters required to reach

Choice of PMU placement technique is not only dictated by the characteristics of the technique but also by the type of application and the size of the power system. Another factor to be taken into consideration is the state of the system itself, e.g. whether the system contains existing PMUs. In this paper, the authors have chosen Genetic Algorithm (GA) which is categorized as an evolutionary technique and Binary Integer Linear Programming (BILP) which is a numerical technique. Both software are tested on a hypothetical 4-bus test system, IEEE 14-bus system and IEEE 30-bus system. Software development in GA and BILP are detailed in the following sections. For both approaches, only the case of placement without flow and zero injection measurements is considered.

Proceedings of the 19th Southern African Universities Power Engineering Conference
SAUPEC 2010, University of the Witwatersrand, Johannesburg

TOPIC C. POWER SYSTEMS

3. DEVELOPMENT OF GA SOFTWARE

The GA code for PMU placement [21] is developed as follows:

t=0

      Input a *connectivity matrix A*

      Initialize a population P (t)

           While not finished do

           t=t+1

      Evaluate P (t) for *observability* through the *fitness function* to be minimized

      Perform *selection* according the fitness scores

      Perform *crossover* to produce a new population

      Perform *mutation*

       end

Each italicized terms are explained in the following paragraphs.

3.1 Formation of Connectivity Matrix

Connectivity matrix is a node-node matrix whose contents are 0s and 1s. An entry of 1 indicates a connection between nodes or buses while 0 means no connection. This matrix is deduced from the topology of the system on which the PMUs are to be placed. The candidate solutions are each tested using this matrix. The 4-bus test system is shown in Fig. 2 below.
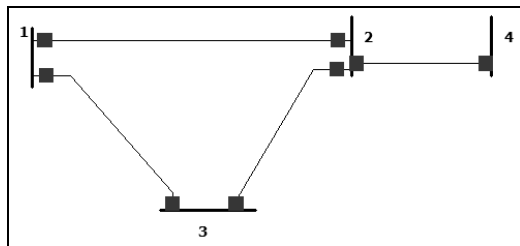
Fig.2: 4-bus test system

For this system the connectivity matrix takes a 4 x 4 form as shown below:

Node	1	2	3	4
1	1	1	1	0
2	1	1	1	1
3	1	1	1	0
4	0	1	0	1

3.2 Initial Population Generation

An initial population of individuals is created. The individuals are represented as a binary string of length n, where n is the number of buses in a power system. These individuals are each a candidate solution. For example, a candidate string for the 4-bus system is:
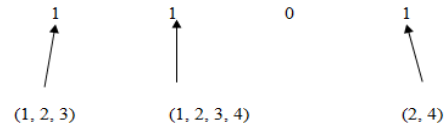
In the string, the bit positions indicate the bus numbers and a binary 1 represents a PMU placement at that bus number. Thus in the above string, PMUs are placed in buses 1, 2 and 4.

In the software, an initial population of a 100 is generated by creating a *(N_pop×N_bus)* matrix consisting of random binary strings, where, *N_pop* is the number of populations and *N_bus* is the numbers of buses in the system.

3.3 Observability Analysis and Fitness Function

The objective of PMU placement problem is to minimize the number of PMUs to be placed in the system under the constraint of full system observability. Thus in GA, a specific objective function or fitness function is be specified. The fitness scores from the function indicate the fitness of each candidate solution. In this study, an objective function *C* and fitness function *f* , as given by Equation (1) and (2) respectively are adapted from reference [18]

$$C=w1*N\_pmu+w2*N\_ou \qquad (1)$$
$$f=inverse(C) \qquad (2)$$

The best results are recorded for *w1=1* and *w2=3*. The candidate solutions with the lowest fitness scores are undesirable as it means that either *N_pmu* or *N_ou* is high [7]. This also means that the selection for the next population should be based on these scores as the objective is to generate a better, fitter population for the next generation, which will eventually end up in a convergent solution, which is the fittest. In this study, this is achieved by updating the best fitness in each generation. The corresponding string is also updated.

To define the above function its inputs *N_pmu* and *N_ou* must be determined. This is done using the population and the connectivity matrix. A flowchart of determining these inputs and thus testing for observability is included in the Appendix as Fig. A-1.

It is from the connectivity matrix A that the number of buses that are observed by a certain bus *b* is determined. For example, the connectivity matrix for the 4-bus system indicates that placing a PMU at bus 1 enables the system to observe buses 1, 2 and 3. Again a PMU at bus 2 enables the system to see buses 1, 2, 3 and 4. From bus 3, it is possible to observe buses At 1, 2 and 3 while from bus 4, buses 2 and 4 can be observed. This means that

each candidate solution string should be assigned the number of buses it allows the system to see according to its position. As an example, the authors consider a random solution string X as shown below:
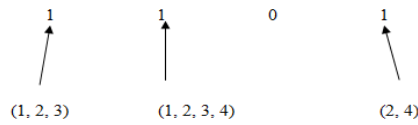
This string places a PMU at bus 4 and allows the system to see two buses. In this case N_ou is 2 and N_pmu is 1. From the topology of Fig. 2, it is clear that this string does not allow the system to observe the state of buses 1 and 3. The fitness value here with $N\_pmu = 1$ would be 0.143. Thus it is deduced that the strings with a large number of N_ou result in a very small fitness value. But in practice, highest fitness values are desired and the strings corresponding to these are more likely to be chosen as parents in the selection process.

3.4 Selection

In selection process, out of a population, the individuals with the better fitness scores are chosen as parents for the next generation.

The roulette wheel method is used to perform selection in this software. The roulette wheel represents all the strings of the current population on a wheel according to their fitness values. The best fitness value occupies the largest portion in the wheel and the probability of selection is proportional to the fitness value [21]. In this study, this is illustrated using the following matrix consisting of the candidate solution set with the corresponding fitness values:

Candidate string	Fitness value
1 1 0 1	0.3
0 0 0 1	0.143
0 0 1 0	0.25
1 1 1 1	0.25
1 0 1 0	0.2
1 0 0 1	0.5

The corresponding roulette wheel is shown in Fig. 3 below.
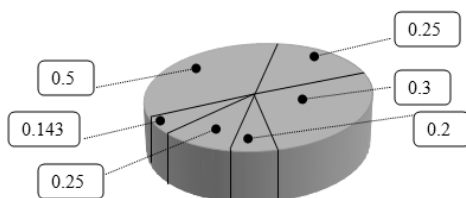
Fig.3 : Roulette wheel representation

The string thus selected is a parent and is then made to crossover with another selected string to produce children. Since the selection is random,

some strings are selected more than once as parents.

3.5 Crossover

Each parent performs a crossover with the next parent to form two children. In this study, single-point crossover is used. To illustrate this crossover two 7-bit long parent strings, String 1 and String 2 are considered as shown below:

String1: 1 1 0 0 1 1 1

String2: 1 1 1 0 1 0 1

The crossover point is chosen randomly.   If crossover point is 2, the resulting children are:

parents	Children
1 1|0 0 1 1 1	1 1|1 0 1 0 1
1 1|1 0 1 0 1	1 1|0 0 1 1 1

The parents merely swop their tails, which are demarcated by the crossover point. In this way, a new set of possible solutions is obtained. However in keeping with the natural process of evolution the strings must be mutated.

3.6 Mutation

The mutation probability [22] used is the reciprocal of N_bus. A random number is generated. If it is bigger than the mutation probability, then the genes which were 1s become 0s and vice versa. At this stage, one generation is complete and the next goes in with the mutated children as the new candidate strings. In every generation, the best fitness value is stored and updated with its corresponding string. This leads to an optimal solution.

4. DEVELOPMENT OF BILP SOFTWARE

BILP software is implemented in MATLAB. The PMU placement objective function is stated in Equation (3) as [16, 17, 22, 23, 24] :

$$\text{Minimize } \sum_i^m x_i, \quad \text{while } f.x \geq 1 \qquad (3)$$

This objective function must minimize the sum of x as long as $f.x$ is greater than 1. In this problem constraints must ensure that $f.x \geq 1$. This technique is implemented for 4-bus test system as follows:
Given a node-to-node connection matrix A of the form,

Node	1	2	3	4
1	1	1	1	0
2	1	1	1	1
3	1	1	1	0
4	0	1	0	1

Proceedings of the 19th Southern African Universities Power Engineering Conference
SAUPEC 2010, University of the Witwatersrand, Johannesburg

TOPIC C. POWER SYSTEMS

the constraints are formed as follows:

$$f(X) = A.X$$
$$=f1=x1+x2+x3 \qquad \geq 1$$
$$f2=x1+x2+x3+x4 \qquad \geq 1 \qquad (4)$$
$$f3=x1+x2+x3+x4 \qquad \geq 1$$
$$f4=x2+x4 \qquad \geq 1$$

Equation(4) implies that for observing node 1 or bus 1, PMU must be is placed at either bus 1, 2 or 3. The 1 on the right hand side of the inequality ensures that there is at least 1 PMU placed at this node or bus. For MATLAB implementation, the constraints are modified as inequalities of the form $A.x \leq b$. This is done by multiplying Equations(4) by -1 to give Equation (5) as follows:

$$-f(X) = -1 \, x \, A.X$$
$$= -f1=-x1-x2-x3 \qquad \leq -1$$
$$-f2=-x1-x2-x3-x4 \leq \quad -1 \qquad (5)$$
$$-f3=-x1-x2-x3-x4 \quad \leq -1$$
$$-f4=-x2-x4 \qquad \leq -1$$

The BILP algorithm implemented in MATLAB only minimizes x and not the sum of x. Therefore, the code is extended to do both. Reference [20] indicates that PMUs need to be installed at 1/5 to 1/3 of the number of buses for the system to be observable. These values are used as the stopping criteria for the test systems. The overall flowchart for BILP software is shown in Fig. A-2 of Appendix A.

5. RESULTS AND DISCUSSION

5.1 Results of GA Technique

Table-2, 3 and 4 shows the results for 4-bus test system, IEEE 14-bus system and IEEE 30-bus system respectively for GA technique.

Table-2: GA Results for 4-Bus System

# of branches	#PMUs	Location of PMUs	Time to converge	Number of generations	Number of population
4	1	2	0.011903 sec	10	10

Table-3 : GA Results for IEEE 14-Bus System

# of branches	#PMUs	Location of PMUs	Time to converge	Number of generations	Number of population
20	4	2,6,8,9	0.502822	2000	100

Table-4 : GA Results for IEEE 30-Bus System

# of branches	#PMUs	Location of PMUs	Time to converge	Number of generations	Number of population
41	12	3,6,7,9,10,12,14,15,20,21,25,29	15.637067 sec	49	1000

5.2 Results of BILP Technique

Table-5, 6 and 7 shows the results for 4-Bus test system, IEEE 14-bus system and IEEE 30-bus system respectively for BILP technique.

Table-5: BILP Results for 4-Bus System

# of branches	# of PMUs	Location of PMUs	Time to converge	Stopping criteria for convergence
4	1	2	0.568210 sec	1/5×(N_bus)

Table-6: BILP Results for IEEE 14-Bus System

# of branches	#PMUs	Location of PMUs	Time to converge	Stopping criteria for convergence
20	6	2,4,7,8,10,13	1.110082 sec	1/2×(N_bus)

Table-7: BILP Results for IEEE 30-Bus System

# of branches	#PMUs	Location of PMUs	Time to converge	Stopping criteria for convergence
41	16	2,4,7,8,10,11,13,15,16,19,21,22,24,25,26,27	0.672286 sec	5/6×(N_bus)

5.3. Comparison of Results

5.3.1 4-bus System

Table-2 and Table-5 show that both techniques optimally place a PMU at bus 2 of the 4-bus system for complete system observability. However BILP converges in 0.568s whereas GA converges in 0.011s. Thus BILP take almost twice time to converge with respect to GA. This is because GA searches a number of possible solutions simultaneously, whereas BILP searches for one solution at a time. Moreover, BILP converges within the stopping criterion which dictates that the number of PMUs should be about 1/5 to 1/3 of the number of buses depending on the size of the system. As 4-bus system is a small system, BILP converges at stopping criteria of 1/5 of the number of buses. This means that the BILP algorithm keeps on searching as long as the number of PMUs is greater than 0.8 rounded to 1 as the number of PMUs can only be whole numbers.

5.3.2 IEEE 14-bus system

For this system, BILP optimally places 6 PMUs while GA places 4 PMUs. In both cases, the placement renders the system observable, however BILP does not give the optimal solution as it places 2 more PMUs. Moreover, the disadvantage of BILP is it can be trapped in the local minima and not converge to the optimal solution [8,17]. This is reflected in the results of Table-3 and Table-6. When an attempt is made to stop at a criterion of 1/3 of 14, the program stalls. At ½ the number of PMUs, the program reaches a local minimum of 6 PMUs and that is the minimal solution it can achieve. Here also, the time to reach the optimal solution for BILP is 1.11s against 0.5s for GA with a population of a 100 and 2000 generations. The difference is also noted in placement positions.

Proceedings of the 19th Southern African Universities Power Engineering Conference
SAUPEC 2010, University of the Witwatersrand, Johannesburg

TOPIC C. POWER SYSTEMS

5.3.3. IEEE 30-bus system

In this case BILP places PMUs at 16 buses whereas GA places PMUs at 12 buses. Convergence time for BILP is 0.672s while that for GA is 15.637s which is far greater. Still, BILP does not provide the optimal solution as it places 4 more PMUs in the system. BILP algorithm stalls at a stopping criterion 1/5 of the number of buses. Result is obtained for a stopping criterion of 5/6 of the number of buses.

6. CONCLUSION

It can be concluded from results that GA performs better than the BILP as GA optimally places lesser number of PMUs for complete system observability. Thus the solution provided by GA is more economic. It is however noted that there is still room to improve the overall convergence times of the software. It is observed that GA converges in different times for different number of populations and generations. This is because the population of guesses might not contain the optimal solution owing to the random generation of the population. This becomes a big challenge in larger systems as there are more combinations to search through. However the advantage of GA is that if the optimal solution exists in the search space then convergence is guaranteed and the programme will not be trapped in the local minima. This problem can be overcome by carefully tuning the number of generations and populations [8,21].

It has also been seen here that high mutation rate has resulted in non-convergent generations and that the solution pattern becomes lost across the generations.

Moreover, increased solution time is most likely due to the code not being vectorised. Therefore the authors recommend the following for further improving the performance of the GA code only, owing to its better performance than BILP.
To improve the response time of the code:
(a) Turn the GA code into a function
(b) Vectorise the code
To improve the performance of the code:
(c) In GA tune the initial variables such as N_pop and N_iter to give maximum performance
(d) Create a search space that allows 2^{n_bus} possible number of solutions
(e) Identify candidate solutions by eliminating the buses where PMU placement is not necessary.

ACKNOWLEDGMENT

REFERENCES

[1] A.Abur & A. ExpÓsito. *Power System State estimation: Theory and implementation,* New York: Marcel Dekker, 2004.

[2] M. Zhou, A. V. Centeno, J. S. Thorp et al, "An Alternative for Including Phasor Measurements in State Estimators", *IEEE Trans. Power Systems*, Vol. 21, No. 4, Nov. 2006.

[3] F. Aminifar, C. Lucas, A. Khodaei et al., "Optimal Placement of Phasor Measurement Units Using Immunity Genetic Algorithm", *IEEE Trans. Power Delivery*, Vol. 24, No. 3, July 2009.

[4] K. Seethalekshmi, S.N.Singh and S.C.Srivastava, "Wide-Area Protection and Control: Present Status and Key Challenges", *Proceedings of the Fifteenth National Power Systems Conference (NPSC),* IIT Bombay, India,. December 2008.

[5] I.C.Decker, A.S.Silva, M.N.Agostini et al. *Development and experimental use of a wide area measurement system.* : www.labplan.ufsc.br/~agostini/publicacoes/In duscon_MedFasee.pdf.[2009 July 15].

[6] D. Karlsson, "Wide-Area Protection and Emergency Control: Cascading Failures and Blackouts", *Proceedings of the T&D Conference and Exposition,* Dallas, USA, May 2006.

[7] GE consumer and Industrial, *Wide Area Monitoring Network stability & Synchrophasors*, April 2005.

[8] "Dawn of the grid synchronization: Benefits, Practical Applications and Deployment Strategies for Wide Area Monitoring, Protection and Control", *IEEE Power and Energy Magazine*, January/ February, 2008.

[9] North American Synchrophasor Initiative, Actual and Potential Phasor Data Applications, March 2009.

[10] S. Chakrabarti and E. Kyriakides, "PMU Measurement Uncertainty Considerations in WLS State Estimation", *IEEE Trans. Power Systems*, Vol. 24, No. 2, May 2009.

[11] M. A. Donolo and V. A. Centeno, "Accuracy Limits for Synchrophasor Measurements and the IEEE standard", *IEEE Trans. Power Delivery*, Vol. 23, No. 1, January 2008.

[12] S. Chakrabarti and E. Kyriakides, "Optimal Placement of Phasor MeasurementUnits for Power System Observability", *IEEE Trans. Power Systems*, Vol. 23, No. 3, August 2008.

[13] W. Jiang, V. Vittal, and G. T. Heydt, "'Diakoptic State Estimation Using Phasor Measurement Units", *IEEE Trans. Power Systems*, Vol. 23, No. 4, November 2008.

[14] J. Chen and A. Abur, " Placement of PMUs to Enable Bad Data Detection in State Estimation", *IEEE Trans. Power Systems*, Vol. 21, No. 4, November 2006.

[15] J. Chen and A. Abur, "Enhanced Topology Error Processing via Optimal Measurement Design", *IEEE Trans. Power Systems*, Vol. 23, No. 3, August 2008.

[16] B.Xu and A.Abur, "Optimal Placement of Phasor Measurement Units for State Estimation", Final Project Report, available at: https://www.actapress.com/PDFViewer [2009 July 15].

[17] B. Gou, "Optimal Placement of PMUs by Integer Linear Programming", *IEEE Trans. Power Systems*, Vol. 23, No. 3, August 2008.

[18] F. Aminifar, C. Lucas, A. Khodaei et al. "Optimal Placement of Phasor Measurement Units Using Immunity Genetic Algorithm", *IEEE Trans. Power Delivery*, Vol. 24, No. 3, July 2009.

[19] J. E. Tate and T. J. Overbye, "Line Outage Detection Using Phasor Angle Measurements", *IEEE Trans. Power Systems*, Vol.23, No. 4, November 2008.

[20] R. F.,Nuqui and A. G. Phadke, "Phasor Measurement Unit Placement Techniques for Complete and Incomplete Observability", *IEEE Trans on Power Delivery*, Vol. 20, No. 4, October 2005.

[21] D. Coley, *An introduction to Genetic Algorithms for Scientists and Engineers*, USA, Hackensack: World Scientific, 1999.

[22] D.Devesh, S.Dambhare and R.K.Gajbhiye, "Optimal multistage scheduling of PMU placement: An ILP approach", *IEEE Trans. Power Systems*, Vol. 23, No. 4, Oct. 2008.

[23] N.H. Abbasy and H.M. Ismail, "A unified Approach for the optimal PMU location for power system state estimation", *IEEE Trans. Power Systems*, Vol. 24, No. 4, May 2009.

[24] MATLAB.2006. Optimization box: Bintprog. Mathworks. [September 2009].

Proceedings of the 19th Southern African Universities Power Engineering Conference
SAUPEC 2010, University of the Witwatersrand, Johannesburg

TOPIC C. POWER SYSTEMS

APPENDIX A

(i) Observability Flow Chart for GA Software

Fig. A-1 : Observability flow chart

TOPIC C. POWER SYSTEMS

Proceedings of the 19th Southern African Universities Power Engineering Conference
SAUPEC 2010, University of the Witwatersrand, Johannesburg
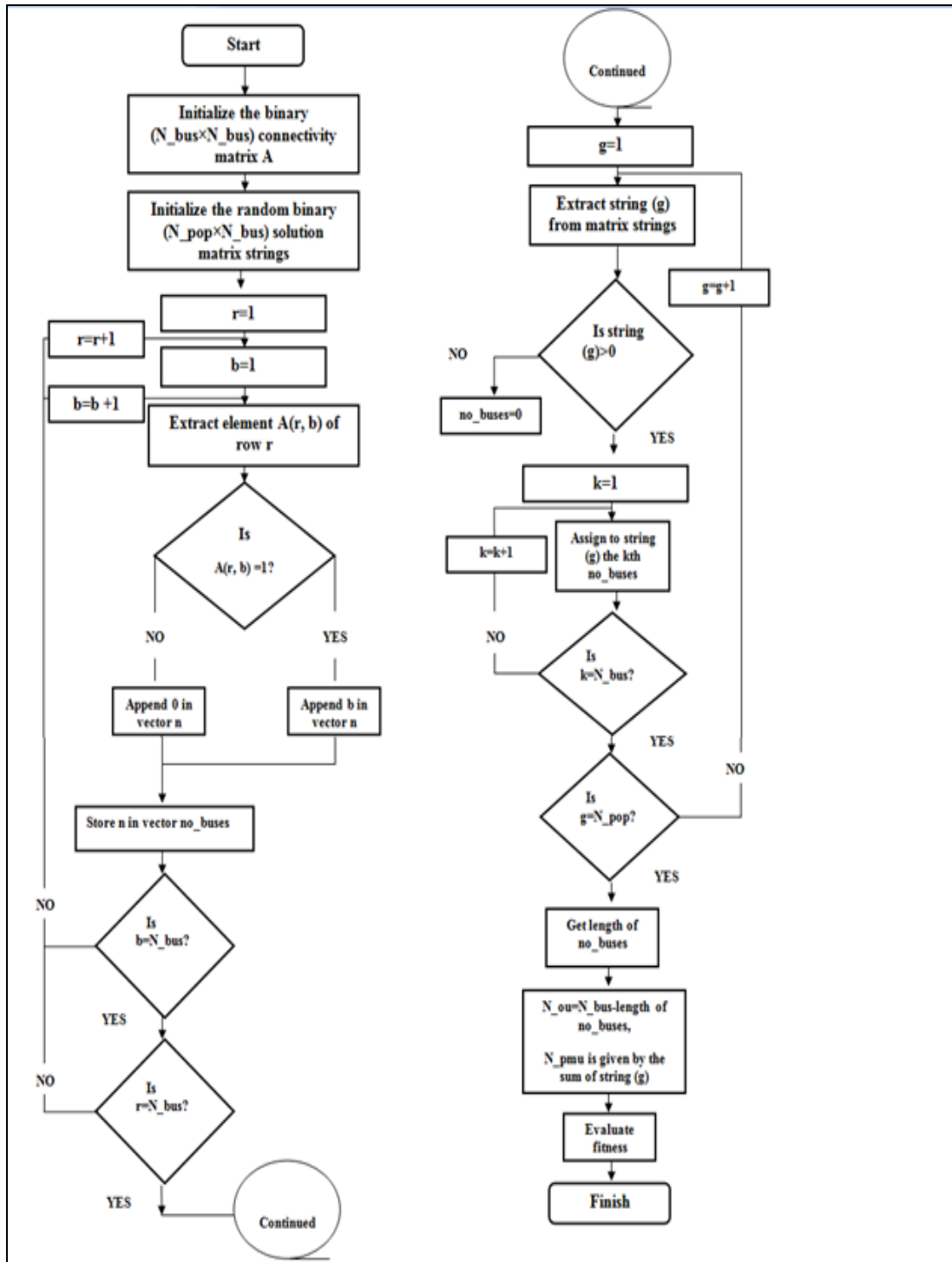
(ii) Flowchart for BILP Software

Fig. A-2 : Observability flow chart

Proceedings of the 19th Southern African Universities Power Engineering Conference
SAUPEC 2010, University of the Witwatersrand, Johannesburg

TOPIC C. POWER SYSTEMS
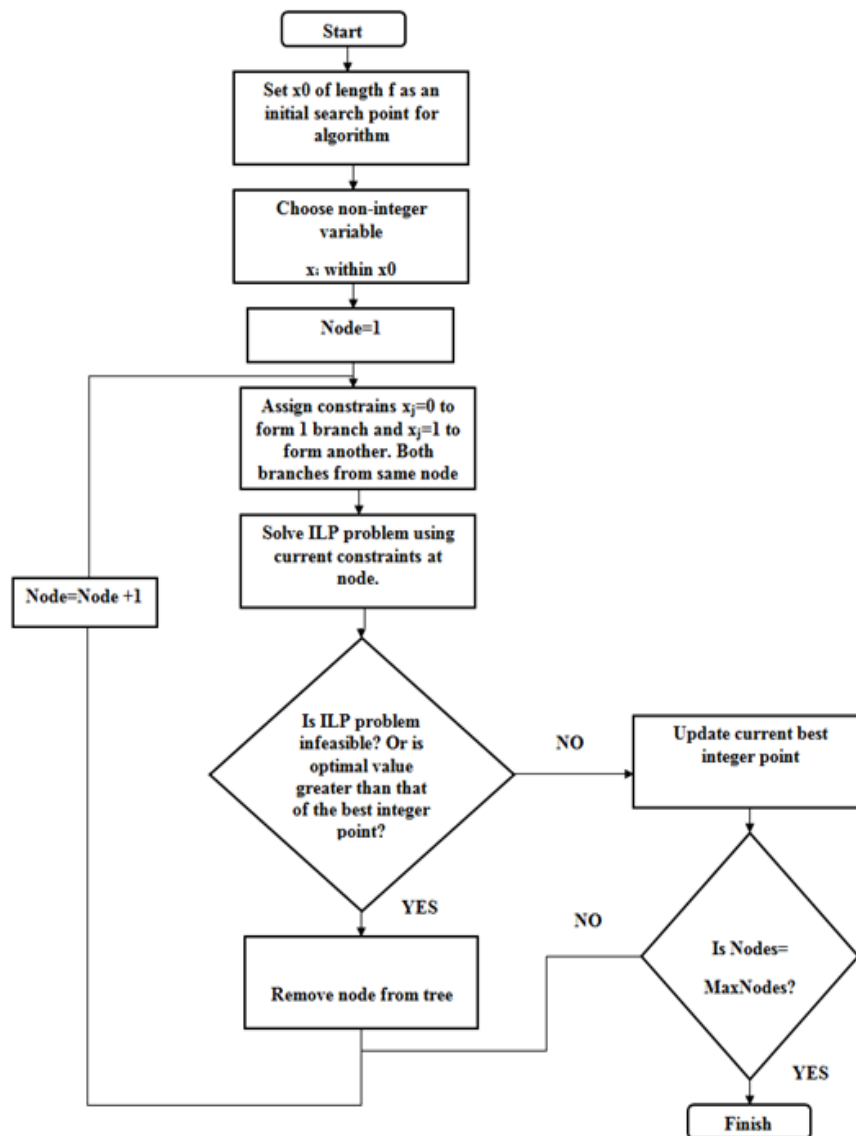
A REVIEW OF SIGNAL PROCESSING TOOLS FOR VOLTAGE DIP ANALYSIS

UJ Minnaar*   CT Gaunt** and F Nicolls

*Eskom Holdings, South Africa

**University of Cape Town, Department of Electrical Engineering, Cape Town, South Africa

Abstract. This paper investigates the characterization of voltage dips with aim of selecting suitable feature extraction tools for the analysis of events. The symmetrical component method, ABC classification and the voltage dip segmentation method are discussed and a list of characteristics identified. Signal processing tools are reviewed and the Kalman filter and Ziarani algorithm selected as suitable feature extraction tools based on the analysis requirements of the dip segmentation method.

1.   INTRODUCTION

Voltage dip characterization can be described as *"the description of voltage dip events through a limited number of parameters"* [1].

The requirements of characterization vary depending on application, and include [1]:

- Utility statistical dip performance reporting for its transmission and distribution systems,
- The description of dip performance at a particular site for use by utility customers.
- Contracting with end-customers,
- Definition of equipment dip immunity requirements,
- Definition of equipment dip immunity test requirements.

These characterisation applications are primarily driven by the response of end-user equipment to voltage dips and the ability of the utility to monitor and report voltage dip performance and analyse causes.

Additionally, characterisation can be conducted as an input to automated classification techniques, with the purpose of saving time spent by specialists manually analyzing data recorded by power quality monitors, protection relays and digital fault recorders [2].

In light of this requirement of characterisation, the aim then becomes "to find common features that are likely related to specific underlying causes in power systems" [3].

This paper investigates the characterization of voltage dips with aim of selecting suitable feature extraction tools for the analysis of events.

The structure of the paper is as follows: Section 2 reviews characterization of voltage dips, Section 3 discusses signal processing tools that are commonly applied in characterizing voltage dips. Section 4 discusses the selection of tools for feature extraction. Section 5 concludes.

2.   CHARACTERISATION OF VOLTAGE DIPS

2.1 Residual Voltage and Longest Duration

Voltage dips are commonly characterised by the lowest voltage and longest duration measured across all channels [4].

IEC 61000-4-30 identifies this characterisation of voltage dips as a useful way of reducing data, interpreting and categorizing events [5]. Voltage dip duration is defined by IEC 61000-4-30 as the time from when the R.M.S. voltage on one phase drops below the dip threshold to the time when all three phases are above the dip threshold. This is illustrated in Figure 1.
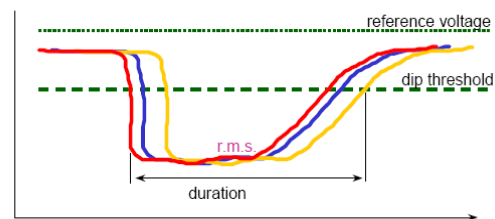
Figure 1: Dip Duration Characterisation [1]

Many utilities record only R.M.S voltage for statistical purposes and it is not possible to determine voltage characteristics without phasor information [6].   Bollen et al. [6] recognises that this limits the information on the voltage dip as seen at the end-user terminal. In practice a power quality monitor recording only RMS voltages may be the only information available to analyse voltage dips. This makes feature extraction from RMS data a key concern.

2.2 Symmetrical Component Method

The symmetrical component method [7, 8] classifies voltage dips in terms of changes in both the magnitude and phase angle. A dip is classified by a characteristic voltage and a PN factor and the method attempts to classify it into one of two main categories C (2-phase dips) and D (single phase dips). It is further identified by a subscript that indicates the symmetrical phase i.e. the least dipped phase for type C and most dipped for type D.
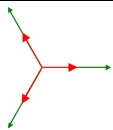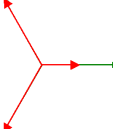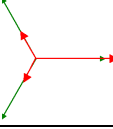
2.3 ABC Classification

The ABC classification [9] distinguishes between 7 different types of unbalanced three-phase voltage

TOPIC C. POWER SYSTEMS

Proceedings of the 19th Southern African Universities Power Engineering Conference
SAUPEC 2010, University of the Witwatersrand, Johannesburg

dips (A-G). Table 1 illustrates   the dipped phases for each dip type according to the ABC classification and provides a comparison with the symmetrical component method.

Table 1: Examples of Dip Vectors for ABC Classification

ABC Dip Classification	Vector Diagram	Symmetrical Component Classification
A		ANY
B		Da
C		Ca

The ABC classification is a special case of the symmetrical component method and has a number benefits including [9]:

- It is a more intuitive classification that does not require the study of symmetrical component theory,

- It provides an easy to understand graphical interpretation of the propagation of unbalanced voltage dips through transformers. This is illustrated in Figure 2 for the translation through Dy transformers.
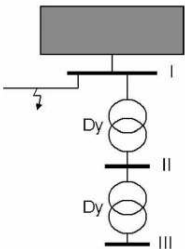
FAULT TYPE	DIP LOCATION		
	I	II	III
3-Phase	A	A	A
3-Phase-to-ground	A	A	A
2-Phase-to-ground	E	F	F
2-Phase	C	D	C
1-Phase-to-ground	B	C	D

Figure 2: Dip Propagation [9]

2.4 Dip Segmentation Method

Styvaktakis [10] introduces segmentation of power quality events as part of an automated classification method   based on the underlying causes of voltage dips.

Djokić and Bollen [11] present the *dip segmentation method* as an approach for the analysis, description and characterisation of voltage dips in power systems and at end-user equipment terminals.

It is introduced to allow an improved assessment of factors and parameters possibly influencing the sensitivity of equipment at different voltage levels. The method is introduced with the intention of helping users and designers of electrical equipment to *"quantify, test and compare performance of their equipment in a simple, consistent, transparent and reproducible manner...."* [11].

The method aims to extend the description of dips beyond a single magnitude and duration as [11]:
- Differences between the 3 phase voltages are not considered,
- Voltage dips are not always rectangular ,
- Phase-shift and point-on-wave are not considered.

The method is based on the separation of recorded dip events into "dip segments" where a segment is described as a period of time during which the voltage magnitude and other properties of the voltage waveform remain more or less constant. The general description of a dip, regardless of type based on the dip segmentation method consists of [11]:

- **One pre-event segment** – provides a description of the relevant voltage characteristics immediately before the dip occurs
- **Zero, one or more during-event segments** – provide a description of dip characteristics during which the voltage magnitude is constant
- **One or more transition segments** – provides a description of dip characteristics during the transition between two steady states.
- **One post-event or voltage recovery segment** – provides a description of voltage characteristics after the cause of the dip is cleared or eliminated

Figure 3 illustrates the segmentation of a multi-stage voltage dip.
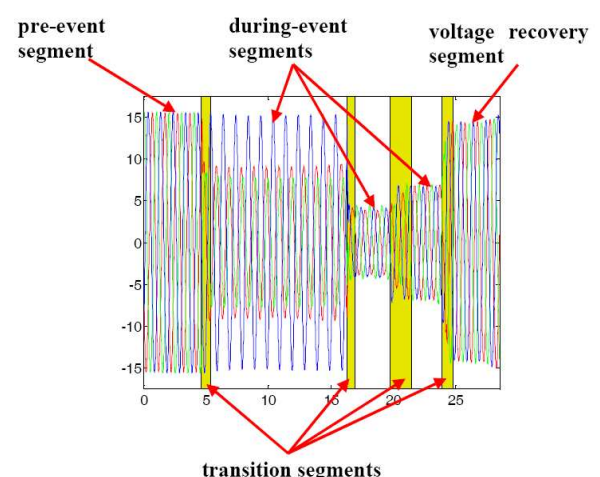
Figure 3: Segmentation of a multi-stage voltage dip [11]

The description of voltage dips in the dip segmentation method consists of [12]:
- Number of transition segments, duration of event segments
- Characteristics of the pre-event segment

Proceedings of the 19th Southern African Universities Power Engineering Conference
SAUPEC 2010, University of the Witwatersrand, Johannesburg

TOPIC C. POWER SYSTEMS

- Characteristics of the event segments
- Characteristics of the transition segments
- Characteristics of the voltage recovery segments

A feature of the dip segmentation method is that it includes the pre- and post-dip segments which fall outside of the time period of the actual voltage dip.

CIGRE/CIRED/UIE working group C4.110 introduces a table of voltage dip characteristics based on the dip segmentation method to *be "used as a "check-list" for a fast and transparent assessment of equipment and process sensitivity to voltage dips during all stages of equipment and process design"* [12].

Table 2: Dip Segment Characteristics [12]

Dip Segment	Characteristics
Pre-Event Segment	Voltage magnitude Phase angle Harmonics Voltage unbalance Frequency
During Event Segment	Dip magnitude Dip Duration Dip Shape Dip Voltage Unbalance Dip phase angle unbalance Dip phase shift Distortion Transient
Transition Segment	Dip Initiation Point-on-wave of dip initiation Phase shift at the dip initiation Phase shift at the dip initiation Multistage dip initiation Dip ending Point-on-wave of dip ending Multistage dip ending Rate-of-change of voltage Damped oscillations
Post-Event Segment	Voltage recovery Post-fault dip (prolonged voltage recovery) Post-dip phase shift Multiple dip events (dip sequences) Multiple dip events Composite dip events Rate-of-change of voltage Voltage recovery time constant RMS voltage

The C4.110 checklist provides a structured list of characteristics for detailed analysis of voltage dips as a starting point for further characterisation and analysis of voltage dip events.

2.5 Summary and Conclusions of Characterisation

Four methods of characterisation of voltage dips have been presented and their key features discussed:

- The RMS voltages may be the only information available to analyse voltage dips. This makes feature extraction from RMS data a key concern.

- The ABC classification provides an intuitive insight into three phase unbalanced dips and their propagation through the network.

- The dip segmentation provides a methodology to conduct detailed analysis and characterisation

of voltage dips and understand propagation through a network.

- A basic list of requirements to meet analysis in line with the dip segmentation method is outlined.

Any further analysis for feature extraction purposes will require that the tools used for feature extraction have the capacity to meet the analysis requirements of the individual dip segments, namely:

- High speed capability for transition segments
- Extraction of phase angle for point-in-wave analysis,
- Extraction of voltage magnitude and rate of change.

3. SIGNAL PROCESSING TOOLS FOR CHARACTERISATION

The methods for analysis and classification of power quality events consist of a number of steps each requiring specific tools [10]:

- Segmentation,
- Feature extraction,
- Additional processing,
- Classification.

The process and individual steps for analysis and classification are illustrated in Figure 4.
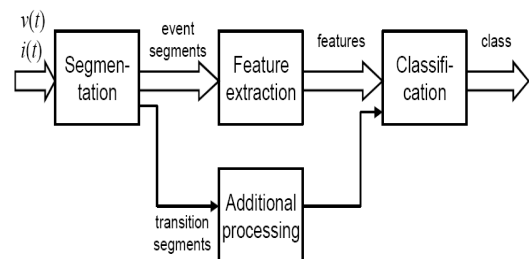
Figure 4: Analysis and Classification of Power Quality Events [10]

This discussion will focus on the tools required for segmentation and feature extraction of event data for input to classification.

Triggering (event detection) and segmentation commonly treated as two separate topics in the literature [13] but both these processes require the detection of nonstationarity in a signal. A signal is stationary when it is statistically time invariant [13] i.e. its statistical properties do not change as a function of time. A non-stationary signal is therefore a signal for which the statistical properties change with time.

Event detection is commonly used in for online capturing of events and event segmentation takes place afterwards during event analysis [13]

3.1 Methods for Analysis

The following tools are commonly discussed in literature for analysis of power quality events [10, 13].

3.1.1 RMS Method

The general equation used to calculate RMS is:

$$V_{rms}(t_k) = \sqrt{\frac{1}{N}\sum_{t_k = t_k - N + 1}^{t_k} v^2(t)} \cdot$$

Event identification via RMS is done by comparing change in magnitude with a predetermined threshold. Application of RMS requires simple signal processing and is recognised as being very efficient. It is widely used in power quality instruments that monitor RMS

Bollen et al [6] recognise the importance of phasor information and introduce a method to deduce phasors from RMS voltages for analysis purposes.

For analysis purposes a method of segmentation based of rate of change is introduced in [10] and finds application in a classification system based on RMS voltage only.

3.1.2 Short -Time Fourier Transform (STFT)

The short time Fourier transform of a signal $v[k]$ is:

$$V_{STFT}(m,\omega) = \sum_k v[k] \cdot w[k-m]e^{-jwk},$$

Where $\omega = 2\pi n/N$, N is the length of $v[k]$, $n = 1......N$, and w[k-m] is a selected window that slides over the analysed signal

The STFT has limitations due to its fixed window length, which has to be chosen prior to the analysis. This drawback is reflected in the achievable frequency resolution when analysing non-stationary signals with both low and high-frequency components [14].

3.1.3 Park Vector - DQ Transform

Park's vector is based on the instantaneous vector sum of all of the three phase vectors (v1, v_2, v_3). The Park transform finds general application in the field oriented control of induction motors. The vector components (v_d, v_q) are given by [14]:

$$v_D = \sqrt{\frac{2}{3}}v_1 - \sqrt{\frac{1}{6}}v_2 - \sqrt{\frac{1}{6}}v_3,$$

$$v_Q = \sqrt{\frac{1}{2}}v_2 - \sqrt{\frac{1}{6}}v_3.$$

3.1.4 *Wavelet analysis*

The wavelet transform is based on the decomposition of a signal into daughter wavelets derived from the translation and dilation of a fixed mother wavelet. The general formula is given by:

$$V_{WT} = \int_{-\infty}^{+\infty} v(t) \cdot \varphi_{a,b}^*(t) \cdot dt\,.$$

Wael et al. [15] point out that the application of wavelets to feature extraction is well researched and documented. The most popular applications of wavelets in literature as [16]:

- Power system protection
- Power quality
- Power system transients
- Partial discharge
- Load forecasting
- Power system measurement

3.1.5 Multi-resolution S-Transform

The S-Transform is described as being either a phase-corrected version of the wavelet transform or a variable window Short Time Fourier transform that simultaneously localizes both real and imaginary spectra of the signal [17]. It is defined by convolving the analyzed signal, v[k], with a window function. The S-transform of a discrete signal *v[k]* can be calculated as:

$$V_{ST}[k,\frac{n}{N}] = \sum_{m=0}^{N-1} V[\frac{m+n}{N}] \cdot e^{\frac{-2\pi^2}{n^2}} \cdot e^{j\alpha k},$$

where k,m and $n = 0,1......N\text{-}1$ and V[m+n/N] is the fourier transform of the analyzed signal *v[k]* $\omega = 2\pi n/N$, N is the length of *v[k]*[17] .

3.1.6 *Extended Kalman filter*

Kalman filtering is a parameter based modelling of an assumed process. If the process is non-linear then a linearization process is carried out and this leads to the extended Kalman filter.

Extended Kalman filtering provides good performance in both the detection of events and the estimation of event magnitude and duration [17]. Power system applications of Kalman filtering include [13]:

- Continuous real-time tracking of harmonics,
- Estimation of voltage and current harmonics for protection systems,
- Estimation of transient parameters.

Styvaktakis [10] discusses the application of Kalman filters to:

- Voltage magnitude estimation and the limitations in the presence of harmonics and short duration events,
- Segmentation of disturbance recordings and
- Voltage dip detection.

He concludes that the order of the model used by the Kalman filter significantly affects the magnitude estimate for the types of changes he identifies (fast, slow and fast repeating).

Further parameter-based methods for feature extraction discussed in the literature include multiple signal classification method (MUSIC), estimation of

Proceedings of the 19th Southern African Universities Power Engineering Conference
SAUPEC 2010, University of the Witwatersrand, Johannesburg

TOPIC C. POWER SYSTEMS

signal parameters via rotational invariances (ESPRIT), stochastic models e.g. auto regressive (AR), auto-regressive moving-average (ARMA) and state space [13].

3.1.7 Method of Ziarani and Konrad

Ziarani and Konrad present a method of extracting nonstationary sinusoidal signals via a nonlinear adaptive filter and estimate the following parameters [18]: amplitude, phase and frequency.

The Ziarani algorithm demonstrates the following characteristics [18]:
- Simple structure,
- Low computational requirements hence easily implemented in hardware and software,
- High degree of noise immunity and robustness,
- High speed,
- Effectiveness in tracking large variations in parameters.

Figure 5 illustrates a block diagram of the Ziarani Algorithm.
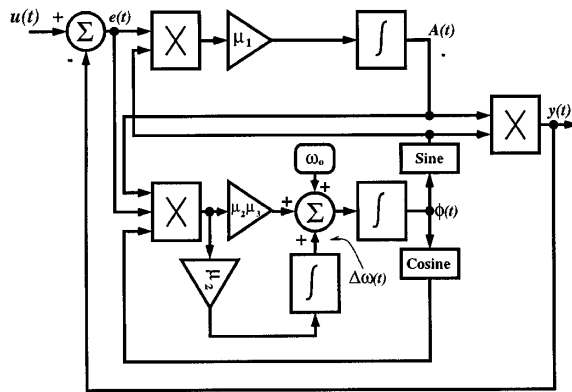
Figure 5: Block diagram of the Ziarani Algorithm [18]

Naidoo and Pillay [19] review the application of this algorithm for power systems applications and identify the following advantages:
- Phase lock loop is not required,
- Simple structure and easy to implement,
- No windowing of data required,
- Less processing power is required as compared to FFT and wavelets.

It has the following disadvantages:
- Limited convergence speed posing problems for processing of short duration events,
- The co-efficients have to be optimized for a particular application,
- Errors associated with the algorithm are not known and require investigation.

3.1.8 Forward Clarke Transform and Space Vector Definition

The Clarke transform is commonly used in real-time motor control applications. It transforms a 3-phase system to an equivalent two phase representation. Gargoom et al. [20] identify its advantages as being able to analyze all three phases of a power system simultaneously as well as its simplicity and speed.

The Clarke transform is commonly used for the analysis of transient disturbances in three-phase systems. It relates the phase-to-neutral voltages and component voltages through a matrix expression [9]. Aller et al. [21] demonstrate the derivation of the space vector where the first two components $(x_\alpha(t), x_\beta(t))$ form the space vector and the third one $(x_0(t))$ representing the zero sequence voltage:

$$\begin{pmatrix} x_\alpha(t) \\ x_\beta(t) \\ x_0(t) \end{pmatrix} = \frac{2}{3} \begin{pmatrix} 1 & -\frac{1}{2} & -\frac{1}{2} \\ 0 & \frac{\sqrt{3}}{2} & -\frac{\sqrt{3}}{2} \\ \frac{1}{2} & \frac{1}{2} & \frac{1}{2} \end{pmatrix} \begin{pmatrix} v_a(t) \\ v_b(t) \\ v_c(t) \end{pmatrix}$$

The space vector of the Forward Clarke Transform is then represented as:

$$S_v = x_\alpha(t) + j x_\beta(t).$$

The magnitude and angle of the space vector is then:

$$|S_v(t)| = \sqrt{(v_\alpha(t)^2 + v_\beta(t)^2)},$$

$$angle\_S_v = \arctan\left(\frac{v_\beta}{v_\alpha}\right).$$

Gargoom et al. [20] utilise the mean and standard deviation of the space vector magnitude as features for event classification.

3.2 Comparative Analysis of Methods

Perez et al. [17] discuss the comparative performance of the most commonly used techniques for detection and analysis of voltage events in power systems, namely:
- RMS method,
- Discrete Fourier Transform and Short Time, Fourier Transform,
- Kalman Filtering,
- Wavelet Analysis.

Their conclusions [17]) are that RMS and STFT show limited performance for short duration and low magnitude voltage events.

Wavelet analysis is deemed to provide the best performance in terms of detection and estimation of time-related parameters but has the drawback of requiring an additional method to discriminate between voltage events and other high frequency disturbances.

Gargoom et al. [14] conduct a comparative study on signal processing tools for feature extraction purposes and Table 3 summarize the performance of various signal processing techniques [14].

Table 3: Comparative analysis of Techniques [14]

	STFT	Wavelet	S - Transform	Park's Vector
Speed	Moderate	Moderate	Low	High
Sensitivity	Low	Moderate	High	High
Practical Implementation	Difficult	Difficult	Difficult	Easy
3-ph signals simultaneous	No	No	No	Yes

Proceedings of the 19th Southern African Universities Power Engineering Conference
SAUPEC 2010, University of the Witwatersrand, Johannesburg

TOPIC C. POWER SYSTEMS

4.   SELECTION OF AN ANALYSIS METHOD

The selection of a suitable feature extraction method should meet the analysis requirements   of the dip segmentation method. These are:

- High speed capability for transition segments
- Extraction of phase angle for point-in-wave analysis
- Extraction of voltage magnitude and rate of change

The analysis of nonstationary signals are a requirement for detailed analysis of the transition segments and the associated segmentation of voltage dips.

Another factor to be taken into consideration is the application of the tool i.e. whether it will be an online or offline analysis application and the ease of implementation.

Based on the abovementioned criteria the tools identified for analysis and feature extraction are the Kalman filter and the method of Ziarani and Konrad.

5.   CONCLUSION

This paper has provided a review of voltage dip characterisation with the aim of selecting suitable signal processing tools for feature extraction

Requirements for selection of suitable signal processing tools for feature extraction are discussed and signal processing tools reviewed and comparative studies of performance are presented.

The Kalman filter and Ziarani and Konrad algorithm are selected as suitable feature extraction tools based on the characterisation requirements.

REFERENCES

[1] Koch RG, Botha A, Johnson PA, McCurrach R, Ragoonanthun R, *"Developments In Voltage Dip (Sag) Characterisation And The Application To Compatibility Engineering Of Utility Networks And Industrial Plants"*, Proceedings of the 3rd Southern African Power Quality Conference, Livingston, Zambia, 31 October - 2 November 2001

[2] Axelberg P, Gu I, Bollen M, *"Automatic Classification of Voltage Events Using the Support Vector Machine Method",* Paper 888,19th International Conference on Electricity Distribution ,CIRED, Vienna, 2007

[3] Bollen, M.H.J.; Gu, I.Y.H.; Santoso, S.; Mcgranaghan, M.F.; Crossley, P.A.; Ribeiro, M.V.; Ribeiro, P.F., *"Bridging the gap between signal and power,"* Signal Processing Magazine, IEEE , vol.26, no.4, pp12-31, July 2009

[4] Bollen M, *"Algorthims For Characterising Measured Three-Phase Unbalanced Voltage Dips"* IEEE Transactions on Power Delivery, Vol.18, No.3, July 2003

[5] IEC 61000-4-30, Power Quality Measurement Methods, IEC, Geneva, Switzerland, 2003

[6] Bollen M, Goossens P, Robert A, *"Deduction of Complex Voltages from Measured RMS Voltages"*, IEEE Transactions on Power Delivery, Vol. 19, No.2, April 2004

[7] Zhang L,Bollen M, *"Characteristic Voltage Dips(Sags) in Power Systems"*, IEEE Transactions on Power Delivery, Vol. 15 No. 2, Apil 2000

[8] Bollen, M.H.J., *"Algorithms for characterizing measured three-phase unbalanced voltage dips"*, IEEE Transactions on Power Delivery, Vol. 18, No. 3, July 2003, pp. 937-944.

[9] Bollen M, Gu I, *"Signal Processing of Power QualityDisturbances"*, Wiley-IEEE Press, New York, 2006

[10] Styvaktakis E, *"Automating Power Quality Analysis"*, PhD thesis, Dept. of Signals and Systems, Chalmers University of Technology, Gothenburg, Sweden, 2002

[11] Djokić S, Bollen M, *"Dip Segmentation Method"*, 13th International Conference on Harmonics and Quality of Power, Wollongong, 2008

[12] Bollen M, Stephens M, Stockman K, „ CIGRE/CIRED/UIE JWG C4.110, Voltage Dip Immunity of equipment in Installations , scope and status of work, January 2008", Cigre 2008

[13] Bollen M, Gu I, *Analysis and classification of Power Quality Events: Ideas, Methods and Techniques", in Proc. 12th International conf. on harmonics and quality of power (ICHQP 06), Cascais, Portugal, Oct. 1-5, 2006*

[14] Gargoom A, Ertugrul N, Soong W, *"A Comparative Study in Effective Signal Processing Tools for Power Quality Monitoring"*, 11th European Conference on Power Electronics and Applications, Dresden, 2005

[15] Wael R, Ibrahim A, Morcos M, *"Aritficial Intelligence and advanced Mathematical Tools for Power Quality Applications: A Survey"*, IEEE Transactions on Power Delivery Vol. 17 No2, April 2002

[16] Fernandez Rm Rojas H, *"An Overview of Wavelet Transform Application in Power Systems"*, 14th Power Systems Computation Conference (PSCC), Session 1, paper 6, Sevilla, Spain, June 2002

[17] Perez, E, Barros J, *"Voltage Event Detection and Characterization Methods: A Comparative Study"*, Transmission & Distribution Conference and Exposition: Latin America , 2006

[18] Ziarani A, Konrad A, *"A Method of extraction of nonstationary sinusoids"*, Elsevier Signal Processing Vol. 84, April 2004

[19] Naidoo R, Pillay P, "A nonlinear adaptive filter for improved power system operation and protection", IEEE Power Engineering Society Meeting, , Denver, USA, 6-10 June, 2004.

[20] Gargoom A, Ertugrul N, Soong W, *"A Comparative Study on Effective Signal Processing Tools for Optimum Feature Selection in Automatic Power Quality Events Clustering"*, IEEE- IAS, Industry Applications Conference, 1, pgs. pp 52–58

[21] Aller J, Bueno A, Paga T, *"Power System Analysis Using Space-Vector Transformg"*, IEEE Transactions on Power Systems, Vol. 17, No. 4, November 2002

Proceedings of the 19th Southern African Universities Power Engineering Conference
SAUPEC 2010, University of the Witwatersrand, Johannesburg

TOPIC C. POWER SYSTEMS

Comparison Matlab PST, PSAT and DigSilent for Power Flow Studies on Parallel HVAC-HVDC Transmission lines

A V Ubisse, K A Folly, K. Awodele, L Azimoh, D T Oyedokun, S P Sheetekela

University of Cape Town, Department of Electrical Engineering, Cape Town.

Abstract. This paper presents the comparative results of load flow studies on HVAC and hybrid HVAC-HVDC transmission lines. Three different software packages are used to conduct this investigation, namely DigSilent, Matlab PST and Matlab PSAT. A two-area four-machine system model is used to validate the results obtained from the three software packages.

Key Words: Power transmission, PSAT, PST, DigSilent, HVAC-HVDC transmission.

1. INTRODUCTION

With the increase in power demand, HVDC has become a preferred alternative for the conventional AC transmission system to transmit bulk power over long distances. This is due to its economical and technical advantages in long distance power transfer. HVDC links offer suitable solutions for interconnecting HVAC systems with different frequencies and it can deliver more power over longer distances with fewer losses. HVDC systems also offer high controllability on the power transmitted.

Since HVDC is a relatively new technology when compared to HVAC for power transmission, not all existing software packages can model this type of system accurately and reliably. For this reason only a limited number of packages that allow HVDC modeling are used in this research.

Two scenarios are investigated. The first one is an HVAC system and the second is a combination of the HVAC in parallel with the HVDC system (i.e, hybrid (HVAC-HVDC).

To validate the results obtained by the software packages, the HVAC load flow results are compared to the results given in reference [1]. The results for the Hybrid network are compared between the software packages.

The paper is organized as follows: Section 2 gives a brief introduction of the transmission models; section 3 describes the software packages used to conduct the simulations. Section 4 discusses the different case studies and their respective results and section 5 gives a conclusion to the paper.

2. BASIC PRINCIPLES OF TRANSMISSION LINES

The different scenarios of power transmission systems are discussed below.

2.1 HVAC system

Conventionally, electric power is transferred from generating stations to the consumer ends through HVAC transmission lines. Fig.1 depicts the HVAC transmission system, in its equivalent π circuit with lumped parameters, used for the study.
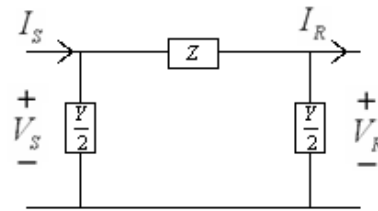
Figure 1: HVAC transmission equivalent model

From figure 1, the following equations are deduced:

$$V_S = \left(1 + \frac{ZY}{2}\right)V_R + ZI_R \tag{1}$$

$$I_S = \left(Y + \frac{1}{4}Y^2 Z\right)V_R + \left(1 + \frac{1}{2}YZ\right)I_R \tag{2}$$

where,
V_S- sending -end voltage
V_R - receiving-end voltage
I_S - sending end current
I_R - receiving end current
Z - equivalent impedance
Y - equivalent admittance

For the above circuit, the transfer matrix for the ABCD parameters becomes

$$\begin{bmatrix} A & B \\ C & D \end{bmatrix} = \begin{bmatrix} 1 + \frac{1}{2}YZ & Z \\ Y + \frac{1}{4}Y^2 Z & 1 + \frac{1}{2}YZ \end{bmatrix} \tag{3}$$

therefore,

$$\begin{bmatrix} V_S \\ I_S \end{bmatrix} = \begin{bmatrix} A & B \\ C & D \end{bmatrix}\begin{bmatrix} V_R \\ I_R \end{bmatrix} \tag{4}$$

2.2 HVDC system

The power transfer on a DC system is a function of the voltage magnitude between the sending and receiving end. On a DC system, power flows from high to low voltage magnitudes.

Fig. 2 shows a monopolar HVDC configuration with a rectifier station and its transformers, the transmission line and an inverter station and its transformers. The transformers at the rectifier station connect to area 1 side and the transformers on the inverter station are connected to the area 2 side. The DC transmission line is modeled as a π equivalent circuit.

Proceedings of the 19th Southern African Universities Power Engineering Conference
SAUPEC 2010, University of the Witwatersrand, Johannesburg

TOPIC C. POWER SYSTEMS
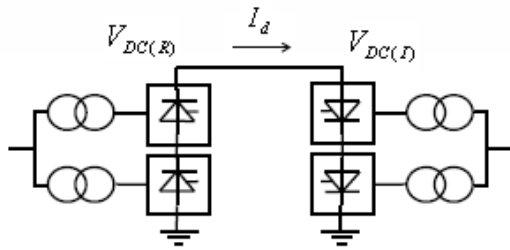
Figure 2: HVDC monopolar configuration

The voltages at the converter stations are given by [1]:

$$V_{DC(R)} = \frac{3\sqrt{2}}{\pi} V_S \cos\alpha \qquad (5)$$

$$V_{DC(I)} = \frac{3\sqrt{2}}{\pi} V_R \cos\beta \qquad (6)$$

where
$V_{DC(R)}$ - rectifier DC voltage
$V_{DC(I)}$ - inverter DC voltage
α - rectifier firing or delay angle,
β - inverter advance angle
The firing angle is normally $\alpha < 18^o$ [2].

The current flowing through the DC link is given as [1]:

$$I_d = \frac{V_{DC(R)} - V_{DC(I)}}{R_{cr} + R_L + R_{ci}} \qquad (7)$$

where
I_d - HVDC current
R_{cr} - rectifier resistance
R_L - line resistance
R_{ci} - inverter resistance

The power output at the rectifier is hence given by:

$$P_{DC(R)} = V_{DC(R)} I_d \qquad (8)$$

The reactive power consumed by the converter stations is between 50% and 60% [1, 3] of the converted power, and is given by

$$Q_{DC(R)} = P_{DC(R)} \tan(\theta) \qquad (9)$$

where θ is the power factor angle

3. SOFTWARE PACKAGES
The software packages used are briefly described below:

3.1 DigSilent
DigSilent stands for Digital Simulation and Electrical Network calculation program. It is a computer aided engineering tool that is widely used for industrial, utility, commercial and academic applications.
DIgSILENT has the ability to simulate load flow, fault analysis, harmonic analysis and stability analysis for AC-DC systems.
The load flow is performed using Newton Raphson method for power flow solutions [4].
DigSilent does not however allow the user to model the components from basic component levels, but

gives a choice of built-in configurations that are already modeled.

3.2 Matlab PST
Power System Toolbox (PST) is Matlab run software that was developed by Joe Chow. It allows users to model components and perform AC-DC system analysis within Matlab. It consists of Matlab m-files, data files and power system application files. It provides dynamic models of machines and controls for performing damping controller designs, transient and small-signal stability simulations [5].

3.3 Matlab PSAT
PSAT is a Matlab toolbox for static and dynamic analysis and control of electric power systems. It was developed by Federico Milano and is an open source software.
PSAT includes power flow, continuation power flow, optimal power flow, small-signal stability analysis and time domain simulation tools. It uses Newton Raphson algorithm to perform power flow analysis. All operations can be assessed by means of graphical user interfaces (GUIs) and a Simulink-based library provides a user friendly tool for network design [6].

4. CASE STUDIES
Two case studies are investigated in this paper. The first is an HVAC consisting of a two-area system with four machines and two AC lines that transmit power from area one to area two. The results obtained from the different software packages are tabled with the results in reference [1] for comparison. The second is a parallel operation of an HVAC and an HVDC line. On the second case, one of the AC lines is changed by an HVDC line. Figure 3 depicts the simple two area system used in scenario 1.

4.1 HVAC system (scenario 1)
This system is taken from [1].
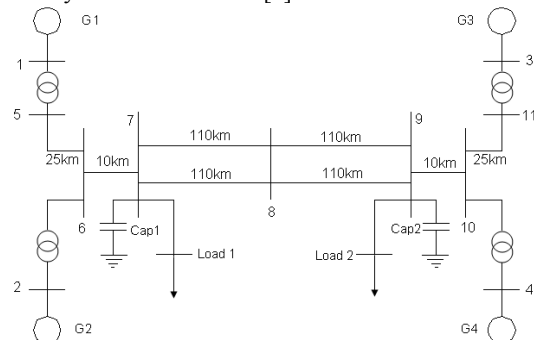
Figure 3: HVAC two area multi machine system

The generators have been modelled using the 6th order machines. Each machine is rated at 900MVA and set to supply 700 MW (see appendix for machine data). Machines G1 and G2, connected to buses 1 and 2, are in area 1 and machines G3 and G4, connected to buses 3 and 4, are in area 2. These

two areas are connected through a weak tie. For the HVAC transmission line, Machine 3 is set to be the slack bus for this system and all other machines are modelled as PV buses. The machines are rated at 20 kV and transmission lines are rated to 230 kV. There are 2 loads in the system, Load 1 = 976 + j100 MVA in area 1 and Load 2 = 1767 + j100 MVA in area 2. To boost up the voltage in the system, capacitor banks Cap 1 = 200 Mvar and Cap 2 = 350 Mvar are connected to the same buses as the loads. Area 1 and area 2 are connected by a double set of transmission lines that are 220km long. The lines are modelled as equivalent π circuits. The parameters for the transmission lines are given in the Appendix. Power is transferred from area 1 to area 2 to supply Load 2 that is much bigger than the total generator capacity of area 2.

Table 1: HVAC two area multi machine system voltage profile

Element	Rated Voltage (kV)	Voltage magnitude and angle (pu)			
		DigSilent	PST	PSAT	Ref[1]
Bus 1	20	1.03∠2 0.25°	1.03∠2 0.25°	1.03∠2 0.27°	1.03∠2 0.20°
Bus 2	20	1.01∠1 0.49°	1.01∠1 0.51°	1.01∠1 0.5°	1.01∠1 0.5°
Bus 3	20	1.03∠- 6.8°	1.03∠- 6.8°	1.03∠- 6.8°	1.03∠- 6.8°
Bus 4	20	1.01∠- 16.99°	1.01∠- 16.99°	1.01∠- 16.99°	1.01∠- 17°
Bus 5	230	1.01∠1 3.79°	1.01∠1 3.79°	1.01∠1 3.8°	*
Bus 6	230	0.98∠3 .71°	0.98∠3 .71°	0.98∠3 .72°	*
Bus 7	230	0.96∠- 4.7°	0.96∠- 4.69°	0.96∠- 4.68°	*
Bus 8	230	0.95∠1 8.56°	0.95∠1 8.57°	0.95∠1 8.56°	*
Bus 9	230	0.97∠- 32.15°	0.97∠- 32.17°	0.97∠- 32.15°	*
Bus 10	230	0.98∠- 23.73°	0.98∠- 23.73°	0.98∠- 23.73°	*
Bus 11	230	1.01∠- 13.43°	1.01∠- 13.44°	1.01∠- 13.43°	*

*: Not displayed in reference [1]

Table 2: HVAC two-area multi machine system active power profile

Element	Active Power (MW)			
	DigSilent	PST	PSAT	Ref[1]
Gen 1	700	700	700	700
Gen 2	700	700	700	700
Gen 3	719.05	719.11	719.09	719
Gen 4	700	700	700	700
HVAC 1	190.69	190.67	190.67	*
HVAC 2	190.69	190.67	190.67	*
Load 1	967	967	967	967
Load 2	1767	1767	1767	1767
Cap 1	0	0	0	0
Cap 2	0	0	0	0

*: Not displayed in reference [1]

Table 3: HVAC two-area multi machine reactive power profile

Element	Reactive Power (Mvar)			
	DigSilent	PST	PSAT	Ref[1]
Gen 1	184.64	185.26	185.01	185.00
Gen 2	233.77	234.84	234.59	235.00
Gen 3	175.6	176.26	176	176
Gen 4	201.18	202.35	202.05	202.00
HVAC 1	-53.17	-53.79	-53.56	*
HVAC 2	-53.17	-53.79	-53.56	*
Load 1	100	100	100	100
Load 2	100	100	100	100
Cap 1	200	200	200	200
Cap 2	350	350	350	350

*: Not displayed in reference [1]

All generators supply 700MW except generator 3 which supplies close to 719MW. The total power generated is approximately (2819 + j798) MVA for all the software packages, from which about half of this power is generated in each area. Since the 1767MW load in area 2 cannot be fully supplied by what is generated in area 2, about 380MW is imported from area 1. Approximately 185Mvar is supplied from generator 1, 234Mvar from generator 2, 176Mvar from generator 3 and 202Mvar from generator 4. Each of the lines carries half of the power to area 2. The negative sign on the transmission lines reactive power indicates that the respective lines are absorbing reactive power. The power generated in the different packages by all machines is very close to the values presented in the literature.

4.2 HVDC system (scenario 2)

The HVDC system is a monopolar 500 kV, 230 MVA, 0.46 kA link with 12 pulse converters on both rectifier and inverter sides. This HVDC system is modified from the CIGRE benchmark model [7, 8]. The HVDC line is modeled as a π equivalent circuit. Each converter has its own converting transformer. The HVDC transmission line is 220km long and its parameters are given in the Appendix. To control the power transmitted across the HVDC link the rectifier is modelled using current control. Apart from the HVDC system, the rest of the structure of the system and the parameter is similar to the HVAC system.

Figure 4: Hybrid two area multi machine system

TOPIC C. POWER SYSTEMS

Proceedings of the 19th Southern African Universities Power Engineering Conference
SAUPEC 2010, University of the Witwatersrand, Johannesburg
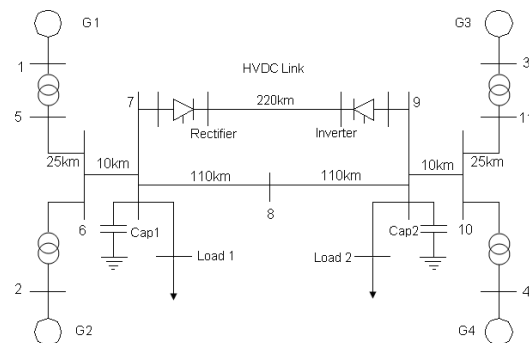
Figure 4 depicts the parallel combination of the HVAC and HVDC transmission lines. The current control on the rectifier station is set to 0.4kA so that the power flow between the lines is quasi equally split. The power flow results for this system are presented below.

Table 4: Hybrid two area multi machine system voltage profile

Element	Rated Voltage (kV)	Voltage and angle (pu)		
		DigSilent	PST	PSAT
Bus 1	20	1.03 ∠21.36°	1.03 ∠21.43°	1.03 ∠21.32°
Bus 2	20	1.01 ∠11.51°	1.01 ∠11.57°	1.01 ∠11.48º
Bus 3	20	1.03 ∠-6.8º	1.03 ∠-6.8º	1.03 ∠-6.8º
Bus 4	20	1.01 ∠-16.87º	1.01 ∠-16.88º	1.01 ∠-16.86º
Bus 5	230	1.00 ∠14.86º	1.00 ∠14.92º	1.00 ∠14.83º
Bus 6	230	0.97 ∠4.64º	0.96 ∠4.68º	0.97 ∠4.6º
Bus 7	230	0.94 ∠-4.02º	0.94 ∠-4º	0.94 ∠-4.06º
Bus 8	230	0.93 ∠-18.31º	0.93 ∠-18.33º	0.93 ∠-18.33º
Bus 9	230	0.96 ∠-32.19º	0.96 ∠-32.23º	0.96 ∠-32.18º
Bus 10	230	0.98 ∠-23.67º	0.98 ∠-23.69º	0.98 ∠-23.66º
Bus 11	230	1.01 ∠-13.38º	1.01 ∠-13.39º	1.01 ∠-13.38º
Rectifier	500	1.01 ∠0°	1.01 ∠0°	*
Inverter	500	1.01 ∠0°	1.01 ∠0°	*

*: No display of the results in PSAT

The voltage magnitudes for machines 1 and 3 are 1.03pu and 1.01pu for machines 2 and 4. The lowest voltage for this syetem is 0.93pu on the HVAC line at bus 8. The voltages on the DC side of the rectifier and inverter are 1.01pu respectively in DigSilent and Matlab PST. Matlab PSAT does not display the voltage profile for the HVDC converter stations.

Table 5: Hybrid two area multi machine system active power profile

Element	Active Power (MW)		
	DigSilent	PST	PSAT
Gen 1	700	700	700
Gen 2	700	700	700
Gen 3	712.06	712.27	712.09
Gen 4	700	700	700
HVAC Line	187.43	187.15	187.04
HVDC Line	201.1	201.25	201.96
Rectifier	202.09	202.24	202.95
Inverter	201.1	201.25	201.96
Load 1	976	976	976
Load 2	1767	1767	1767
Cap 1	0	0	0
Cap 2	0	0	0

Table 6: Hybrid two-area multi machine reactive power profile

Element	Reactive Power (Mvar)		
	DigSilent	PST	PSAT
Gen 1	216.79	219.56	217.03
Gen 2	311.17	317.33	311.7
Gen 3	192.94	195.02	193.53
Gen 4	246.9	251.34	248.53
HVAC Line	-57.88	-58.53	-57.86
HVDC Line	0	0	0
Rectifier	62.76	43.68	47.629
Inverter	77.24	77.02	56.028
Load 1	100	100	100
Load 2	100	100	100
Cap 1	200	200	200
Cap 2	350	350	350

The power generated by all machines with the exception of machine 3 in the hybrid system is 700MW. Machine 3 produces roughly 712 MW, and the total generated power is approximately (2812 + j971) MVA. Machine 3 is supplying less power than in the HVAC system. This is due to the fact that the HVDC line only looses approximately 1.8MW losses while the HVAC line looses approximately 9.2MW across all packages, hence more power is delivered to area 2 on the hybrid system. The HVDC line transfers approximately 201MW across all software packages. The reactive power obtained in Matlab PST is slightly higher when compared to DigSilent and Matlab PSAT.

5. CONCLUSIONS

For AC power flow, all software packages perform satisfactorily. The results for the voltage power profile for the HVAC system across all software packages agree with what is given in literature, hence validating their power flow results. Generators 1, 2 and 4 supply 700MW and the slack bus (generator 3) supplies close to 719MW. The voltage drop across the hybrid is a result of the interaction of a weak AC system with a DC system. The lack of reactive power, which is consumed by the converter stations, in the weak AC system leads to a fall in the AC voltage. The hybrid system is a combination of an HVAC and HVDC transmission systems. Generators 1, 2 and 4 each supply 700MW, and generator 3 supplies close to 712MW across all software packages as the HVDC has fewer losses than the HVAC transmission system.
The active power generated by the hybrid system reduces by nearly 7MW overall across all packages. All software packages agree in the results obtained. Both for HVAC and a parallel combination, power flow studies can confidently be performed using any of the packages.
Limitations: Matlab PST and PSAT do not allow HVDC systems to be modeled without an HVAC system in parallel connected to it. Matlab PSAT does not display the results for the rectifier and inverter buses when the HVDC load flow is performed.
Future work: All software packages will be used to perform small-signal and transient stability studies

on the HVAC and Hybrid two-area multi machine systems.

REFERENCES:

[1] P. Kundur, "Power System Stability and Control", McGraw-Hill, Inc., 1997

[2] D. A. Woodfrod, "HVDC Transmission", Manitoba HVDC Research Centre, Canada, 18 March 1998

[3] J. Arrilaga, Y. H. Lin, N. R. Watson, "Flexible power transmission The HVDC options", John Wiley & Sons, ISBN 978-0-470-05688

[4] DigSilent Power Factory Version 12.0.194 Basic User's Manual, 2001

[5] Joe Chow, Power system Toolbox Version 2.0 Load Flow Tutorial and Functions Manual, 2003

[6] Federico Milano, Power System Analysis Toolbox Quick Reference Manual for PSAT version 2.1.2, June 26, 2008

[7] M. O. Faruque, Y. Zhang and V. Dinavahi, "Detailed Modelling of the CIGRE HVDC Benchmark System Using PSCAD/EMTDC and PSB/SIMULINK", IEEE Transactions on Power Delivery, Vol. 21, No. 1, January 2006

[8] Working Group 14.02, "The CIGRE benchmark model – A new proposal with revised parameters", December 2003

APPENDIX

Synchronous generator data

$X_d = 1.8$ $X'_d = 0.3$ $X''_d = 0.25$ $X_q = 1.7$ $X'_q = 0.55$ $X''_q = 0.25$ $X_l = 0.2$ $R_a = 0.0025$ $T'_{do} = 8s$ $T''_{do} = 0.03s$ $T'_{qo} = 0.4s$ $T''_{qo} = 0.05s$ $A_{sat} = 0.015$ $B_{sat} = 9.6$ $\psi_{TI} = 0.9$ $S_{1.0} = 0.039$ $S_{1.2} = 0.223$ $K_D = 0$ $H = 6.5$(For machines 1 and 2) $H = 6.175$(for machines 3 and 4)

HVAC line parameters:

R = 0.0529 Ω/km, X = 0.529 Ω/km and B = 3.371 μS/km.

Using an S_{base} = 100MVA and a V_{base} = 230kV, the equivalent parameters in per unit values are R = 0.0001 pu, X = 0.001 pu and B = 0.00175 pu.

HVDC line parameters:

R = 0.0281 Ω/km, X = 0.02 Ω/km, B' = 0.44 μS/km.

Using a S_{base} = 230MVA and a V_{base} = 500kV, the equivalent parameters in per unit values are R = 0.000025 pu, X = 0.000022 pu and B = 0.000021 pu.

TOPIC C. POWER SYSTEMS

Proceedings of the 19th Southern African Universities Power Engineering Conference
SAUPEC 2010, University of the Witwatersrand, Johannesburg

APPLICATION OF PREDICTIVE RELIABILITY ANALYSIS TECHNIQUES IN DISTRIBUTION NETWORKS

N Mathebula*,   K Awodele**, S.P Chowdhury+ and S Chowdhury++

University of Cape Town, Department of electrical engineering, University of Cape Town Private Bag X3 7701 Rondebosch

*ntiyiso.mathebula@gmail.com **kehinde.awodele@uct.ac.za + *sp.chowdhury@uct.ac.za*
++sunetra.chowdhury@uct.ac.za

Abstract.   This paper evaluates the reliability of bus 4 of the RBTS and also a portion of a typical Cape Town network. The RBTS is evaluated using both Monte Carlo simulations (MCS) and Failure Mode and Effects Analysis (FMEA). Failure frequency and duration distributions are computed for load point 1 using MCS. The duration distribution for feeder 1 is also computed. Two other cases on the RBTS are evaluated. The typical Cape Town network load point indices are also evaluated using MCS. From the evaluation of the cases on the RBTS, conclusions are made. Conclusions are also made about the reliability of the real network.

Keywords: Monte Carlo Simulations; Failure Modes and Effects Analysis; Failure frequency and Duration Distributions.

1. INTRODUCTION

Power systems are expected to deliver electrical energy continuously to the customer as and when necessary [1]. For this reason, power systems are designed as meshed systems with redundancy occurring at different points in the network. The power system components are usually overdesigned so that they are operated at levels below their design capacity in order to decrease the probability of failure. Intelligent protection systems minimise or eliminate power outages and interruptions in case of faults. All these precautionary measures are used to ensure that the network is able to deliver electrical energy continuously to the customer. With all these efforts, still outages and blackouts occur. In the year 2003 there were six blackouts within five different countries that affected approximately 112 million people. All these occurred in a period of six weeks [2]. This was certainly an unacceptable level of reliability in power systems across the globe. Blackouts and power interruptions have a negative impact on the economy, environment and safety in general [3]. Some other factors that contribute to a need for reliable distribution systems include:

(i) Sensitivity of loads to poor power quality (voltage and frequency deviations) and supply interruptions [4].
(ii) Implementation of reliability standards by state regulatory authorities [5].The implementation of reliability standards stems from concern from agencies as they anticipate that deregulation will have negative impact on reliability [6].

Power systems reliability evaluation is concerned with power outages and interruptions [7]. This assesment can be subdivided into two key studies: system security and system adequacy [1]. Power system security describes the ability of the system to respond to system disturbance. The way in which the system would respond to a lightning strike for example, is a security problem. Power system

adequacy on the other hand, evaluates if a network has sufficient facilities to supply the customers load demands and is associated with static conditions. Proper generation, transmission and distribution capacity all relate to power system adequacy [1]. Most statistical reliability analysis techniques available address power systems adequacy [1]. Power system security can however be assessed and reference [8] presents this assessment by using fuzzy logic.

Techniques that can be used to evaluate the reliability of distribution systems are subdivided into analytical and simulation techniques. Simulation methods recreate the actual process and systems random behavior. This is done to estimate the reliability indices [1]. Analytical approaches represent the system by a mathematical model and compute reliability indices from the mathematical equations [6]. In this paper, both analytical and simulation techniques are used to determine the reliability of the Roy Billinton Test System (RBTS). Failure Mode and Effect Analysis (FMEA) is used as the analytical technique and Monte Carlo Simulation (MCS) is used as the simulation technique. The objectives of this paper are to use Monte Carlo Simulations and Failure Mode and Effect Analysis (FMEA) to evaluate the reliability of bus 4 on the Roy Billinton test system (RBTS); and also to evaluate the reliability of a real network, a typical network in Cape Town, using Monte Carlo Simulations.

2. DEVELOPMENT OF PREDICTIVE RELIABILITY ANALYSIS TECHNIQUES

2.1 Failure modes and effect analysis (FMEA)

FMEA analyses the potential failures of components in order to determine the effects that these have on the system [7]. This method essentially evaluates the different contingencies. FMEA method is demonstrated here by the network shown in figure 1 below.

Proceedings of the 19th Southern African Universities Power Engineering Conference
SAUPEC 2010, University of the Witwatersrand, Johannesburg

TOPIC C. POWER SYSTEMS

This network consists of a feeder with distributors and load points connected to them. The feeder has 4
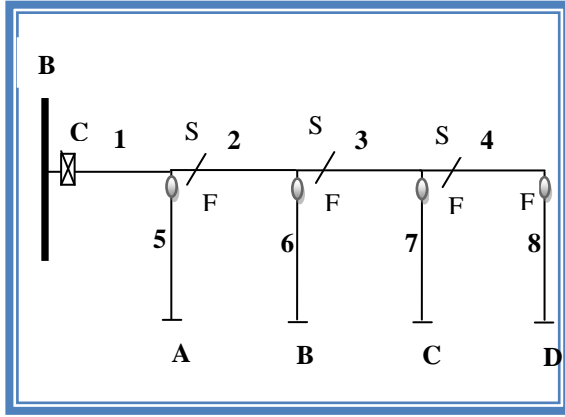
Figure 1: Simple network with 4 load points [9]

sections labelled 1-4 as shown in figure 1. The distributors are labelled 5 – 8. The network has fuse gears (F) at the tee-point in each lateral distributor. A circuit breaker (C) connects the feeder to bus 1. Switches are provided to isolate faulted part of network whenever faults occur. There are 4 load points labelled A, B, C and D. The operating procedure for the network is as follows: If any section of the main feeder fails, then the circuit breaker will be activated and all load points will be without supply. When this happens, the relevant switches will be opened to isolate the faulted part of the network. Then the circuit breaker will reclose and supply to healthy parts of the system will be restored. The faulted part of the system will only be restored once the component is repaired. If one of the distributors fails, the fuse gear will isolate the fault and hence only the local load point will be affected. To simplify the evaluation, it is assumed that the circuit breaker and the fuse gears do not fail.

FMEA is used to evaluate the contingencies of each of the 8 components failing and to see how this affects the load points. The network in figure 1 is a series network and therefore series equations can be used to calculate the load point indices. These equations are as follows [9]:

$$\lambda_s = \sum_{i=1}^{n} \lambda_i \tag{1}$$

$$r_s = \frac{U_s}{\lambda_s} = \frac{\sum_{i=1}^{n} \lambda_i r_i}{\sum_{i=1}^{n} \lambda_i} \tag{2}$$

$$U_s = \lambda_s \times r_s = \sum_{i=1}^{n} \lambda_i \times r_i \tag{3}$$

Using the component failure rate, component outage time and switching time, the FMEA table can be computed. Below is a reduced version of the table for the network in figure 1. Only load point A is represented here.
The following are to be noted:

(i) The rows of Table 1 represent components 1 to 8. The columns represent the indices for each load point.

Table 1: FMEA table for load point A

Component no.	Load pt A		
	λ (f/yr)	r (hours)	U (hours/yr)
1	0.2	4	0.8
2	0.1	0.5	0.05
3	0.3	0.5	0.15
4	0.2	0.5	0.1
5	0.2	2	0.4
6			
7			
8			
Overall	1	1.5	1.5

(ii) If the component failure affects a particular load point, then the indices are inserted (U is calculated using equations) into the columns of that load point and the row of that component. If a component failure does not affect that load point, then the columns of that load point and the row of that component will be blank. For example, failure of components 6-8 do not affect load point A so the three columns for load point A are blank in rows 6-8.

(iii) The outage time can either be the repair time or switching time. This is determined by the load point being evaluated and its location in the network. For example, when evaluating load point A, if component 2 fails, the outage time is equal to switching time. But if component 1 fails, the outage time is equal to repair time.

(iv) The last row of the table is the actual value of the different indices of the load points. These actual values of the different load point indices are calculated using the series equations. The FMEA table ensures that only the indices for the components that affect load point failures are included in the calculation. The failure rate of load point A for example is given by the summation column 1 of load point A (0.2 +0.1+0.3+0.2+0.2=1)

2.2 Monte Carlo Simulation (MCS)

MCS essentially creates an artificial history of the system. Predictable and random behaviour of the systems components are modelled and these models are used to simulate the system's behaviour (with respect to reliability). The load point indices are calculated using data collected in this artificial history [10].

TOPIC C. POWER SYSTEMS

Proceedings of the 19th Southern African Universities Power Engineering Conference
SAUPEC 2010, University of the Witwatersrand, Johannesburg

The following algorithm is used for implementing MCS [9]:

1. Generate a random number
2. Convert this number into a value of up time using a conversion method on the appropriate TTF (Time to Failure) distribution of the component. The method of conversion is detailed in [11].
3. Generate a new random number.
4. Convert this number into a value of repair time using a conversion method on the appropriate TTR (Time to Repair) distribution. The method of conversion is detailed in [11].
5. Repeat steps 1 – 4 for the desired simulation period. In order to obtain distributions, this should be a period of time which is able to capture the outage events under consideration. According to [9], a period of one year is usually sufficient for radial systems.
6. Repeat steps 1 – 5 for each component in the system.
7. Repeat steps 1 – 6 for the desired number of simulated periods. These steps create scenarios from which the load point reliability indices can be deduced. The principles of the subsequent procedure are as follows:
8. Consider the first simulated period lasting n years.
9. Consider the first component (feeder section or lateral distributor).
10. Deduce which load points are affected by the failure of this component.
11. Count the number of times this component fails during this period. Let this be N. The failure rate is calculated as follows:

$$\lambda = \frac{N}{\sum TTF} \tag{4}$$

12. Evaluate the total down time of the load point. This will equal the total downtime (i.e. repair time) of the component if it cannot be isolated and the load point restored to service by switching. If the component can be isolated, the down time of the load point is taken as the total time to restore the load point by switching. The latter value can be considered either as a deterministic value of time or itself sampled from an assumed distribution .

In either case, define the value as $\sum TTR$, total time taken to restore the load point in n – year period.

13. The average down time is given by:

$$r = \frac{\sum TTR}{N} \tag{5}$$

13. The annual unavailability (U) is given by:

$$U = \lambda \times r \tag{6}$$

14. Steps 8 – 13 create the first row of the FMEA (table 1) for one simulated period.
15. Repeat steps 9 – 14 for each system component to produce the complete the FMEA table.
16. Calculate the load point indices from the FMEA table using the equation for series system. This set of indices represents one point on each of the probability distributions.
17. Repeat steps 8 – 16 for each of the simulated periods. This produces a series of individual points from which the complete probability distributions can be determined. Generally, these distributions are plotted as frequency histograms or probability distributions.
18. The average values, standard deviations and any other statistical parameter of these distributions can be evaluated.

3. RESULTS

Reliability of bus 4 of the RBTS and a real network in Cape Town are evaluated in this paper. Three case studies are performed for the RBTS. These cases are variations of how the network can be operated and maintained. The RBTS network and network parameters are reported in [12].

3.1 Base Case for RBTS

In this case the network has alternate supply, fuse gears, switches and faulted transformers are repaired. Table 2 shows the system indices for the base case. The load point indices for the base case are can be found in table A1 in the appendix and are discussed below. The MCS expected values for the load point indices are simulated over a period of 10000 years.

This is done in order to increase the data (total number of failures, time to failure, time to repair) computed in the simulation and hence increases accuracy of the results at the end of the simulation. This however increases the simulation time which is a disadvantage.

It took 54 seconds to simulate for a long feeder. The computational time for the analytical method was

Table 1: System Indices For Base Case of RBTS

Feeder number	SAIFI (Interruptions/customer yr)		SAIDI (hrs/customer yr)		CAIDI (hrs/customer interruption)		ENS (kWhr/yr)	
	MCS	FMEA	MCS	FMEA	MCS	FMEA	MCS	FMEA
1	0.3010	0.301	3.4772	3.4681	11.5526	11.521	1.2216e+004	1.22E+04
2	0.1895	0.1896	0.3759	0.3759	1.9836	1.98286	1.3210e+003	1.32E+03
3	0.2932	0.2933	3.4685	3.4683	11.8281	11.8266	1.2006e+004	1.20E+04
4	0.3076	0.3075	3.4776	3.4746	11.3058	11.2987	1.3943e+004	1.39E+04
5	0.1863	0.1863	0.3726	0.3727	1.9996	2	1.1177e+003	1.12E+03
6	0.1950	0.195	0.3640	0.364	1.8668	1.86667	1.2659e+003	1.27E+03
7	0.2966	0.2967	3.4687	3.4723	11.6932	11.7045	1.2456e+004	1.25E+04
Overall system	0.3	0.2938	3.4672	4.3619	11.5676	22.5541	5.43E+04	5.43E+04

Proceedings of the 19th Southern African Universities Power Engineering Conference
SAUPEC 2010, University of the Witwatersrand, Johannesburg

TOPIC C. POWER SYSTEMS

negligible. The maximum error in the MCS results is 0.00603%. This error was the error in outage time at load point 2.

The highest failure rate is 0.311 f/yr. This failure rate occurred on several load points connected to feeder 4 (via distributors). It is also noted that feeder 4 is a long feeder with the most number of components and load points. Feeders 1, 3 and 7 have comparable failure rates (all comparable to feeder 4) and are also long feeders containing many components. The lowest failure rate was 0.179 which occurred on feeder 5, load point 28. It is also noted that feeder 5 is a small feeder with fewer components. Feeders 2 and 6 have comparable failure rates (comparable to feeder 5) and are also short feeders with fewer components.

The longest outage time was 12.0044 hours, which occurred in load point 14, feeder 3. This feeder is one of the long feeders but has slightly less number of components than feeder 4. Feeders 1, 4 and 7 have comparable outage times (comparable to feeder 3). These feeders have 11/0.415 kV transformers on their distributors. These transformers are repaired whenever they fail with an outage time of 200 hours.

The lowest outage time was 1.8135 hours which occurred in load point 29, feeder 6. Feeders 2 and 5 have comparable outage times (comparable to feeder 6). These 3 feeders do not have 11/0.415 kV transformers on their distributors. Consequently, feeders 1, 3, 4 and 7 have load points with the highest unavailability. Feeders 2, 5 and 6 have load points with lower unavailability i.e. higher availability.

Feeders 1, 3, 4 and 7 supply power to load points with residential and commercial customer types. These feeders have comparable SAIFI, SAIDI and CAIDI. This follows from the similarities in the load point indices and also from the similarity in number of customers. The ENS of these feeders is also comparable in that they are of the same order of magnitude ($\times 10^4$ kWhr/yr). This is partly due to the fact that these feeders have load points with comparable unavailability indices and also due to the fact that these load points have comparable average loads. Similarly, feeders 2, 5 and 6 have comparable SAIFI, SAIDI, CAIDI and ENS. These feeders supply power to load points with small users. Figure 2 below shows the failure frequency histogram for load point 1. The expected failure rate of load point 1 is 0.295 f/yr. This means that it is expected that 1 failure will occur every 3.38 years. The failure frequency distribution is shown in figures 2. The failure duration distribution is in figure 3.

This duration distribution spans over a wide range of duration times. The expected outage duration is 11.731. It can be seen from the distributions above that the outage duration can be as high as 22 hours . This is the extreme case and the probability of this happening is less than 0.01.
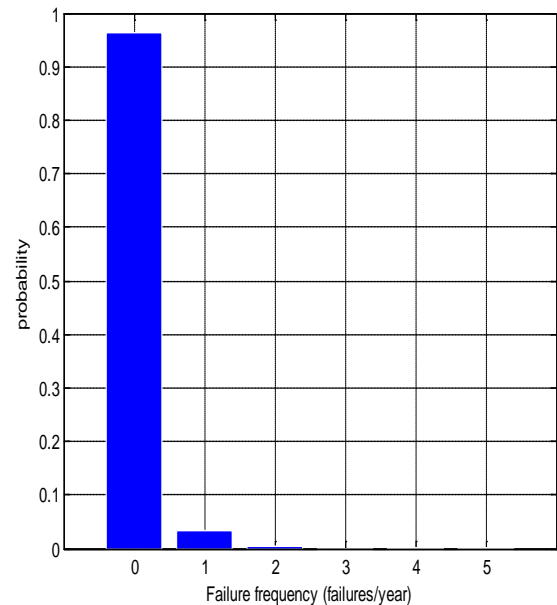
Figure 2: Failure frequency distribution
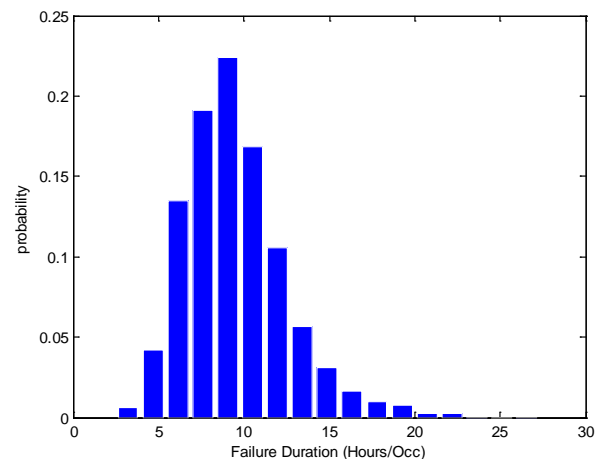
Figure 3: Load point 1 failure duration distribution

3.2 Case 2 of RBTS

Case 2A: In this case the network has alternate supply, fuse gears, switches; and faulted transformers are replaced. The difference between this case and the base case is that faulted transformers are replaced instead of repaired. The input data for the transformer repair time thus decreases from 200 hours (which was used for the base case) to 10 hours. All other data do not change and are the same as in the base case. Case 2A uses overhead lines as in the base case. Case 2B uses cables. When cables are used, the failure rate of all the lines in the network decreases from 0.065 failures/year.km (base case) to 0.04 failures/year.km. The repair times of all the lines in the network increases from 5 hours to 30 hours. All the data used in this case and all other cases was taken from reference [12].

Comparing these results to the base case results, it is observed that there is a negligible change in SAIFI.

TOPIC C. POWER SYSTEMS

Proceedings of the 19th Southern African Universities Power Engineering Conference
SAUPEC 2010, University of the Witwatersrand, Johannesburg

The overall system SAIDI decreases from 3.4672 hrs/customer yr to 0.6209 hrs/customer yr. This drastic change is due to the decrease in SAIDI on feeders 1, 3, 4 and 7. These feeders were affected because they have the 11/0.415 kV transformers on their distributors and the short replacement times on their transformers changed SAIDI. Note also that CAIDI and ENS on these feeders also decrease and hence overall system CAIDI and ENS decrease. Feeders 2, 5 and 6 are not affected (as they have no distribution transformers connected to the distributors).

Case 2B: Comparing the results of case 2B to Case 2A, it is observed that SAIFI decreases for all feeders. This is because cables are less prone to fault than overhead lines (i.e. the failure rate of the cables is lower). However, SAIDI increases. This is due to the increased outage time of the cables (since cable repair rate is low). CAIDI and ENS increase. CAIDI increased because the failure rate decreased and Unavailability increased. ENS increased because the total unavailability of the all load points increased.

3.3 Case 3 of RBTS

Case 3A: In this case it is assumed that there is no alternate supply, no fuse gears, no switches and faulted transformers are repaired. In Case 3A, the network is designed using overhead lines. In Case 3B, the network is designed using cables. It is observed that all system indices increase and are very high compared to the previous cases.

Case 3B: SAIFI decreases as compared to case 3A but is still higher than all other cases. It decreases because the cables are less prone to fault than overhead lines (i.e. the failure rate of the cables is lower). It is however still higher than other cases because this case has the worst system conditions. SAIDI increases just like in case 2B. In this case however, SAIDI is higher than all other cases because this case has the worst system conditions.
CAIDI and ENS also increase and are higher than all other cases. Just like in case 2B, CAIDI increases because the unavailability increases and failure rate decreases when compared to case 3A. ENS increased because the total unavailability of the all load points increased.

3.4 Typical Cape Town network

The data of a typical Cape Town network was used to calculate the component indices of all the components in the network. The calculated component indices served as the input data to the MCS. Table 3 shows the results of the simulation of the network.

Load points G, H, I and G have the highest load point indices. These load points are all connected to the same feeder. This feeder was the longest feeder in the reduced network. These load points are expected to

experience approximately 1 failure every two years for duration longer than 4 hours.

Table 3: Results for the Typical Cape Town network

Load	λ (f/yr)	r (hrs)	U (hrs/yr)
E	0.2960	3.0000	0.8879
F	0.2949	3.6236	1.0685
G	0.4799	4.3673	2.0959
H	0.4798	4.3691	2.0963
I	0.4798	4.3531	2.0889
J	0.4799	4.3673	2.0959
K	0.3966	5.5687	2.2083
L	0.3963	5.0892	2.0171
M	0.3961	5.0551	2.0024
N	0.1575	1.6494	0.2598
O	0.1574	1.6454	0.2590

4. CONCLUSIONS

MCS had the major disadvantage of high computational time. MCS can however yield distributions which show how the indices vary. Both MCS and FMEA are suitable for computing system and load point indices, however if distributions are not required, it is better to use FMEA. For example, if a cost/worth analysis was carried out for industrial customers with critical processes or commercial customers with non-linear cost functions then distributions would be required [14].

4.1 Reliability of RBTS

 (i) In all study cases, feeders 1, 3, 4 and 7 were identified to have the highest load point and system indices. The reason for this was that these feeders have many components which can fail and affect load points connected to these feeders. These feeders therefore are the least reliable section of the RBTS based on the indices used.

 (ii) It is better to replace transformers instead of repair them from a duration of interruption point of view. Feeders 1, 3, 4 and 7 SAIDI, CAIDI and ENS reduced significantly when transformers were replaced instead of repaired.

(iii) Cables reduce load point failure rate and feeder SAIFI. They however increase SAIDI, CAIDI and ENS. It is therefore better to use cables for customers that have less tolerance (based on their needs) for number of interruptions but can tolerate fewer interruptions for longer durations.

(iv) The way the network is operated and the protection and isolating components affect the reliability of a network drastically. Case 3 had the worst indices because the protection and

isolating devices were removed and there was no alternative supply.

(v) The failure frequency distribution for load point 1 (base case) showed that there is a greater than 0.95 probability of having 0 failures in a year and the probability of having 1 failure was less than 0.05.

(vi) The failure duration distribution for the base case for load point 1 showed that the durations of failures varied over a wide range and the expected value had a low probability. This lowers the confidence in the expected value.

4.2 Reliability of the Typical Cape Town Network

Based on the results in section 3.4, the following load points are the worst performing load points in the typical Cape Town network: G, H, I and J.

5. RECOMMENDATIONS

This paper demonstrated how predictive techniques can be used to evaluate the reliability of a network. The information that can be obtained from such studies can help planners, designers and managers in South Africa to make the following decisions: Selection of components and design type, Maintenance philosophy and Protection schemes.

Although reliability is a very important topic and deserves attention and focus, it is not enough just to evaluate the reliability of a network. Planners, designers and managers of distribution systems have to make decisions based on both the reliability of the network and the associated customer and utility costs. It is therefore recommended to investigate the customer and utility cost associated with the different levels of reliability in cases 1 to 3 of the RBTS.

Any reliability improvement program planned for the typical Cape Town network in this study should give load points G, H, I and J priority.

ACKNOWLEDGEMENTS

REFERENCES

[1] R.Billinton, R.N.Allan and L.Salvaderi, *Applied Reliability Assessment In Electtric Power Systems*, IEEE Press, 1991.

[2] *"Power System Reliability And Adequacy"*, Notes prepared by T.Gaunt, Department of Electrical Engineering, , UCT, Cape Town 2009.

[3] H.L.Willis, G.V.Welch and R.R.Schrieber, *Aging Power Delivery Infrastructres,* CRC Press, 2001.

[4] M.G Da Silva et al, "An application of predictive reliability analysis techniques in Brazil's northeast distribution networks", *Energy power and Energy Systems*, Vol. 29, pp 155 – 162, 2007.

[5] N.Balijepalli, S.S.Venkata, and R.D.Christie, "Modeling and Analysing of Distribution Reliability Indices", *IEEE Transactions On Power Delivery*, Vol. 19(4), pp 1950 – 1955, 2004.

[6] R.E.Brown, M.V.Engel, J.H.Spare, "Making Sense of Worst-Performing Feeders" , *IEEE Transactions On Power Systems*, Vol. 20, pp 1173 -1178, 2005.

[7] R.E.Brown, *Electrical Power Distribution System Reliability*, CRC Press, 2008..

[8] B.P.Lang and A.Pahwa, "Power Distribution System Reliability Planning Using a Fuzzy Knowledge-Based Approach", *IEEE Transactions On Power Delivery*, Vol. 15, pp 279 – 284, 2000.

[9] R.Billinton and R.N.Allan, *Reliability Evaluation of Power Systems,* Plenum Press, 1996.

[10] "Distribution System Reliability Evaluation", Slides prepared by S.R.Yeddanapudi, , Iowa State University of Science and Technology.

[11] R.Billinton and R.N.Allan, *Reliability evaluation of Engineering Systems: Concepts and Techniques*, Plenum Press, 1992.

[12] R.N.Allan, R.Billinton, I.Sjarief, L.Goel and K.S.So, "A Reliability Test System for Educational Purposes – Basic Distribution System Data and Results", *IEEE Transactions on Power Systems* , Vol. 6, pp 813 – 820, 1991.

[13] N.Mathebula, *Application of Predictive Reliability analysis Techniques in Distribution Networks,* Undergraduate Thesis, Dept of Electrical Engineering, UCT, 2009.

[14] R.Billinton and P.Wang, "Teaching Distribution System Reliability Evaluation Using Monte Carlo Simulation", *IEEE Transactions on Power Systems*, Vol. 14, pp 397 – 403, 1999.

APPENDIX

Table A-1:Results for Base Case

TOPIC C. POWER SYSTEMS

Proceedings of the 19th Southern African Universities Power Engineering Conference
SAUPEC 2010, University of the Witwatersrand, Johannesburg

Load point	Failure rate (f/yr)			Outage time (hrs)			Unavailability (hrs/yr)		
	MCS	FMEA	%DIFF.	MCS	FMEA	%DIFF	MCS	FMEA	%DIFF
Feeder 1									
1	0.295	0.295	0	11.731	11.666	0.00561	3.455	3.436	0.00562
2	0.304	0.304	0.00148	11.521	11.452	0.00603	3.501	3.484	0.00469
3	0.295	0.295	0	11.6466	11.666	0.00162	3.43	3.436	0.00157
4	0.308	0.308	0.00033	11.4069	11.384	0.00203	3.509	3.501	0.00234
5	0.304	0.304	0.00049	11.4729	11.452	0.00183	3.492	3.484	0.00222
6	0.307	0.308	0.00195	11.3867	11.384	0.00026	3.495	3.501	0.00154
7	0.305	0.304	0.00115	11.4462	11.452	0.0005	3.487	3.484	0.00073
Feeder 2									
8	0.182	0.182	0	1.861	1.8571	0.00208	0.339	0.338	0.00178
9	0.192	0.192	0.00078	2.0163	2.0169	0.00032	0.386	0.387	0.00116
10	0.195	0.195	1.4E-16	2.066	2.0667	0.00032	0.403	0.403	0.00025
Feeder 3									
11	0.298	0.298	0.00084	11.7414	11.724	0.0015	3.493	3.491	0.00076
12	0.295	0.295	0	11.7407	11.798	0.00485	3.457	3.475	0.00501
13	0.295	0.295	0	11.8049	11.798	0.00059	3.477	3.475	0.00058
14	0.285	0.285	0.00018	12.0044	12.031	0.00219	3.419	3.426	0.00191
15	0.295	0.295	0	11.8273	11.798	0.00249	3.483	3.475	0.00253
16	0.285	0.285	0.00088	12.0012	12.031	0.00245	3.42	3.426	0.00162
17	0.294	0.295	0.00068	11.8007	11.798	0.00023	3.474	3.475	0.00029
Feeder 4									
18	0.311	0.311	0.00016	11.2224	11.233	0.00097	3.486	3.491	0.00125
19	0.301	0.301	0.00066	11.4169	11.435	0.0016	3.439	3.442	0.0009
20	0.31	0.311	0.00113	11.2268	11.233	0.00058	3.485	3.491	0.00176
21	0.311	0.311	0.00048	11.2619	11.233	0.00255	3.498	3.491	0.00202
22	0.301	0.301	0.001	11.4261	11.435	0.0008	3.442	3.442	8.7E-05
23	0.311	0.311	0.00048	11.2317	11.233	0.00014	3.489	3.491	0.00059
24	0.311	0.311	0.0008	11.2473	11.233	0.00125	3.498	3.491	0.00193
25	0.301	0.301	0.00066	11.4586	11.435	0.00204	3.446	3.442	0.00128
Feeder 5									
26	0.189	0.189	0.00053	2.0326	2.0345	0.00093	0.383	0.384	0.00052
27	0.192	0.192	0.00026	2.0857	2.0847	0.00046	0.4	0.4	0.00038
28	0.179	0.179	0.00084	1.8745	1.8727	0.00095	0.335	0.335	0.00194
Feeder 6									
29	0.192	0.192	0.00078	1.8135	1.8136	3.3E-05	0.348	0.348	0.00101
30	0.202	0.202	0.0005	1.9704	1.9677	0.00135	0.397	0.397	0.00202
31	0.192	0.192	0.00078	1.816	1.8136	0.00135	0.348	0.348	0.00187
Feeder 7									
32	0.301	0.301	0.00066	11.6464	11.608	0.00331	3.504	3.494	0.00272
33	0.301	0.301	1.8E-16	11.6255	11.608	0.00151	3.5	3.494	0.00157
34	0.288	0.288	0.00069	11.9024	11.906	0.00032	3.43	3.429	0.00026
35	0.301	0.301	0.00133	11.6012	11.608	0.00058	3.496	3.494	0.00063
36	0.288	0.288	1.9E-16	11.9208	11.906	0.00122	3.433	3.429	0.00122
37	0.301	0.301	0.00033	11.6205	11.608	0.00108	3.499	3.494	0.00146
38	0.288	0.288	0.00069	11.9331	11.906	0.00226	3.434	3.429	0.00143

Proceedings of the 19th Southern African Universities Power Engineering Conference
SAUPEC 2010, University of the Witwatersrand, Johannesburg

TOPIC C. POWER SYSTEMS

Evaluation of the Generator Circuit Breaker applications

J F Fourie* and J A de Kock**

North-West University, School of Electrical, Electronic and Computer Engineering, Potchefstroom, South Africa.

Abstract. The use of generator circuit breakers in power stations was evaluated. A feasibility study to determine if the additional capital cost required to use a generator circuit breaker in a power station can be justified by the possible saving in equipment damage, was completed. To ensure practical results, commonly used layouts were used to determine the effect of using a generator circuit breaker on the reliability, availability and the mean time to repair of a power station layout. The effect on zone protection on the generator and generator transformer increased selectivity of the protection system through the use of the generator circuit breaker.

Practical layouts were used to determine the effect on reliability using assumed values of operational costs to determine the cost incurred through the change in reliability of the power station. By adding a generator circuit breaker, the station transformer and associated equipment are regarded as back-up or redundant equipment. This increases the reliability of the power station dramatically and limits the risk of income lost due to failures. With the increased protection, higher availability and the possible omission of power station equipment, the use of generator circuit breakers will result in more power delivered and more income generated by a power station.

The study proved that the generator circuit breaker is a critical part of a power station layout and is a necessary capital requirement to ensure the sustainability of the power station.

Key Words. Generator circuit breaker, Power station layout, reliability, circuit breaker

1. INTRODUCTION

A circuit breaker is "a mechanical device capable of making, carrying and breaking currents under normal circuit conditions and also making, carrying for a specific time and breaking currents under specified abnormal circuit conditions such as those of short-circuits" [1]. The definition describes a circuit breaker's purpose in an electrical circuit. For this specific reason, this device has been used in most electrical circuits for more than a century. This paper focuses on a special type of circuit breaker, the generator circuit breaker (GCB). This circuit breaker is classified as a medium voltage breaker with a high current application. The circuit breaker is used in the circuit directly between the generator and the generator (step-up) transformer. This paper evaluates circuit breaker literature, specific characteristics of GCBs, compiles a reliability analysis, and the resulting capital and operational costs were evaluated. With this evaluation the aim was to determine the feasibility of the using of a GCB in various layouts. This paper aims to clarify and quantify these effects and impacts in a practical simulation.

The implication of installing a GCB is to improve the protection of the generator and associated equipment. This circuit breaker facilitates additional changes within the power station layout, changing the capital cost and the reliability of the layout. In this paper, these questions and the interaction of various elements will be quantified and evaluated, resulting in a practical layout of a power station. The effect of the using of a GCB will finally be determined by the comparison of the layouts with and without a GCB using the cost and availability of the system.

2. LITERATURE STUDY

2.1 Generator circuit breakers

This circuit breaker is located between the generator and the step-up transformer in generating stations. These breakers are usually for generators between 50 MVA and 1 800 MVA, and the primary goal is to protect the generator and transformer in a fast,

economic and reliable way. The operation of the circuit breaker is complicated as they should be able to carry load current of 6.3 kA to 40 kA. These circuit breakers should also be able to break enormously large short-circuit currents, up to 275 kA. GCBs belong to the medium voltage range of circuit breakers, but due to the high transient recovery voltage the circuit breakers should incorporate high voltage breaker design principles. The X/R ratio of the fault current may be very high.

Another requirement for GCBs is the direct performance implications to the generating plant, increasing the need for reliable and repeatable operation. The availability of a power plant is thus an essential performance indicator, and with a GCB included within a generating system the differential protection zones ensures maximum selectivity [3]. This ensures that generator fed short-circuit current is interrupted within 40 ms and limits damage to the step-up transformer [3]. These requirements are aggravated due to the possibilities of switching out-of-phase currents or low power factor loads. An advantage is the relative ease of synchronisation on the generator voltage level in relation to synchronisation on high voltage levels [4].

Associated with the lower voltage levels, is the extreme high current levels continuously carried by the GCB. This breaker must be able to break generator and system fed short circuits in the shortest possible time. The pressure build-up through breaking fault currents of 200 kA can result in premature failure of the device [3]. Therefore, overpressure relief valves are essential to generator breakers to limit the mechanical damage associated with pressure build-up. The opposite to high pressure is the lack thereof; this can occur with breaking of small currents and thus the normal puffer principles still needs to exist to resolve this problem [3].

The most important components of a GCB are the arcing contacts. The design and construction of this

TOPIC C. POWER SYSTEMS

Proceedings of the 19th Southern African Universities Power Engineering Conference
SAUPEC 2010, University of the Witwatersrand, Johannesburg

device is critical to the life expectancy of the GCB. This contact material has to withstand the repeated plasma conditions over the lifetime of the breaker [3]. This material should also not vaporize with the arc exposure as this will contaminate and degrade the insulating gas. To further complicate this seemingly simple device, the mechanical stability is also important. These devises have to stay in position and ensure minimal power losses through the balance of repulsive and attractive forces, or anti-parallel and parallel current paths [3].

To extend the life and the capabilities of a GCB thermal aspects of normal and fault conditions should be considered. The heat generated by the continuous current through the device must be less than the capability of the insulating resins to withstand heat. These effects can be limited by optimising the design to limit heat generation, using an external housing to dissipate heat through cooling fins, and an encapsulated design to limit external field strength leading to heat generation [3]. This generated heat can limit the life of a circuit breaker dramatically due to the degrading of the insulation. New insulation have been developed to withstand temperatures of $105\,^{\circ}$C for 30 years to prolong circuit breaker life [3].

One of the greatest differences between generator breakers and medium voltage circuit breakers is the effects of the X/R ratio of the power system. This causes a high magnitude of DC components within the fault current, creating some difficulty because the current does not pass through zero [5]. Most circuit breakers are rated to break their rated symmetrical current at a maximum X/R ratio of 17. The X/R ratio partly determines the needed opening time, maximum RMS current and the time constant of the system, and is a critical requirement associated with GCBs as high X/R ratios are regularly associated with faults close to large generators. High X/R ratios can cause high alternating current exponential components, and high DC components. To ensure the generator breaker specified in the system is designed to withstand and is capable of interrupting system faults, the rating of the breaker must be adapted to the system conditions.

2.2 Generator operation modes
Beyond the normal operating conditions of conducting the normal generator current, GCBs are also required to synchronise the generator with the system and in other cases switch no-load currents. This is critical as the overvoltages resulting from closing an unloaded line, opening an isolating switch and breaking low inductive and capacitive currents can cause damage to equipment [2]. Overvoltages can be controlled through external or internal devices to limit the effects on insulation systems.

When closing any circuit breaker within a system the load and parameters of the network changes resulting in the "shift" in the power system to accommodate these changes. The equipment connected through the circuit breaker can contain a trapped charge and

result in additional overvoltages within the system. The factors that have an effect on the overvoltage are the length of the line, high source reactance, number of parallel-connected lines, switching unloaded lines, and re-closing after fault clearing. When a single line-to-ground fault occurs there is significant charge stored on the other phases. This charge creates the conditions that the line functions as a capacitor, and with the reconnection of the disconnected system the resulting overvoltage could be severe [2].

Overvoltages can occur through interrupting small currents, as the capability of the circuit breaker is much greater than what is needed in short-circuit fault conditions. Interrupting of small capacitive currents can cause the breaker to interrupt the current while the distance needed to prevent a re-strike or re-ignition has not been reached. This will result in the transient recovery voltage over the breaker to breakdown the dielectric medium of the breaker [2]. This is due to the energy stored within the capacitance and the source side of the breaker oscillates according to the system frequency. After the current reached zero, assuming peak voltage within the system due to capacitive load, the load side will continue the oscillating frequency and reach the maximum amplitude at reverse polarity a half cycle later. This will result in a 2 p.u. to 2.5 p.u. voltage over the open contacts of the breaker depending on grounding configuration of the capacitors.
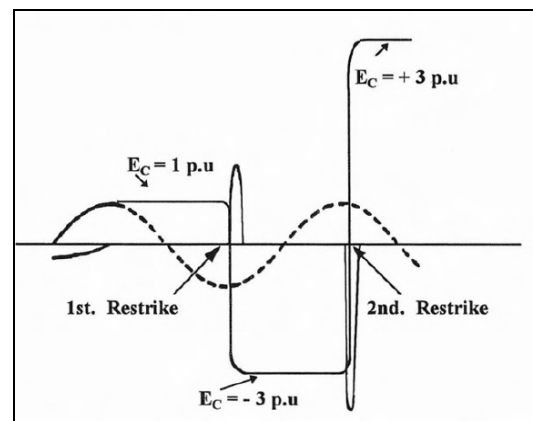
Figure 1: Voltage escalation due to re-strikes during capacitive load switching [2].

As can be seen in Figure 1, a re-strike will result in an in-rush current, due to the inductance within the system and aim to swing the capacitor voltage to the system voltage. A second interruption on the following zero crossing of the applied voltage on the capacitor will be 3 p.u. and result in an applied voltage of 4 p.u. over the opening circuit breaker contacts assuming no damping within the system [2]. This can result in damage to the circuit breaker, capacitor or unloaded line due to severe over-voltages applied to the system.

The same scenario can be applied to switching low inductive currents with a greatly oversized circuit breaker. This will also cause the current to be interrupted while the contact is not sufficiently separated to withstand the recovery voltage, but due to the expected damping within the system the over-voltages will under normal conditions not exceed the 2 p.u. level. Although breakers that can interrupt the high frequency re-strike or re-ignition current, it can cause the build-up of magnetic energy within the system inductance load, while the contact movement advances, creating the opportunity for a re-strike to occur at higher voltage levels. This scenario can occur after the high frequency re-strike is interrupted and the system voltage is recovering over the contacts, this can then result in another re-strike. These consecutive re-strikes can cause the build-up of energy stored within the inductance of the load and this results in the cumulative rise in overvoltage within the system.

2.3 Simulations

To understand the impact of a GCB on the protection within a generating station, the situation was simulated to identify the effect various faults and the protection system have on the system performance. The system consisted of a 200 MW generator with a GCB feeding a 250 MVA step-up transformer and a 10 MVA unit transformer. The station transformer was connected to a simulated load of the appropriate size.

The basic elements of the power station simulation include:
Generator: P = 200 MW; V = 11 kV; I = 13.13 kA, H = 3 s; P_{iron} = 1/300 p.u. and $R_{neutral}$ = 1200 p.u.
Generator Transformer: S = 250 MVA, X = 14%; V = 11 kV/400 kV; P_{iron} = 1/200 p.u.; P_{load} = 0.01 p.u.
Simulated HV Load: R = 800 Ω; L = 0.8 H

Simulated Faults:
single phase-to-earth and three phase-to-earth faults
Fault locations = Generator terminals, primary (LV) transformer terminals, load terminals
Fault resistance = 1 mΩ phase-to-earth

The system was modelled after a steady state was reached after 1 s, and after another 0.5 s a fault was applied to one of the locations. Depending on the location, the relevant circuit breaker will operate with a 40 ms time delay, and the other breakers 160 ms later. Within the simulated system three circuit breakers are present: the GCB, unit transformer LV circuit breaker and the HV circuit breaker of the step-up transformer. Various faults were applied to the simulated system with and without the GCB, thus determining the system response.

In the scenario of the fault applied to the load side of the HV busbar, independent of type of fault, the response to the fault current is similar. As the supply of the energy is isolated in similar fashion the in- or exclusion of a GCB has limited effect. Large differences in results occur when a fault is applied to

the generator side of the HV circuit breaker. This is due to no circuit breaker not interrupting the supply from the generator.

To demonstrate the impact of this scenario, see figure 2, 3, 4 and 5. The study was conducted with a three phase-to-ground fault. In both scenarios the fault results in a dramatic decrease in system voltage and a rise in fault current. The fault current has a high DC offset resulting in the exponential decay of the fault currents, as a result of the high X/R ratios in the system.
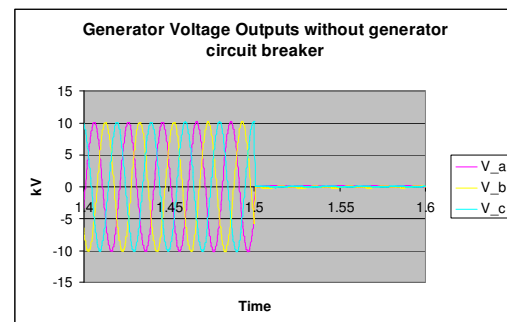
Figure 2: Voltage output of the simulated generator without a GCB
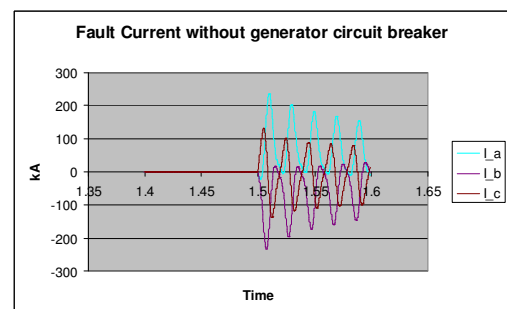
Figure 3: Simulated fault current without a GCB installed

The generator and the step-up transformer could possibly be damaged as the extremely high currents must be withstood for prolonged periods. The simulation results only display the decay over a 0.1 s period, but the decay will continue until the energy stored within the system is dissipated.

In figure 4 and 5 on the other hand, a similar three-phase fault, results in similar magnitude fault currents, but the difference resulting from the additional protection provided by the GCB can be seen in the duration of the fault current.

This minimizes the impact of a failure within the transformer differential zone, the consequential damage to the generator and limits the down time due to such a fault. The transient recovery voltage is shown in figure 4. This is due to the change from loaded to unloaded conditions. The increase in recovery voltage is the result of the high X/R ratio when the load is disconnected. The transient recovery voltage (TRV) is less the 2 p.u., but as

TOPIC C. POWER SYSTEMS

Proceedings of the 19th Southern African Universities Power Engineering Conference
SAUPEC 2010, University of the Witwatersrand, Johannesburg

explained in previous sections can be dramatically higher depending on the load conditions. Normally the rated short time withstand voltage is approximately 5 p.u. for GCBs due to the occurrence of high X/R ratio faults close to the generator terminals.
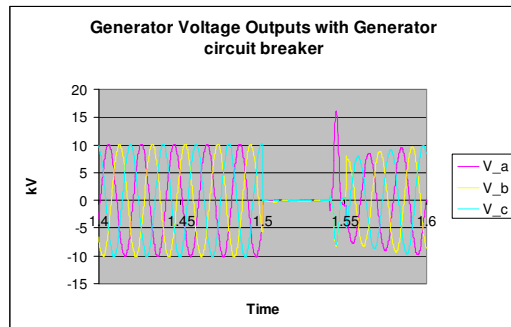
Figure 4: Generator terminal voltage with GCB installed
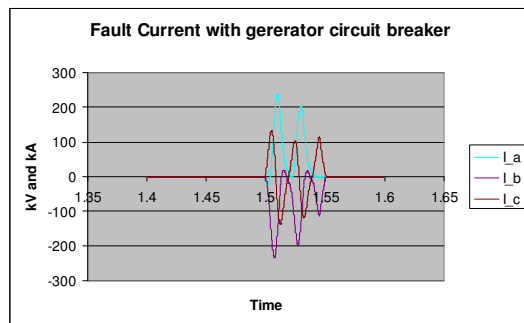
Figure 5: Simulation outputs of fault currents with a GCB

This is not the case when the fault is on the generator terminals and where the interrupted current through the GCB only forces the system contribution to zero, but does not isolate the fault. In this case, the effect of GCB is limited. For this reason, the effects of various layouts with and without GCBs should be evaluated, incorporating in addition to the protection of the system the cost, ease of operation, availability and mean time to repair of a layout.

In short, the GCB reduces the risk associated with faults occurring between the step-up transformer high voltage terminals and the generator output terminals. Furthermore, the protection system can be more selective and effective. This also reduces the risk of consequential equipment failures due to prolonged exposure to fault conditions.

3. GENERATION LAYOUT ANALYSIS

Figure 6 shows a thermal power station layout without a GCB. With this configuration, or a similar derivative, the areas where differential protection is needed are for five differential zones, i.e. each transformer and the generator has its own differential zone and the overall differential zone that includes the generator, the generator transformer and the unit transformer. Within a unit-configured system, the station transformer usually supplies auxiliaries on

start-up or shutdown of the generator unit. These transformers can be utilised for various units in a power station, resulting in a cost saving.
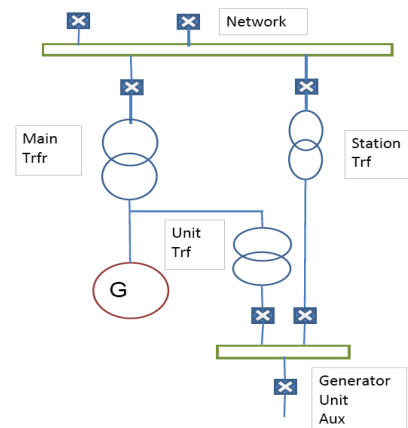
Figure 6: Layout of a thermal power station without a GCB

The scheme in Figure 6 also requires rapid changeover equipment, to transfer the auxiliary load fed from the station transformer to the generator fed unit transformer, using as high-speed bus transfer (HBT) system [6]. This device evaluates the voltage on the unit board busbar and ensures the quick and timely switching between the supplies. This device monitors the status of the various controlled circuit breakers and uses three distinctly different algorithms to achieve this changeover [6]. The first option after the change signal is received is a change of supply within the angle window. This automatic changeover usually occurs within approximately 100 ms, to limit the voltage amplitude and phase angle difference, and the current on breaker closure. The second option allows switching to occur at a complete phase rotation cycle, but within set phase angle and voltage limits. If the load is not transferred, the remaining option is to transfer the supply when the residual bus voltage is below 30%. This transfer equipment is required in all layouts without a GCB.

If a GCB is included in the layout of a generating station the station transformer and associated HV and LV breakers can be eliminated. If a non-unity configuration is used, a station transformer can be inserted as a standby supply for multiple generating units. Costs are reduced as the number of transformers, high voltage breakers and control equipment is reduced.

4. RELIABILITY ANALYSIS

To compare the available time to generate power between various power station layouts, an analysis of the availability and reliability of the various components was done. The IEEE recommended practice for the design of reliable industrial commercial power systems [7] was used to determine the availability and reliability of layout in generating stations.

The failure rate and mean time to repair per component was used to determine the system failure rate and mean time to restore plant. For the major components functioning in series, the failure rates directly affect other components, but for components in parallel, this is not the case, as the system as a whole will only be affected if both the systems fails at the same time.

For the comparison, the units (see table 3) will be evaluated as parallel units and operated as totally independent entities. The reliability data in table 1 was used and the entire system unit was evaluated as a whole unit in parallel with a similar unit.

Table 1: Results of unit configuration of parallel unit with and without GCBs

	Dual Unit Layouts without GCBs	Dual Unit Layouts with GCBs	
Failure rate of layout	0.00788603	0.00354509	per year
Downtime per failure	79.9	82.8	Hours
Reliability	0.99214498	0.99646118	p.u.
Availability	0.99992809	0.99996651	p.u.
Downtime per year	0.63	0.29	Hours per year

Using parallel units to produce power decreased the failure rate dramatically. Although this is true for both the evaluated scenarios, in this case the less equipment required for the layout with GCB means are a more reliable method of generating power. The advantages of such fully redundant system, although substantial, are not feasible as the cost overshadows the benefits. A more practical approach is to have two units share one station transformer to limit costs. This configuration was compared with a unit-configured station with GCBs included, but with a single station transformer as a backup system. Although the layout with the GCB has more equipment that could possibly fail, the layout results in the station transformer serving as a parallel supply to the unit transformer. This parallel system is of low probability to fail and is the main reason for the better performance of this system (see table 3).

From the results the addition of a GCB does not in any way degrade the reliability or dramatically affect the repair time of generator station equipment. The addition of a GCB and either the decreased importance or the total exclusion of the station transformer and associated equipment relates to a significant increase in reliability and availability of generation systems. This was attributed to the decreased equipment need for the system to function in any one unit. The possibility of creating redundancy within the system if the standard configuration is followed with the addition of the breakers further increases the system capability.

Through the evaluation of the tested data from the suppliers [5] and the practical data obtained from the IEEE recommended practice [7] the results obtained from all evaluations with GCBs included were validated. The effect of the parallel components was dramatic in the improvements in reliability and availability of the plants as a whole. This concept can rarely be achieved or sustained in practise. This is due to the initial cost for installation of additional capacity, and the rapidly growing demands for electricity engulfing most or all redundant capacity. The preventative expansion of power station capacity is also not as feasible as the theory might suggest.

5. COST CALCULATIONS

To complete the analysis of various power station layouts the effects of the cost on the choice of implementing GCBs were determined. From the reliability data tables the failure rate and the mean time to repair were used. The initial cost of each of the layouts and reliability cost for each layout was compared. A plant delay time of 10 hours per start up was assumed, irrespective of the cause of the delay [7]. The IEEE recommends an average revenue of R120 000/h, variable cost of R105 000/h and expenses of failures amounting to R300 000 is applied to resolve this unreliability cost. The sent-out generating capacity was assumed to be 97% at R0.95/kWh. Assuming a 30% marginal income on all sales of electricity delivered to the network, this amounts to R55 005/h lost due to plant delays. Delay time for a power station also reduces some variable expenses due to the station downtime. Thus, if assumed that 25% of cost of generation can be saved after the marginal income was deducted from the cost of a kWh, the saving due to not producing power amounts to R32 086/h. Finally, an approximation is required to estimate the cost per failure of a generating plant, and is a fixed value of R110 000 was chosen and a 10-hour start-up time is required per failure. To ensure that the capital investment of a power station can be returned to the investors within 20 years including the interest, a return on investment of 12% was used to meet this requirement.

To evaluate the impact on capital cost only the differences were considered, i.e. the inclusion of the GCB and the exclusion or sharing of the station transformer. Thus, to evaluate the impact the increased availability resulting form the additional investment cost these elements should considered (see Table 2). All cost was obtained as budget quotes from various suppliers and conversion rates of R7.50/$ and R10.50/€ were applied.

From Table 2 it is clear for the scenario in Figure 6, where the station transformer and the associated breakers are exchanged for a generator breaker that the least capital cost option was to include the GCB. The capital cost as well as the costs due to failures must be evaluated. According to IEEE [7] the standard analysis to determine the cost of power stations is performed as indicated in Table 3.

TOPIC C. POWER SYSTEMS

Proceedings of the 19th Southern African Universities Power Engineering Conference
SAUPEC 2010, University of the Witwatersrand, Johannesburg

Through the time to repair, income lost and variable cost gained through the delay duration, the cost of downtime can be established. With the addition of all the variable expenses incurred and the failure rates, the cost per annum can be obtained. By adding the capital expenditure per layout, included a return on investment of 12%, a total cost per annum was calculated. The results show that the lowest cost of the unit configuration included a GCB. The evaluation proves that the additional capital spent GCBs is similar to the loss in production capacity of the unit without a GCB.

Table 2: Summary of budget quotations for power station equipment

	Type	Cost
GCB	12 kV, 100 kA	R3 000 000
HV Breaker	420 kV	R1 375 000
MV Breaker	72 kV	R165 000
Generator Transformer	250 MVA, 12/400 kV	R34 500 000
Unit Transformer	20 MVA, 12/6.6 kV	R4 900 000
Station Transformer	20 MVA, 400/6.6 kV	R12 500 000

6. CONCLUSION

In this study various aspects of circuit breaker technology was investigated, to assist in the evaluation of the generator circuit breaker (GCB) as an option in a power station layout. The effect, extent and the cost implications of using a GCB were evaluated. The evaluation focused on the combination of individual pieces of equipment and the effect of including and excluding a GCB on the reliability, availability and mean time to repair of the power station. An example using a 200 MW generator was used to demonstrate the significant advantages of including a GCB in the power station

topology, despite its cost. Using a GCB means less equipment, shorter fault current duration, less damage during faults and improved functionality.

The choice of interrupting medium is based in the size of the unit, using vacuum up to 100 MVA, SF_6 for units producing fault currents up to 200 kA and for the extreme cases air blast circuit breakers can be used.

REFERENCES

[1] Definition for power switchgear, ANSI/IEEE C37.100-1981, New York, USA, 1981..

[2] Garzon, R.D., HV Circuit Breakers: Design and applications, Square D Co., Marcel Dekker, 1996, pp 129-222.

[3] Zehnder, L., Kiefer, J., Braun, D., Schoenermann, T., "SF6 generator circuit breaker system for short-circuit currents up to 200kA", Technologies for the utility industry, 2002, ABB review 3.

[4] Canay, M., Braun, D., Koppl, G.S., "Delayed current zeros due to out of phase synchronizing", IEEE Transactions on Energy Conversion, New York, vol. 13, No. 2, 1998, pp 124-132.

[5] Braun, D., Guerig, A., "Life Management for Generator Circuit Breakers", ABB High Voltage Technologies Ltd, 1994, Switzerland.

[6] ANON. (a.d.). ABB Switzerland Ltd, Synchrotact HBT, www.abb.com/synchrotact, accessed 2 September 2009, pp 1-14

[7] IEEE Standards Board, IEEE recommended practice for the design of reliable power systems, IEEE Std 493-1990, pp 7-85, pp 213-300.

Table 3: Summary of costing data for all evaluated solutions

Descriptions	Dual Thermal layout without GCB	Dual Thermal layout with GCB	Dual Thermal layout without GCB with single station transformer	Dual Thermal layout with GCB and single station transformer
R = average time to repair failure	79.88	82.75	248.61	67.93
S = plant start up time per failure	10	10	10	10
R + S	89.88	92.75	258.61	77.93
Gp - Xp= income lost per hour of plant downtime – variable expenses saved	R22 919	R22 919	R22 919	R22 919
(R+S)(Gp-Xp)	R2 059 935	R2 125 711	R5 927 010	R1 786 056
Xi = Variable expenses per failure	R110 000	R110 000	R110 000	R110 000
Sub Total	R169 9345	R2 235 711	R6 037 010	R1 896 056
Failure rate per year	0.007886032	0.003545092	0.094847063	0.004407044
X = Annual Sub total cost	R17 112	R7 926	R572 593	R8 356
F = Capital investment excluding generator	R109 960 000	R87 880 000	R95 920 000	R101 920 000
CF = Fixed investment charges (12%)	R13 195 200	R10 545 600	R11 510 400	R12 230 400
G = X + CF Minimum requirement per year	R13 212 312	R10 553 526	R12 082 993	R12 238 756

Proceedings of the 19th Southern African Universities Power Engineering Conference
SAUPEC 2010, University of the Witwatersrand, Johannesburg

TOPIC C. POWER SYSTEMS

EVALUATION OF SHUNT REACTIVE COMPENSATION OF LINE VOLTAGE

F M Welgemoed, H J Beukes

University of Stellenbosch, Dept. of Electrical and Electronic Engineering, Stellenbosch, South Africa

Abstract. This paper discusses the mitigation of voltage-dips on 400V three phase transmission lines using a shunt connected voltage source inverter (VSI). Compensation is done by injecting reactive power at the end of a radial transmission line where the voltage is to be regulated. Space vector pulse width modulation (SV-PWM) based control is implemented in the static reference frame. A predictive current controller and dual proportional integral (PI) voltage controllers are used to successfully control the converter. Parts of this paper include: theory on this compensation method, controller design, simulations results and practical implementation results.

Key words. Reactive Compensation, Voltage Source Inverter, var Control, Regulation

1. INTRODUCTION

Voltage dips are classified into various categories based on the depth and duration of the dip [1]. According to the NRS-048 a dip is generally classified as a reduction in voltage to a level below 0.9 pu lasting longer than 20 ms and shorter than 3 seconds. An under-voltage event is classified as a reduction in voltage to below 0.85 pu for more than 3 seconds. This reduction in the amplitude of the voltage may be for either one, multiple or all three phases.

Voltage dips are generally caused by network faults. The large currents in fault conditions cause a voltage drop across the transmission line impedance. Where the transmission line is very long or it has high impedance, the connection of much smaller loads can cause equally large voltage dips. This reduction in voltage is then experienced by customers further down the line.

Whatever the class or origin of the dip, a reduction in the supply voltage at a customer may cause damage to voltage sensitive equipment or cause interruptions in the working of such equipment.

To prevent this, the voltage has to be regulated to within a few percent of the nominal voltage.

In this paper only balanced voltage dips are considered, which means that the reduction in the voltage amplitude is the same for each of the three phases. In practice, large loads that cause voltage dips are usually balanced three phase loads.

The voltage V_F at the end of the radial transmission line, under discussion here, can be effectively regulated by loading the line with the correct reactive load [2]. Shunt-connected controllable var generators can be used to supply this variable reactive load. Using a controllable var generator ensures that steady-state and dynamic voltage regulation can be achieved.

The var generator discussed in this paper is a three phase IGBT voltage source inverter (VSI). It draws a small amount of active power to compensate for losses in the inverter while supplying or consuming reactive power [2].

It is well known that reactive compensation can be implemented by means of a VSI. The generation and absorption of reactive power by means of a VSI is achieved by generating a voltage at the inverter output that is in phase with the supply voltage. By varying the magnitude of the generated voltage reactive power is either absorbed or generated by the inverter [2]. When the inverter voltage magnitude is greater than that of the supply voltage a lagging (inductive) current is drawn from the supply while a leading (capacitive) current is drawn when the opposite is true. The inverter is thus either seen as a reactor or capacitor by the ac network. The value of this so called capacitance or inductance is proportional to the amplitude of the generated inverter voltage.

If we assume that the amount of active power drawn by the inverter is negligible compared to its maximum rating the maximum amount of reactive power is available for compensation. The maximum voltage dip that can be handled can then be calculated from this amount of available power and the transmission line impedance.

In this paper a 250kVA, 3 phase VSI and 800V dc bus is implemented for this purpose.

2. CONTROL ALGORITHM DESIGN

Using the Clarke-transformation, equation (1), the three phase voltages and currents can be represented as vectors in the stationary (αβ) reference frame [3].

$$\begin{bmatrix} x_\alpha \\ x_\beta \\ x_\gamma \end{bmatrix} = \sqrt{\frac{2}{3}} \begin{bmatrix} 1 & -\frac{1}{2} & -\frac{1}{2} \\ 0 & \frac{\sqrt{3}}{2} & -\frac{\sqrt{3}}{2} \\ \frac{1}{\sqrt{2}} & \frac{1}{\sqrt{2}} & \frac{1}{\sqrt{2}} \end{bmatrix} \begin{bmatrix} x_a \\ x_b \\ x_c \end{bmatrix} \tag{1}$$

Figure 1 shows the filter voltage space vector, V_F, in the αβ plane. The active and reactive reference currents can be set up accordingly based on their angular relationship with V_F and their magnitudes.

TOPIC C. POWER SYSTEMS

Proceedings of the 19th Southern African Universities Power Engineering Conference
SAUPEC 2010, University of the Witwatersrand, Johannesburg
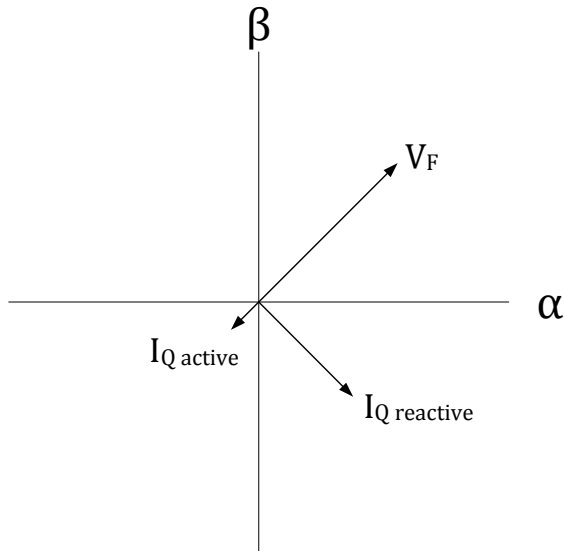
Figure 1 – Space vector representation of the active and reactive currents with respect to the filter voltage.

It is then obvious that active current vector should be in phase with the voltage vector and that reactive current vector should be 90° out of phase with respect to the voltage vector.

2.1 Current Controller

A predictive (dead-beat) current controller is designed for the VSI to operate in the stationary reference frame. Analysis of the inverter output filter, figure 2, is the key to the predictive controller [4]. Unlike [4] a more detailed version of the output filter is used by not neglecting the series resistance of the filter inductor.
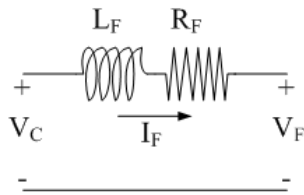
Figure 2 – VSI output filter inductor and equivalent series resistance.

Simple circuit analysis produces equation (2).

$$V_C - V_F = L_F \frac{dI_F}{dt} + R_F I_F \qquad (2)$$

Further manipulation leads to the control algorithm for the dead-beat current controller as shown in equation (3). There are, however several issues, beyond the scope of this paper, that need to be addressed before this controller can simply be implemented. These include the prediction of the filter voltage at instance *k+1* and the handling of the reference current with respect to the calculation delay.

The discrete predictive control algorithm is calculated to be:

$$V_C^{\alpha\beta}[k+1] = \frac{L_F}{T_s}\left(I_{REF}^{\alpha\beta}[k] - \left(1 - \frac{R_F T_s}{L_F}\right)^2 I_F^{\alpha\beta}[k]\right) + \left(1 - \frac{R_F T_s}{L_F}\right)V_F^{\alpha\beta}[k]$$
$$+ V_F^{\alpha\beta}[k+1] - \left(1 - \frac{R_F T_s}{L_F}\right)V_C^{\alpha\beta}[k] \qquad (3)$$

Where:

V_C is the voltage generated by the inverter,

V_F is the filter output voltage,

I_F is the filter current,

I_{REF} is the filter reference current,

L_F is the filter inductance,

R_F is the filter inductor's series resistance,

T_s is the sample period (200μs).

The reference current for the dead-beat controller is determined by two separate proportional and integral (PI) controllers. The first is designed to regulate the dc–bus voltage at a steady 800V. This controller thus generates an active current reference flowing into the inverter. The design of this controller is beyond the scope of this paper and is thus not discussed here.

The second PI controller is used to regulate the ac voltage at 400V and thus generates a reactive current reference. The two reference currents are added in the alpha-beta plane to form a space vector representing both the active and reactive reference current. The aim of the predictive controller is to generate a voltage at the inverter output that allows this reference current to be realized.

2.2 Voltage Controller

This second PI controller thus generates a reactive current reference which is either capacitive or inductive. A capacitive current is drawn when the voltage is less than the reference while an inductive current is drawn when the voltage is higher than the reference. With this PI controller the voltage error is calculated based on the amplitude of the space vector. This is true for the assumption that the supply voltage is balanced and that the magnitude of the space vector is thus constant. The reactive current is then based on the voltage magnitude error and is set to be 90 degrees out of phase with respect to the filter voltage.

For a balanced three phase supply and transmission line impedance the reactive current (capacitive or inductive) required to maintain a certain voltage at the inverter will be balanced.

By considering only reactive components the control diagram in figure 3 can be obtained. $X_L=2\pi fL$ is the transmission line impedance and H_c, in figure 3, translates the filter voltage to the filter capacitor current.

Proceedings of the 19th Southern African Universities Power Engineering Conference
SAUPEC 2010, University of the Witwatersrand, Johannesburg

TOPIC C. POWER SYSTEMS
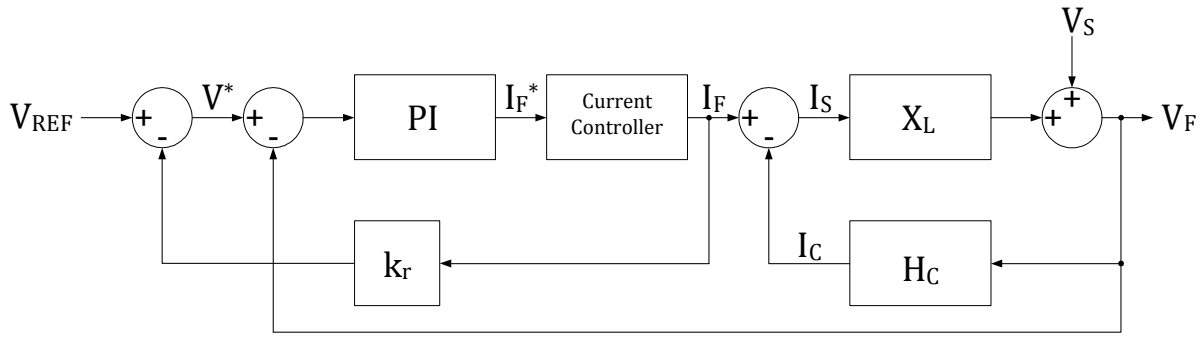
Figure 3 – Reactive compensation control diagram.

The constant k_r is introduced to allow for a regulation slope. This essentially adjusts the reference voltage when the converter is supplying larger reactive currents. According to [2] this allows for a greater linear operating range of the VSI with a given maximum rating and a better defined operating point. By correctly choosing the value of k_r a 3% deviation in the nominal reference voltage at 360 A_{RMS} (reactive) is allowed as it is the aim here to regulate the voltage within 3% of the nominal value.

The predictive current controller is assumed to have only a pure delay without any tracking error. This is a valid assumption considering that calculation-delay compensation as well as dead-time compensation has been done to the controller. The converter and the current controller are thus modelled as a pure delay with unity gain.

With all parameters, except for the transmission line impedance, exactly known the PI controller gains in this loop can be calculated. V_{REF} is set to zero as the controller should be designed to optimally respond to variations in V_S. This is shown in figure 4, where disturbances, caused by network faults, are modelled as a variation ΔV_s in the magnitude of the voltage.
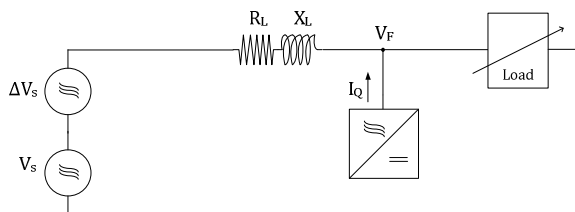
Figure 4 – A single phase representation showing a three phase VSI used as a shunt compensator at the end of a radial transmission line.

The loop is analyzed and the proportional and integral gains calculated using the weakest system impedance (minimum short circuit capacity). This means that the controller should be stable for all line impedances lower than the designed value. Here the load connected to the line at the point of compensation as well as the filter capacitance is ignored.

Simplifying the control diagram in figure 3 as mentioned above, a transfer function describing the

response of the system based on variation in filter voltage can be obtained. Substituting the PI controller with a pure unity gain and considering the open-loop bode plot shows that the system is already stable. Placing the zero has little effect on the magnitude plot but reduces the phase margin. The phase margin is already sufficiently large and the effect of the zero does not pose a problem. The gain of the PI controller needs to be set to achieve a 0 dB crossing that is as high as possible while still maintaining a sufficient gain margin. A gain margin of roughly 20 dB is chosen for this design. Figure 5 shows the bode plot for this controller. The effect of a variation in the transmission line impedance is shown in figure 6 when the transmission line impedance is reduced to 200 µH.
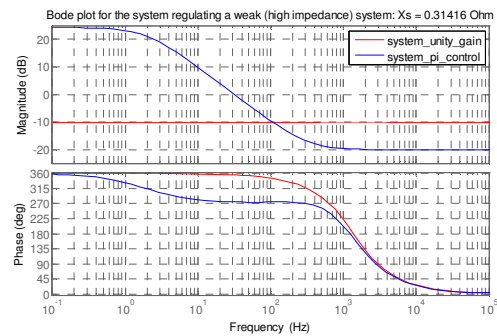
Figure 5 – Bode plot of system with high transmission line impedance. *GM*: 19.7dB *PM*: 94.6° f_{0dB}: 31.3Hz.
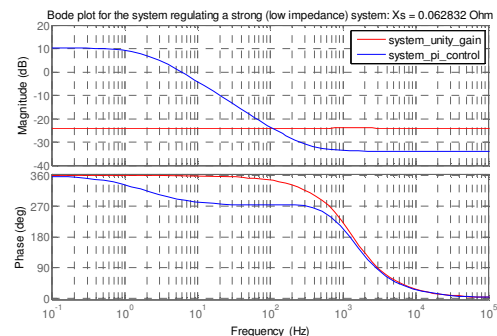
Figure 6 – Bode plot of system with low transmission line impedance. *GM*: 33.7 dB *PM*: 108° f_{0dB}: 6.01Hz.

TOPIC C. POWER SYSTEMS

Proceedings of the 19th Southern African Universities Power Engineering Conference
SAUPEC 2010, University of the Witwatersrand, Johannesburg

3. SIMULATION AND EXPERIMENTAL RESULTS

Simulation of the VSI and transmission line has been done in Simplorer. Large loads were connected at a point on the transmission line between the grid and the point of regulation (PCC) as shown in figure 7. This is to simulate practical step changes in the voltage. Although a step change in voltage is not very common in practice, it does provide a means to measure the performance, in terms of response time, of the compensator.
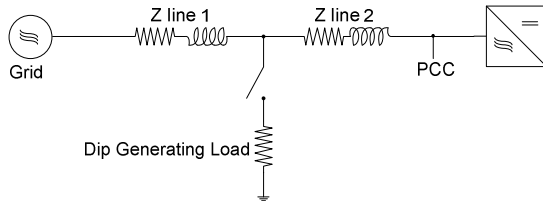
Figure 7 – The system as set up for simulation and practical testing.

Table 1: Simulation and Practical Test Parameters

Symbol	Value	Description
$V_{(AC)REF}$	400 V	AC Line Reference Voltage
$V_{(DC)REF}$	800 V	DC Reference Voltage
L_F	400 µH	Filter Inductance
C_F	100 µF	Filter Capasitance
L_1	200 µH	Line Inductance (part 1)
L_2	800 µH	Line Inductance (part 2)
R_1	0.16 Ω	Line Resistance (part 1)
R_2	0.004 Ω	Line Resistance (part 2)
F_s	5 kHz	Swithing/Sample Frequency

Figure 8 shows the RMS filter voltage when a load is connected without reactive compensation. The voltage drops from almost 230 V_{RMS} to 195 V_{RMS} thus a 0.15 pu voltage drop.
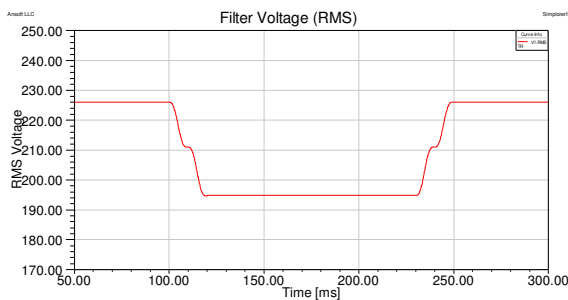
Figure 8 – Filter RMS voltage during a dip without reactive compensation.

Figure 9 shows the same plot as figure 8 but with reactive compensation being done. As can be seen the voltage now does not drop below 216 V_{RMS} and the voltage error is reduced to zero after just 45 ms.

Figure 10 shows the voltage and current waveforms of one phase during this same time.
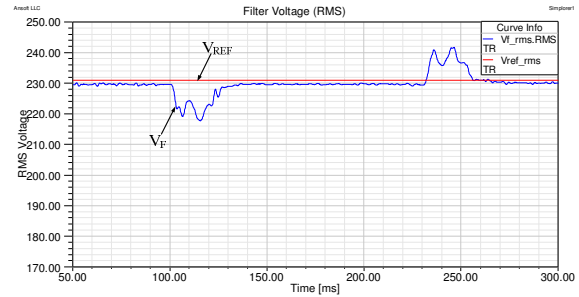
Figure 9 – Filter RMS voltage during a simulated dip with reactive compensation. V_{REF}: Fixed reference voltage.
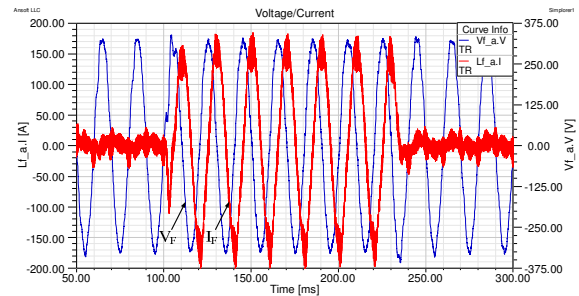
Figure 10 – Filter voltage and current during a simulated voltage dip.

Practical tests were performed to verify the working of the above described control. The transmission line was simulated by using reactors and resistors of the same values as used in the Simplorer simulation. The load connected to generate the voltage dip is switched in by firing thyristors for 250 ms. The voltage dip generated is exactly the same as the simulated dip in figure 8.

Figure 11 shows the RMS filter voltage before, during and after the dip. The RMS voltage has been calculated by moving a 20 ms window over 10 ms intervals as specified by the NRS-048 standard. It is possible to determine the exact time it takes the system to reduce the voltage error to zero, but what is more evident is that the depth of the voltage dip is reduced substantially.

Figure 12 shows the 3 phase voltages and one phase current during this time. It can be confirmed that the practical test results coincide with the simulated results depicted in figure 9.
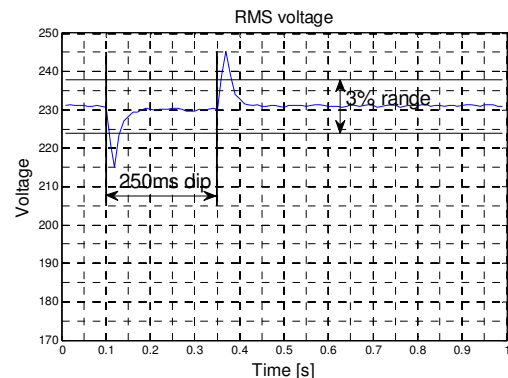
Figure 11 – Filter RMS voltage during a practical test dip with reactive compensation.

Proceedings of the 19th Southern African Universities Power Engineering Conference
SAUPEC 2010, University of the Witwatersrand, Johannesburg

TOPIC C. POWER SYSTEMS
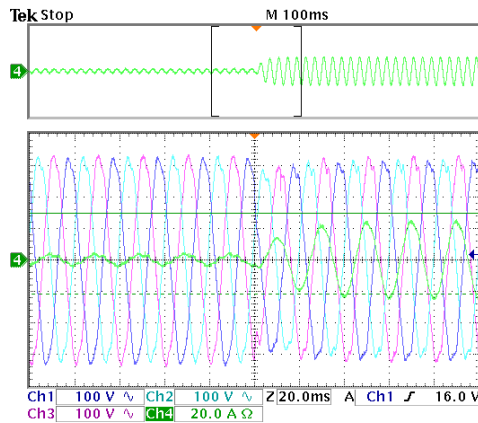
Figure 12 – Filter voltage and current during a practical test dip with reactive compensation. Ch1, Ch2, and Ch3: Phase voltages. Ch4: Current (÷10).

4. CONCLUSION

In this paper the concept of reactive compensation is explained. A brief overview is given on the current control while the design of a PI controller for the regulation of the filter voltage is discussed in more detail. The control was simulated and practically tested to verify its working and performance. Practical tests confirm simulation results.

Despite critique that var generators have large transport delays [5], a shunt connected VSI can compensate for steady over and under voltage to well within the 3% specification. Dynamic performance is however also important and as shown by the results, the magnitudes of the dips are reduced substantially.   Dips can thus be sufficiently compensated for with the response being dependant on accurate knowledge of the system parameters.

REFERENCES

[1] NRS-048-2:2004, "Part 2: Voltage Characteristics, Compatability Levels, Limits and Assessment Methods".

[2] N.G Ningorani and L. Gyugyi, "FACTS: Concepts and Technology of Flexible AC Transmission Systems", Piscataway, New York, 2000.

[3] S. Buso and P. Mattavelli, "Digital Control in Power Electronics", Morgan & Claypool, USA, 2006.

[4] S. Buso, S. Fasolo and P. Mattavelli, "Uninterruptible Power Supply Multiloop Control Employing Digital Predictive Voltage and Current Regulators", *IEEE Transactions on Industry Applications*, vol. 37, no. 6, pp. 1846-1854, Nov/Dec. 2001.

[5] M. Bongiorno, "On Control of Grid-connected Voltage Source Converters", Chalmers University of Technology, Sweden, 2007.

TOPIC C. POWER SYSTEMS

Proceedings of the 19th Southern African Universities Power Engineering Conference
SAUPEC 2010, University of the Witwatersrand, Johannesburg

AC HARMONIC FILTER DESIGN METHODOLOGY FOR HVDC SYSTEMS

WC Stemmet, J Smith & G Atkinson-Hope

Cape Peninsula University of Technology, Electrical Engineering Department, P.O. Box 652, Cape Town, 8000

Abstract. The HVDC CIGRE benchmark network and published literature thereon discloses the use of harmonic filters and parameter values are given for the components. The methodologies on how to design the filters used is not disclosed. The focus of this paper is to identify the types of AC harmonic filters applied and to develop design methodologies for the CIGRE filter used. At both the converter stations, a combination of a 2nd order high-pass damped filter and a CIGRE C-type filter is identified. Methodologies were developed for these filters. The developed methodologies were compared and evaluated to ascertain discrepancies in filter components and results that arose due to the CIGRE using a non generalised C-type filter. The methodologies were adapted to accommodate these changes, and the results then became the same. The filter performances were evaluated in terms of the individual and total harmonic distortion indices and frequency sweeps. The filter design methodology was shown to be effective and can serve as a benchmark.

Key Words: 2nd Order high- pass damped harmonic filters, C-Type filters, CIGRE HVDC Benchmark

1 INTRODUCTION

The CIGRE Benchmark was the first attempt to create a reference network for HVDC simulation studies. The benefit of a reference network is that it allows for the comparison of different simulation methods, mostly control systems [3] and [4].

In 2006, a detailed modelling of the CIGRE benchmark using PSCAD software was published [9]. Little emphasis was placed on the design methodology of the harmonic filters at both ends of the converter stations. The CIGRE network does not include harmonic filters on its DC transmission network, only on the rectifier and inverter AC sides.

The types of filters used and their parameters are given for the CIGRE network. The shortcoming in literature is that the design methodology for the filter types is not described. There is thus a need to develop a design methodology for these filter types and test this methodology by applying it to the CIGRE system. Also to demonstrate that the developed methodology leads to the parameter values that agree with 2nd order high-pass damped filter and a C-type filter used in the benchmark.

2 RESEARCH STATEMENT

The emphasis of this paper is to develop a design methodology for the 2nd order high-pass damped and C-type filters for both the converter stations of the CIGRE HVDC benchmark, apply the methodology and compare the filter parameters to that of the published filter data. The effectiveness of the filters will also be demonstrated through analysis of the results when the design is applied and simulation studies are conducted.

3 CIGRE HVDC BENCHMARK

The benchmark is a 12-pulse monopolar system with the following operating parameters: 500 kV, 1000 MW and 2 kA. The rectifier is connected to a 345 kV, 50 Hz, AC system and the inverter is connected to a 230 kV AC system [3].

HVDC systems transfer bulk power using large nonlinear equipment (converter valves) causing harmonic penetration into its associated AC networks. Harmonic mitigation equipment has to be installed. With 12-pulse converters two techniques are used for mitigation, transformer configurations and harmonic filters. These techniques prevent harmonics from entering the rest of the power system [1] and [8]. Line commutated HVDC systems draw large amount of reactive power and therefore must have capacitive reactive compensation to supply the converters. To save costs this capacitor bank forms part of the harmonic filter design, thus reactive power compensation is provided by a combination of capacitor banks and harmonic filters [4].

The focus for the research is to design high-pass damped harmonic filters for HVDC systems. In Figure 1, the typical configuration of these harmonic filters is illustrated:
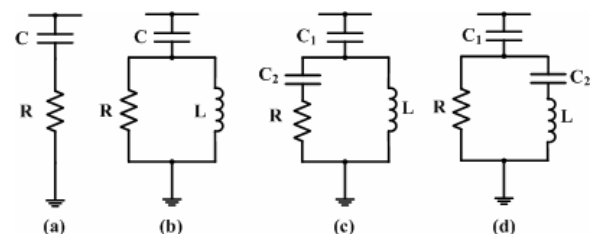
Fig.1: High-pass damped filters: (a) First order; (b) second order; (c) third order; (d) C-type

The CIGRE benchmark uses the 2nd order high-pass damped filter (Figure 1b) and the C-type filter (Figure 1d) at both the rectifier and inverter ends.

Proceedings of the 19th Southern African Universities Power Engineering Conference
SAUPEC 2010, University of the Witwatersrand, Johannesburg

TOPIC C. POWER SYSTEMS
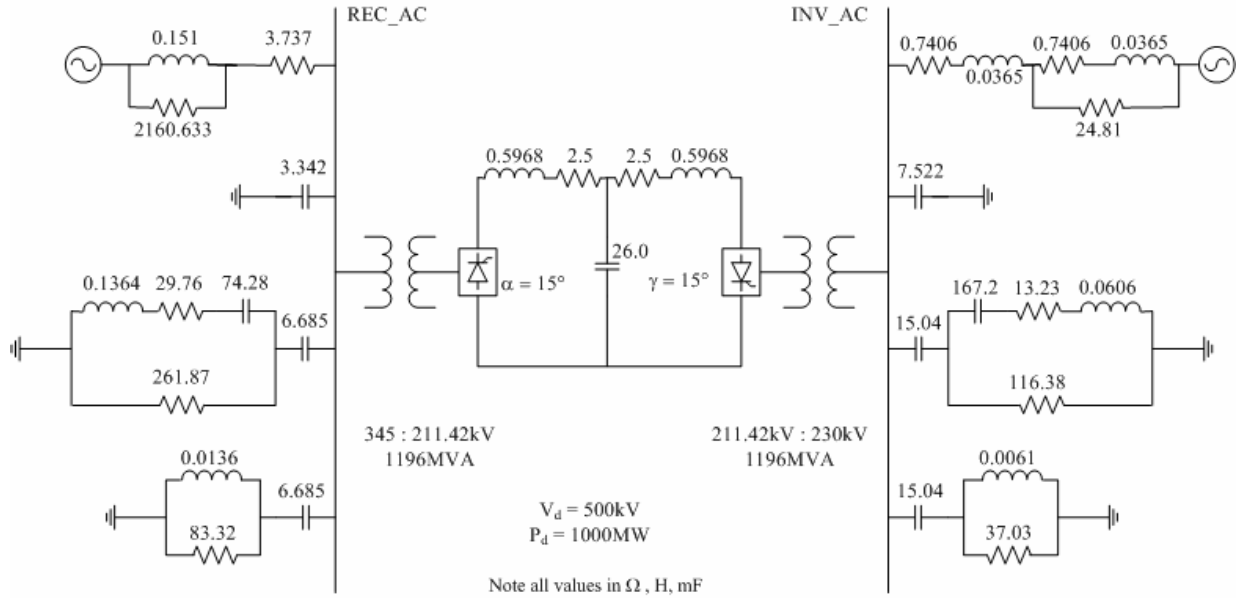
Fig. 2: CIGRE HVDC Benchmark

4 MITIGATION SOLUTIONS

4.1 Transformer vector groups

The 12-pulse monopolar configuration for the benchmark is obtained by connecting two 6-pulse rectifiers in series. Six-pulse converters generate characteristic harmonic currents of the order:

$$h = np \pm 1 \qquad (1)$$

Where n is any positive integer and p is the pulse number. The first mitigation technique is the use of transformer configurations to prevent the 5th and 7th harmonics penetrating into the AC system (primary side).
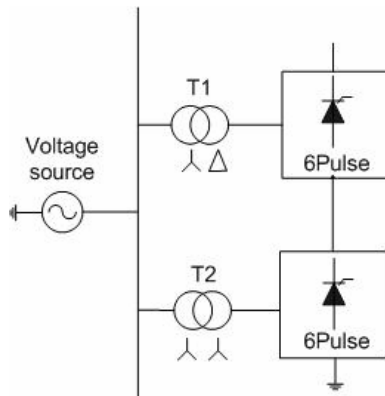
Fig.3: Commutating transformer vector groups

The total AC current flowing into the AC network has the following Fourier components shown in (2):

$$i_T = C_1 \cos\left(\omega t + \frac{\pi}{6}\right) + C_{11} \cos\left(11\omega t - \frac{\pi}{6}\right) +$$
$$C_{13} \cos\left(13\omega t + \frac{\pi}{6}\right) + \dots \qquad (2)$$

The AC current waveform contains characteristic 12-pulse harmonic currents (11th, 13th and higher) and the lower order 6-pulse harmonics (5th and 7th) are eliminated in the arrangement shown in Figure 3:

4.2 Reactive power compensation

The reactive power compensation for the converter is supplied by the capacitor bank and the two filters.

The rating of a harmonic filter is defined by the amount of reactive power the filter supplies at fundamental frequency. The direction of reactive power flow in a HVDC system can be seen in Figure 4.
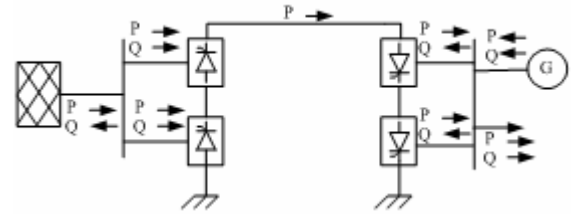
Fig. 4 HVDC Transmission Network Power Flow Diagram

The power factor for a converter station is calculated by (3):

$$\cos(\phi) = \frac{\cos(\alpha) + \cos(\alpha + \mu)}{2} \approx 0.866 \qquad (3)$$

For the benchmark the firing angle (α) is 15° and the overlap angle (μ) is 25°, thus the approximate power factor is 0.866 lagging. The amount of reactive power required for the converter station is often expressed as a percentage of the DC power to be transmitted and is given by (4) [8]:

$$\tan(\phi) = \frac{Q_1}{P_1} = 0.577 \approx 0.6 \qquad (4)$$

For CIGRE, a 1000MW is to be transferred from the rectifier side to the inverter side. Thus 600Mvar has to be supplied from the capacitor bank and the two harmonic filters connected to a converter station.

5 METHODOLOGY

The ideal objective for filter design is to nullify all waveform distortion; however, the ideal criterion is impractical for technical and economical reasons. A more practical approach is to reduce the distortion problem to an acceptable level.

In a real world, characteristic harmonics occur in systems but when they are asymmetrical and unbalanced the converters also generate third harmonic currents. They pass through transformer configurations as they act like positive sequence and are not blocked. In order to eliminate characteristic and low order harmonic currents, HVDC systems typically use C-type and 2nd order damped filters to eliminate all these harmonics.

These types of filters (Figures 1 and 2) contain capacitors and the determination of amount of reactive power that they must supply needs initially to be fixed. From the CIGRE benchmark and (4) the converters requires approximately 600 Mvar. Allowing for tolerances the value of 625 Mvar is selected. The ratio for the contribution and from a cost point of view, the filters and the reactive compensation is as follows:

- 40 % from second order high pass filter
- 40 % from C-type high pass filter
- 20 % from compensation capacitor bank

Thus the two harmonic filters connected to the rectifier station contribute 500 Mvar (80 %), and assuming that the capacitance is equally divided between them, each filter should contribute 250 Mvar (40 %). The reactive power compensation bank contributes the remaining 20 % (125 Mvar). Similar approach is followed on the inverter side.

Three methodologies are needed to be developed for the design of the filters for CIGRE benchmark:

- 2nd order high-pass damped filter
- General C-type damped filter
- CIGRE C-type damped filter

5.1 Second order high- pass damped filter
- **Step1:** Filter design criteria for lowest characteristic harmonic order. The filter at the rectifier station is designed with the following parameters: voltage rating (V_1) of 345 kV, reactive power (Q_1) of 250 Mvar, angular velocity (ω) of 314.159 rad/s, resonant harmonic order (h_r) for the 11th H/O and a quality factor (q): 2.5, typically ($0.5 < q < 5$).

In Figure 5, are the configuration and the impedance characteristic for the filter:
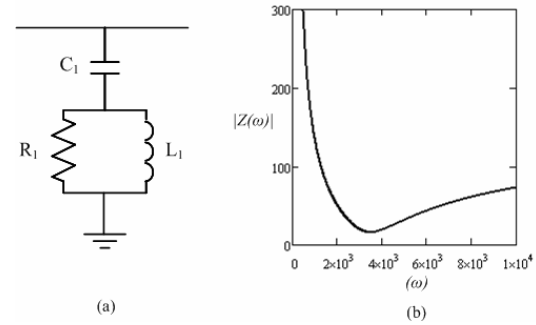
Fig. 5: 2nd order high-pass damped filter: (a) configuration; (b) impedance characteristic

- **Step 2:** Obtain filter component values. The filter components are determined with the use of the following (5) to (10), [6], The capacitive reactance is:

$$X_C = \frac{V_1^2}{Q_1} \qquad (5)$$

The value for the capacitor (C_1) is:

$$C_1 = \frac{1}{\omega \cdot X_C} \qquad (6)$$

The inductive reactance is:

$$X_L = \frac{X_C}{h_r^2} \qquad (7)$$

The value for inductor is:

$$L_1 = \frac{X_L}{\omega} \qquad (8)$$

The characteristic reactance is:

$$X_N = \sqrt{X_L \times X_C} = \sqrt{\frac{L_1}{C_1}} \qquad (9)$$

The value for the resistor is:

$$R_1 = X_N \times q \qquad (10)$$

Step3: Compare harmonic filter parameters based on Step 1 to CIGRE published filter values.

Harmonic filters are usually tuned slightly lower than the harmonic component to be filtered to provide a margin of safety in case there is some change in system parameters that would alter the resonant frequency. If they were tuned exactly to the resonant frequency of the system, changes in either capacitance or inductance with temperature or failure might shift the resonance from the harmonic component being filtered [8].

Proceedings of the 19th Southern African Universities Power Engineering Conference
SAUPEC 2010, University of the Witwatersrand, Johannesburg

TOPIC C. POWER SYSTEMS

Step 4: Redesign the filter to accommodate potential changes in system parameters.

Step 5: Evaluate the performance of the filter.

A similar methodology is followed to design the 2nd order high- pass damped filter at the inverter station, but at a different voltage level.

5.2 General C-type damped filter

Figure 6, shows the configuration and the impedance characteristic for a general filter of this type:
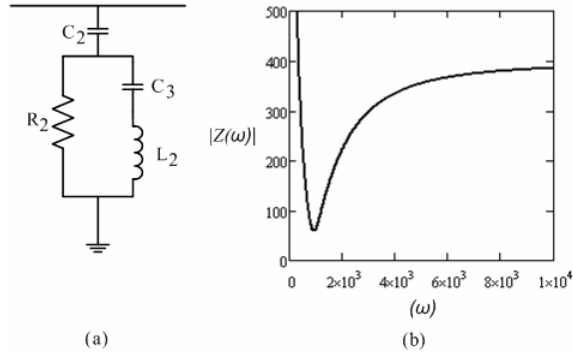
Fig. 6: C-type damped filter: (a) configuration; (b) impedance characteristic

It is necessary to first review the general design methodology.

- **Step 1:** Filter design criteria for lowest characteristic harmonic order including the intermediate factor (m). The filter at the rectifier station is designed with the following parameters: voltage rating (V_1) of 345 kV, reactive power (Q_1) of 250 Mvar, angular velocity (ω) of 314.159 rad/s, resonant harmonic order (h_r) for the 3rd harmonic order, a quality factor (q) of 2.5, typically ($0.5 < q < 5$) and an intermediate factor (m) of ∞.

- **Step 2:** Obtain filter component values for the filter. The filter. The filter components are determined with the use of the (11) to (15), [5]: The capacitive reactance is:

$$X_C = \frac{V_1^2}{Q_1} \tag{11}$$

The value for the capacitor (C_2) is:

$$C_2 = \frac{1}{\omega \cdot X_C} \tag{12}$$

The value for the capacitor (C_3) is:

$$C_3 = \frac{h_r^2 - 1}{m^2 - m\sqrt{m^2 - 1}} \times \frac{Q_1}{2 \cdot V_1^2 \cdot \omega} \tag{13}$$

The value for the inductor (L_2) is:

$$L_2 = \frac{m^2 - m\sqrt{m^2 - 1}}{h_r^2 - 1} \times \frac{2 \cdot V_1^2 \cdot \omega}{Q_1} \tag{14}$$

The value for the resistor (R_2) is:

$$R_2 = \frac{q \cdot V_1^2}{h_r \cdot Q_1} \tag{15}$$

- **Step 3:** Obtain the equivalent series tuned filter with the intermediate factor (m), ($m \geq 1$). According to (17), these final parameters are based on the assumption that the factor (m), is infinite.

$$g(m) = m^2 - m\sqrt{m^2 - 1} \tag{16}$$

If $m \to \infty$, then (15) resolves to:

$$\lim_{m \to \infty} g(m) = \lim_{m \to \infty} (m^2 - m\sqrt{m^2 - 1}) = 0.5 \tag{17}$$

This means there are no resistance (R_2), in parallel, thus the C-type filter become a single tuned filter as shown in Figure 7.
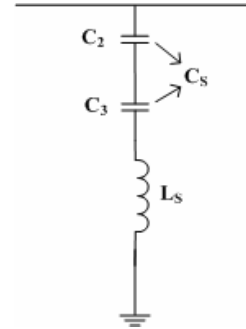
Fig. 7: Equivalent single tuned filter

From the single-tuned filter (Figure 7) the following components can be calculated: The parameters (C_3) and (L_S) for the filter can be obtained using (18) to (21).

$$C_S = \frac{(h_r^2 - 1) \cdot Q_1}{\omega \cdot V_1^2} \tag{18}$$

The inductor (L_S) is calculated by:

$$L_S = \frac{V_1^2}{(h_r^2 - 1) \cdot \omega \cdot Q_1} \tag{19}$$

From (20) and (21) the filter components of the general C-type filter can be obtained;

$$C_S = \left(\frac{1}{C_2} + \frac{1}{C_3}\right)^{-1} = \frac{(h_r^2 - 1) \cdot Q_1}{h_r^2 \cdot \omega \cdot V_1^2} \tag{20}$$

TOPIC C. POWER SYSTEMS

Proceedings of the 19th Southern African Universities Power Engineering Conference
SAUPEC 2010, University of the Witwatersrand, Johannesburg

The value for the inductor (L_2) is:

$$L_S = L_2 \qquad (21)$$

A similar process was followed to design the general C-type damped filter at the inverter station, but at a different voltage level.

5.3 CIGRE C-type damped filter

The CIGRE benchmark does not use the general C-type damped harmonic filter. It uses the type shown Figure 8b.
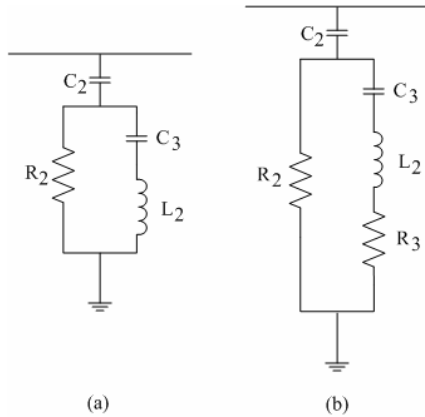
Fig. 8: C-type damped filters: (a) Section 4; (b) Default CIGRE benchmark

The CIGRE has an additional resistance (R_3) in the series tuned arm of the filter and its value needs to be determined. This is obtained using:

The characteristic reactance is:

$$X_N = \sqrt{\frac{L_2}{C_3}} \qquad (22)$$

Resistor (R_3) is:

$$R_3 = \frac{X_N}{q_S} \qquad (23)$$

6 HARMONIC FILTER EVALUATION

The methodologies are now applied.

The 2nd order high-pass damped harmonic filter components are compared to that of the filter components provided with the CIGRE benchmark (Section 5.1, Step 3) is shown in Table 1.

The respective design methodologies for the filters are applied, and to check the effectiveness the following equation is used:

$$|\%Change| = \frac{CIGRE - Design}{CIGRE} \times 100\% \qquad (24)$$

TABLE 1: Comparison of the 2nd order high-pass harmonic filter components

Rectifier			
2nd Order HP Filter			
Component	Designed	CIGRE	|% Change|
C_1 (μF)	6.686	6.685	0.015
L_1 (H)	0.0125	0.0136	8.088
R_1 (Ω)	108.205	83.32	29.867
Inverter			
2nd Order HP Filter			
Component	Designed	CIGRE	|% Change|
C_1 (μF)	15.04	15.04	0
L_1 (H)	0.0056	0.0061	8.196
R_1 (Ω)	48.091	37.03	29.870

TABLE 2: Comparison of C-type damped harmonic filters components

Rectifier			
C-type damped filter			
Component	Designed	CIGRE	|% Change|
C_2 (μF)	6.686	6.685	0.015
C_3 (μF)	53.49	74.28	27.989
L_2 (H)	0.1894	0.1364	38.856
R_2 (Ω)	396.75	261.87	51.506
R_3 (Ω)	---	29.76	---
Inverter			
C-type damped filter			
Component	Designed	CIGRE	|% Change|
C_2 (μF)	15.04	15.04	0
C_3 (μF)	120.3	167.2	28.050
L_2 (H)	0.0842	0.0608	38.487
R_2 (Ω)	176.33	116.38	51.512
R_3 (Ω)	---	13.23	---

From Tables 1 and 2, it can be seen that the designed parameters differ from the CIGRE values, thus adapted filters need designing. To adapt the 2nd order high-pass damped harmonic filter it is required to change the design criteria. This is achieved by reducing the resonant harmonic order (h_r) from 11 to 10.55 and the quality factor (q) from 2.5 to 1.85.

TABLE 3: Comparison of the 2nd order high-pass harmonic filter components

Rectifier			
2nd Order HP Filter			
Component	Re_designed	CIGRE	|% Change|
C_1 (μF)	6.685	6.685	0
L_1 (H)	0.0136	0.0136	0
R_1 (Ω)	83.487	83.32	0.2
Inverter			
2nd Order HP Filter			
Component	Re_designed	CIGRE	|%Change|
C_1 (μF)	15.04	15.04	0
L_1 (H)	0.0061	0.0061	0
R_1 (Ω)	37.11	37.03	0.2

Proceedings of the 19th Southern African Universities Power Engineering Conference
SAUPEC 2010, University of the Witwatersrand, Johannesburg

TOPIC C. POWER SYSTEMS

With the C-type damped filter, Figure 8 (b), an additional resistor (R_3) has to be added to the filter. In order to obtain similar results to that of the CIGRE benchmark model, the resonant harmonic order (h_r) was increased from 3 to 3.5 and the quality factor (q) was decreased from 2.5 to 2. For R_3, a quality factor of 1.5 was used. The results are displayed in Table 4.

TABLE 4: Comparison of C-type damped harmonic filter components at both the rectifier and inverter station

Rectifier			
C-type damped filter			
Component	Designed	CIGRE	|% Change|
C_2 (μF)	6.685	6.685	0
C_3 (μF)	75.22	74.28	1.27
L_2 (H)	0.1347	0.1364	1.25
R_2 (Ω)	272.06	261.87	3.89
R_3 (Ω)	28.21	29.76	5.21
Inverter			
C-type damped filter			
Component	Designed	CIGRE	|% Change|
C_2 (μF)	15.04	15.04	0
C_3 (μF)	169.23	167.2	1.21
L_2 (H)	0.0601	0.0608	1.31
R_2 (Ω)	120.91	116.38	3.89
R_3 (Ω)	12.54	13.23	5.21

For the quality factor (q_S) of 1.5 the error for R_3 is approximately 5%. If the q-factor is adjusted, more accurately, then error will disappear.

7 HARMONIC FILTER PERFORMANCE

Now that the filter parameters have been established, the performance of the filters together with the reactive compensation and the AC network needs to be checked for effectiveness.

The characteristic harmonic currents generated by the each of the 6-pulse converters at the rectifier side (commuting transformer secondary) are shown in Figure 9 and 10.
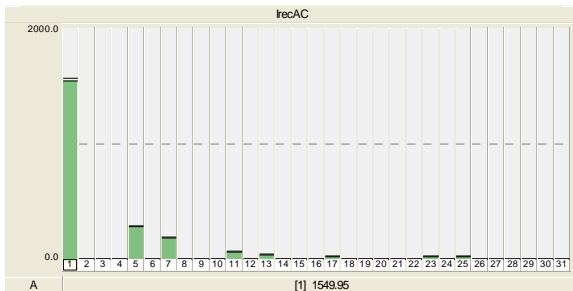
Fig. 9: Harmonic currents at the commutating transformer secondary (Delta/Wye)
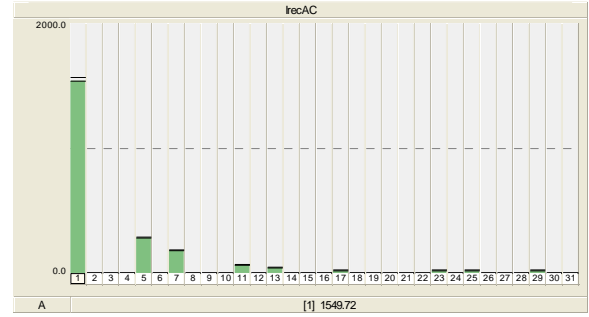
Fig. 10: Harmonic currents at the commutating transformer secondary (Wye/Wye)

To demonstrate that the AC current waveform contains characteristic 12-pulse harmonic currents (11th, 13th and higher) and the lower order 6-pulse harmonics (5th and 7th) are eliminated at REC_AC is shown in Figure 11:
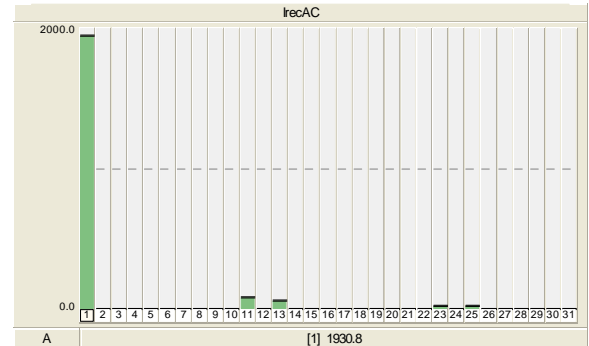
Fig. 11: Harmonic currents at REC_AC

The same characteristic 12- pulse harmonic currents (11th, 13th and higher) were present at INV_AC at the inverter side.

To evaluate the combined performance of the 2nd order high-pass damped filter and the C-type filter at the rectifier and inverter sides of the HVDC system, the following voltage and current indices were used (25) and (26):

Individual Harmonic Distortion (*HD*) is:

$$HD_M = \frac{M_h}{M_1} \times 100\%$$ (25)

The Total Harmonic Distortion (*THD*) is:

$$THD_M = \frac{\sqrt{\sum_{h=2}^{31} M_h^2}}{M_1} \times 100\%$$ (26)

TOPIC C. POWER SYSTEMS

Proceedings of the 19th Southern African Universities Power Engineering Conference
SAUPEC 2010, University of the Witwatersrand, Johannesburg

The harmonic voltage index results at REC_AC and INV_AC are shown in Tables 5 and 6.

TABLE 5: Harmonic voltage index results at REC_AC

REC_AC			
Harmonic Voltage Index Results			
Index	Design	Adapted	CIGRE
HD_5 (%)	0.018	0.018	0.017
HD_7 (%)	0.002	0.006	0.001
HD_{11} (%)	0.622	0.777	0.778
HD_{13} (%)	0.551	0.620	0.617
HD_{17} (%)	0.003	0.001	0.002
HD_{19} (%)	0.001	0.002	0.001
HD_{23} (%)	0.432	0.347	0.348
HD_{25} (%)	0.367	0.303	0.297
THD (%)	1.008	1.101	1.103

TABLE 6: Harmonic voltage index results at INV_AC

INV_AC			
Harmonic Voltage Index Results			
Index	Design	Adapted	CIGRE
HD_5 (%)	0.012	0.031	0.074
HD_7 (%)	0.005	0.025	0.005
HD_{11} (%)	0.484	0.606	0.619
HD_{13} (%)	0.380	0.462	0.447
HD_{17} (%)	0.004	0.006	0.004
HD_{19} (%)	0.002	0.006	0.002
HD_{23} (%)	0.440	0.339	0.355
HD_{25} (%)	0.349	0.277	0.270
THD (%)	0.836	0.915	0.894

The harmonic current index results at REC_AC and INV_AC are shown in Tables 7 and 8.

TABLE 7: Harmonic current index results at REC_AC

REC_AC			
Harmonic Current Index Results			
Index	Design	Adapted	CIGRE
HD_5 (%)	0.022	0.040	0.026
HD_7 (%)	0.003	0.023	0.004
HD_{11} (%)	4.444	4.376	4.392
HD_{13} (%)	2.906	2.843	2.850
HD_{17} (%)	0.007	0.008	0.008
HD_{19} (%)	0.004	0.011	0.002
HD_{23} (%)	0.966	0.957	0.975
HD_{25} (%)	0.863	0.868	0.853
THD (%)	5.467	5.378	5.397

TABLE 8: Harmonic current index results at INV_AC

INV_AC			
Harmonic Current Index Results			
Index	Design	Adapted	CIGRE
HD_5 (%)	0.005	0.018	0.042
HD_7 (%)	0.021	0.021	0.036
HD_{11} (%)	3.393	3.365	3.447
HD_{13} (%)	2.023	2.039	2.047
HD_{17} (%)	0.006	0.005	0.010
HD_{19} (%)	0.005	0.006	0.009
HD_{23} (%)	0.951	0.930	0.958
HD_{25} (%)	0.793	0.795	0.756
THD (%)	4.145	4.131	4.203

Small differences were found in the results obtained for the individual voltage and current harmonic distortion results, and similar results were obtained for the total voltage and current harmonic current distortion index results obtained at both REC_AC and INV_AC. The low percentage values demonstrate that the combined performance of the filters is effective proving that the developed design methodology for the filters is correct.

To show the frequency response of the integrated HVAC/HVDC system that includes the AC source impedance, harmonic filters and reactive compensation, a frequency sweep study was conducted at both REC_AC and INV_AC buses in the network.

The role of the AC source impedance on both the rectifier and inverter sides influences the performance of the harmonic filters used. Due to the nature of these impedances (R-R-L and R-L-L, configuration types, Figure 2, respectively) the resonant frequency point and the damping are effected. The R-L-L type reveals a higher damping at the lower harmonic orders, thus sweeps are conducted to evaluate responses.

In Figure 12 and 13, the frequency responses at REC_AC are displayed.
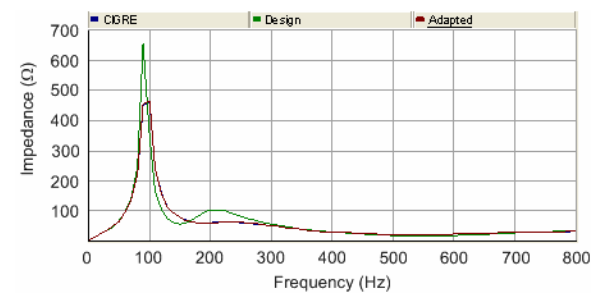
Fig. 12: Impedance magnitude obtained at REC_AC
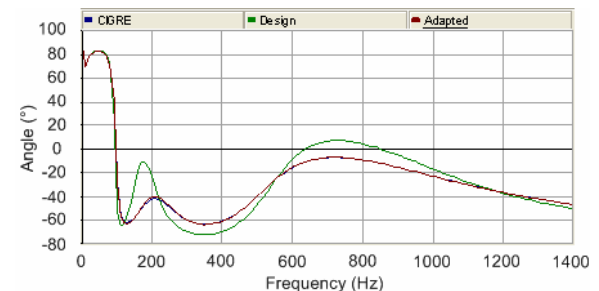
Fig. 13: Impedance angle obtained at REC_AC

From literature [3], a second harmonic resonance at the AC side should be present, due to the weak inverter side. From Figure 12, a harmonic resonance close to the 2nd harmonic order (94 Hz) can be seen for the designed harmonic filters as well as the adapted harmonic filters compared to the CIGRE harmonic filters, proving the work conducted.

The process was repeated and in Figure 14 and 15, the frequency responses at INV_AC are displayed.
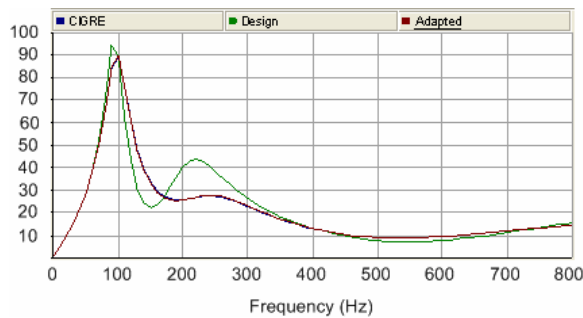
Fig. 14: Impedance magnitude obtained at INV_AC
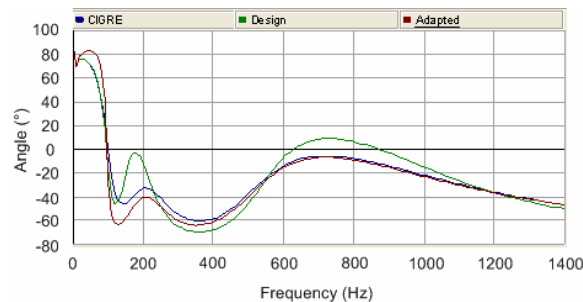
Fig. 15: Impedance angle obtained at INV_AC

With the dominant R-L-L AC system configuration present at the at the inverter side, the higher damping for lower harmonic orders can be seen in Figure 14, where the impedance magnitude at the resonant frequency is below 100 Ω, compared to the impedance (near 500 Ω) at the rectifier side.

8   CONCLUSIONS

It was found necessary to identify the harmonic filter types used with the HVDC CIGRE benchmark network. They were identified as a 2nd order high-pass damped filter and a C-type damped filter at both the rectifier and inverter sides. On closer inspection it was found that the C-type used with the CIGRE network differed from the general C-type filter.

From this finding design methodologies for the 2nd order high-pass damped and CIGRE C-type filters for both the converter stations needed development. It was thus found necessary to develop three methodologies so that proper understanding of the design details is known.

The first methodology was for the 2nd order high-pass damped filter where choice of the resonant harmonic order (h_r) and the quality factor (q) are decisive in the design.

Before developing the CIGRE C-type methodology it was necessary to develop a methodology for a generalised C-type filter, especially as the design is more complex than the 2nd order high-pass filter. As with this filter it is necessary to include the intermediate factor (m) besides choosing the harmonic resonant order (h_r) and quality factor (q).

With HVDC systems typically there are two harmonic mitigation solutions, transformer vector groups and harmonic filters. These are reviewed and evaluated using the designed filters and the results demonstrated their effectiveness. The three methodologies were compared to ascertain discrepancies using a developed percentage change formula. Discrepancies were found and this was because general theory of filters is based on the elimination of the lowest characteristic harmonic order present. This is not true for the CIGRE benchmark, where filters are tuned to frequency other than a characteristic harmonic.

Filter performance was evaluated in terms of voltage and current individual and total harmonic distortion index results and frequency sweeps. The filters effectively reduced distortion, by shifting resonant frequency points and by providing suitable damping.

REFERENCES

[1]   J. Arrillaga and N.R. Watson, "Power System Harmonics", 2nd Edition, pp. 219-258, 2003. ISBN: 0-470-85129-5

[2]   K.W. Huddart and G.L. Brewer, "Factors influencing the harmonic impedance of a power system", *IEE Conference*, No.22, pp. 450-452, 1966.

[3]   M.Szechtman, T. Wess and C.V.Thio, "First benchmark model for HVDC control", *Electra*, No. 135, pp.55-73, 1991.

[4]   M.Szechtman, T. Wess and C.V.Thio, "A benchmark for HVDC studies", *International conference on AC and DC power transmission*, pp.374-378, 1991. ISBN:0-85296-517-6

[5]   Y. Xiao, J. Zhao and S. Mao, "Theory for the design of C-type filter", *11th International Conference on Harmonics and Quality of Power,* USA, ICHQP#010, 2004.

[6]   G.J. Wakileh, " Power Systems Harmonics: Fundamentals, Analysis and filter design", Springer-Verlag, Berlin, pp. 105-136, ISBN: 3-540-42238-2.

[7]   C.H. Stanley, J.J. Price and G.L. Brewer, "Design and performance of a.c. filters for 12-pulse HVdc schemes", *IEE Conference Publication*, No. 154, pp. 158-161, 1977.

[8]   R.C Dugan, M.F. McGranaghan, S. Santoso and H.W. Beaty," Electrical power systems quality, MacGraw-Hill, 2nd Edition, pp.255, 2002, ISBN: 0-07-138622-X.

[9]   M.O. Faraque, Y. Zhang and V. Dinavahi, "Detailed modelling of CIGRE HVDC system using PSCAD/EMTDC and PSB/Simulank", *IEEE Transactions on Power Delivery*, Vol.21, No.1, pp.378-387, January 2006.

BIOGRAPHIES

- **Willem Stemmet**
  E-mail: stemmetw@cput.ac.za
- **Johan Smith**
  E-mail: smithj@cput.ac.za
- **Prof. G. Atkinson-Hope**
  E-mail: atkinsonhopeg@cput.ac.za

Topic D

Renewable and Alternative Energy

GRID INTEGRATION OF WIND ENERGY : IMPACT ON NETWORK STABILITY

S P N Kanyemba*,   S P Chowdhury* and S Chowdhury*

*University of Cape Town, Electrical Engineering Department, Cape Town, South Africa.

Abstract. Penetration of wind power plants to utility grids are increasing day by day for a drive to generate clean power and cut down on carbon emissions caused by fossil-fuelled power plants. This is leading to extensive research on impact of wind penetration on utility power network stability particularly in terms of voltage and frequency. As wind power plants use different types of electric generators ranging from synchronous machines, induction machines and permanent magnet machines, it is likley that the nature of the impact will depend on the type of generator employed. Due to robustness and easy controllability, Doubly-Fed Induction Generator (DFIG) is widely used in commercial wind turbines. This paper presents the impact of grid integration of wind turbines with DFIG on stability of utility grid networks. The impacts are investigated for wind turbines of different capacities at different load conditions for different points of integration.

Key Words. Doubly Fed Induction Generators, power system stability, wind power generations, simulation, PWM, grid integration.

1. INTRODUCTION

Penetration of wind turbines in distribution grids is increasing worldwide. The drive for cleaner energy sources, the economic opportunities presented for investors in the deregulated electric industry environment and the potential benefits for utilities (peak shaving, congestion alleviation, reduction of losses, better asset utilization, etc.) are contributing to this trend [11]. Over 13900 MW of capacity is now installed worldwide with an annual increase averaging 35.7% from 1998 to 2002 [6]. The most widely used wind turbine in wind farm is based on Doubly Fed Induction Generator (DFIG) due to noticeable advantages: the various speed generation, the decoupled control of active and reactive power and the improvement of the power quality [2, 10]. However, the integration of wind turbines to utility grids has given rise to different kinds of voltage and frequency instability problems other than the ones already reported for conventional vertically integrated grid operation. Hence there is ample need to adequately assess the impact of wind integration on network voltage and frequency stability.

2. INTEGRATION OF DFIG BASED WIND TURBINE

Fig. 1 shows how a DFIG-based wind turbine is integrated to the grid [4]. The DFIG consists of a pulse-width modulated converter connected to the rotor side of the generator. The converter is connected to the three winding transformer before connecting to the grid [4]. The mechanical power generated by the wind turbine is converted into electrical power by an induction generator and is fed into the grid through the stator and the rotor windings [3]. The rotor winding is connected to the main grid by self commutated AC/DC converters allowing controlling the slip ring voltage of the induction machine in magnitude and phase angle [3].
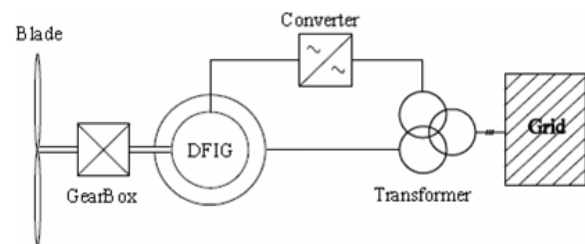
Fig.1: Doubly Fed Induction Generator [4]

In contrast to a conventional, singly fed induction generator, the electrical power of a DFIG is independent from the speed. This is because the rotor of the generator is connected to the grid by a back to back electronic inverter. This gives an advantage that only a part of the power production is fed through the inverter. That means the nominal power of the inverter system can be less than the nominal power of the wind turbine. In general the nominal power of the inverter is the half of the power of the wind turbine, enabling a rotor speed variation in the range of half the nominal speed. Hence, the DFIG can supply power at constant voltage and constant frequency while the rotor speed varies. Therefore, it is possible to realize a variable speed wind generator by adjusting the mechanical speed to the wind speed and hence operating the turbine at the aerodynamically optimal point for a certain wind speed range [3].

3. DFIG MODEL
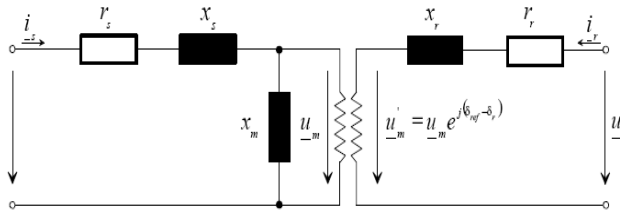
Fig.2: Equivalent circuit of the doubly fed induction generator [3]

The equivalent circuit diagram for DFIG as shown in Fig. 2 is used to derive the basic modeling equations (1)-(3) as below:

Voltage equations [3]:

$$u_{-s} = r_s i_{-s} + \frac{d\psi_{-s}}{\omega_n dt} + j\frac{\omega_{ref}}{\omega_n}\psi_{-s} \qquad (1)$$

$$u_{-r} = r_r i_{-r} + \frac{d\psi_{-r}}{\omega_n dt} + j\frac{\omega_{ref} - \omega_g}{\omega_n}\psi_{-r} \qquad (2)$$

where,
u_{-s} = stator voltage
u_{-r} = rotor voltage
ω_n = nominal frequency
ω_g = angular speed of the rotor
ω_{ref} = dq - reference frame speed

Equation of motion [3]:

$$J\frac{d\omega_g}{dt} = t_m + t_{el} \qquad (3)$$

Electrical torque is calculated from the stator current and the stator flux [3] using Equation(4) below:

$$t_{el} = \text{Im}(\psi_{-s} \quad i^*_{-s}) \qquad (4)$$

4. PULSE WIDTH MODULATION (PWM) CONVERTER MODEL

The rotor and grid side converters are self-commutated PWM converters and are usually set up by six pulse bridges as shown in Fig. 3 [8].
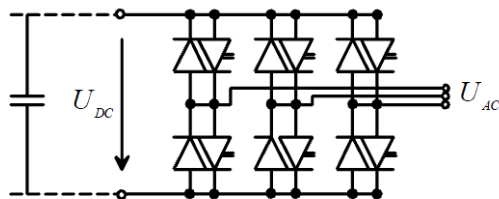
Fig.3: PWM converter [8]

Assuming an ideal DC-voltage and an ideal PWM modulation (infinite modulation frequency), the rms value of fundamental frequency line to line AC voltage (U_{AC}) and the DC voltage (U_{DC}) can be related by Equation(5) as follows [8]:

$$|U_{AC}| = \frac{\sqrt{3}}{2\sqrt{2}} pm U_{DC} \qquad (5)$$

The pulse width modulation factor P_m is the control variable of the PWM converter. Equation (5) is valid for $0 <= P_m < 1$. For values larger than 1 the converter starts saturating and the level of lower order harmonics starts increasing [10].

5. VOLTAGE STABILITY

A network experiences a state of voltage instability when there is a progressive or uncontrollable drop in voltage magnitude after a disturbance, increase in load demand or change in operating condition. The main factor, which causes these unacceptable voltage profiles, is the inability of the distribution system to meet the demand for reactive power. Under normal operating conditions, the bus voltage magnitude increases as reactive power injected at the same bus is increased [12].

However, when voltage magnitudes of any one of the network buses decreases with an increase in reactive power for the same bus, the system is said to be unstable. Although the voltage instability is a localised problem, its impact on the system can be wide spread as it depends on the relationship between transmitted power, injected reactive power and receiving end voltage [12].

Disturbances occur in different ways such as short circuit on a transmission line, loss of a transmission line between two substations or loss of a generator or a big load. Short circuits vary in type and severity and are usually cleared by the system protection either by disconnection and fast reclosure, or by disconnection of the faulty equipment. All these situations result in a fault period with low or no voltage followed by a post-fault period where the voltage is restored to the specified value [7, 12].

Loss of transmissions lines due to overload or component failure disrupts the balance of active and reactive power flow to the adjacent areas. Though the capacity of the operating generators is adequately large, voltage drops may occur suddenly. The reactive power following new paths in a highly loaded transmission grid may force the voltage operating point of the network in the area beyond the border of stability. This is manifested again as a period of low voltage likely to be followed by complete loss of power [5,7].

Proceedings of the 19th Southern African Universities Power Engineering Conference
SAUPEC 2010, University of the Witwatersrand, Johannesburg

TOPIC D. RENEWABLE AND ALTERNATIVE ENERGY

The major factors that have a possible impact on voltage stability as a result of wind integration are as follows [9]:

- The point of integration of wind turbine on the grid has considerable impact on voltage stability. As a result of this integration, power flows may be considerably altered by high winds and therefore the dynamic response of the system does no longer primarily depend on the conventional generator but also get influenced by the presence of wind generators.

- Electric generators might be technologically widely different from the conventional synchronous generators.

6. TEST SYSTEM

In this paper, the authors investigate the impact of integrating DFIG-based wind turbines on the voltage and frequency behaviour of the grid following a disturbance event. The base test system, shown in Fig. 4, consists of a 100MW and 40MVAR conventional synchronous generator representing the bulk power source. Power generated at 13.8 kV from the synchronous generator is stepped up to a suitable distribution voltage of 230 kV through a 230kV/13.8kV transformer. A double line 230kV feeder supplies the four loads, each rated at 40MW and 20MVAR. The external grid at 230kV is considered as the infinite bus for the study.
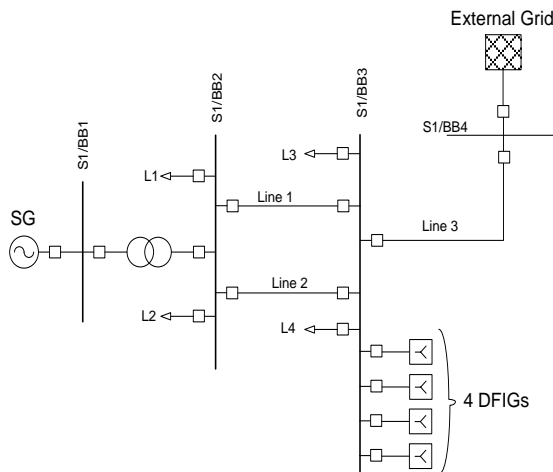
Fig.4: Test system [9]

7. RESULTS AND DISCUSSIONS

Two sets of studies have been conducted, Case-1 for investigating the effect of wind energy penetration level and Case-2 for investigating the effect of point of integration of the wind turbines on the grid following a disturbance. For Case-1, the voltage and frequency responses of the bus at which the wind turbines are integrated are plotted. For Case-2, the wind turbines are integrated at two different points on thre grid and their voltage and frequency responses are compared following the same disturbance event.

7.1 Case - 1: Effect of Wind Energy Penetration Level

Different numbers of DFIG-based wind turbines, each rated at 10MVA are connected at bus 3 (BB3) of the test system in Fig.4 in order to simulate different levels of wind penetration. The DFIGs are connected to the grid through a short transmission line. The penetration level is increased by increasing the number of DFIGs from 2 to 8 in the system, in steps of two DFIGs at a time. Fig. 5 shows a detailed model of a DFIG as realised in DIgSILENT Power Factory.
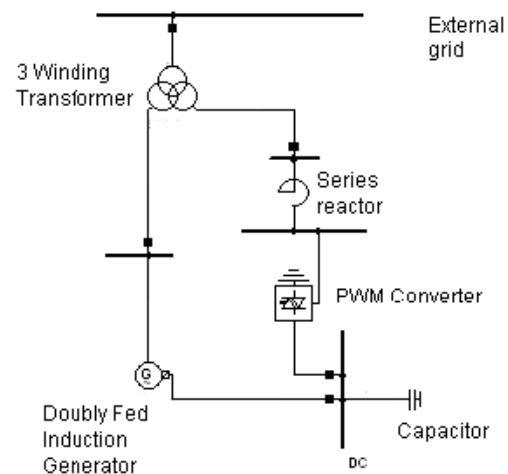
Fig.5: DFIG model for simulation [1]

No internal PQ and current controllers are included in the DFIG model. The disturbance event is simulated as a three-phase fault on Line 2 of the base system applied at t=1s starting from the time of simulation and again clearing the same fault at t=1.2s. The simulations are run for a total time of 10s. The voltages responses at bus 3 for different penetration level of DFIGs are plotted in Fig. 7.

7.1.1 Voltage Responses

Fig. 6 indicates that the post-fault voltage at bus 3 (BB3) increases with increasing number of DFIGs confirming that DFIGs improve the voltage profile. The pre-fault voltage of the base system when no DFIG is connected is at 0.9 pu which improves to 0.99 pu when 6 DFIGs are connected. However, the post-fault voltage starts oscillating and the oscillation increases with increasing DFIG penetration level. This is due to the PWM converters, reactors and capacitor banks which are likely to introduce oscillations in the voltage. When

8 DFIGs are connected the system performs well before the fault with a pre-fault voltage at 1 pu. However, after the fault the voltage drops to a value of 0.82 pu which is much below the specified voltage of 1 pu. Hence, the system does not meet its performance criteria with respect of bus voltage level.
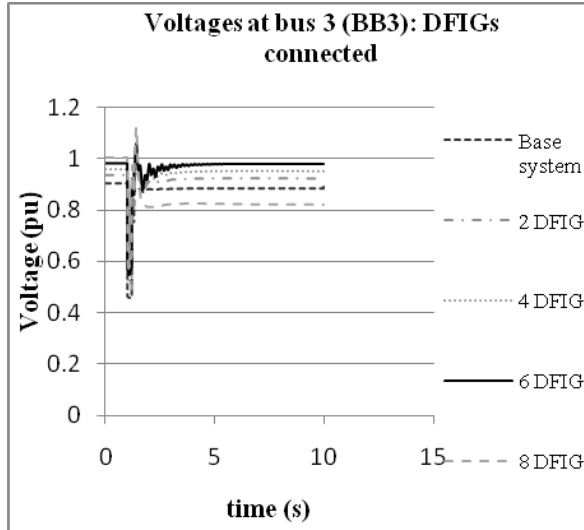
Fig.6: Voltages at bus 3 when DFIGs are connected

7.1.2 Frequency Responses

Post-fault frequency responses at bus 3 for the base system and four different peneration levels (2,4,6 and 8 DFIGs) are plotted in Fig.7 to Fig.11.
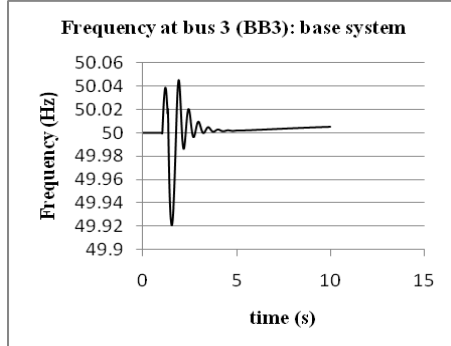
Fig.7: Base system frequency at bus 3
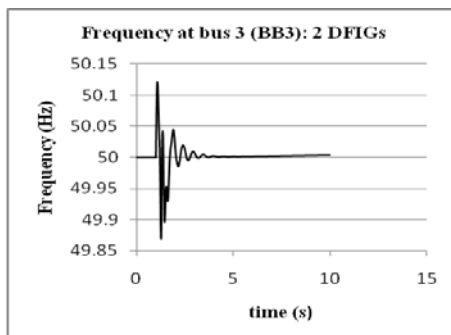
Fig.8: frequency at bus 3 with 2 DFIGs
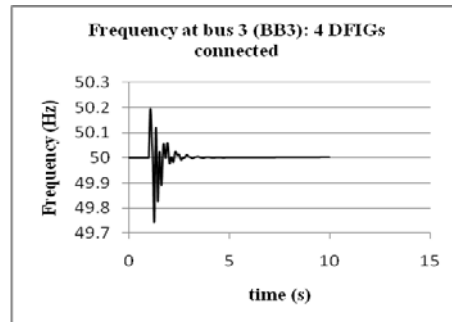
Fig.9: frequency at bus 3 with 4 DFIGs
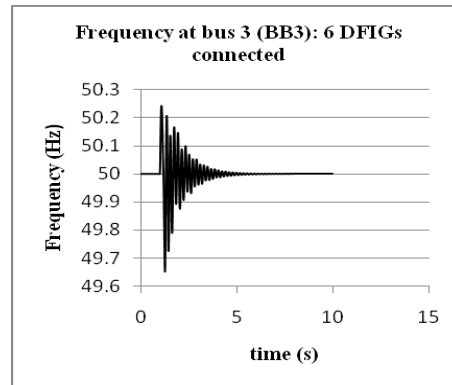
Fig.10: frequency at bus 3 with 6 DFIGs
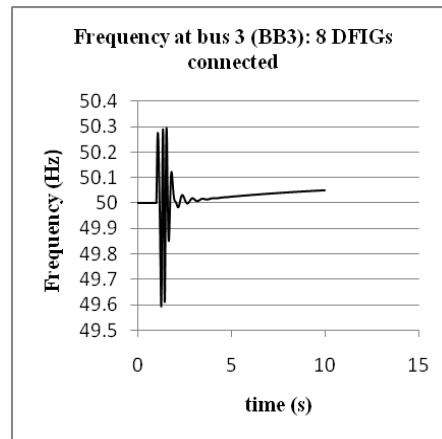
Fig.11: frequency at bus 3 with 8 DFIGs

Fig.7 to Fig.11 indicates that after the post-fault frequency oscillations increase with increasing number of DFIGs. When 2 DFIGs are connected, the first swing reached a frequency below 50.15Hz, while it reached 50.2Hz when there are 4 DFIGs connected. When 6 DFIGs are connected, the frequency oscillates more than when 2 or 4 DFIGs are connected, with the first swing above 50.2Hz. However, when 8 DFIGs are connected, the frequency swings up to 50.25 Hz, slowly increasing in magnitude before it suddenly drops to the pre-fault value and starts increasing again at a constant slope, hence forcing the system into instability.

7.2 Case - 2: Effect of Point of Integration of DFIG-based Wind Turbines

Case-2 investigates the impact of the wind turbine integration point relative to the position of the conventional synchronous generator. Bus 2 (BB2) and Bus 3 (BB3) of the base system are selected as two different points of integration of DFIG-based wind turbines. The number of DFIGs is increased from two units to four units in both cases. For simulating the disturbance, a three phase fault is applied on the middle of Line 2 at t=1s from starting of simulation and cleared at t=1.2s. Voltage and frequency responses at Bus 1 where the synchronous generator is connected are plotted for all the simulations.

7.2.1 Voltage Responses
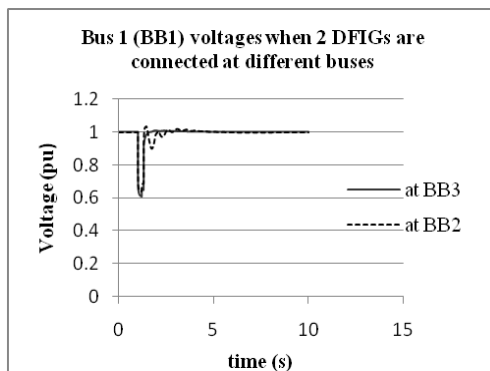
Fig.12: Voltages at bus 1 when 2 DFIGs are connected at BB2 and BB3
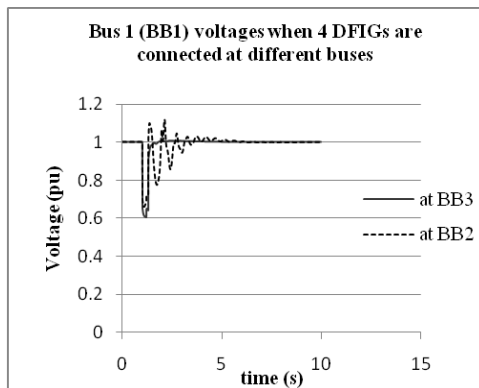
Fig.13: Voltages at bus 1 when 4 DFIGs are connected at two different buses

Voltage responses at bus 1 as shown in Fig. 12 and Fig. 13 indicate voltage stability performance of the system is better when the wind farm is connected far from the synchronous generator. In both cases when the wind farm is connected at bus 3 which is the furthest from the synchronous generator, the bus voltage returns to the pre-fault value of 1 pu within 2-3s after the fault is cleared. However, when the wind farm is connected at bus 2 which is closer to the synchronous generator than

bus 3, the bus voltage oscillates before recovering to a pre-fault value of 1pu and only settles after 6-7s. It can also be observed from the two figures that the oscillations after the fault is cleared increases with increasing DFIG penetrations level in the system. The system is said to be stable in both cases, but more voltage oscillation is there when the wind farm is connected close to the synchronous generator and at higher penetration level.

7.2.2 Frequency Responses
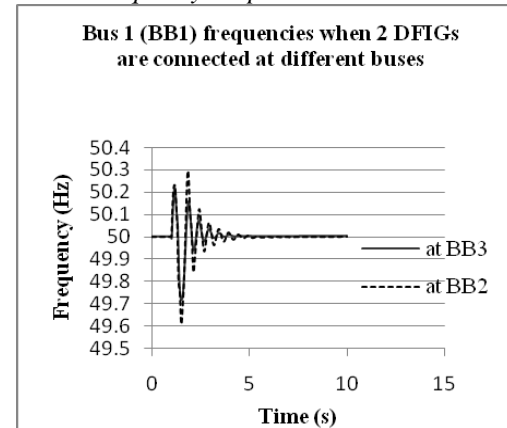
Fig.14: Bus 1 frequencies when 2 DFIGs are connected at BB2 and BB3
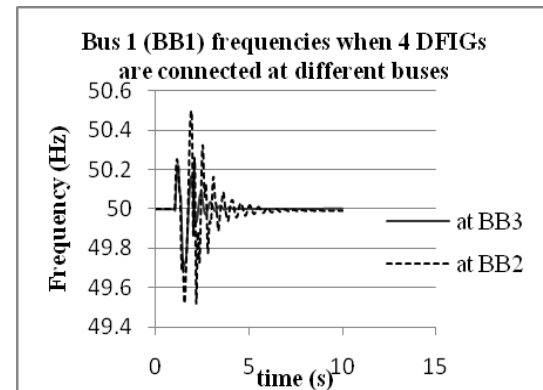
Fig.15: Bus 1 frequencies when 4 DFIGs are connected at two different buses

Fig. 14 and Fig. 15 show the frequency responses of Bus 1 for wind turbine integration at Bus 2 and Bus 3. It can be seen from these two figures that again the frequency performance of the system is better when the wind farm is connected far from the synchronous generator. When two DFIGs are connected at bus 2 the magnitudes of oscillations are higher than when the wind farm is connected at bus 3, with the same number of oscillations. However, when four DFIGs are connected at bus 2 both the magnitude and number of oscillations increases comparing to when the wind farm is connected at bus 3.

8. CONCLUSION

In this paper, the authors investigate the impact of level of peneration (i.e. wind farm capacity) and point of integration of wind turbines on voltage and frequency stability of utility grid. The authors have modeled the base grid network and the DFIG-based wind turbine in DIgSILENT Power Factory and the case studies simulated for analysing the voltage and frequency responses of the system without and with the wind turbines following a fault event.

The results of the case studies show that the stability performance of the grid network depends on the penetration level of the wind energy, i.e. on the total capacity of wind turbines or wind farms connected. At a high penetration level the system tends to lose stability easier than at low penetration level. However, high penetration level also has a beneficial impact on the voltage profile. The bus voltage profile improves with increasing number of wind turbines.

The integration point of DFIGs relative to the position of a conventional synchronous generator also has an impact on stability performances of power networks. The stability performance of the system is better when the wind turbines are connected far from the synchronous generator as compared to the wind turbines connected close to the synchronous generator.

ACKNOWLEDGMENT

REFERENCES

[1]   DIgSILENT GmbH, *DIgSILENT Technical Documentation, Doubly-Fed Induction Generator*. Germany, 2007

[2]   How difficult is it to integrate wind turbine with utilities. Available: http://www.awea.org/faq/putnam.html [20 July 2009].

[3]   A.P.Markus. *Doubly-Fed Induction Machine Models for Stability Assessment of Wind Farms*. Electrical Power Systems Research 77 (2007) 24-34.

[4]   K.Mngxuma, *The power quality of wind turbines in South Africa and their impacts on distribution networks,* Msc. Thesis. University of Cape Town, South Africa, 2005.

[5]   J.D.Glover, M.S.Sarma and T.J.Overbye, *Power System Analysis and Design*, 4th ed.USA:Cengage Learning, 2009.

[6]   Poul A. Ø. Poul, "Ancillary services and the integration of substantial quantities of wind power", *Applied Energy*, Vol.83, pp.451-463, 2006.

[7]   F. Santjer and J.G.Gerhard, *Wind Turbines Grid Connection and Interaction*. Available: http://www.dewi.de/dewi.php, 2000 [29 July 2009].

[8]   A.Sebastian and P.Markus, *Direct Drive Synchronous Machine Models for Stability Assessment of Wind Farms* Electrical Power Systems Research 77 (2007) 22-34.

[9]   S.P.N.Sheetekela, *Impact on network stability: transient stability.* Bsc. Thesis, University of Cape Town, South Africa, 2007.

[10] P.C.Sen, *Principles of Electrical Machine and Power Electronics*. 2nd ed. Kingston, Ontario, Canada: John Wiley & Sons, 1996.

[11] A.P.Stavros, "A technical evaluation framework for the connection of DG to the distribution network", *Electric Power Systems Research*, Vol.77, pp.24-34, 2007

[12] T.C.Trinh, "Voltage Stability Investigation of Grid Connected Wind Farm", World Academy of Science, Engineering and Technology 42, 2008.

DESIGN AND DEVELOPMENT OF A SMALL WIND TURBINE GENERATOR FOR URBAN-ENVIRONMENTS

by Nivashnee Pillay and Matthew Song

School of Electrical & Information Engineering, University of the Witwatersrand, Private Bag 3, 2050, Johannesburg, South Africa

Abstract. This report presents a design strategy that is applied to a grid connected wind turbine generator system to facilitate harnessing maximum power. The recommended system is built as a proof of concept and limited to the electrical and mechanical engineering disciplines. The design and development process involved three major components: sourcing, building and testing. Rotor blades were sourced and utilized to build a test rig, to evaluate its performance. The amount of power generated by the rotor blades upon testing was found to be 500 W at a wind speed of 9 m.s-1, but is capable of 3.5 kW at a wind speed of 18 m.s-1. An existing induction machine rated at approximately 3.7 kW was utilized for testing and with suitable modifications; a generator was made for the application. The design involves implementing an automatic Maximum Power Point Tracker (MPPT) concept into the generator by means of curve matching. A simulation program to obtain a decent overlap between the torque-speed profile's of the induction generator and the rotor blades was required. Curve matching was achieved by adding a rotor resistance of 0.5 Ω per phase. A flaw in the simulation program however causes the torque-speed profile of induction generator to not follow the normal profile. The system is capable of 3 kW peak power generation but can only do 500 W on average.

Key Words. Induction generator, Maximum Power Point Tracker (MPPT), Curve matching, Wind turbine

1. INTRODUCTION

The global energy demand is expected to increase to 44 % by 2030 with approximately 70 % of this demand coming from developing nations like China and India [1]. New power plants are investments that can last 25 to 50 years, requiring major processing and fine-tuning on the plant to make raw materials into useful forms of energy. Renewable energy sources, in particular wind, can be used in small sources locally. Small sources of wind power help supplement grid electricity and reduce the dependency on the local electrical utility. Wind energy systems are one of the most cost-effective home-based renewable energy systems [1].

The document proposes a simple design strategy that is applied to a grid connected wind driven system to facilitate harnessing maximum power and is described in three subsystems. The document begins with a description of the social and environmental impacts of the wind power system suitable for an urban environment. Thereafter, a description of each subsystem's contribution to the development of the entire wind turbine generator system is accounted for. This is followed by critical analysis. Finally recommendations are made for future work and conclusions are drawn.

2. SOCIAL AND ENVIRONMENTAL IMPACT

2.1 Siting and Visual Impact

The 'visual pollution' of wind turbines is a subjective one. In a large-scale power generation network, the presence of steel and technology against a mountainous background is not appealing. Objection from the local public need not be considered in this situation as the site is often windy and mountainous and sparsely populated [2]. However, in urban areas, small turbines may take their place alongside television antennae which are tolerated as mild visual pollution.

Social acceptance of these wind turbines would be influenced by its aesthetics and the potential for free energy.

2.2 Emissions and Pollution

The purpose of wind turbines is not to supply the base load but rather as a fuel saver. One of the benefits of the wind turbine is that it releases no pollutants into the atmosphere. According to the water usage and carbon dioxide emissions of Eskom for the year ending March 2009, installing a wind turbine would save 1,03 kg/kWh in terms of carbon dioxide emissions and 1,35 L/kWh for water usage [3].

3. OVERVIEW OF SUBSYSTEM 1
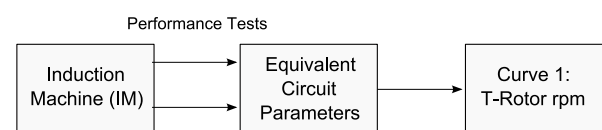
Figure 1: Block diagram indicating subsystem 1 of wind turbine generator system

The block diagram in Figure 1 represents subsystem 1 of the wind turbine generator system.

3.1 Induction Generator

A comprehensive understanding of the induction machine is required to design an induction generator. Essential to the operation of induction machine: three-phase stator currents are responsible for creating a stator rotating magnetic field in the air gap. According to Faraday's Law, a voltage is induced in the rotor that is proportional to the rate of flux linkage between the stator and rotor. The current establishes a magnetic field in the air gap which interacts with the stator rotating magnetic field. The interaction between the

Proceedings of the 19th Southern African Universities Power Engineering Conference
SAUPEC 2010, University of the Witwatersrand, Johannesburg

TOPIC D. RENEWABLE AND ALTERNATIVE ENERGY

stator and the rotor magnetic rotating fields give rise to torque in the rotor which allows the rotor to move. An interesting characteristic is that if the motor is run at a higher speed than its synchronous speed, the motor becomes a generator.

A number of generator technologies exist in wind power applications to produce electricity. The generator best suited for the proposed urban application is the induction generator. The preliminary design incorporated the use of a three-phase squirrel-cage induction machine to avoid maintenance issues when dealing with brushes and slip rings as in the wound rotor induction machine. Three-phase power offers some advantages over single-phase power. For instance, three-phase power allows more power to be generated from a smaller generator making it quite efficient for domestic use.

3.2 Reasons for Choice of Technology Chosen

The three-phase induction generator was found to be the most appropriate generator for urban use. The reasons in favour of the generator are as follows:

1) It is robust and needs little maintenance. In particular the squirrel cage induction motor has no brushes and has less wear and tear due to friction.
2) A three-phase induction motor produces more power per unit material than the single-phase induction motor variety.
3) In terms of manufacturability, an induction machine is simple to construct and with mass production is inexpensive [4].
4) The material cost for a permanent magnet machine with rare earth magnets is significantly more expensive than the material required for an induction machine.
5) The output AC voltage of an induction motor is regulated. The generator can be connected directly to the grid without power electronics.
6) An induction machine would not be a safety hazard under fault conditions. Induction machines will cease to operate in a few milliseconds if the windings failed. In contrast, a permanent magnet machine would continue to draw power until the machine has stopped [5].

The induction motor commissioned for modification has the specification shown in Table 1 below. The motor is a slip-ring motor with access to the rotor windings.

3.3 Induction Machine Equivalent Circuit Parameters

The equivalent circuit parameters required for computing the performance of the three-phase induction machine can be determined from the no load test and the locked rotor test. These tests were performed on the wound rotor induction machine provided.

Table 1: Motor Specifications

	Specification	Value
1.	3Φ Connection	Y
2.	Pole Number	4
4.	Frequency	50 Hz
5.	Horse Power	5
6.	Rated RPM	1400
7.	Rated voltage	380 V
8.	Rated Current	14.8 A
9.	Class	E

3.4 Development of Torque-Speed Profile

A simulation program using the software package Matlab, was developed to run through the specified set of circuit parameter values. The torque versus speed (T-Rotor RPM) characteristic curve was obtained for the motor at stock configuration (rotor resistance unaltered).

4. OVERVIEW OF SUBSYSTEM 2
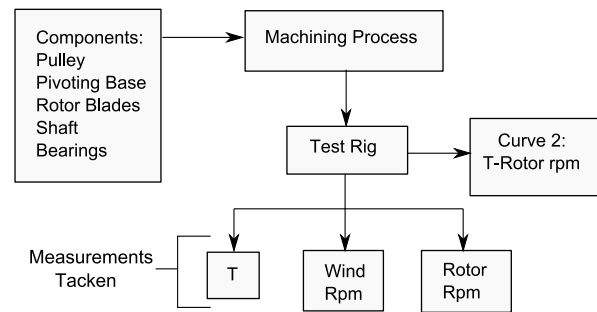
Figure 2: Block diagram indicating subsystem 2 of wind turbine generator system

4.1 Test Rig Design and Construction

Approximately 30 percent of the project was dedicated to designing and building the test rig represented in Figure 3. A drawing package, Solid Edge V19, was used to design the rig. Design considerations included:

1) Location: a suitable location, approximately 24 m high was found to mount the test rig with no trees or other obstructions near the site. The area also gave a good indication of the prevailing wind speed and direction.
2) Height of tower: the test rig was mounted on a tower which was extremely sturdy, well anchored and tall enough (approximately 5 m) to get above any obstructions.
3) Dimensions: the physical dimensions of all components making up the test rig can be obtained from [6]. Careful decisions on sizes and lengths of components were made to accommodate for the rotor blades and pulley.
4) Mass of test rig - the total mass of test rig was [6] obtained and a simple balancing exercise was applied to it to find the rig's balance point so that the pivoting base could be mounted on.

Proceedings of the 19th Southern African Universities Power Engineering Conference
TOPIC D. RENEWABLE AND ALTERNATIVE ENERGY
SAUPEC 2010, University of the Witwatersrand, Johannesburg
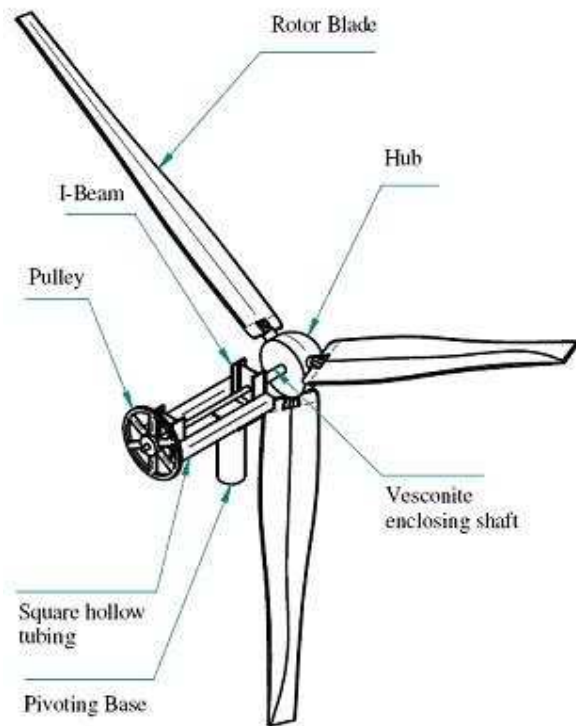
Figure 3: Physical arrangement of test rig

The framework, not including the rotor blades, was constructed from machined metallic material (steel, iron and aluminium). This material provided a sturdy structure to support the rotor blades. The square, hollow tubing composed of mild steel forms the base of the framework. The bearings were mounted on machined I-Beams, which served to hold the bearings in place thereby allowing the shaft to be aligned and fixed appropriately. The shaft is composed of bright mild steel. A machined piece of hollow steel cylinder tubing was mounted on the base of the structure and it formed a pivot thereby allowing the structure to rotate in and out of the direction of the wind. A disk of vesconite was mounted on the shaft between the I-Beam and the rotor blades to prevent friction. The machining process consisted of welding, drilling, sawing, cutting and soldering.

4.2 3WTR Rotor Blades

The rotor blades were donated by a manufacturer of wind turbine blades [7]. The type of rotor blades shown in Figure 3 form part of the horizontal axis wind turbine (HAWT) [8]. HAWT's are upwind, ensuring that the wind hits the blade before it hits the tower. The rotor blades primarily determine the amount of power obtained from the turbine [8]. There are some variables that determine how much energy the blade can capture. The main blade variables include:

1) Material - blades are usually made of a hard, stiff composite material [7].

2) Weight - lighter or less material is used in an effort to reduce the weight of the blades. Each blade weighs 1.2 kg each.
3) Number - most wind turbines today have three blades. This number proves to be most efficient and economical.
4) Length - the blades are 1.75 m in length.
5) Pitch - this variable is the angle at which the blades are oriented into the wind and dramatically effects torque and rotor speed ratio. Upon testing, it was found that by increasing the pitch, the blades slowed down, and had a higher starting torque.

4.3 Wind Turbine Pulley- Gear System

A pulley-gear system was used in series with the rotor blades. It serves as a mechanical advantage for the wind turbine; responsible for controlling the speed of the rotor blades as seen by the induction machine. A set up of two pulleys were utilized - a fixed pulley attached to the boundary to change the direction of the applied force and a movable pulley (see Figure 3) to multiply the applied force. The pulley-gear system is not very efficient because of the slip and friction generated in the string attached to the pulleys

4.4 Yawing

Passive yawing uses the force of the wind to push the turbine into place [8]. A wind vane was made and mounted onto the frame close to the pulley (Figure 3) end and used to orient the test rig into the wind.

4.5 Furling

When the wind became gusty, the blades had to be turned out of the direction of the wind to slow it down, a process called furling. This was achieved by attaching a rope to the wind vane and physically pulling on the rope to get it in or out of the direction of the wind.

4.6 Measurement System

Once the test rig was built and erected, a series of measurements for torque (T), rotor speed (Rotor RPM) and wind speed (Wind RPM) were taken (refer to Figure 2). These actual measurements were taken under non-steady state conditions, implying that wind speed is not constant. Special environments like a wind tunnel would have been an ideal option for testing, however due time and financial constraints, this could not be done. The data received upon measurement was manipulated to obtain a torque versus speed characteristic curve for rotor blades.
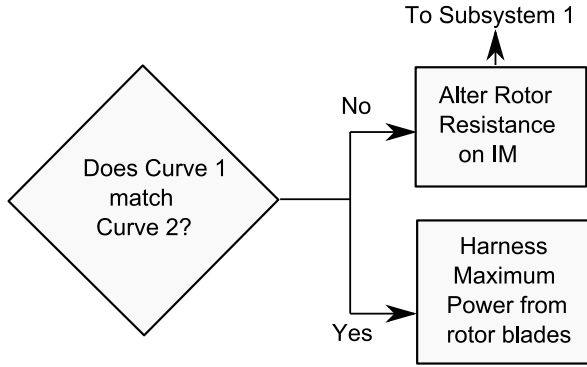
Figure 4:   Block diagram indicating subsystem 3 of wind turbine generator system

Table 2: Equivalent Circuit Parameters

Parameter	Stock Motor Value (Units)	Motor (modified) Value (Units)
Stator winding resistance (R_S)	1.098 Ω	1.098 Ω
Stator leakage reactance (X_S)	4.46 Ω	5.55 Ω
Rotor leakage reactance (X_R)	4.46 Ω	5.55 Ω
Rotor winding resistance(R_R)	2.87 Ω	3.53 Ω
Stator magnetizing reactance (X_m)	61.78 Ω	58.87 Ω
Starting Torque (T_S)	21.8 N.m	42.98 N.m
Starting Current (I_{Start})	23 A	18.29 A

5. RESULTS AND EVALUATION OF RESULTS

The torque-speed profiles obtained from subsystem's 1 and 2 respectively were compared and a process of altering rotor resistance had to be followed to get a decent overlap (matching) of the two profiles. Subsystem 3 in Figure 4 illustrates this. Results and evaluation of the results obtained for subsystem's 1 and 2 are documented.

5.1 Induction Machine Parameters

The equivalent circuit parameters obtained from the performance tests discussed in section 3.4 are presented in Table 2. Values were obtained for the stock (rotor resistance not altered) motor as well as the motor after rotor resistance was altered.

5.2 Rotor Blade Characteristic

Utilising the actual measurement data obtained from using the test rig, a mechanical power versus speed characteristic curve was developed for the rotor blade (see Figure 5). A maximum of approximately 500 W at a rotor speed of 500 RPM could be harnessed from the rotor blades under the non-steady state conditions (wind speed of approximately 9 m.s^{-1}). The rotor blades are however capable of harnessing 3.5 kW at a rotor speed of 1200 RPM and a wind speed of 18 m.s^{-1} [7]. Owing to the inaccuracies of measurements taken under the non-steady state conditions, the manufacturer's data was utilised for matching purposes.

Analysing the manufacturer's rotor blade mechanical power versus speed characteristic curve (see Figure 6), it can be noted that the optimal curve has a steady exponential growth. For ease of analysis a straight line approximation to the optimal curve was obtained. Since the straight line approximation to the steeper part of the curve, corresponding to the speed between 600 and 800 RPM gives better matching characteristics, it was decided to utilize this speed range.

Figure 5: Actual Wind Data

Figure 6:   Manufacturer's Power Versus Speed Graph At Different Wind Velocities

The corresponding torque versus speed characteristic curve was also obtained for the rotor blade by making use of the mechanical power developed at the mentioned speeds. The following equation was used:

$$T = \frac{P}{\omega_{syn}} = \frac{60P}{2\pi n_{syn}} \quad (1)$$

where:

T = mechanical torque [N.m]
P = mechanical power [W]
ω_{syn} = synchronous speed [rad.s-1]
n_{syn} = synchronous speed [rpm]

This is shown on the simulation program developed for creating the straight line approximation. A negative gradient is used for the straight line approximation for matching purposes.

Ideally the generating portion of the torque versus speed characteristic curve of the motor must overlap the torque versus speed characteristic curve of the rotor blade. This overlap ensures that maximum power is drawn from the rotor blades. On comparison of the two curves upon simulation, no overlap occurred as illustrated in Figure 7.
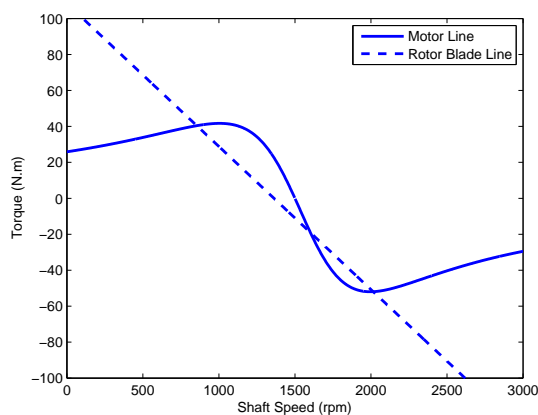
Figure 7: Comparison Of Stock Motor And Optimal Generation Line

When the Motor line is under the Rotor Blade line, it implies that the torque of the motor exceeds the torque of the rotor blades. The torque of the rotor blades must exceed the breaking torque of the motor to ensure that the rotor blades accelerate to an elevated power operation point. The empty area between the two curves is indicative of no power being harnessed. By altering the rotor resistance through an external resistor bank setup, the torque-speed characteristic curve can be altered. Rotor resistance has direct influence on the gradient of torque-speed profile at low slip.

Upon initial simulation, an external rotor resistance value of 4.5 Ω per phase added to the stock rotor resistance value allowed an overlap between the two curves to occur. Three variable resistors set at 4.5 Ω were connected to the rotor terminals through slip rings and brushes in a star connected configuration. When the performance test (locked rotor test) was repeated, results obtained from prediction and actual measurement did not correspond.

5.3 Investigation of errors

By adding resistance, the starting current decreases and the starting torque increases as is apparent in Table 2. Resistance decreases the torque available

at full running speed. A test was performed to see the effect of rotor resistance to starting torque and hence to see if this normal profile was followed. Actual torque measurements: direct on line (DOL) starting was used to start the motor every time a measurement for starting torque and speed was taken at each resistance starting from 0 Ω to 4.5 Ω. A tachogenerator was used in conjunction with a differentiator to obtain speed and torque measurements upon testing. The differentiator was calibrated to yield 1 V at 21.8 N.m (stock motor configuration). A graph of the starting torque with varying rotor resistance is illustrated in Figure 8. This characteristic curve indicates that too high a resistance affects the starting torque in a negative way. This implies that there is an optimum resistance for maximum starting torque and anything greater than this optimum value causes torque to decrease.
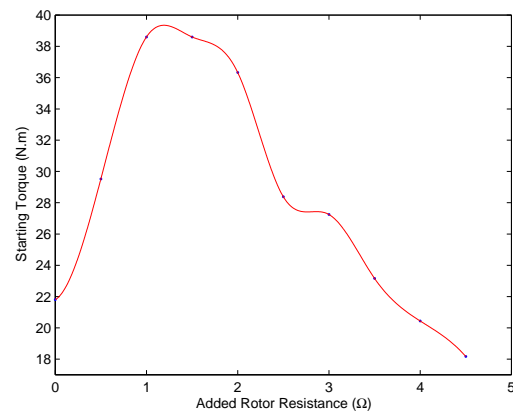
Figure 8: Starting Torque with Varying Rotor Resistance

Table 2 shows a measured rotor resistance of 3.53 Ω. Theoretically, when 0.5 Ω is added rotor resistance at stock configuration (2.87 Ω), 3.37 Ω is expected (predicted value). Thus a percentage error of 4.7 % is found. Upon simulation, a rotor resistance value of 3.53 Ω allowed an overlap between the two curves to occur (see Figure 9). A gear ratio of 1.9:1 proved (upon simulation) to be suitable to maintain this overlap. The graph of actual torque measurements with speed also follows the simulated curve almost exactly (see Figure 10).

It was noticed that the torque-speed profile did not change according to the normal torque-speed profile when resistance was altered. Yet upon actual torque-speed measurements done, the profile behaved as normal.

Conclusions drawn from actual testing and simulation:

1) There is a flaw in the simulation program to plot torque-speed profile, because upon simulation only rotor resistance was changed, other equivalent circuit parameters were kept the same. However, it was found upon actual testing that

all the equivalent circuit parameters change and this was not taken into account in the simulation. This affects the overall torque-speed profile.

2) The more resistance added, the greater the losses incurred, hence efficiency decreases.

3) The initial assumption to neglect core resistance in the induction machine equivalent circuit model could also be a possible reason for the inefficient simulation model.
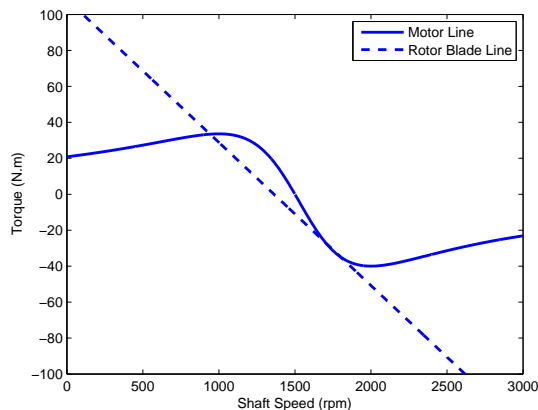
Figure 9:   Torque versus Rotor speed for 0.5 Ω added resistance to rotor
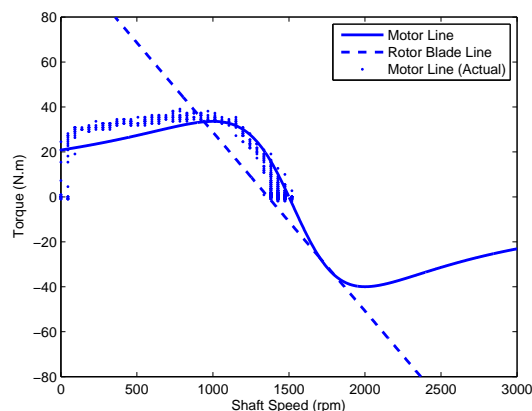
Figure 10:   Comparison between actual and simulated data for 0.5 Ω added resistance to rotor

6. EVALUATION OF SOLUTION

An induction machine is inherently a fixed-speed machine. A fundamental part of the machine operating as a generator is that the speed of the shaft must exceed the synchronous speed of the machine. In the design, this was achieved by using a fixed gear ratio of 1.9:1 whereby the shaft speed of the generator is increased relative to the shaft of the rotor blades. The drawback with using a fixed gear ratio is that the opportunity to harvest energy is limited to a small window. In this design the window is between 600 and 800 rpm.

Since the generator is connected directly to the grid, care must be taken that the generator is only energized once the the shaft speed exceeds the synchronous speed. The machine would be operating as a motor if the shaft speed were to fall below synchronous and power would be consumed as apposed to being generated.

7. FUTURE WORK AND RECOMMENDATIONS

To increase the window of opportunity for harvesting, an intelligent variable-speed gearbox may be installed to replace the fixed gears. The gearbox can measure the speed of the rotor blade and change gears accordingly to maintain a speed higher than the synchronous speed. Since the generator is intended for urban use, the cost and capability of the gearbox must be considered and matched to the target market.

Implementing a two-speed drive can improve energy capture. The most economical and efficient way of designing such a drive would be to use a single rotor cage with two stator windings of differing pole numbers. Two synchronous speeds would then be available and each stator may be energized individually according to the rotor speed whilst still using the fixed gear ratio.

8. CONCLUSION

Three subsystems were used to describe a design strategy that is applied to an on-grid wind driven system to facilitate drawing maximum power from the rotor blades. This strategy involved obtaining an overlap between the torque-speed profile for the induction generator and the torque-speed profile for the rotor blades. A decent overlap occurred when an external rotor resistance of 0.5 Ω was added. A percentage error of 4.7 % was found between predicted and measured values of rotor resistance. However, a flaw in the simulation program causes the torque-speed profile of induction generator to not follow the normal profile. Further investigation is required for this. The wind turbine generator system is capable of 3 kW peak power generation but can only do 500 W on average.

REFERENCES

[1] "Wind energy," last accessed 12 October 2009. [Online]. Available: http://windeis.anl.gov/guide/concern/index.cfm

[2] D. R. Inglis, *Wind Power and Other Energy Options*. John Wiley & Sons Canada, Limited, 1982.

[3] Eskom, "Annual report 2009," 2009, last Accessed: 13 October 2009. [Online]. Available: http://www.eskom.co.za/annreport09/

[4] G. L. Johnson, *Wind Energy Systems*. Prentice-Hall Inc, 1985.

[5] J. Vaidya and E. Gregory, "Advanced electric generator & control for high speed micro/mini turbine based power systems," 2002, last Accessed: 13 October 2009. [Online]. Available: http://www.electrodynamics.net/

[6] N. Pillay, *ELEN 4002, Engineering Notebook*. School of Electrical and Information Engineering, University of Witwatersrand, Johannesburg, 2009.

[7] Multi-Wing, "3wtr series datasheet," 2007, last Accessed: 15 October 2009. [Online]. Available: http://www.multi-wing.pl

[8] "Wind energy lessons," last accessed 12 October 2009. [Online]. Available: http://www.KidWindLessons/WindEnergy

MODELING AND SIMULATION OF A STAND-ALONE PV SYSTEM WITH BATTERY BACKUP

N W Vanden Eynde*, S Chowdhury* and S P Chowdhury*

*University of Cape Town, Electrical Engineering Department, Cape Town, South Africa

Abstract. This paper reports on the modeling and simulation of a stand-alone photovoltaic (PV) system with its own battery backup. The system consists of a polycrystalline PV module, a battery bank, MPPT module for maximum power point tracking, controller, inverter and a resistive load. The load is supplied by both the PV and the battery bank. The output power of the PV module is controlled and held at maximum power output by the MPPT module. The battery controller is used to control the charging and discharging of the battery and deciding in what schedule the PV and the battery will supply the load. The overall system model is an integration of individual PV, MPPT, batter, controller, inverter and load models. The proposed model is used to determine the voltage, current and power at the maximum power point and then investigate the quality of voltage available at load terminals for different operating scenarios. The system model is found to be accurate to reflect satisfactorily the system behaviour for different loads. Response of the stand-alone PV system to various changes in load demand as well as changes in solar irradiance and ambient temperature are presented along with the analysis of the simulated results.

Key Words. PV module, Battery bank, Stand-alone System, MPPT module, Inverter.

1. INTRODUCTION

The world wide drive to combat climate change, global warming and environmental pollution has led to the deployment of renewable energy resources for clean power generation. Recently, solar photovoltaic, wind turbines and hydrogen fuel cells have become popular as alternative sources of energy [1]. Solar photovoltaic (PV) have several advantages such as sunlight as highly sustainable source of fuel, no fuel costs, pollution-free energy, less maintenance requirements and quiet operation [1]. Due to rapid growth in renewable energy resources across the world, the development of stand-alone PV system becomes inevitable [2]. Implementing stand-alone PV plants as distributed generation (DG) systems have several advantages such as supplying power to remote load centres which do not have access to national utility grid networks. Their modular size and proximity to loads also helps to reduce the cost of transmission and distribution lines and line losses. However, as the power output from PV modules fluctuate mainly due to variation in solar irradiance and slightly due to variation in ambient temperature, it must be backed up by its own battery storage. Battery storage helps to obtain a steady power output from the system [3].

Existing research literature reports on several PV models with various levels of accuracy for different purpose [4][5][6][7][8][12][13]. Single diode model is a very popular way of modeling the cell as it offers a good compromise between accuracy and simplicity. An extra diode is added in the double exponential model [6] and it is used to represent the effect of recombination of carriers. A three-diode model is proposed in reference [7] to include the

influence of effects that are not considered by the previous models. An MPPT technique is implemented to maximize solar energy capture by the PV module. Various MPPT algorithms are analysed in references [8] and [9]. It has been reported in existing literature that the battery component is necessary in stand-alone PV system due to the fluctuating nature of the power delivered by the PV arrays. At night, or during a period of low sunlight (such as cloud cover or rain), load is supplied from the battery. Several battery models have been proposed by authors [10][11]. Some models are phenomenological and therefore do not depend on the internal structure of the system [10]. Battery model reported in [10] represents the sensitivity of storage capacity to the rate of discharge. No extensive measurements of voltage or current are required. A control strategy is implemented in some work in order to manage the load flow of the system. The controller scheme reported in [10] includes a protection scheme for excessive charge on the battery. The inverter is modeled as a simple DC-AC power converter and load is modeled as a purely resistive load. The system is simulated both in Matlab Simulink as well as in the form of Matlab m-files. The stand-alone system is designed as a steady power source which operates at maximum efficiency for various environmental factors and load requirements.

In this work, the authors report on the modeling and simulation of a stand-alone inverter-interfaced PV system, consisting of a polycrystalline PV module, maximum power point tracking (MPPT) module and a dedicated battery bank. The model is used for determining the voltage, current and maximum power at the maximum power point for different solar irradiance and ambient temperature values and then study the phase-to-phase voltage

Proceedings of the 19th Southern African Universities Power Engineering Conference
SAUPEC 2010, University of the Witwatersrand, Johannesburg

TOPIC D. RENEWABLE AND ALTERNATIVE ENERGY

waveform at load terminals for various operating scenarios. The proposed system operates as follows: During daytime and periods of bright sunshine, PV module supplies the load and charges the battery. At night and during low sunlight, load is supplied from the battery. The integrated operation of the PV module and the battery and the charging and discharging cycles of the battery is controlled by the proposed controller. For the PV module, maximum power point tracking is performed by the MPPT module.

For overall system modeling and simulation, the authors have reviewed the existing PV models and battery models and chosen them in such a way as to make a compromise between accuracy and simplicity. Since stand-alone PV systems are usually designed to supply domestic type of loads operating at almost unity power factor, the authors have assumed resistive load model for this work.

2. MODELING OF STAND-ALONE PV SYSTEM

2.1 Modeling the PV Module

The authors have selected double exponential model for the PV module owing to its high level of accuracy. Figure 1 shows the equivalent circuit of the double exponential model of a PV cell. The model takes into account the irradiance (E), ambient temperature (T), photocurrent (I_{ph}), both diode saturation currents (I_{s1} and I_{s2}), series resistance (R_s) and the parallel resistance (R_p), all of which have a large impact on the I-V curve as well as the accuracy of the model.
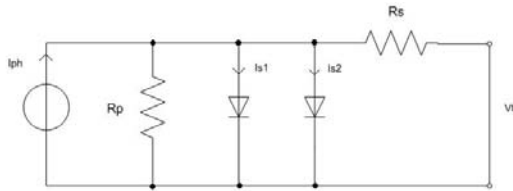
Fig.1: Double Exponential Model of PV Cell

The model is described by the following equation (1):

$$I = I_{ph} - I_{s1}\left(e^{\left[\frac{V+IR_s}{vt}\right]} - 1\right) - I_{s2}\left(e^{\left[\frac{V+IR_s}{Avt}\right]}\right) - \frac{V-IR_s}{R_p} \quad (1)$$

where,

$$vt = kT/e \quad (2)$$

Equation (1) describes the effects of the five electrical parameters I_{ph}, I_{s1}, I_{s2}, R_s, R_p and the terminal voltage V have on the terminal current I. The diode constant A is set to 2 in order to approximate the Shockley–Read-Hall

recombination in the space-charge layer. The five electrical parameter values are directly related to irradiance E (W/m^2) and temperature T (^{o}K) using the empirical relationships found in reference [6] for a polycrystalline cell. Reference [6] also derives and provides the values for the various K constants from cell characterisation of polycrystalline cells. In this paper, the authors assume the PV module to be of polycrystalline type and hence adopt the same K values (as given in Table 1) and the Equations (3)-(7) as reported in [6]. Equations (3)-(7) for calculating I_{ph}, I_{s1}, I_{s2}, R_s, and R_p are given below:

$$I_{ph} = K_0 E(1 + K_1 T) \quad (3)$$

$$I_{s1} = K_2 T^3 e^{\frac{K_3}{T}} \quad (4)$$

$$I_{s2} = K_4 T^{\frac{3}{2}} e^{\frac{k_5}{T}} \quad (5)$$

$$R_s = K_8 + \frac{K_9}{E} + K_{10} T \quad (6)$$

$$R_p = K_{11} e^{K_{12} T} \quad (7)$$

Table 1 : K Coefficient Values used in Modeling

Parameter	Coefficient Value	Coefficient Value
$I_{ph} = K_0 E(1 + K_1 T)$	K_0 = -5.729e-7	K_1 = -0.1098
$I_{s1} = K_2 T^3 e^{\frac{K_3}{T}}$	K_2 = 44.5355	K_3 = -1.2640e4
$I_{s2} = K_4 T^{\frac{3}{2}} e^{\frac{k_5}{T}}$	K_4 = 11.8003	K_5 = -7.3174e3
$A = K_6 + K_7 T$	K_6 = 2	$K_7 = 0$
$R_s = K_8 + \frac{K_9}{E} + K_{10} T$	K_8 = 1.47 K_{10} = -4.47e3	K_9 = 1.6126e3
$R_p = K_{11} e^{K_{12} T}$	K_{11} = 2.3034e6	K_{12} = -2.8122e-2

A PV module is basically a series-parallel combination of PV cells. Owing to very low power output of a single PV cell, several PV cells are connected in a series (N_s) and parallel (N_p) configuration to realize a PV module with a much higher power capacity. These multiplicative constants affect the voltage, current and power as displayed by the equations (8) – (10) where 'c' and 'm' denote a cell and module, respectively:

$$V_{OC,n} = V_{OC,c} * N_s \quad (8)$$

$$I_{SC,m} = I_{SC,c} * N_p \quad (9)$$

$$P_m = P_c * N_s * N_p \quad (10)$$

The module used in this paper use the following configuration parameters:

$N_s = 2000$ (11)

$N_p = 400$ (12)

2.2 Modeling the MPPT Module

The authors have modeled the Maximum Power Point Tracking (MPPT) module and integrated it to achieve the overall system model. Due to the nonlinear relationship between the current and the voltage of the PV cell, it is noted that there is a unique maximum power point (MPP) at a particular environmental condition (i.e. for a particular solar irradiance and particular ambient temperature). The MPPT module reads in the values of voltage and current produced by the PV module and then outputs the MPP values for the specific irradiance and temperature condition. The model is implemented by a search function for determining the maximum voltage, current and power for a given irradiance E and temperature T. The flow chart below outlines the steps that the MPPT component follows.
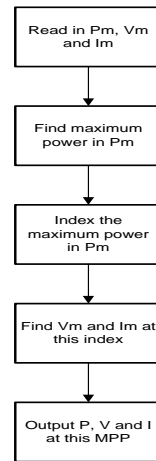
Fig.2: Flow Chart of the MPPT Module

The technique starts by reading in the voltage, current and power arrays produced by the PV module. The power array is then searched for the maximum power and this position in the array is then indexed. The voltages and currents are then searched for their respective values at this maximum power index. Once all of the indexed values have been determined they are output as the MPP values of the PV module.

2.3 Modeling the Battery

The authors first investigated the Kinetic Battery Model (KiBaM) for use in this system. However, though accurate, the model proved to be overly complex for this system. Hence to reduce computational burden of overall system model, the authors have modeled the battery as two independent R-C circuits, one for charging and the other for discharging.

Since the battery's primary use is to provide the load with power in periods of no irradiance, such as that of night time, the battery only needs to be able to provide the load for a few hours. Hence, the battery is assumed to be a 48Ah battery which can provide 6A for 8 hours. The secondary task of the battery is to absorb excess power from the PV module when the load is smaller than the output power of the PV module. These two states are known as discharging and charging, respectively. A circuit is designed for each state. The discharging model is composed of a DC voltage source which outputs 330V DC and a resistor representing the internal resistance R_0. R_0 in this case is assumed to be 0.0026 ohm. The power equation during discharge is given by the following equation (13) below.

$$P_{batt} = I_{batt} V_{batt}$$ (13)

where, P_{batt} is the power output and I_{batt} the current output from the battery. V_{batt} is the DC voltage available at the battery terminals connected to the load. V_{batt} is calculated from the following equation (14) below

$$V_{batt} = E - I_{batt} R_0$$ (14)

where, E is the open circuit e.m.f. of the battery and R_0 is the internal resistance.

The charging state circuit of the battery is very similar to the discharging state circuit albeit two differences:

(i) The DC-voltage source is set by the controller which determines the excess voltage to the battery.

(ii) An R-C circuit simulates the non linear charging property of the battery in place of R_0. The time constant for the charging effect of the battery is chosen to be 0.05 seconds. The battery modelling resistor is set at 10 ohm and the capacitor at 5mF.

2.4 Modelling the Controller
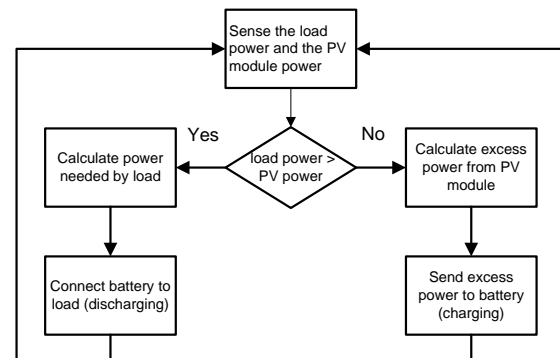
Fig.3: Flow Chart for the Controller

The controller is designed to manage the power flow from the PV module and the battery to the inverter and the load. When the load draws less power than that produced by the PV module, the excess power is utilised for charging the battery. The controller also connects the battery to the load

when the power generated by the PV module is less than the load power demand. The flow chart of Figure 3 shows the functioning of the controller.

2.5 Modelling Inverter and Load
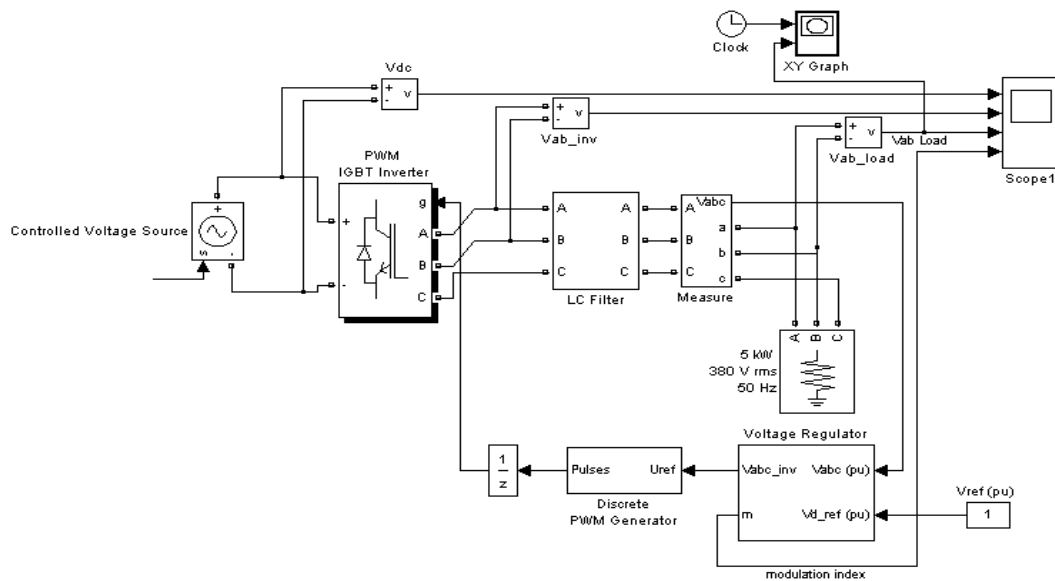
Fig.4: Simulation of the Inverter and the Load
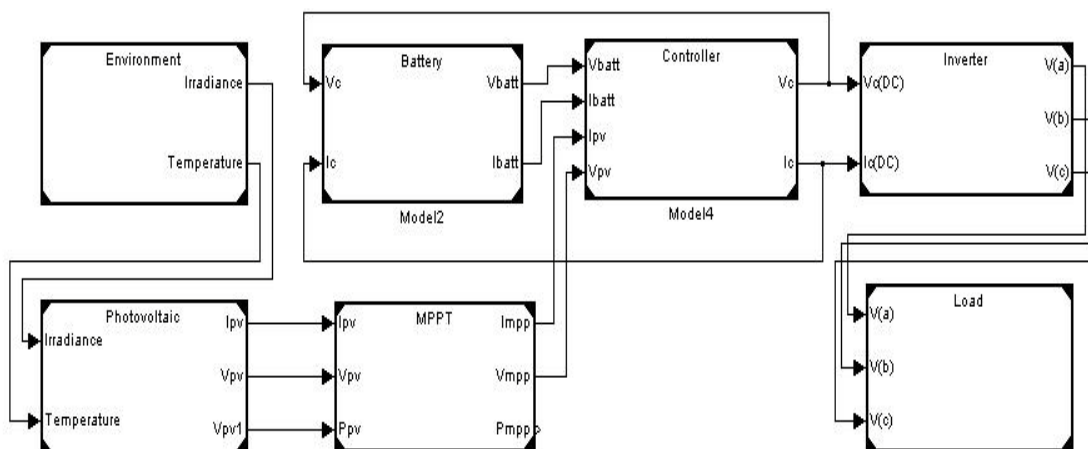
Fig.5: PV System Structure in Simulink

The overall PV system with battery includes an inverter circuit to converts the DC output to three-phase, 50Hz AC power. The inverter output is connected to the purely resistive three-phase load. A PWM IGBT inverter is used together with a voltage regulator. The direct AC outputs of the inverter are fed into an L-C filter, with the inductor set at 2mH and a three phase parallel capacitor branch set at 3kvar. In order to keep the voltage at

load terminals at 1 p.u., a PI regulator is included. The inverter chopping frequency is set to 2000Hz. For load following study, the load active power in Watts in manually set by the user.

2.6 Modelling the Overall PV System

The overall PV system is simulated in Matlab. Individual models for PV module, MPPT module, battery bank, controller, inverter and load. Fig.5 shows how the various component models are interconnected in order to form the complete system.

By connecting the model blocks together it is easy to see that the total system has only two input variables, temperature and irradiance, which are situated in the environment model block. These variables determine the output current, voltage and power of the PV module. The outputs of the PV module are then fed into the maximum power point tracking model block where the MPP values of the PV module are calculated. From here the MPP values are fed into the controller model block. The battery voltage and current output are also fed into the controller block. The controller block has another input in the form of the load and it the controller then determines how much of the voltage from the PV module must go to either the battery or the load. It also determines when the battery should supply the load. The output of the controller is connected to the DC/AC inverter. Here the power is converted from DC to AC and then delivered to the load where load studies can be performed.

3.   CASE STUDIES

The model is tested for its performance for different values of solar irradiance and temperature. Firstly, maximum power point voltage, current and maximum power is calculated for varying solar irradiances and temperature and variation of the maximum power point is noted. Secondly, phase-to-phase r.m.s. voltage waveform at load terminals, i.e. at the inverter output is investigated for different operating scenarios. For Case-2, solar irradiance is taken to be $1000 W/m^2$ and temperature to be $298^0 K$ at standard test conditions (STC). As calculated from the model, maximum power provided by the PV at this irradiance and temperature is 4.125kW and maximum power provided by battery is 1.98kW.

3.1   Generating I-V and P-V curve for varying solar irradiance and constant temperature

Table 2 demonstrates the values of V_{OC}, I_{SC}, V_{MPP}, I_{MPP} and P_{MPP} for a temperature of $298^0 K$ and irradiance of E = 200, 400, 600, 800 and 1000 W/m^2 obtained from the model simulation.

Table 2 : Values obtained for varying irradiance and constant temperature

Irradiance (W/m^2)	Open Circuit Voltage (V)	Maximum Power Point			Short Circuit Current (A)
		Voltage (V)	Current (A)	Power (W)	
1000	878	662.5	6.226	4125	7.243
800	864	650.2	4.899	3185	5.789
600	843	631.2	3.597	2270	4.335
400	815	598.6	2.324	1391	2.882
200	752	540.4	1.062	574	1.431

3.2 Generating I-V and P-V curve characteristics for varying temperature and constant irradiance

The values obtained from the simulated model for a constant irradiance of $1000 W/m^2$ and temperatures T = 278, 288, 298, 308, 318 $^0 K$ are represented in Table 3. The values include V_{OC}, I_{SC}, V_{MPP}, I_{MPP} and P_{MPP}.

Table 3 : Values obtained for varying temperature and constant irradiance

Temperature (°K)	Open Circuit Voltage (V)	Maximum Power Point			Short Circuit Current (A)
		Voltage (V)	Current (A)	Power (W)	
278	976	767.1	5.965	4576	6.751
288	927	710.9	6.135	4361	6.998
298	878	662.5	6.266	4125	7.243
308	829	614.3	6.295	3867	7.485
318	780	566.3	6.340	3591	7.724

3.3   Study of Voltage Waveform at Load Terminals for Various Operating Scenarios

3.3.1 Scenario 1

In this scenario load power drawn is just less than the power provided by the PV module. Only the PV module is connected to the load and it operates at maximum power under the standard irradiance and temperature conditions. In this scenario, load power drawn is 4.1kW, voltage to inverter input is 662.5V DC and power provided by system: 4.125kW. The phase-to-phase load voltage waveform for Scenario 1 is shown in Figure 6.
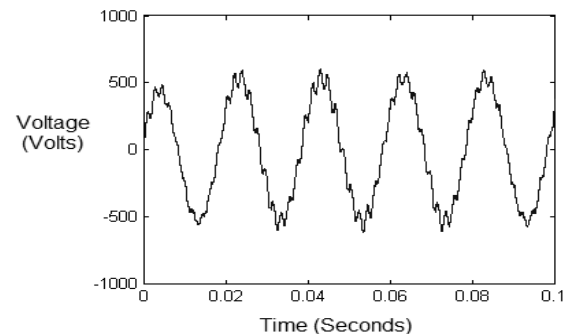
Fig.6: Phase-to-phase load voltage waveform for Scenario 1

3.3.2 Scenario 2

In this scenario, load power required is just less than the maximum battery output power. To simulate night time operation, only the battery is connected to the load with irradiance set at 0 W/m^2. Figure 7 shows the phase-to-phase load voltage. Here, load power drawn is 1.95kW, voltage to inverter input is 330V DC and power provided by system is 1.98kW. The phase-to-phase load voltage waveform for Scenario 2 is shown in Figure 7.
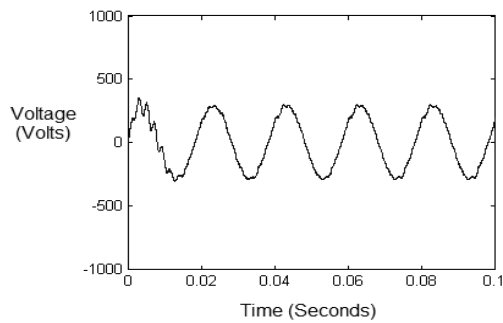
Fig.7: Phase-to-phase load voltage waveform for Scenario 2

3.3.3 Scenario 3

In scenario 3, the PV module supplies half its maximum power with the load requirement just under this value. The remaining power produced is fed to the battery for charging.   Only the PV module is connected. Here, load power drawn is 2.05kW, voltage to inverter input is 290.7V DC and power provided by system: 2.07kW. The phase-to-phase load voltage waveform for Scenario 3 is shown in Figure 8.
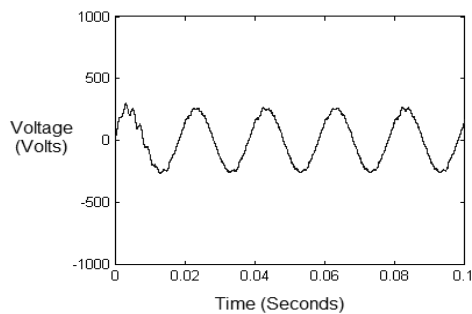
Fig.8: Phase-to-phase load voltage waveform for Scenario 3

3.3.4 Scenario 4

In this scenario both the battery and the PV module are delivering their maximum power outputs of 4.125kW and 1.98kW respectively to the load. The load is rated at just under this value. Both the PV module and the battery are connected to the load. Here load power drawn is 6.1 kW, voltage to inverter input: 992.5V DC and power provided by system is 6.105kW
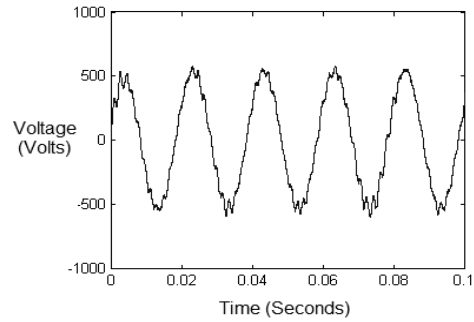
Fig.9: Phase-to-phase load voltage waveform for Scenario 4

The phase-to-phase load voltage waveform for Scenario 4 is shown in Figure 9.

The results of the four scenarios have been summarized and presented in Table 4 below. Both the DC and AC voltages are provided as well as the modulation indexes and the load power drawn.

Table 4 : Summary of Results of the Scenarios

Scenario	DC Voltage Input to Inverter (V)	Phase-phase Volt at Load (V)	Modulation Index		Load Power (W)
			Mean	Std. Dev.	
1	662.5	600	0.925	0.05	4100
2	330.0	300	1.000	0.00	1950
3	290.7	260	1.000	0.00	2050
4	992.5	580	0.630	0.05	6100

4. CONCLUSION

The results indicate that the overall model of the stand-alone PV system performs well to reflect the system behaviour for different operating scenarios. This model does not require storage of the PV module characteristics as data points but calculates the maximum power generated by the PV module and battery power required from solar irradiance, temperature and load values. The double exponential model proves to be the most accurate and efficient PV cell model over the various reviewed cell models. The developed PV model reflects properly the I-V and P-V characteristics of a photovoltaic module. It is able to take into account variances in the environmental variable such as temperature and irradiance. This is found to be useful as datasheets only predict expected performance under standard test conditions (STC). The MPPT model that is developed performs a search for the MPP and output the values of power, voltage and current at this point. It is found to be a much simpler and faster alternative to the initial perturb-and-observe technique. The battery model simulates the effects of charging and discharging sufficiently. However, detailed modelling of the battery for stand-alone PV system will be

undertaken as future work. The battery model will be able to monitor the available and bound charge levels of the battery and thus the battery behaviour will be more accurately represented than that by R-C battery model. The simplified battery model however is sufficient for simulating with moderate accuracy the voltages and powers produced by this stand-alone PV system. More accurate load modelling with different load power factors will also be undertaken as future work. However, resistive load model here satisfactorily represents domestic loads as assumed in this paper.

REFERENCES

[1] J. Li, H. Wang, "A Novel Stand-alone PV Generation System Based on Variable Step Size INC MPPT and SVPWM Control," *IEEE,* 2009.

[2] A.Jager-Waldau, "Photovoltaics and Renewable Energies in Europe," *European Commission, Renewable Energy Unit,* 2005.

[3] S.Chowdhuy, S.P.Chowdhury and P.Crossley, *Microgrids and Active Distribution Networks*, IET Renewable Energy Series 6, The IET (UK), 2009.

[4] M.G. Villalva, J.R. Gazoli, E.R. Filho, "Comprehensive Approach to Modelling and Simulation of Photovoltaic Arrays," *IEEE Transactions on Power Electronics,* Vol. 24, No. 5, 2009.

[5] Y.T. Tan, D.S. Kirschen, N. Jenkins, "A Model of PV Generation Suitable for Stability Analysis," *IEEE Transactions on Energy Conversion,* Vol. 19, No. 4, 2004.

[6] J.A. Gow and C.D. Manning, "Development of a Model for Photovoltaic Arrays Suitable for Use in Simulation Studies of Solar Energy Conversion Systems," *Power Electronics and Variable Speed Drives, Conference Publication,* No. 429, 1996.

[7] K. Nishioka, N. Sakitani, Y. Uraoka, and T. Fuyuki, "Analysis of multicrystalline silicon solar cells by modified 3-diod equivalent circuit model taking leakage current through periphery into consideration," *Solar Energy Matter. Solar Cells,* Vol. 91, No. 13, pp. 1222-1227, 2007.

[8] J.M Enrique, E. Duran, M. Sidrach-de-Cardona, J.M. Andujar, "Theoretical Assessment of Maximum Power Point Tracking Efficiency of Photovoltaic Facilities with Different Converter Topologies", *Solar Energy,* vol. 81, pp. 31-38, 2007.

[9] D.P. Hohm, M.E Ropp, "Comparative Study of Maximum Power Point Tracking Algorithms Using an Experimental, Programmable, Maximum Power Point Tracking Test Bed", *Proc. of Photovoltaic Specialist Conference, 2000, Conference Record of the Twenty-Eighth IEEE,* pp. 1699-1702, 2000.

[10] A.D. Hansen, P. Sorenson, L.H. Hansen and H. Bindner, "Models For a Stand-alone PV System," *Riso-R-1219(EN),* 2001.

[11] J.F Manwell, J.G McGowan, "Extension of the Kinetic Battery Model for Wind/Hybrid Power Systems," *In Proceedings of EWEC,* pp. 284-289, 1994.

[12] S. Chowdhury, S.P. Chowdhury, G.A. Taylor, Y.H. Song, "Mathematical Modelling and Performance Evaluation of a Stand-alone Polycrystalline PV Plant with MPPT Facility," *Proc. of IEEE PES General Meeting 2008,* Pittsburgh, USA, July 2008.

[13] M.G Villalva, J.R Gazoli, E.R Filho, "Comprehensive Approach to Modelling and Simulation of Photovoltaic Arrays," *IEEE Transactions on Power Electronics,* Vol. 24, No. 5, 2009.

ECONOMIC AND EFFICIENCY EVALUATION OF DIFFERENT BATTERY CHARGING WIND GENERATOR SYSTEMS

JA Stegmann and MJ Kamper

Department of Electrical and Electronic Engineering, Stellenbosch University, Stellenbosch, South Africa.

Abstract.   In this paper three different small wind generator systems for low voltage battery charging stand-alone inverter supplies are evaluated and compared in terms of energy production and cost. One of the systems proposed in the paper consists of a fixed speed wind generator system that is connected directly to the stand-alone inverter supply. The comparative study is based on two wind sites with different wind speed distributions. The generator considered in all three systems is an air-cored permanent magnet direct drive generator. It is found, amongst other things, that the energy production per cost of the proposed fixed speed wind generated system is substantially better than the variable speed maximum power point generator system.

Key Words.   Wind generator, battery charging; efficiency, cost.

1.   INTRODUCTION

Many designers of small wind turbines (typically sub 50 kW) emphasize the simplistic design of the wind generators so as to allow for little or no maintenance. These generators are usually direct-drive permanent magnet (PM) synchronous machines which are directed windward by a simple tale vain yaw system. Small wind turbines are used amongst others in water pumping, electrification of fencing and small weather station power. The dominant share of the market for small wind turbines, however, lies in off-grid residential properties [1]. These homes are usually powered by hybrid systems incorporating wind, solar and in some cases diesel generators.

In developing countries, especially, many non-grid connected rural areas are in need of reliable and low cost electrical power. To solve this problem numerous wind power systems have been developed and implemented over the years to supply farms and rural settlements with high quality electrical power. For these applications, direct-connected battery charging systems are used the most. The wind generators are used to charge the battery banks, whilst the battery banks allow for an uninterrupted inverter-fed power supply without requiring continuous turbine operation. Typically, these stand-alone systems are used where a grid connection would be too expensive. Many of these systems have shown that the energy capture of the wind turbine fall short of expectations based on only the generator rating and rotor size [1], [4], [7].

In this study three different battery charging wind turbine systems are investigated and compared in terms of efficiency and energy-production per cost. The paper explains the method whereby the total yearly energy capture for each of the systems is calculated. The paper illustrates how the system components affect the total energy supply to the electrical load. An explanation of the estimated costs and the energy production per cost of each of the three systems are given.

2.   WIND TURBINE POWER

Electricity production obtained from a wind source at a given wind speed and with a particular wind turbine, varies a lot depending on the site's wind speed distribution. For example, a wind turbine would produce much more power at a site where the wind speed is 12 m/s for 50 % of the time and 0 m/s for the other 50% of the time than on a site where the wind speed is 6 m/s for 100 % of the time. This is due to the fact that the power available in the wind is proportional to the cube of the wind speed [5]. Even though the annual average wind at two different sites may be equal, the site with the higher wind speeds will still have a higher average kinetic wind energy.

For most areas the wind speed distribution can be approximated by a Weibull plot as shown in Fig. 1. The Weibull curve can be calculated by

$$ p(v) = \frac{k}{c}\left(\frac{v}{c}\right)^{k-1} e^{-\left(\frac{v}{c}\right)^{k}} , \qquad (1) $$

where $p(v)$ is the probability density function of the wind speed v, k is the shape parameter and c is the scale parameter. By changing these two variables, the wind plot can be altered to represent almost any site. In Fig. 1, site 1 (Weibull distribution 1) has a better annual power production capability than site 2. Depending on the wind speed, v, at a particular site, the turbine power production can be calculated by considering the turbine blade power curves. In this study 1.9 m turbine blades are used. This equates to a swept area of 11.3 m^2. The blade's power curves are represented in Fig 2. The power curves are obtained by calculating the mechanical power of the turbine rotor by [5]
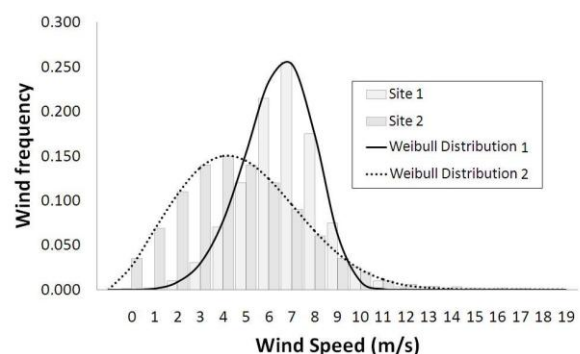
Fig. 1: Weibull wind distribution at two different sites.

TOPIC D. RENEWABLE AND ALTERNATIVE ENERGY

Proceedings of the 19th Southern African Universities Power Engineering Conference
SAUPEC 2010, University of the Witwatersrand, Johannesburg

$$P_m = \frac{1}{2}\rho\pi C_p R^2 v^3, \qquad (2)$$

where ρ is the density of air, C_p is the power coefficient [C_p has a theoretical maximum value of 0.593 known as the Betz limit] and R is the rotor blade radius. The power coefficient is the ratio of the available power of the turbine rotor to the power available in the wind, and is affected largely by the blade profile design. C_p is usually given as a function of the tip speed ratio [5]

$$\lambda = \frac{\omega R}{v}, \qquad (3)$$

where ω is the angular speed of the turbine. A typical power coefficient versus tip-speed-ratio for a fixed pitch turbine is shown in Fig. 3. Hence, rewriting (3) and substituting into (2) results into

$$P_m = \frac{1}{2}\rho A C_p \left(\frac{R}{\lambda}\right)^3 \omega^3. \qquad (4)$$

Thus, for a given wind speed and blade radius the available rotor power can be plotted versus the turbine speed. The peak power at each wind speed can be realized if the turbine's optimal tip speed ratio, λ_{opt}, is maintained. This implies a maximum power coefficient, C_{pm}, as shown in Fig. 3. This results in [9]

$$P_m = \frac{1}{2}\rho A C_{pm} \left(\frac{R}{\lambda_{opt}}\right)^3 \omega^3. \qquad (5)$$

The optimum tip-speed-ratio can be guaranteed by using an electronic active rectifier to control the generator at the optimum turbine-load speed [10].
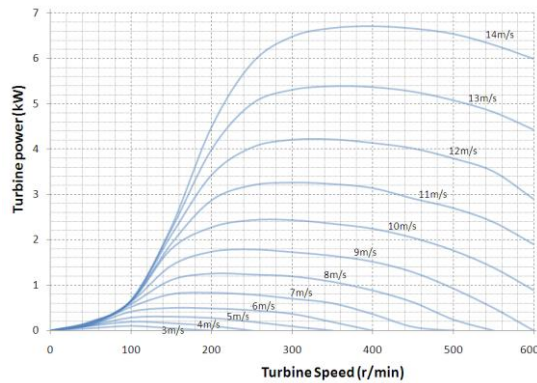
Fig. 2: 1.9 m wind turbine blade power curves.
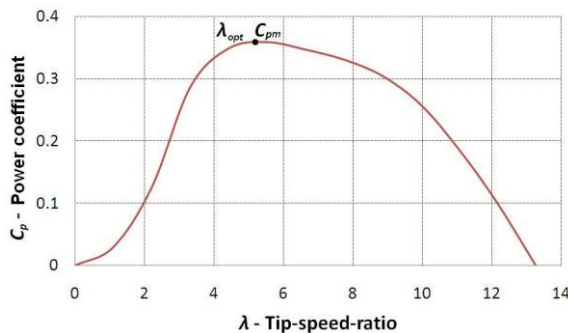
Fig. 3: Power coefficient versus tip-speed-ratio.

3. WIND GENERATOR SYSTEMS

In this section the three wind generator systems are described. Each of the systems utilizes the same type of generator namely an air-cored permanent magnet (PM) direct drive generator. Research has shown that this type of generator is a good alternative to iron cored generators, particularly in small rural wind energy systems [2]. The air-cored PM generator has numerous advantages such as no core losses, zero cogging torque and no attraction forces between the rotor and stator.

Each of the systems also employs the same turbine blades and, thus, has the same energy capture potential. Further aspects to be noted, similar to all three systems, is the presence of a battery charge controller. The charge controller ensures save operating conditions for the batteries by dumping surplus power in resistors when the batteries are near a state of full charge [4]. This component is usually inactive most of the time and for the purpose of this study is omitted.

3.1 Passive controlled system

The first system to be addressed is known as a passively controlled system. A simplified illustration of the passive controlled system is depicted in Fig 4. It is the most widely used system because of its simplicity. Such a system is used by [6] and [7] to provide power to a 230 V grid connection. A 32 – 46 V battery bank coupled to the grid or stand-alone load via an inverter and transformer is common practice.

The system in Fig. 4 comprises of an air-cored PM generator with a generated back-EMF voltage E_g, a cable with an impedance Z_c, an external inductance with a reactance X_e, and a diode rectifier that is directly connected to a battery bank. From the battery bank the inverter and transformer converts the power to a fixed frequency, fixed voltage, three-phase stand-alone power supply, to be connected to the loads.

In this system maximum power point tracking cannot be realized due to the passive diode rectifier control. The external inductance is used to ensure sinusoidal phase currents to reduce generator noise and to obtain better power matching with the turbine at all wind speeds [2]. The external inductance, however, causes the generator to be oversized in its design, which increases the cost of the generator in this system [2].
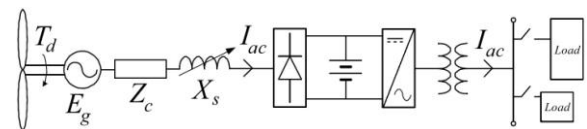
Fig. 4: Passively controlled system.
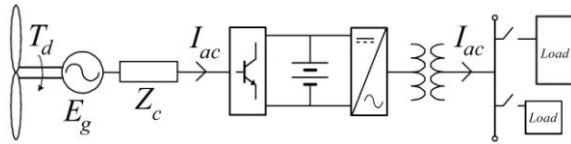
Fig. 5: Active controlled system.
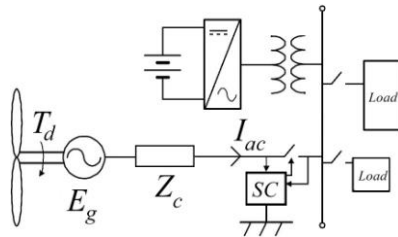
Fig. 6: Fixed speed system.

3.2 Active controlled system

A simplified illustration of the active controlled wind generator system using an active synchronous rectifier is depicted in Fig. 5. This system comprises of the same components as the passively controlled system, with the exception of the external inductance and the diode rectifier. The external inductance is no longer needed and the diode rectifier is replaced with a current controlled active rectifier.

In contrast with the passive system, the active controlled system utilizes turbine speed control by adjusting the load on the wind turbine and generator [1]. The load on the generator is adjusted by controlling the current of the generator by means of the active rectifier. By loading the generator in an optimum way, maximum power transfer from the turbine to the battery bank is obtained.

This system is considerably more expensive due to the active rectifier. However, this system produces maximum power at each wind speed, a feat that makes it an attractive option. The generator also does not have to be oversized in its design as in the case of the passive system; the reason is that the generator is controlled at maximum power conversion efficiency by means of the active rectifier.

3.3 Fixed speed system

A simplified illustration of the fixed speed wind generator system is depicted in Fig. 6. As is shown the generator in this case is connected directly to the fixed voltage and fixed frequency battery powered stand-alone grid inverter supply. The turbine and generator, thus, operates at a fixed speed at all wind speeds. The synchronization controller (SC) in Fig. 6 synchronizes the generator with the stand-alone grid inverter-fed supply and keeps the generator synchronized with the supply. In the cases of gust winds or no wind conditions the SC will disconnect the generator from the mini-grid supply.

Unlike the previous two wind generator systems, the generator in this case is a high voltage generator. It is, therefore, connected to the mini-grid inverter-fed supply by means of a much thinner high voltage cable; this results in considerably lower I^2R cable losses. A further advantage of the high voltage transmission cable is that it allows for a much longer distance between the wind turbine and the mini-grid supply.

The inverter in the fixed speed system is used to charge the batteries in the case of a surplus amount of power supplied form the turbine to the mini-grid. When the wind generator stops producing power, the battery bank will act to produce power to the stand-alone grid via the inverter and transformer. The inverter-transformer combination will insure a steady grid voltage and frequency.

It should be noted however, that this system's inverter needs to be rated according to two different conditions. Firstly, it has to be rated according to the maximum electric load condition of the fully utilized grid. Secondly, it has to be able to handle the highest amount of generated power from the wind turbine when a strong wind is blowing and all the loads are switched off. This latter condition can be overcome if a simple controller switches on a load, e.g. a water heating geyser, to dump the additional power when a surplus is generated.

The optimum speed of the fixed speed wind generator system is determined by obtaining the speed at which the turbine produces the highest annual energy. The method of calculating the annual energy produced by the turbine is described in the next section. The operating speed at which the highest energy is produced for site 1 in Fig. 1 and the turbine power curves of Fig. 2 is found to be at 310 r/min.

4. SYSTEM PERFORMANCE AND COST

4.1 Annual energy production

The annual energy production can be calculated from the site's annual wind speed distribution and the turbine's performance at these wind speeds. In Fig. 7, the turbine power of each of the three wind generator systems are plotted at each wind speed, for wind speeds of 3 – 14 m/s. The optimum power points of the actively controlled system are calculated by (5), while the fixed speed system's power points are calculated by (4). The power points of the passive controlled system are calculated from the known system parameters of Fig. 4 and using (3) and (4) in an iterative way.
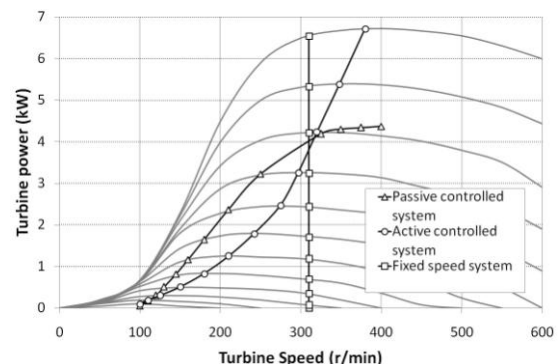
Fig. 7: Generated wind power curves for three systems.

Proceedings of the 19th Southern African Universities Power Engineering Conference
TOPIC D. RENEWABLE AND ALTERNATIVE ENERGY
SAUPEC 2010, University of the Witwatersrand, Johannesburg
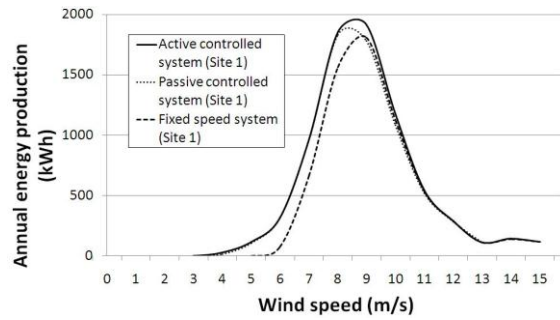
Fig. 8: Annual system energy versus wind speed of site 1.
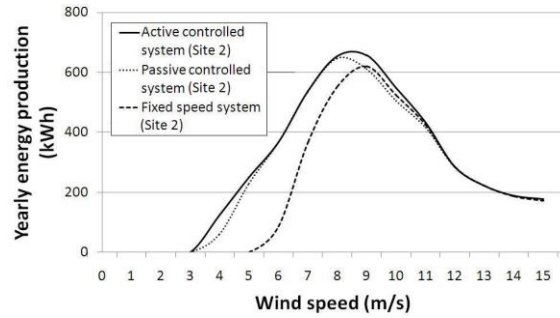
Fig. 9: Annual system energy versus wind speed of site 2.
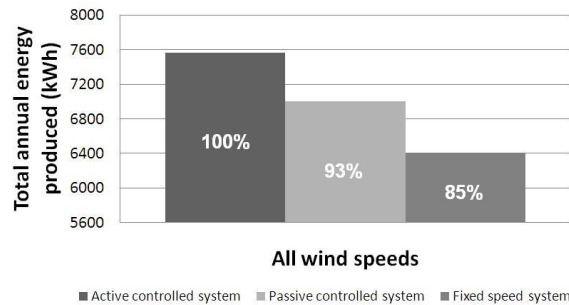
Fig. 10: Total annual system energy captured at site 1.
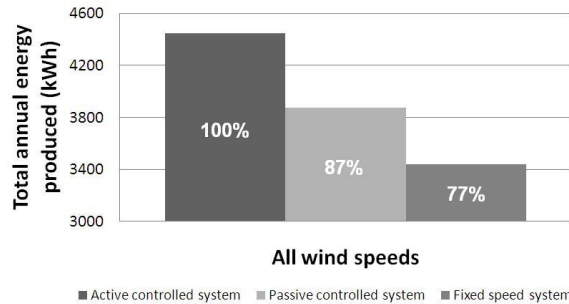
Fig. 11: Total annual system energy captured at site 2.

To obtain the annual system energy produced versus wind speed, the three power plots in Fig. 7 are multiplied by the annual wind speed distributions of Fig. 1. The results for site 1 and site 2 are shown in Figs. 8 and 9 respectively. These two figures show how site 1 produces more energy than site 2 because of its higher wind speeds. It is clear that the fixed speed system performs considerably better at higher wind speeds. All three systems show to have similar energy plots for wind speeds of 9 m/s and above.

The total annual energy per site is calculated by integrating the curves of Fig. 8 and Fig. 9. The total annual energy, in kWh, produced at site 1 is shown in Fig. 10. As expected, the actively controlled turbine performs the best of the three systems as it converts maximum power at each wind speed. The passively controlled system performs second best at 93 % of

the actively controlled system. Lastly, the fixed speed system produces 85 % of the maximum possible energy. Fig. 11 shows the total annual energy produced of each of the three systems at site 2. In this case the fixed speed system produces only 77 % of the maximum possible energy.

A good way to quantify the delivered energy per annum is known as the capacity factor. It is defined as the ratio of actual average power to the rated power of the wind generator system, measured over a year period [3]. The capacity factor, thus, is given by

$$C_f = \frac{P_a}{P_r}, \qquad (6)$$

where P_a is the annual average power [calculated from Fig. 10 and Fig. 11] and P_r is the rated generator power of 4.2 kW from Fig. 7. Table 1 lists the capacity factor of the three systems at the two wind sites.

Table 1: Turbine capacity factor C_f.

Site	Turbine capacity factor		
	Passive	Active	Fixed
Site 1	19%	20.6%	17.4%
Site 2	10.5%	12.1%	9.4%

4.2 System efficiency

The conversion efficiency of a system, from the kinetic energy in the wind to the useful electrical power delivered to the load, is the product of all the individual component efficiencies present in the system [5]. Various power losses occurring throughout the system decreases its power conversion efficiency. Fig. 12 shows a power flow diagram of a wind generator system together with its losses. P_w is the power available in the wind. P_m is the extracted power from the turbine that is supplied to the sub-system. P_o is the useful power delivered to the stand-alone mini-grid.

The efficiencies of the components of the sub-system used in the calculations are estimated averaged values of common of the shelf available components. Table 2 gives the estimated efficiencies of each of the components as well as the overall efficiency of the systems for the two wind sites considered. Note that the efficiencies should be taken ideally at the annual average power level, P_a, of (6).

Table 2 shows some interesting differences between the passive, active and fixed speed wind generator systems. Firstly, the transmission cable needed for a high voltage system is much more effective than a low voltage high current cable. Secondly, since the components of the passive and active wind generator systems are connected in series, all the efficiencies are multiplied to give the overall system efficiency.
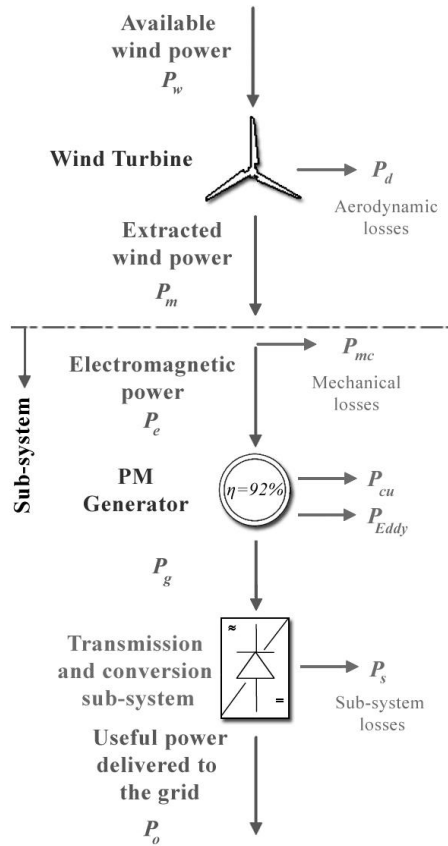
Fig. 12: System component losses.
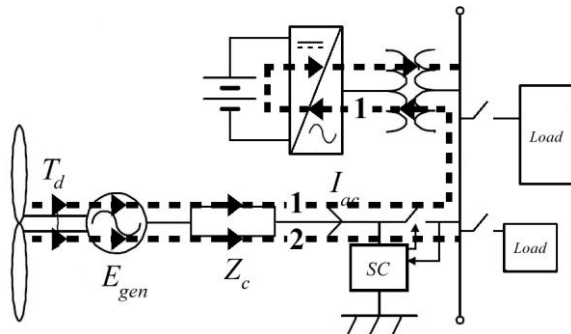
Fig. 13: Power paths in the fixed speed system.

The fixed speed system, on the other hand, has two parallel power flow paths as shown in Fig. 13. This implies that two scenarios must be considered. The first scenario (path 1 in Fig. 13) is where the turbine produces power to the batteries with all the loads switched off, followed then by a time-period where the batteries supply power to the load with no power from the wind turbine. This scenario is the worst in terms of efficiency as it takes seven conversions (including the battery) before the power reaches the load.

The second scenario (path 2 in Fig. 13) is where the turbine produces all its power to the stand-alone grid load. In this case the generated wind power is directly supplied to the load, consequently at a high efficiency as only two conversions take place. To simplify the efficiency calculation of the fixed speed system, the average efficiency of the two power flow paths is taken as the overall efficiency of this system, as given in Table 2.

From the overall efficiency results in Table 2 it is clear that the efficiency of the fixed speed wind generator system is the same or higher than that of the passive controlled system. If the sub-system efficiency is taken into account in the calculation of the capacity factor of (6), called the sub-system capacity factor, C_{fs}, then this factor can be used as a merit of comparing wind generator systems. The C_{fs}-percentages of the three wind generator systems are compared in Table 3.

Table 2: Efficiency of system components.

Components	Component efficiencies		
	Passive	Active	Fixed
Wind turbine energy capture (site 1, Fig. 10)	93%	100%	85%
Wind turbine energy capture (site 2, Fig. 11)	87%	100%	77%
RFPM Generator efficiency	92%	92%	92%
Transmission cable	96%	96%	99%
External Inductor	95%	-	-
Diode rectifier	98%	-	-
Active rectifier	-	96%	-
Inverter and transformer	93%	93%	93%
Total component efficiency (site 1)	71%	79%	70%
System efficiency between turbine and grid (site 1)	71%	79%	77%
Average system efficiency (site 1)	-	-	74%
Total component efficiency (site 2)	67%	79%	61%
System efficiency between turbine and grid (site 2)	67%	79%	70%
Average system efficiency (site 2)	-	-	66%

Table 3: Sub-system capacity factor C_{fs}

Site	Sub-system capacity factor		
	Passive	Active	Fixed
Site 1	14.5%	16.2%	15.2%
Site 2	8.1%	9.5%	8.1%

4.3 System component cost

The cost of each system component should also be investigated to determine the energy production per cost of each wind generator system. Generic costs are formulated for the components based on industry averages. Table 4 shows the per unit cost of each component of the systems based on the PM generator cost of the passively controlled wind generator system.

Proceedings of the 19th Southern African Universities Power Engineering Conference
TOPIC D. RENEWABLE AND ALTERNATIVE ENERGY
SAUPEC 2010, University of the Witwatersrand, Johannesburg

From Table 4 one can see that the most economical system in terms of component cost is the fixed speed system. The passive controlled system is also cheaper than the active controlled system. This system is easy to install and to maintain, these being the primary reasons for its wide use. The active controlled system has a very expensive active rectifier. Current rule of thumb estimates a cost of R2500/kW for power electronic converters in renewable energy applications.

The per unit annual energy production per cost of the systems can be determined by dividing the overall system efficiency of Table 2 with the per unit system cost of Table 4. These results are given in Table 5. It is clear that the fixed speed system outperforms completely the other systems in this regard.

Table 4: Per unit system component costs.

Components	Sub-system component costs		
	Passive	Active	Fixed
PM Generator	1	0.9	0.9
Transmission cable	0.22	0.22	0.1
External Inductor	0.05	-	-
Diode rectifier	0.05	-	-
Active rectifier	-	0.9	-
Inverter and transformer	1	1	1
Synchronizing controller	-	-	0.2
Total cost	2.32	3.02	2.2

Table 5: Per unit annual energy production per cost.

Wind sites	Per unit annual energy production per cost		
	Passive	Active	Fixed
Site 1	0.31	0.26	0.34*
Site 2	0.29	0.26	0.3*

*Depends on the matching of the load and delivered wind power.

5. CONCLUSIONS

From the results of the comparative study of the three considered 4 kW air-cored PM wind generator systems for battery charging stand-alone inverter supplies, the following conclusions are drawn:

- For good and moderate wind sites it is found that the fixed speed wind generator system capture 15 – 23 % less annual wind turbine energy than the variable speed maximum power point wind generator system.

- If the subsystem efficiency, however, is taken into account in the calculations, then the annual energy produced to the load by the fixed speed wind generator system is only 6 – 16 % less than the variable speed maximum power point wind generator system.

- It is shown that the capacity factors of the wind generator systems and wind sites can only be used as a merit of comparison if the subsystem efficiency is included in the calculation.

- The cost of the fixed speed wind generator system is found to be substantially lower than the other two wind generator systems considered. Hence, with the annual energy delivered to the load less, but the cost of the system also less, the energy production per cost of the fixed speed wind generator system is shown to be much better than the other two systems.

REFERENCES

[1] AM de Broe, S Drouilhet and V Gevorgain, "A Peak Power Tracker for Small Wind Turbines in Battery Charging Applications", *IEEE Transactions on Energy Conversion*, vol. 14, no. 4, pp. 1630-1635, 1999.

[2] JA Stegmann and MJ Kamper "Design Aspect of Medium Power Double Rotor Radial Flux Air-Cored PM Wind Generators", *1st International Energy Conversion Congress and Expo (ECCE)*, San Jose, CA, pp. 3634-3640, 2009.

[3] DNV Risø, *Guidelines for design of wind turbines – Second edition*. Det Norske Veritas, Copenhagen and Wind Energy Department, 2002.

[4] S Drouilhet, E Muljadi and R Holz, "Optimizing Small Wind Turbine Performance in Battery Charging Applications", *25th Annual Conference and Exhibition on Wind Power*, Washington, DC, 27-30 Mar. 1995.

[5] JF Manwell, JG McGowan and AL Rogers, *Wind Energy Explained*, Wiley, 2003.

[6] JR Bumby, N Stannard, J Dominy and N McLeod, "A Permanent Magnet Generator for Small Scale Wind and Water Turbines", *18th International Conference on Electrical Machines (ICEM)*, Sydney, Australia, 2008.

[7] E Muljadi, S Drouilhet, R Holz and V Gevorgain "Analysis of Wind Power for Battery Charging", *Proceedings of the 15th American Mechanical Engineering Wind Energy Symposium,* Houston, TX, 1996.

[8] B Sareni, A Abdelli, X Roboam and DH Tran, "Model Simplification and Optimization of a Passive Wind Turbine Generator", *Renewable Energy*, vol. 34, pp. 2640-2650, 2009.

[9] FM Rodrigo, LC Herrero de Lucas, S de Pablo Gómez, JM González de la Fuente, "Analysis of the Efficiency Improvement in Small Wind Turbines when Speed is Controlled", *IEEE International Symposium on Industrial Electronics*, pp. 437-442, 2007.

[10] A Koyanagi, H Nakamura, M Kobayashi, Y Suzuki and R Shimada, "Study on Maximum Power Point Tracking of Wind Generators using a Flywheel", *IEEE Power Conversion Conference (PCC)*, Osaka, Japan, pp. 322-327, 2002.

INTEGRATION OF PEM FUEL CELL AND MICROTURBINE IN DISTRIBUTED GENERATION

S N Ngema*,   A K Saha*

*University of KwaZulu-Natal, School of Electrical, Electronic and Computer Engineering, Durban, South Africa.

Abstract. This paper reports the study of dynamic behaviour of an integrated distributed generation (DG) system comprising proton exchange membrane fuel cell (PEMFC) and microturbine (MT) under variable loading profile. PEMFC dynamic model includes independent control of active power and inverter output voltage to meet the load demand. The MT supplies the peak demand of the system. For MT, GAST (Gas Turbine) model coupled to PMG is used. Responses of the system to variable load demand are presented with the analysis of the results.

Key Words: PEMFC, microturbine, distributed generation, renewable energy sources

1. INTRODUCTION

Integration of non-conventional and renewable energy resources in DG applications is now significantly important to meet the rapidly increasing power demand and changing environmental policies [1]. Renewable energy sources utilized in DG systems provide better service reliability, better economics and less dependence on utility. However, there is trade-off between economic benefits and related stability, protection and safety issues [2]. DG systems located at or near to consumers' sites may use a variety of emerging generation technologies, such as fuel cells (FCs), MTs, photovoltaics, WTs etc. with capacities ranging from 1KW to 10MW along with storage devices. FCs are popular because they have the advantages of being modular, efficient, quiet and environmentally friendly. Also, they can be used as portable on-site power generators. Presently, MTs are being utilized in DG applications due to their quick-start capability and easy controllability which are very much useful for efficient peak-shaving [3].

From literature survey on PEMFC, it has been observed that Zhong, Z.D. et al. reported a hybrid multivariable model composed of least square-support vector machine for PEMFC [4]. A description was given in [5] to model dynamic behavior of PEMFC as an initial step to prescribe internal design modifications and/or external controller designs to improve its transient behavior. Jemei, S. et al. described the modeling of PEMFC using artificial neural network (ANN) [6]. Mathematical model and characterization of the transient behavior of a PEMFC was described by Wolfgang, F. et al. [7]. Georgakis, D. et al. described modeling and control of a small scale grid-connected PEMFC system [8].

Research areas on the application of MT for DG include development of MT for power generation [9], test results [10], active filter [11], control mechanism for FC and MT [12], simulation model and operation in islanded and grid-connected modes [13] [14].

In this work, authors report the modeling of an integrated DG system of hybrid nature comprising PEMFC and MT and study of its dynamic behavior under variable load conditions.

2. MODELING OF PEMFC-BASED PLANT

The PEMFC system is a nonlinear, multivariable electrochemical system that is hard to model. A convenient PEMFC model can help greatly to control, simulate and diagnose its behavior [4]. While developing the model for the PEMFC, the following assumptions are made [15, 16]:
The Nernst equation is applicable.

- The gases are ideal.
- The FC is fed with hydrogen and oxygen.
- The FC temperature is stable.
- The electrode channels are small enough so that the pressure drop across them is negligible.
- The ratio of pressures between the inside and outside of the electrode channels is large enough to assume choked flow.
- Ohmic loss and activation losses are taken into consideration.

Ideal gas law is used to find out the partial pressures of the gases flowing through the electrodes. The same formula is applicable to all the gases. Hence the expression for hydrogen is expressed as [16]:

$$p_{H_2} V_{an} = n_{H_2} RT \tag{1}$$

It is possible to isolate the pressure and to take time derivative of the previous expression (1), obtaining [16]:

$$\frac{d}{dt} p_{H_2} = \frac{RT}{V_{an}} q_{H_2} \tag{2}$$

The relationship of molar gas flow through the valve is proportional to its partial pressure inside the channel and for hydrogen it can be expressed as [16]:

$$\frac{q_{H_2}}{p_{H_2}} = \frac{K_{an}}{\sqrt{M_{H_2}}} = K_{H_2} \tag{3}$$

For hydrogen flow, there are three significant factors: hydrogen input flow, hydrogen output flow and hydrogen flow during reaction . The relationship among these factors with the derivative of partial pressure of hydrogen can be represented as [16]:

$$\frac{d}{dt} P_{H_2} = \frac{RT}{V_{an}} (q_{H_2}^{in} - q_{H_2}^{out} - q_{H_2}^{r}) \tag{4}$$

Now, according to the basic electrochemical relationship, the molar flow of hydrogen that reacts can be calculated as [16]:

$$q_{H_2}^{r} = \frac{N_0 I}{2F} = 2K_r I \tag{5}$$

Proceedings of the 19th Southern African Universities Power Engineering Conference
TOPIC D. RENEWABLE AND ALTERNATIVE ENERGY
SAUPEC 2010, University of the Witwatersrand, Johannesburg

Using the equations (3) and (5) and applying Laplace transform, hydrogen partial pressure can be written in s-domain as [16]:

$$p_{H_2} = \frac{1/K_{H_2}}{1+\tau_{H_2}s}(q_{H_2}^{in} - 2K_r I) \qquad (6)$$

and $\tau_{H_2} = \dfrac{V_{an}}{K_{H_2}RT}$ \qquad (7)

τ_{H_2} is expressed in seconds. It is the value of the system pole associated with the hydrogen flow [16]. The partial pressures of water and oxygen can also be calculated in the similar way.

Polarization curves can be expressed by the equation:

$$V_{cell} = E + \eta_{act} + \eta_{ohmic} \qquad (8)$$

The activation over voltage, η_{act} is a function of the oxygen concentration, CO_2 and stack current I (A) whereas ohmic over voltage, η_{ohmic} is a function of the stack current I (A) and the stack internal resistance R int (Ohm).

Assuming constant temperature and oxygen concentration, the fuel cell output voltage, V_{cell} can be rewritten as:

$$V_{cell} = E - B\ \ln\ (CI) - R\text{int}\ I \qquad (9)$$

The Nernst's voltage can be expressed as [13]:

$$E = N_o[E_o + \frac{RT}{2F}(\ln \frac{p_{H_2}p_{O_2}^{0.5}}{p_{H_2O}})] \qquad (10)$$

The potential difference between the anode and cathode is calculated using Nernst's equation and Ohm's law [16] along with activation over voltage,

$$V = N_o[E_o + \frac{RT}{2F}(\ln \frac{p_{H_2}p_{O_2}^{0.5}}{p_{H_2O}})] - rI - B\ln(CI) \qquad (11)$$

Now, using the expression (11) the model of the fuel cell can be illustrated as in Fig. 1 [16].
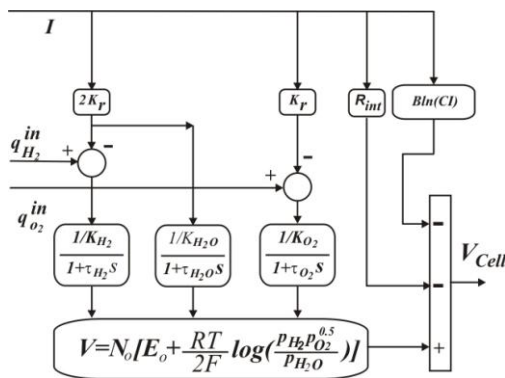
Fig. 1: PEMFC model

2.1 Reformer Model

A developed model is used for the reformer, which generates hydrogen for FC system. The reformer model is a second-order transfer function. The mathematical representation of the model is expressed as [17],

$$q_{H_2} = q_{methane}[\frac{CV}{\tau_1\tau_2s^2+(\tau_1+\tau_2)s+1}] \qquad (12)$$

In reformer model, a feedback from the stack current is considered to control the flow of hydrogen according to the output power from the fuel cell. A controller controls the flow rate of methane in the reformer. Oxygen flow is determined by the use of hydrogen-oxygen ratio (r_{H-O}) [17].

2.2 Power Conditioning Unit

The power-conditioning unit (PCU) is used to convert dc output voltage to ac. The power-conditioning unit includes a dc/dc converter to raise dc output voltage to dc bus voltage, followed by a dc/ac inverter to convert dc bus voltage to ac.

Fig. 2: FC, inverter and load

Only a simple model of a dc/ac inverter is considered in this work as illustrated in Fig. 2 for the following reasons: the dynamic time constant of inverter is of the order of microseconds or at the most milliseconds. The time constants for the reformer and stack are of the order of seconds. Hence, including the inverter time constant will have negligible effect on the time response accuracy. On the other hand, it complicates the systems [17]. The simple model of the inverter is provided in [17, 18], where the output voltage and the output power are controlled using the inverter modulation index and the phase angle of the ac voltage [17]. In this work, output ac voltage of the inverter is taken as 230 volt as it is suitable for residential use.

The ac voltage output of the inverter can be expressed as [17]:

$$V_{ac} = mV_{cell}\angle\delta \qquad (13)$$

The active and reactive power between the source and the load can be expressed by the following expression respectively [17],

$$P_{ac} = \frac{mV_{cell}V_S}{X}\sin\delta \qquad (14)$$

$$Q_{ac} = \frac{mV_{cell}^2 - mV_{cell}V_S Cos\delta}{X} \qquad (15)$$

The inverter for the system has been modeled using equations (13), (14) and (15) which has three inputs - FC DC voltage (V_{cell}), phase angle of the ac voltage (δ) and modulation index (m) with active power, reactive power and ac voltage as outputs.

2.3 Power and Voltage Control Strategy

From the FC system the voltage is taken as input to the control functions which generate inverter phase angle of the ac voltage and the modulation index. The quantities are obtained using the following relationship.

Assuming a lossless inverter, the expression for power can be written as [17]:

$$P_{ac} = P_{dc} = V_{cell}I \qquad (16)$$

Now, the relationship between the stack current and molar flow of hydrogen can be written using electrochemical relationship as [17]:

$$q_{H_2} = \frac{N_0 I}{2FU} \quad (17)$$

Now, considering the equations (14) and (16), we get,

$$\frac{mV_{cell}V_s}{X}\sin\delta = V_{cell}I \quad (18)$$

Therefore, the current can be written as:

$$I = \frac{mV_s}{X}\sin\delta \quad (19)$$

Now, putting the value of current in equation (17), we get,

$$q_{H_2} = \frac{N_0 mV_s \sin\delta}{2FUX} \quad (20)$$

which can be rewritten as:

$$Sin\delta = \frac{2FUX}{N_0 mV_s} q_{H_2} \quad (21)$$

Using the above relationship, the following expression for the phase angle of ac voltage can be written where this angle is very small [17],

$$\delta = \frac{2FUX}{N_0 mV_s} q_{H_2} \quad (22)$$

This expression (22) provides the relationship by which the phase angle can be controlled by controlling the hydrogen flow to the fuel cell.

Two separate PI controllers are used to control the fuel flow to the fuel cell system to meet the power demand set by the user of the system and to maintain the inverter output ac voltage.

With the expressions of ac power and phase angle, it is now possible to control the active power output by the use of hydrogen flow. The active power controller is a PI controller which takes P_{ref} and P_{ac} as inputs and controls the phase angle of the ac voltage as output. On the other hand, actual inverter ac voltage is given as one input to the voltage controller to generate the modulation index (m) while the other input is the reference voltage set by the user. The expression for controlling the modulation index can be expressed as:

$$m = [K_p + \frac{K_i}{s}][V_{ref} - V_{ac}] \quad (23)$$

3. MICROTURBINE MODELING

MTs are small and simple-cycle gas turbines. Their output ranges typically from around 25 to 300 kW. They are available as single or split-shaft units. Single shaft MT is a high speed (50,000 to 120,000 r.p.m) synchronous machine with compressor and turbine mounted on the same shaft. On the other hand, the split-shaft configuration uses a power turbine rotating at 3,000 r.p.m. and a conventional generator connected via a gear box. They can supply a customer's base-load requirements or can be used for standby, peak shaving and cogeneration applications. Usually an MT consists of the following parts [3]:

(a) Turbine: Single shaft or split-shaft gas turbines.
(b) Alternator: Single shaft units use an alternator directly connected to the turbine. The rotor is either

2-pole or 4-pole permanent magnet design and the stator is copper wound. In split-shaft units, a conventional induction or synchronous machine is used through the gearbox.

(c) Power electronics: In single shaft machines, the generated high frequency power is converted to standard frequency power through power electronic interfaces. However, in the split-shaft design, these are not required.

(d) Recuperator: It transfers heat from exhaust gas to compressed air before it enters combustor to improve the energy efficiency of the MT.

(e) Control and communication: It includes the entire turbine control mechanism, inverter interface, start-up electronics, instrumentation and signal conditioning, data logging, diagnostics and user control communications.

In this work, the focus is on slow dynamic performance of the system and not on the transient behaviors. Therefore, MT modeling is based on the following assumptions:

(a) System is operating under normal conditions.
(b) Recuperator model is not included as it only raises efficiency.
(c) The temperature and acceleration controls have no impact on the normal operation and hence, those are omitted.
(d) The governor model is not included as the MT does not use any governor [1] [3] [14] [19]. Instead, a speed controller is incorporated to keep the speed constant. The simplified MT model is shown in Fig. 3. The main emphasis is on active power control. Therefore, the entire control system is simplified and represented as a PI-controller.
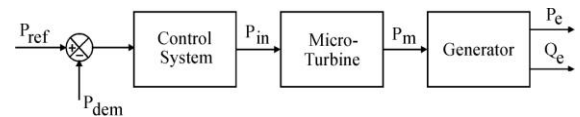
Fig. 3: MT model
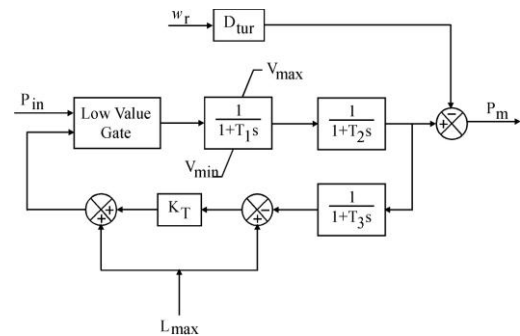
Fig. 4: Turbine model

This work used widely accepted GAST model as shown in Fig. 4 to represent the dynamic behavior of a gas turbine. The advantages of GAST model are that it is simple and follows typical modeling guidelines. It is a Western System Coordinating Council compliant model that can directly be used in specific commercial simulation programs [1] [19].

Proceedings of the 19th Southern African Universities Power Engineering Conference
TOPIC D. RENEWABLE AND ALTERNATIVE ENERGY
SAUPEC 2010, University of the Witwatersrand, Johannesburg

The PMG connected to the MT is modelled using a second order transfer function.

4. INTEGRATED DG SYSTEM

In this work, an integrated DG system is modelled and simulated in Matlab Simulink which comprises three 5 kW PEMFC, a 30 kW MT operating in parallel and power controller as shown in Fig. 5. The power control section is implemented using switches in Matlab Simulink.
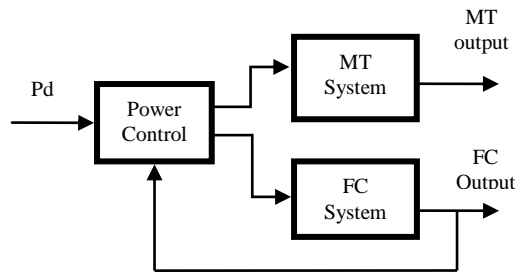
Fig. 5: Integrated DG system

The system operating strategy is such that the PEMFCs supply the power when the load demand is less than their rated capacity. If the power demand rises above the rated output of the PEMFCs, the deficit is supplied by the MT. A power controller is used to control the power to be generated by the MT accordingly as the power demand on the system varies with time. The MT then generates the required power to meet the increased demand. However, should there be any decrease in demand from this condition; the MT is controlled by the power controller so that the demand is met accordingly. The peak power demand is efficiently supplied by the MT utilizing its standby capacity, quick-start capability and easy controllability.

5. SIMULATION AND RESULTS
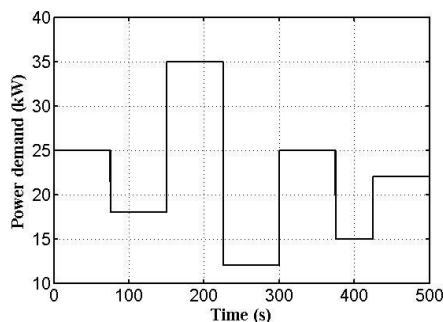
Fig. 6: Changes in power demand

The changes in power demand considered in simulation are as shown in Fig. 6, which shows that from t=0 s to t= 75 s, the power demand is 25 kW, it drops to 18 kW at t=75 s. Again it increases to 35 kW at t=125 s and finally settles at 22 kW. Fig. 7 illustrates the corresponding power generated by the PEMFCs. It has been observed that PEMFCs are delivering their rated output of 15 kW as and when the demand is above 15 kW. The excess demand is met by the MT as observed from the MT output

power illustrated in Fig. 8. Fig. 8 also shows that the MT is supplying power according to the demand placed by the power control section.
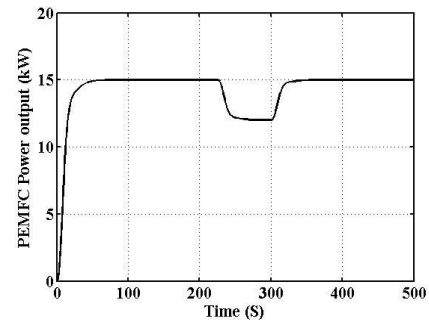
Fig. 7: PEMFC power output
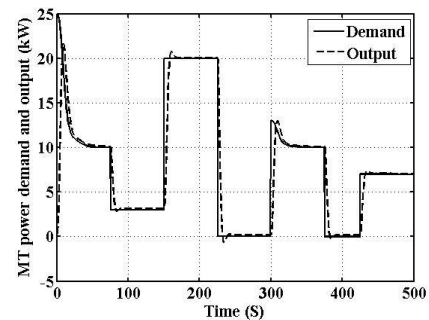
Fig. 8: MT demand and power output

Fig. 9 shows the power demand, FC output and MT output at a glance. From which it is clear that the total power output obtained from FCs and MT is equal to meet the power demand on the system.
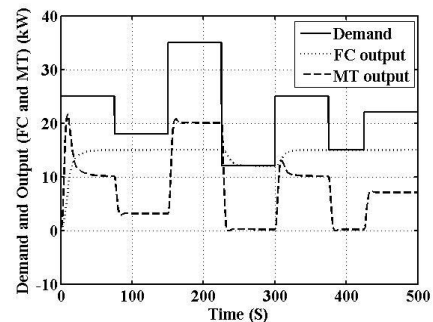
Fig. 9: Power demand, PEMFC and MT power output

Figs. 10 and 11 illustrate the FC stack output and inverter voltage respectively. The stack voltage decreases as current increases due to increase in power output by the cells. From Fig. 11, it has been observed that the inverter voltage is maintained at 230 V by the control action of the voltage control.
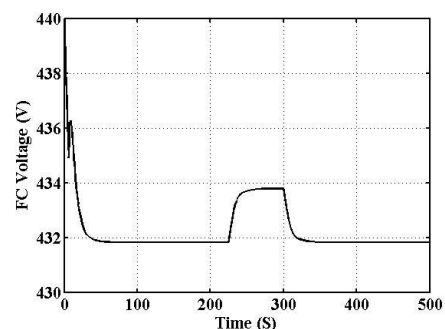
Fig. 10: FC stack voltage
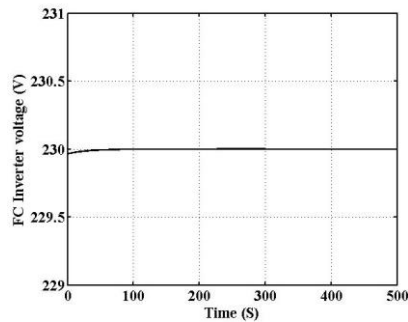
Fig. 11: FC inverter voltage
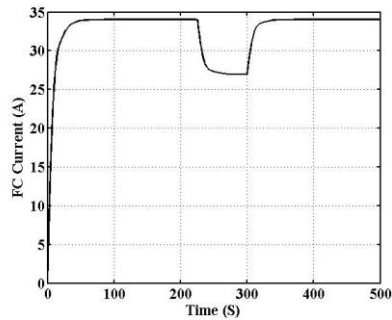
Fig. 12: FC current
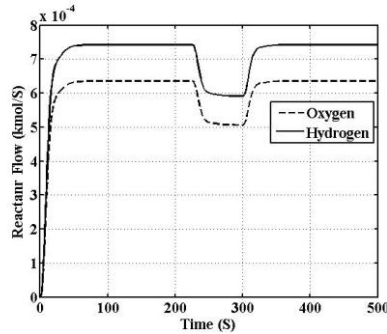
Fig. 13: FC hydrogen and oxygen flow

Figs. 12 and 13 show the changes in FC current and reactant flow. It has been observed that with increase in power demand the current increases and decreases as the power demand decreases. The change in current in turn changes the hydrogen and oxygen flow accordingly to meet the power output.

6. CONCLUSION

Dynamic simulation of PEMFC has been performed along with a MT to analyze their load following behavior in a hybrid power system. The response of the system to step changes in load demand are presented along with the analysis of the simulated results. It has been observed that the system can meet the load demand efficiently using the power controller. The output from each of the system is controlled in such a way that the total power output becomes equal to the load demand. An efficient dynamic model of PEMFC has also been described which can supply active power maintaining inverter voltage as desired. The combined system reduces the cost of power generation as well as the level of pollution reducing the fuel consumption. Also, the

MT has been utilized efficiently to meet the peak demand of the system utilizing its standby capacity, quick start-up capability and easy controllability.

REFERENCES

[1] Y. Zhu, and K. Tomsovic, "Development of models for analyzing the load-following performance of microturbines and fuel cells," *Electric Power System Research*, vol. 62, pp. 1-11, May 2002.
[2] S. Li, K. Tomsovic, and T. Hiyama, "Load following functions using distributed energy resources," *Proc. of IEEE/PES 2000 Summer Meeting*, Seattle, Washington, USA, pp. 1756-1761, July 2000.
[3] S. R. Guda, C. Wang and M. H. Nehrir, "A simulink-based microturbine model for distributed generation studies", *Proc. of IEEE Power Symposium*, pp. 269-274, October 2005.
[4] Z.D. Zhong, X.J. Zhu, G.Y. Cao, and J.H. Shi, "A hybrid multi-variable experimental model for a PEMFC", *Journal of Power Sources*, Vol. 164, 2, pp. 746-751, 2007.
[5] L.Y. Chiu, and B.M. Diong, "An improved small signal model of the dynamic behavior of PEM fuel cells", *IEEE Conf. on Industry Applications*, 38th IAS Annual Meeting, Vol. 2, pp. 709-715, 2003.
[6] S. Jemei, D. Hissel, M.C. Pera, and Kauffmann, "Black-box modeling of proton exchange membrane fuel cell generator", *IEEE Conf. of Industrial Electronics Society*, Vol. 2, pp. 1474-1478, 2002.
[7] W. Friede, S. Raël, and B. Davat, "Mathematical model and characterization of the transient behavior of a PEM fuel cell", *IEEE Trans. on Power Electronics*, Vol. 19, No. 5, pp. 1234-1241, 2004.
[8] S. Papathanassiou, and D. Georgakis, "Modeling and control of a small scale grid-connected PEM fuel cell system", *IEEE Conf. of Power Electronics Specialists*, Recife, pp. 1614-1620, 2005.
[9] J. Peirs, D. Reynaerts and F. Verplaetsen, "A microturbine for electric power generation", *Sensors and Actuators*, A 113, pp. 86-93, 2004.
[10] D. K. Nichols and K. P. Loving, "Assessment of microturbine generators", *Proc. of IEEE PESGM*, Vol. 4, pp. 2314-2315, July 2003.
[11] M. Suter, "Active filter for a microturbine", *Proc. of IEE, Telecom. Energy Conf.*, pp. 162-165, October 2001.
[12] F. Jurado and J. R .Saenz, "Adaptive control of a fuel cell-microturbine hybrid power plant", *IEEE, Trans. on Energy conversion*, Vol. 18, No. 2, pp. 342-347, June 2003.
[13] D. N. Gaonkar and R. N. Patel, "Modeling and simulation of microturbine based distributed generation system", *Proc. of IEEE, Power India Conf.*, April 2006.
[14] D. N. Gaonkar and R. N. Patel, and G. N. Pillai, "Dynamic model of microturbine generation system for grid connected/islanding operation", *Proc. of IEEE, Int. Conf. on Industrial Technology*, pp. 305 − 310, December 2006.
[15] C. Boccaletti, G. Duni, Fabbri, G., and E. Santini, "Simulations models of fuel cell systems", *Proc. ICEM, Electrical Machines*, Chania, Greece, (pages) 6 pp, September 2006.
[16] J. Padulles, G.W. Ault, and R. McDonald, "An integrated SOFC plant dynamic model for power systems simulation", *Journal of Power Source*, Vol. 86, pp. 495-500, March 2000.
[17] M.Y.E. Sharkh, A. Rahman, M.S. Alam, P.C. Byrne, A.A. Sakla, and T. Thomas, "Analysis of active and reactive power control of a stand-alone PEM fuel cell power plant", *IEEE Trans. on Power Systems*, Vol. 19, No. 4, pp. 2022-2028, November 2004.
[18] C.J. Hatziadoniu, A.A. Lobo, F. Pourboghrat, and M. Daneshdoost, "A simplified model of a grid-connected fuel cell generators", *IEEE Trans. on Power Delivery*, Vol. 17, 2, pp. 467-473, April 2002.
[19] N. Hatziargyriou, G. Kariniotakis et al., "Modelling of microsources for security studies", *Proc. of CIGRE Session*, Paris, France, August-September 2004.

Topic E

Electromagnetics

TOPIC E. ELECTROMAGNETICS

Proceedings of the 19th Southern African Universities Power Engineering Conference
SAUPEC 2010, University of the Witwatersrand, Johannesburg

Fields and Common-mode Currents in the Vicinity of Measurement Probes

H.C. Reader, D.J. Rossouw and J. Badenhorst

University of Stellenbosch, Dept. of Electrical and Electronic Engineering, Stellenbosch, South Africa

Abstract. We are interested in the characterisation of E-fields, H-fields and common-mode (CM) currents in the vicinity of typical measurement probes. To illustrate these points, we verify a computational electromagnetic code in a defined probing environment. Our ultimate interest is in reducing the dependency of, or defining, the conditions surrounding typical probes to improve high frequency metrology.

Key Words. EM modelling, HF-probes, CM-currents, HF-Metrology

1. INTRODUCTION

There are numerous examples of invasive probing techniques in high frequency metrology [1],[2]. Our earlier work on EMC current probes (CP) [3], [4] directed our focus to this general metrology issue. We are interested in studying the electromagnetic environmental conditions surrounding typical probes. A specific material properties probe is used to illustrate key points in this regard. In our work, we place a standard SMA flanged probe in a cylindrical shield with interior length of approximately 200 mm and diameter of 80 mm, see Fig. 1. This setup has been both modelled and measured and the results are used to illustrate our findings.
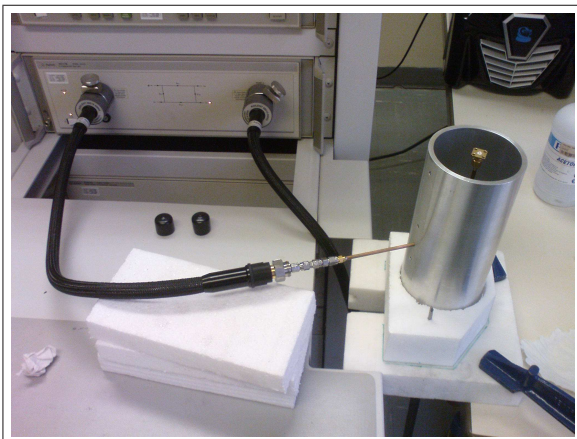
Figure 1: Measurement setup to illustrate a defined probe measurement environment. A flanged SMA-probe, surrounded by a cylinder, can be seen, along with a semi-rigid E-field probe on the side wall.

2. CURRENT PROBE CHARACTERISATION

Fig. 2 shows a collection of high frequency (HF) CM current probes, similar to those used in our earlier work [3]. Summarising [3], we used a measurement setup shown in Fig. 3 to measure the transfer impedance of a CP for an open cable environment [3]. Use is made of a commercial full-wave, finite volume time domain (FVTD) simulation code, to visualise field and current behaviour in the system. Fig. 4 reveals the spatial dependance of current at 400 MHz which hampers accurate calibration. Final measured transfer impedance shows up to 2.5dB discrepancies, Fig. 5, compared to published probe data. This is related to capacitive coupling effects

between the CP and recognised enclosures used for standard calibration. This point highlights the importance of understanding EM environments surrounding HF probes in general and spurred the investigation and related methodology presented here.

Figure 2: Typical HF CM current probes.
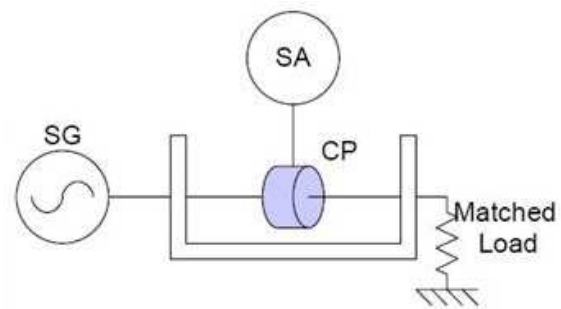
Figure 3: Illustration of measurement setup for current probe characterisation [3].

3. DIFFERENT APPROACH TO CM CURRENT AND FIELD MEASUREMENT

To examine small levels of CM current and fields surrounding measurement probes a different approach may be required. We have constructed a carefully controlled measurement setup around an SMA flanged probe to illustrate our alternative method. The overall system needs to be sensitive and must support fixed reference positions for measurements exterior to the probe face. With this in mind a metallic

Proceedings of the 19th Southern African Universities Power Engineering Conference
SAUPEC 2010, University of the Witwatersrand, Johannesburg

TOPIC E.   ELECTROMAGNETICS
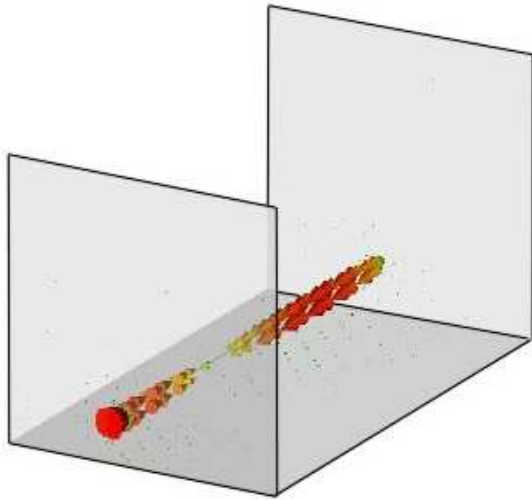
Figure 4:   CST model of current probe calibration jig showing current distribution [3].
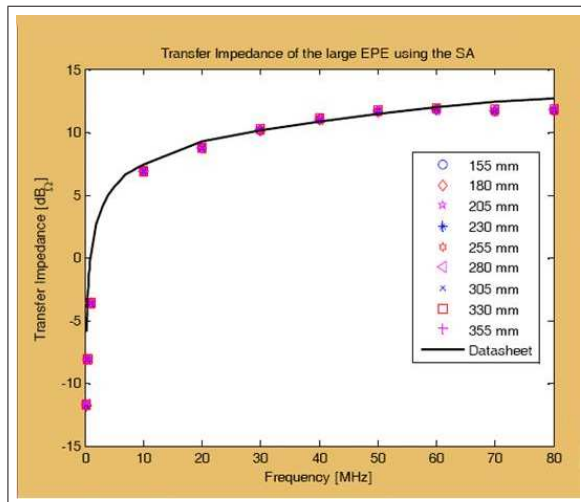
Figure 5:   Measured and simulated transfer impedance of the current probe [3].

Figure 6: E-field magnitude of shielded flanged probe at 3 GHz.

4.   Flanged Probe and Cavity Simulation

Fig. 6 shows a cut-plane view of the four simulated probing positions numbered from top to bottom. Superimposed on the image is the E-field magnitude at 3 GHz. These field levels are small and the scale is clamped to make the values visible within the cavity. The contours indicate positions of equal field magnitude and should not be interpreted as vector field lines in the cut-plane.

Every possible detail of the system geometry is modelled while making suitable simplifications to reduce computation times. Cable, connector, probe flange and side-probe outer characteristics were obtained from manufacturers' data. Waveguide ports were specified with the bottom port embedded slightly below the face plane of the probe. This allows the use of CST's port-offset function and accommodates higher-order modes that occur in the dielectric bead near the face. Open boundaries using a Perfect Boundary Approximation were defined. We ran the Transient solver with the energy criteria accuracy set to -50 dB. Model regularity supports the use of quarter symmetry in meshing and suitable iterations ensured result convergence.

5.   Field Simulations and Measurements

We performed a two-port SOLT (short-open-load-through) calibration with the reference planes established between the feeding SMA port below the shield base and the SMA port of the E-field probe at the side wall.

A 1 - 3 GHz comparison between the simulation and measurement for side-probe position four is seen in

cylindrical shielding cavity surrounding the flanged probe was designed. The removable shield isolates the probe structure from vector network analyser (VNA) cabling.

To characterise the system, we made use of an E-field probing technique described in [5]. The extended-centre-conductor coaxial probe allows a second port to be established in the side wall of the cavity. The E-field probe is made sufficiently long to obtain a reasonable measurement dynamic range, but not long enough to disturb the fields significantly. This second port allows a measurement of S21 versus frequency which can be compared to computation. Using the E-field probe we also evaluated the cavity field spatial distribution at four positions as shown in Fig. 6. We modelled the complete setup including the probe geometry in the full-wave FVTD code CST [6].

TOPIC E. ELECTROMAGNETICS

Proceedings of the 19th Southern African Universities Power Engineering Conference
SAUPEC 2010, University of the Witwatersrand, Johannesburg

Figure 7: Field probe |S21| dB versus frequency: Simulation and VNA measurement at probe position four.
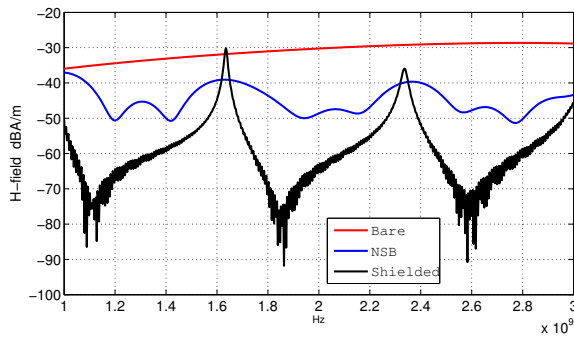
Figure 8: Simulated H-field strength (dBA/m) versus frequency for the H-field probe in the three environments depicted in Fig. 9
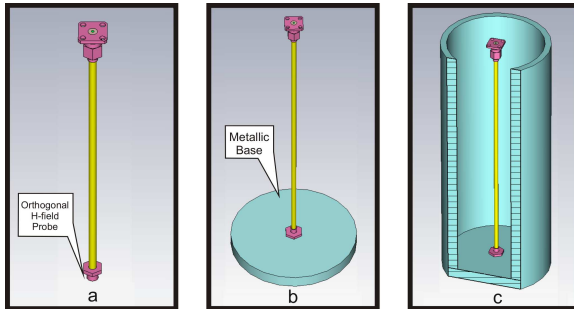
Figure 9: Three levels of defined probe environment: a) bare probe: undefined environment; b) probe with shield base only: loosely defined and c) cut-plane view of fully-shielded probe: well defined. a) also shows the placement of the H-field probe for all three cases.

Fig. 7. This agreement is reached down to levels of -100 dB on the reference 0 dB and required great care in the measurement process. Two cavity resonant modes at 1.67 and 2.38 GHz are identifiable and change with dimensions of the cylinder. Similar results are achieved for all the other field-probing positions. We can now discuss the physics of the problem trusting simulations alone. From the side-probing, we observe the following: 1) the level of energy escaping the flanged probe face; 2) the field moding; 3) the containment of these fields within the cavity; and, 4) even on this amplified scale, the small amount of CM current on the feeding coaxial cable. The CM current is determined from the orthogonal H-fields close to the feed cable of interest. Fig. 8 shows the simulated H-field strength around the feed cable for the three external environments illustrated in Fig.

9. The position for the H-field indicator is depicted in Fig. 9 a). The CM current on cabling is one of the issues that we found interferes with accurate measurements when using many types of probes. The measurement probe, a flanged SMA probe in this case, does not just sample a material-under-test (MUT), it also is affected by the fields and currents along the cables. As this CM current distribution varies according to measurement configuration, we wish to explore techniques to minimise and then quantify this effect.

The bare flanged probe, shown in Fig. 9 a), represents an undefined measurement environment, similar to that used in [1]. H-field levels of -30 dBA/m, Fig. 8, are seen. The same probe with No Shield and metallic Base (NSB), Fig. 9 b), typifies a loosely defined environment and shows 10 dB lower CM levels on the cabling. This can be compared to the fully shielded case, shown in Fig. 9 c), which constitutes a well-defined situation with levels of -60 dBA/m or better apart from resonant features.

These results indicate that the CM current propagating on the feed cable can be significantly reduced by placing shielding environments around the probe. Even the simple metallic base of Fig. 9 b) improves the situation. The full cylindrical shield can attenuate the current by 30 to 40 dB. At the two cavity resonances, the shield appears as a high impedance and the CM currents cannot be prevented. The features seen in the NSB and the shielded case of Fig. 8 will ultimately give rise to incorrect MUT permittivity data at these frequencies.

6. FACE-PLANE CALIBRATION AND MATERIAL PROPERTY DERIVATION

With the effect of the environment now better understood we extend our investigation to SOL (short-open-load) calibrated face-plane measurements of dielectric solids. We focus on the two better-defined setups. The first is the NSB case shown in 9 b), and the second is the fully-shielded case shown in 9 c). Specific measurement precautions stated in [1] are applied. We have improved the repeatability of the matched load and short circuit standards through an in-house clamp, see Fig. 10. The clamp is similar to one reported by Gregory and Clarke [7].

CST is used to compute open-circuit (OC) data from which we obtain VNA calibration coefficients for both the NSB and fully-shielded cases. After performing SOL calibrations described in [1], we recorded face-plane-referenced S11 data for a well-known material standard, Teflon®.

To look into the consequences of CM energy in the region surrounding the probe, we use a full-wave inversion algorithm described in [1]. This converts our measured reflection data set into complex permittivity. We show the real permittivity result for Teflon® in Fig. 11.

Proceedings of the 19th Southern African Universities Power Engineering Conference
SAUPEC 2010, University of the Witwatersrand, Johannesburg

TOPIC E. ELECTROMAGNETICS
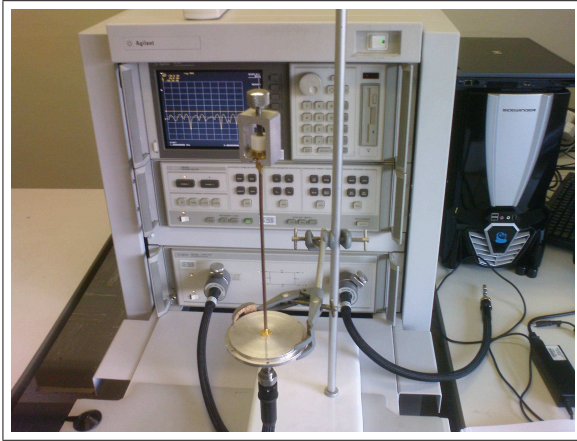
Figure 10: Measurement setup with SMA flanged probe and supporting jig. In-house clamp used during calibration, visible at probe face.
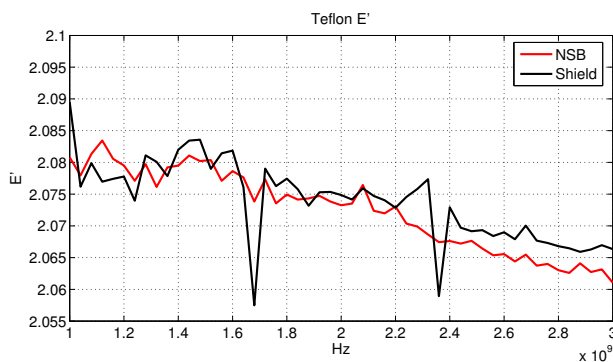
Figure 11: ϵ' for Teflon®: NSB and Shield data

The two shield-cavity modes form the resonances seen in the ϵ' data. Without giving a detailed discussion on the permittivity result, the derived values seen here are close to the published data of around 2.08.

7. DISCUSSION ON PROBE CM CURRENTS AND FIELDS

Concerning the two shield-cavity modes, these resonances disappear when the shield is removed. On detailed scrutiny, a small resonant effect can also be determined for the NSB case. This is more evident from the measurements on higher relative permittivity materials which we do not present here. However, for a completely exposed flanged probe with no shield or base, resonances in the data are due to the cabling environment and cannot be predicted. We find that with a known boundary provided by a shield, the ϵ' results compare well with published data except in the regions of resonance, which are now known.

Probe external effects should be considered more carefully both in the physical experiments and in the data processing. With uncontrolled environments, unexpected features and uncalibrated results can arise. This occurs because of CM currents, or exterior capacitive coupling to the environment through E-fields. It is arguably better to define the probe measurement

region, as we have demonstrated here, and know that the results will be slightly in error, than to have unpredictable results. It is also conceivable that, for a given measurement probe, appropriate corrections could be made to compensate for the defined measurement region.

8. CONCLUSION

We have established the characteristics and levels of CM energy exterior to the face-plane of a flanged coaxial probe. This was accomplished through verified modelling of the probe system. A cylindrical shield was used to isolate the environment from the measurements. Without this, unpredictable features will appear in data sets. The shield introduces identifiable resonances. Regions either side of these frequencies yield good ϵ' information when using a well-prepared, flanged probe with good calibration procedures.

Our original intention in this work was to use a CM current probe to measure cable currents in a reliable fashion. On closer study we discovered that the probe gave slightly different results depending on how we measured. This paper has explored the reasons for probe inaccuracies. With these insights, it alerts metrologists to possible methods of obtaining better results.

9. ACKNOWLEDGEMENTS

REFERENCES

[1] H. C. Reader and M. D. Janezic, "Coaxial probe dielectric measurements: Practical dotting "i's" and crossing "t's"," *68th ARFTG Conference Omni Interlocken Resort, Broomfield, Colorado*, Dec 2006.

[2] D. J. Rossouw, H. C. Reader, and J. Badenhorst, "Flanged coaxial material probes: Characterizing exterior cm energy," *74th ARFTG Conference Omni Interlocken Resort, Broomfield, Colorado*, 2009.

[3] H. C. Reader, R. H. Geschke, J. Badenhorst, and E. Laubscher, "Issues in calibrating sensors for emi and suppression of unwanted modes," *Saupec Conference Paper 2007*, 2007.

[4] H. C, Reader, R. H. Geschke, A. J. Otto, and J. Badenhorst, "Transfer impedance and EM bandgap structures in EMI suppression," *Saupec Conference Paper 2008*, 2008.

[5] T.V. Chow Ting Chan and H. C. Reader, *Understanding Microwave Heating Cavities.* Artech House Publishers, 2000.

[6] Computer Simulation Technology (CST), Microwave Studio, CST website available on internet search.

[7] A. P. Gregory and R. N. Clarke, "Dielectric metrology with coaxial sensors," *IOP Publishing - Measurement Science and Technology*, vol. 18, pp. 1372–1386, 2007.

TOPIC E. ELECTROMAGNETICS

Proceedings of the 19th Southern African Universities Power Engineering Conference
SAUPEC 2010, University of the Witwatersrand, Johannesburg

L.P. Kibet and H.C. Reader

Department of E&E Engineering, University of Stellenbosch, South Africa

Abstract- The spectral and radiation characteristics of power-line sparking noise are reported in this paper. Spark-gap tests are carried out in both a high-voltage laboratory and on an active 22kV power-line. Time domain measurements are made on an oscilloscope and on a spectrum analyzer in zero-span mode. Frequency spectra, which include the lateral and longitudinal profiles of the noise from a radiating line, are recorded on a spectrum analyzer. The influence of varying the measurement position from the source and the line is considered. The consequence of varied voltage level applied to a given gap length is discussed. Radiation characteristics of a power line are examined through simulations done using FEKO® EM software.

Key Words – Power line, radiation pattern, radio frequency interference, sparking noise.

1. INTRODUCTION

This paper reports an ongoing effort to characterize South Africa's SKA (Square Kilometre Array) system's electromagnetic environment. We are concerned about power-line sparking and its radio frequency interference (RFI). The SKA will operate over a very wide frequency range and is expected to achieve unprecedented sensitivity and resolution [1].

Power line interference is known to be caused by corona and gap-type discharges. The gap-type (commonly known as sparking noise) discharge is the major cause of wideband power line interference. It is mainly encountered on wooden pole lines, which are usually operated below 70 kV AC [2]. At this voltage level, the voltage gradients on the lines are insufficient to generate conductor corona [3].

We describe some of the characteristics of sparking noise measured on active lines in the field and in a high-voltage laboratory. In both environments, an artificial sparking-gap device was used as a noise generator. The field measurements were conducted on a 22 kV power line. The important parameters considered were the frequency spectrum and time domain characteristics of the radiated noise. This yields information concerning the pulse repetition rate, and lateral and longitudinal profiles of the noise.

The radiation characteristics of a power line due to a noise source injecting energy onto it were also examined using FEKO® EM software to evaluate the far-field radiation patterns.

2. FIELD MEASUREMENT SETUP

The spark-gap noise measurements were carried out on a 22kV grid test power line at the SKA Karoo support base near Carnarvon. This line had 13 spans of approximately 100m long each. It is suspended on wooden poles. This was designed with various specifications for the wooden section of the main grid 22/33 kV supply line for the SKA precursor, MeerKAT, in mind.

The measurement site was scanned for background noise before taking sparking noise measurements.

Some broadcast and cell phone transmitter signals were present but were not strong enough to saturate the measuring equipment. The sketch of the site is shown in Fig. 1 with various measurement points. These points were chosen according to the terrain and our modelling capabilities. The spark-gap device was attached to the middle conductor of the power-line as shown in Fig. 2 with a 2mm gap spacing set. One electrode was connected to the active line while the other electrode was left floating.

The instrumentation used included an LPDA antenna (300 MHz – 6GHz) with a gain of 5dB and a low-noise pre-amplifier (50 MHz – 3GHz) with up to 22dB of gain. The pre-amplifier was used together with the LPDA to improve the system's measurement sensitivity at higher frequencies. Portable and battery driven FSH3 handheld (100 kHz – 3GHz) and FSH8 (9 kHz – 8GHz) spectrum analyzers and a scope-meter (100MHz bandwidth) were used to make frequency and time domain measurements. In addition to these measurements we also studied results using a magnetic loop antenna (100 kHz – 30 MHz). The information derived from this is not reported here, but it fills in our understanding of the sparking noise.
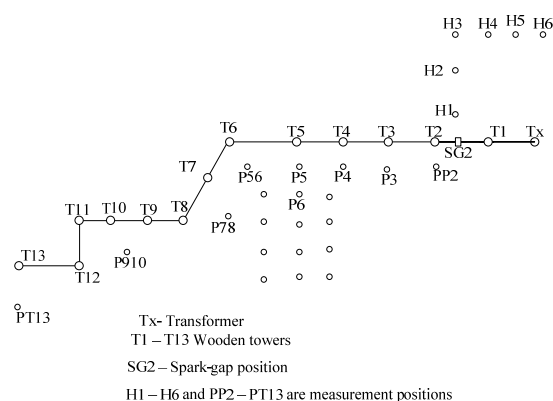
Fig 1: Sketch of measurement site at Carnarvon

Fig 2: Spark-gap device mounted on the line at point SG2

3.   MEASURED RESULTS AND DISCUSSION

3.1 Field measurements

3.1.1   Longitudinal profile

Sparking noise decay along the line length and away from the noise source was examined by taking measurements at points along and near the power line. Here, E-field strength was recorded at locations that are parallel to the power line. These locations were P4, P56, P78, P910 and PT13, as shown in Fig. 1, and are 10m away from the line. Another set of points were H3, H4, H5 and H6, which are 100m away from the line and 50m apart.

(a)

(b)
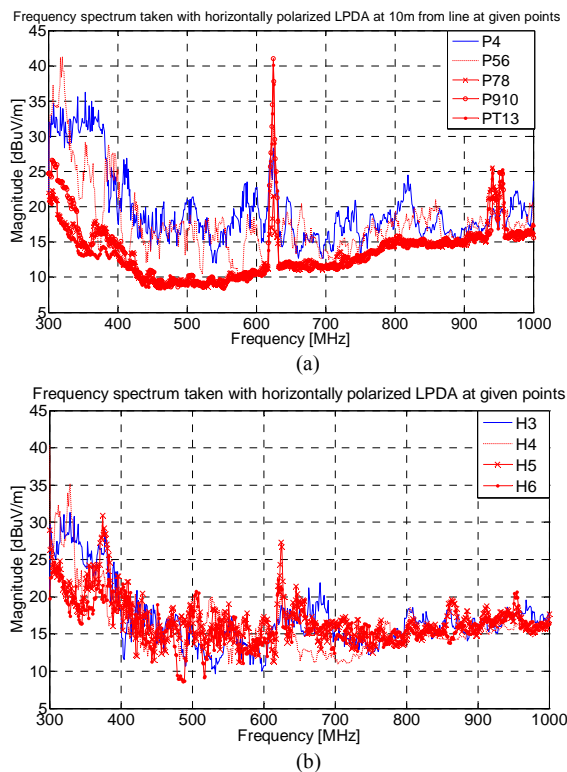
Fig. 3: Spark-gap longitudinal profile at a) 10m and b) 100m from the line (RBW = 30 kHz)

Typical frequency spectrum results are given in Fig. 3. Here the LPDA antenna and FSH8 spectrum analyzer with resolution bandwidth (RBW) = *30 kHz*, preamplifier off and clear/write mode were used. It can be seen that the measured noise levels extend up to 1GHz. It was also observed, though not recorded here, that the radiated noise energy was detectable and filled up the entire frequency band up to 3GHz. The spectrum was also found to decay with frequency as measurement position moved away from the spark-gap device, as shown in graphs P4 and PT13.

3.1.2   Lateral Profile

The measurement results for the lateral profile were taken at positions perpendicular to the line axis. H1, H2 and H3, are 50m apart with H1 being 10m from, and perpendicular to, the point where the spark-gap source is attached to the line.

Typical frequency spectra at each measurement position are given in Fig. 4. This shows that the noise levels decrease with distance from the source.
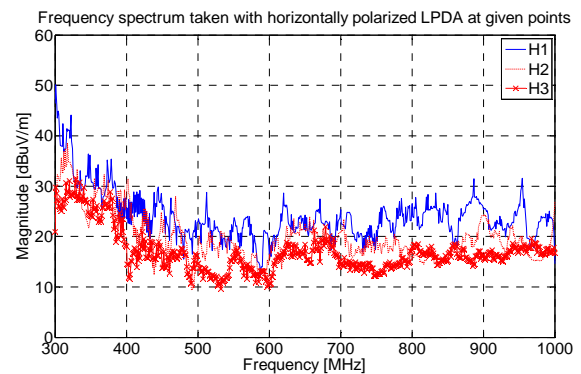
Fig 4: Spark-gap lateral profile at given points (RBW= 30 kHz)

3.2 High-voltage lab measurements

The sparking-gap noise measured in the high voltage laboratory utilized the spark-gap device attached to an ac voltage source and raised about 7m above the ground. A 2mm gap length was set on the device. Measurements were taken 10m away from the spark-gap. The voltage level applied to the device was varied from when there was intermittent sparking to when the gap was continuously sparking. These voltages are given in the captions or legends of each graph and are the values of $AC_{Peak}/\sqrt{2}$. This voltage representation is one of the formats available in the voltage supply controller used. The frequency spectrum was taken with an LPDA antenna and a spectrum analyzer. A voltage level that is much higher than the breakdown value of a specific gap size resulted in a higher noise level, but the shape of frequency spectrum is about the same as shown in Fig. 5.

TOPIC E. ELECTROMAGNETICS

Proceedings of the 19th Southern African Universities Power Engineering Conference
SAUPEC 2010, University of the Witwatersrand, Johannesburg
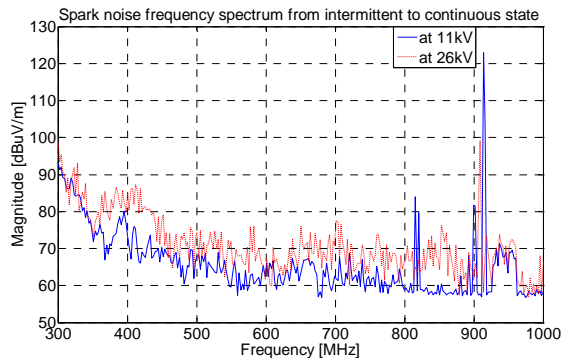
Fig 5: Frequency spectrum for spark-gap noise during intermittent and continuous states

The pulse repetition in time domain is given in Fig. 6. This was taken with a zero-span setting at 300 MHz on the spectrum analyzer.
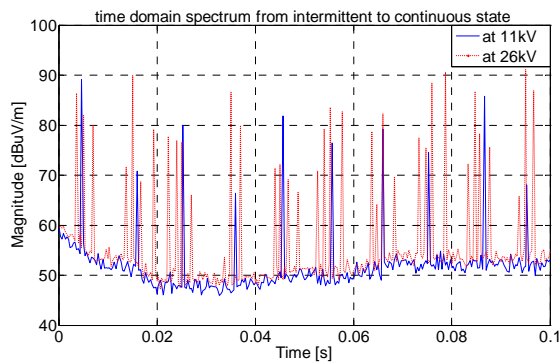
Fig 6: Time domain for spark-gap noise during intermittent and continuous states – measured at 300 MHz on spectrum analyzer in zero-span mode

(a)

(b)
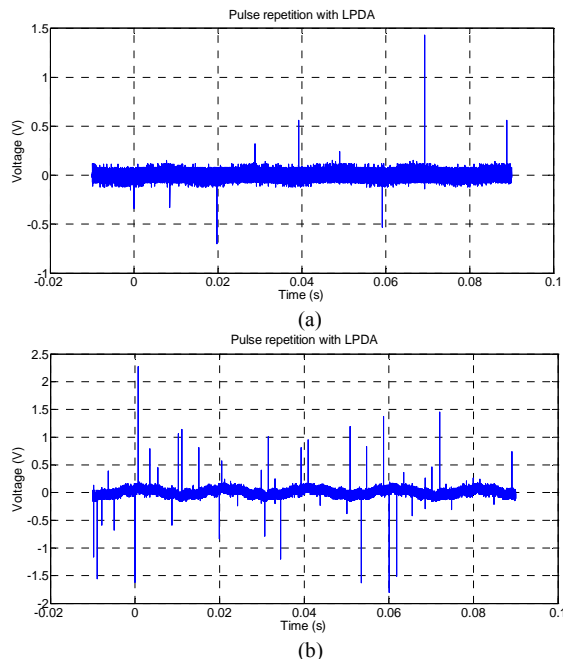
Fig 7: Time domain spectrum measured with a scope with RMS supplied voltage of a) 14kV and b) 49kV

It can be seen that as the voltage is increased far beyond the breakdown value, a higher pulse repetition rate is achieved. This is also confirmed by the oscilloscope data given in Figs. 7a and 7b. The oscilloscope used here had a bandwidth of 350 MHz. It can be concluded that a higher pulse repetition rate results in a higher noise level.

3.3 Power-line simulated radiation characteristics

If a time varying current, such as the sparking current pulses, couples on to an overhead power line, the line will act as both an antenna and transmission line. The modes of propagation of the resultant noise are by direct radiation, conduction, RF induction, and re-radiation [4]. The radiation characteristics of this line depends on such factors as the frequency of the source, spacing between the conductors, load impedance, presence or absence of a grounded neutral conductor, ground properties and mode of current injection.

Antenna radiation characteristics of a power line with a noise source were modelled using FEKO® EM software. By varying some of the described parameters, their contribution to the far-field radiated energy from the line was examined.

In the simulations, a full-scale model was configured with three equal length 20 mm PEC wires placed 12m above a PEC finite ground plane. The horizontal conductors were parallel to each other to represent a simplified version of a power line with a line spacing of 1*m*. The line length used was 300m, equivalent to a 3-span section of a real line with each span being 100m long. 500 Ω impedances were connected between each end of the wires and the ground, to terminate the approximate line surge impedances.

Simulation of this electrically large model requires substantial computing resources. The required discretization of the finite ground plane and long wires in FEKO limits the higher simulation frequency range.

A typical horizontal radiation pattern is as shown in Fig. 8 for 35 MHz. It exhibits an end-fire pattern whose shape, level and orientation vary with source frequency. We also observed that the pattern shape does not change with termination impedance.

Proceedings of the 19th Southern African Universities Power Engineering Conference
SAUPEC 2010, University of the Witwatersrand, Johannesburg

TOPIC E. ELECTROMAGNETICS
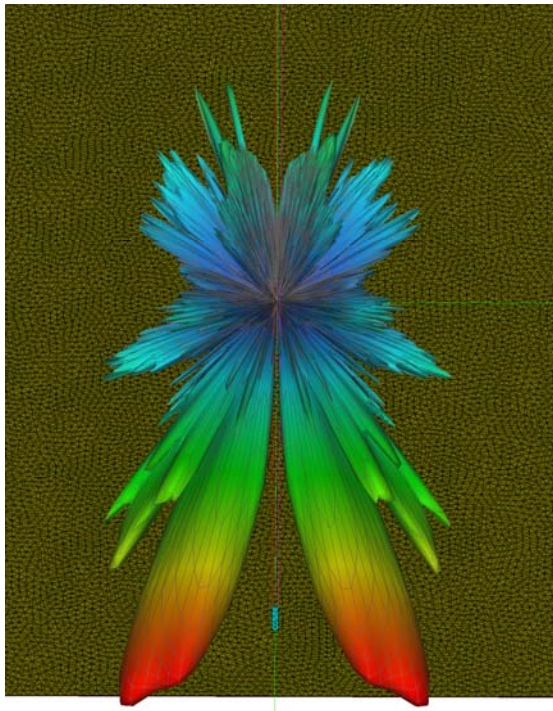
Fig 8: A typical horizontal radiation pattern for the FEKO modelling at 35 MHz

The radiation pattern shape was found to be affected by line configuration. The precise point of injection on the line contributed to the variation in field patterns. As shown in Fig. 9, there is symmetry in the pattern for a line that is excited on the centre conductor. With the excitation on the outer line, the radiation pattern becomes pulled to that side.
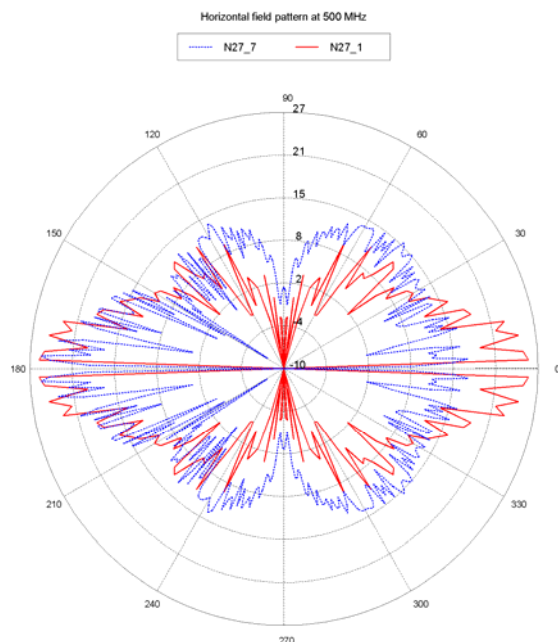
Fig 9: Horizontal field patterns for models with pulse injection point at the centre of middle line (*N27_1*) and at the end of the middle conductor (*N27_7*) at 500MHz

4. CONCLUSION

This paper presents results of radiated sparking noise from a spark-gap device in a laboratory and on a 22kV test power line. Time and frequency domain characteristics of the sparking pulse are given along with lateral and longitudinal profiles.

Far-field radiation characteristics of the line were evaluated through simulations and it was noted that the pattern exhibited end-fire characteristics. Work is currently underway to investigate radiation properties of a physical scale-model line where measurements will be done in an anechoic chamber. The measured radiation pattern results will then be correlated with simulations.

ACKNOWLEDGEMENTS

REFERENCES

[1] P. J. Hall, "The Square Kilometre Array: An international engineering perspective," Experimental Astronomy, vol. 17, no. 1–3, pp. 5–16, Jun. 2004.

[2] W. E. Pakala and V. L. Chartier, "Radio noise measurements on overhead power lines from 2.4 to 800 kV," IEEE Trans. Power App. Syst., vol. PAS-90, no. 3, pp. 1153-1165, 1971.

[3] R.T. Harrold, "The Spectrum Analyzer Applied to the Measurement of EHV Power Line Radio Noise," IEEE Transactions on Power Apparatus and Systems, Vol. PAS-90, No. 4 pp. 1837-1847, 1971.

[4] M. Loftness, KB7KK, "*AC Power interference Handbook*," Third Edition, Percival Technology, Revised, 2007.

TOPIC E. ELECTROMAGNETICS

Proceedings of the 19th Southern African Universities Power Engineering Conference
SAUPEC 2010, University of the Witwatersrand, Johannesburg

NON-ACTIVE POWER IN A TRANSFORMER CARRYING GEOMAGNETICALLY INDUCED CURRENTS

P. O'Donoghue, C.T. Gaunt

Department of Electrical Engineering, University of Cape Town, Private Bag, Rondebosch 7701

Abstract. Geomagnetic disturbances associated with space weather events induce earth surface potentials that drive geomagnetically induced currents (GICs) through transmission systems. This paper reports an investigation into the effects of GICs on transformers, especially in respect of non-active power. A new definition of non-active power is applied to laboratory measurements in a transformer with direct current injection equivalent to GICs.

Key Words. Geomagnetically Induced Currents (GICs), Transformer, Geomagnetic Disturbance, Saturation, Non-Active Power.

1.   INTRODUCTION

Solar activity phenomena include filaments, coronal holes, solar flares and coronal mass ejections, all resulting in a stream of matter through space known as the solar wind [1]. The overall solar activity appears to follow an 11 year cycle, illustrated in Figure 1.
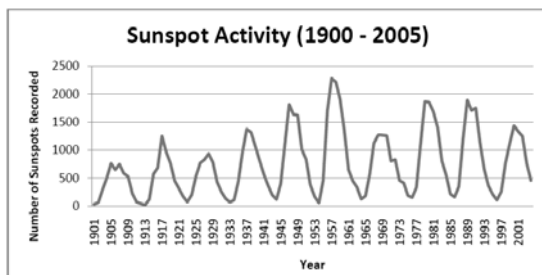
Figure 1: Recorded Sunspot Activity from 1900 to 2005 [2]

Fluctuations in the solar wind cause fluctuations in the shape and strength of the earth's magnetic field. Within the solar cycles, over periods of minutes, hours and days, increased solar activity results in intense geomagnetic field fluctuations, known as magnetic storms [2]. During these magnetic storms a potential difference is induced on the earth's surface. This is known as an Earth Surface Potential (ESP). This ESP appears as an ideal voltage source between the grounded neutrals of wye-connected transformer and reactor windings. This ESP causes quasi-direct current, called geomagnetically induced current (GIC), to flow in transmission lines and between the grounded neutrals in substations. In a simple model, the GIC splits evenly and flows in all three phases of a transformer [3].

The severity of the GIC is determined by the extent, strength and variation of the horizontal magnetic field, and the electrical network characteristics [3].

The electrical system characteristics affecting GIC severity are the power system orientation, transmission line length, component resistances and the transformer type, connection and grounding [1].

2.   GIC's EFFECTS ON TRANSFORMERS

Power transformers are designed to operate close to the magnetisation curve knee-point for economic reasons. The presence of a direct current offset on the winding of the transformer causes a core flux offset. The core flux offset may cause the transformer to operate in half-cycle saturation mode [4].
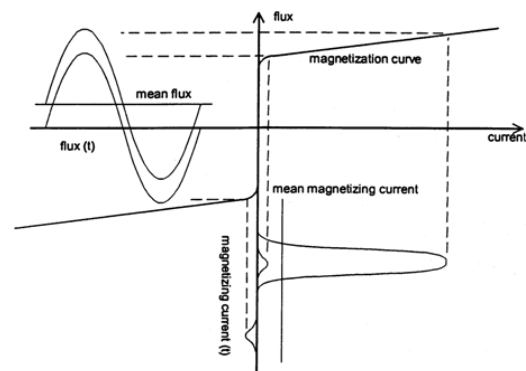
Figure 2: Transformer Magnetising Current due to Half-Cycle Saturation [5]

Half-cycle saturation in a transformer is the root cause of the detrimental effects of a GIC event [6]. The half-cycle saturation may cause increases in audible noise, generation of odd and even harmonics, and increased losses and heating in the transformer [7]. Other detrimental power system effects include protective relaying problems,

Proceedings of the 19th Southern African Universities Power Engineering Conference
SAUPEC 2010, University of the Witwatersrand, Johannesburg

TOPIC E. ELECTROMAGNETICS

communications problems and unusual and variable flows of 'reactive' power [8].

The measurement of apparent power, non-active power and power factor in multi-phase systems with harmonics, phase unbalance and dc components has been a matter of debate for many years. A new approach, differing from the standard definitions of apparent power, has been proposed [9]. This paper reports on an investigation of the non-active power in transformers, based on the new definition of apparent power and power factor.

3. TRANSFORMER MODEL

The transformer is one of the most common non-linear elements in the power system. The non-linearity is caused by the non-linear core magnetisation characteristic. The model we use consists of three single-phase shell type transformers [8]. The magnetic flux distribution for a shell-type transformer is shown in Figure 3 below.
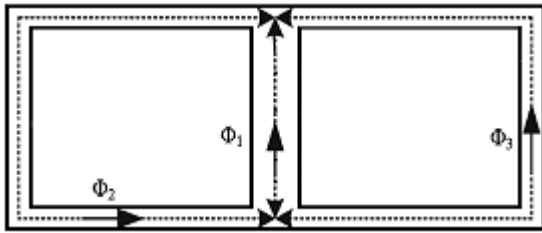
Figure 3: Magnetic Flux Distribution for a Shell-Type Transformer [7]

The approximate equivalent circuit can be derived using a reduction process. It is assumed that the transformer is symmetrical. As such the opposite yoke and limb reluctances are assumed to be equal. The yoke and limb reluctances are represented by $\mathcal{R}_Y$ and $\mathcal{R}_L$ respectively while $\mathcal{R}_C$ models the centre limb reluctance. The air gap reluctance is represented by $\mathcal{R}_0$.

$$\mathcal{R}_{Y1} = \mathcal{R}_{Y2} \, , \mathcal{R}_{L1} = \mathcal{R}_{L2}$$
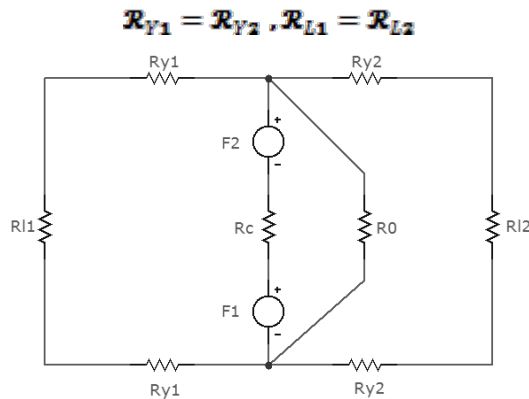
Figure 4: Equivalent Circuit for Single-Phase Shell-Type Transformer

The equivalent reluctance at specific conditions is given by $\mathcal{R}_{eq}$. The equation for equivalent reluctance is derived using simple network reduction principles. The equivalent reluctance can be determined by the transformer dimensions and magnetic characteristics.

$$\mathcal{R}_{eq} = \mathcal{R}_c + \left(\frac{2}{\mathcal{R}_{eq1}} + \frac{1}{\mathcal{R}_0} \right)^{-1}$$
$$\mathcal{R}_{eq1} = 2\mathcal{R}_Y + \mathcal{R}_L$$

For the laboratory testing, the 3-phase transformer is modelled as a bank of three single-phase 100 VA transformers, which is consistent with the practical arrangement of very large power transformers.

4. AVERAGE POWER THEORIES

Instantaneous and general power theory was developed with the aim of being applied to active power compensators. The theory has also been used to establish energy transmission properties in asymmetrical and distorted conditions [10].

The two basic properties of every non-active component of the apparent power are that they cause power loss and the amplitude of oscillation of power which does not contribute to a continuous unidirectional transfer of energy [11].

The nomenclature was revised and the term reactive power has been replaced with the term non-active power. This is done since the term reactive power implies some element of energy storage which may, or may not, be the case when non-active power is considered [9].

Instantaneous and average power theories typically decompose currents into active and non-active components. Malengret and Gaunt [9] have developed a general theory of instantaneous power that can be applied to m-wire systems with unequal impedances.
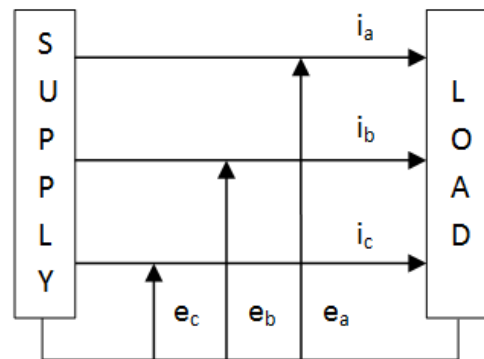
Figure 5: Three Phase Supply Connected to Load

Proceedings of the 19th Southern African Universities Power Engineering Conference
SAUPEC 2010, University of the Witwatersrand, Johannesburg
TOPIC E. ELECTROMAGNETICS

The values required for analysis are the load impedances, the line currents, phase voltages and information regarding the neutral wire.

The instantaneous power theory can be extended to the average power domain. The components of apparent power consist of an active component and two non-active components. The components of the non-active current are distinguished by the fact that one component can be compensated without energy storage elements while the other component requires energy storage for compensation [9].

5. INVESTIGATION TECHNIQUES

The investigation process involved simulations using the SIMULINK package from MATLAB. The laboratory model was built using three single-phase 100 VA transformers connected to form a three-phase transformer. The laboratory setup is illustrated in Figure 6.
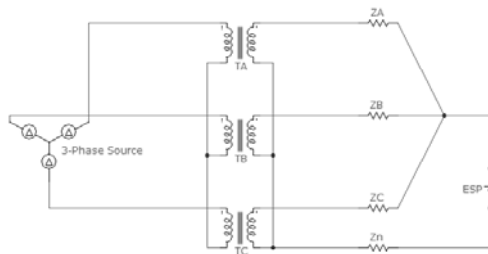
Figure 6: Laboratory Apparatus Circuit Diagram

The loads Z_A, Z_B and Z_C were set up using a combination of incandescent lamps and compact fluorescent lamps (CFLs).

The neutral impedance Z_N consisted of a variable resistor. The earth surface potential (ESP) was simulated using a 12 V battery.

Currents and voltages were sampled with a digital signal processor (DSP) card and processed in real time in a standard computer.

6. RESULTS

The power transfer characteristics were investigated for an unbalanced complex load using the conventional laboratory three-phase meter and the new definition - Table 1. The results for non-active power and power factor did not agree, illustrated in Figure 7 and Figure 8.

Table 1: Calculated Results for Unbalanced Load

S (Old)	S (New)	Q (Old)	Q (New)	PF (New)	PF (Old)
180	228	166	217	0.302	0.383
199	232	181	217	0.301	0.418
198	245	180	230	0.340	0.419
203	251	183	235	0.349	0.433
205	254	184	238	0.354	0.438
203	253	183	237	0.347	0.434
218	267	193	247	0.381	0.467
222	269	196	248	0.387	0.468
238	290	206	265	0.403	0.499
262	318	219	283	0.453	0.549
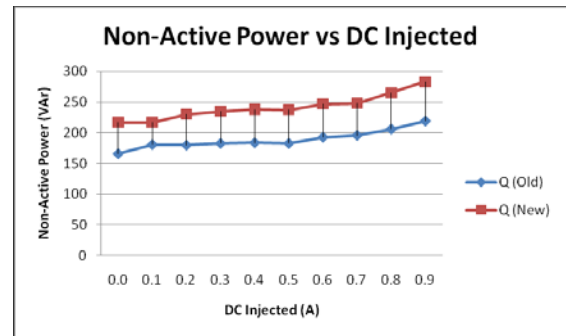
Figure 7: Non-Active Power versus DC Injected

The non-active power is higher using the new method indicating that the effect of non-active power in transformers has previously been underestimated.
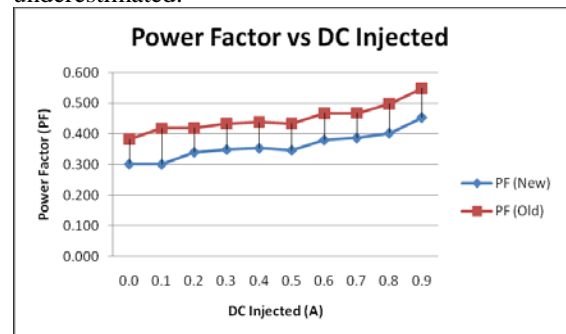
Figure 8: Power Factor versus DC Injected

The results obtained for a balanced complex load are plotted in Figure 9 and Figure 10.
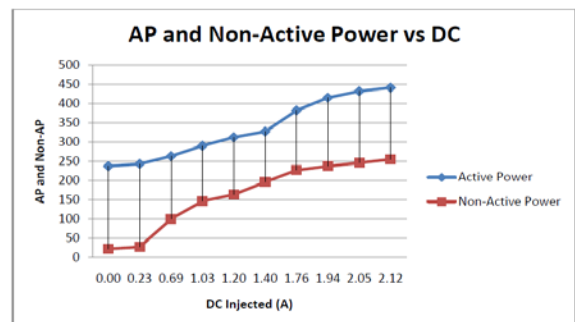
Figure 9: AP and Non-AP versus DC Injected   (Balanced Complex Load)

Proceedings of the 19th Southern African Universities Power Engineering Conference
SAUPEC 2010, University of the Witwatersrand, Johannesburg

TOPIC E. ELECTROMAGNETICS
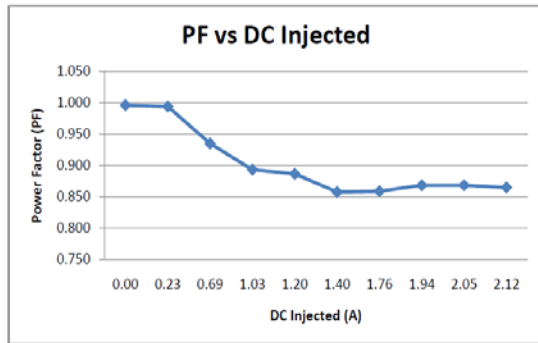
Figure 10: Power Factor versus DC Injected   (Balanced Load)

There is an increase in both active and non-active power as the DC injection increases. There is a corresponding decrease in the power factor.

The results obtained for an unbalanced complex load are plotted in Figure 11 and Figure 12.
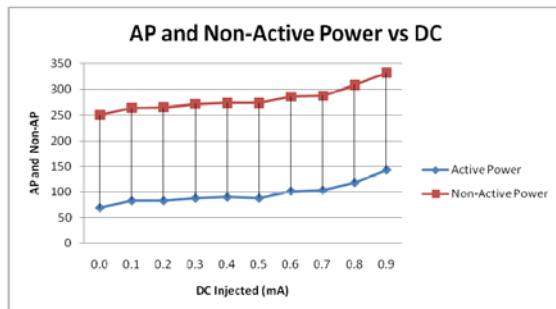
Figure 11: AP and Non-AP versus DC Injected (Unbalanced Load)
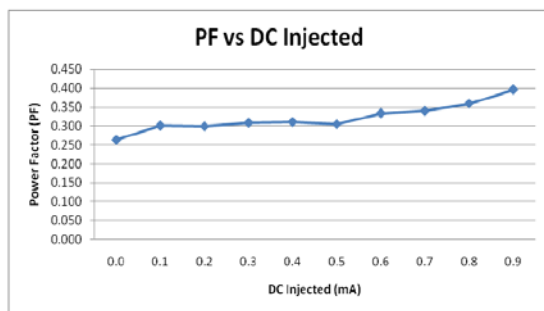
Figure 12: Power Factor versus DC Injected   (Unbalanced Load)

There is an increase in the power factor corresponding to an increase in the DC injection in the case of an unbalanced complex load.

7.   CONCLUSIONS AND RECOMMENDATIONS

The presence of geomagnetically induced currents (GICs), modelled as DC injection in this work, have an effect on the non-active power in a transformer.

The non-active power in a transformer is affected by the presence of harmonics as well as DC injection. The harmonics generated and the consequent total harmonic distortion (THD) is, however, a complicated function of the DC injection.

Further investigation should be undertaken using different transformer and load configurations.

REFERENCES

1   Molinski, T.S., "Why Utilities Respect Geomagnetically Induced Currents", Journal of Atmospheric and Solar-Terrestrial Physics 64 (2002) 1765-1778

2   Gombosi, T.I., "Physics of the Space Environment", Cambridge University Press, 1998

3   Breckenridge, TH., Cumming, T., Merron, J. "Geomagnetically Induced Current Detection and Monitoring", Seventh International Conference on Power System Protection, London, UK: IEE, 2001. Pp 250-253

4   Ahfock, A., Hewitt, A.J., "DC Magnetization of Transformers", IEE Proc. Electric Power Applications

5   Bolduc, L., Gaudreau, A., Dutil, A., "Saturation Time of Transformers under DC Excitation", Electric Power Systems Research 56 (2000) 95–102

6   Walling, R.A., Khan, A.H., "Characteristics of Transformer Exciting-Current During Geomagnetic Disturbances", IEEE Transaction on Power Delivery, Vol. 6, No.4, October 1991, pg. 1707-1713

7   Amuanyena, L.A.T., Gaunt, C.T., "Effects of Geomagnetically Induced Currents (GICs) on Power Transformers and Reactors", University of Cape Town

8   Price, P.R., "Geomagnetically Induced Current Effects on Transformers", IEEE Transactions on Power Delivery, Vol. 17, No. 4, October 2002

9   Malengret, M., Gaunt, C.T., "Decomposition of Currents in Three- and Four-Wire Systems", IEEE Transactions on Instrumentation and Measurement, Vol. 57, No. 5, May 2008

10 Emanuel, A.E., "On the Definition of Power Factor and Apparent Power in Unbalanced Polyphase Circuits with Sinusoidal Voltage and Currents", IEEE Transactions on Power Delivery, Vol. 8, No. 3, July 1993

11 Salmerón, P., Herrera, R.S., "Instantaneous Reactive Power Theory – A General Approach to Poly-Phase Systems", Electric Power Systems Research 79 (2009) 1263–1270

TOPIC E. ELECTROMAGNETICS

Proceedings of the 19th Southern African Universities Power Engineering Conference
SAUPEC 2010, University of the Witwatersrand, Johannesburg

HVDC ELECTROSTATIC FIELD MILL DEVELOPMENT

R Warrington*,   A J Otto**, H C Reader*** and R van Zyl*

*Cape Peninsula University of Technology, Department of Electrical Engineering, Bellville, South Africa

**Eskom, Research and Innovation Department, Lower Germiston Road, Roscherville, South Africa

***University of Stellenbosch, Dept. of E&E Engineering, Stellenbosch, Western Cape, South Africa

Abstract. It is important to be able to characterise the electrical environment under HVDC lines when doing line design. To achieve this we need to measure the electric field strength, space charge and ion current densities. We consider the design and development of a low-cost, robust electric field mill for measurement of especially the electric field at ground level under HVDC transmission lines. This work forms part of a larger project of long term measurement, monitoring and testing under HVDC lines. The measurements are compared to analytical and numerical results.

Key Words. Charge Simulation Method, Electric Field Sensor, Field Mill, High Voltage Direct Current

1. INTRODUCTION: AN INDUSTRY PERSPECTIVE

Prospects of new high-voltage direct current (HVDC) transmission schemes to transfer large amounts of power over long distances in sub-Saharan Africa has introduced a renewed interest in HVDC research. South Africa's only operational experience with HVDC is that of the Cahora Bassa hydroelectric scheme connecting Songo (Mozambique) and the Apollo converter station in Tshwane (South Africa) over a distance of approximately 1400km [1]. The bipolar transmission scheme has two transmission line spaced roughly 1km apart, effectively operating as two monopolar schemes of positive and negative polarity. To fully characterize the electric environment under HVDC transmission lines, one has to accurately measure the electric field ($\vec{E}$), ion current density ($\vec{J}$) and space charge density (ρ) [2, 3] that builds up during corona discharges. The space charge plays a critical role in the formation and suppression processes of direct current (DC) corona [4]. The electric field under HVDC lines therefore has an electrostatic space charge free component, as well as a space charge component [2]. Field mills are often used for the measurement of electric fields, charges and potentials [5]. The work in this paper forms part of a larger project of long term measurement, monitoring and testing under HVDC transmission lines similar to the work in [6]. We consider the design and development of a low-cost, robust electric field mill to measure the electric field at ground level under HVDC lines. The field mill will also be used to study the effect of space charge build-up on the electrical environment under the lines.

2. FIELD MILL: DESIGN AND DEVELOPMENT

A field mill is an electro-mechanical device used to measure high voltages, electric charge, atmospheric effects and electric field strength. It measures electric field by measuring the modulated, capacitively induced charge on metal electrodes.

The first phase of the research was greatly enhanced by a field mill electrode shell provided by *Grant et. al.* [7] to test the developed signal conditioning circuits. Next, using computer aided design (CAD); an electrode shell was designed and integrated with a power supply, data logger and global system for mobile communications (GSM) network. The CAD design is shown in Fig. 1.
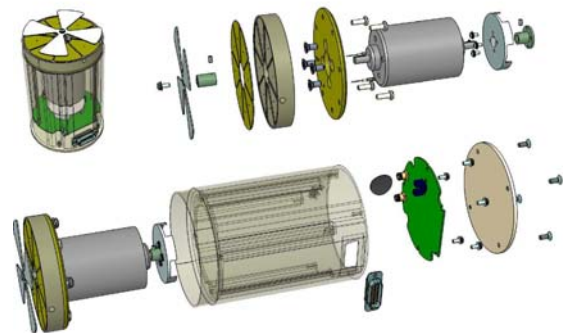
Fig. 1: Computer aided design (CAD) of the field mill electrode shell

2.1 Sensing Electrode

The sensing aperture of the field mill consists of 8 photo-etched brass electrodes connected in 2 pairs of 4 each, as shown in Fig. 2.
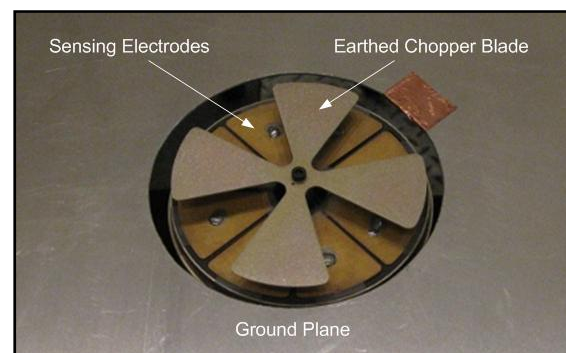
Fig. 2: Electrode pairs and earthed chopper blade flush with aluminum ground plane (top view)

Proceedings of the 19th Southern African Universities Power Engineering Conference
SAUPEC 2010, University of the Witwatersrand, Johannesburg
TOPIC E. ELECTROMAGNETICS

Each electrode pair is periodically exposed by an earthed chopper blade, modulating the incident E-field at the electrodes. The periodic signal induced on each electrode pair is 180° out of phase with respect to each other. Gauss's law dictates that the induced charge on a metal surface due to an incident electric field is given by equation 1 [5]:

$$Q(t) = \varepsilon_0 E(t) A(t) \qquad (1)$$

In equation 1, Q is the surface charge in C, ε_0 the permittivity of free space F/m, E the incident electric field V/m perpendicular to the surface and A the surface area in m^2.

2.2 Conditioning Circuit Design

The charge induced on the electrodes will vary with time and generate an alternating current with amplitude proportional to the electric field strength. The signals from each electrode pair is separately amplified using charge amplifiers, which convert the induced charge to a voltage.

A differential amplifier adds the two signals by compensating for the 180° phase shift, which is then fed to a non-inverting amplifier and rectification section. This section adjusts the gain and converts the output signal from AC to DC. A flow diagram of the conditioning circuitry is shown in Fig. 3.
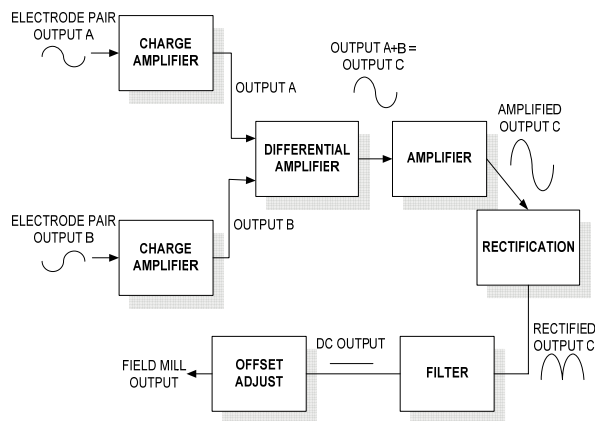
Fig. 3: Conditioning circuitry flow diagram

2.3 EMC Housing and Shielding

The signal processing circuitry is housed inside the grounded field mill electrode shell as it provides electromagnetic (EM) shielding against radio frequency interference (RFI). The bottom view, looking into the shell, is shown in Fig. 4. For the printed circuit board (PCB) layout of the conditioning circuit, an electromagnetic compatibility (EMC) design guide [8] was followed to improve the circuit's susceptibility to internal and external interference. The data logger is housed in an unpainted diecast aluminum EM shielded box with power filtering and 360° bonding for cable entry into the box. Cable braiding is placed between the lid and box for improved EM shielding from surface currents induced by the nearby electric fields.

The developed field mill prototype manufactured from the CAD design in Fig. 1 is shown in Fig. 5.
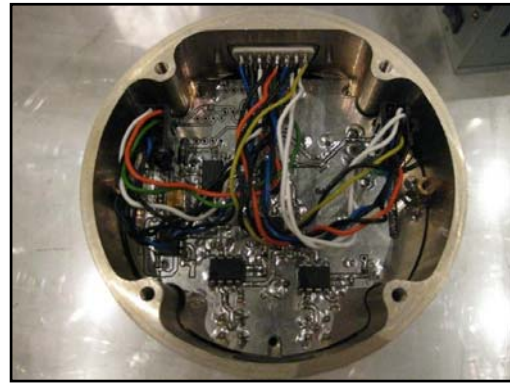
Fig. 4: The signal conditioning circuitry housed inside the electrode shell for electromagnetic shielding (bottom view looking into electrode shell)

Fig. 5: Developed field mill prototype for E-field measurements

2.4 Power Supply

The biasing requirements are: 5V for the humidity, temperature and opto-sensors, +/-12V for the op-amp circuitry. The 5V was also used to power the motor which required a start-up current of between 4 and 5A. A 200W desktop computer power supply was modified to supply 5V, 12V, -12V and, if needed, 3.3V. The reliability of the supply was tested over a prolonged period, supplying power to a number of devices during the test. The current handling capability of the power supply exceeded the field mill current requirements, but served as a cost-effective and robust solution.

2.5 Data Logger and System Integration

The DT80 data logger [9] was used during measurements. It has a USB interface for on site data extraction and a RS232 communications port for connecting a GSM module. The functionality of the telemetry part of the system was successfully tested in a laboratory. Fig. 6 shows the integrated field mill and remote data logging system.

TOPIC E. ELECTROMAGNETICS

Proceedings of the 19th Southern African Universities Power Engineering Conference
SAUPEC 2010, University of the Witwatersrand, Johannesburg
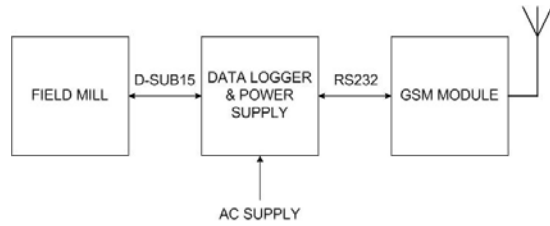
Fig. 6: Field mill system with remote data logging functionality.

The data logger was configured via a USB interface and software package called "*DeLogger*". Logged data was then processed using a software package called "*DeView*". DeView provides quick access to charts and tabulated data. The field mill was powered and interfaced through a D-sub15 connector pair, while the system was powered from an external 220V AC source.

3. CALIBRATION

The procedure for calibrating the electric field sensor was done according to the standard in [10] and is discussed in section 3.1. The calibration was done in a screened room environment to ensure that no background radio interference (RI) coupled to the measurement system.

3.1 IEEE Standard: DC Electric Field Measurement

Because of the space charge in the vicinity of HVDC transmission lines, a known DC electric field with space charge is desirable for calibrating the instrument. It is suggested in [10] that the region of uniformity at the location of the sensing probe is sufficiently large to reduce the uncertainty in the value of the field strength. The electric field should not be perturbed in any way by nearby objects. The dimensions of the calibration apparatus should be sufficiently large that the sensing electrode does not disturb the charge distributions on the electrodes producing the electric field. An experimental arrangement that satisfies the above criteria is the parallel plate configuration and both a calibration procedure with and without space charge present is discussed in [10]. It is suggested, however, that for ion current densities and electric fields near HVDC transmission lines, the measurement error due to space charge may be negligible or small. The simpler space charge free system is considered adequate for the calibration processes and is discussed in section 3.2.

3.2 Parallel Plate Arrangement

The space charge free parallel plate arrangement for the calibration of the field mill is shown in Fig. 7. According to [10] the earthed chopper blade must be flush with the ground plane and the plate spacing must be no less than three times the radius of the aperture for the sensing electrodes. The outer edge of sensing electrode must be no closer than two times the plate spacing.

The plates were chosen such that it was at least ten times the diameter of the sensing aperture with a spacing of 150mm between the plates.
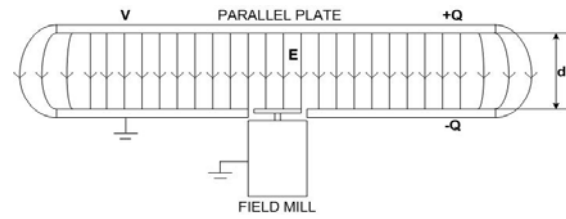
Fig. 7: Space charge free parallel plate arrangement for field mill calibration

The capacitance of the parallel plate arrangement is then given by

$$C = \frac{\varepsilon_0 A}{d} \qquad (2)$$

where ε_0 is the permittivity of free space in *F/m*, *A* is the area of the plates in m^2 and *d* is the distance between the plates in *m*. The charge voltage relationship is given by

$$C = \frac{Q}{V} \qquad (3)$$

where *Q* is the charge in *C*, *V* is the voltage in *V* and *C* is the capacitance in *F*. The electric field between two parallel plates in *V/m* is calculated using equation 4:

$$E = \frac{V}{d} \qquad (4)$$

where *V* is the applied voltage in *V* and *d* is the distance between the plates in *m*.

3.3 Calibration Results

Various voltages were applied to the parallel plate configuration shown in Fig. 8 while the field mill output was recorded. The output was then correlated with the calculated magnitude of the electric field. The linear relationship between the applied electric field and field mill voltage output is shown in Fig. 9 for two measurement sets of increasing and decreasing applied voltage levels.
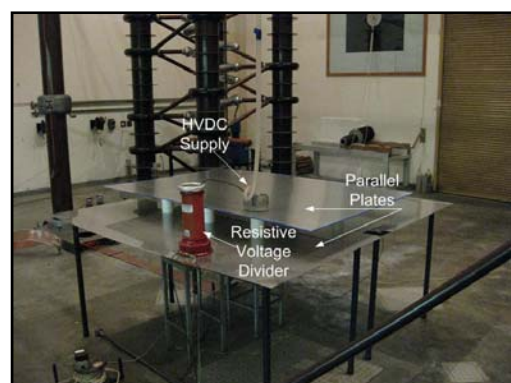
Fig. 8: Experimental parallel plate arrangement for calibration of field mill

Proceedings of the 19th Southern African Universities Power Engineering Conference
SAUPEC 2010, University of the Witwatersrand, Johannesburg

TOPIC E. ELECTROMAGNETICS
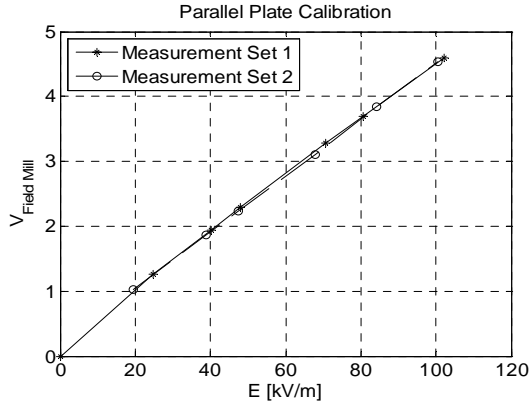
Fig. 9: Parallel plate calibration results: linear relationship between applied electric field and field mill voltage output

4. WIRE PLANE NUMERICAL SOLUTION

4.1 Charge Simulation Method

The charge simulation method (CSM) is a numerical method used for the computation of electrostatic fields [11]. This method is based on the use of fictitious line charges as particular solutions of Laplace's and Poisson's equations [12]. The electrostatic potential at any point in the simulated region can be found by the summation of the potentials resulting from the individual charges. The CSM has been proven to be an effective numerical method where good accuracy in highly divergent fields are required [13], and was used to compute the space charge free electrostatic field of the wire-plane configuration discussed in section 4.2.

4.2 Wire-Plane Configuration

The wire-plane arrangement is shown in Fig. 10 with the sensing electrode placed flush with the ground plane and placed directly below the artificial source on the conductor. This will ensure maximum exposure of sensing electrodes to space charge during corona events. The capacitance C of the line is given by equation 5.

$$ C = \frac{2\pi\varepsilon_0}{\ln\left(\frac{h}{R} + \sqrt{\left(\frac{h}{R}\right)^2 - 1}\right)} \quad (5) $$

In equation 5, h is height of the conductor centre above the ground plane and R is the conductor radius in m. The potential Φ at a point (x, y) in the two dimensional Cartesian coordinate system is given in [12, 13] by equation 6.

$$ \phi(x, y) = -\frac{\lambda_l}{2\pi\varepsilon_0} \ln \frac{\sqrt{(a - y)^2 + x^2}}{\sqrt{(a + y)^2 + x^2}} \quad (6) $$
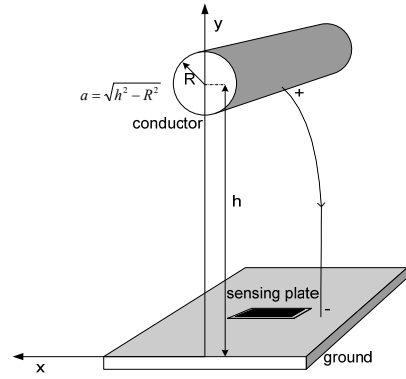
Fig.10: Wire-plane configuration and sensing electrode flush with ground plane

In equation 6 $\lambda_l = CV$ *is* the charge per unit length of the conductor, $a = \sqrt{h^2 - R^2}$ is a constant, V is the applied voltage and C is the capacitance of the line. The electric field between the conductor and ground plane can be described by a line charge in the centre of the conductor and its image below the ground plane. In the physical situation, however, the charge per unit length is induced on the surface of the ground plane. The electric field vector at a point (x, y) is given in equation 7 by the negative gradient of the scalar potential in equation 5.

$$ \vec{E}(x, y) = -\vec{\nabla}\phi(x, y) = -\left(\frac{\partial\phi}{\partial x}\hat{x} + \frac{\partial\phi}{\partial y}\hat{y}\right) \quad (7) $$

The computed scalar potential distribution for a wire plane configuration is shown in Fig. 11, while the vector E-field distribution is shown in Fig. 12. The values of the space charge free electrostatic E-field for various applied conductor surface voltage gradients were computed and compared to field mill measured values in Fig. 15.

5. WIRE PLANE MEASUREMENT RESULTS

The wire plane experimental arrangement with a conductor height of *h=0.6m* is shown in Fig. 13. To investigate the effect of the space charge created during corona events on the electric field at ground level, a smooth copper conductor with an artificial corona source shown in Fig. 14 was used. Electric field measurements with and without space charge present in the electrode gap were conducted. The artificial source was a *1mm* steel sphere with half of its surface protruding out of an otherwise smooth copper conductor. This will result in an enhancement of the field in the close vicinity of the surface irregularity that will result in the various ionization and electron avalanche processes. These processes give rise to corona discharge and space charge formation, and will occur at a much lower surface voltage gradient at the artificial source than that necessary to put the whole conductor into corona. This also means that the regional location of the space charge formation is known.

Proceedings of the 19th Southern African Universities Power Engineering Conference
SAUPEC 2010, University of the Witwatersrand, Johannesburg

TOPIC E. ELECTROMAGNETICS

Streamer discharges at the artificial source for various applied conductor surface voltage gradients captured with an ultra violet (UV) intensifying corona camera is shown in Fig. 15. The streamer discharges made part of a visual investigation. As applied voltage was increased a increase in streamer length as well as brightness of the glow could clearly be noted.
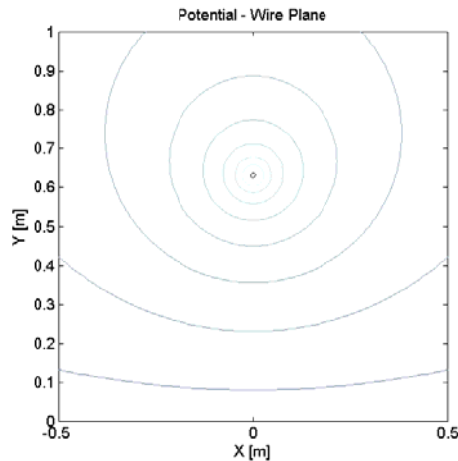
Fig. 11: Computed scalar potential for wire-plane geometry
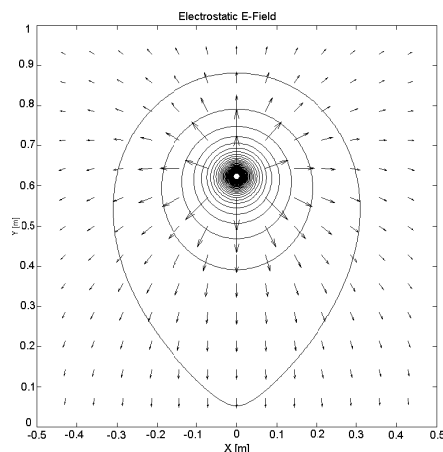
Fig. 12: Computed vector electric field for wire-plane geometry

Fig. 13: Experimental setup of wire-plane configuration and sensing electrode flush with ground plane

The parallel lines in the top of the image are a side view reference of the conductor while the vertical scale on the left of each discharge image is in 1cm increments.

Fig. 14: Smooth copper conductor with artificial corona source
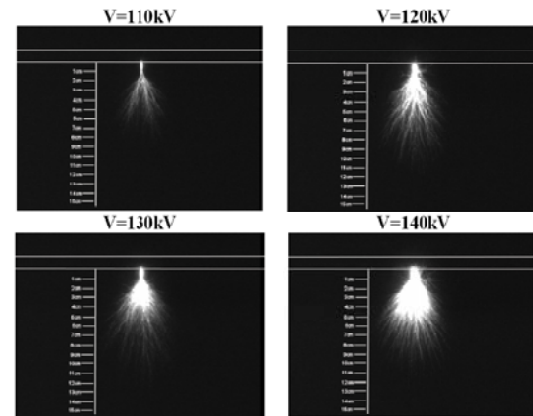
Fig.15: Set of corona streamer discharges captured with UV intensifying corona camera (vertical 1cm scale increments)

The space charge free measurements were made by removing the artificial source, resulting in only a smooth copper conductor above a ground plane. The measured and numerically computed space charge free electrostatic E-field results correlate well and are shown in Fig. 16. The enhancement of the electric field in the electrode gap, as well as the variation due to the formation of the ion space charge is evident in Fig. 16 for surface voltage gradient beyond the corona inception level. The sensing electrodes not only experience the induced charge due to the electrostatic field, but also both a displacement and conduction current component due to the movement and neutralisation of the ion space charge on the sensing electrodes. The variation in the electric field gives an indication of the amount of ion space charge created during corona events.

6. DISCUSSION AND CONCLUSIONS

The work discussed in this paper provides an overview of the steps and investigation performed during the development and calibration of a field mill.

Proceedings of the 19th Southern African Universities Power Engineering Conference
SAUPEC 2010, University of the Witwatersrand, Johannesburg

TOPIC E. ELECTROMAGNETICS

Using the field mill, changes in electric field as well as the effects of space charge due to corona on the incident electric field were recorded. The space charge free measurements related well to numerical results using the charge simulation method (CSM).
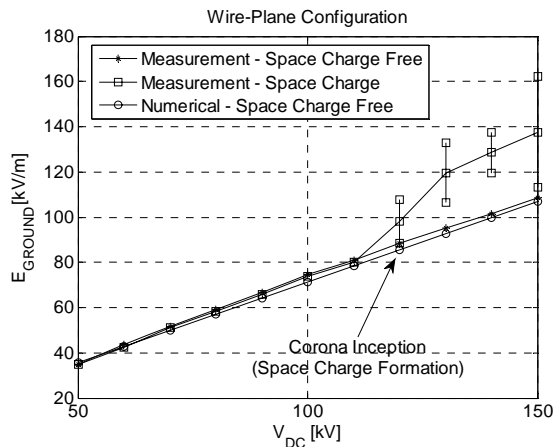
Fig.16: Wire-plane configuration measurements and computation with and without space charge present in the electrode gap

The recorded results obtained by the field mill met all expectations in providing stable and linear readings for the whole space charge free E-field range. The effects of space charge formation and movements during corona discharge can now be investigated by studying the variation of the E-field. The field mill and integrated logging system can be used for long term monitoring, testing and measurements under HVDC lines and the results will be used in the study to predict corona radio interference excitation functions.

REFERENCES

[1] A. J. Otto, P. J. Pieterse, H. C. Reader, "*An Electrometer to Measure Ion Space Charge*", in the Proceedings of the 18th South African Universities Power Engineering Conference (SAUPEC), Stellenbosch, Western Cape, South Africa, January 2009, pp. 117-121

[2] T. D. Bracken, A. S. Capon, D. V. Montgomery, "*Ground Level Electric Fields and Ion Currents on the Celilo-Sylmar ±400kV DC Intertie During Fair Weather*", IEEE Transactions on Power Apparatus and Systems, vol. PAS-97, March/April 1978, pp. 370-378

[3] P. S. Maruvada, R. D. Dallaire, R. Pedneault, "*Development of Field-Mill Instruments for Ground-Level and Above-Ground Electric Field Measurement under HVDC Transmission Lines*", IEEE Transactions on Power Apparatus and Systems, vol. PAS-102, no. 3, March 1983

[4] A. J. Otto, H. C. Reader, P. J. Pieterse, "*Ion Space Charge Measurement and Simulation*", in the Proceedings of the 16th International Symposium of High Voltage (ISH), Cape Town, South Africa, 24-28 August 2009

[5] P. Tant, B. Bolsens, T. Sels, D. Von Domellen, J. Driesen, R. Belsmans "*Design and Application of a Field Mill as a High Voltage DC Meter*", IEEE Transactions on Instrumentation and Measurement, vol. 56, no. 4, 2007

[6] V. L. Chartier, L. D. Dickson, L. Y. Lee. R. D. Stearns, "*Performance of a Long Term Unattended Station for Measuring DC Fields and Air Ions from an Operating HVDC Line*", IEEE Transactions on Power Delivery, vol. 4, no. 2, April 1989

[7] M. D. Grant, J. M. Garrad, K. M. Nixon, "*Low Cost Electric Field Mill: Design, Construction and Testing*", Proceedings of the 15th South African Universities Power Engineering Conference (SAUPEC), Durban, KwaZulu-Natal, South Africa, January 2006, pp. 163-166

[8] "*Electromagnetic Compatibility Design Guide*", Design Guide by TECKNIT, 1998, pp. 3-13

[9] "*DT80/81/85 Users Manual*", dataTaker - Intelligent Data Logging Products, Datasheet UM-0085-A7, 2008

[10] "*IEEE Guide for Measurement of DC Electric Field Strength and Ion Related Quantities*", IEEE Std 1227-1990 (R2001)

[11] A. J. Otto, "*Direct Current Conductor Corona Modelling and Metrology*", PhD Dissertation, University of Stellenbosch, Western Cape, South Africa, September 2009

[12] H. Singer, H. Steinbigler and P. Weiss, "*A Charge Simulation Method for the Calculation of High Voltage Fields*", IEEE Power Engineering Society Winter Meeting, 1973, pp. 1660-1668

[13] E. Kuffel, W. S. Zaengel, J. Kuffel, "*High Voltage Engineering: Fundamental*", 2nd edition, Butterworth-Heineman, 2005

[14] H. A. Haus, J. R. Melcher, "*Electromagnetic Fields and Energy*", Prentice-Hall, Inc., 1989

[15] S. Ramo, J. R. Whinnery, T. van Duzer, "*Fields and Waves in Communication Electronics*", 3rd edition, John Wiley & Sons, Inc., 1994

Topic F

Control and Applications

ESTIMATING THE EMBODIED ENERGY AND ENERGY PAYBACK PERIOD WHEN REPLACING AN ELECTRIC MOTOR

C. Smythe and W. A. Cronje

School of Electrical & Information Engineering, University of the Witwatersrand, Private Bag 3, 2050, Johannesburg, South Africa

Abstract: With the recent energy shortages in South Africa, the need to save energy has become a national priority. Eskom has implemented an Energy Efficient Motors Programme which aims to save energy by offering subsidies to users who replace old motors with new energy efficient motors. This paper aims to investigate the deeper implications of such a policy. The approach to estimating the embodied energy is described in detail. By including the embodied energy of the replacement motors, an upfront energy loss must therefore be recovered before any actual savings take effect. We can therefore determine the energy payback period for a particular size motor.

Key Words: Embodied Energy, Induction Motor, Efficiency, Energy Payback Period.

1. INTRODUCTION

The aim of this research was to estimate the embodied energy of various sized electric motors.

This research was prompted by the recent Energy shortages in South Africa, and is in response to the Energy Efficient Motors (EEM) Programme run by Eskom Demand Side Management (DSM). The programme offers motor users subsidies when trading in an old motor for a new energy efficient motor. The old motors are then scrapped to ensure that those "inefficient" motors cannot be used for any future applications [1].

Industry is a major consumer of electricity where an estimated 100 000 motors consume up to 10 GW of electrical power. This accounts for about 60% of all electrical energy used by industry. Clearly improving the efficiency of these motors could play a pivotal role in reducing the South African electricity demand [1].

We however also need to consider the deeper implications of such a policy. Energy is required to manufacture any replacement motors. Essentially we need to weigh up the expected energy savings against the upfront embodied energy that goes into manufacturing the replacement motor. Additionally an old working motor is scrapped when the trade-in takes place, and therefore any other applications which could have used that motor will now need another new motor.

2. EMBODIED ENERGY

The term embodied energy is the total energy necessary to produce and maintain a product for its entire lifecycle. The embodied energy of an electric motor is therefore the total energy which goes into manufacturing and maintaining the motor [2].

Embodied energy can be divided into two categories:

- The initial embodied energy represents the non-renewable energy consumed in the acquisition of raw materials, their processing, transportation and finally the manufacture of the motor itself.
- The recurring embodied energy represents the non-renewable energy consumed to maintain, repair, restore, refurbish or replace components during the life of the motor.

This paper only considers the initial embodied energy.

3. APPROACH AND ASSUMPTIONS

With the assistance of some reputable motor manufacturers, the embodied energy of various induction motors ranging from 200 kW to 6 500 kW were estimated. The data covered a one year period.

The mass of all copper and steel purchases over that period were tallied. Although other materials form part of the motor, steel and copper are by far the largest contributors so all others have been neglected. Various sources estimate the embodied energy in copper and steel, and these values were used for the estimate. Additionally the utility bills for the plant have also been made available, and the monthly energy costs (electricity and gas) were included in the analysis.

By adding the raw materials component of embodied energy (steel and copper) to the energy used by the factory (electricity and gas) over the period, we could estimate the total embodied energy for all motors produced during the period. Finally this total embodied energy needed to be divided appropriately between all motors manufactured during that period so that the embodied energy for a single motor could be obtained.

Table 1: The Manufacturers Motor Data

Motor Class	kW Rating Range		Total kW Ratings			Number Manufactured			Average kW Rating		
	Min	Max	Cage	Wound	Total	Cage	Wound	Total	Cage	Wound	Total
A	200	720	46 827	-	46 827	138	-	138	339.33	-	339.33
B	660	1 700	34 060	-	34 060	30	-	30	1 135.33	-	1 135.33
C	683	2 700	80 306	37 238	117 544	46	20	66	1 745.79	1 861.90	1 780.97
D	2985	6 500	13 200	64 803	78 003	4	15	19	3 300.00	4 320.20	4 105.42
Total	-	-	174 393	10 2041	276 434	218	35	253	799.968	2 915.46	1 092.63

Since the steel and copper are large contributors to the embodied energy of each motor, it is reasonable to assume that the raw materials component of the embodied energy of each motor is proportional to its mass.

Also since the electricity and gas can only contribute to the embodied energy while the motor is actually being manufactured, we assumed that the gas and electricity portion of the embodied energy was proportional to the lead time for that motor.

Finally since the lead time of some of the larger motors can be up to 9 months, it is likely that some of the motors which are considered to be manufactured during the period were started many months earlier. Also many of the motors started during the period will not be finished and therefore not counted. We assumed that the factory output from month to month over the period and for a few months leading up to the period was fairly constant, and therefore the two effects cancel out.

4. THE MOTOR DATA

Table 1 shows the motors which were manufactured over the considered 1 year period. The motors were divided into 4 classes, where each class includes a different range of motor ratings. The motors were also divided into squirrel cage and wound rotor induction motors. Since Class A and B do not include wound rotor motors. A total of 6 groups therefore should be considered.

4.1. Generating a List of Motors

Since only a summary of the motors manufactured during the period was made available, the next step was to generate a list of motors to fit the data given in Table 1.

This was achieved by assigning Probability Density Function PDF (and associated Cumulative Density Function (CDF)) to fits the data for each group. PDFs and CDFs are most commonly used in statistics to describe probabilities, in this instance however we are simply using them as a tool to generate a list of motors to fit the data. It is a deterministic algorithm, and has nothing at all to do with probability [3].

The PDFs were developed as follows:

1. Assign a temporary function (this function should be strictly non-negative).

$$f(x) = e^{\frac{k}{X_{range}}(x - X_{av})} \tag{1}$$

2. Find the area under the curve.

$$F(x) = \int_{X_{start}}^{x} f(\alpha)\ d\alpha \tag{2}$$

3. Convert $f(x)$ into a PDF by ensuring that the area under the curve is 1.

$$pdf(x) = \frac{f(x)}{F(X_{end})} \tag{3}$$

4. Convert $F(x)$ into a CDF.

$$cdf(x) = \frac{F(x)}{F(X_{end})} \tag{4}$$

The following four functions were used in the analysis. They were all chosen since they have horizontal asymptotes, so it is easy to ensure that the functions are strictly non-negative. Four different functions were chosen since we are unsure which distribution best models the data.

$$f_0(x) = 1 \tag{5}$$

$$f_1(x) = \text{DiracDelta}(x - X_{av}) \tag{6}$$

$$f_2(x) = e^{\frac{k}{X_{range}}(x - X_{av})} \tag{7}$$

$$f_3(x) = 1 + \tanh\left(\frac{k}{X_{range}}(x - X_{av})\right) \tag{8}$$

Where:
- $f(x)$: Temporary function which describes the shape of the PDF (un-normalised PDF)
- $pdf(x)$: The PDF used to generate a list
- $cdf(x)$: The corresponding CDF
- X_{start}: The minimum kW rating for the motor class
- X_{end}: The maximum kW rating for the motor class
- X_{av}: The average kW rating for the group of motors
- $X_{range} = X_{end} - X_{start}$
- $X_{mid} = \frac{X_{end} + X_{start}}{2}$
- k: The slope constant

Proceedings of the 19th Southern African Universities Power Engineering Conference
TOPIC F. CONTROL AND APPLICATIONS
SAUPEC 2010, University of the Witwatersrand, Johannesburg
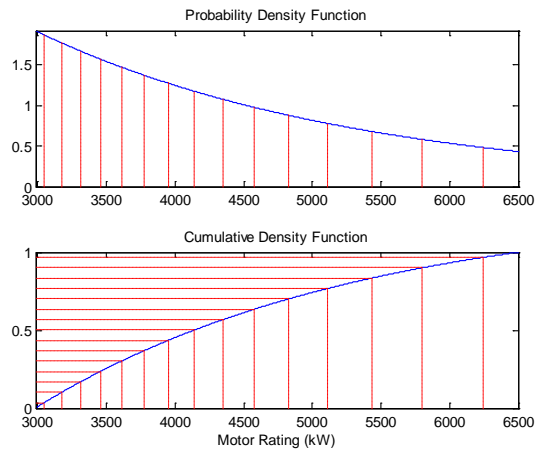
Figure 1: Generating a List of Motors

Figure 1 illustrates how the PDF and CDF were used to generate a list of motors. The example above uses the exponential function (Equation (6)) for the class D wound rotor motors. The 15 vertical dashed lines show the list of motors. The horizontal dotted lines on the CDF are equally spaced, and were used to generate the list of motors. They all lie in the specified range (from 2985 to 6500), and as expected are bunched closer together at higher probabilities.

The final step is to adjust the slope constant k, to ensure that the sum of all kilowatt ratings corresponds to Table 1. This is an iterative process.

The function $f_1(x)$ is the simplest and will result in a list in which all motors lie on the average value of each group. The function $f_2(x)$ is more realistic since the list of motors will be spread over the entire range. Since the exponential function has a steep slope at one end, the motors will tend to clump towards one edge of the range. For this reason the hyperbolic tangent function was used for $f_3(x)$ since they have horizontal asymptotes at both ends.

The function $f_0(x)$ will uniformly distribute the motors of each group. The average rating for each will therefore always be at the midpoint of the range. Since the average rating of each group was not necessarily at the midpoint, the function was not used as it fails to accurately model the data supplied by the manufacturers.

5. TOTAL EMBODIED ENERGY

Once the list of motors has been generated, each motor in the list was assigned an embodied energy. The total embodied energy of all the motors in the list must correspond to raw materials, gas and electricity used during the period.

5.1. Raw Materials Component

Over the period, the manufacturers used about 3 248 000 kg of steel and 215 000 kg of Copper. Although the embodied energy depends on the grade of steel and copper used, and also where and how the raw material was mined from the earth, we shall assume a constant for the energy content of both the steel and copper.

The embodied energy of steel was estimated to be 32.0 MJ/kg (8.89 kWh/kg), and 70.6 MJ/kg (19.6 kWh/kg) was used for copper [2].

Table 2: Embodied Energy of Raw Materials

	Mass kg	Embodied Energy MJ	kWh
Steel	3 248 000	103 936 000	28 871 111
Copper	215 000	15 179 000	4 216 389
Total	-	119 115 000	33 087 500

5.2. Electricity and Gas Component

The manufacturers also used about 3 863 200 units of electricity and 193 314 units of gas. Each unit of electricity corresponds to 3.6 MJ (1 kWh). For gas each unit refers to 1 m^3 and has an energy content of 40.393 MJ/m^3 (11.220 kWh/m^3)

Table 3: Embodied Energy of Raw Materials

	Units	Embodied Energy MJ	kWh
Electricity	3 863 200	13 907 520	3 863 200
Gas	193 314	7 808 532	2 169 037
Total	-	21 716 052	6 032 237

Therefore the total embodied energy for all motors manufactured during the period was 140 831 052 MJ (39 119 737 kWh).

6. EMBODIED ENERGY OF EACH MOTOR

As discussed earlier we assumed that the raw materials component of the embodied energy is proportional to the mass of the motor. The electricity and gas component of the embodied energy was assumed to be proportional to the lead time for the motor. A relationship for the mass and lead time of a motor as a function of its power rating must therefore be determined. A second order polynomial is used to fit the mass and lead time data.

Table 4: Mass and Lead Time Data

Motor Rating (kW)	Motor Mass (kg)	Motor Lead Time (Weeks)	Weight	
425	3 350	10	(A)	138
995	4 250	10	(B&C)	10+11
1 000	5 680	10	(B&C)	10+11
1 500	8 100	15	(B&C)	10+11
1 800	9 680	15	(C)	11
2 000	12 100	15	(C)	11
2 240	16 060	18	(C)	11
2 985	22 380	21	(D)	6.3
3 300	29 680	23	(D)	6.3
4 476	32 300	25	(D)	6.3

Figure 3: Mass and Lead Time Fit Using Weights

We are now able to determine the embodied energy of each of the motors in the list.

$$E_{mass}(X_i) = \frac{mass(X_i)}{\sum mass(X_i)} E_{mass\ total} \qquad (9)$$

$$E_{time}(X_i) = \frac{time(X_i)}{\sum time(X_i)} E_{time\ total} \qquad (10)$$

$$E(X_i) = E_{mass}(X_i) + E_{time}(X_i) \qquad (11)$$

Where:

X_i: The power rating of a particular motor in the list of motors

$E_{mass}(X_i)$:   The raw materials component of the embodied energy of that motor

$E_{time}(X_i)$:   The electricity and gas component of the embodied energy of that motor

$E(X_i)$:   The total embodied energy of that motor

$mass(X_i)$:   The mass of that motor

$time(X_i)$:   The lead time of that motor

$E_{mass\ total}$:   The total raw materials component of embodied energy

$E_{time\ total}$:   The total electricity and gas component of embodied energy

Figure 2: Mass and Lead Time Fit (Ignoring Weights)

Figure 2 shows the least squares fits of the data from Table 4 (with the weights ignored). We can see that the Mass fit goes negative for the small motor power ratings. This is clearly incorrect, and the problem is exaggerated since the most of the motors in the data provided fall in the smallest category. Clearly if anything we want the fit to be most accurate at these lower values where the bulk of the motors are situated, and therefore we must assign weights to the data points we want to fit.

The weights should be assigned to be proportional to the number of motors around that point. Let us start with the 138 motors in Class A (200 to 720 kW). Only the first point in Table 4 falls in that range, and must take the weight of all the Class A motors. The next three points fall in the range of Class B, so the 30 Class B motors are evenly distributed over those points (10 each). The 66 Class C motors and the 19 Class D motors are used to assign weights in the same way. Note that three of the points fall in the range of both Class B & C, and will therefore receive weights from both. Weighting the points like this ensure that the fit is most accurate in the regions where the bulk of the motors lie.

TOPIC F. CONTROL AND APPLICATIONS

Proceedings of the 19th Southern African Universities Power Engineering Conference
SAUPEC 2010, University of the Witwatersrand, Johannesburg

Figure 4: Plot of Embodied Energy as a Function of Motor Power Rating

Figure 4 shows the embodied energy as a function of motor power rating for each of the four functions (Equations (5)-(8)). It appears as though there are only three curves in the figure, however the results from $f_2(x)$ and $f_3(x)$ are just too similar to distinguish. We will use the results from $f_3(x)$ for the next section

Table 5: Embodied Energy and Power Rating

Motor Rating (kW)	Embodied Energy (kWh)
200	50 960
1 000	126 800
6 500	1 132 000

7. ENERGY PAYBACK PERIOD

Finally we are ready to compare the energy savings due to a possible increase in efficiency against the upfront embodied energy of a new replacement motor.

We shall assume a constant service level, therefore the output power will remain constant with both the new and old motors. (Although this is not necessarily a realistic assumption as the service level is usually related to the efficiency, it illustrates the point.)

$$T_{payback} = \frac{E_{embodied}}{P_{in\ old} - P_{in\ new}} \qquad (12)$$

$$\eta = \frac{P_{out}}{P_{in}} \qquad (13)$$

$$T_{payback} = \frac{E_{embodied}}{P_{out}} \frac{\eta_{new}\ \eta_{old}}{\eta_{new} - \eta_{old}} \qquad (14)$$

Where:

$T_{payback}$: The payback period of the new motor
$E_{embodied}$: The embodied energy of the new motor

P_{in} : The input power of the motor
P_{out} : The output power of the motor (this is the motor's power rating)
η : The efficiency of the motor

Clearly the payback period depends on the efficiencies of both motors (old and new), as well as the embodied energy and power rating.
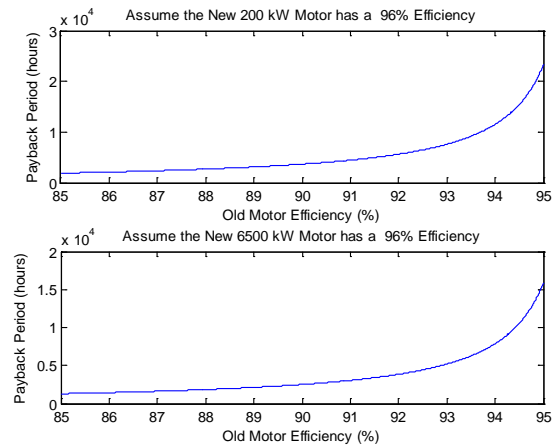
Figure 5: The Energy Payback Period Assuming the New Motor is 96% Efficient [4]

The curves in Figure 5 are hyperbolic and with asymptote at 95%, therefore as the efficiency of the old motor approaches the efficiency of the new motor it takes longer and longer to pay back the embodied energy of the new motor.

The above payback periods are stated in hours, so with 730 hours per month the payback periods of Figure 5 start at around 2.5 months. If we say that the motor only runs 5 hours per day, 5 days per week, then we should multiply by 6.7 and we are now looking at about 17 months. Additionally many motors in industry are overrated to give a comfortable safety margin, since these motors are not operating below their rated value. Since the embodied energy of the motors is a function of the rated power and not the operating power, the payback periods may be even higher.

8. ANALYSIS OF RESULTS

The Eskom DSM Energy Efficient Motors (EEM) programme only covers motors in the range from 1.1 kW to 90 kW. The smallest motors covered by this investigation are 200 kW and therefore we would need to extrapolate these results to cover the range of motors specified in the EEM programme. Since the manufacturing processes for smaller motors may be very different it is difficult and unwise to simply extrapolate the results of this analysis. However this research does show that the energy savings may be less than expected

when accounting for the embodied energy.

In order to accurately evaluate the EEM programme one would need to perform a similar investigation with a manufacturer producing the correct range of motors. The method presented in this paper however illustrates an approach that could be taken, and certainly indicates that further research in this area should be done to justify the EEM programme.

On the other hand many of the motors in the range covered by the EEM programme are manufactured overseas and imported. Eskom could therefore correctly say that the programme will help to reduce the South African demand. They are however only shifting that energy demand to some other country overseas. From a global perspective this may not reduce the global energy demand.

9. CONCLUSION

This paper defines embodied energy and describes how it can be used to make energy saving related decisions with regard to electric motors. A detailed description of how to determine the embodied energy for a motor of a particular size is then discussed. The data provided by has allowed us to estimate the embodied energy of any motor in the range from 200 kW to 6 500 kW.

Finally we are able to estimate the energy payback period of upgrading a motor to a new energy efficient motor. The energy savings due to increased efficiency are compared to the upfront embodied energy spent in manufacturing the motor. This gives an indication of how many hours the new motor will most likely need to operate before its energy savings cover the energy required to manufacture that motor.

ACKNOWLEDGEMENT

Special thanks go to our contacts from the different motor manufacturers for going out of their way to provide the data required for this research.

REFERENCES

[1] Eskom Demand Side Management (DSM). *Energy Efficient Motors programme*, http://www.eskomdsm.co.za/sites/default/files/u1/EEMPfactsheet.pdf, Last accessed 3 December 2009.

[2] *Measures of Sustainability – Embodied Energy*, http://www.canadianarchitect.com/asf/perspectives_sustainibility/measures_of_sustainablity/measures_of_sustainablity_embodied.htm, Last accessed 3 December 2009.

[3] G. M. Clark and D. Cook. *A Basic Course in Statistics*, Fourth Edition, Arnold Publishers, Inc., England, 1998.

[4] W. Deprez. *Energy Efficiency of Induction Machines: A Critical Assessment*, December 2008, https://repository.libis.kuleuven.be/dspace/bitstream/1979/2011/2/DoctoraatWD.pdf , Last accessed 3 December 2009.

TOPIC F. CONTROL AND APPLICATIONS

Proceedings of the 19th Southern African Universities Power Engineering Conference
SAUPEC 2010, University of the Witwatersrand, Johannesburg

TRANSFORMER VIBRATION MONITORING USING A WIRELESS SENSOR NETWORK

S Kaplan, J Davies, G de Jager and R Wilkinson

Centre for Instrumentation Research, Cape Peninsula University of Technology, Cape Town, South Africa

Abstract. Transformer vibration monitoring is often at present implemented under laboratory conditions. If it is to be used for preventative maintenance in the field, remote access, limited energy usage and data communications have to be taken into consideration. The present work describes results of a system using an IEEE 802.15.4 based wireless sensor network, a matrix of accelerometers and a communications gateway to measure the distribution of frequency amplitudes across a transformer tank surface. Frequency spectra at different positions on the surface show harmonics and the variation of vibration amplitudes across the surface are presented. With a change in load conditions the distribution of frequency amplitudes varies. The system can be installed on a remote transformer with only minor adaptations to ruggedise it.

Key Words. transformer monitoring, vibration sensing, wireless sensor network

1. INTRODUCTION

Electrical power network downtime due to unscheduled interruptions in the supply line can cause major economic disruption. Transformer breakdowns can cause such interruptions and a system that can act as a predictor for imminent transformer breakdown or failure would allow preventative maintenance or replacement of faulty equipment. Before such a predictive system can be implemented a system has to be developed that can monitor the performance of a transformer in the field under varying load conditions. A wireless sensor network (sensornet) that can remotely monitor the performance of power line transformers is proposed here.

Transformer condition monitoring through sensing various characteristics has been an ongoing area of research [1] and can be implemented by various methods. Abu-Elanien and Salama [2] published a survey of all methods such as thermal, vibration, partial discharge, dissolved gas and frequency response analysis. They concluded that dissolved gas analysis was "well defined, well understood and no more enhancements are to be expected" but the special arrangements it required limited its application to on-line monitoring. They furthermore concluded that other techniques needed more development before an on-line system of condition monitoring and fault diagnosis could be realised. This project initially concentrates on vibration analysis.

Remote monitoring of equipment has been greatly enhanced in recent years through the application of sensornets. Applications to power transformers have recently been explored by Baker et. al. [3] who sensed partial discharge and Nasipuri et.al. [4] who sensed temperature and bushing voltage phase differences. Behaviour of transformers in the field (not only in the laboratory) can be determined in much greater detail due to (a) smaller sized sensors, (b) wireless remote monitoring, (c) low power requirements and (d) long term monitoring. Considerations that have to be taken into account on vibration monitoring of power transformers are discussed in part 2. The system described in part 3 goes some way towards

this goal. In part 4 experimental results are presented and part 5 concludes that the proposed system could greatly enhance real-time vibration condition monitoring on power transformers in the field.

2. VIBRATION MONITORING OF POWER TRANSFORMERS

There have been several studies into using vibration methods to check conditions of power transformers [5], [6], [7], [8], [9]. Magnetostriction and electrodynamic forces acting on the core and windings of the transformer cause vibrations that are transmitted through the transformer oil to the tank walls. The tank walls therefore oscillate and the two-dimensional distributions of these oscillations are to some extent influenced by the normal modes of the tank wall. The mechanical deformations in the transformer are non-linear causing the generation of harmonics of the fundamental frequency. There is little evidence for significant harmonics above 1000Hz [5], [6], [7] when high frequency responses (up to 1MHz) used for diagnostics [8] are not considered for on-line monitoring. The distribution of amplitude vibrations over the tank surface has not been investigated in any detail other than positioning sensors over each core [5], [7].

In the system presented here we sampled the vibrations at about 500 samples per second restricting the frequency range to 250Hz. In order to determine the two-dimensional surface distribution of vibration amplitudes a matrix of accelerometers were deployed over the surface.

3. SYSTEM DESCRIPTION

To effectively map the vibration behaviour across the tank of a transformer, a low power, low maintenance, wireless sensor network was required that could easily be deployed in remote locations. The architecture for this system was developed using a sensornet of IEEE 802.15.4 nodes (motes) capable of

Proceedings of the 19th Southern African Universities Power Engineering Conference
SAUPEC 2010, University of the Witwatersrand, Johannesburg

TOPIC F. CONTROL AND APPLICATIONS
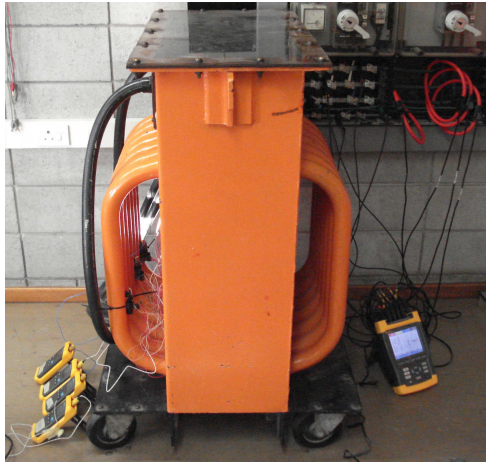
Fig. 1: Transformer during testing.
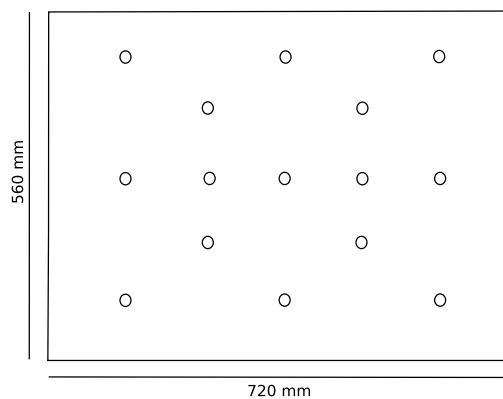
Fig. 2: Positioning of accelerometers in the area underneath the transformer cooling tubes.

communicating data across a gateway to a PC for post processing.

The sensornet was designed using TelosB wireless sensing nodes, each running an MSP430 processor and using the 2.4 GHz Chipcon CC2420 radio for spread spectrum 802.15.4 communication. Attached to the 12 bit ADC of each mote were five LIS352AX 3-axis accelerometers capable of measuring 0-2 g within a bandwidth of 2 kHz. The sensors were chosen predominantly for their operating voltage range and relatively wide sensing bandwidth.

The laboratory transformer under test was a 3 phase, star-delta, 47 kVA, 220 V, 50 Hz, isolation transformer with dimensions 720 mm by 960 mm by 335 mm (see figure 1). Each of the 15 sensors were mounted on small PCBs that were attached in a grid-like pattern to the side of the transformer tank (as in figure 2) on an area between the cooling tubes using thin double-sided tape. Lightweight wires were used to connect the sensors to individual motes mounted on the cooling tubes surrounding the plate. By placing the motes away from the vibrating plate, any additional mass loading effects were minimised.

The software for the network was implemented using

TinyOS in which a designated mote was chosen as a master. This mote polled for the required number of motes to be active, before sending out a synchronisation packet. The synchronisation packet informed each mote of the time period before a sample set is to be taken.

Sampling is performed at approximately 500 Hz with 600 samples recorded per channel. All ADC channels are sampled sequentially as fast as the ADC permits facilitating almost instantaneous sampling. The sample sets from each mote were then transmitted to a computer for logging and post processing at intervals of approximately 9 seconds.

Matlab was used as a post-processing tool to map the sampled acceleration data as a snapshot of displacement. The method used for this involved capturing the time domain sample sets for each sensor and performing a Fast Fourier Transform on the data. Absolute magnitude and phase were calculated and the dominant resonant modes for the plate were extracted by performing a maximum amplitude search of the power spectrum. Initial observation revealed distinct mechanical resonances caused by magnetostriction and interwinding vibration [5] typically present at around 100Hz. By dividing the absolute magnitude spectrum by $-\omega^2$ it was possible to transform the acceleration data to displacement. In order to display a smoothed two-dimensional surface plot of amplitude vibrations an array of data points was created with dimensions those of the unencumbered tank surface (the area inside the cooling tubes). This array was populated at each sampling point with the measured amplitude at that point of each selected frequency. Convolving this "bed of spikes" with a Gaussian kernel yielded a smooth surface distribution of the vibration amplitude.

Power density spectra contain no information on the relative phases of the deviations at different positions. To determine this the amplitude and phase of the vibrations at each accelerometer site were determined and could be compared.

4. VIBRATION SPECTRA

Data from each of the fifteen accelerometers show the fundamental vibration frequency at close to 100 Hz and harmonics at close to 200 Hz. In order to get a clear estimate of the spectrum a separate experiment was performed to sample 3000 data points at 1000 samples per second at one sensor. This data provided a frequency spectrum plot as shown in figure 3. This is similar to spectra reported elsewhere [5].

The natural modes of vibration of the transformer tank surface were unknown. To investigate the amplitude distribution over the surface using fifteen accelerometers the sampling rate had to be reduced to 500 samples per second. Amplitudes as a function

Proceedings of the 19th Southern African Universities Power Engineering Conference
SAUPEC 2010, University of the Witwatersrand, Johannesburg

TOPIC F. CONTROL AND APPLICATIONS
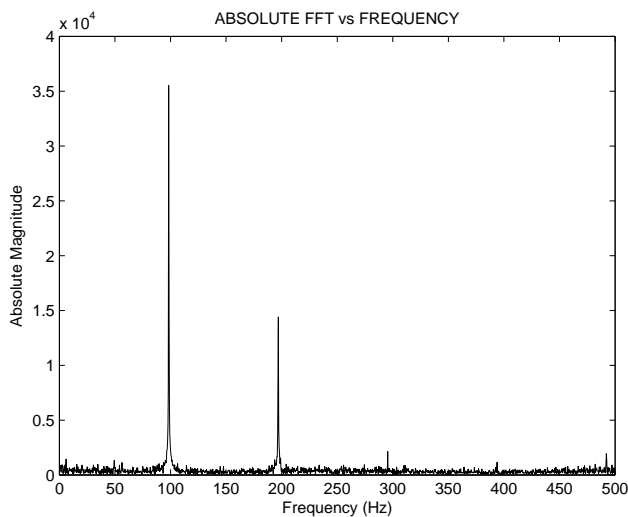
Fig. 3: Frequency spectrum plot from an accelerometer near the centre of the transformer tank surface.
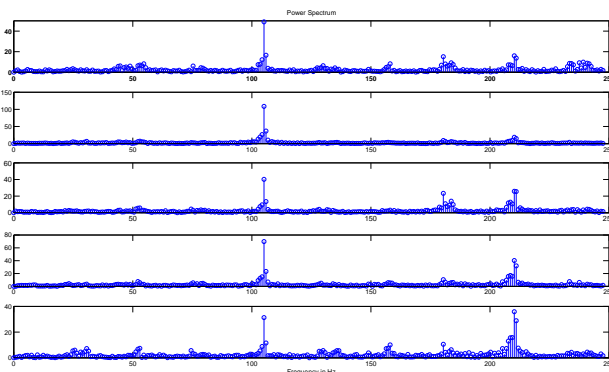
Fig. 4: Power spectral density plots of a mote's 5 accelerometers.

Fig. 5: Data from two accelerometers indicating phase differences.

Fig. 6: Amplitude distribution plot for the transformer under varying loads.

of frequency were calculated and these showed the fundamental frequencies at about 100 Hz and second harmonics at 200 Hz as shown in figure 4. The corresponding amplitude displacements could be positive or negative and hence the phases of the displacements were calculated. From the phase values the signs of the displacements were determined. Figure 5 shows the phase difference evident from readings sampled from two accelerometers.

Selecting the peak amplitude near 100 Hz for each position allowed a surface amplitude distribution plot to be generated. By changing the loading on the different phases of the transformer, different amplitude distributions were observed. Examples of these distributions are shown in figures 6 and 7. In figure 6 the top plot shows no-load condition with the lower plot showing only the white phase loaded. Figure 7 shows only the blue and red phases loaded in the top and bottom plots respectively. Notice the marked difference in amplitude distributions in the unloaded and loaded plots.

5. CONCLUSIONS AND FUTURE WORK

We have implemented a sensornet to evaluate a transformer whilst online using a grid of accelerometers. From this we are able to measure the vibration over a surface of the transformer tank and visualise the amplitude and frequency of its vibration. It can be seen that the amplitude distribution changes under varying conditions.Further analysis of the data is required.

Future work includes modifying the sensornet and logging and analysis software to facilitate long term
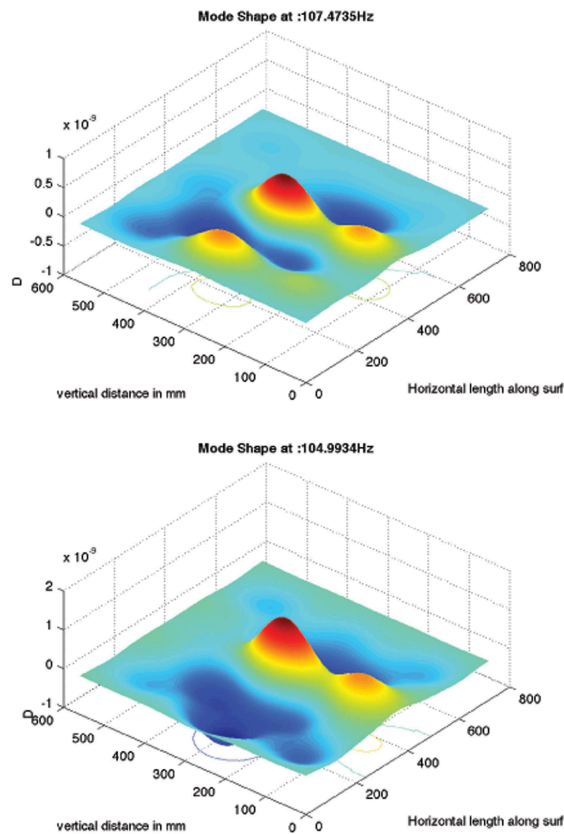
Fig. 7: Amplitude distribution plot for the transformer under varying loads.

unsupervised monitoring to further analyse the state of the transformer over time. Ruggedisation will be required to move the system out into the field.

REFERENCES

[1] V. Rusov and S. Zhivodernikov, "Transformer condition monitoring," in *International Conference on Condition Monitoring and Diagnosis, 2008. CMD 2008*, Apr. 2008, pp. 1012–1014.

[2] A. E. B. Abu-Elanien and M. M. A. Salama, "Survey on the transformer condition monitoring," in *Large engineering systems conference on power engineering*. IEEE, Oct. 2007, pp. 187–191.

[3] P. Baker, S. McArthur, and M. Judd, "Data management of online partial discharge monitoring using wireless sensor nodes integrated with a multi-agent system," in *International Conference on Intelligent Systems Applications to Power Systems, 2007. ISAP 2007*, Nov. 2007, pp. 1–6.

[4] A. Nasipuri, R. Cox, H. Alasti, L. Van der Zel, B. Rodriguez, R. McKosky, and J. A. Graziano, "Wireless sensor network for substation monitoring: design and deployment," in *SenSys '08: Proceedings of the 6th ACM conference on Embedded network sensor systems*. New York, NY, USA: ACM, 2008, pp. 365–366.

[5] J. Shengchang, L. Yongfen, and L. Yanming, "Research on extraction technique of transformer core fundamental frequency vibration based on olcm," *IEEE Transactions on Power Delivery*, vol. 21, pp. 1981–1988, Oct. 2006.

[6] B. Garcia, J. C. Burgos, and A. Alonso, "Winding deformations detection in power transformers by tank vibrations monitoring," *Electric power systems research*, vol. 74, pp. 129–138, Apr. 2005.

[7] C. Bartoletti, M. Desiderio, D. Di Carlo, G. Fazio, F. Muzi, G. Sacerdoti, and F. Salvatori, "Vibro-acoustic techniques to diagnose power transformers," *IEEE Transactions on Power Delivery*, vol. 19, no. 1, pp. 221–229, Jan. 2004.

[8] P. Nirgude, B. Gunasekaran, Channakeshava, A. Rajkumar, and B. Singh, "Frequency response analysis approach for condition monitoring of transformer," in *Conference on electrical insulation and dielectric phenomena*, Oct. 2004, pp. 186–189.

[9] J. A. Garcia-Souto and H. Lamela-Rivera, "Comparative analysis of optical-fibre interferometric sensors versus accelerometers: application to vibrations inside high-power transformers," *Journal of optics A: Pure and applied optics*, vol. 4, pp. S318–S326, Nov. 2002.

EVALUATION OF THE PERFORMANCE OF A POWER TRANSFORMER UNDER VARYING DC INJECTION AND MITIGATION OF ADVERSE EFFECTS

Emma Françoise ISUMBINGABO, Dr. M.MALENGRET

Department of Electrical Engineering,
University of Cape Town,
Cape Town, South Africa

Abstract .*The presence of the DC in a power transformer results in adverse effects such as harmonic distortion, an increase in reactive power losses, and an increase in magnetizing current, among others which affect the performance of the power transformer. The aims of the study were, therefore, to investigate (1) the effects that a DC injection can have on the operational characteristics of a 6 kVA power transformer and (2) how some of the adverse effects can be mitigated. Six main tests were performed. these were: (1) power transformer magnetizing characteristics measurements (i) at zero AC load and (ii) when AC circulates with DC in the secondary windings (2) determination of the effects that dc bias has on the secondary of a power transformer (3)evaluation of the magnetizing current distortion resulting from DC bias (4) shift in the operating point of the core steel characteristics (b-h) through hysteresis tests on a 6 kVA single phase power transformer (5) harmonic contents of the magnetizing current of a power transformer under different DC injections and (6) harmonics mitigation using extra windings. Results obtained showed an increase in each characteristic with increased DC applied. The cancellation of some of the adverse effects such as reactive power, magnetizing current, THD and waveform in the windings was achieved by applying DC injection to opposite terminals at a high level. A hundred per cent of harmonics cancellation was achieved as the cancellation current was increased. Harmonics analysis revealed that harmonics of orders greater than 10 were less significant to the study.*

Key Words: Current; Injection; Mitigation; Transformer; Harmonics.

1. INTRODUCTION

The performance of a power transformer can be affected by a DC voltage which can originate from many sources including [1-14]:

(i) power electronics converter systems
(ii) geomagnetic induced voltages which result in DC currents when they enter into a power transformer by its earth point.
(iii) non-linear loads and loads that have a DC voltage source in their circuit.

The DC in a power transformer's windings causes a shift in the operating point of the core steel characteristics (which causes an asymmetrical B-H Curve) and the power transformer may go into half-cycle saturation. This causes the power transformer to draw a large asymmetrical exciting current which results in increased reactive power consumption as well as the generation of significant levels of harmonic currents [5, 6]. The increased reactive power in a power transformer may result in several adverse effects on the power system. Some of the adverse effects due to the increase in the reactive power are [7]:

(i) intolerable system voltage depression
(ii) unusual swing in active and reactive power flow into transmission lines
(iii) problems with generator reactive power limits in some instances

The generation of both odd and even harmonics in the power transformer may result in several adverse effects on the power system including:

(i) shunt capacitor banks come to be seen as low impedance paths for the higher harmonics and this causes a large portion of the harmonic currents to go through capacitor banks. Since some protection schemes could see this as an overload, they could trip out capacitor banks in an attempt at overload protection
(ii) The undesired operation of other protective relays may respond to sequence voltages or currents which are not frequency selective. Undesired operations can be of three types; detection of fault where none exists, failure to detect a fault and failure to detect a fault in an adequate time period.

Another adverse effect that can occur is drastic leakage flux effect in the transformer with resulting excessive localized heating which could result in the following:

(i) increase in losses
(ii) degradation of insulation

This paper aims to evaluate the performance of a power transformer under varying DC injection and mitigation of any adverse effects. This will be achieved by:

(i) investigating the effects that DC injection can have on the operational characteristics of a 6 kVA power transformer.
(ii) investigating the likely occurrence of sources of DC in a power transformer incorporated in distributed generator(DG) inverter systems
(iii) investigating how the adverse effects of DC injection in a 6 kVA power transformer can be mitigated.
(iv) creating software that can mitigate the effects of DC injection in a power inverter transformer.

2. METHODOLOGY

The following experiments were performed in the laboratory:

(i) determination of 6 kVA power transformer magnetizing characteristics under AC magnetization and measurement of the power transformer's magnetizing characteristics under DC bias in two situations (a) at zero AC in the secondary windings, (b) when AC circulates with DC in the secondary windings using a 12V battery with a variable resistor
(ii) determination of the effects that DC bias in the secondary of a power transformer has on the load current, and its corresponding primary component.
(iii) evaluation of the magnetizing current distortion resulting from DC bias, injected from the secondary

winding when the power transformer output is cancelled. The magnetizing current was measured on the primary side by means of an Agilent Technologies DS06012A Oscilloscope. A transcend USB was used to capture the magnetizing current waveform in different scenarios where a DC is injected through the secondary windings. The same magnetizing current waveforms were captured in the scenario when AC was superimposed on the DC in the secondary windings of the power transformer.

(iv) Determination of the shift in the operating point of the core steel characteristics (B-H Curve). The non-linear magnetic characteristics of a power transformer core are needed to predict distortion of its primary current due to DC injection. A transformer's magnetization curves can also be obtained by measurements.

Here the focus is on the measurement of hysteresis to prove that DC introduces a shift in the operating point of the magnetizing characteristics.

Hysteresis loops were measured with 50Hz sinusoidal excitation on a grain oriented silicon steel toroidal core at room temperature. the test core has the following dimensions: outer diameter =240mm, inner diameter=120mm, height=80mm,mean path length=180mm and cross section of 516mm^2 ,the primary windings has 178 turns wound on the toroidal core and the secondary windings has 20 turns also wound on the same toroidal core.

(v) Determination of the magnetizing current harmonic contents in the power transformer under different DC injection in two instances:

(a) When the transformer output is zero and only DC circulates in the secondary windings. The test set up consisted of two identical 6 kVA single phase power transformers, connected in such a way that their secondary voltages oppose each other and therefore cancel each other out. The DC injected in the secondary winding was made from a DC-DC Converter in series with a variable resistor to help in varying the amount of DC injected.

The supply voltage was varied, from 21.5V AC (under voltage operation), to 25.8VAC which is the power transformers nominal voltage.

The DC injection was then varied for different values of voltage. Readings of total magnetizing current, harmonic contents, reactive power, and Total Harmonic Distortion (THD) were taken and (b) when DC current is superimposed on the AC in the power transformer's secondary windings.

In this test an AC non-linear load consisted of a half-wave rectifier with a passive LC filter and a resistor load. A constant DC current with little ripple resulted. This led to a distortion in the B-H curve and hence an asymmetrical magnetizing current on the primary of the power transformer. The DC injected was varied using a variable resistor.

(vi) Harmonics cancellation using extra windings.

The main objective of this experiment was to determine the level of cancellation that could be achieved by using extra windings to cancel the harmonics effect in a power transformer subjected to DC current injection.

3. PRESENTATIONS OF THE RESULTS AND DISCUSSION

3.1 Magnetizing characteristics under sinusoidal supply voltage   and effects of DC current injection on magnetizing characteristics

The results were obtained on the 6 kVA power transformer under AC magnetization as well as by imposing a varying amount of DC current on the secondary of the power transformer and are presented in the figures below:
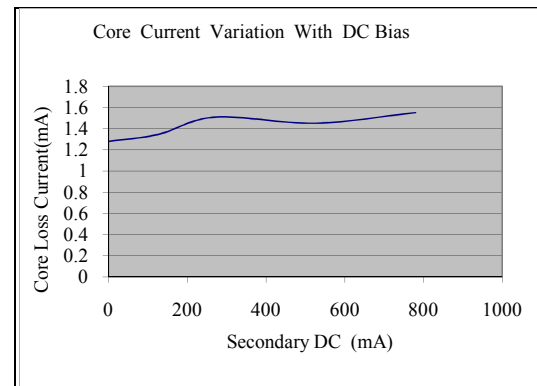
Figure 3.1: Core Current Variation with DC Bias
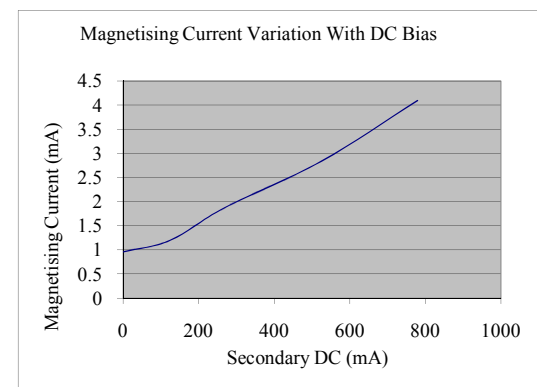
Figure 3.2: Magnetizing Current Variation with DC bias

Figure 3.1 illustrates the effect that DC Bias has on the core current of a power transformer. Since the core current in a power transformer is frequency dependent, it is evident that the core current will not vary much since the frequency was kept constant during the tests.

By observing the graph shown in Figures 3.2, it is evident that the magnetizing current increases considerably with the increase of the DC injected. This explains the basic theory which states that the transformer enters half cycle saturation due to DC bias since the excess flux in the secondary winding is not cancelled by any corresponding component in the primary winding. The transformer therefore has to increase its own magnetizing current to keep the flux stable. The variation in the magnetizing current causes an increase in the power transformer's reactive power. The increase in the reactive power results in the increase in the apparent power drawn from the primary source. The real (Active) power depends on the core material. The current in the core being constant, the real power does not vary much. Figures 3.3, 3.4 and 3.5 show the variation in apparent power and reactive power respectively with DC Bias.
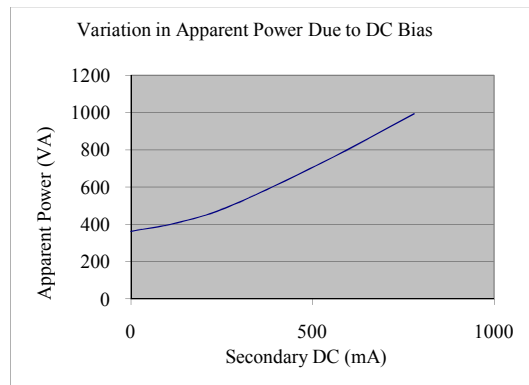
Figure 3.3: Variation in Apparent Power of a Transformer Due to DC Bias
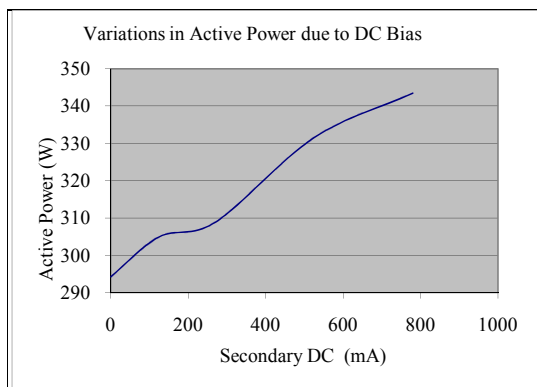
Figure 3.4: Variation in Active Power in a Transformer Due to DC Bias
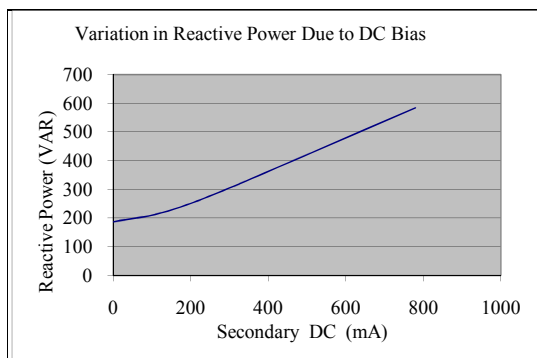
Figure 3.5: Variation in Reactive Power Due to DC Bias
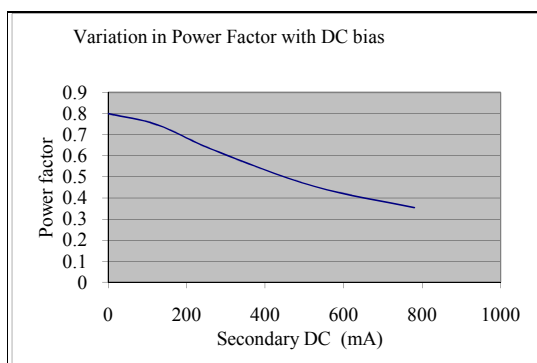
Figure 3.6: Power Factor Variation with DC current Bias.

Figure 3.6 shows the relationship between the power factor and the increase in injected DC. The power factor decrease can be accounted for by the increase in distortion and asymmetry of the primary current.

3.2 Evaluation of the Magnetizing Current Distortion Resulting from DC Offset
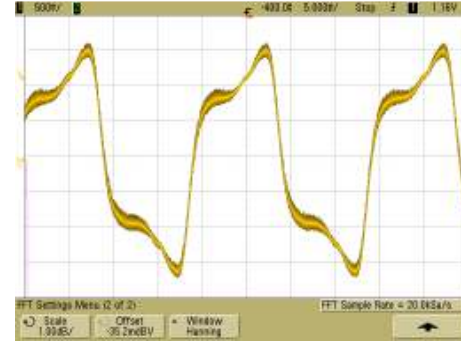
Figure 3.7: Measured magnetizing current of a 6 kVA power transformer on no load and with no DC current injection

It can be seen that the magnetizing current is symmetrical around the x-axis, which means that the mean value of the current is zero, that is, there is no DC current component. That situation changes once a DC current is injected into the secondary windings. The waveform which is not sinusoidal but symmetrical becomes more distorted and there is an increase in the average value (figure 3.8), as the DC current injected increases. Figures below show different waveforms according to different DC current injected values for two main situations:

(i)   when only a DC circulates in the transformer secondary windings

(ii) when DC and AC are superimposed in the transformer secondary windings.
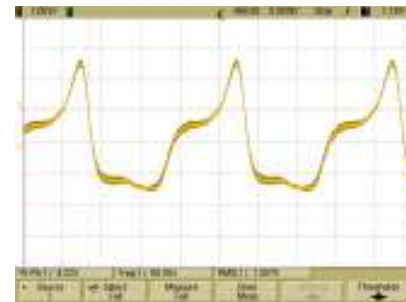
Figure 3.8: Measured magnetizing current waveform with 100mA DC injection
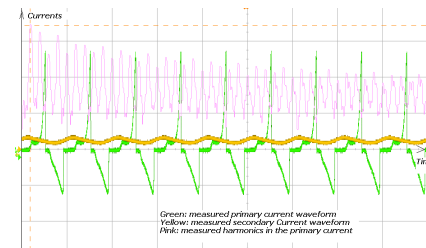
Figure 3.9: Measured Magnetizing Current Waveform and average magnetizing current (with an LC filter)

3.3 Shift in the operating point on the core steel characteristic (B-H) Curve, of the 6 kVA power transformer

While the hysteresis models are usually in terms of field variables, such as magnetic flux density (*B*) and magnetic field intensity (*H*), experimental data are usually in terms of circuit variables, such as voltages (*v*) and currents (*i*). In this experiment, circuit variables were measured from a sample toroidal core.

Photo 3.1: Hysteresis loop of a 6 kVA, (230/25) V power transformer operating at nominal voltage
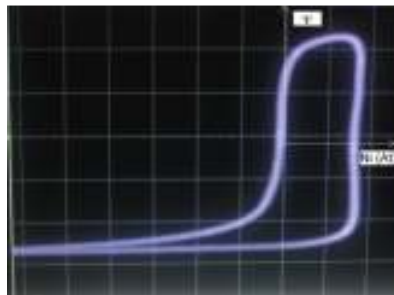
Photo 3.2: Hysteresis Loop of a 6 kVA power transformer Operating at Nominal Voltage and Subjected to a 540mA positive DC current Injection
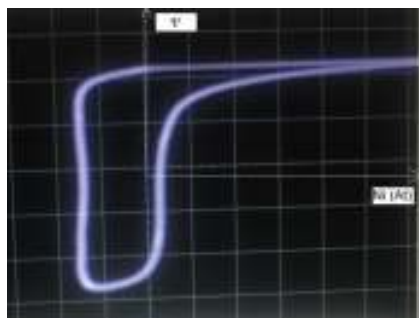
Photo 3.3. Hysteresis Loop of a 6 kVA power transformer with a negative DC injection

With the voltage fixed at its nominal value (230V primary), a varying constant DC voltage supply resulted in a DC current in the secondary windings through a variable resistor. Plots of the resulting hysteresis loops were then captured (see photos above). The hysteresis at nominal voltage was necessary to provide an indication of the transformer's performance when operating under normal conditions compared with the situation where a DC is injected which results in the core flux being biased.

It has to be noted however that these plots are not a complete representation of hysteresis characteristics exhibited by the core when DC is injected in the secondary. The integrator works out the flux by means of measurements of the integral of the supply voltage.

The integral measures only the AC flux and is unable to provide the DC flux. Although the integrator is unable to provide the true representation of biased flux, the resulting flux shown in photo 3.2 indicate a large increase in the peak value for the negative half cycle of the magnetizing current.

3.4 Harmonic contents in the magnetizing current of a transformer under different DC injection

The aim of this section is to analyze the level of primary current harmonics distortion created in a single phase transformer when exposed to a DC current. The level of distortion will be compared to relevant standards. The harmonic spectrum will be investigated to determine which harmonic orders dominate and why. The results obtained during the tests performed to determine the harmonic contents on the primary side current of a 6 kVA power transformer, are presented below:
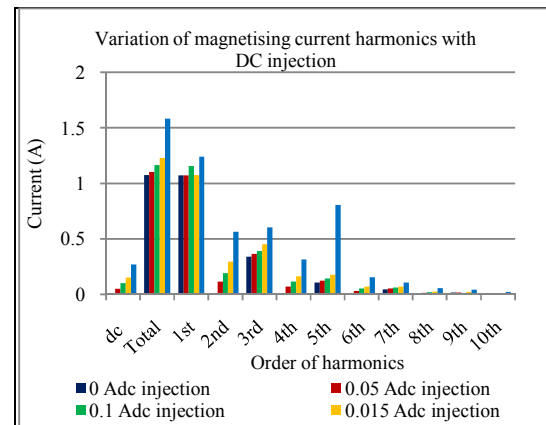
Figure 3.10: Measured primary current harmonic contents in the 6 kVA power transformer in nominal voltage operation, when only DC circulates in the secondary windings
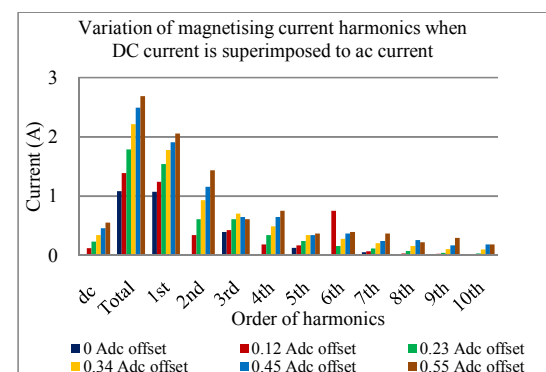
Figure 3.11: Measured primary current harmonic contents in the 6 kVA power transformer in nominal voltage operation, when an AC circulates with DC in the secondary windings

Harmonic contents in the primary current are presented as figures 3.10 and 3.11.
In recording the results it was decided to present up to the 10th harmonic since further order of harmonics were less significant to the interest of the work.

Proceedings of the 19th Southern African Universities Power Engineering Conference
TOPIC F. CONTROL AND APPLICATIONS
SAUPEC 2010, University of the Witwatersrand, Johannesburg

The results confirm the generation of even harmonics in the supply voltage side current and as the graphs depict, the harmonics of 2nd, 4th and 6th order increase considerably when a varying DC is injected whereas the harmonics of the 7th and 9th, order show little variation with respect to the DC injected. The asymmetry in the secondary current due to DC bias caused a significant increase in the 2nd and 4th even harmonics. The 3rd and the 5th harmonics have also experienced a significant increase. The increase in the 7th and 9th harmonics is due mostly to the existing distortion of the power laboratory supply voltage waveform, and also due to the no-load magnetizing current distortion.

3.5 Harmonics cancellation using extra windings

The results obtained during the tests performed to investigate the level of cancellation of harmonics in the power transformer are presented in figures 3.12 and 3.13 below:
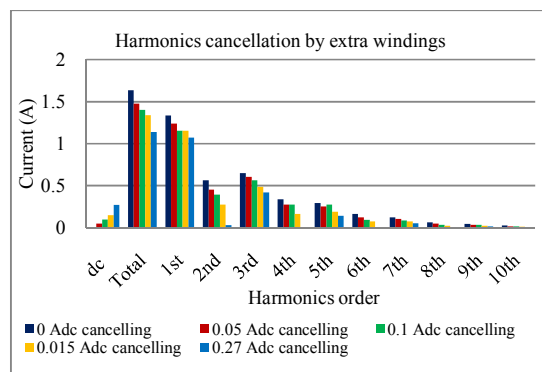
Figure 3.12: Cancellation of Magnetizing Current Harmonic Contents using Extra Windings
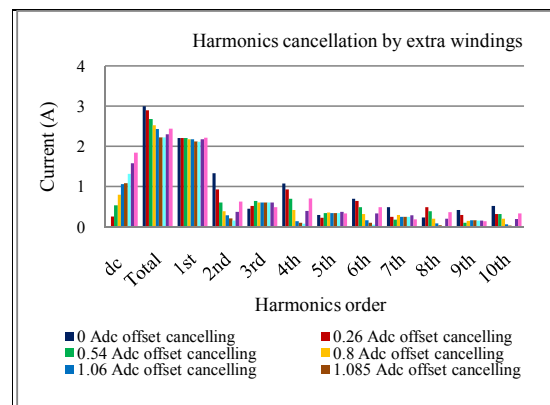
Figure 3.13: Harmonics cancellation using an extra coil. The figure also shows the over-canceling which results in harmonics re-generation

The results show that by applying the same DC injection on extra windings wound on the same core of a power transformer subjected to a DC bias, the generated harmonics can be cancelled out.

4. CONCLUSION

The study of the performance of a power transformer under varying DC injection and the mitigation of adverse effects has revealed positive results and validate the theories tested

here. Main conclusions than can be drawn from the laboratory tests performed are that:

(i) a DC current component in the secondary windings is not transferred onto the primary windings.

(ii) a DC component in the secondary windings of a power transformer causes increased distortion, asymmetry and displacement factor in the transformer non load primary current.

(iii) on the evaluation of the transformer's magnetizing current the following effects were noted:
  ➢ there is a change in the duration of the negative or positive cycle depending on the direction of the offset
  ➢ the duration of the positive half cycle was reduced from 10ms of Zero DC injection to 8ms as result of the positive duration of the current waveform.
  ➢ the peak amplitude of the positive half cycle waveform was larger than the positive one.

(iv) tests on the shift in the magnetizing curve (B-H) through the measurements of the hysteresis indicate that, although the RC integrator was unable to provide a true representation of a biased flux, the resulting flux suggests a large increase in the peak value of the positive cycle of the magnetizing current. When a positive bias is applied to the core, the large peak value of the negative magnetizing current is necessary to maintain symmetry of the primary current.

(v) with reference to the mitigation measures, it was observed that that the complete restoration of the magnetizing current to its original no DC bias was possible as the cancellation current was increased. The other observation was that DC injection is only cancelled by similar DC injection with opposing polarities through the use of extra windings.

(vi) harmonics analysis revealed that harmonics of orders greater than 10 were less significant with respect to the research work. The analysis also showed that harmonics of the 2nd, 4th and 6th orders vary considerably with the injection of varying DC. On the other hand, harmonics of the 7th and 9th orders show little variation with respect to the DC injection.

(vii) mitigation of adverse effects of a power transformer under varying DC injection is achievable.

5. RECOMMENDATIONS

(i) for tests on the shift in the magnetizing curve (B-H), further investigations are necessary to provide more details on the shift of the transformers operating point.

(ii) software which controls the DC injection and even harmonics is necessary for the cancellation of the DC current injection effects in a power transformer.

REFERENCES

[1] Gregory A. Kern, August 2001. "*DC Injection and Even Harmonics Control Systems*" United State Patent 6, 282,104 B1.

[2] Kirchberg, Jr. et Al, December 1990. "*Suppression of Switching Harmonics*" United States Patent 4, 977,492.

[3] Jayasinghe, R.N. *et al*. 2003. "*Power system harmonic effects on distribution transformers and new design considerations for K factor transformers.*" IEEE Sri Lanka Annual Sessions.

[4] Shunji Yanase, Yasuo Okazaki, Takeyoshi Asano, 2000. "*AC Magnetic Properties of Electrical Steel Core under DC-Biased Magnetization*". Journal of Magnetism and Magnetic Material 215-216.

[5] Patrice Hurlet, Frédérique Berthereau, 2007. "*Impact of Geomagnetic Induced Currents on Power Transformer Design*" JST Transformateurs (FRANCE),

[6] W.Chandrasena, P.G McLaren, U.D.Annakkage, and R.P. Jayasinghe, ___ "*Modeling GIC Effects on Power Systems: The Need to Model Magnetic Status of Transformers*", IEEE Transactions on Power Delivery.

[7] Jayasinghe, R.N, "*Investigation of Protection Problems due to Geomagnetically Induced Currents*" PhD, University of Manitoba,Canada, 1996

[8] Shu Lu (Student M) Yilu Liu (M) Jaime De La Ree (M), April 1993. "*Harmonics generated from a DC biased transformer*", IEEE Transactions on Power Delivery, vol.8, No.2.

[9] Xuzhu Dong, Yilu Liu, John G. Kappenman, 2001. "*Comparative Analysis of Exciting Current Harmonics and Reactive Power Consumption from GIC Saturated transformer*" IEEE Transactions on Power Delivery

[10] W.C. Viana, R.J.Micaleff, S.Young, F.P. Dawson, September 1999. "*Transformer Design Considerations for Mitigating Geomagnetic Induced Saturation*", IEEE Transactions on Magnetics, Vol.35, No 5.

[11] Geomagnetic Induced Current Principle. On http://en.wikipedia.org/wiki/image:GIC consulted on 03/07/2008 at 01:50 pm.

[12] Salih, T.M. *et al.* 2000. "*The Effect of the harmonic components upon transformer active losses in the case of (non) sinusoidal sources and (non) linear loads*." Department of Electrical Engineering Yildiz Technical University, Istanbul, Turkey.

[13] Maswood, I.A. *et al*. 2002. "*Harmonics, Sources, Effects and Mitigation Techniques*". Second Intl. Conf. on Electrical and Computer Engineering, ICECE 2002, Dhaka, Bangladesh, pp: 26-28.

[14] D.Gallo, Langella,A. Testa,A.Emanuel.____ " *On the Effects of Voltage Subharmonics on Power Transformers: a preliminary study*" IEEE Transactions on Power Delivery.

TOPIC F. CONTROL AND APPLICATIONS

Proceedings of the 19th Southern African Universities Power Engineering Conference
SAUPEC 2010, University of the Witwatersrand, Johannesburg

VOLTAGE DEPENDENCY OF THE POWER CONSUMPTION OF TUBULAR FLUORESCENT LAMPS WITH ELECTRONIC BALLASTS

A Jakoef and H J Vermeulen

Stellenbosch University, Department of Electrical and Electronic Engineering, Stellenbosch.

Abstract. A significant proportion of Industrial and Commercial Energy Efficiency (ICEE) projects conducted as part of Demand Side Management (DSM) interventions involve the retrofit of inefficient lighting technologies with modern, more efficient lighting technologies with the view to reduce the overall energy consumption. These interventions typically include the replacement of magnetic ballasts used to drive Tubular Fluorescent Lamps (TFLs) with more efficient electronic ballasts. The Measurement and Verification (M&V) of the load reduction and energy savings impacts of such interventions requires that baseline and post-implementation energy consumption profiles are determined for the lighting technologies removed and installed in the intervention. Ideally, this requires that the relationships between the active power consumption of the technologies and the supply voltage magnitude are taken into consideration. This paper presents the results of a laboratory investigation to determine the effects of supply voltage variation for a voltage range of 90 % to 110 % of the nominal supply voltage of 230 V on the active, reactive and apparent power consumption of 36 W and 58 W TFLs with electronic ballasts. The results show that the active power consumption of the different TFLs tested ranges from 82 % to 120 % of rated power.

Key Words. Energy-efficiency; Tubular Fluorescent Lamps; Lamp ballasts,

1 OVERVIEW

1.1 Introduction

The exchange of magnetic ballasts with electronic ballasts for driving tubular fluorescent lamps (TFLs) represents an important part of the current Demand Side Management (DSM) strategy designed to achieve energy savings and reduce the electrical demand during peak periods when generation and network capacity constraints are experienced. A typical TFL fixture consists of either a magnetic ballast with a Power Factor Correction Capacitor (PFCC) or an electronic control circuit that drives one or more fluorescent tubes [1]. From a Measurement and Verification (M&V) perspective, the voltage dependency of the active power consumption of TFL loads with magnetic ballasts differs from those with electronic ballasts and this may impact on the methodology applied in determining the savings impacts of such interventions. This paper presents the results of a laboratory investigation undertaken to determine the supply voltage dependency of the active power consumption of individual TFLs with electronic ballasts experimentally, similar to experiments done with Compact Fluorescent Lamps (CFLs) [2].

1.2 Test arrangement and test samples

A number of tests were conducted on commercial TFLs using the generic test arrangement shown in Figure 1. The arrangement supplies a variable sinusoidal voltage to the load, measures the active and reactive power consumption and records the voltage and current waveforms.
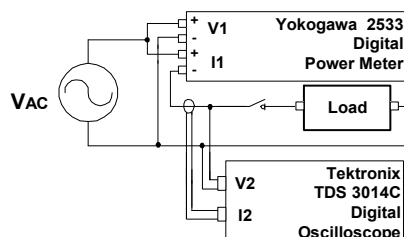
Figure 1: Functional block diagram of the test arrangement.

The supply voltage V_{AC} was obtained from the local mains supply network through a variac that facilitates the control of the magnitude of the supply voltage applied to the TFL and ballast under test. The supply network exhibited a degree of harmonic voltage distortion, as is common for typical Low Voltage (LV) supply networks [3]. The effects of this distortion on the main results, i.e. the voltage dependency of the active power consumption, however, have been determined to be minimal.

The load is represented by a single TFL with an electronic ballast. A variety of commercial TFLs of different ratings and from different manufacturers were tested. Electronic ballasts from a single manufacturer were used in the tests. In order to determine whether the test results are consistent, three samples of each rating per manufacturer were tested. Table I summarizes the test samples considered in the investigation.

Table II gives details of the measuring instrumentation used in the investigation, including the relevant critical measuring specifications obtained from their respective datasheets. Table III summarizes the applicable power calculation formulas used by the Yokogawa 2533 Digital Power Meter [4]. The supply voltage and current waveforms to the test specimens were recorded using a digital oscilloscope for subsequent processing in MATLAB.

Table I: Summary of the test samples considered in the investigation.

Manufacturer / Model	Ballast Type	Power Rating [W]
A	Electronic	36
		58
B	Electronic	36
		58

Table II: Specifications of the measuring equipment used in the test arrangement.

Equipment	Max. Voltage	Max. Current	Bandwidth
Tektronix P3010 voltage probe	300 V_{RMS}	-	DC to 100 MHz
Tektronix TCP202 current probe	300 V_{RMS}	Max DC + Peak AC Current of 15 A.	DC to 50 MHz
Tektronix TDS 3014C Digital Oscilloscope	300 V_{RMS} with a standard 10x probe	-	DC to 100 MHz
Yokogawa 2533 Digital Power Meter	1000 V peak or 2x maximum range (V_{RMS})	50 A peak or 3x maximum range (I_{RMS})	DC, 10 Hz to 20 kHz

Table III: Yokogawa 2533 Digital Power Meter power calculation formulas.

Variable	Formula
Average real power (P_{AVG}) [W]	$\frac{1}{T}\int_{0}^{T} v(t)\cdot i(t)\,dt$
Reactive power (Q) [Var]	$\sqrt{\left(V_{RMS} \times I_{RMS}\right)^2 - P_{AVG}}$
Apparent power (S) [VA]	$V_{RMS} \times I_{RMS}$
Power factor	$\dfrac{P_{AVG}}{V_{RMS} \times I_{RMS}}$

2 MEASUREMENT PROCEDURES AND RESULTS

2.1 Measurement procedure

The TFL and ballast under test is energized with a supply voltage of 230 V and the lamp is allowed to stabilize. The voltage is then reduced to 207 V, i.e. 90 % of the nominal supply voltage of 230 V [3], before being gradually increased in 1 % increments to 253 V, i.e. 110 % of the nominal supply voltage. The RMS supply voltage, RMS current, active power, reactive power, apparent power and power factor are measured with the digital power meter and the voltage and current waveforms are recorded for each increment. The recorded voltage and current waveforms are processed using MATLAB to extract spectral information and to verify the measured RMS values.

2.2 Modelling of the voltage dependency of the active power consumption of TFLs

The samples of TFLs with equivalent power ratings from the same manufacturer exhibit slight differences in the measured results. The following procedure was used to arrive at a representative model for the active power consumption of the TFLs versus RMS supply voltage for each of the manufacturers and ballast type:

- The measured results for each sample are modelled using a polynomial curve fitting algorithm.

- The power consumption over the supply voltage range of interest is determined for each sample from the individual curve derived.

- The average of the power consumption of the test samples are obtained and then modelled with another polynomial curve fitting in order to

realize an active power versus supply voltage model for the specific TFL and ballast type.

2.3 Results for TFLs with electronic ballasts

Figure 2 shows the voltage and current waveforms of a typical TFL with an electronic ballast. The supply current exhibits a degree of high frequency distortion.
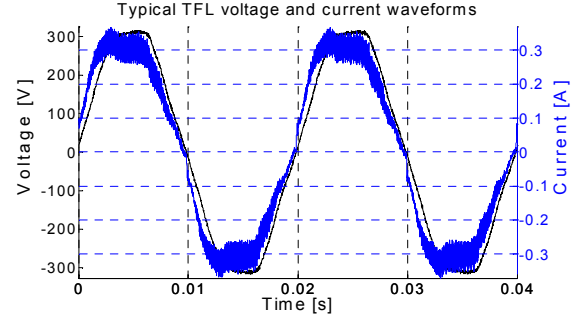
Figure 2: Typical supply voltage and current waveforms of a TFL with an electronic ballast.

Figure 3 to Figure 6 show the normalized RMS supply current as a function of the supply voltage for the samples tested, denoted by S1, S2 and S3 respectively, for the ratings listed in Table I. The base value for the current I_{Base} is determined by the relationship

$$I_{base} = \frac{P_{rated}}{V_{nom}} \tag{1}$$

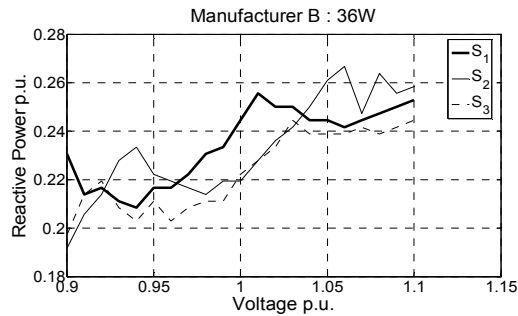where P_{rated} and V_{nom} denote the rated power and rated voltage respectively.
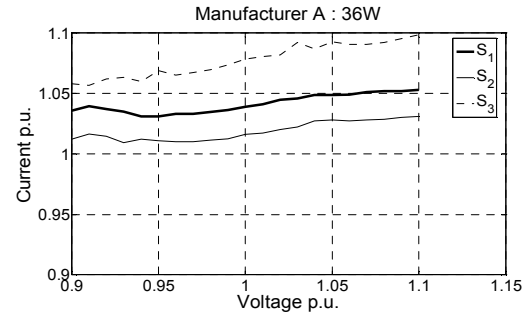
Figure 3: RMS current versus RMS supply voltage for three 36 W TFL samples from manufacturer A with an electronic ballast.
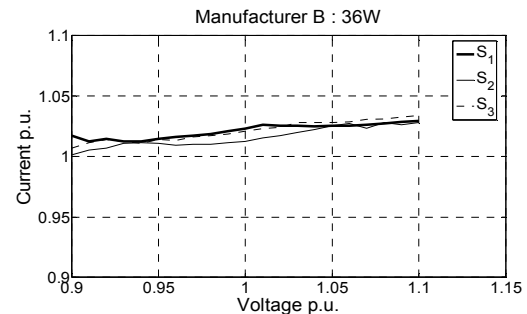
Figure 4: RMS current versus RMS supply voltage for three 36 W TFL samples from manufacturer B with an electronic ballast.
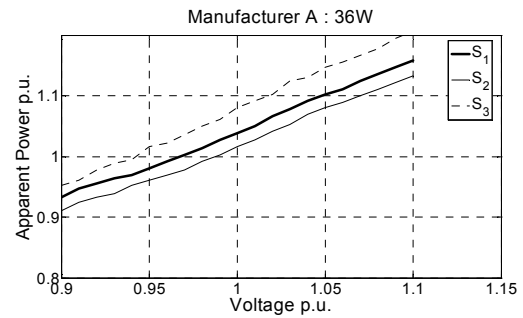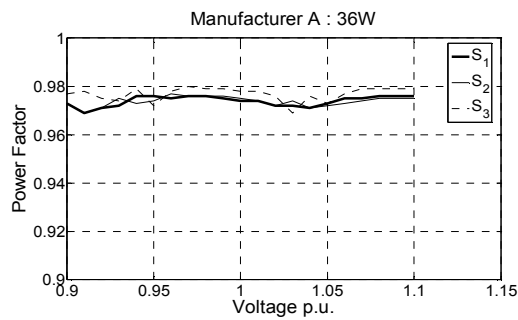
Proceedings of the 19th Southern African Universities Power Engineering Conference
SAUPEC 2010, University of the Witwatersrand, Johannesburg

TOPIC F. CONTROL AND APPLICATIONS
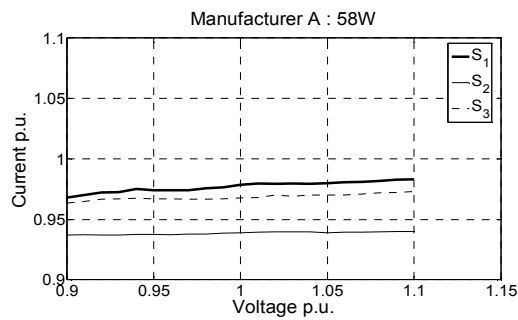
Figure 5: RMS current versus RMS supply voltage for three 58 W TFL samples from manufacturer A with an electronic ballast.
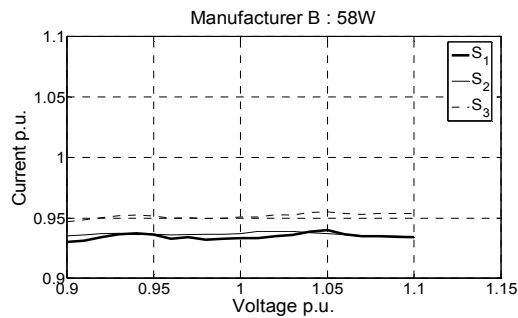
Figure 6: RMS current versus RMS supply voltage for three 58 W TFL samples from manufacturer B with an electronic ballast.

The RMS supply current relationships generally exhibit a slight increasing trend with increased RMS supply voltage for all samples tested. This trend is most pronounced for the 36 W samples from manufacturer B. The results also show a fair degree of difference between the curves for the same rating from the same manufacturer, e.g. a difference exceeding 6% is recorded at nominal voltage for the 36 W samples from manufacturer A.

Figure 7 to Figure 10 show the normalized active power consumption as a function of supply voltage for the samples tested for the ratings listed in Table I. The base value for the active power is the rated power of the TFL.
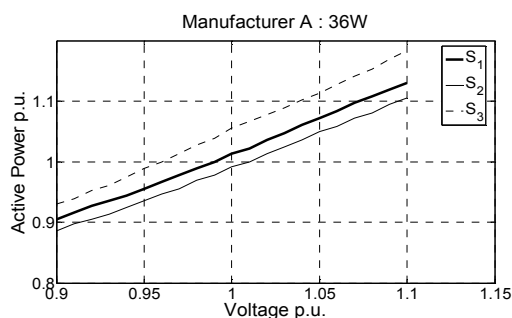
Figure 7: Active power versus RMS supply voltage for three 36 W TFL samples from manufacturer A with an electronic ballast.
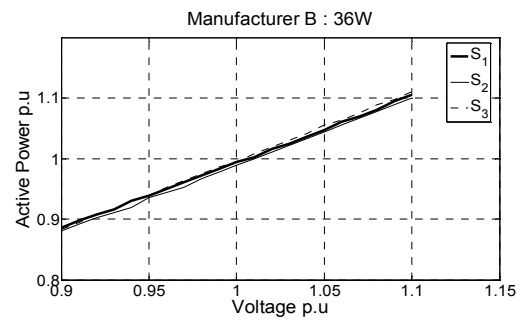
Figure 8: Active power versus RMS supply voltage for three 36 W TFL samples from manufacturer B with an electronic ballast.
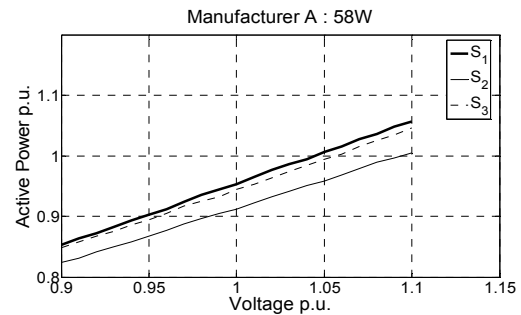
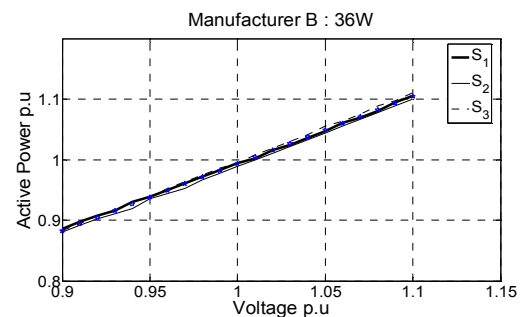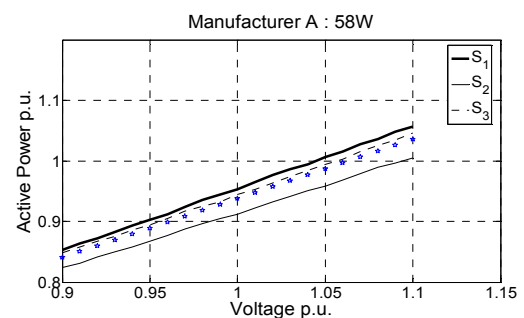

Figure 9: Active power versus RMS supply voltage for three 58 W TFL samples from manufacturer A with an electronic ballast.
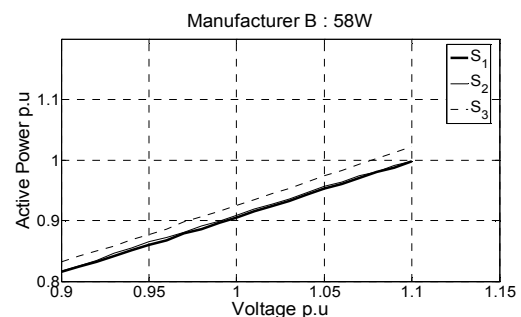
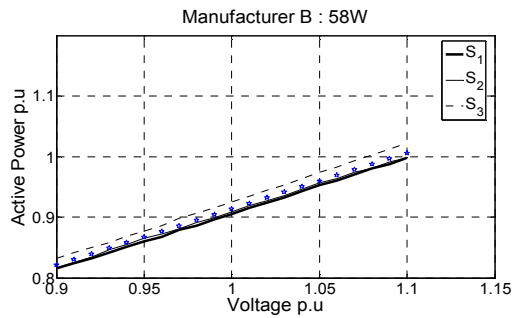Figure 10: Active power versus RMS supply voltage for three 58 W TFL samples from manufacturer B with an electronic ballast.

As expected, based on the supply current trends, the active power consumption relationships exhibit a linear trend trend with increased RMS supply voltage for all samples tested. The differences between the curves for the same rating from the same manufacturer reflect the trends for the supply current, e.g. a difference of approximately 6% is recorded at nominal voltage for the 36 W samples from manufacturer A.

Figure 11 to Figure 14 show the normalized reactive power consumption as a function of supply voltage for the samples tested for the ratings listed in Table I. The base value for the reactive power is the rated power of the TFL.

The reactive power relationships exhibit an increasing trend with increased RMS supply voltage for all samples tested.

Proceedings of the 19th Southern African Universities Power Engineering Conference
SAUPEC 2010, University of the Witwatersrand, Johannesburg

TOPIC F. CONTROL AND APPLICATIONS
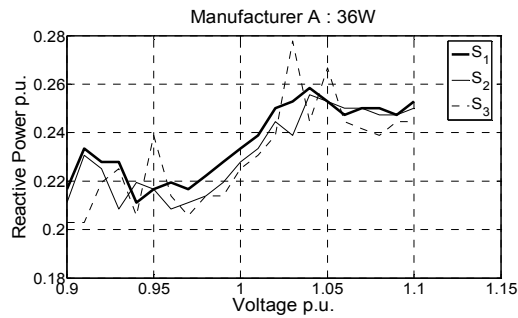
Figure 11: Reactive power versus RMS supply voltage for three 36 W TFL samples from manufacturer A with electronic ballast.

Figure 12: Reactive power versus RMS supply voltage for three 36 W TFL samples from manufacturer B with an electronic ballast.
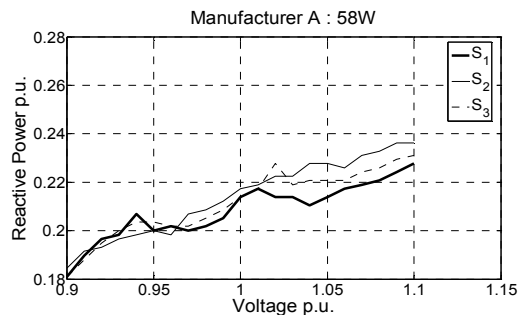
Figure 13: Reactive power versus RMS supply voltage for three 58 W TFL samples from manufacturer A with an electronic ballast.
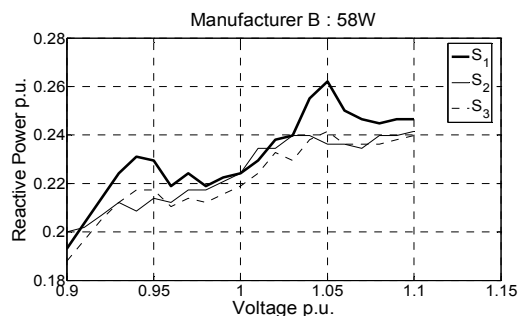
Figure 14: Reactive power versus RMS supply voltage for three 58 W TFL samples from manufacturer B with an electronic ballast.

Figure 15: Apparent power versus RMS supply voltage for three 36 W TFL samples from manufacturer A with an electronic ballast.
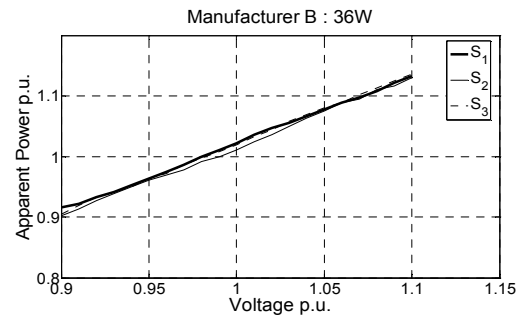
Figure 16: Apparent power versus RMS supply voltage for three 36 W TFL samples from manufacturer B with an electronic ballast.
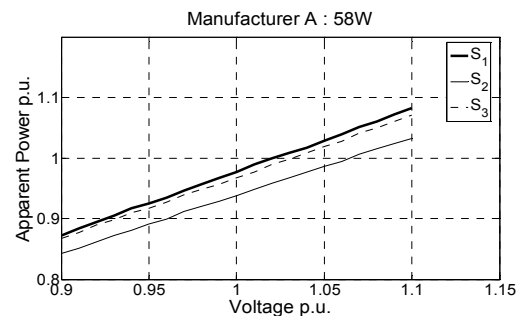
Figure 17: Apparent power versus RMS supply voltage for three 58 W TFL samples from manufacturer A with an electronic ballast.
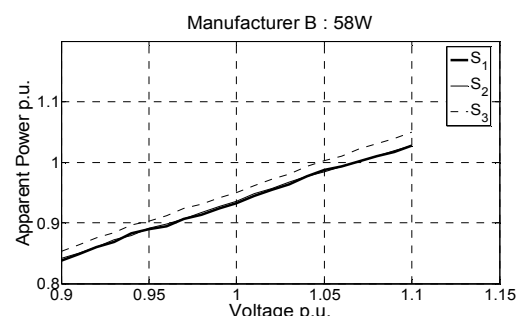
Figure 18: Apparent power versus RMS supply voltage for three 58 W TFL samples from manufacturer B with an electronic ballast.

Figure 15 to Figure 18 show the apparent power consumption as a function of supply voltage for the samples tested for the TFL ratings listed in Table I. The base value for the apparent power is the rated power of the TFL.

The apparent power relationships exhibit an increasing trend with increased RMS supply voltage for all samples tested.

Figure 19 to Figure 22 show the power factor as a function of supply voltage for the samples tested for the TFL ratings listed in Table I.

The power factor relationships exhibit an inconsistent trend.

Proceedings of the 19th Southern African Universities Power Engineering Conference
TOPIC F. CONTROL AND APPLICATIONS
SAUPEC 2010, University of the Witwatersrand, Johannesburg

Figure 19: Power factor versus RMS supply voltage for three 36 W TFL samples from manufacturer A with an electronic ballast.
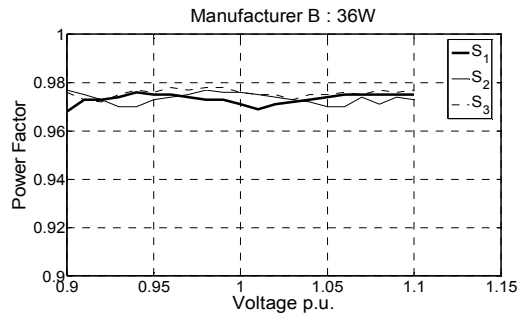
Figure 20: Power factor versus RMS supply voltage for three 36 W TFL samples from manufacturer B with an electronic ballast.
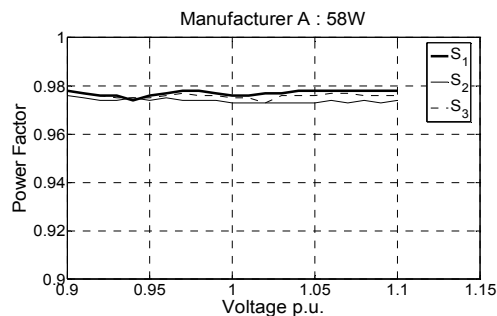
Figure 21: Power factor versus RMS supply voltage for three 58 W TFL samples from manufacturer A with an electronic ballast.
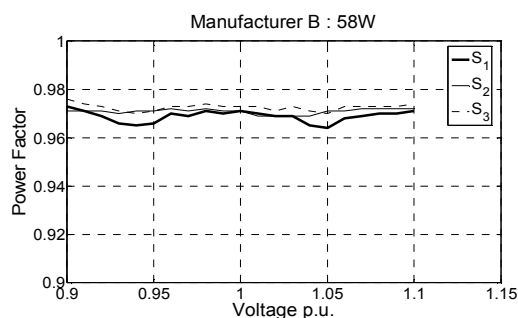
Figure 22: Power factor versus RMS supply voltage for three 58 W TFL samples from manufacturer B with an electronic ballast.

Table IV summarizes first order regression models (denoted by M) for the normalized active power consumption for the averaged results measured for the specimens listed in Table I. The models exhibit linear increasing trends with increased RMS supply voltage, as is expected based on the active power consumption measurements.

Figure 23 to Figure 26 compare the normalized active power versus RMS supply voltage responses

of the models (M) to the original measurements obtained for each TFL sample.

Table IV: First order regression models for the voltage-dependent normalized active power consumption of the samples tested.

Manufacturer / Model	Ballast type	Power Rating [W]	Active power model [W]
A	Electronic	36	$0.12614V + 7.7155$
		58	$0.24593V - 2.1523$
B	Electronic	36	$0.17357V - 4.153$
		58	$0.23329V - 0.6607$
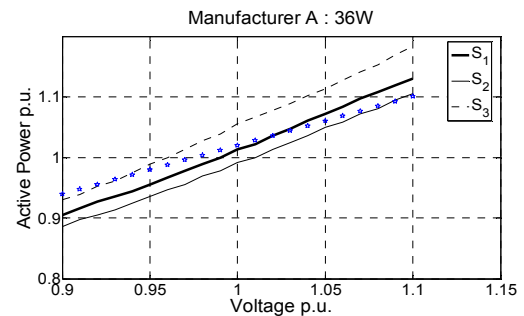
Figure 23: Measured and modelled active power consumption versus RMS supply voltage for three 36 W TFL samples from manufacturer A with an electronic ballast.

Figure 24: Measured and modelled active power consumption versus RMS supply voltage for three 36 W TFL samples from manufacturer B with an electronic ballast.

Figure 25: Measured and modelled active power consumption versus RMS supply voltage for three 58 W TFL samples from manufacturer A with an electronic ballast.

Figure 26: Measured and modelled active power consumption versus RMS supply voltage for three 58 W TFL samples from manufacturer B with an electronic ballast.

3   CONCLUSIONS

The RMS supply current of TFLs with electronic ballasts exhibit moderately increasing linear characteristics with increased supply voltage. The active and reactive power consumption of TFLs with electronic ballasts similarly exhibit approximately linear increasing trends with increasing supply voltage. The power factor measurements exhibit fluctuating trends with increased supply voltage.

Table V summarizes the active power consumption for the different TFLs at 207 V, 230 V and 253 V respectively. TFLs with magnetic ballasts show a maximum deviation of 19 % from the rated power [5]. This could impact on energy saving calculations.

The active power models for each manufacturer and ballast type show a reasonable degree of accuracy by staying within a 10 % range of any sample. The results presented in this paper apply for the samples listed in Table I only.

Table V: Active power consumption for the different TFLs at 207 V, 230 V and 253 V respectively.

Manufacturer / Model	Ballast type	Power Rating [W]	Sample #	% of rated power		
				at 207 V	at 230 V	at 253 V
A	Electronic	36	1	90.56	101.39	113.06
			2	88.61	99.167	110.06
			3	93.06	105.56	118.33
		58	1	85.34	95.35	105.69
			2	82.41	91.21	100.52
			3	84.83	94.48	104.66
B	Electronic	36	1	88.61	99.44	110.56
			2	90.28	98.89	110
			3	90.56	99.44	111.11
		58	1	81.55	90.517	99.83
			2	81.72	90.86	99.82
			3	83.27	92.5	102.24

REFERENCES

[1]   A. Vitanza, R. Scollo, A. Hayes, Technical Literature, "Application Note – Electronic Fluorescent Lamp Ballast", http://eu.st.com, STMicroelectronics, 1999.

[2]   A. Jakoef, H.J. Vermeulen, M Bekker, "Compact Fluorescent Lamp (CFL) Voltage Dependency Test", SAUPEC 2008, Durban University of Technology, Durban, South Africa, Proceedings of the 17th Southern African Universities Power Engineering Conference: 134-139, 2008.

[3]   NRS, "NRS048-2 Electricity Supply-Quality of Supply Part2: Voltage characteristics, compatibility levels, limits and assessment methods", 2nd Edition, Standards South Africa, 2003.

[4]   Yokogawa, "Instruction Manual Models 2533 11 and 2533 21 Digital Power Meter (Single-Phase AC and DC/AC)", 3rd Edition, 1987.

[5]   A. Jakoef, H.J. Vermeulen, "Voltage Dependency of Tubular Fluorescent Lamps with Magnetic Ballasts". SAUPEC 2009, Stellenbosch University, Stellenbosch, South Africa, Proceedings of the 18th Southern African Universities' Power Engineering Conference: 1-7, 2009.

PARALLEL DC-DC CONVERTERS AS A LINK BETWEEN PHOTOVOLTAIC PANELS AND A VARIABLE SPEED DRIVE

D J du Toit and P-J Randewijk

University of Stellenbosch, Dept. of Electrical and Electronic Engineering, Stellenbosch, South Africa

Abstract: In the dry regions of South Africa, boreholes tend to be very deep. The use of wind pumps to draw water at such great depths is unpractical and photovoltaic panels (PV) can be used instead. The panels can be connected directly to a low voltage DC motor that powers a positive displacement pump. However, the use of this high power, low voltage system can lead to high losses in the long cables feeding the DC motor at the bottom of the borehole.

The solution developed in this paper uses a DC-DC converter to step-up the low voltage from the PV panels. The high voltage DC is converted to three phase power using a commercial variable speed drive (VSD) in order to power a three phase induction motor instead of the DC motor. The higher voltage and the use of three phases lowers the losses in the cables. The DC-DC converter considered features a parallel topology of half bridge converters. Maximum power point tracking (MPPT) is also incorporated.

The parallel topology proved to be invaluable in the implementation of the MPPT. Some recommendations are made to improve the concept further.

Key Words: DC-DC converter, half bridge, photovoltaic panels, variable speed drive, maximum power point tracking

1. INTRODUCTION

In dry regions of South Africa and in places where the water table is very low, boreholes tend to be very deep. Depths of 150 m or more are common. Due to the depths of the boreholes, wind pumps cannot be used as the length of the pipe that would be needed is too long.

The simplest solution is to use photovoltaic (PV) panels together with a DC motor to power a positive displacement pump (PDP) as shown in Fig. 1. However, this is a high power, low voltage setup which leads to I^2R losses in the long cables that feed the motor situated at the bottom of the borehole.
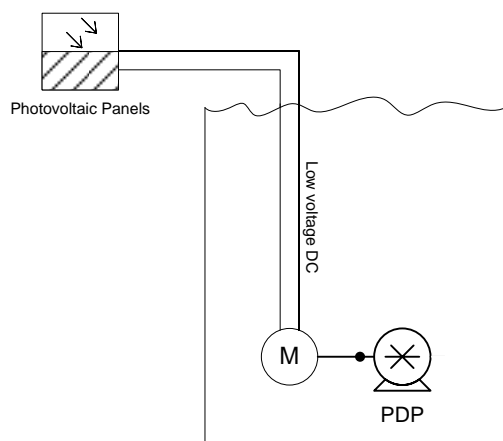
Fig. 1: Photovoltaic panels directly connected to a DC motor to power a positive displacement pump.

Previous work done by [1] and [2] provided an alternative to this lossy setup. The solution replaces the low voltage DC motor with a 400 V, three phase induction motor. The combination of the higher voltage and use of three phases will lower the current and thus lower the I^2R losses in the cable. The setup of the proposed system is shown in Fig. 2. The system consists of photovoltaic panels, a DC-DC- and a DC-AC converter, and a motor and PDP pump combination. The DC-AC converter is a standard commercial variable speed drive (VSD) used to do speed control on the motor. Although the VSD usually requires a 400 V three phase input it can also operate from a 500 V DC input. In this project the 500 V DC was supplied by the DC-DC converter. The photovoltaic panels, VSD, submersible induction pump motor and the PDP are standard components that can be bought. Only the DC-DC converter therefore had to be custom designed for this application.
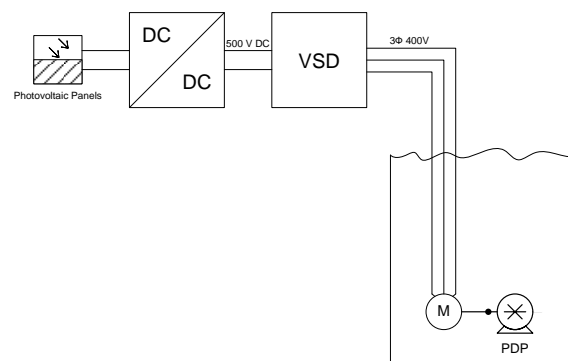
Fig. 2: Photovoltaic panels' low voltage DC converted to high voltage AC to power the three phase submersible induction motor

The complete system was successfully implemented by [1] but some recommendations were made. A single half bridge converter with three PV panels connected in series was used. The most important recommendations that were made were the addition of maximum power point tracking (MPPT) to the system. This will ensure that the photovoltaic panels are utilized to their optimum efficiency. Also the use of individual converters, one for each PV panel, should be considered.

In this paper different algorithms for MPPT are discussed as well as the converter topology used to implement the MPPT. Recommendations for future work will also be given.

Proceedings of the 19th Southern African Universities Power Engineering Conference
SAUPEC 2010, University of the Witwatersrand, Johannesburg

TOPIC F. CONTROL AND APPLICATIONS

2. MAXIMUM POWER POINT TRACKING

The output voltage and current of any PV panel is a function of the atmospheric conditions and the load connected to the system [3]. Because of the changing conditions it is necessary to constantly control the load so that the maximum amount of power is drawn from the panel. The typical voltage-current characteristic of a PV panel is shown in Fig. 3. It can clearly be seen that by changing the load connected to the panel the output power of the panel is also changed. The goal of MPPT is to actively control the operating voltage and current of the PV panel in order to supply maximum power to the load.

Different methods to do MPPT have been developed of which some are listed in [4].

2.1 Look-up Table

Measured output voltages and currents at the MPP under different conditions are stored in a table. A microprocessor can then use these values to operate the system at the MPP.

Large amounts of memory are needed and the values that are stored are only valid for a specific PV panel. However, it provides very fast MPPT because the exact values are instantly available.
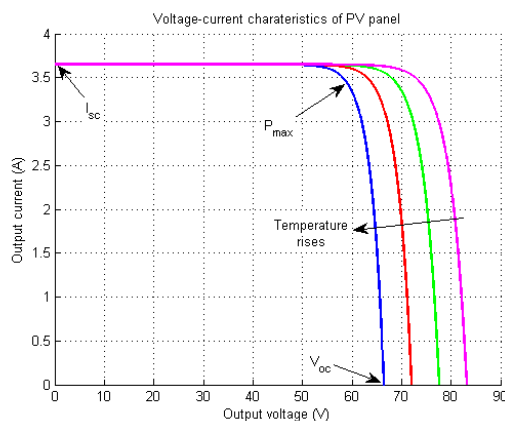
Fig. 3: Voltage-current characteristics of a photovoltaic panel with the maximum power point shown.

2.2 Constant Voltage or Current Tracking

From the voltage-current characteristics it can be derived that at the MPP the output voltage or current is an approximately constant factor of the open circuit voltage or short circuit current. The required output voltage and current for operation at the MPP can thus be calculated.

This method cannot track the MPP exactly because no factor can be found that will be true for all possible conditions. The factor is usually assumed to be between 60% and 80%. Furthermore, the PV panel will have to be periodically short circuited or open circuited to be able to measure the short circuit current or open circuit voltage. This will disrupt the power supply to the load that can have damaging effects.

A solution to overcome the decoupling of the panels is to use a test panel. This panel is not connected to the load and is only used to take the measurements of the open circuit voltage or short circuit current. However, this is not a viable solution as PV panels are expensive and one will not want to install a panel that will not provide any power.

2.3 Mathematical Model

By using a mathematical model of the PV panel and by measuring all the required parameters, the exact output voltage and current at the MPP can be calculated. The accuracy of the calculated values will depend on the accuracy of the model being used as well as the accuracy of the obtained measurements. All the necessary measurements should represent the exact conditions that the panel will be exposed to. Any measurement noise or offset will render the calculated MPP inaccurate.

2.4 Perturb and Observe

This is an iterative process to search for and track the MPP. The output voltage and current of the panel is measured and the output power calculated. The MPPT controller then disturbs the system. These disturbances include changing a duty cycle in a converter or changing something mechanically. The system is then given time to settle before the output power is measured again. If the power increased the direction of the disturbance, positive or negative, was correct. If the power decreased the direction for the following disturbance should be reversed.

This algorithm is PV panel independent but provides slow MPPT that may be seen as a disadvantage. It should however be stated that PV panels are not subjected to rapidly changing conditions. The response of the tracking can be altered by changing the step size of the disturbances. The fixed step size does cause the tracker to oscillate around the MPP but that can be corrected by using a variable step size. As the panel is operated closer to its MPP, the changes in the output power will decrease as the step size stays constant. The controller can then adjust the step size so that at the MPP it will disturb the system by zero.

2.5 Implemented Algorithm

As stated earlier, the conditions that the PV panels will be exposed to do not change very rapidly. It is therefore acceptable to use a slower tracking algorithm with higher accuracy. This motivates the use of the perturb and observe method of MPPT.

Some changes were made to the described working of the algorithm. The VSD in the proposed system setup requires a constant input voltage. The assumption was made that this voltage could be regulated by controlling the speed of the induction motor. Simple volt-per-hertz control [5] was used. The faster the motor rotates the more power it consumes and the voltage will decrease. If the motor slows down the voltage will increase. The VSD has

Proceedings of the 19th Southern African Universities Power Engineering Conference
TOPIC F. CONTROL AND APPLICATIONS
SAUPEC 2010, University of the Witwatersrand, Johannesburg

an analogue input for setting the speed of the motor connected to it.

As the output voltage of the DC-DC converter is not regulated by the converter itself, it leaves the duty cycle at which the switching elements operate as a freely controllable entity. By utilizing the duty cycle of the converter to implement current control, rather than voltage control, the converter can control the output current while the output voltage is regulated by the VSD and the motor. The MPPT algorithm should then maximize the output current in order to maximize the power delivered to the motor and thus maximizing the amount of water pumped.

The maximizing of the output current is done with the perturb and observe method. The current reference is disturbed after which the output power of the converter is measured. A fixed step size was used.

3.   CONVERTER

The successful implementation of the half bridge converter in [1] motivated the choice to continue with the half bridge. This was done so that more time could be spent on the development of the MPPT. The recommendation of using individual converters was however followed.

3.1 Parallel Topology

By using individual converters [5] each PV panel can be operated at its MPP. By connecting the panels in series all the panels carry the same current. This current is not necessarily each panel's current at its MPP, therefore each panel will not be able to operate at its MPP. A similar scenario occurs when the panels are connected in parallel. The PV panels are the most expensive components in the system, therefore their efficiency should be optimised as far as possible. The cost of the extra converters are only a fraction of the total cost of the system, and considering the better performance of the PV panels the extra cost is permissible.
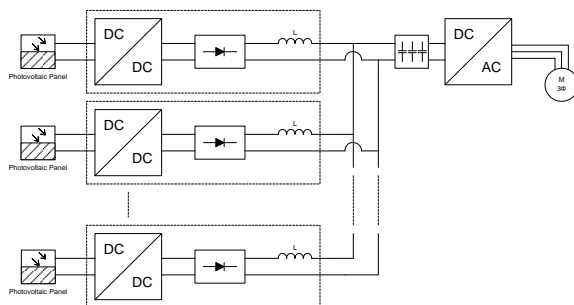
Fig. 4: Parallel topology used. Each PV panel's converter module has switching elements, a transformer and rectifier and filter inductor. The outputs feed the VSD in parallel.

The parallel topology proposed, converts each PV panel's output voltage to the 500 V as required by the VSD. The outputs of the individual converters are fed into a capacitor bank in parallel. The VSD is also connected to the capacitor bank. The topology is shown in Fig. 4. Each PV panel has its own converter module. The module consists of the switching

elements, the transformer, a full bridge diode rectifier as well as the filter inductor. The capacitor bank fulfils the function of filter capacitors.

3.2 Half Bridge Converter

The circuit of the half bridge converter is shown in Fig. 5. The transformer's winding ratio is of utmost importance. Theoretically it is possible to choose such a ratio that the converter will be able to provide the 500 V output voltage for almost any input voltage from the PV panel.
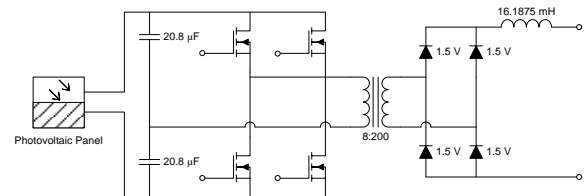
Fig. 5: Half bridge converter used in each PV panel's module.

The Sanyo HIT 180B panels that were used, have a maximum output voltage of 66.4 V. The minimum output voltage that still needs to be converted to 500 V determines the winding ratio. Special care should however be taken, as the larger the winding ratio, the higher the transformer's output voltage at the secondary side. This output voltage must be withstood by the rectifier diodes. The winding ratio is thus limited by the rectifier diodes' maximum blocking voltage. A safety factor of two was used in determining the ratio. A list of the components that were used in the half bridge converter is shown in Table 1.

Table 1: List of specifications for the half bridge converter.

Component	Value
Output voltage	500 V
Input voltage (max)	66.4 V
Input voltage (min)	44 V
Power	180 W
Output current ripple	100 mA
Output voltage ripple	1 V
Filter inductor	16.1875 mH
Filter capacitor	312.5 nF
Switching frequency	40 kHz

4.   CONTROL

The system was built using four of the Sanyo PV panels. A TMS320F28027 microprocessor from *Texas Instruments* was used for the control of the system. It features an eight channel pulse width modulation (PWM) port and twelve channel analogue to digital converter (ADC). The eight channel PWM provided the switching signals for the four half bridge converters as each converter requires two unique signals. The ADCs were used to measure the voltages and currents.

A representation of the control system for the system is shown in Fig. 6. Each of the four converter modules has a current controller with one voltage controller, which controls the speed of the motor.

The MPPT algorithm also forms part of the control system.
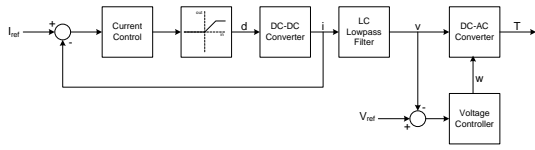
Fig. 6: Block diagram of control system.

4.1 Current Control

From [1] the output voltage to duty cycle transfer function of the half bridge is given in (1).

$$\frac{V_o(s)}{d(s)} = V_d \frac{N_2}{N_1} \frac{sCr_C + 1}{LCs^2 + \left(\frac{1}{RC} + \frac{r_L + r_C}{L}\right)s + \frac{1}{LC}} \quad (1)$$

Current control was needed, so the transfer function should be output current over duty cycle. By dividing the output voltage by the load resistance and setting that into (1), the output current to duty cycle transfer function in (2) was obtained.

$$\frac{I_o(s)}{d(s)} = \frac{N_2}{N_1} \frac{V_d}{R} \frac{sCr_C + 1}{LCs^2 + \left(\frac{1}{RC} + \frac{r_L + r_C}{L}\right)s + \frac{1}{LC}} \quad (2)$$

To be able to do MPPT on the individual PV panels each DC-DC converter's output current should be measured, and not only the total load current. Each converter's current was measured in the return path to the diode rectifier. This was done because of the instrumentation's common mode voltage limit of 80 V while the output's high side voltage was 500 V. Current in the return path is the same as the inductor current which has an average value equal to the load current but with the ripple current added to it. The assumption was made that the average current flows through the load and the ripple current through the filter capacitor. In order to remove this ripple current, a low pass filter was used between the measurement instrumentation's output and the ADC of the microprocessor. This made it possible to measure the average value of the current.

The measured average current, which is the output of the converter, can then be used for control purposes. The output current had to follow a reference value therefore an integral compensator was implemented. The loop gain was determined via a root locus design. The root locus of the converter's transfer function as well as the integral compensator is shown in Fig. 7.
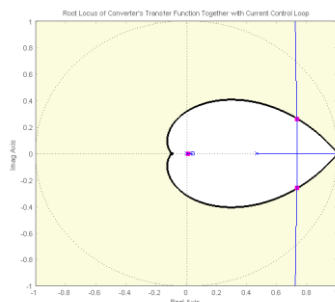
Fig. 7: Root locus of the converter's current to duty cycle transfer function together with the current control loop's transfer function

The marked area on the root locus represents an overshoot of 10%. The loop gain was determined and the final current control compensator is shown in (3) in difference equation form.

$$d(k) = 9.45 \times 10^{-3} e(k-1) + d(k-1) \quad (3)$$

4.2 Voltage Control

The voltage control compensator was also implemented as an integrator, but the loop gain was determined via experimentation. The output voltage was measured for different values of the loop gain. Some results are shown in Fig. 8. For the loop gain equalling 0.5 the output voltage was regulated to within 20 V of the reference value. The reference was taken to be 450 V.
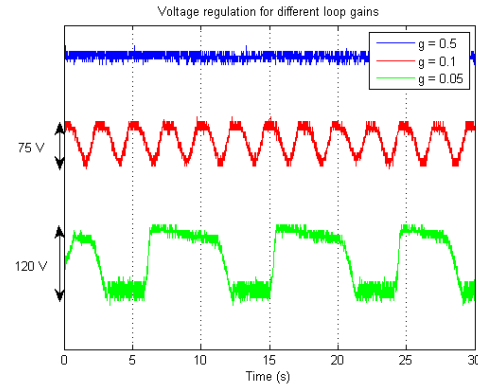
Fig. 8: Regulation of the output voltage for different values of the loop gain of the voltage control loop

The fact that the compensator was able to regulate the output voltage proves that the assumption that was made in section 2.5 is valid. The controller was indeed able to regulate the output voltage by controlling the speed of the motor. These tests were done with one converter powering the VSD.

4.3 MPPT

The functioning of the MPPT algorithm has already been stated in section 2.5. The working of the MPPT algorithm can be put in flow diagram form as shown in Fig. 9. Each DC-DC converter has such a process to find the MPP of the PV panel connected to it.

The MPPT that was implemented had a repeat rate of once every second. This made the tracking slow but it gave the voltage control loop sufficient time to regulate the output. It should be noted that some start-up procedure was necessary to bring the whole system into operation. For the first 30 seconds after reset the DC-DC converters' duty cycles, not the speed of the motor, were used to regulate the output voltage to 500 V. While the voltage was being regulated the motor was started and set to a predefined, slow speed. This is needed so that the control system will be able to regulate the voltage by changing the speed of the motor. If the motor is not running the speed cannot be altered. After the start-up time had elapsed, the current that each of the converters provide to the VSD was taken as their reference current, and the control system shown in

Proceedings of the 19th Southern African Universities Power Engineering Conference
SAUPEC 2010, University of the Witwatersrand, Johannesburg

TOPIC F. CONTROL AND APPLICATIONS

Fig. 6 was activated. At this time the MPPT algorithm also took effect.

The MPPT algorithm also included actions to take when the output voltage of a PV panel dropped below the threshold of being able to step it up to the required 500 V. At this point the controller will shutdown the PWM signals provided to the specific converter which will then cease to provide power to the VSD. The controller will however continue to monitor the panel's voltage in order to bring it online as soon as its voltage increases above the threshold.
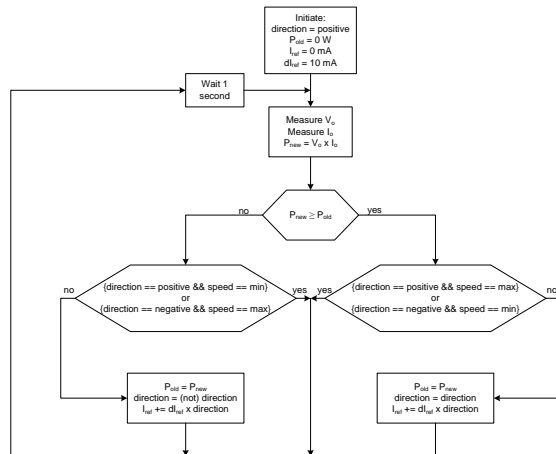
Fig. 9: Flow diagram of the MPPT algorithm. Each DC-DC converter has such a flow diagram to track its PV panel's MPP.

5. RESULTS

Some simulations were done to verify the designed values for components. Simulations were done in SIMPLORER® 7.0.5. The measurements were taken with a TDS3014B oscilloscope from Tektronix.

5.1 Simulations

The ability of the converter to regulate the output voltage to the required 500 V was simulated. Two simulations were done: one with ideal components with no series resistances or forward voltages and another with practical components. The results in Fig. 10 show that the converter can output the required 500 V for both instances. The switching elements were switched at a duty cycle that was ramped from zero to the theoretical value needed to result in a 500 V output voltage.
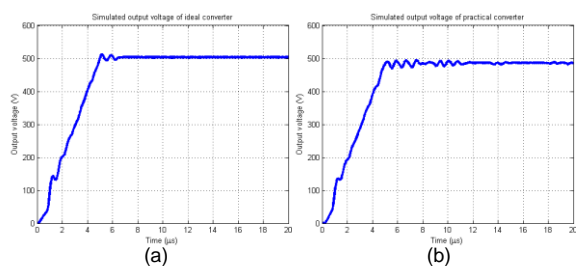
Fig. 10: Simulated values for the output voltage of the converter. (a) ideal components, therefore no series resistances or forward voltages for diodes; (b) practical components, therefore resistances and forward voltages taken into account.

5.2 Diode Rectifier Reverse Voltage

The high winding ratio of the transformer posed a serious problem. By having a low minimum output voltage from the PV panels and therefore a high winding ratio, the reverse voltage across the rectifier diodes was high. The higher the peak reverse voltage the diodes would have to withstand, the slower their reverse recovery time. The slower the recovery time, the more power gets dissipated. This is not favourable as the diodes need to rectify an 80 kHz square wave.

The results shown in Fig. 11(a) are the reverse voltages experienced by the rectifier diodes. The peak value of 1 600 V is more than the 1 500 V diodes can handle. One would preferably not use the diodes at more than 1 250 V in order to leave some margin for safety. A voltage limiting snubber needed to be added.
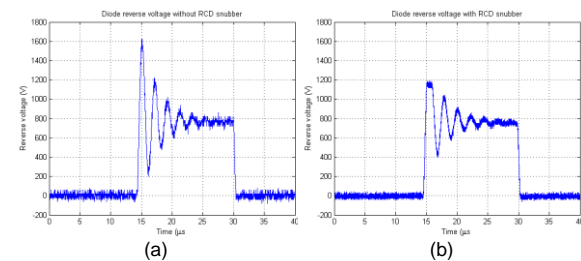
Fig. 11: Reverse voltage for the rectifier diodes (a) without and (b) with a RCD voltage limiting snubber.

The snubber chosen was a resistor-capacitor-diode (RCD) snubber [6]. From the circuit shown in Fig. 12 the additional components can be identified. L_{leak}, r' and C' are parasitic components in the circuit. The RCD snubber is made up from D_{ov}, r_{ov}, C_{ov} and R_{ov}. The OV subscript designates the components as part of the "overvoltage" snubber.

The threshold voltage above which the snubber will clamp the voltage is controlled by the voltage over C_{ov}. If the reverse voltage of a diode exceeds this threshold, D_{ov} will become forward biased. The voltage across a capacitor cannot change instantaneously, so C_{ov} will clamp the voltage. R_{ov} is used to program the threshold voltage and r_{ov} is used to limit the current into C_{ov}.
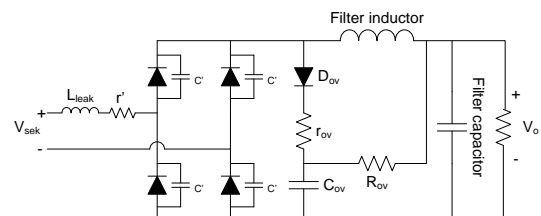
Fig. 12: RCD overvoltage snubber.

5.3 Efficiency

The efficiency of the DC-DC converters was measured. At full load an efficiency of 87% was achieved.

Proceedings of the 19th Southern African Universities Power Engineering Conference
SAUPEC 2010, University of the Witwatersrand, Johannesburg

TOPIC F. CONTROL AND APPLICATIONS

5.4 MPPT Algorithm

The MPPT algorithm was tested using three DC-DC converters. The output voltage, current and power is shown in Fig. 13. In the time between 10 seconds and 40 seconds the MPPT is inactive and the system only regulates the output voltage. The voltage dip at 20 seconds is due to the motor being switched on. From 40 seconds onwards, the MPPT is increasing the current references of the three converters while the motor's speed increases to regulate the voltage. The load used could only dissipate around 180 W, which can be seen at 85 seconds as the output power no longer increases.

The system was able to keep the output voltage of the DC-DC converters constant while it increased the power delivered to the load. This result proves the correct working of the implemented MPPT algorithm.
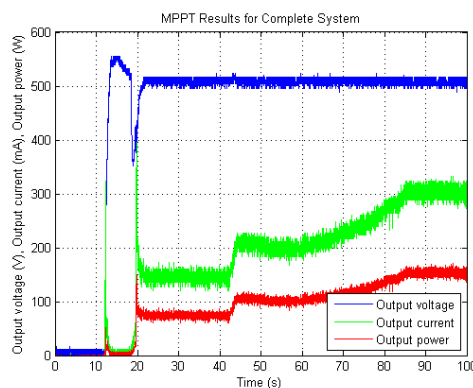
Fig. 13: MPPT results for three converters used. The DC-DC converters' output voltage, current and power is shown.

6. RECOMMENDATIONS

The major cause for the problems experienced was due to the high input voltage which the VSD required. The high voltage meant high winding ratios on the transformers, which resulted in too high reverse voltages for the rectifier diodes. By lowering the winding ratio, the minimum output voltage from the PV panels that can be regulated to 500 V becomes higher. This means that the system will operate for a shorter period of time during the day.

The proposed solution is to design (or modify) a VSD that does not require such a high minimum input voltage but will still be able to implement speed control on the motor. When low power is available from the PV panels, for example at sundown or rainy days, their output voltages will also be low. When low power is available the speed of the motor will be slow. If a motor is turning slowly and volt-per-hertz control is used the amplitude of the voltages from the VSD will be low. Therefore at times when the PV panels' output voltage is low, the amplitude of the output voltage of the VSD is also low. As more power becomes available and the output voltages of the PV panels increases, the VSD's output can also increase as the motor's speed increases.

By using such a VSD as described above the output, voltages from the PV panels does not have to be stepped up 25 times as was done in this project. The much lower winding ratio will solve the problems regarding the overly high voltages.

Another recommendation is to change the MPPT algorithm to make use of a self adjusting step length. This will provide the system with better tracking and thus better utilization of the PV panels.

In addition, the half bridge converters should be replaced by full bridge converters with a phase shift switching scheme. The full bridge converter does not have the expensive bus capacitors that the half bridge has. These are expensive due to the large currents they have to be able to handle. The phase shift switching scheme provides zero voltage switching (ZVS) that will reduce switching losses, and thus increase the efficiency of the system.

7. CONCLUSION

In this paper, an attempt was made to design a parallel DC-DC converter system to provide power to a VSD that powers a three phase induction motor to operate a PDP. The power source was PV panels. The system needed to include MPPT for the PV panels.

The parallel topology used in this project proved to be successful and worthwhile. The slightly more expensive converters were able to operate the PV panels, which were the most expensive components, to their optimum efficiency.

The project outcomes were met but further attention should be given to the recommendations made.

REFERENCES

[1] Johannes Cornelius Bekker, "Halfbrug GS-na-GS Omsetter as Koppelvlak Tussen Fotovoltaïse Panele en Drie-fase Omsetter," Stellenbosch University, Stellenbosch, Final Year Project 2008.

[2] Marko Wolf, "A Solar DC-DC Converter Front-end for a BLDC Water Pump," Stellenbosch University, Stellenbosch, Final Year Project 2007.

[3] Y.H. Lim and D.C. Hamill, "Simple Maximum Power Point Tracker for Photovoltaic Arrays," Electronics Letters, vol. 36, no. 11, May 2007.

[4] H.P. Desai and H.K. Patel, "Maximum Power Point Algoritm in PV Generation: An Overview," IEEE, vol. PEDS, 2007.

[5] T. Wildi, Electrical Machines, Drives and Power Systems.: Pearson, 2006.

[6] B. Liu, S. Duan, and Y. Kang, "A DC-Module-Based Power Configuration for Residential Photovoltaic Power Application," IEEE, vol. PEDS, 2007.

[7] Marko Wolf, "Design and Implementation of a Solid State Transformer," Stellenbosch University, Stellenbosch, 2009.

TOPIC F. CONTROL AND APPLICATIONS

Proceedings of the 19th Southern African Universities Power Engineering Conference
SAUPEC 2010, University of the Witwatersrand, Johannesburg

TRANSFER FUNCTION BASED INTEGRATION OF DERS AND DYNAMIC STABILITY ANALYSIS OF MICROGRID

Prasenjit Basak*,   S Chowdhury** and S P Chowdhury**

Calcutta Institute of Engineering & Management, Electrical Engineering Department, Kolkata, India.

** *University of Cape Town, Electrical Engineering Department, Cape Town, South Africa.*

Abstract.   A microgrid is an integrated form of distributed energy resources (DERs) which are connected together to serve electrical power to the selected consumers or can exchange power with the existing utility grid suitably under standalone or grid connected mode. The microgrid can be cited as a physical system which is a combination of DERs such as, Photovoltaic Generator, Wind turbine, Fuel Cell, Electrolyzer system, Microturbine etc. and can be modeled   with suitable assumptions depending upon specific operational condition to be studied. Interconnection of several kinds of power sources would impact the quality of power within the microgrid. Since voltage and frequency are not the only factors for a system delivering good quality power, the capacity of the same to withstand instability due to transient condition is one of the prime factors to be considered to accept a system as a stable system. Before practical integration of distributed energy resources, it would be essential to check the stability of the system at the design stage. In this paper, the authors have presented the microgrid based on control system engineering. To represent the individual components of microgrid, the DERs (Distributed Energy Resources) have been represented with their transfer functions and they have been simulated using Simulink-Matlab. To observe the response of the DERs, the frequency fluctuation due to step and random change in output power/load are considered as the main factors for stability analysis. All the DERs are integrated forming the microgrid which is represented with an equivalent transfer function based model. The models are studied and results are discussed with the waveforms. This paper shows one feasible method to check the dynamic stability of a proposed microgrid.

Key Words.   Dynamic Stability of Microgrid, Integration of DERs, Microgrid, Pole-Zero Plots, Polynomial Stability Test.

1.   INTRODUCTION

The stability of a microgrid, which is interconnection of several distributed energy resources, is its ability to return to normal or stable operation after having been subjected to some form of disturbance. Conversely, instability means a condition denoting loss of synchronism or falling out of step. Stability considerations have been recognized as an essential feature of microgrid planning. For proper working of microgrid, the stability problems are to be taken care, covering the steady state, dynamic and transient condition. The study of steady state stability mainly concerned with the calculation of maximum limit for the DER loading before losing synchronism, provided the loading is increased gradually [1]. In microgrid, dynamic instability is more probable than steady state instability. The dynamic instability may occur due to sudden fluctuation of load and the system oscillation may occur which has to die out completely within a short time. If the oscillation of the system output persists for a longtime, then the microgrid will be dynamically instable, which may be a serious threat to the interconnection of DERs. This paper shows a feasible method to study the dynamic stability of a microgrid. Initially, the individual DERs are presented with their first order transfer functions based on assumption on the linearity of the systems with reference from the study of Battery Energy Storage (BES) facility system [2][3].

2.   RESPONSE OF DISTRIBUTED ENERGY RESOURCES AGAINST FREQUENCY AND POWER FLUCTUATION

The widespread use of various kinds of distributed power sources would impact the quality of the power supply within a microgrid power system, causing many control problems. This paper discusses the dynamic stability of microgrid operation and presents the control scheme of combining fuel cell, electrolyzer system and micro-turbine as a hybrid system to enumerate the microgrid system's ability to solve power quality issues resulting from frequency fluctuations due to sudden and random load fluctuation [4].

With reference to [3], large Battery Energy Storage (BES) facility may provide significant dynamic operation benefits for electric utilities. One area in which a BES facility could be useful is the frequency regulation requirement. This feature is significantly important in island power systems. In [3], D. Kottick, M. Blau and D. Edelstein quantified the effects of a 30 MW battery on frequency regulation in the Israeli isolated power system. The study was performed on a single area model representing the whole power system and containing a first order transfer function that represented the BES performance. In reference to [2] and [3], in this paper, each source is presented with their first order transfer functions. Next section focuses on the stability of each system against fast frequency fluctuation and sudden output power unbalance. Each system is observed with their output waveforms showing overshooting due to sudden power fluctuation and finally reaching steady state condition.

2.1 Fuel Cells

With reference to [5], in order to introduce and apply small fuel cell cogeneration to a building, it is necessary to investigate the response characteristics of the power and heat power with load fluctuations. In particular, the power demand pattern of an individual house is a load that has usually gone up and down rapidly for a short time. If a system is controlled to follow such a load, the difference in the response and load increases. As a result, the power quality (voltage and frequency) of this power system may worsen. "Fluctuation in a short period, such as an inrush current" and "fluctuation in a long period to cause in change of demand" are included in the power load. "Change over a long period" means a step change in the power demand. With the change factor of the transient power demand, such as with an inrush current, there is a change over a long period in the demand. When "transient power demand" is defined as load fluctuation and "change over a long period" is defined as demand fluctuation, the power load changes of an individual house have large fluctuations of both. If the transient response of a single cell of a fuel cell is examined, it seems that stable response characteristics are acquired for the load fluctuation characteristics of the household appliance items used in common homes [5]. As referred in [2], the sudden real power fluctuation of a fuel cell generator can be represented by its transfer function $\Delta P_{FC} = [K_{FC} / (1 + T_{FC} S)] \Delta f$

where,

ΔP_{FC} = Real time power fluctuation
Δf = Frequency fluctuation due to sudden fluctuation of real power
P_{FC} = Output power of Fuel Cell
K_{FC} = Gain of Fuel Cell
T_{FC} = Time Constant of Fuel Cell

Fig.1.1: Output Power versus Frequency Control of Fuel Cell for Step Change in Output

Fig. 1.2: Output Power versus Frequency Control of Fuel Cell for Random Change in Output

In the Fig. 1.1 and Fig. 1.2, the fuel cell is presented with the Proportional plus Integral control scheme where the sudden fluctuation of output power is simulated with a step and random change of output respectively. Due this step change in output power, the fluctuation of frequency is shown in Fig. 2.

Fig.2: Frequency Variation in Fuel Cell for Step Change in Load

Sudden fluctuation of frequency due to that disturbance in output is shown with overshooting and damping and finally reaching steady state. The variation of output power and system response due to random & step variation of output power is shown in Fig. 3 and Fig. 4 respectively.

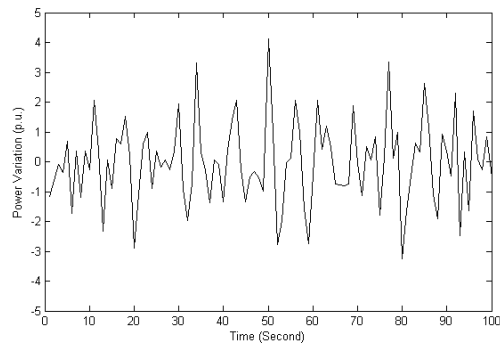Fig.3: Output Power Variation in Fuel Cell for Random Change in Load

Fig.4: Output Power Variation in Fuel Cell for Step Change in Load

2.2 Electrolyser System and Microturbine

As referred in [6], it is well known that the power output of microturbine can be controlled to compensate for load change and alleviate the system frequency fluctuations. Nevertheless, the microturbine may not adequately compensate rapid load change due to its slow dynamic response. Moreover, when the intermittent power generations from wind power and photovoltaic are integrated into the system, they may cause severe frequency fluctuation [6].

In order to study the fast dynamic response, each system is studied separately to observe the absorption of the frequency and power fluctuations. Simulation results exhibit the robustness and stabilizing effects of electrolyzer and microturbine.

The sudden real power fluctuation of an Electrolyser system can be presented as [2],

$\Delta P_{ES} = [K_{ES} / (1 + T_{ES} S)] \Delta f$;

where,

ΔP_{ES} = Real time power fluctuation

Δf = Frequency fluctuation due to sudden fluctuation of real power

P_{ES} = Output power of Electrolyser system

K_{ES} = Gain of Electrolyser system,

T_{ES} = Time Constant of Electrolyser system

Fig. 5.1: Scheme for Step Change in Output of Electrolyser

Fig.5.2: Scheme for Random Change in Output of Electrolyser

The proportional integral control schemes are shown in Fig.5.1 and Fig. 5.2. Disturbance is created at the output in two modes; one is sudden fluctuation which is simulated with sudden step change in output and the other is random power fluctuation simulated by random noise signal generated by Simulink tool box. The frequency fluctuation for step change in load and power variation due to random and step load fluctuation are shown in the following Fig. 6, Fig. 7 and Fig. 8 respectively.

Fig.6: Frequency Variation in Electrolyser System for Step Change in Load

Fig.7: Output Power Variation in Electrolyser System for Random Change in Load

Fig. 8: Output Power Variation in Electrolyser for Step Change in Load

The above outputs show the satisfactory damping of the overshoot occurred due to disturbances applied as mentioned above.

A Microturbine block which is normally intended for base load supply is shown in the Fig. 9.

Fig.9: Output Power versus Frequency Control Scheme for Microturbine

Considering the linear power versus frequency droop characteristic, the transfer function based formulation is shown below [2].

$\Delta P_{MT} = (-1 / K_{MT})\, \Delta f;$

where, ΔP_{MT} = Real time power fluctuation,

Δf = Frequency fluctuation due to sudden fluctuation of real power,

K_{MT} = Droop property of Microturbine output

Variation of output power in Microturbine due to step change and random fluctuation of load is shown in Fig. 10 and Fig. 11 respectively. The waveform obtained shows zero error after damping off the overshoot.
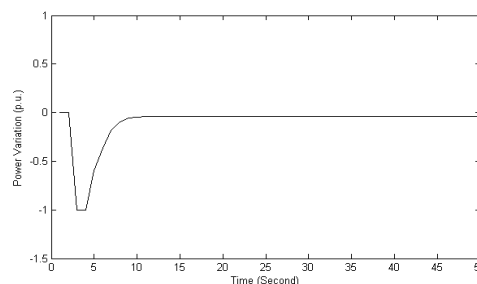
Fig.10: Output Power Variation in Microturbine for Step Change in load

Fig.11: Output Power Variation in Microturbine for Random Change in load

3. TRANSFER FUNCTION BASED MODEL OF MICROGRID: STUDY OF FREQUENCY AND OUTPUT POWER FLUCTUATION

In the previous sections, the Fuel Cell, Electrolyser system and Microturbine are studied separately and are simulated to observe the dynamic instability.

In this section, the transfer functions of DERs are integrated as shown in the Fig. 12 forming microgrid. The integrated system is tested for dynamic instability with a step change in the output power. Proportional plus integral control strategy is used and the output power wave form obtained is shown in the Fig. 13 below. The result shows satisfactory performance of the microgrid model against dynamic instability. The model is studied for random load fluctuation and the response is observed as shown in Fig. 14. Step response output data are shown in Table 1.

Fig.12: Transfer Function based Model of Microgrid

Fig.13: Output Power variation in Microgrid due to Step Change in Load

Fig.14: Output Power Variation in Microgrid due to Random Change in Load

Table-1 : Step Response obtained after Linear Analysis of Microgrid

	FC	ES	MT	MG
Peak Amplitude	0.887	0.95	-25	-3
Overshoot (%)	Infinity at t=0	Infinity at t=1.09	$2.5*10^3$	$7.7*10^3$
Rise Time (Second)	0	0	0.845	0.902
Settling Time (Second)	11.7	14.2	1.5	10.4
Final Value	0	0	-0.962	-0.0385

FC = Fuel Cell, ES= Electrolyser, MT= Microturbine, MG=Microgrid

4. STABILITY ANALYSIS OF MICROGRID

The microgrid shown in Fig. 12 are studied for stability analysis with Pole-Zero mapping [7] using Matlab-Simulink. The main objective of this section is to check if there is any root of the characteristic equation on the right half of s-plane. The step change in output power is considered as input and the output power variation is considered as output. The result is shown in Fig. 15. It shows that no pole is located on the right hand side of the imaginary axis of S-plane, supporting stability of the microgrid system.

Polynomial Stability Test: The microgrid shown in Fig. 12 above also studied for "Polynomial Stability Test" using Matlab Simulink tool box. This block is used to check the pole locations of the denominator polynomial, A(z), of a transfer function, H(z) as mentioned below.
Mathematical Formulation:
$$H(Z) = [B(Z)/A(Z)]$$
$$= \{b_1+b_2Z^{-1}+....+b_mZ^{-(m-1)}\}/\{a_1+a_2Z^{-1}+....+a_nZ^{-(n-1)}\}$$

Fig.15: Pole-Zero Mapping of Microgrid

The poles are the n-1 roots of the denominator polynomial, A(z). As is typical in DSP applications, the transfer function above is specified in descending powers of z-1 rather than z. "The Polynomial Stability Test Block" uses the Schur-Cohn algorithm to determine whether all roots of a polynomial are within the unit circle. If any poles are located outside the unit circle, the transfer function H(z) is unstable showing zero(0) at the output of the Simulink test block. For the system to be stable, the output of the block should display one (1). After simulation of the current system, the value 1 is obtained at the output of the "Polynomial Stability Test Block" indicating that the polynomial in the corresponding column of the input is stable.

5. CONCLUSION

Renewable energies are environmentally focused but the output power fluctuation of renewable energies may cause excess variation of voltage or frequency of the grid. Increase in the amount of renewable energies would violate the quality of the grid [8]. To maintain the quality of the grid, the design of a microgrid should meet some specific criteria which can judge its performance. There are many factors responsible towards smooth integration of the DERs to form microgrid. Eventually, all the possible factors should be considered at the stage of research and development prior to the system put in actual operating mode for effective utilization of R&D cost.

Among many prime factors, a microgrid must be studied for stability at design level. It is necessary to develop suitable tool or method to check the stability criteria of a proposed grid. In this paper, the authors have suggested few methods to study the dynamic stability of a proposed microgrid due to sudden fluctuation of load by representing each component of the microgrid in the form of their transfer function. It is realized from this work, that there are many features such as linearity or non linearity of the system, gain, time constants, etc. which decide the transfer function of a DER and the transfer function may vary as per the assumptions considered for those factors even for the same system. So the stability analysis has many dimensions to be dealt with in the future research work. Further research efforts will attempt to accumulate all the possible factors for integration of distributed energy resources and stability analysis of microgrid. Progress of this research will be reported in due course.

ACKNOWLEDGMENT

REFERENCES

[1] D.P. Kothari, I.J. Nagrath, "Modern Power System Analysis", 3rd Edition, Chapter 12, pp 433-434.

[2] Xiangjun Li, Yu-Jin Song, Soo Bin Han, "Study on Power Quality Control in Multiple Renewable Energy Hybrid Microgrid System," in *Proc. PowerTech 2007*.

[3] D. Kottic, M. Blau and D. Edelstein, "Battery Energy Storage for Frequency Regulation in an Island Power System" in IEEE Transactions on Energy Conversion", Vol.8, No3, pp- 455-459, Sep. 1993.

[4] Xiangjun Li, Yu-Jin Song and Soo-Bin Han; Frequency control in micro-grid power system combined with electrolyzer system and fuzzy PI controller; Journal of Power Sources, Volume 180, Issue 1, 15 May 2008, Pages 468-475, Copyright © 2008 Elsevier B.V.

[5] S.Obara, Fuel Cell Microgrids, © 2009 Springer, Power Systems Series, Chapter 7: Load Response Characteristic of the fuel cell for individual Cold-region houses; p- 113.

[6] Sitthidet Vachirasricirikul, , Issarachai Ngamroob and Somyot Kaitwanidvilaib, Application of electrolyzer system to enhance frequency stabilization effect of microturbine in a microgrid system, International Journal of Hydrogen Energy, Volume 34, Issue 17, Pages 7131-7560 (September 2009)*Pages 7131-7142,* Crown copyright © 2009 Published by Elsevier Ltd.

[7] I.J. Nagrath, M. Gopal, "Control Systems Engineering", 2nd Edition, Chapter 9, pp 274-318.

[8] M. Matsubara, G. Fujita, T.Shinji, T. Sekine, A. Akisawa, T. Kashiwagi & R. Yokoyama, "Supply and Demand Control of Dispersed type Power Sources in Microgrid", in Proc. 13th Int.. Conf. ISAP'05, pp 67-72.

[9] R.H. Lasseter and P. Paigi, "Microgrid: A Conceptual Solution", in Proc. 35th Annv. Conf. IEEE, PESC'04, pp 4285-4290.

IMPACT OF INTEGRATED HVAC-HVDC TRANSMISSION ON THE ROTOR ANGLE STABILITY OF A POWER SYSTEM NETWORK

D T Oyedokun, K A Folly, S P Sheetekela, L C Azimoh, A V Ubisse

University of Cape Town, Department of Electrical Engineering, Rondebosch, 7700, South Africa

Abstract.   The technical and economic benefits of using HVDC for power transmission, together with the advancement in thyristor design, lead to the increase in HVDC application in different power utilities world wide. In this paper, the rotor angle stability of a two-area power system with two different transmission line scenarios is investigated. Firstly, HVDC transmission is implemented between two areas of a power network with no connection of HVAC transmission line and secondly, HVDC transmission is implemented between the two areas of the network which already has a connecting HVAC transmission tie- line. To determine the rotor angle stability of the above described two scenarios of transmission line, AC and DC faults are applied to system. The simulation results have proved that the use of integrated HVAC-HVDC transmission schemes will reduce the amplitude of the first rotor angle swing and subsequent oscillations after a DC or AC fault. It takes longer for the system to recover from a 3-phase fault and a fault on the HVDC line when HVDC alone is used for power transmission between the two areas. The use of integrated HVAC-HVDC transmission reduces this time. Therefore, the integrated HVAC-HVDC transmission scheme is a preferred over HVDC transmission.

Key Words. Rotor angle, HVDC, HVAC, transmission, transient stability

1.   INTRODUCTION

The 21st century is characterized by industrialization and growth across the globe. The consequence to this is the increase in load demand and the need to increase generation and transmission capacity. The commencement of HVDC transmission in the 1950's and its rapid development had make the bulk power transmission over long distances a possibility [1,2,3].

Examples of HVDC schemes include the HVDC pacific inter-tie in the USA which has a total of 3100 MW over a distance of 1360 km [4], the Hydro Quebec New England link which exchanges 2250 MW via HVDC transmission, Itaipu HVDC scheme in Brazil with a capacity of 6300 MW [4, 5], the cross channel UK- France scheme with a capacity of 2000 MW and Wybord in Russia with a capacity of 1050 MW, etc. [4]. The scheme between North and South Islands of New Zealand is of 1240 MW capacity. In China, the first HVDC transmission scheme known as the GESHA scheme has a capacity of 1200 MW which interconnects central China and Eastern China over a distance of 1045 km [6, 7, 8].

The advantages of HVDC transmission includes; reduced power losses, economic benefit for long distance transmission, ease of bulk power transfer, the ability to connect asynchronous power networks, under-sea power transmission and reduced servitude requirements [9, 10, 11, 12].

HVDC transmission can be implemented in two major scenarios. The first implementation is interconnecting areas of a power system which has no AC tie. The second form of implementation is a scenario where HVDC transmission is used to interconnect areas of a power system that already has an AC tie-line. In this paper, the latter of the two forms will be regarded as the integrated HVDC transmission scheme.

Just like HVAC transmission lines, HVDC transmission lines are susceptible to faults. The most common causes of HVDC line faults are lightning, field fire, bird droppings, un-kept trees along the servitude of the HVDC transmission line, etc. Other faults associated with HVDC transmission are faults within the converter stations. These faults will have an impact on the rotor angle stability of the generators within the power system. Moreover, the location and the duration are very important in that they affect the severity of the fault [10, 11, 13, 14, 15].

In this paper, the rotor angle stability of a two-area power system with two different transmission line scenarios is investigated. In the first scenario, HVDC transmission is implemented between two areas of the power network with no connection of HVAC transmission line and in the second scenario, HVDC transmission is implemented between the two areas of the network which already has a connecting HVAC transmission tie- line To determine the rotor angle stability of the above described two scenarios of transmission line, three-phase to ground AC fault and DC converter   faults are simulated. The simulation results indicated that the use of integrated HVAC-HVDC transmission schemes will reduce the amplitude of the first rotor angle swing and subsequent oscillations after a DC or AC fault. It takes longer for the system to recover from a 3-phase fault and a fault on the HVDC line when HVDC alone is used for power transmission between the two areas. The use of integrated HVAC-HVDC transmission reduces this time. Therefore, the integrated HVAC-HVDC transmission scheme is a preferred over HVDC transmission.

2. OVERVIEW ON HVDC TRANSMISSION

2.1 Converter equations

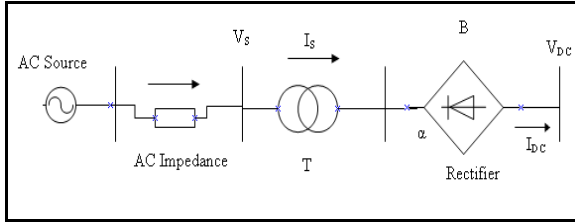Fig.1 shows the schematics of the rectifier side of a HVDC scheme.

Fig.1 Rectifier side of a HVDC scheme

$$V_{DC} = \frac{3\sqrt{2}}{\pi} V_S BT \cos\alpha \qquad (1)$$

Where: B = Number of converter bridges
        T = Transformer turns ratio

$$V_{DC(R)} = \frac{3\sqrt{2}}{\pi} V_{SR} BT \cos\alpha \qquad (2)$$

$$V_{DC(I)} = \frac{3\sqrt{2}}{\pi} V_{SI} BT \cos\gamma \qquad (3)$$

$$I_{DC} = \frac{V_{DC(R)} - V_{DC(I)}}{R_R + R_L + R_I} \qquad (4)$$

Where $V_{DC(R)}$ is the rectifier DC voltage, V_{SR} is the rectifier AC Voltage, $V_{DC(I)}$ is the inverter DC voltage, V_{SI} is the Inverter AC Voltage, γ is the inverter extinction angle, R_R is the resistance of the Rectifier, R_I is the resistance of the Inverter, R_L is the resistance of the HVDC Line, I_{DC} is the DC line current, α is the firing angle.

From (3) and (4), the DC power output from the rectifier is given as follows:

$$P_{DC} = V_{DC(R)} \cdot I_{DC} \qquad (5)$$

$$Q_R = P_{DC} \cdot \tan(\phi) \qquad (6)$$

Where Q_R is the reactive power absorbed by the rectifier and ϕ is the power factor angle.

3. ROTOR ANGLE STABILITY

Rotor angle stability is the ability of synchronous machines in a power system to remain in synchronism after been subjected to a disturbance. This stability also depends on the ability of the machines to maintain equilibrium between the electromagnetic torque and the mechanical torque. The movement of the rotor is governed by the Newton's second law of motion given by equation 7 [1, 16].

$$J\alpha_m(t) = T_m(t) - T_e(t) = T_a(t) \qquad (7)$$

Where J is the total moment of inertia of the rotating mass, kgm^2, α_m is the rotor angular acceleration, rad/s^2, T_m is the mechanical torque, Nm, T_e is the electrical torque, Nm and T_a is the net accelerating torque, Nm.

The rotor angular acceleration is given by equation 8.

$$\alpha_m(t) = \frac{d^2\theta_m(t)}{dt^2} \qquad (8)$$

Where θ_m is the rotor angular position

After substituting equation 8 into equation 7, converting from toque to power, the swing equation can be given in per unit as:

$$2H\omega_{p.u}(t)\frac{d^2\delta(t)}{dt^2} = P_{m\,p.u}(t) - P_{e\,p.u}(t) = P_{a\,p.u}(t) \qquad (9)$$

where:
H is the normalized inertia constant (sec), P_a is the accelerating power, P_m and P_e are the mechanical and electrical power respectively.

When the power system is in steady state of equilibrium, the mechanical power and the electrical power of the generator in equation 9 remain the same, so is the speed of the generator [1]. Hence, there is no accelerating power. This means that the rotor angle of the synchronous machines in the interconnected power system will be at a fixed angular position. If the systems is perturbed by a disturbance such as a three-phase to ground fault, HVDC line fault or the loss of a generating unit, the equilibrium between P_e and P_m is lost and the speed of the generator changes. This change will lead to an imbalance in the active power generation by all the machines in the power system [1, 16, 17, 18, 19].

3.1 Responses of the System AC and DC faults

Power systems with HVDC transmission schemes are not completely infallible to faults. The stability of such power systems are affected by DC line faults, converter faults. In AC systems, relays and circuit breakers are used for fault detection and clearance. On the contrary, most of the faults in DC systems are self-clearing or are cleared through the action of converter controls [19]. In some cases though, it may become necessary to take out a bridge or an entire pole out of service.

A)   DC line Faults

The most common type of faults on DC lines is pole-to-ground faults. This faults blocks power transfer on the affected pole with the rest poles remaining intact. During this fault, the short circuit causes the rectifier current to increase while the inverter current decrease. The rectifier current control acts to reduce the direct voltage and also reduce the current back to the current set point (normal operation current level). At the inverter side of the scheme, the current level reduces below its current reference value

$(I_{ord} - I_m)$. This causes the inverter to change from Constant Extinction Angle (CEA) control to Constant Current (CC) control. As a result, the voltage of the inverter reduces to zero and then reverses its polarity as shown by line B in fig. 2 [10, 14, 15, 20].
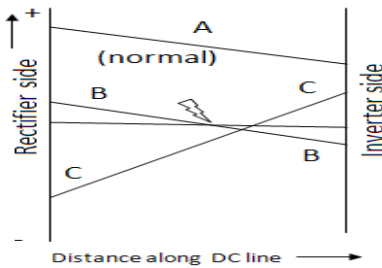

Fig.2 Voltage profile on a DC line

Under normal control action, the fault arc is not extinguished while limiting the fault current to the current margin [10]. With fast acting line protection, the fault is detected by the drop in DC voltage and current at the rectifier and the inverter respectively. After the fault has been detected, the angle beta of the inverter is changed to a maximum limit of 80^0 to allow the inverter voltage reduce to zero but not to reverse polarity as explained under normal control action. At the rectifier side, the rectifier firing angle is changed above 90^0. This is shown by line C in figure 2. Although the current in the pole may attempt to change polarity, this will not be successfully as a result of the unidirectional current characteristics of converter valves. Consequently, the current is reduced to zero in a very rapid manner. This process is called "forced retard". Following this, the DC line is restarted with time for de-ionisation taken into consideration.

B)   Rectifier side AC fault

The DC system response to AC fault is faster than that of the AC system. The DC system is capable of self sustenance through the AC system fault or in severe cases, there will be a reduction in power or a complete shut down till the AC system recovers from the fault [10]. When the AC fault is a distant 3-phase fault, there will be a reduction in the rectifier commutation voltage, which will lead to a reduction in the DC voltage and current. If the firing angle reaches its minimum value, the control measure will switch the rectifier from CC mode to Constant Ignition Angle (CIA) mode while the inverter changes to CC mode. The Voltage Dependent Current Order limit (VDCOL) regulates the transfer of current and power depending on how low the voltage at the rectifier drops during the rectifier side AC fault. Although in theory, DC power may be transmitted via the HVDC transmission line when the rectifier voltage is very low, the resulting increase in reactive power consumption could damage the generators. This is mainly because the inverter would have to change from CEA to CC mode by lowering its voltage and increasing β [10].

4.   SYSTEM MODEL

DigSILENT power factory was used in the simulations. Area 1 has two generating stations, G3 and G4 which are connected to bus 3 and bus 4, respectively in area 2, via a double-circuit transmission hybrid HVAC-HVDC as shown in Figure 3 and figure 4. Each of the generating stations in area 1 has a capacity of 1700 MW. Area 2 has a total local generating capacity of 600 MW of which 400 MW is from G2 and the rest from G1. Furthermore, area 2 has two distribution centers. The first distribution center is at bus 7 which is connected to bus 5 via a 1600 MVA 500/11 kV step down transformer. The second distribution center is at bus 8 which is connected to bus 5 via a 1600 MVA 500/11 kV step down transformer. The load at bus 7 is 1064MW while the load at bus 8 is 1379 MW. Capacitor banks are connected to Bus 5 and Bus 6 contributing a total reactive power compensation of 1000 Mvar. The HVDC scheme is given in Figure 4 with two series rectors, each of 0.86 H connected to each end of the HVDC transmission line. A combination of two 6-pulse converters is used for the rectifier and the inverter.
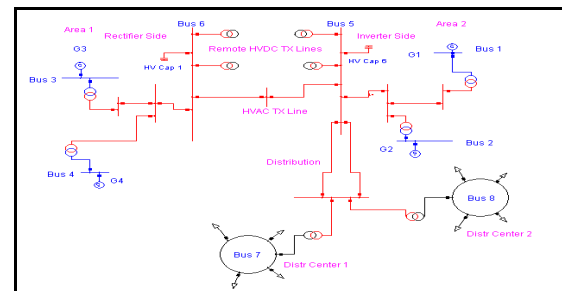

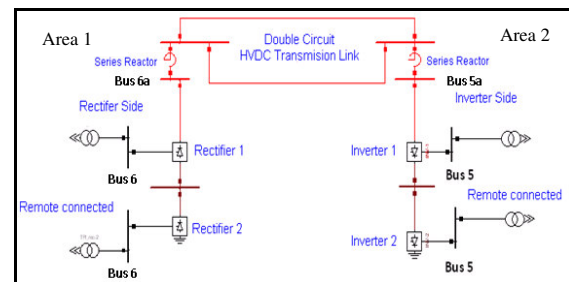Fig.3 Hybrid HVAC-HVDC power network

Fig. 4 Remote HVDC scheme between area 1 (bus 6) and area 2 (Bus 5)

5.   SIMULATION RESULTS

5.1 Response to DC fault on HVDC TX line

Figure 5 to figure 10 show the results obtained from generator G3 and G2, when a DC fault was initiated mid way on the HVDC transmission line for 50 ms. During the fault on one of the HVDC transmission lines, the first swing of rotor angle of G3 reaches 170^0 before settling at 120^0. When the same fault was applied to the transmission scenario 2 (integrated HVAC-HVDC), the first swing of the rotor angle was at -25^0. This is 97% less than when the transmission line scenario 1 was used.
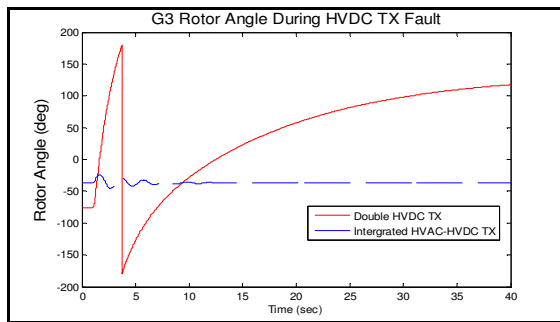
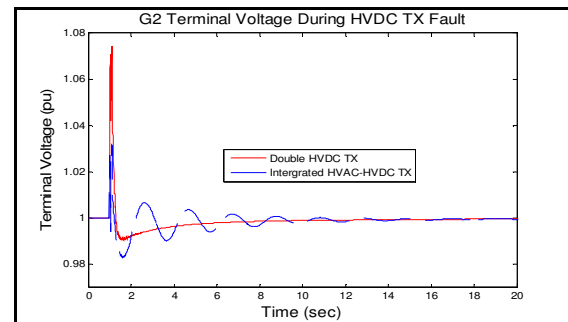Proceedings of the 19th Southern African Universities Power Engineering Conference
TOPIC F. CONTROL AND APPLICATIONS
SAUPEC 2010, University of the Witwatersrand, Johannesburg
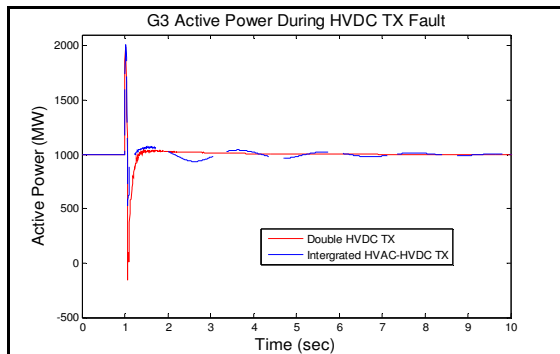

Fig.5 G3 Rotor angle

Fig.6 G3 Active Power
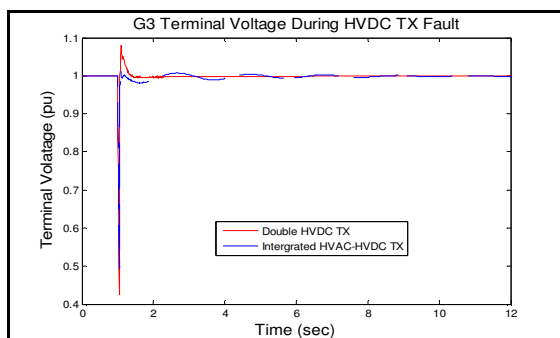
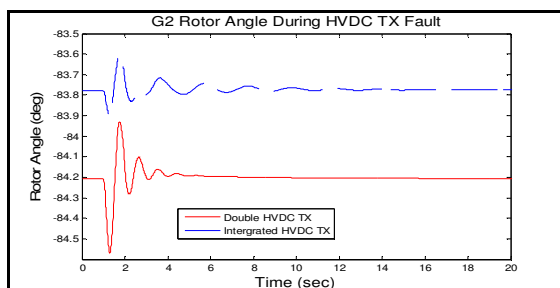Fig.7 G3 Terminal Voltage
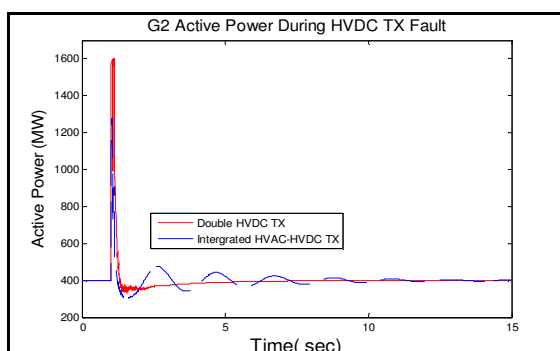

Fig.8 G2 Rotor angle

Fig.9 G2 Active Power

Fig.10 G2 Terminal Voltage

It took 45 seconds in the first transmission scenario (HVDC), before the rotor angle of G3 stabilized as shown in figure 5. Figure 6 shows the active power generated at G3 for the two transmission scenarios. In the first scenario, the electrical power output stabilized at about 2 seconds. For the second scenario (integrated HVAC-HVDC transmission), the rotor angle of G3 had more oscillations with smaller amplitudes, which stabilized in 10 seconds. At this point, the electrical power output at G3 in the second scenario as seen in figure 6 reached the value of its mechanical power, thereby leading to zero accelerating power and stability of the rotor angle within 10 seconds.

The terminal voltage at G3 when the HVDC transmission scheme (i.e., scenario 1) was used stabilized in about 1.5 seconds with no oscillation, and faster than when the integrated HVAC-HVDC scheme was used, as shown in figure 7, where the terminal voltage at G3 stabilized at 10 seconds into the simulation with small oscillations whose amplitude decreased. At G2, in area 2 of the power system, the amplitude of the first swing of the rotor angle after the DC fault, when the integrated HVAC-HVDC transmission scheme was used is found to be 51.6% less than the amplitude of the first swing of the rotor angle when the HVDC transmission scheme is used. This is because of the damping effect that HVDC has when integrated with HVAC for power transmission It reduces the amplitude of the rotor angle oscillation. The time taken for the balance of mechanical and electrical power after the DC fault when the integrated HVAC-HVDC transmission scheme was used was found to be 14 seconds as indicated by the time it took the rotor angle in figure 8, the active power in figure 9 and the terminal voltage in figure 10 to reach steady state. This consistency was not observed when the HVDC transmission scheme was used. In this case, the rotor angle as seen in figure 8 stabilized 9 seconds before the terminal voltage stabilized. The post fault angular position of the rotor for the first transmission scenario corresponded with its pre fault rotor angular position at -84.2^0. Similarly, the post fault angular position of the rotor for the second transmission scenario corresponded with its pre fault rotor angular position at -83.78^0.

5.2 Response to 3-phase to ground AC fault at G4 (Rectifier AC)

Figure 11 to figure 16 show the results obtained from generator G3 and G2, when a 3-phase to ground fault was initiated at G4 which is at the rectifier AC side. The fault lasted for 50 ms.
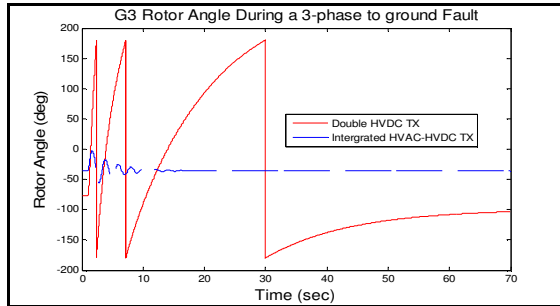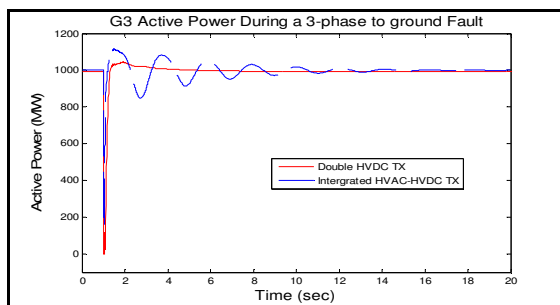

Fig.11 G3 Rotor Angle
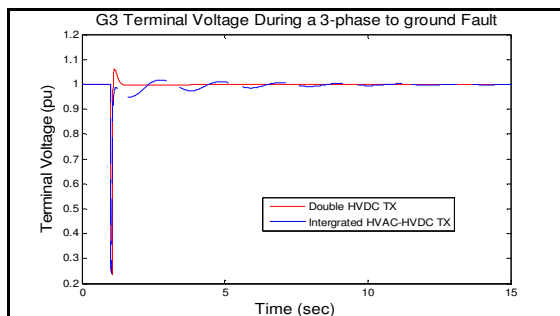

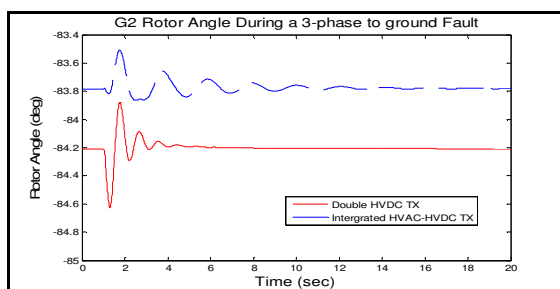Fig.12 G3 Active Power

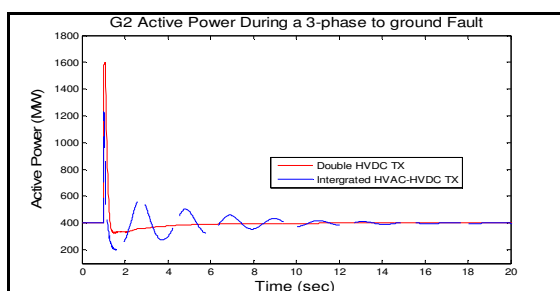Fig.13 G3 Terminal Voltage

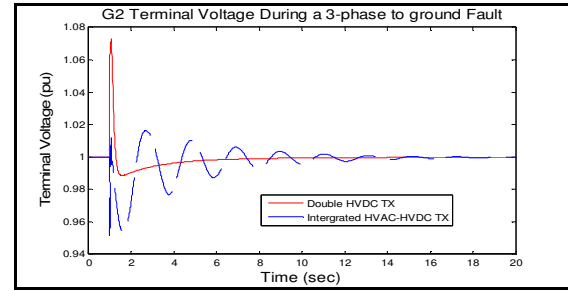Fig.14 G2 Rotor Angle

Fig.15 G2 Active Power

Fig.16 G2 Terminal Voltage

During the 3-phase to ground fault at G4 on the AC side of the rectifier station, for the HVDC transmission (scenario 1), the rotor angle first swing of G3 oscillates between -170^0 and 170^0 with two consecutive large oscillations. This period took about 30 seconds. After that, the rotor angles slowly increased from -170^0 to -100^0 (new operating point), which is 20^0 larger than the pre fault rotor angle as shown in figure 11. The total time taken for the rotor angle to stabilize at -100^0 was 70 seconds. For the integrated HVAC-HVDC transmission scheme, the first rotor angle swing of G3 was between -55^0 and 0^0, followed by smaller oscillations which stabilized in 13 seconds. The post fault rotor angle position was the same as the pre fault rotor angle position of -47^0.

The first rotor angle swing for G3 when the integrated HVAC-HVDC transmission scheme (scenario 2) is used is 83.8% less than first rotor angle swing of G3 when the HVDC transmission scheme (scenario 1). Figure 12 and 13 shows that for the integrated scheme, the time taken by G3's rotor angle to stabilize was equivalent to the time taken for electrical power output to balance the mechanical power. At this point, the accelerating power of G3 became zero. This time took 13 seconds. From figure 14 which shows the rotor angle of G2, the amplitude of the first swing of the rotor angle after the DC fault, when the HVDC transmission scheme was used is found to be 57.1% more than the amplitude of the first swing of the rotor angle when the integrated HVAC-HVDC transmission scheme is used. This is because of the amplitude of the rotor angle oscillation at G2 is reduced by the damping effect that HVDC has on the integrated HVAC-HVDC transmission scheme. The time taken for the balance of mechanical and electrical power after the DC fault when the integrated HVAC-HVDC transmission scheme was used was found to be 16 seconds which was also the same as the time it took the rotor angle in figure 14, the active power in figure 15 and the terminal voltage in figure 16 to reach steady state. Similar to the post DC fault equilibrium, the post fault angular position of the rotor for the first transmission scenario corresponded with its pre fault rotor angular position at -84.2^0. Similarly, the post fault angular position of the rotor for the second transmission scenario corresponded with its pre fault rotor angular position at -83.78^0. When HVDC transmission scheme was used, the time it took the terminal voltage and active power to stabilize was twice the amount of time it took the rotor angle to

TOPIC F. CONTROL AND APPLICATIONS

Proceedings of the 19th Southern African Universities Power Engineering Conference
SAUPEC 2010, University of the Witwatersrand, Johannesburg

stabilize. The rotor angle as seen in figure 14 stabilized 7 seconds into the simulation while the active power and terminal voltage stabilized at 14 seconds.

6. CONCLUSION

The impact of integrated HVAC-HVDC transmission scheme on the rotor angle stability of the power system has been shown. The simulation results have proved that the use of integrated HVAC-HVDC transmission schemes will reduce the amplitude of the first rotor angle swing and subsequent oscillations after a DC or AC fault. It takes longer for the system to recover from a 3-phase fault and a fault on the HVDC line when HVDC alone is used for power transmission between the two areas. The use of integrated HVAC-HVDC transmission reduces this time. Therefore, the integrated HVAC-HVDC transmission scheme is a preferred over HVDC transmission.

APPENDIX

HV Transmission lines parameters

Table 1: Transmission line Parameters [46]

Line	Resistance (Ω/km)	Reactance (Ω/km)	Susceptance (µS/km)	Length (km)
HVAC	0.028	0.325	4.35	500
HVDC	0.015	0.025	0.45	500

REFERENCES

[1] P Kundur et al, "Definition and Classification of Power System Stability - IEEE/CIGRE Joint Task Force on Stability Terms and Definitions", IEEE Trans. on Power Systems, Vol.19,No. 2, May, 2004.

[2] P. F de Toledo, et all, "Multiple Infeed Short Circuit Ratio- Aspects Related to Multiple HVDC into One AC Network", ABB Power Systems, HVDC Division, Sweden, 2005.

[3] L. Guangkai et al, "Research on Hybrid HVDC", 2004 International Conference on Power System Technology, POWERCON. Singapore, 21-24 November, 2004.

[4] Ashraq Husain, "Electrical Power Systems",5th Edition, CBS Publishers & Distributors, 2007.

[5] M. Hausler, "Multi terminal HVDC for High Power transmission in Europe", Presented at CWPEX99, Pozan, Poland, March 1999.

[6] S.V. Bozhko, R. Blasco-Gimenez, R. Li, "Control of Offshore DFIG- Based Wind Farm Grid With Line-Commutated HVDC Connection", IEEE Transactions on Energy Conversion, voll 22, No. 1, March 2007.

[7] A. Hammad, H Koelsch, P Daehler, "Active and Reactive Power controls for the GEZHOUBA-SHANGHAI HVDC Transmission scheme", 6th International conference on AC and DC Transmission, IEE. May, 1997.

[8] J.M Perez de Andres et all, "Prospects for HVDC- Getting more power out of the grid", Jornadas Tecnicas sobre la "Sesion Plenaria Cigre 2006", Madrid, 29-30 November, 2006.

[9] P. Bresesti, W.L. Kling, R.L Hendriks, "HVDC Connection of Offshore Wind Farms to the Transmission System", IEEE Transactions on Energy Conversion, Vol 22, No. 1, March 2007.

[10] D T Oyedokun, K.A Folly, "Power Flow studies in HVAC and HVDC Transmision Lines" , IASTED AfricaPES 2008, Garborone,Botswana, 2008.

[11] P Kundar, Power System Stability and Control (McGraw-Hill, Inc, 1993).

[12] Brian K. Johnson, The ABCs of HVDC Transmission Technologies, IEEE power and energy magazine, March/April 2007.

[13] F. F Wu, " Technical Considerations for Power Grid Interconnecxtion in Northeast Asia", University of Hong Kong and California at Berkely, http://www.nautilus.org/archives/energy/grid/abs tracts/wu_technical.pdf,April 27th, 2009.

[14] R. Joetten et al, "On the fault recovery of HVDC Systems", European Conference on Power Electronics and its applications (EPE) Aachen, 1989.

[15] J. Senthil, K.R. Padiyar, "A simulator Study of Recovery of HVDC Links following AC system fault", 5th International conference on AC and DC Transmission, IEE. May, 1996.

[16] EPRI Report EL-3004, " Methodology for intergration of HVDC links in Large AC Systems- Phase 1: Reference Manual", Prepared by Ebasco Services Inc., March 1983.

[17] J. Duncan Glover and Sarman, "Power System analysis and Design", 3rd edition, Brooks/cole, 2002, pp 608-643.

[18] D.L Aik, G Andersson, "Voltage and Power Stability of HVDC Systems- Emerging Issues and New Analytical Methodologies", VII SEPOPE, Curtiba, Brazil, 23-28 May, 2000.

[19] G.Liu, Z.Xu,Y.Huang, " Analysis of Inter-area oscillations in the South China Interconnected Power System", Journal of Electrical Power Systems Research 70, pp38-45, 2004.

[20] K.R Padiyar, "HVDC Power Transmission systems: technology and system interactions" Willey, pp84-90, 1990.

[21] Michael P. Bahrman, "The ABCs of HVDC Transmission Technologies." IEEE power and Energy Magazine, March/April 2007.

ENHANCEMENT OF POWER SYSTEMS STABILITY OF A HVAC NETWORK USING HVDC AND VSC-HVDC LINKS

L C Azimoh, K. Folly, SP Chowdhury, D T Oyedokun, A Ubisse, SP Sheetekela

Electrical Engineering Department, University of Cape Town
Private Bag X3, Rondebosch, Cape Town 7701, South Africa
leonard.azimoh@uct.ac.za, komla.folly@uct.ac.zaSP.Chowdhury@uct.ac.za

Abstract.   This paper investigates the effects of high voltage direct current (HVDC) and voltage source converter-high voltage direct current (VSC-HVDC) on a HVAC network. In other to study the transient stability and voltage stability of the system, a three phase short circuit fault was applied to the HVAC link. The study shows that for a weak (low short circuit ratio) hybrid ac-dc network, the VSC-HVDC is the most viable alternative to the HVDC system. VSC-HVDC systems improved the voltage and transient stability of the ac link; although the HVDC system improved the transient stability, it was problematic with the voltage stability due to the weak tie with HVAC link. Furthermore, the study shows that for bulk power transmission HVDC link is the best alternative due the inherent limitations of the of VSC-HVDC in transmitting power beyond 250MW¬300MW.

Key Words: HVAC, HVDC, VSC-HVDC, Voltage Stability, Transient Stability

1. INTRODUCTION

To attain the status of a smart grid a power system must be able to enhance grid power stability and efficiency by automatically anticipating and responding to system perturbations. HVDC and HVDC light, or HVDC[PLUS] also known as VSC-HVDC are one of such electronic devices for improving stability and quality of power supply to the grid. HVDC systems is normally used for transmission of bulk power over a long distance, for asynchronous tie of networks with different frequencies and for under water transmission using submarine cable (VSC-HVDC can also be used for this purpose) these can be found in [1, 2].The advantages of HVDC over HVAC in transmission of power are given in [2, 3] and also, classical application of HVDC projects is stated comprehensively in [4] with the development of semiconductors and various control devices, HVDC with voltage source converter (VSC-HVDC) based on insulated gate bipolar transistor (IGBT) have recently attracted a lot of attention in the industry. Projects and commercial applications of VSC-HVDC are described in [5, 6] and the first commercial HVDC Light installation is described in [7].

HVDC[PLUS] is the preferred technology for interconnection of Islanded grids to the power system, such as offshore wind farms, the technology utilizes the use of "Black-Start" feature of the voltage source converter (VSC) [8]. In power systems literature, a number of papers have analyzed the functions and different control capabilities of VSC-HVDC. Ref [9] investigates the impact of HVDC and VSC-HVDC on power systems stability of HVAC systems network. In ref [10] it was shown that even when HVAC and HVDC are separately stable their interaction could be unstable if there is a weak tie (low short circuit ratio) between them, this study proves that with VSC-HVDC link the weak tie between them will not create any problem, since the VSC-HVDC can automatically regulate the reactive power and the ac voltage independent of the real power flow. Therefore, the SCR of the hybrid network does not need to be high. This paper investigates the transient and voltage stability of the system using two case scenarios, hybrid HVAC-HVDC and hybrid VSC-HVDC-HVAC systems. The study shows that transient stability is enhanced with VSC-HVDC and HVDC links. The voltage stability study was conducted on buses 4,5,7,8 and 12 used for transmission of power from area A to area B in the HVAC network (figure 3 refers), from the result of the voltage profile, voltage angle, voltage magnitude and the maximum load-ability point it is evident that bus 7 at the centre of transmission line has the highest proximity and sensitivity to voltage instability. The voltage stability and transient stability was improved by the VSC-HVDC link, whilst the HVDC link improved transient stability but was problematic with voltage stability as a result of effect of the control actions of the converter stations on the weak HVAC link and the consumption of reactive power by the HVDC converter stations.

2. FUNDAMENTALS OF HVDC TRANSMISSION

In HVDC transmission, the conversion of AC to DC occurs at the transmitting end (rectifier) and the inversion of DC to AC occurs at the receiving end (inverter). Converters consist of high voltage bridges and tap changing transformers, the valve bridges consist of high voltage valves connected in 6-pulse or 12-pulse arrangement. One of the advantages of this technology is the fault-blocking characteristics of the system which enables it to serve as an automatic firewall for blackout prevention in case of cascading events, which is impossible with flexible alternating current transmission system (FACTS) [12].

In this study the hybrid HVDC-HVAC solution was investigated and the HVDC link used was the mono-polar link system as shown in figure1.
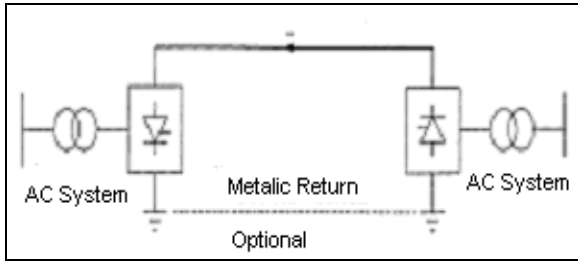
Figure 1: Shows HVDC mono-polar link system

Power flow equation of HVDC line is given as follows

$$P_d = V_d . I_d \tag{1}$$

$$Q_R = P_d . \tan \phi \tag{2}$$

$$I_d = \frac{V_{dor} Cos\alpha - V_{doi} Cos\gamma}{R_{cr} + R_L - R_{ci}} \tag{3}$$

And

$$V_d = V_{do} \cos \gamma - \frac{3}{\pi} X_c I_d B \tag{4}$$

Where

B is number of bridges in series and ϕ is the power factor angle. V_{dor}, V_{doi} are the voltages at rectifier and inverter respectively, Z_C, X_C are the characteristic impedance and commutating reactance respectively. And R_{cr}, R_{ci} and R_L are the resistances at rectifier, inverter and the DC line respectively. P_d represents the active power transmitted, while Q_R represents the reactive power at the AC bus.

V_d, I_d is the direct voltage and current per pole α is the firing angle of the rectifier. In HVDC power transmission, the time taken for the current to move from one phase to another is known as overlap time or commutation time because the line inductance of AC source phase currents do not change instantly. The angle associated with this is known as overlap angle or commutation angle (μ). In normal operation μ is less than 60^0. Typical full load values are in the range of 15^0 to 25^0 and normal operation is 15^0-45^0 therefore, the range $15^0 \angle \mu \angle 60^O$ [13].

3. FUNDAMENTALS OF VSC-HVDC TRANSMISSION

The controlled voltage source can be derived from the control system of the converter where the amplitude, the phase and the frequency can be controlled independently; the operation of the VSC-HVDC can be described by the following equation [14].

$$P_f = \frac{u_f u_v \sin \delta}{X_v} \tag{5}$$

u_v is the controlled voltage source from the AC side and Equation (9) shows active power flow Pf neglecting losses in the phase reactor, where u_f is the ac voltage on the

secondary side of the transformer and u_v is the voltage generated by the VSC, X_v is the reactance of the VSC. The reactive power and the dc current of VSC is given by.

$$Q_f = \frac{u_f (u_f - u_v \cos \delta)}{X_v} \tag{6}$$

$$i_{DC}(t) = \frac{u_f^{(q)}(t) . l_v^{(q)*}(t)}{u_{DC}(t)} \tag{7}$$

Where $l_v^{(q)}$ is the VSC source current and i_{DC} and u_{DC} are the VSC dc current and voltage respectively.
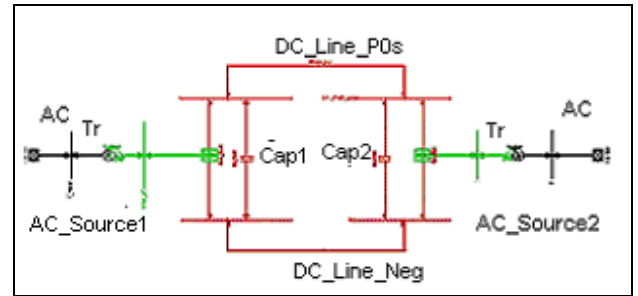

Figure 2: VSC-HVDC-Configuration

4. PV CURVE

Equations 8 below determine the maximum loading point (MLP) in a power transmission network. It shows the receiving end power as a function of load demand as stated in [11].

$$P_R = \frac{Z_{LD}}{F} (\frac{E_S}{Z_{LN}})^2 \cos \phi \tag{8}$$

Where

$$F = 1 + (\frac{Z_{LD}}{Z_{LN}})^2 + 2(\frac{Z_{LD}}{Z_{LN}}) \cos(\theta - \phi) \tag{9}$$

P$_R$ is the receiving end power, θ is the power transmission angle, Z_{LN} and Z_{LD} represents line and load impedance respectively, maximum power transfer occurs when $\frac{Z_{LD}}{Z_{LN}} = 1$, E$_S$ is the source voltage

As the load demand increases Z_{LD} decreases and P$_R$ increases initially before getting to maximum and then decreases. The PV curve thus represents the variation in voltage at critical bus in load area prone to instability as function of the active power load. This curve is produced by using series of power flow solutions at different load level, the MPL is at the knee of PV curve at this point the voltage drop rapidly and power fails to converge, indicative of voltage instability.

5. VQ CURVE

The VQ curve is used to show the variation of reactive power with respect to the voltage magnitude, as shown in bellow.

$$\frac{dQ}{dV} = 0 \qquad\qquad\qquad 10$$

Equation 10 represents a stable operation of the system; the bottom of VQ curve represents the voltage stability limit of the system under study. Q represents reactive power and V the voltage magnitude, also when $\frac{dQ}{dV} < 0$ the system is unstable system and when $\frac{dQ}{dV} > 0$ the system is stable. QV sensitivity at a bus represents the slope of the VQ curve at the given operating point, a positive sensitivity is indicative of stable operation [11].

6. POWER FLOW FOR THE TWO AREA POWER NETWOTK

Fig. 3 shows the power systems network used in the simulation. The Power flow result indicates that total power generated into the network is about (2835.50+j404.76) MVA and the installed capacity is around 3240 MVA. Power amounting to (400+j100) MVA flows from area A to area B in order to meet the load demand of (1788+j100) MVA of area B, which is greater than the generated power (1586.60+j261.48) in area B. The additional reactive power requirement of the network is compensated by the (j350) MVAR from capacitor (C9) to reduce the characteristics impedance in order to improve the apparent power level. Generators at Area-A supplied (1404 – j72.40) MVA to meet the demand of (967 + j 100) MVA of the load GL7. The excess power is transmitted by both the HVDC and HVAC (when in hybrid with HVDC) and VSC-HVDC (when in hybrid with VSC-HVDC) to meet the demand at area B. The total power loss in the system is (50.32 + j276.36) MVA
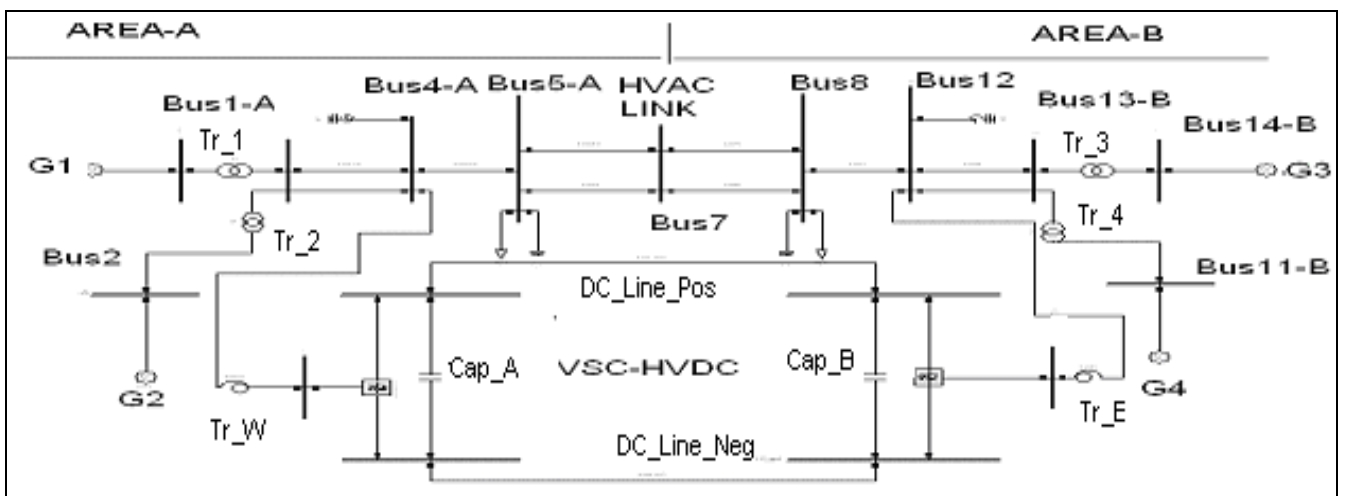
7. VOLTAGE STABILITY RESULT

Figure 4: voltage angle for Bus7
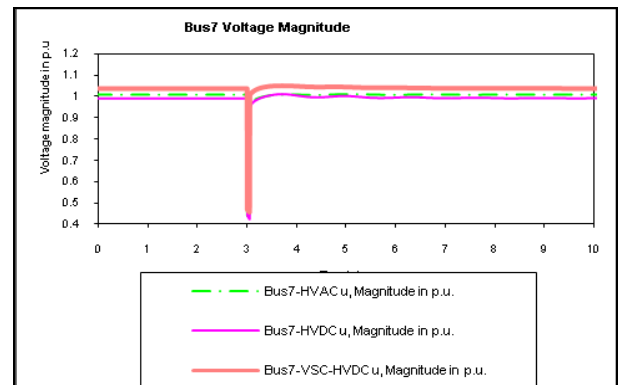
Figure 5: voltage magnitude at Bus7

Figure 3: Two area HVAC link interconnected with VSC-HVDC link

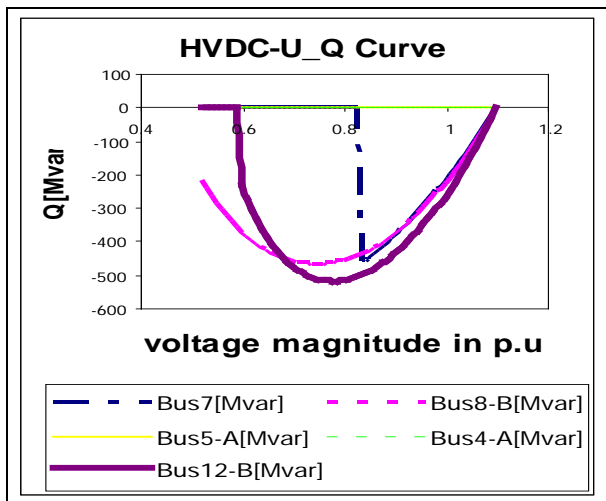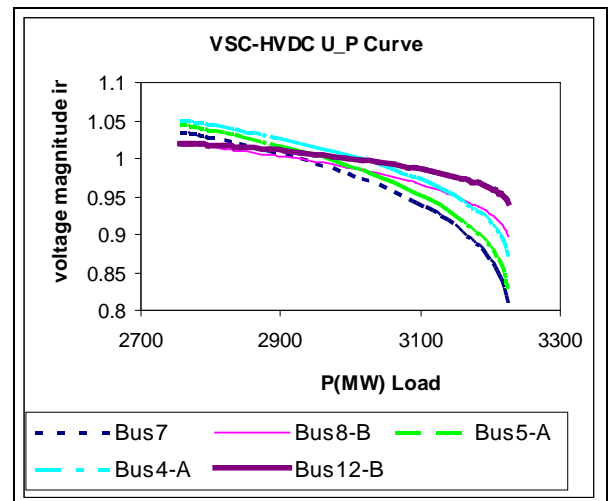**Figure 6: VQ curve under HVDC Interaction**

Fig 8: PV Curve under VSC-HVDC Interaction
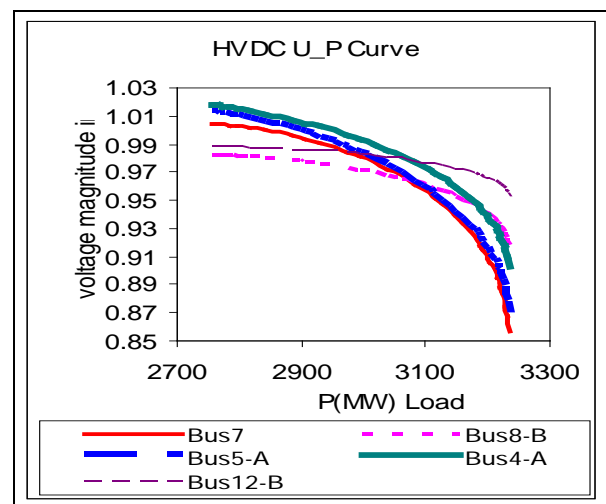

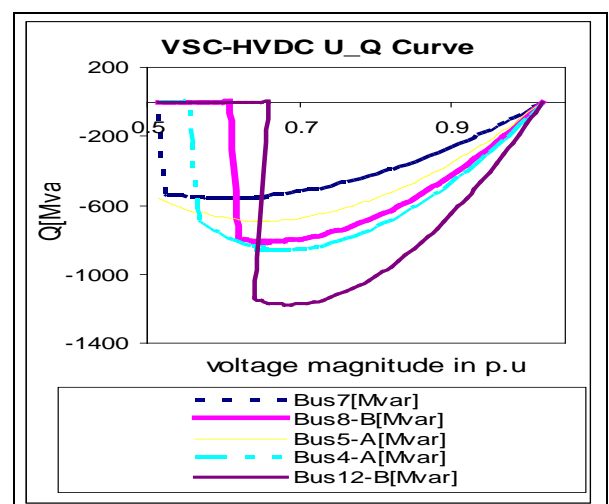**Figure 7: PV curve under HVDC Interaction**

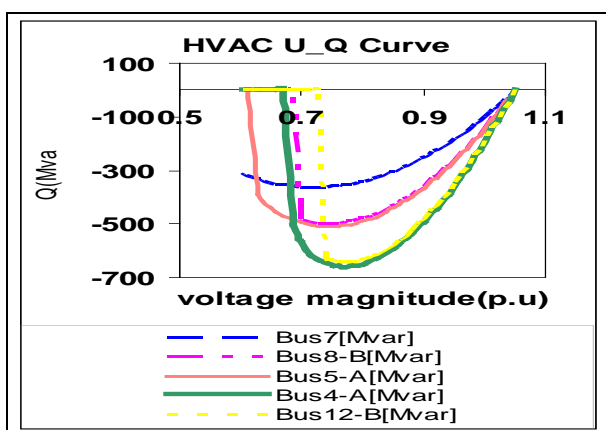**Figure 9: VQ Curve under VSC-HVDC**

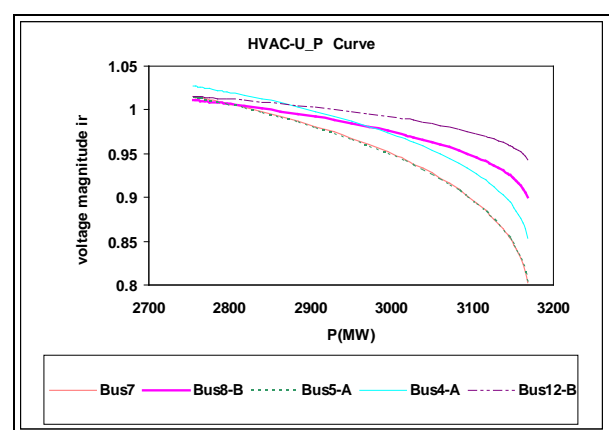**Figure10: VQ Curve under HVAC**

Figure11: PV Curve under HVAC

Note: Q [Mvar] is represented by Y(axis) in Figures 6, 9 & 10

Note: Voltage Magnitude [p.u] is represented by Y(axis) in figures. 7, 8 & 11

8. INTERPRETATION OF RESULTS (Voltage Stability)

The VSC-HVDC has the advantage of being able to almost instantly change the active and reactive power independently [15, 16] It behaves like an ideal generator to the grid with flexible working point and no inertia. This capability helps it in improving the Voltage stability as shown in figs. 4-11: The voltage stability of the system was investigated using Voltage angle, Voltage magnitude, PV and QV curves for the analysis. As shown from figure 4 to figure 11, in Figure 4 the voltage angle of VSC-HVDC operating at about 2^0 was able to come to a steady state within 3 seconds after perturbation. On the other hand, HVDC operating at about 6^0 with a settling time of about 7-8 seconds after the fault and the HVAC operating at about -7.5^0 settles at about 11 seconds after the fault. This shows the robustness of VSC-HVDC over HVDC operating at a lower voltage angle to deliver the same amount of power from Area A to Area B as shown in figure 3. Figure 5 shows the voltage magnitude of VSC-HVDC to be about 1.05 p.u and it came to steady state after the fault in about 2 seconds, the HVAC voltage magnitude is 1.0 p.u and came to a steady state after 4 seconds of perturbation, also the HVDC voltage magnitude was about 0.98 p.u the difference is as a result of reactive power consumption by the converter stations. Figs. 6-11 shows VQ and PV Curves, they were used to investigate the sensitivity to voltage collapse and the maximum loading points (MLP) respectively on buses 4,5,7,8 and 12 and the result are as follows: Figure 6 shows HVDC VQ Curve, bus7 has the highest sensitivity to voltage instability with a critical point of 0.8353p.u (voltage magnitude), -456.13Mvar(reactive power). The voltage collapsed at this point due to insufficient reactive power, (this bus is often recommended for the location of compensators like Static var compensators (SVC) and synchronous condensers,) the second critical bus is bus 8 (0.7453p.u, -464.6246Mvar) and the third critical bus is bus12 (0.7653p.u, -515.8819Mvar) in that order, buses 4 & 5 collapse due to the fact that reactive power flowed from Area B to Area A in the network, after the collapse of bus7 no reactive power flowed in buses 4 & 5 Also, these two buses are located close to converter station on the AC side that consumes reactive power, the control action of the converter station affects the voltages and power transmitted by the buses close the converter station. In a weak system with low effective short circuit ratio (ESCR) changes in HVAC network or in HVDC transmission power could lead voltage collapse necessitating the need for special control strategies i.e. dynamic reactive power control at the sensitive ac bus or near the HVDC substations [17]. The PV curve depicted in figure 7 shows the maximum loading points on the buses. The MLP achieved with HVDC network was 3234.37MW for all the buses (active power load) and bus 12 had the highest voltage magnitude at 0.9532p.u, followed by bus8 (0.9142p.u), bus4 (0.9028p.u), bus5 (0.8679p.u) and bus7 with (0.8572) this also shows that bus 7 at the centre has the lowest voltage profile and therefore, more prone to voltage instability. The VSC-HVDC PV Curve in Figure 8 shows the MLP under VSC-HVDC, the MLP achieved here for all the buses was 3226.11MW (active load power), bus 12 have the highest voltage profile at 0.9415 p.u (voltage magnitude) and the lowest was bus7 at 0.8069 p.u. Figure 9 shows QV Curve under VSC-HVDC the curve shows the sensitivity of the buses to voltage collapse, like in the previous cases the sensitivity of

bus 7 to voltage collapse was the highest with 0.6595 p.u and -534.02 Mvar and bus12 has the lowest with 0.700197 p.u, -1174.403 Mvar followed by bus4 with 0.680197 p.u, -862.8795 Mvar. Figure10: Shows the VQ Curve for HVAC system, bus 12 had the lowest sensitivity with 0.77102 p.u, -642.1245 Mvar and the highest was bus7 with 0.7510 p.u, -359Mvar followed by bus4 with 0.7610p.u, -642.12Mvar. Figure11: Shows PV Curve for HVAC system, the MLP achieved with HVAC was 3168.25MW, and bus12 achieved this at 0.9431p.u and buses 7 & 5 achieved this with lowest voltage profile of 0.8028p.u this makes them more susceptible to voltage instability during perturbation.
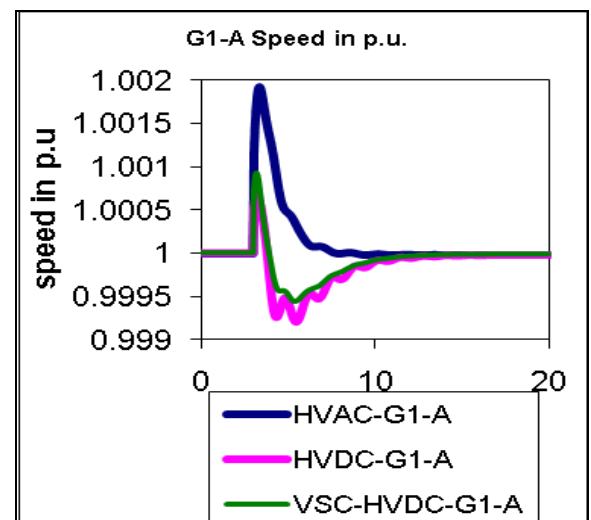
9. TRANSIENT STABILITY RESULTS

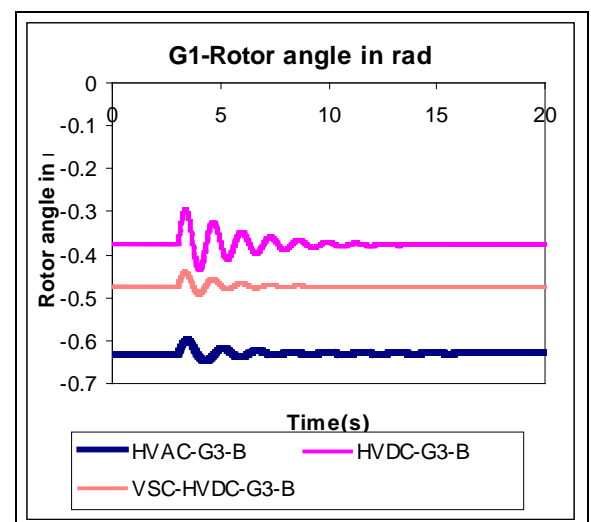**Figure12: Generator1 Speed**

Figure13:Gnerator1 Rotor angle

Transient stability is the ability of a power system to maintain synchronism when subjected to a severe transient disturbance [11] the generator1 in area-A (Slack bus) was used to investigate the responses of the speed and rotor angle of the network under transient (three phase short circuit) fault situation. From figure12 it is evident that the VSC-HVDC reduced the systems oscillation better than the rest, with a speed

Proceedings of the 19th Southern African Universities Power Engineering Conference
TOPIC F. CONTROL AND APPLICATIONS
SAUPEC 2010, University of the Witwatersrand, Johannesburg

of (1.001p.u) and came to a steady state of operation 7 seconds after perturbation. The HVDC also reduced the first swing oscillation from 1.001p.u to 0.9997 before coming to a steady state of operation at about 9 seconds after perturbation. Figure 13 shows generator1 rotor angle, from the result HVAC rotor angle was -0.65rad and it to a steady state of operation at about 15 seconds after perturbation. HVDC rotor angle was -0.35rad and it reaches a steady state of operation after about 10 seconds and VSC-HVDC rotor angle was -0.47rad it came to a steady state of operation 5seconds after perturbation. The result shows that the VSC-HVDC system improves the transient stability of the power system. The fast power run back capability of VSC-HVDC is very useful in helping the system to overcome transient instability after a system fault [18] Also, the instant power reversibility of VSC makes it possible for it to change up to 2 times the power of its rated value.

10. CONCLUSION

Several interesting features of HVDC, VSC-HVDC and HVAC has been shown, VSC-HVDC is able to improve voltage stability and transient stability of its hybrid with HVAC system. Also in a weak ac link interaction it overcomes the problems of low short circuit ratio, which was not achievable using the HVDC system. The HVDC system hybrid with HVAC also improved the transient stability but was problematic with the voltage stability. The HVDC system was able to extend the maximum loading point of the network beyond the capability of the VSC-HVDC. Therefore, for bulk power transmission it is advisable to use the HVDC link. Further research is recommended to find a way of improving the power transfer capability of VSC-HVDC system, since bulk power transfer is one its greatest limitation at the moment.

REFERENCES

[1] A. Ekstrom, "High power electronics HVDC and VSC" Electric Power Research Centre, Royal Institute of Technology, Stockholm, Sweden, 1990.

[2] J.Arrillaga,"High Voltage Direct Current Transmission" London: The Institute of Electrical Engineers, 1998.

[3] R. Rudervall, J.P Charpentier, and R. Sharma,"High voltage direct current (HVDC) transmission systems technology review paper" in Energy week 2000, Washington, D.C, U.S.A, March 2000.

[4] D.A Woodford, "HVDC transmission," Manitoba HVDC Research Center, Tech. Rep., 1998.

[5] "Other ABB HVDC Light systems in operation" http://www..abb.com, January 2007, Tech. Rep.

[6] B. Jacobson, Y. Jiang-Haner, P. Rey. G. Asplund, M. Jeroense, A. Gustafsson, and M. Bergkvist,"HVDC with voltage source converters and extruded cables for up to -/+300Kv and 1000MW," CIGRE conference, Paris, France, August 2006.

[7] Andrew Williamson, Olaf Saksvik, Bo Westman, Hans Tunehed Geo Vista;" HVDC for Power

Transmission" Power Africa 2007 Tutorial T3: 19 July 2007, Johannesburg, South Africa.

[8] Juan Miguel Perez de Andres, Miguel Muhlenkamp et al: " Prospect for HVDC-Getting more power out of the grid" Jornadas Technicas Sobre LA 'Session Plenaria CIGRE 2006' Madrid, 29-30 November 2006

[9] L. Lamont and D. Jovcic," Multivariable interaction indicators for VSC transmission controller design," IEEE Power Engineering Society General Meeting, June, 2006.

[10] L.C Azimoh, D.T Oyedokun, S. Chowdhury, S.P Chowdhury, K.A Folly,"transient and small signal stability of a two area HVAC power network interconnected with a HVDC link .Proceedings of the ninth IASTED European Conference. Power and Energy Systems (EuroPes 2009) September 7-9, 2009 Palma de Mallorca, Spain.

[11] Prabha Kundur: "Power system stability and control" 1994 Edition.

[12] W. Breuer, D. Povh, D. Retzmann, Teltsch and X. Lei, "Role of HVDC and FACTS in future power systems review paper".CEPSI Shanghai, 2004.

[13] J. C Das: Power systems analysis", New York, Marcel Dekker, 1934, c2002.

[14] G.Asplund, K. Eriksson, H. Jiang, J. Lindberg, R. Palsson, and K. Svensson, "DC transmission based on voltage source converters" in International Conference on Large High Voltage Electric Systems. CIGRE 98, VOL.4, Paris, France, 1998.

[15] G. Asplund, K. Erikson, H. Jiang, J, Linberg, R. Palsson, and K, Svensson, "DC Transmission based on Voltage Source Converters," CIGRE Conference in Paris France, 14-302, 1998.

[16] S. Johannsson, G. Asplund, E. Jansson, and R. Rudervall, "Power System Stability Benefits with VSC-HVDC-Transmission Systems," CIGRE Conference in Paris, France, B4-204, 2004.]

[17] Dennis A. Woodford," HVDC Transmission" Manitoba HVDC Research Centre, 400-1619 Pembina Highway, Winnipeg, Manitoba, R3T 3Y6, Canada, 18 March 1998.]

[18] Lidong Zhang, Lennart Harnefors, Pablo Rey,"Power System Reliability Transfer Capability Improvement by VSC-HVDC (HVDC Light© "Security and Reliability of Electric Power Systems, CIGRE Regional Meeting, June 18-20, 2007, Tallinn, Estonia.

[19] J. Duncan Glover and Sarman, "Power system analysis and design", 3rd edition, 2002 pp 608-643]

[20] X.I Koutva, T.D Vrionis, Nicholas A. Vovos, Gabriel B. Giannakopoulos,"Optimal Integration of an Offshore Wind Farm to a Weak AC Grid". IEEE Transaction on Power Deliivery, VOL. 21. NO. 2, April, 2006.]

1

Proceedings of the 19th Southern African Universities Power Engineering Conference
SAUPEC 2010, University of the Witwatersrand, Johannesburg   TOPIC F. CONTROL AND APPLICATIONS

ANALYTICAL SIZING OF AN ELECTROLYSER FOR A SMALL SCALE WIND ELECTROLYSIS PLANT

J.G. Wanjiku[a][*], M.A. Khan[*], P.S. Barendse[*] and A.B. Sebitosi[**]

[*]University of Cape Town, Department of Electrical Engineering, Rondebosch 7701, South Africa
[**]University of Stellenbosch, Department of Mechanical and Mechatronic Engineering, Matieland 7602, South Africa

Abstract. This paper presents an analytic way of sizing an electrolyser by considering the load requirements and efficiencies of the electrolyser, fuel cell and their ancillaries. Current density and the size of the active area of the membrane are optimised to ensure thermal self-sustaining mode of the electrolyser for stand alone applications. This eliminates the need of heating the feed water. Correlations between the voltages and currents of the generator and the electrolyser are also established. Simulation results for electrolyser parameters are then presented. From these results it can be inferred that by maintaining the current density at $0.8A/cm^2$, the electrolyser can meet its hydrogen production rate and maintain the temperature in the operating range of 70-90°C.

Key Words. Electrolyser; wind energy; environment.

1. INTRODUCTION

The world's consumption of the already declining fossil fuels is increasing unabated. The demand is forecast to increase by 71% by 2030 [1]. Global warming effects, increased pollution levels, energy security and sustainability are the major challenges facing the energy sector globally. It is therefore imperative to have alternative solutions which are sustainable and are in line with the United Nations Intergovernmental Panel on Climate Change (IPCC) [2].

Adopting renewable energies (REs), such as wind, solar, hydro and tidal waves can reduce dependency on fossil fuels especially when considering that over 70% of oil deposits are found in OPEC countries, while developing countries are rich in REs [2]. This will lead to development of their economies by channelling finances meant to import fossil fuels to development projects.

Most REs are inherently intermittent. To ensure a steady supply of power, Electrical Energy Storage (EES), like batteries, supercapacitors, pumped hydro-storage, flywheels and recently hydrogen via fuel cells, allow load levelling and thus reduces the cost of the plant [3]. Hydrogen (H_2) is considered to be the best energy storage media due to the following: its versatility for end use, it has higher conversion efficiency at zero-emissions, it is well suited for long term storage and it can be an excellent alternative to fossil fuels [3]. H_2 can be combusted in a fuel cell (FC) at efficiencies of over 80% when combined heat and power generation (CHP) is employed and has zero-emissions and water as the only by-product [3]. Hydrogen can also be combusted to provide thermal energy for space heating, cooking and in internal combustion engines (ICEs).

Hydrogen is derived, among other methods, from fossil fuels, electrolysis and thermolysis of water. The energy needed in the electrolysis process can be supplied by nuclear plants and RE sources. To reap the benefits of using H_2 as a 'clean' energy carrier; carbon dioxide (CO_2) sequestration is employed if H_2 is derived from fossil fuels [1,3]. REs provide the best solution in the long term and therefore, this industry is expected to grow with the adoption of a 'clean' hydrogen economy.

The major challenges facing the hydrogen economy are: lack of transport, storage and distribution infrastructure, high capital cost, technological challenges in storage and electrodes, safe end-use of hydrogen and reliability of technologies for large scale implementation [1,3]. Distributed hydrogen generation near load points will reduce transportation and distribution infrastructure while mass production will lower the production cost. The hydrogen economy will be favoured by the increasing demand and cost of transport fossil fuels with declining supply. As the deficit increases, the hydrogen technology will become affordable with added benefits of being clean. Other fuels such as landfill gases, bio-fuels and bio-diesel will form part of the energy mix for the transport industry and distributed generation.

2. SYSTEM DESCRIPTION

A schematic diagram showing the various components of a small scale wind-hydrogen plant is shown in Fig. 1. The wind energy conversion system (WECS) converts wind power to AC electrical power. This is converted to DC power by the maximum power point tracker (MPPT) which consists of a rectifier and a DC/DC converter that ensures maximum power is extracted for a particular wind speed. This allows for variable operation of the WECS. The input voltage to the electrolyser should be held constant to ensure that the cells are held above the thermoneutral voltage. A battery bank can be used to hold the DC bus constant and power auxiliary devices. The dump load dissipates excess energy from the WECS. This energy can be used to heat the feed water. From the electrolyser, H_2 is then stored as a compressed gas or liquid or as a hydride compound. It is then used to power thermal loads and/or electrical loads. In this set-up oxygen from the

---

[a] Corresponding author.
E-mail address: John.Wanjiku@uct.ac.za (J.G. Wanjiku)

2

Proceedings of the 19th Southern African Universities Power Engineering Conference
TOPIC F. CONTROL AND APPLICATIONS
SAUPEC 2010, University of the Witwatersrand, Johannesburg

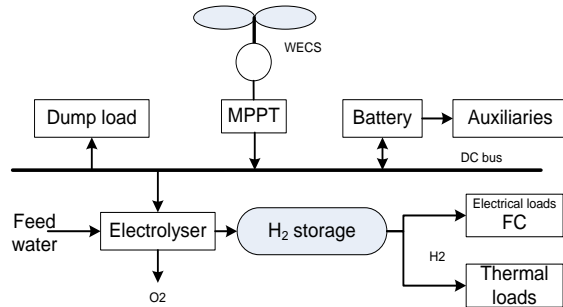electrolyser, water and heat from the FC are not recovered.

Fig. 1 A small scale wind-hydrogen SAPS system

PEM/SPE electrolysers have a thin polymer membrane (Nafion®) sandwiched between the anode and the cathode. The membrane contains the electrolyte and allows the conduction of H^+ ions from the anode to the cathode. It also separates hydrogen and oxygen. PEM electrolysers are small in size due to higher current densities (1-2A/cm^2) when compared to alkaline electrolysers and have efficiencies in the range of 50-90%. Their start-up/shut-down time and response time is short since there is no recirculation of the electrolyte and they have a reduced mass. PEM electrolysers can also operate at high pressures, reducing the need for auxiliary compression. These benefits over alkaline electrolysers make them to be well suited for stand-alone systems [1,3]. References [1] to [4] give more information on hydrogen technology.

3. THERMAL AND ELECTRICAL LOADS

This section considers the flow of power or energy, from the load to H_2 liberation (working backwards), which results to the power rating of an electrolyser. The scenarios to be analysed are: a *H_2-biogas system* which can be implemented in rural areas by utilising existing biogas infrastructure, a *H_2-storage (and FC) combination* for residential applications both in rural and suburban areas, and finally a *H_2-storage system* fit for utility companies specializing in hydrogen production and bottling.

All the cases will involve small-scale hydrogen production. The H_2-biogas system will be analysed using cooking and lighting loads; where H_2 is burnt, while the rest will consider electrical loads.

3.1 H_2-biogas system
Biogas is a mixture of 50-60% methane, 30-40% carbon dioxide and other trace elements like hydrogen sulphide, oxygen, hydrogen and water vapour among other elements [1]. Biogas has a heating value of 4713kCal/m^3 (= 20MJ/m^3) [6,7] and H_2 has a low heating value of 10MJ/m^3 at 1 atm and 15°C [8]. The sizing and efficiency of a biogas system will not be considered in this paper.
According to [6], the biogas requirement for cooking per day per person is 0.3m^3 and 0.15m^3/hr for lighting with an illumination equivalent of 60W [6].

A family of five is used as a representative of an average family in rural Africa [9]. If the family needs five hours of lighting (3½ hours in the evening and 1½ hours in the morning) for two lamps; the total biogas demand for cooking and lighting is
$$3m^3 = \left(0.3m^3 \times 5\,persons\right) + \left(0.15m^3/hr \times 5hrs \times 2lamps\right)$$
per day with an energy content of $60MJ \approx 14MCal \approx 4713kCal/m^3 \times 3m^3$. Using an efficiency value of 60% for the burners and lamps [6,7], results to a biogas requirement of 5.0m^3/day with an approximate energy content of 24MCal = 100 MJ biogas.

Biogas can be blended with hydrogen to improve on combustion efficiency and emissions [10,11]. unfortunately for every 10% increase in hydrogen content there is a corresponding 10% increase in NO_x emissions [10] which can be reduced by using catalytic burners [2].Values of 15-20% by volume are preferred according to [2,11]. Values above 30% have a reduced energy density coupled with potential pre-ignition of hydrogen [11]. 10-50% blending will be considered in this paper. Figure 2 is a comparison of two blending modes - by volume and by energy. Blending by energy gives a wide range of blending ratios compared to the other.

If an already existing biogas plant has a capacity of 5m^3 (100 MJ), the maximum electrolyser rating can only be obtained if the blending ratio is 2 (from Fig. 2). Thus the electrolyser is rated to produce 5m^3 of H_2 equivalent to $0.42kg = 5m^3 \times 0.08376kg/m^3$ of H_2 per day, where 0.08376 kg/m^3 is the density of H_2 at 1atm [8]. From this ratio, the daily biogas requirement reduces to 2.5 m^3. The rating is computed from the high heat value (HHV = 49.25kWh/kgH$_2$) assuming electrical energy is the sole source of energy and no heat is derived from the ambient as
$$1.5kW \approx \left(0.42kg \times 49.25kWh/kgH_2\right)/\left(24hrs \times 0.56\right).$$
An electrolyser efficiency of 56% is assumed [12]. If there is no biogas system, the electrolyser rating is 3kW; in order to meet the load requirements.
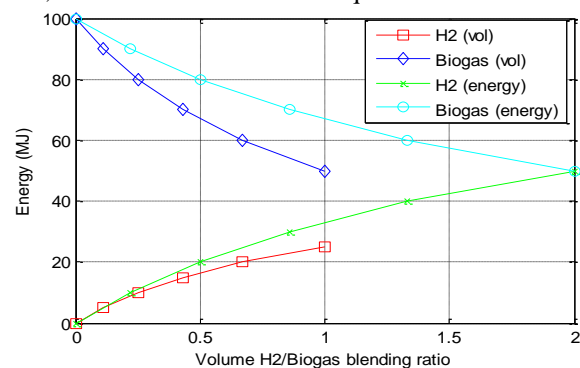

Fig. 2: Energy requirements for H_2/Biogas blending ratios by volume and by energy.

3

Proceedings of the 19th Southern African Universities Power Engineering Conference
SAUPEC 2010, University of the Witwatersrand, Johannesburg   TOPIC F. CONTROL AND APPLICATIONS

This system has a reduced capital cost by eliminating storage, FCs and their ancillaries. The use of biogas infrastructure for storage and distribution of the gas further reduces the costs. Blending improves energy content, combustion efficiency and prolonged usage of biogas.

3.2 H₂-FC Combination

This set-up consists of an electrolyser and a FC that uses hydrogen immediately it is produced. Storage is eliminated and a buffer tank may be provided to ensure continuous flow of H₂. The peak and base electrical load requirements for a single household are obtained from [13] as 0.42kW and 0.17kW respectively. This is taken as a representative of a typical rural load profile in Africa. For this combination, the electrolyser is rated from the peak power demand to allow the system to respond to transients since there is no storage. Using efficiency values of 56% for the electrolyser, 50% [14] for the FC and 90% [14] for the auxiliaries gives a rating of $1.7kW \approx 1.66kW = 0.42kW/(0.56 \times 0.50 \times 0.90)$.   If other forms of EES are incorporated to meet the peak load, the rating is obtained as 0.67kW (~0.7kW) from the base load.

This system reduces the storage costs and it has a higher efficiency than a system incorporating H₂ storage. It has a higher capacity rating if other forms of EES are not incorporated and it cannot respond to transients adequately due to fuel starvation.

3.3 H₂-Storage (and FC) combination

This section considers a *H₂-storage-FC system* and a *H₂-storage system*. The daily energy demands corresponding to the base and peak loads are $14.7MJ = 4.08kWh = (0.17kW \times 24hrs)$ and   36MJ = 10kWh respectively. This translates to $0.12kg = 4.08kWh/(33.3kWh/kgH_2)$ and   0.30kg of H₂ by using the low heat value (LHV = 33.3 kWh/kgH₂), since there is no heat and water recovery in the FC.

Compressing a unit mass of H₂ requires 10-15MJ/kg (~ 12MJ/kg) and 50.4MJ/kg for liquefaction [15]. Hydrides can utilize the waste heat from FCs and ICEs to supply 15MJ/kg at 20 atm [15]. By using the daily energy demand, the storage efficiencies are computed as 90% for compression, 59% for liquefaction and 88% for metal hydrides utilising waste heat. These efficiencies are comparable to others found in literature. According to [14], the efficiency of compression is 90%, that of liquefaction is about 65%. If electrical energy from the FCs is used to charge the metal hydrides, the efficiency reduces to about 50% [16] and by utilising waste heat or an independent secondary thermal system, the efficiency approaches 90% [16].

3.3.1 H₂-storage-FC combination

Efficiencies of storage, electrolyser, FC and ancillaries are used in computing the electrolyser rating. For compression, the electrolyser rating is $0.8kW \approx 0.75kW = 0.17kW/(0.56 \times 0.50 \times 0.90 \times 0.90)$ and for liquefied hydrogen it is 1.1kW. Metal hydrides using electrical power from the FC gives a rating of 1.4kW, and by using waste heat or a secondary thermal system, the rating becomes 0.8kW. The above are computed using the base load demand. Ratings obtained by using the peak power demand are 1.9kW, 2.8kW, 3.3kW and 1.9kW respectively.

3.3.2 H₂-storage combination

In future, some of the utilities will provide bottled hydrogen for applications like FCs, cooking, space heating and filling of hydrogen vehicles and ICEs. This negates the need of FCs and their ancillaries in this set-up. The electrolyser ratings are obtained as 3.7kW, 5.8 kW, 6.7kW, 3.4 kW and 3.8 kW when thermal loads (cooking and lighting) are considered. For electrical loads, the ratings are 0.4kW, 0.6kW, 0.7kW and 0.4kW for base load demand and ~1.0kW, 1.4kW, 1.7kW and ~1.0kW for peak power demand. These values correspond to systems incorporating compression, liquefaction and hydride (use of power from the FC and independent thermal system or use of waste heat) storages.

H₂-storage (and FC) systems can respond to transients due to the availability of fuel in storage. It is also practical especially for residential applications and adaptable to any locality unlike biogas systems that entirely depend on the availability of biodegradable materials. It is versatile, that is, it can meet electrical and thermal loads and fuel ICEs. The H₂-storage system will find applications in refuelling fuel cell vehicles and other ICEs which are hydrogen based. Compression of hydrogen reduces space requirements significantly. This set-up however, has higher losses due to more ancillaries. A summary of all the scenarios is shown in Table 2.

4. ELECTROLYSER DESIGN PARAMETERS

The H₂-compression storage-FC (electrical load) topology is selected from Table 2 whose rating is 0.749kW ≈ 0.8kW. The hydrogen requirement per day is $0.5398kgH_2/day = (0.749kW \times 24hrs)/(33.3kWh/kgH_2)$ giving a hydrogen production rate of $0.0225kg/h = (0.5398kgH_2/day)/24hrs$. The relationship between the production rate per hour, the number of electrolyser cells η_c and the electrolyser stack current I_{ely} is given as [17,18]

4

Proceedings of the 19th Southern African Universities Power Engineering Conference
TOPIC F. CONTROL AND APPLICATIONS   SAUPEC 2010, University of the Witwatersrand, Johannesburg

Table 2: A comparative summary of the electrolyser ratings for different scenarios

Scenario	Load	Ely. 56%	F.C. 50%	Aux. 90%	Comp. 90%	Liq. 59%	Hydride 50%*	Hydride 90%+	Hydride 88%×	Ely. rating kW	Comment
Biogas Th	4.17MJ									-	Biogas system only; 5 m³ capacity
H₂-biogas Th	0.86kW	✓								1.5	5m³H₂ at 1atm; 2.5m³Biogas (50MJ)
H₂ Th	1.72kW	✓								3.0	10m³H₂ at 1atm
H₂-FC El	0.17kW	✓	✓	✓						0.7	Immediate use of H₂ by FC
	0.42kW	✓	✓	✓						1.7	
H₂-Storage-FC El *Note:* 0.17kW-base load 0.42kW-peak load Th Thermal load El Electrical load	0.17kW	✓	✓	✓	✓					0.8	Compressed H₂
		✓	✓	✓		✓				1.1	Liquefied H₂
		✓	✓	✓			✓			1.4	Electrical thermal system powered by FC
		✓	✓	✓				✓		0.8	Independent thermal system
		✓	✓	✓					✓	0.8	Use of waste heat
	0.42kW	✓	✓	✓	✓					1.9	Compressed H₂
		✓	✓	✓		✓				2.8	Liquefied H₂
		✓	✓	✓			✓			3.3	Electrical thermal system powered by FC
		✓	✓	✓				✓		1.9	Independent thermal system
		✓	✓	✓					✓	1.9	Use of waste heat
H₂-Storage Th	1.72kW	✓		✓	✓					3.7	Compressed H₂
		✓		✓		✓				5.8	Liquefied H₂
		✓		✓			✓			6.7	Electrical thermal system powered by FC
		✓		✓				✓		3.4	Independent thermal system
		✓		✓					✓	3.8	Use of waste heat
H₂-Storage El	0.17kW	✓		✓	✓					0.4	Compressed H₂
		✓		✓		✓				0.6	Liquefied H₂
		✓		✓			✓			0.7	Electrical thermal system powered by FC
		✓		✓				✓		0.4	Independent thermal system
		✓		✓					✓	0.4	Use of waste heat
	0.42kW	✓		✓	✓					1.0	Compressed H₂
		✓		✓		✓				1.4	Liquefied H₂
		✓		✓			✓			1.7	Electrical thermal system powered by FC
		✓		✓				✓		1.0	Independent thermal system
		✓		✓					✓	1.0	Use of waste heat

Key: **Ely.** – Electrolyser; **F.C.** – Fuel Cell; **Aux.** – Auxiliary; **Comp.** – Compression, **Liq.** – Liquefied.

*Hydride storage powered by an electrical system (FC), a part of the primary system.

+Hydride storage powered by an independent system such as a solar water heater system.

×Hydride storage utilising waste heat from a FC or ICE.

$$H_2(kg/h) = \frac{2.106\,g/molH_2 \times 3600s}{1000g} \cdot \frac{\eta_c I_{ely}}{zF}$$
$$= 7.5816 \cdot \frac{\eta_c I_{ely}}{zF} = 0.0225\,kg/h \tag{1}$$

where z is the number of electrons transferred per mole of H₂O ($z = 2e^-$) and F = 96485 C/mol or As/mol is Faraday's constant. The number of moles/sec is $\sim 3.0\times10^{-3}\,mols/s = \eta_c i A_{elc}/zF$, where $I_{ely}(A) = i(A/cm^2) \times A_{elc}(cm^2)$ with A_{elc} being the active area of electrodes. A_{elc} for a typical stand-alone PEM electrolyser cell is about 100cm² with a maximum current density i of 1.0A/cm² at an operating cell voltage of about 2.0-2.2V [1]. Therefore, $\eta_c = 5.7891/i$. At low current densities hydrogen generation is low; otherwise it is high at the expense of degrading membranes [1]. The operating current density is chosen in the mid-band of 0.4-0.8A/cm². Setting it to 0.55A/cm² gives 11 electrolyser cells. The maximum stack voltage U_{ely} is therefore, $24V \approx 11cells \times 2.2V$. Substituting $\eta_c = 11$ into eqn (1) gives a nominal stack current I_{ely} of 52A which is close to 55A computed from the current density and an active area of 100cm². The resulting DC power rating of the electrolyser is in the range of 0.80-1.25kW corresponding to 1.5-2.2V cell voltage for a rated current of 52A. 1.5V is an

approximation of the thermoneutral voltage U_{tn} = 1.48V - the minimum cell voltage above which current starts flowing. Below this voltage hydrogen is not produced [1].

Temperature response for a 14-cell stack with 100cm² active area without insulation was done by [1] in thermally self-sustaining mode. The temperature of the feed water was at 22°C. The stack reached its operating temperature as the current density increased to 1.0A/cm², with the water exiting at 85-86°C. From the temperature and current density data adopted from [1], the variation of temperature as a function of current density was modelled using MS Excel as a polynomial of degree 2 as

$$T_{ely}(°C) = -83.333i^2 + 151.67i + 12 \tag{2}$$

An optimum current density of 0.8A/cm² at an operating temperature of 80°C [1] can be achieved by adjusting the current or the active area. For a rated current of 52A, the active area reduces to 65cm² or the current can be increased to 80A for an active area of 100cm².

The efficiency of hydrogen production is referenced to the lower heating value (LHV) of hydrogen as [17]

5

Proceedings of the 19th Southern African Universities Power Engineering Conference
SAUPEC 2010, University of the Witwatersrand, Johannesburg

TOPIC F. CONTROL AND APPLICATIONS

$$eff = \frac{LHV\ of\ H_2\ (33.3kWh/kgH_2)}{sp.\ energy\ use\ (kWh/kgH_2)} \quad (3)$$

Specific energy use, *sp. energy use,* is the ratio of the input power of the electrolyser over the actual content of hydrogen generated. It is given as [17]

$$sp\ energy\ use\ (kWh/kgH_2) = \frac{U_{ely}I_{ely}\ (kW)}{H_2\ (kg/h)} \quad (4)$$

Combining eqns (1), (3) and (4), the efficiency becomes

$$eff = 7.5816 \cdot \frac{1000}{zFU_{cell}}(33.3kWh/kgH_2) \quad (5)$$

It is therefore dependent on the cell voltage U_{cell} and it is highest when the cell voltage approaches 1.48V. Faradic efficiency which is usually high (over 90%) [1] for non-degraded cells, is neglected in this analysis.

Figure 3(a) shows the effect of cell voltage on the stack voltage and power for constant current and H_2 production rate. Figure 3(b) illustrates the effects of cell voltage on efficiency and specific energy use.

(a)

(b)
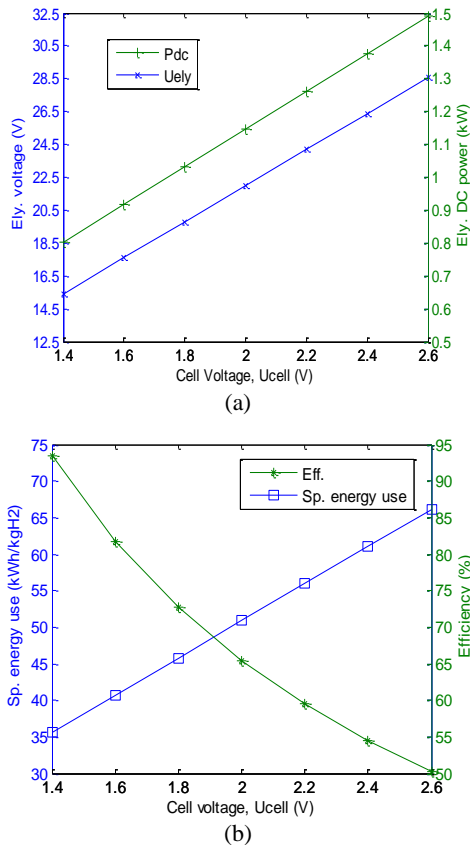
Fig. 3: Electrolyser parameters vs. cell voltage for $\eta_c = 11$ cells at $I_{ely} = 52A$ at a H_2 production rate of 22.5g/hr

A buck-boost converter with continuous conduction mode (CCM) is selected for regulating the input voltage to the electrolyser. It can boost low voltages (for low wind speeds) and buck high voltages (for high wind speeds). The relationship between the output voltage of the converter V_o which is the input voltage U_{ely} of the electrolyser, the phase voltage V_{ac} of the generator, number of cells η_c and the cell

voltage U_{cell} is given as

$$\left. \begin{array}{l} V_o = U_{ely} = \dfrac{D}{1-D} \cdot \dfrac{3\sqrt{2}}{\pi} \cdot \sqrt{3} \cdot V_{ac} = \eta_c \times U_{cell} \\[3mm] I_{ely} = \dfrac{1-D}{D} \cdot \dfrac{1}{0.816} \cdot I_{s(rms)} \end{array} \right\} \quad (6)$$

The electrolyser current I_{ely} is also expressed in eqn (6) as a function of the phase $I_{s(rms)}$ (or line current) for a wye connected generator. The equations are derived by manipulating buck-boost and rectifier equations found in [19]. V_{ac} changes depending on the wind speed; hence to hold V_o constant, the duty ratio D can be varied to correspond to the available wind speed. At lower duty ratios, there is poor switch utilisation hence D_{min} is set to 0.30. Parasitic effects reduce D_{max} to less than unity [19]; hence it is set to 0.75. The phase voltage range is obtained as 3-24V giving a converter input range of 8-56V. The inductor and output capacitor of the converter are computed as 13.5µH and 7.4mF for a load current of 52A at $24V \approx 11cells \times 2.2V$.

The H_2 production rate (H_2g/hr) from eqn (1), the converter output voltage (V_o) and the output voltage of a PEM electrolyser analytic model ($U_{ely-model}$) derived from [20,21,22] were simulated using Simulink® and the results are shown in Fig. 4. A current density of 0.8A/cm^2 (rated current of 52A and an active area of 65cm^2) and eqn (2) are used to predict the temperature giving the plots in Fig. 5. For these simulations, the duty cycle was set to 37% at a converter input voltage of 56V.
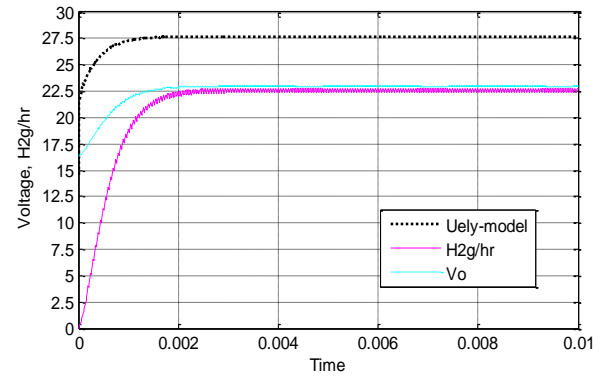

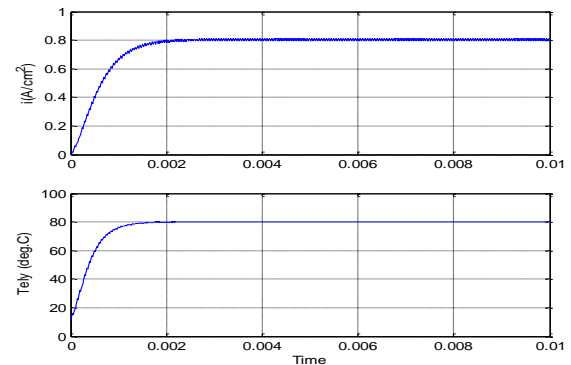Fig. 4: Model voltage $U_{ely-model}$, converter ouput voltage V_o and production rate (H_2g/hr) vs. time

Fig. 5: Current density i (A/cm^2) and Temperature (˚C) vs. time

6

Proceedings of the 19th Southern African Universities Power Engineering Conference
SAUPEC 2010, University of the Witwatersrand, Johannesburg

TOPIC F. CONTROL AND APPLICATIONS

CONCLUSIONS

A PEM electrolyser contains inherent advantages like fast start up/down times and fast response to transients makes it favourable for REs. The rating of an electrolyser was found to be dependent on the load and efficiencies of system components. A H_2-compression storage-FC system is selected whose rating falls within 0.8-1.25kW, therefore a 1kW 11-stack PEM electrolyser can be selected to meet the electrical load requirements. Maximum operating efficiency solely depends on the minimum acceptable cell voltage.

An optimum current density of $0.8A/cm^2$ can be obtained by either varying the active area or the electrolyser current. From the simulations in Figures 4 and 5, the current density was able to maintain the operating temperature at 80˚C; ensuring self-sustaining thermal mode of the electrolyser at a hydrogen production rate of 22.5g/hr. The converter output voltage was found to be lower than the PEM electrolyser voltage. In the model, the overpotentials are dependent on a number of variables such as pressure, temperature, and current density which may have affected the results of the model.

The generator and electrolyser currents and voltages are related using eqn (6). The nominal current of the generator will have to ensure electrolyser operating conditions like the current density, temperature and hydrogen production rate are achievable. Similarly the rated voltage of the generator will also have to ensure the electrolyser voltage is met while keeping the efficiency maximum. This can be achieved by limiting the electrolyser voltage using a converter and allowing the current to fluctuate according to the wind speed.

A study should be done to optimise the selection of the generator and EES to ensure the effects of varying wind are mitigated. The use of wind profile data (which was not available during the writing of this paper) in the sizing of the system components should be considered.

This paper serves as guide and in the event of sizing an actual system, it is important to get the power requirements and efficiencies of all the system components before making the final decision on the topology to select.

REFERENCES

[1]   S.P.S. Badwal, S. Giddey, P. Bandopadhayay, "Hydrogen, Fuel Cells and Renewable Energy," *CSIRO Energy Technology, Australia*.

[2]   B. Kruse, S. Grinna, C. Buch, "Hydrogen – Status and Possibilities", *The Bellona Foundation*, 2002. http://www.bellona.org/filearchive/fil_Hydrogen_6-2002.pdf. (11 May, 2009)

[3]   S.P.S. Badwal, S. Giddey, F.T. Ciacchi, "Hydrogen and oxygen generation with polymer electrolyte membrane (PEM)-based electrolytic technology," *Ionics*, vol. 12, pp 7-12, 2006.

[4]   Ø. Ulleberg, "Modelling of advanced alkaline electrolyzers: a system simulation approach," *Int. J. Hydrogen Energy*, vol. 28, pp 21-33, 2003.

[5]   M. Newborough, "A Report on Electrolysers, Future Markets and the Prospects for ITM Power Ltd's Electrolyser Technology", *Heriot-Watt University, Edinburgh*, Feb, 2004. http://www.h2fc.com/Newsletter/PDF/ElectrolyserTechnologyReportFINAL.doc   (18 May, 2009)

[6]   NIIR Board, *Hand book on Biogas and its Applications*, 1st Edition, Delhi, India, National Institute of Industrial Research (NIIR), 2004.

[7]   U. Gautam, "Biogas Technology: A training manual," *Food and Agricultural Organisation (FAO) of the United Nations*, 1996.

[8]   "Hydrogen Fuel Cell Engines and Related Technologies," *College of the Desert, Monterey Avenue, Palm Desert, CA 92260, USA*, Rev 0, Dec 2001.

[9]   Population Reference Bureau: http://www.prb.org/Articles/2008/kenya.aspx?p=1 (24 Sep, 2009).

[10] G.P. McTaggart-Cowan, S.R. Munshi, S.N. Rogak, P.G. Hill, W.K. Bushe, "Hydrogen-Methane Blend Fuelling of a Heavy-Duty, Direct-Injection Engine," *Proceedings of IMECE2007, 2007 ASME Int. Mechanical Engineering Congress and Exposition, Seattle, Washington, USA*, 2007.

[11] S.O.B. Shrestha, G.A. Karim, "Hydrogen as an additive to methane for spark ignition engine applications," *Int. J. Hydrogen Energy*, vol. 24 pp 577-586, 1999.

[12] B. Kropotkin, J. Levene, K. Harrison, P.K. Sen, F. Novachek, "Technical report on Electrolysis: Information and Opportunities for electrical Power Utilities," *National renewable energy Laboratory (NREL), A National Laboratory of the U.S. Department of Energy*, Sept, 2006. http://www.osti.gov/energycitations/advancedsearch.jsp (18 May, 2009)

[13] A. B. Sebitosi, "Application of advances in automotive technologies to electrification in rural sub-Saharan Africa, PhD Thesis" *Electrical Engineering, University of Cape Town, South Africa*, Chapter 7, 2004.

[14] U. Bossel, "Efficiency of Hydrogen Fuel Cell, Diesel-SOFC-Hybrid and Battery Electric Vehicles," *European Fuel Cell Forum*, 2003.

[15] L.K. Heung, "Using Metal Hydride to Store Hydrogen," *Savannah River Technology, Aiken, SC 29808 USA*, 2003. http://sti.srs.gov/fulltext/ms2003172/ms2003172.pdf (24 Sep, 2009)

[16] Hydride hydrogen storage: http://www.ika.rwth-aachen.de/r2h/index.php/Hydride_Hydrogen_Storage (24 Sep, 2009).

[17] L.M. Gandía, R. Oroz, A. Ursúa, P. Sanchis, P.M.Diéguez, "Renewable Hydrogen Production: Performance of an Alkaline Water Electrolyzer Working under Emulated Wind Conditions," *Energy & Fuels,* vol. 21, pp 1699-1706, 2007.

[18] N.A. Kelly, T.L. Gibson, D.B. Ouwerkerk, "A solar powered, high-efficiency hydrogen refuelling system using high-pressure electrolysis of water: Design and initial results," *Int. J. Hydrogen Energy*, vol. 33, pp 2747-2764, 2008.

[19] N. Mohan, T.M. Undeland, W.P. Robbins, *Power Electronics: Converters, Applications, and Design*, 3rd Edition, USA, John Wiley & Sons, 2003.

[20] P. Choi, D.G. Bessarabov, R. Datta, "A simple model for solid polymer electrolyte (SPE) water electrolysis," *Solid State Ionics*, vol. 175, pp 535-539, 2004.

[21] H. Görgün, "Dynamic modelling of a proton exchange membrane (PEM) electrolyzer," *Int. J. Hydrogen Energy*, vol. 31, pp 29-38, 2006.

[22] R.A. Costa, J.R. Camacho, "The dynamic and steady state behaviour of a PEM fuel cell as an electric energy source," *Journal of Power Source*, vol. 161, pp 1176-1182, 2006.

Topic G

High Voltage

TOPIC G. HIGH VOLTAGE

Proceedings of the 19th Southern African Universities Power Engineering Conference
SAUPEC 2010, University of the Witwatersrand, Johannesburg

AN INVESTIGATION INTO THE RELATIONSHIP BETWEEN BREAKDOWN PROBABILITY AND TIME-TO-BREAKDOWN FOR VARIOUS GAP GEOMETRIES UNDER LIGHTNING IMPULSE CONDITIONS

Hugh G.P. Hunt, Trevor D. ter Wolbeek, Nick J. West and Ian R. Jandrell

School of Electrical & Information Engineering, University of the Witwatersrand, Private Bag 3, 2050, Johannesburg, South Africa

Abstract. The process of electrical breakdown in an air gap is not always a predictable event and is dependent on the strength of the electric field applied to the gap. When the event does occur, there is also a time delay from when the electric field is applied to when breakdown occurs. A Marx generator is used to apply lightning impulses to three electrode geometries (12 mm Rogowski profile, a 12 mm rod-rod geometry and a 125 mm Rogowski profile) in order to investigate the relationship between breakdown probability and the time-to-breakdown. It was seen that the uniformity of the electric field within the geometry had the greatest affect on the predictability of the time-to-breakdown. This has direct application in the design of gap geometries since a uniform geometry will allow for much more predictable times.

Key Words. Breakdown Probability, Rogowski profile, Time-to-Breakdown, Uniform Electric Field

1. INTRODUCTION

The subject of this paper is based on phenomena observed during the investigation of laser-induced breakdown in spark gaps. During the experiments, it was observed that the interaction between the laser-induced plasma and the resulting arc was heavily dependent on the electric field strength as well as the time delay until breakdown [1].

In these experiments, the breakdown event was guaranteed since the gap was triggered by the laser beam. However, in the case of overvoltages or impulses, breakdown may or may not occur. This is due to the many factors that may affect the process of breakdown and is most easily dealt with by attributing a probability to the breakdown event [2]. The probability of breakdown increases as the electric field strength within the gap is increased [3].

It has also been shown that there exists a relationship between the electric field strength and the time-lag to breakdown [4, 5]. As the electric field strength becomes greater, the time-to-breakdown decreases [6]. Since the behaviour of both these parameters affects the interaction between the plasma and the arc, it is of interest to establish their relationship.

Using the relationship between the electric field strength for both breakdown probability and the time-to-breakdown, experiments were designed to investigate the relationship between breakdown probability and time-to-breakdown under impulse conditions.

In this paper, these experiments and the consequent results are investigated and discussed. Differing spark gap geometries are used in order to see how the nature of the electric field affects the relationship. The experimental setup is provided and the results are presented as time-to-breakdown distributions for increasing levels of breakdown probabilities together with an explanation for the behaviour of the distributions.

2. BACKGROUND

2.1 Process of Breakdown

Electrical breakdown in a gas is essentially the flow of current (electrons) through the gas [7]. A gas such as air, however, is an excellent insulator at standard temperature and pressure. When a strong enough electric field is applied to an air gap, it can influence any electrons present in the gap. These electrons then collide with the air molecules and cause them to release electrons. This process is known as ionisation and will eventually lead to electrical breakdown across the gap [2, 8].

The appearance of an electron in the gap is statistical in nature due to the many conditions and factors that affect it [3, 9]. There is, therefore, a probability associated with the process of breakdown. As the strength of the electric field is increased, the likelihood that the breakdown process will occur increases [2, 3].

Also associated with the breakdown process is a time delay or the time-to-breakdown as given by [3, 5]:

$$T_{Total} = T_S + T_F \tag{1}$$

The statistical time, T_S, is the time it takes for an electron to present itself in the gap and is dependent on the amount of pre-ionisation [3, 6]. The formative time lag, T_F, is the time taken for breakdown to occur and is determined by the mechanism of breakdown in the gap. This is in turn, dependent on the gap geometry [3, 7, 10].

2.2 Lightning Impulse

Figure 1 shows the $1.2/50$ μs lightning impulse as defined in the IEC60060-1 standard [11].

This voltage waveform is used for many testing applications and is well understood [2]. For this reason it is chosen for this experiment.
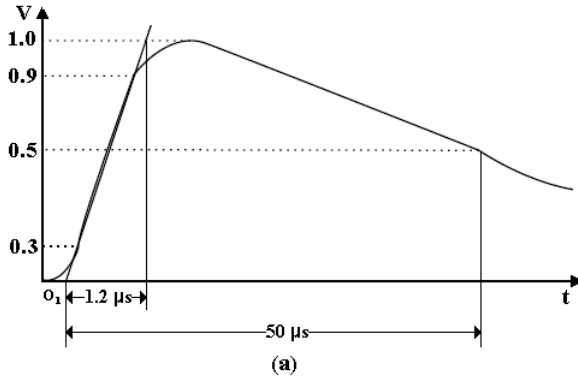
Proceedings of the 19th Southern African Universities Power Engineering Conference
SAUPEC 2010, University of the Witwatersrand, Johannesburg

TOPIC G. HIGH VOLTAGE

Fig. 1.   1.2/50 μs lightning impulse waveform as defined in the IEC60060-1 standard.

The waveform is applied across the spark gap - if the gap withstands, the full waveform as shown the figure can be viewed. However, if breakdown occurs, the waveform shown in figure 2 can be viewed.

This is because the breakdown process has begun and the gap quickly approaches a short circuit.

The experiment is performed by applying the 1.2/50 μs lightning impulse to different gap geometries. By viewing the waveform across the gap, it can be determined whether or not breakdown occurred. If so, the time from the application of the impulse to when breakdown occurs can then be measured as the time-to-breakdown.
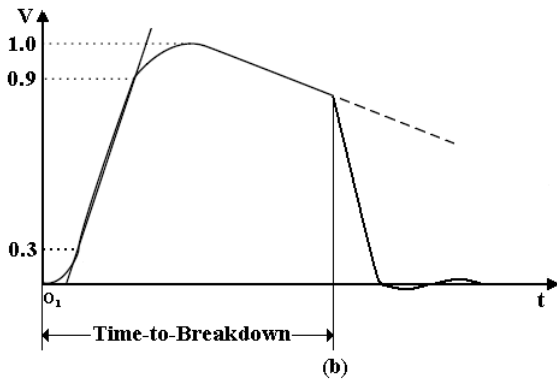
Fig. 2.   1.2/50 μs lightning impulse waveform under breakdown conditions.

2.3 Probability Distributions

Figure 3 shows a generalised probability density function for a Gaussian distribution [2]. This shows the probability that a value of the variable Z occurs and is given by:

$$p(Z) = \frac{1}{\sigma\sqrt{2\pi}}e^{-\frac{(Z-Z_{Mean})^2}{2\sigma^2}} \qquad (2)$$

The mean value, Z_{Mean} of the distribution is the average of all the possible values that may occur. The standard deviation (or variance), σ, is a measure of the greatest variation from the mean value. This

distribution is described as symmetrical since the variance is equal on both sides of the mean.
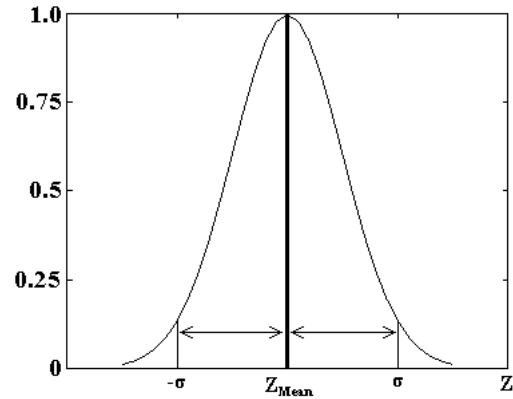
Fig. 3.   Generalized probability density function for a Gaussian distribution

The mode of the distribution is the value with the greatest probability of occurring. In this case, this is the same as the mean since the distribution is symmetrical. If the distribution was not symmetrical about the mean, it would be said to be 'skewed' in the direction where the most values occurred. If these values are much larger than most of the other values in the distribution, they are referred to as extreme values.

3. EXPERIMENTAL SETUP

3.1 Impulse Generation

A diagram of the experimental setup is shown in figure 4.
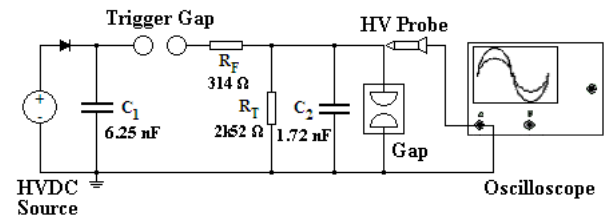

Fig. 4.   Circuit Diagram of the Single-Stage Marx Generator.

The circuit shown is a single-stage Marx generator and was used for the generation of the lightning impulses. It was used for testing of the 12 mm electrode gaps. The generator was charged using a 50 kV Cockroft-Walton High Voltage DC (HVDC) source (Spellman SA4). A diode, rated at 160 kV, was used to provide protection for the source. Maximum impulse peaks of 40 kV were achieved and this was sufficient for the testing of the 12 mm gaps.

A Tektronix® P6015 probe was used to measure the high voltage across the spark gap and was connected to a Tektronix® TDS 320 oscilloscope in order to view the waveform. The probe has a 1000:1 ratio and a voltage rating of 40 kV.

For the larger gap geometry, a multi-stage Marx generator circuit used. Using five stages, voltage peaks of

TOPIC G. HIGH VOLTAGE

Proceedings of the 19th Southern African Universities Power Engineering Conference
SAUPEC 2010, University of the Witwatersrand, Johannesburg

200 kV were achieved which was sufficient to break-down the 125 mm gap [2]. To achieve a $1.2/50$ μs impulse, two resistors of 340 Ω and 15.8 $k\Omega$ as well as a capacitor of 1.0 nF were required. For this multi-stage generator, a resistor divider network with a ratio of 150355:1 was connected to the scope to measure the voltage.

3.2 Gap Geometries

Testing was performed on three different electrode geometries:

- A 12 mm Rogowski profile
- A 12 mm rod-rod geometry
- A 125 mm gap using the Rogowski profile electrodes

The Rogowski profile was used to provide a fairly uniform electric field in the gap [12]. A diagram of the electrodes is shown in figure 5. They are made from aluminum with a tungsten carbide coating for heat resistance. As shown in the figure, the electrodes have a diameter of 104 mm and a height of 70 mm. These same electrodes were tested with a gap of 125 mm. However, given the surface area of the electrodes, the Rogowski profiling no longer simulates a uniform electric field at this gap length and the geometry can be considered a weakly non-uniform field.
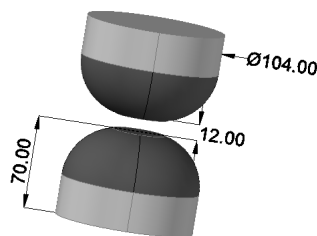
Fig. 5.   Diagram of Rogowski profile electrodes [13].

Figure 6 shows a diagram of the rod-rod electrode geometry. This geometry was used to examine the effects that an non-uniform electric field has on the time-to-breakdown. Each rod has a diameter of 3.24 mm and are set 12 mm apart so as to compare with the 12 mm Rogowski geometry.
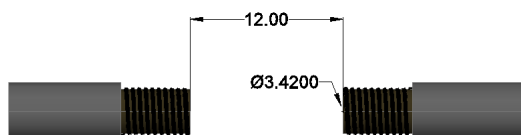
Fig. 6.   Diagram of rod-rod electrode geometry [13].

4. EXPERIMENTAL RESULTS

Using the experimental set-up as described above, the relationship of breakdown probability to time-to-breakdown was investigated as follows:

- The impulse voltage peak was set.
- Multiple impulses were applied to the electrode geometry consecutively. A period of one minute was left between each shot so as to allow the self-healing process of air take place [2].
- For each impulse that was applied, it was recorded whether the electrode geometry withstood or broke down. If breakdown occurred, the time-to-breakdown was recorded.
- The laboratory atmospheric conditions were then recorded using a Davis Perception II weather station.

By examining the relative frequency of breakdowns that occurred out of the total sample, the probability of breakdown given the applied electric field was established. The time-to-breakdown readings were plotted as a distribution for this probability of breakdown. The magnitude of the impulse voltage was then increased and the same method was repeated in order to view how the time-to-breakdown distribution changed as probability of breakdown was increased.

4.1 Low Probability of Breakdown

Figure 7 shows the time-to-breakdown distributions for the three electrode geometries at a low probability of breakdown.

The time-to-breakdown distribution for the 12 mm Rogowski profile is shown by the solid line. As can be seen, the distribution obtained approaches a symmetrical distribution with a mean time-to-breakdown of 2.76 μs. The rod-rod electrode geometry, however, produced a very different distribution as shown by the dotted line. As can be seen, the distribution is skewed to the right with many extreme values occurring. Consequently, the time-to-breakdown is far less predictable than that of the Rogowski profile geometry.

The distribution for the 125 mm Rogowski profile is also shown, using the dotted-dashed line. This distribution is also slightly skewed to the right with some extreme time-to-breakdown values. The electric field strength was then increased increasing the probability of breakdown.

4.2 Mid Level Probability of Breakdown

Figure 8 shows the time-to-breakdown distributions obtained for a mid level probability of breakdown.

The 12 mm Rogowski profile distribution still approaches a symmetrical distribution, however, as can be seen, the standard deviation of the distribution has decreased. The mean time-to-breakdown has also become shorter, now 2.25 μs, and the probability of it occurring has increased.

The rod-rod geometry's distribution is still skewed to the right but with far less extreme values occurring.

Proceedings of the 19th Southern African Universities Power Engineering Conference
SAUPEC 2010, University of the Witwatersrand, Johannesburg
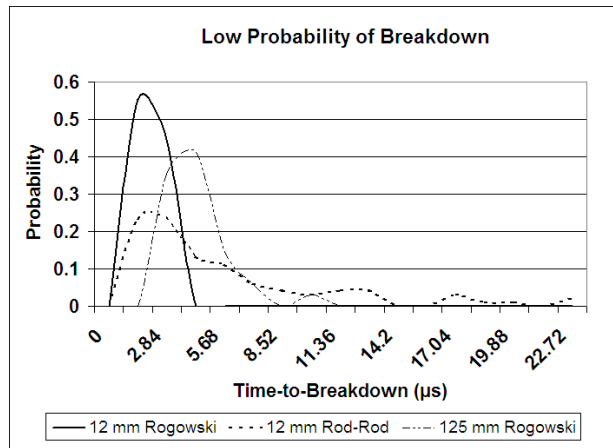
TOPIC G. HIGH VOLTAGE

Fig. 7.   Time-to-Breakdown Distributions for the Electrode Geometries for a Low Probability of Breakdown
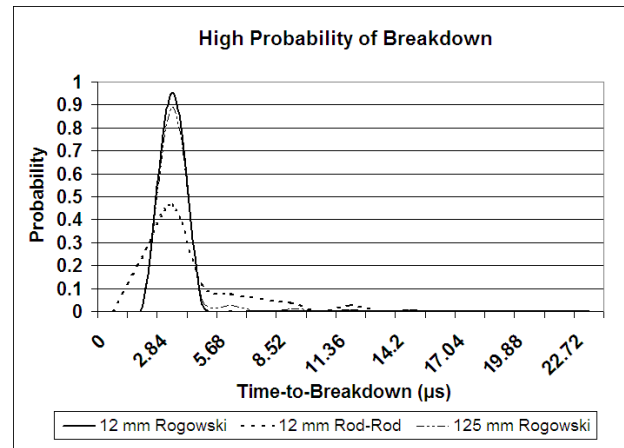

Fig. 9.   Time-to-Breakdown Distributions for the Electrode Geometries for a High Probability of Breakdown

The peak value (or mode) has also shortened. Similarly, the distribution for the 125 mm Rogowski profile also has less extreme values and is approaching that of the 12 mm Rogowski profile.
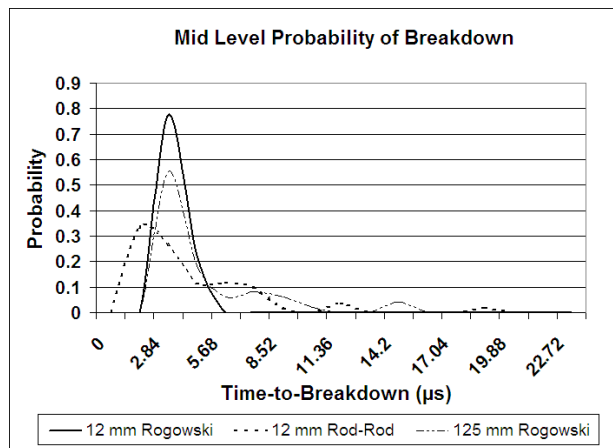
Fig. 8.   Time-to-Breakdown Distributions for the Electrode Geometries for a Mid Level Probability of Breakdown

4.3 High Probability of Breakdown

Figure 9 shows the time-to-breakdown distributions obtained for a high probability of breakdown.

As can be seen, the 12 mm Rogowski profile's distribution is still symmetrical. The standard deviation has decreased again as well as the mean value which is now 1.95 μs. Even fewer extreme values occur in the rod-rod distribution. The same is seen for the 125 mm Rogowski profile in which almost all of the extreme values have fallen away and the distribution is almost exactly the same as that of the 12 mm geometry.

4.4 Discussion and Analysis

Firstly, it was seen that the most common time-to-breakdown value or the mode of the distribution became less as the probability of breakdown increased. This was particularly noticeable in the case of the

Rogowski profile. This observation confirms what was expected given the literature [3, 4].

The other observation that became apparent is that the time-to-breakdown was heavily dependent on the uniformity of the electric field. For the uniform field (Rogowski profile), the time-to-breakdown distribution approached a symmetrical distribution and was, therefore, more predictable. The extremely non-uniform field (rod-rod gap) had a skewed distribution with many extreme values. This is likely due to the nature of non-uniform fields. While there may be occurrences of much higher intensity fields in the rod-rod gap, they are limited to small particular locations. If a seed electron enters the uniform gap, the field will have the same effect on the electron at any point leading to a similar breakdown process every time. In the case of the non-uniform gap however, a seed electron may enter at a point of low electric field and no breakdown will occur. It may then move into a high intensity field later and only then cause a breakdown. As a result, the time taken for breakdown in a non-uniform field is unpredictable [3].

Also notable is the comparison between the 125 mm geometry and the 12 mm geometry. Firstly, the larger gap had some extreme values which is most likely due the slight non-uniformity in the electric field as discussed in section 3.2. Of more interest is the observation that, on average, the larger gap takes the same amount of time for breakdown to occur as the smaller gap.

4.5 Applications

These results have application in the design of any gap geometry in which the time-to-breakdown is of interest. For example, surge protection devices (SPD's) and more specifically, gap arresters. The time it takes for the arrester's gap to breakdown and conduct current to ground is critical to the protection the device can offer [14, 15]. Using uniform electrode geometries for the arrester gaps may lead to more predictable breakdown times.

TOPIC G. HIGH VOLTAGE

Proceedings of the 19th Southern African Universities Power Engineering Conference
SAUPEC 2010, University of the Witwatersrand, Johannesburg

5. CONCLUSION

An experiment has been performed in order to investigate the relationship between breakdown probability and the time-to-breakdown for various gap geometries under lightning impulse conditions. It was seen that, for the three electrode geometries (Rogowski profile, rod-rod and a 125 mm gap) there was a decrease in the average time-to-breakdown as the probability of breakdown increased. However, it was seen that the uniformity of the electric field in the gap had the greatest effect on the time-to-breakdown. For a uniform field, the time-to-breakdown data was seen to approach a symmetrical distribution whereas the distribution was skewed to the right for the non-uniform electric field data. This observation becomes relevant to design of gap geometries where time-to-breakdown is of interest since a uniform electric field will yield far more predictable times than a non-uniform field. More specifically, this is of particular interest in the design of gap arresters.

6. ACKNOWLEDGEMENTS

REFERENCES

[1] N. J. West and I. R. Jandrell, "Arc shapes observed during the laser-induced breakdown of spark gaps," in *Proceedings of the 16th International Symposium on High Voltage Engineering*, 2009.

[2] E. Kuffel, W. S. Zaengl, and J. Kuffel, *High Voltage Engineering Fundamentals*. Butterworth Heinemann, 2008, ch. 5, 8.

[3] R. Arora and W. Mosch, *High Voltage Insulation Engineering*.   New Age International, 1995, ch. 2, pp. 124–126.

[4] H. Raether, "The electron avalanche and its development," *In Applied Scientific Research*, vol. 5, sec. B, pp. 23–33, December 1956.

[5] M. Pejovic, G. S. Ristic, and J. P. Karamarkovic, "Electrical breakdown time delay in gases at low pressures," *Facta Universities: Physics, Chemistry and Technology*, vol. 2, no. 2, pp. 63–78, 2000.

[6] R. F. Saxe and T. J. Lewis, "Measurement of the statistical time lag of breakdown in gases and liquids," *British Journal of Applied Physics*, vol. 6, pp. 211–216, June 1955.

[7] L. H. Fisher, "Formative time lags of spark breakdown," *In Applied Scientific Research*, vol. 5, sec. B, pp. 281–284, 1955.

[8] J. M. Meek, "The mechanism of growth of spark discharges," *In Applied Scientific Research*, vol. 5, sec. B, pp. 269–276, December 1956.

[9] D. F. McDonald and S. Brient, "Nanosecond pulse breakdown initiation and growth," *Rome Air Development Centre Research and Technology Division*, no. RADC-TDR-63-525, January 1964.

[10] M. S. Naidu and V. Kamaraju, *High Voltage Engineering*.   Tata McGraw-Hill, 2009, ch. 2, pp. 39–42.

[11] IEC60060-1:1989 Part 1: General definitions and test requirements, *High Voltage Test Techniques*.   Standards South Africa, 1989.

[12] J. A. Harrison, "A computer study of uniform-field electrodes," *British Journal of Applied Physics*, vol. 18, pp. 1617–1627, April 1967.

[13] H. Hunt and T. ter Wolbeek, "An investigation into the relationship between breakdown probability and time-to-breakdown for various gap geometries under lightning impulse conditions," *4th Year Laboratory project, University of the Witwatersrand*, 2009.

[14] K. Hill, "Surge arresters and testing," *Doble Engineering Company*, 2004.

[15] Z. Abdul-Malek, A. Haddad, D. M. German, and R. T. Waters, "Co-ordination of spark gaps with zno surge arresters," *International Conference on Lightning Protection*, pp. 701–706, 1998.

Proceedings of the 19th Southern African Universities Power Engineering Conference
SAUPEC 2010, University of the Witwatersrand, Johannesburg

TOPIC G. HIGH VOLTAGE

A PRELIMINARY INVESTIGATION INTO 2D RECONSTRUCTION OF BRANCHED LIGHTNING DISCHARGE CHANNELS IN A 3D ENVIRONMENT

Y.C. Liu and K.J. Nixon

Dept. of Electrical and Information Engineering, University of the Witwatersrand, Johannesburg, South Africa

Abstract.   The study of lightning models provides insight into understanding the behaviour of the natural phenomenon. By producing 3D lightning models, a greater understanding of the spatial propagation of a lightning channel can be obtained. A preliminary study was performed to determine whether branched lightning channels could be modelled from one photograph in a 3D environment. Photographs of lightning strikes were obtained using Axis 207 surveillance cameras. Cross-polarised optical filters were used to limit the captured light intensity of the strike. The digital images captured from the cameras were processed manually using an image editor. Three images were used to create a model; the orginal image, a white straight-line image and a mirrored image of the original. These images were placed with 90° separation in the 3D environment. Fourteen branched models were reconstructed. An average error of 1.68% was calculated for an image comparison between the filtered image and a model image. This paper extends on work performed by Liu and Rapson in 2008.

Key Words.   3D reconstruction model, branched lightning channels, lightning photography, image processing.

1. INTRODUCTION

LIGHTNING models form the basis of research into further investigating the physical behaviour of the natural phenomenon [1]. By obtaining a three dimensional (3D) representation of a lightning discharge, the channel can be properly analysed in a 3D visualised space. A system was implemented to capture two dimensional (2D) images of a discharge channel and represent the lightning discharge as a 3D model. Liu and Rapson designed, developed and implemented a preliminary system [2], which was tested primarily using single-channelled high voltage discharges in a controlled laboratory environment. This paper extends their work, by testing the modelling capabilities of branched lightning channels. This paper provides an overview of the modelling procedure; from photographing the lightning channels, to creating the models in a 3D environment. Examples are provided for each stage using one model dataset. Five models are presented to provide a variation of results.

2. PROBLEM STATEMENT

The nature of lightning occurrences is studied to broaden the understanding of the lightning mechanism. This knowledge provides a beneficial contribution to lightning protection systems and further understanding the nature of this phenomenon. Lightning protection becomes evident with a cloud-to-ground (CG) strike with the potential to cause damage to electrically sensitive devices, power distribution lines and even structural buildings [3]. The physical distribution of lightning events is typically considered using photography of the discharge channel from a single perspective. This solution lacks the ability to fully grasp the spatial propagation of the channel, which highlights a need to develop a system that is capable of reconstructing a discharge channel within 3D space. The reconstruction must ultimately be able to determine the channel's directional data and distinguish between split branches. By constructing a 3D model of a discharge channel, a better understanding of how the path of a large channel or lightning strike develops its pattern.

3. BACKGROUND

The difficulties involved with the photography of lightning, and a brief summary of the 3D modelling solution developed by Liu and Rapson will be briefly discussed.

3.1 Photography of Lightning:

The basis of modelling a lightning discharge requires photographs of the channel. The difficulties involved with capturing images of a lightning strike include: the flash duration and the unpredictability of the occurrence. For research purposes, it is difficult to verify whether the correct data of the channel is captured on the photograph. There are several research solutions to the photographing lightning channel attachments to tall structures, such as studies performed on the Fukui Chimney in Japan [4], CN Tower in Toronto, Canada [5] [6] [7]. These papers investigate lightning attachments to tall structures using digital images from conventional video cameras, or high-speed cameras. These studies provide valuable insight into the photography of lightning discharges. No mention of a 3D model is included in these papers, although some produce images from multiple capture devices to provide a sense of spatial distribution. Cummins et al provide preliminary experimental results that could ultimately lead to producing a time-resolved 3D model of CG lightning discharges [8].

3.2 Liu and Rapson's Solution

The 3D reconstruction of general high voltage channels provides insight into their formation, and ultimately its spatial propagation.

TOPIC G. HIGH VOLTAGE

Proceedings of the 19th Southern African Universities Power Engineering Conference
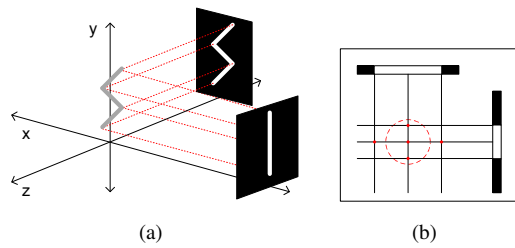SAUPEC 2010, University of the Witwatersrand, Johannesburg

Fig. 1:   A basic representation of the reconstruction method (a) 3D reconstruction algorithm (b) A 2D representation of the algorithm using cylinders for modelling [2].

Liu and Rapson devised a method of recreating the laboratory scenario in a software application, extending normals from the image to the central y-axis, and creating a pixel-high cylinder where the normals meet [2]. *Figure 1 (a) and (b)* illustrate a simplified representation of the algorithm functionality. The system produces a 3D model of a discharge channel samples from in a controlled environment. They focused on reconstructing unbranched high voltage channels in a laboratory environment. This modelling algorithm provided a total error of 11% from 70 tests, through the comparison of the filtered image to an image of the model from the same perspective.

4. SYSTEM OVERVIEW

The system developed by Liu and Rapson [2] was modified to account for a physical investigation, which is the focus of this paper. The physical investigation considers a discharge environment in a real-world scenario, which includes the capturing of image test data from lightning strikes. The system described in *Figure 2* will attempt to render an accurate 2D model of the channel in 3D space. The following lists a summary of the system and contents of this paper.

1) The discharge environment is selected to provide image samples of the lightning strikes.
2) The method of acquiring photographs, and optimising the data is discussed.
3) The image processing required for reconstructing the model is demonstrated, including the data filtering and description of the algorithm used.
4) An example of the reconstructed model will be presented with a discussion on the modelling capabilities.
5) The testing framework and the sampled results will be presented and discussed.
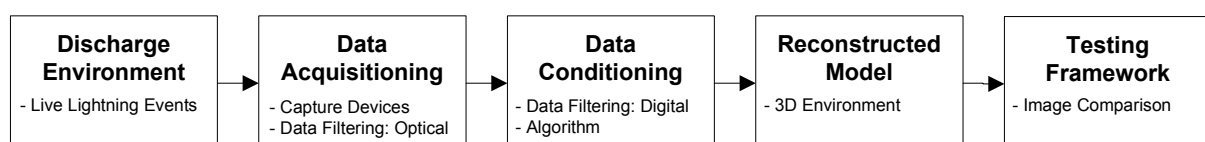
5. DISCHARGE ENVIRONMENT AND DATA ACQUISITION

The test data was taken in the late thunderstorm season in Johannesburg, South Africa. The reason for obtaining test data in this location was due to its high ground flash density. The capture of image data includes the consideration of the devices used and optical filters required. *Figure 3* displays a set of test images resulting from this stage. The images provide a time-resolved lightning strike with multiple strokes. This would provide a scope for future reconstruction of time-resolved models.

Fig. 3:   Consecutive images with 10 ms time separation taken of a cloud-to-cloud (CC) lightning strike.

The camera used for digital capture was the Axis 207W wireless surveillance IP camera [9]. The camera was set according to the settings as demonstrated in *Table 1*. These were chosen as per the implemented system in [2].

Table 1:   Camera configuration for the physical investigation.

Parameter	Value
Frame rate (fps)	15
Pre-Buffer (s)	2
Resolution (pixels)	640×480
Colour	Grayscale
Triggering method	Motion detection

Captured images require the data of only the intense light of the discharge channel. For the purpose of the experiment, only wavelengths of the visible light spectrum were desired for modelling the discharge [10]. The insignificant data needed to be filtered out. Optical filters were required to obtain the usable data in the images. A combination of cross-polarised filters and camera configurations provided images that could be used for the reconstruction. The images in *Figure 4* demonstrated the different variations in the captured images using different layers of optical filters. A disadvantage to using optical filters is the possible loss of image detail brought about by damaged lenses but this is neglected for the purpose of this experiment.
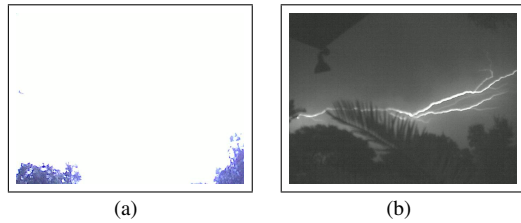

Fig. 2:   Block diagram demonstrating the expected system overview and flow.

Proceedings of the 19th Southern African Universities Power Engineering Conference
SAUPEC 2010, University of the Witwatersrand, Johannesburg

TOPIC G. HIGH VOLTAGE

Fig. 4: Different images taken with and without filters. (a) No filters (b) Cross-polarised filters.

Fig. 6: Amalgamated lightning strike from individual images.

Figure 4 (a) shows the image captured of a lightning discharge channel without optical filters. It is observed that the image is extremely overexposed. Two linearly polarised lenses are placed perpendicularly to construct a cross-polarised filter, which reduces the intensity of light entering the lens. The image captured from this filter is illustrated in *Figure 4 (b)*.

6. DATA CONDITIONING

The images needed be to filtered further so the channel information could be isolated. Due to the greyscale ambiguities from the photographed images, digital filtering was required. Once the images were filtered to explicit black and white images, the relevant data was extrapolated from the images and conditioned to provide a reconstructed model.

6.1 Data Filtering: Digital

The application requires black and white images to extract the relevant data points from the image. The white pixels represent the channel information, and the black pixels are ignored. The digital filtering provides a means to isolate the channel information. The images were manually processed, and then filtered again in the application. This may seem ambiguous, but the purpose of manually filtering the images ensured that the less pronounced branches in the channel were portrayed in the model. The filtering in the application just ensures that the inserted images have usable data.
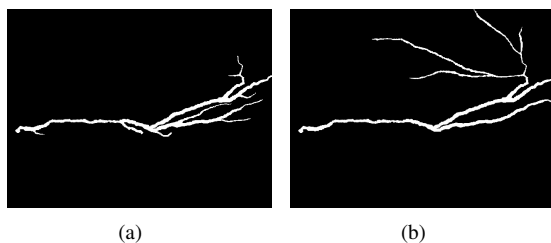
Fig. 5: Manually processed images taken of lightning strike.

The images in *Figure 5* depict the result of manually filtering the photographs from *Figure 3*, using an image editor. These images were overlayed and amalgamated to combine the discharge channel information, as shown in *Figure 6*. Each of these images can be used as individual test samples.

The images were inserted into the modelling framework in the preparation of data conditioning. The filtering process includes a tracking function, to determine the relevant channel information from the image, and crops it to a smaller size, to decrease the processing time of the reconstruction.

6.2 Algorithm

The 3D algorithm was written in C++ programming language, integrated with VTK — an open source, cross-platform visualisation toolkit. The application could reconstruct a model using two or three images; each configuration may have different options for reconstruction. Using the VTK 3D environment, the filtered images were arranged on a set of axes in 3D space, mapping the experimental setup. The algorithm was designed to process the setup in layers over the y-axis. This method eliminated the third dimension, reducing the algorithm to a 2D problem, as demonstrated in *Figure 1*. Normals of the white segments were projected to the centre of the setup, where they were compared to the normals from other perspectives. Each layer of the discharge was assumed to have a cylindrical body. The centres of two images determined the centre point of the cylinder, where the average thickness of the images determined the radius of the cylinder. The third image was used to verify the existence of the cylinder.
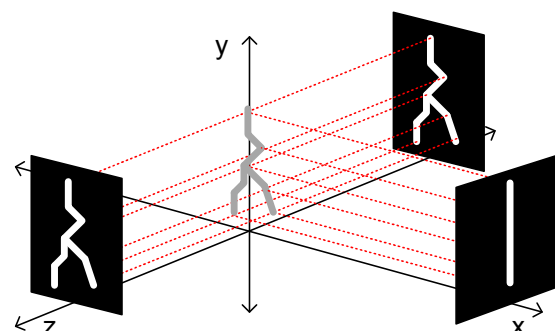

Fig. 7: Algorithm for one image reconstruction.

Since only one image perspective was taken per lightning strike, it was expected that the model could not have any 3D definition. Thus, a white straight-line image was placed 90° from the original image, as depicted in *Figure 7*. Due to algorithm limitations for two images, the split branches in the channel were not accounted for, and only the main channel at which the

TOPIC G. HIGH VOLTAGE

Proceedings of the 19ᵗʰ Southern African Universities Power Engineering Conference
SAUPEC 2010, University of the Witwatersrand, Johannesburg

points intersected was modelled. This was resolved by using three images place with a $90°$ separation. The third image was created using the image editor to provide a mirrored imaged of the original. This was placed $180°$ from the original image to identify the channel branching.

7. MODEL

Fourteen models were constructed using test data obtained in the physical investigation. *Figure 8* provides an example of the models that were created. A visual comparison of the model with the filtered image used for the reconstruction is presented. The image of the reconstructed model was taken from the same perspective as the filtered image for the appropriate comparison.

(a)

(b)
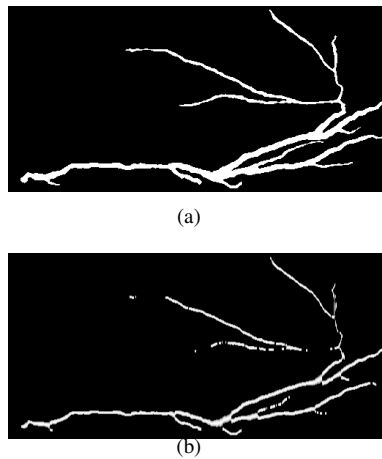
Fig. 8: Filtered image (a) compared to reconstructed model (b).

It can be observed that the algorithm is not perfect, and does not flawlessly reconstruct the channel path, even with the ambiguity of the mirrored image. The reconstruction seems to break down when the channel thickness thins in the path. This could be explained by the fact that the original image and the mirrored image do not get perfectly aligned to receive the logical identifier as an indication that a cylinder exists. This property is confirmed in some of the other samples which produce continuation of thicker channels and corresponding paths.

8. TESTING AND RESULTS

In order to quantitatively verify the model accuracy, the images in *Figure 8* were compared using a tester application. An image difference in pixels was produced, identifying the pixel mismatch between the two images. *Equation 1* provides the error calculation for the model verification, where ε is the pixel mismatch determined by the tester application, h and w account for the height and width of the tested image in pixels.

$$\% \ error = \frac{\varepsilon}{h \times w} \times 100 \qquad (1)$$

Table 2: Testing information for model

Parameter	Value
Image difference ε	321.51
Height h (pixels)	500
Width w (pixels)	160
Percentage Error (%)	**0.40**

There could only be one value for h and w, since the tester application requires identical image sizes. The error calculation takes into account the total error of the entire image, and not only of the significant channel information. This may provide a misleading result, since the calculation is a function of the image size (which includes the redundant black pixels). *Equation 1* presents an error of 0.40% for the created model in *Figure 8* using the information in *Table 2*. All fourteen samples were tested with the results provided in *Figure 9* with an average error of 1.68%. It should be noted that Model 1 in *Figure 9* is the model demonstrated as the running example within this paper. The error ranges from 0.16 to 8.47%, which is a considerably large range and could be accounted for by several different factors. There were a few things that specifically accounted for the error: the thickness of the channel did not match; there were missing links in the channel path; and the image of the model was slightly off-centred, providing a mismatched image for comparison.
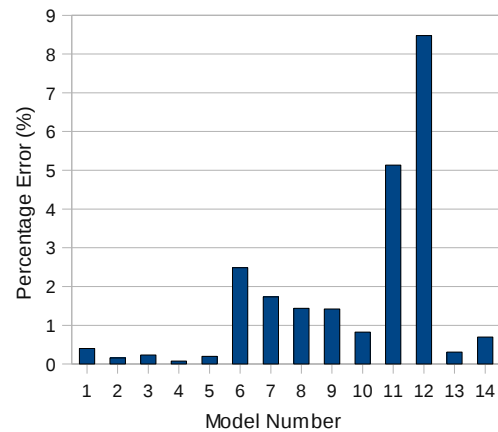

Fig. 9: Results for error calculation of branched test models.

It was only possible to determine the error of the filtered image to the image acquired from the model from the same perspective. Other errors occuring in the system that should be taken into account, but could not be quantified include: lightning to optically filtered images, optically filtered images to manually filtered images, manually filtered images to application filtered images.

9. ANALYSIS

The models of fourteen datasets were successfully reconstructed. The models provided an average error in comparison to the filtered images of 1.68%, even though the error calculation has been identified as

Proceedings of the 19th Southern African Universities Power Engineering Conference
SAUPEC 2010, University of the Witwatersrand, Johannesburg

TOPIC G. HIGH VOLTAGE

being misleading. Also, the cylinder radius for the channel was determined by the thickness of the straight-line image placed 90° relative to the lightning image, which could account for the inaccuracies of the model thickness. This work presents the first recorded testing data of the algorithm using branched channels acquired from a physical investigation. The full system error could not be easily quantified.

The average error of the high voltage discharges from [2] can be seen to differ by an order of magnitude to the average error obtained in the physical investigation of this paper. This could be accounted for by several factors from the laboratory investigation: more tested datasets and a combination of the different algorithm configurations (differing when using 2 or 3 images), more images with possible inaccurate angular placements in the environment setup.

10. FUTURE WORK

More models need to be reconstructed and tested for the physical investigation in order to provide a better perspective on the algorithm performance. This will also provide better comparisons to the test data obtained from the experimental investigation.

A detailed testing platform needs to be established, taking into account only the significant information, instead of testing the entire image. This includes determining the reason for the offsetted image of the model for error comparison, thus providing a better means for comparison. Currently, a more comprehensive testing framework is being developed. This test would compare two images with a branched channel which would determine the points of branching and channel path termination. This would map out the position of the points in question and compare the number of significant points and accuracy of the image of the reconstructed model.

Of course, this paper provides a proof of concept to obtaining 3D models of lightning discharges. This provides a platform for reconstructing the lightning models using multiple-perspective images of a strike. This would require a scaled version of the work performed in [2].

11. CONCLUSION

This paper presented a preliminary investigation into considering the plausibility of modelling a 2D lightning image in a 3D environment. It has been shown that it is possible to capture lightning images using an Axis 207 surveillance camera with a cross-polarised optical filter. The channel information was extracted from the image using manual and application filtering. Fourteen branched discharge channels were successfully modelled using three images per photograph. The algorithm configuration using three images with a 90° -separation provided an error of 1.68% from fourteen test models. A comprehensive

testing method needs to be developed to obtain a more accurate error calculation. Additional test data needs to be obtained in order to provide more models for comparison. And lastly, this proves that in theory, by scaling the system in [2], a 3D model of a branched lightning channel can be obtained.

REFERENCES

[1] V. Rakov and M. Uman. *Lightning — Physics and Effects*. Department of Electrical and Computer Engineering, University of Florida: Cambridge University Press, 2003.

[2] Y. Liu, A. Rapson, and K. Nixon. "Laboratory Investigation into Reconstructing a Three Dimensional Model of a Discharge Channel using Digital Images." *SAUPEC — Stellenbosch, South Africa*, vol. 18, p. 83, 2009.

[3] S. Prentice and R. Golde. *Lightning Volume 1: Physics of Lightning — Frequency of Lightning Discharges*, chap. 100, pp. 100–100. Department of Electrical Engineering, University of Queensland, Brisbane, Australia: Acedemic Press Inc., New York, 1977.

[4] M. Miki, A. Wada, and A. Asakawa. "Observations of Upward Lightning in Winter at the Coast of Japan Sea with a High-speed Video Camera." *ICLP — Avignon, France*, vol. 27, no. 1a2, 2004.

[5] A. Hussein, W. Janischewskyj, F. Noor, and M. Milewski. "Characteristics of Lightning Flashes Striking the CN Tower below its Tip." *ICLP — Avignon, France*, vol. 27, no. 4p8, 2004.

[6] A. Hussein, M. Milewski, A. Abdelraziq, W. Janischewskyj, and F. Jabbar. "Visual Characteristics of CN Tower Lightning Flashes." *ICLP — Kanazawa, Japan*, vol. 28, no. I-11, 2006.

[7] A. Hussein, V. Todorovski, M. Milewski, K. Cummins, and W. Janischewskyj. "Characteristics of Lightning Strikes at and in the Vicinity of the CN Tower." *ICLP — Uppsala, Sweden*, vol. 29, no. 1c4, 2008.

[8] K. Cummins, M. Saba, T. Warner, C. Weidman, L. Campos, S. Fleenor, A. Saraiva, and W. Scheftic. "A Multi-Camera High-Speed Video Study of Cloud-to-Ground Lightning in South Arizona — Preliminary Results." *ICLP — Uppsala, Sweden*, vol. 29, no. 1c1, 2008.

[9] Axis Communications AB. *AXIS207 Users Manual Rev 3.0*, August 2006.

[10] R. Serway and J. Jewett. *Physics for Scientists Engineers with Modern Physics*. Thomson Bokes/Cole, 6th ed., 2004.

TOPIC G. HIGH VOLTAGE

Proceedings of the 19th Southern African Universities Power Engineering Conference
SAUPEC 2010, University of the Witwatersrand, Johannesburg

TRANSFER FUNCTION BASED INTEGRATION OF DERS AND DYNAMIC STABILITY ANALYSIS OF MICROGRID

Prasenjit Basak*,   S Chowdhury** and S P Chowdhury**

* Calcutta Institute of Engineering & Management, Electrical Engineering Department, Kolkata, India.

** University of Cape Town, Electrical Engineering Department, Cape Town, South Africa.

Abstract.   A microgrid is an integrated form of distributed energy resources (DERs) which are connected together to serve electrical power to the selected consumers or can exchange power with the existing utility grid suitably under standalone or grid connected mode. The microgrid can be cited as a physical system which is a combination of DERs such as, Photovoltaic Generator, Wind turbine, Fuel Cell, Electrolyzer system, Microturbine etc. and can be modeled   with suitable assumptions depending upon specific operational condition to be studied. Interconnection of several kinds of power sources would impact the quality of power within the microgrid. Since voltage and frequency are not the only factors for a system delivering good quality power, the capacity of the same to withstand instability due to transient condition is one of the prime factors to be considered to accept a system as a stable system. Before practical integration of distributed energy resources, it would be essential to check the stability of the system at the design stage. In this paper, the authors have presented the microgrid based on control system engineering. To represent the individual components of microgrid, the DERs (Distributed Energy Resources) have been represented with their transfer functions and they have been simulated using Simulink-Matlab. To observe the response of the DERs, the frequency fluctuation due to step and random change in output power/load are considered as the main factors for stability analysis. All the DERs are integrated forming the microgrid which is represented with an equivalent transfer function based model. The models are studied and results are discussed with the waveforms. This paper shows one feasible method to check the dynamic stability of a proposed microgrid.

Key Words.   Dynamic Stability of Microgrid, Integration of DERs, Microgrid, Pole-Zero Plots, Polynomial Stability Test.

1.   INTRODUCTION

The stability of a microgrid, which is interconnection of several distributed energy resources, is its ability to return to normal or stable operation after having been subjected to some form of disturbance. Conversely, instability means a condition denoting loss of synchronism or falling out of step. Stability considerations have been recognized as an essential feature of microgrid planning. For proper working of microgrid, the stability problems are to be taken care, covering the steady state, dynamic and transient condition. The study of steady state stability mainly concerned with the calculation of maximum limit for the DER loading before losing synchronism, provided the loading is increased gradually [1]. In microgrid, dynamic instability is more probable than steady state instability. The dynamic instability may occur due to sudden fluctuation of load and the system oscillation may occur which has to die out completely within a short time. If the oscillation of the system output persists for a longtime, then the microgrid will be dynamically instable, which may be a serious threat to the interconnection of DERs. This paper shows a feasible method to study the dynamic stability of a microgrid. Initially, the individual DERs are presented with their first order transfer functions based on assumption on the linearity of the systems with reference from the study of Battery Energy Storage (BES) facility system [2][3].

2.   RESPONSE OF DISTRIBUTED ENERGY RESOURCES AGAINST FREQUENCY AND POWER FLUCTUATION

The widespread use of various kinds of distributed power sources would impact the quality of the power supply within a microgrid power system, causing many control problems. This paper discusses the dynamic stability of microgrid operation and presents the control scheme of combining fuel cell, electrolyzer system and micro-turbine as a hybrid system to enumerate the microgrid system's ability to solve power quality issues resulting from frequency fluctuations due to sudden and random load fluctuation [4].

With reference to [3], large Battery Energy Storage (BES) facility may provide significant dynamic operation benefits for electric utilities. One area in which a BES facility could be useful is the frequency regulation requirement. This feature is significantly important in island power systems. In [3], D. Kottick, M. Blau and D. Edelstein quantified the effects of a 30 MW battery on frequency regulation in the Israeli isolated power system. The study was performed on a single area model representing the whole power system and containing a first order transfer function that represented the BES performance. In reference to [2] and [3], in this paper, each source is presented with their first order transfer functions. Next section focuses on the stability of each system against fast frequency fluctuation and sudden output power unbalance. Each system is observed with their output waveforms showing overshooting due to sudden power fluctuation and finally reaching steady state condition.

Proceedings of the 19th Southern African Universities Power Engineering Conference
SAUPEC 2010, University of the Witwatersrand, Johannesburg

TOPIC G. HIGH VOLTAGE

2.1 Fuel Cells

With reference to [5], in order to introduce and apply small fuel cell cogeneration to a building, it is necessary to investigate the response characteristics of the power and heat power with load fluctuations. In particular, the power demand pattern of an individual house is a load that has usually gone up and down rapidly for a short time. If a system is controlled to follow such a load, the difference in the response and load increases. As a result, the power quality (voltage and frequency) of this power system may worsen. "Fluctuation in a short period, such as an inrush current" and "fluctuation in a long period to cause in change of demand" are included in the power load. "Change over a long period" means a step change in the power demand. With the change factor of the transient power demand, such as with an inrush current, there is a change over a long period in the demand. When "transient power demand" is defined as load fluctuation and "change over a long period" is defined as demand fluctuation, the power load changes of an individual house have large fluctuations of both. If the transient response of a single cell of a fuel cell is examined, it seems that stable response characteristics are acquired for the load fluctuation characteristics of the household appliance items used in common homes [5]. As referred in [2], the sudden real power fluctuation of a fuel cell generator can be represented by its transfer function $\Delta P_{FC} = [K_{FC} / (1 + T_{FC} S)] \Delta f$

where,

ΔP_{FC} = Real time power fluctuation
Δf = Frequency fluctuation due to sudden fluctuation of real power
P_{FC} = Output power of Fuel Cell
K_{FC} = Gain of Fuel Cell
T_{FC} = Time Constant of Fuel Cell

Fig.1.1: Output Power versus Frequency Control of Fuel Cell for Step Change in Output

Fig. 1.2: Output Power versus Frequency Control of Fuel Cell for Random Change in Output

In the Fig. 1.1 and Fig. 1.2, the fuel cell is presented with the Proportional plus Integral control scheme where the sudden fluctuation of output power is simulated with a step and random change of output respectively. Due this step change in output power, the fluctuation of frequency is shown in Fig. 2.

Fig.2: Frequency Variation in Fuel Cell for Step Change in Load

Sudden fluctuation of frequency due to that disturbance in output is shown with overshooting and damping and finally reaching steady state. The variation of output power and system response due to random & step variation of output power is shown in Fig. 3 and Fig. 4 respectively.

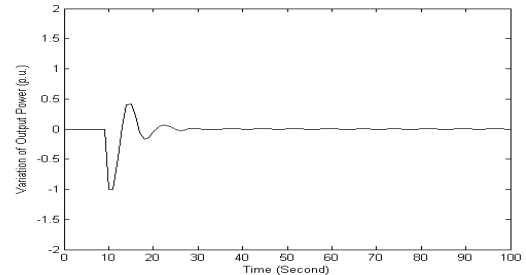Fig.3: Output Power Variation in Fuel Cell for Random Change in Load

Fig.4: Output Power Variation in Fuel Cell for Step Change in Load

2.2 Electrolyser System and Microturbine

As referred in [6], it is well known that the power output of microturbine can be controlled to compensate for load change and alleviate the system frequency fluctuations. Nevertheless, the microturbine may not adequately compensate rapid load change due to its slow dynamic response. Moreover, when the intermittent power generations from wind power and photovoltaic are integrated into the system, they may cause severe frequency fluctuation [6].

In order to study the fast dynamic response, each system is studied separately to observe the absorption of the frequency and power fluctuations. Simulation results exhibit the robustness and stabilizing effects of electrolyzer and microturbine.

The sudden real power fluctuation of an Electrolyser system can be presented as [2],

$\Delta P_{ES} = [K_{ES} / (1 + T_{ES} S)] \Delta f$;

where,

ΔP_{ES} = Real time power fluctuation

Δf = Frequency fluctuation due to sudden fluctuation of real power

P_{ES} = Output power of Electrolyser system

K_{ES}= Gain of Electrolyser system,

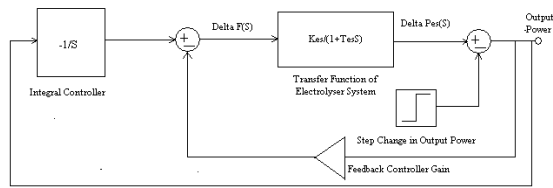T_{ES} = Time Constant of Electrolyser system

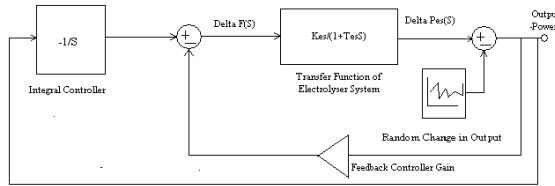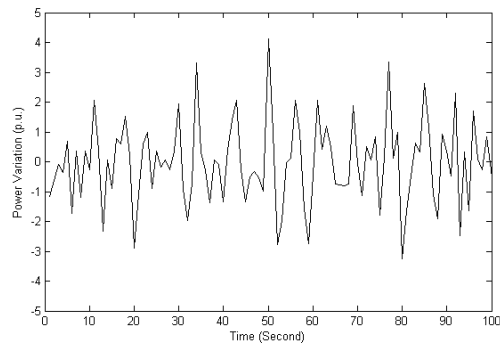Fig. 5.1: Scheme for Step Change in Output of Electrolyser

Fig.5.2: Scheme for Random Change in Output of Electrolyser

The proportional integral control schemes are shown in Fig.5.1 and Fig. 5.2. Disturbance is created at the output in two modes; one is sudden fluctuation which is simulated with sudden step change in output and the other is random power fluctuation simulated by random noise signal generated by Simulink tool box. The frequency fluctuation for step change in load and power variation due to random and step load fluctuation are shown in the following Fig. 6, Fig. 7 and Fig. 8 respectively.

Fig.6: Frequency Variation in Electrolyser System for Step Change in Load

Fig.7: Output Power Variation in Electrolyser System for Random Change in Load

Fig. 8: Output Power Variation in Electrolyser for Step Change in Load

The above outputs show the satisfactory damping of the overshoot occurred due to disturbances applied as mentioned above.

A Microturbine block which is normally intended for base load supply is shown in the Fig. 9.

Fig.9: Output Power versus Frequency Control Scheme for Microturbine

Considering the linear power versus frequency droop characteristic, the transfer function based formulation is shown below [2].

ΔP_{MT} = (-1 / K_{MT}) Δf;

where, ΔP_{MT} = Real time power fluctuation,

Δf = Frequency fluctuation due to sudden fluctuation of real power,

K_{MT} = Droop property of Microturbine output

Variation of output power in Microturbine due to step change and random fluctuation of load is shown in Fig. 10 and Fig. 11 respectively. The waveform obtained shows zero error after damping off the overshoot.
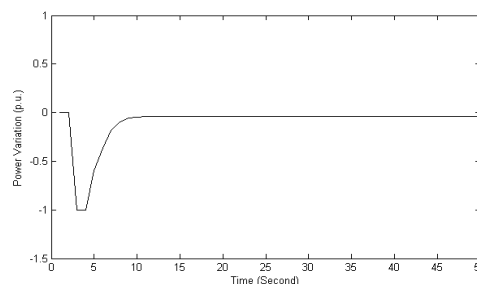

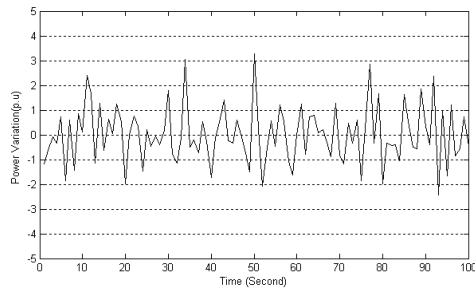Fig.10: Output Power Variation in Microturbine for Step Change in load

Proceedings of the 19th Southern African Universities Power Engineering Conference
SAUPEC 2010, University of the Witwatersrand, Johannesburg

TOPIC G. HIGH VOLTAGE

Fig.11: Output Power Variation in Microturbine for Random Change in load

3. TRANSFER FUNCTION BASED MODEL OF MICROGRID: STUDY OF FREQUENCY AND OUTPUT POWER FLUCTUATION

In the previous sections, the Fuel Cell, Electrolyser system and Microturbine are studied separately and are simulated to observe the dynamic instability.

In this section, the transfer functions of DERs are integrated as shown in the Fig. 12 forming microgrid. The integrated system is tested for dynamic instability with a step change in the output power. Proportional plus integral control strategy is used and the output power wave form obtained is shown in the Fig. 13 below. The result shows satisfactory performance of the microgrid model against dynamic instability. The model is studied for random load fluctuation and the response is observed as shown in Fig. 14. Step response output data are shown in Table 1.

Fig.12: Transfer Function based Model of Microgrid

Fig.13: Output Power variation in Microgrid due to Step Change in Load

Fig.14: Output Power Variation in Microgrid due to Random Change in Load

Table-1 : Step Response obtained after Linear Analysis of Microgrid

	FC	ES	MT	MG
Peak Amplitude	0.887	0.95	-25	-3
Overshoot (%)	Infinity at t=0	Infinity at t=1.09	$2.5*10^3$	$7.7*10^3$
Rise Time (Second)	0	0	0.845	0.902
Settling Time (Second)	11.7	14.2	1.5	10.4
Final Value	0	0	-0.962	-0.0385

FC = Fuel Cell, ES= Electrolyser, MT= Microturbine, MG=Microgrid

4. STABILITY ANALYSIS OF MICROGRID

The microgrid shown in Fig. 12 are studied for stability analysis with Pole-Zero mapping [7] using Matlab-Simulink. The main objective of this section is to check if there is any root of the characteristic equation on the right half of s-plane. The step change in output power is considered as input and the output power variation is considered as output. The result is shown in Fig. 15. It shows that no pole is located on the right hand side of the imaginary axis of S-plane, supporting stability of the microgrid system.

Polynomial Stability Test: The microgrid shown in Fig. 12 above also studied for "Polynomial Stability Test" using Matlab Simulink tool box. This block is used to check the pole locations of the denominator polynomial, A(z), of a transfer function, H(z) as mentioned below.

Mathematical Formulation:

$$H(Z) = [B(Z)/A(Z)]$$
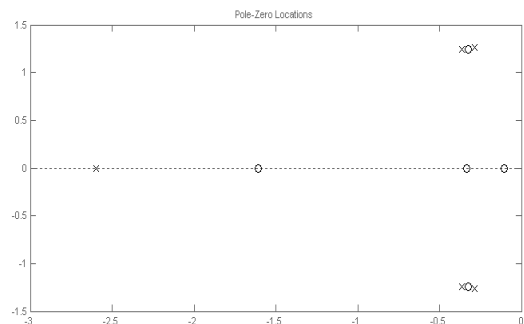$$=\{b_1+b_2Z^{-1}+....+b_mZ^{-(m-1)}\}/\{a_1+a_2Z^{-1}+....+a_nZ^{-(n-1)}\}$$

Fig.15: Pole-Zero Mapping of Microgrid

TOPIC G. HIGH VOLTAGE

Proceedings of the 19th Southern African Universities Power Engineering Conference
SAUPEC 2010, University of the Witwatersrand, Johannesburg

The poles are the n-1 roots of the denominator polynomial, A(z). As is typical in DSP applications, the transfer function above is specified in descending powers of z-1 rather than z. "The Polynomial Stability Test Block" uses the Schur-Cohn algorithm to determine whether all roots of a polynomial are within the unit circle. If any poles are located outside the unit circle, the transfer function H(z) is unstable showing zero(0) at the output of the Simulink test block. For the system to be stable, the output of the block should display one (1). After simulation of the current system, the value 1 is obtained at the output of the "Polynomial Stability Test Block" indicating that the polynomial in the corresponding column of the input is stable.

5. CONCLUSION

Renewable energies are environmentally focused but the output power fluctuation of renewable energies may cause excess variation of voltage or frequency of the grid. Increase in the amount of renewable energies would violate the quality of the grid [8]. To maintain the quality of the grid, the design of a microgrid should meet some specific criteria which can judge its performance. There are many factors responsible towards smooth integration of the DERs to form microgrid. Eventually, all the possible factors should be considered at the stage of research and development prior to the system put in actual operating mode for effective utilization of R&D cost.

Among many prime factors, a microgrid must be studied for stability at design level. It is necessary to develop suitable tool or method to check the stability criteria of a proposed grid. In this paper, the authors have suggested few methods to study the dynamic stability of a proposed microgrid due to sudden fluctuation of load by representing each component of the microgrid in the form of their transfer function. It is realized from this work, that there are many features such as linearity or non linearity of the system, gain, time constants, etc. which decide the transfer function of a DER and the transfer function may vary as per the assumptions considered for those factors even for the same system. So the stability analysis has many dimensions to be dealt with in the future research work. Further research efforts will attempt to accumulate all the possible factors for integration of distributed energy resources and stability analysis of microgrid. Progress of this research will be reported in due course.

ACKNOWLEDGMENT

REFERENCES

[1] D.P. Kothari, I.J. Nagrath, "Modern Power System Analysis", 3rd Edition, Chapter 12, pp 433-434.

[2] Xiangjun Li, Yu-Jin Song, Soo Bin Han, "Study on Power Quality Control in Multiple Renewable Energy Hybrid Microgrid System," in *Proc. PowerTech 2007*.

[3] D. Kottic, M. Blau and D. Edelstein, "Battery Energy Storage for Frequency Regulation in an Island Power System" in IEEE Transactions on Energy Conversion", Vol.8, No3, pp- 455-459, Sep. 1993.

[4] Xiangjun Li, Yu-Jin Song and Soo-Bin Han; Frequency control in micro-grid power system combined with electrolyzer system and fuzzy PI controller; Journal of Power Sources, Volume 180, Issue 1, 15 May 2008, Pages 468-475, Copyright © 2008 Elsevier B.V.

[5] S.Obara, Fuel Cell Microgrids, © 2009 Springer, Power Systems Series, Chapter 7: Load Response Characteristic of the fuel cell for individual Cold-region houses; p- 113.

[6] Sitthidet Vachirasricirikul, , Issarachai Ngamroob and Somyot Kaitwanidvilaib, Application of electrolyzer system to enhance frequency stabilization effect of microturbine in a microgrid system, International Journal of Hydrogen Energy, Volume 34, Issue 17, Pages 7131-7560 (September 2009)*Pages 7131-7142,* Crown copyright © 2009 Published by Elsevier Ltd.

[7] I.J. Nagrath, M. Gopal, "Control Systems Engineering", 2nd Edition, Chapter 9, pp 274-318.

[8] M. Matsubara, G. Fujita, T.Shinji, T. Sekine, A. Akisawa, T. Kashiwagi & R. Yokoyama, "Supply and Demand Control of Dispersed type Power Sources in Microgrid", in Proc. 13th Int.. Conf. ISAP'05, pp 67-72.

[9] R.H. Lasseter and P. Paigi, "Microgrid: A Conceptual Solution", in Proc. 35th Annv. Conf. IEEE, PESC'04, pp 4285-4290.

Proceedings of the 19th Southern African Universities Power Engineering Conference
SAUPEC 2010, University of the Witwatersrand, Johannesburg

TOPIC G. HIGH VOLTAGE

EVOLUTION OF PD FREQUENCY SPECTRA OF TYPICAL DEFECTS IN SOLID DIELECTRICS: Some preliminary results

C Nyamupangedengu and IR Jandrell

University of the Witwatersrand, Johannesburg, School of Electrical and Information Engineering,
Private Bag 3, Wits 2050 South Africa

Abstract. Partial discharges in polymer insulation are known to change in characteristics as the insulation defect progresses in ageing to total failure. In the work reported in this paper the phenomenon was investigated through monitoring the changes in the discharge frequency spectral content as the defects aged under continuous exposure to PD until total failure. The way in which the various features of the frequency spectra evolved depended on whether the defect was cavity, surface or corona discharge. The findings of this work suggest more diligent approach in the interpretation of online partial discharge diagnosis results. A PD defect recognition criterion is then suggested that is based on continuous monitoring and evaluation of PD frequency spectral features.

Key Words: Partial discharges; frequency spectra; evolution; ageing; spectrum analyser; defect recognition

1. INTRODUCTION

Partial discharges (PD) are 'microsparks' that occur in electrical insulation and are caused by enhanced electrical stress due to insulation defects [1]. The discharge process gradually causes physiochemical degradation of the insulation and in most cases progresses to total failure. PDs are therefore, in most cases, precursors of electrical insulation failure and can be considered as indicators of insulation condition integrity.

There are various ways of detecting PD – the common being acoustic, phase resolved, time resolved and frequency domain methods. PD diagnosis in the frequency domain has been studied by various researchers and it is now generally agreed that, in some cases, there are aspects of the method that make it superior over other PD diagnosis techniques [2-6].

This paper presents preliminary results of an experimental investigation into how PD frequency spectra evolve over long time ageing period under continuous PD activity for different defects in polymer electrical insulation. The work intends to contribute to the fundamental understanding of PD phenomena as well as enhance effectiveness of PD diagnosis technologies. It searches for answers to the question: *Can different types and 'ages' of solid insulation defects be uniquely recognised through characterisation of the corresponding PD frequency spectra?*

The rest of the paper is structured as follows: Section 2 gives an overview of the frequency domain PD detection techniques as this was the method used in this work. It is followed by the description of the experimental methodology. Results are then presented and discussed in sections 4 and 5 respectively. The paper is concluded in section 6.

2. AN OVERVIEW OF THE FREQUENCY DOMAIN PD DIAGNOSIS METHOD

Frequency domain PD detection entails displaying discharge signals as spectra of frequency components and these can extend into the GHz range.

2.1 The strengths of the frequency domain PD detection techniques

Some of the features of PD diagnosis in the frequency domain that make it preferable under certain circumstances over other methods include:

i. In the frequency domain it is possible to view the entire bandwidth of the PD together with any other interference. Suitable portions of the spectrum that are free from external interferences can be selected and the rest of the spectra discarded thereby improving detection sensitivity. It is for this reason that PDs are detected in the high or ultra high frequency portions of the PD frequency spectra in high voltage equipment such as GIS (gas insulated systems) and power transformers. These equipments impose minimum frequency dependent distortions in the high to ultra high frequency range [7]. The lower frequency portion of the spectrum can be discarded as it is usually polluted by harmonics from machines and drives and also communication signals.

In power cables the significantly high frequency dependent attenuation characteristics of the cables prevents most high frequency interferences from propagating along the cable. When detecting PDs in a cable accessory with the sensor being close to the accessory, the rest of the power cable filters out any high frequency signal travelling towards the accessory. The accessory is therefore shielded from high frequency interferences. High detection sensitivities can therefore be achieved within the high and ultra high frequency range [8].

ii. In some cases PD defect recognition is more effective in the frequency domain than other methods. PD frequency spectra can exhibit more PD type dependent distinctive features than the corresponding time domain signals [5,6]. An example of success in this regard is that reported by Thayoob and co-workers [3]. They used PD frequency domain signals to successfully recognise various soil conditions under which the power cables with PDs were operating in.

iii. PDs in a cable with water trees can be distinguished from that without water trees by using the frequency domain techniques as

TOPIC G. HIGH VOLTAGE

Proceedings of the 19th Southern African Universities Power Engineering Conference
SAUPEC 2010, University of the Witwatersrand, Johannesburg

reported by Ahmed and Srinivas in [4]. A PD pulse travelling through a cable portion with water trees encounters partial reflections and diffractions caused by the water trees. The phenomenon manifests as increased white noise background on the PD frequency spectrum.

2.2 The use of a spectrum analyser in detecting PDs

Generally there are two ways of detecting PDs in the frequency domain. They can be detected as time-resolved pulses that can then be appropriately transformed into equivalent frequency spectra. Alternatevely PDs can be detected and displayed directly as frequency spectra using a spectrum analyser. The spectrum analyser enables viewing of the PD signal together with the accompanying interfering signals such that the instrument can be tuned to select portions of the signal that give the best S/N ratio. Furthermore, in the zero span mode, the spectrum analyser can display phase-resolved PD and this flexibility makes the instrument more attractive than others. For more detailed studies and discussions of spectrum analyser PD detection methodology in comparison with other conventional methods, the reader is referred to [2] and [4].

In this work, a spectrum analyser was used as described in the next section.

3. THE EXPERIMENTAL INVESTIGATION

3.1 Experimental Setup

The experiment to investigate time variation of broadband PD frequency spectra of different defects was set up as depicted schematically in Figure 1. The setup was an accelerated ageing test rig comprising of an array of test cells being subjected to long term exposure to PD activity. Each test cell had a defect artificially made to simulate the common defects that are found in high voltage solid polymer insulation like in power cables.

In order to compare the PD activities from different defects in different test samples, all the test cells were dimensioned such that PDs would be initiated almost at the same voltage of about 7 kV; this voltage was chosen as it would give discharge conditions similar to those in MV power distribution cables. The cells were simultaneously subjected to continuous voltage stress at twice the PD inception level. Acceleration of the PD induced degradation was achieved through elevation of the supply voltage frequency to 400 Hz. At suitable intervals of 2 hours PD frequency spectra were recorded for each cell in complete isolation from the rest of the other test cells in order to avoid cross-interference. While accelerated ageing was done at elevated frequency of 400 Hz, tests were conducted at 50 Hz power supply voltage giving electrical stress conditions that are similar to those of normal operational conditions of medium voltage power equipment.
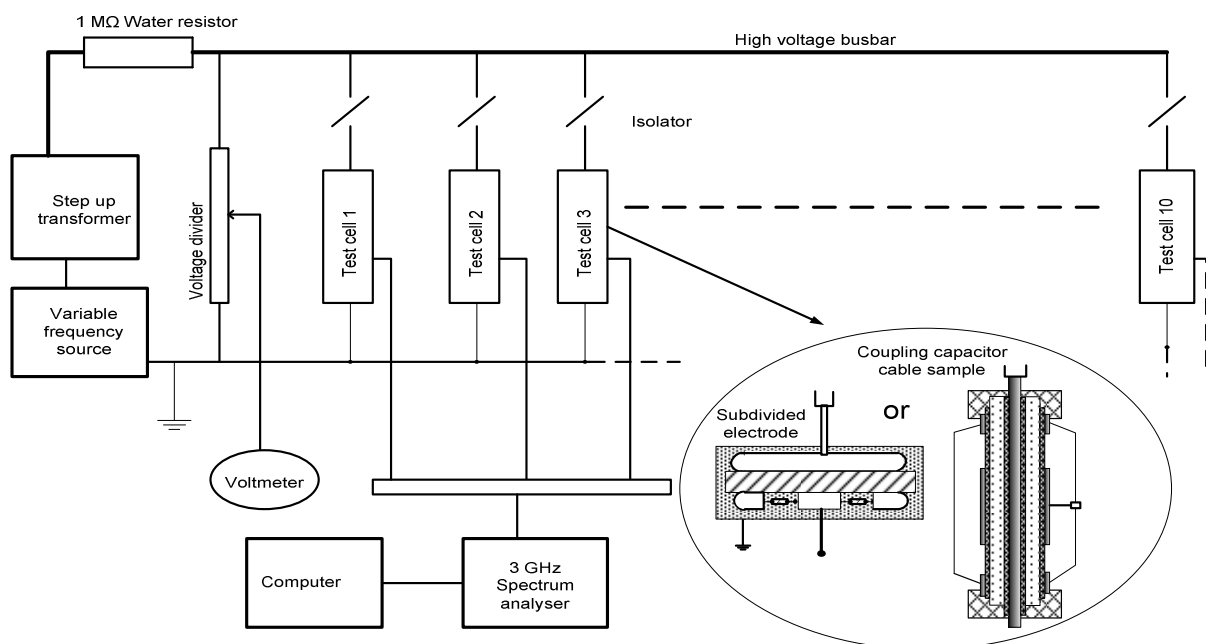
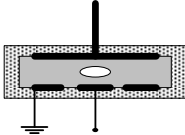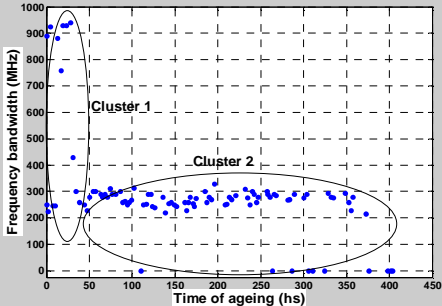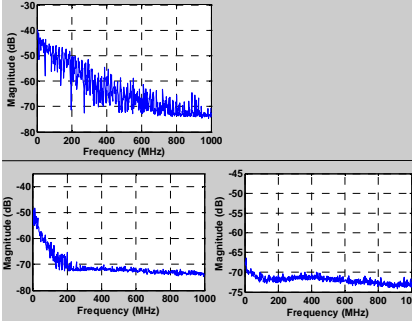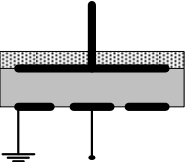**Figure. 1:** PD frequency evolution experimental investigation setup.

Proceedings of the 19th Southern African Universities Power Engineering Conference
SAUPEC 2010, University of the Witwatersrand, Johannesburg

TOPIC G. HIGH VOLTAGE

The 1 MΩ water resistor connected in series with the test cells (as shown in Figure 1) prevented the flow of excessive short circuit currents in the event of complete failure.

The PD signals were detected as power frequency spectra by a 3.5 GHz sweep-tuned spectrum analyser that was connected and controlled through a computer as shown in Figure 1. The spectrum analyser was set to maximum hold mode and with a resolution bandwidth of 1 MHz, traced the frequency spectra for a minute using sweep time of 62 ms.

For each test cell the PD frequency spectra and the corresponding time and date of measurement were recorded and stored for further analysis. All tests were conducted in a Faraday cage type screened high voltage laboratory. Prior to commencement of the tests, the background noise spectrum was recorded while the supply voltage was on but held below the PD inception level. The atmospheric conditions in the test environment, though not deliberately controlled, were monitored such that the temperature and humidity were about 20 ^{0}C and 50% respectively and varied within about 1% throughout the duration of the tests.

4.   RESULTS

All the PD defect types produced frequency spectra that had distinct features. Except for corona in air the frequency spectra of the other defects evolved in different ways depending on the defect type as a function of ageing time from initial inception to total failure. Each PD type had frequency spectra descriptors that clustered distinctly when plotted against the ageing time as shown in the second column of Table 1.

Among possible features or descriptors that characterise a frequency spectrum, the frequency bandwidth, magnitude variance and average magnitude exhibited distinct trends for each defect type as a function of long time ageing. In this paper on the account of space and scope, only the bandwidth results are presented.

The bandwidth of the spectrum, in this work, is defined as the highest frequency component whose magnitude is at least 5% above the background noise level.

Table 1: The simulated defects, their corresponding bandwidth scatter plots and typical frequency spectra at various ageing phases.

Defect type	Scatter plots of the spectral bandwidth as a function of time of ageing	Ageing phase	Typical PD spectra
Insulation bounded cavity		Moderately aged / Severely aged	
Surface discharges on earth electrode & insulation interface		Moderately aged / Severely aged	
Point-to-plane corona in air on earth electrode		Moderately and severely aged	

TOPIC G. HIGH VOLTAGE

Proceedings of the 19th Southern African Universities Power Engineering Conference
SAUPEC 2010, University of the Witwatersrand, Johannesburg

4.1 Void defects
4.1.1   Observations

The time distribution of PD frequency spectra bandwidth exhibited two distinct clusters as shown in the cluster plots in Table 1.

Void PD evolution Cluster 1 occupies the period of about 50 hours of PD activity from the moment of initial inception. This period of PD defect ageing is characterised by distinctly stochastic behaviour. The bandwidth varied randomly within a maximum limit of about 1 GHz and minimum of 200 MHz.

Void PD evolution Cluster 2 is the period that followed 50 hours of continuous ageing (cluster 1). It was the longer of the two time-clusters with a time length of up to 500 hours up to the moment of total failure. In this period of the void defect life the following were noted: The PD frequency spectra bandwidth had relatively narrow variations with a maximum of about 350 MHz and a minimum of 215 MHz. The average bandwidth was much smaller than that of cluster 1. Another interesting characteristic of cluster 2 PD activity is that there were incidences of complete evanescence of PD signals and in some cases for prolonged periods of up to tens of hours.

4.1.2   Possible interpretations and theoretical model

In terms of the space charge dynamics in an insulation gas filled cavity, the evolution of PD mechanisms could be explained using a model that is based on a concept that assumes that all discharges in small cavities are cathode emission sustained processes [9,10]. Figure 2 gives a sketch of a simplified space charge distribution pattern in cavity during a discharge event.
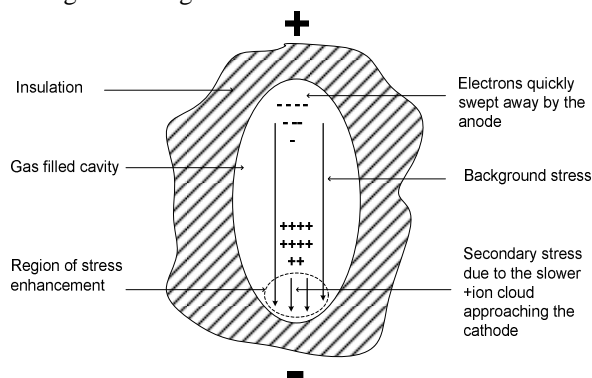
Figure 2: A sketch of simplified space charge distribution with a cathode emission condition in a gas filled insulation cavity during a discharge event initiation process.

The avalanches that are initiated by a seed electron create a cloud of positive ions that drift towards the cathode. As the cloud gets nearer the cathode it enhances the electric field and emits photons. As the photons bombard the cathode, secondary electrons are released that in turn initiate secondary avalanches

eventually resulting in gap discharge. The extent of the cathode effect is a function of the positive ion cloud that in turn depends on the gap overvoltage. In un-aged defect, due to scarce electrons, the overvoltage would relatively be large resulting in bigger and faster avalanches.

Such discharges have been termed spark type, fast, streamer-like etc. Observed in the frequency domain, as in this work, the wide bandwidth would be attributed to the fast rise-time pulses. The random variations of the PD frequency bandwidth could be attributed to the cosmic dependent statistically random availability of discharge seed electrons.

As the defect ages due to continuous PD activity the cavity wall modifications and liquid PD by-products store electrons and act as sources of free electrons. This causes discharges to initiate at smaller gap overvoltages. It results in PD pulses with slower-rise and fall-times, wider widths and smaller heights. Such PD types have been given names such as pseudo-glow, Townsend-like or slow discharges [9-11]. The discharges have slower fall-time and wider width with the latter directly corresponding to the depth of the cavity [9,12]. In the frequency domain as observed in this work, the Townsend-like discharges manifested as spectra with smaller bandwidth and magnitude in cluster 1 of the Table 1 cluster plots. The readily available seed electrons could be responsible for the observed reduction in the extent to which the PD frequency bandwidth varied from one discharge to another.

As the cavity wall becomes extensively 'polluted' many free electrons act as seed electrons and therefore several independent discharge avalanches initiate concurrently on many points on the cathode. In severely aged cavities, the cavity surfaces are littered with solid crystals having been formed from liquid PD byproducts. The crystals cause localised stress enhancement that become PD sources. Such PDs were termed pitting discharges by Morshuis [11] and eventually lead to treeing followed by total failure. Optically the discharges glow over the entire cavity and therefore are also known as glow, pulseless or swarming discharges [7,11]. In this work these PDs could not be detected because of the low frequency response limitations of the spectrum analyser and the largely capacitive (the guard electrode and coupling capacitor cable sample) sensors used to detect the PDs. Consequently no signal was detected and the spectrum analyser displayed only the background noise spectrum as shown in Table 1.

4.2 Surface discharges
4.2.1   Observations

As with void discharges, the time distribution of surface discharges frequency spectra bandwidths

Proceedings of the 19th Southern African Universities Power Engineering Conference
SAUPEC 2010, University of the Witwatersrand, Johannesburg

TOPIC G. HIGH VOLTAGE

exhibited distinct clusters as shown in the second row of Table 1.

Surface discharges evolution Cluster 1 occupied the first 100 hours of continuous accelerated ageing where the frequency spectra bandwidth varied over a wide range bounded by a maximum of about 500 MHz and a minimum of about 200 MHz.

Cluster 2 of the surface discharges occupied the time period after 100 hours of continuous ageing up to the moment of total failure. Discharges in this period were characterised by significantly reduced bandwidth (compared to that in cluster 1). Moreover the random variations of the bandwidth (from one measurement to another) were also greatly reduced and lay within maximum of 200 MHz and minimum of 40 MHz. Another interesting characteristic of cluster 2 surface discharges is that unlike in the case of void discharges, there were no instances of complete discharge evanescence.

4.2.2   Possible interpretations

The evolution of surface discharge spectral signals observed in this work is discussed using the theory of surface discharge mechanisms drawn from similar work done by other researchers such as [13,14].

In the initial stages of the PD activities, the availability of PD seed electrons is dependent on the ionisation of air from cosmic radiation. There is therefore relative scarcity of the seed electrons and this causes discharges to occur at relatively higher overvoltages. Furthermore the discharge initiation delay period varies randomly with a significant scatter. Cases of prolonged delay in discharge initiation would result in big bandwidth and magnitude. In this work this surface discharge phenomenon manifested as a cluster of randomly varying frequency spectra features with wide ranging scatter as shown in cluster 1 of surface discharge cluster plots in Table 1.

As the defect ageing progressed, visible whitish material developed as a coating on the insulation surface as well as splutter on the adjacent metallic electrode surfaces. The corresponding PD signal at this stage had smaller and less varying bandwidths and average magnitudes. The amount of deposits increased with time of ageing and the corresponding signal bandwidth and average magnitudes decreased until the defects completely failed. On the surface discharge cluster plots, this period of evolution is indicated as cluster 2.

On closer examination of the surface discharge areas on the polyethylene insulation sheets, visible signs (cracks and craters) of erosion appeared on the insulation surface that had been close to the edge of the metallic electrode as shown in the photo of Figure 3.

It can be suggested that the coated metallic electrode surface together with the morphological changes of the adjacent insulation surface, reduced the ambient electric field. Consequently the corresponding PDs would be slower and smaller. In this work, measurements that were conducted in the frequency domain showed PDs with narrow bandwidth and small magnitudes. The microcavities seen as craters in the insulation could be sources of localised intense discharges that would eventually create electrical trees to completely bridge the insulation causing a short circuit. Figure 3 shows a portion of a sample that had failed due to surface discharges after about 800 hours of ageing under PD activity.

Figure 3: Portion of some of the surface discharge samples showing visible signs of cracks and microvoids after long term (800 hs) ageing under PD activity.

4.3 Point to plane corona discharges in air

As intuitively anticipated, corona discharges in air did not show any significant evolutional changes during the entire time of observation. This was because the discharge environment had no polymer dielectric boundaries that would undergo physiochemical changes and cause changes in the discharge mechanisms. The corona discharge frequency bandwidth however exhibited consistent narrow variations (as shown in the corona cluster plots in Table 2) that could be attributed to the natural random nature of electrical discharges and possible minor surface erosions of the metallic electrodes.

5.   DISCUSSION

The manner in which the PD frequency spectra evolved with time from initial inception to total failure depended on the type of defect causing the PD. While corona PD, as expected, exhibited no time dependency characteristics, void and surface discharges changed as a function of ageing time.

Based on these experimentally observed phenomena and subject to further tests, as an answer to the research question that motivated this work, a PD defect recognition criterion in solid polymer dielectrics could be tentatively suggested in general terms as follows;

Proceedings of the 19th Southern African Universities Power Engineering Conference
SAUPEC 2010, University of the Witwatersrand, Johannesburg

TOPIC G. HIGH VOLTAGE

When continuously monitoring PD frequency spectral signals under online conditions and taking regular periodical measurements:

i. If an unknown defect gives spectral features (such as bandwidth and magnitude) that significantly change with time **but with no incidences of complete extinction**, then it is likely to be a surface discharge defect that is progressing to total failure.

ii. If an unknown defect gives a PD signal with spectral features (such as bandwidth and magnitude) that significantly change with time **and have incidences of complete extinction**, then it is most likely to be a cavity defect that is progressing towards total failure.

iii. If an unknown defect gives a PD signal with spectral features (such as bandwidth and magnitude) that are **consistent and not significantly changing with time**, then it is likely to be corona in air and may not be a major cause for concern.

6. CONCLUSION

This work has shown that the frequency content of partial discharge signal is a function of the type of insulation defect causing the discharge and is also strongly influenced by the age related physiochemical changes in the defect such as in void and surface discharge defects. Where there are no physiochemical mechanisms such as corona in air discharges, the frequency content of the PDs is generally consistent notwithstanding the natural normal statistically random variations. These phenomena could be used as a basis for developing a novel PD defect recognition criterion.

ACKNOWLEDGEMENTS

REFERENCES

[1] FH Kreuger, *Discharge Detection in High Voltage Equipment*, Temple Place Book Ltd, London 1964, Butterworths, 1989.

[2] S Boggs, "*The case for frequency domain PD testing in the context of distribution cable*", IEEE Electrical Insulation Magazine, Vol. 19, No. 4, pp 13-19, 2003.

[3] YH Md Thayoob, ABA Ghani and PS Ghosh, "*Partial discharge pattern classification using frequency-domain statistical descriptors*", IEEE Proceedings of the 26th Electrical Insulation Conference and Electrical Manufacturing & Coil Winding Conference, Indianapolis 2003, pp 171-175.

[4] NH Ahmed and NN Srinivas, "*On-line partial discharge detection in cables*", IEEE Transactions on Dielectrics and Electrical Insulation, Vol. 5, No. 2, 1998.

[5] Y Cheng, H Xie and W Li, "*Study on characteristics of ultra-wideband partial discharge of typical insulation sample*", Proceedings of the Dielectrics and Electrical Insulation and the 30th Symposium on Electrical Insulation Materials, Toyohashi, Japan, 1998, pp 697-700.

[6] P. Morshuis, "*Ageing of polymers studied by spectral analysis of UWB partial discharge signals*", IEEE Electrical Insulation and Dielectric Phenomena, Annual report. 1995, pp. 226-229.

[7] R Bartnikas, "*Partial discharges: Their Mechanism, detection and measurement*", IEEE Transactions on Dielectrics and Electrical Insulation, Vol. 9, No. 5, 2002, pp. 763-808.

[8] D. Denissov, RG Pfisterer, TK Pfisterer, W Kohler and S. Tenbohlen, "*UHF partial discharge diagnosis of plug-in cable terminations*", Jicable 2007

[9] R. Bartnikas and JP Novak, "*Effect of overvoltage on the risetime and amplitude of PD pulses*", IEEE Transactions on Dielectrics and Electrical Insulation, Vol. 2, No. 4, 1995, pp. 557-565.

[10] JC Devins, "*The physics of partial discharges in solid dielectrics*", IEEE Transactions on Electrical Insulation Vol. EI-19, No. 5, 1984, pp. 475-495.

[11] P. Morshuis, "*Assessment of dielectric degradation by ultrawide-band PD detection*", IEEE Transactions on Dielectrics and Electrical Insulation, Vol. 2, No. 5, 1995, pp. 744-760.

[12] PHF Morshuis and FH Kreuger, "*Transition from Streamer to Townsend mechanisms in dielectric cavities*", J. Phys. D: Appl. Phys., Vol. 23, 1990, pp. 1562-1568.

[13] MA Handala and O Lamrous, "*Surface degradation of styrene acrylonitrile exposed to corona discharge*", European Transactions on Electrical Power Vol. 18, 2008, pp. 494-505.

[14] X. Li and L. Wang, "*Discharge characteristics in atmospheric pressure glow surface discharge in helium gas*", Chin. Phys. Lett. Vol. 22, No.2, 2005, pp. 416-419.

List of Discussion Papers

- Customer interruption costs for the agricultural sector,
  Mphephu, T., Awodele, K.

- The development of a guideline to assist with compiling asset management plans for transmission lines,
  Mansingh, S., Ijumba, N.M., Govender, S.

- FACTS compensation modelling of the Albany-Wesley 66/22kV transmission system for optimal power transfer,
  Ndimurwimo, A., Harris, R.T., Roberts, A.G., Phipps, W.

- Comparison of real-time sofware relay models with the SEL 311C hardware relay for distance protection,
  Kabelo, O., Rigby B.S.

- Digital technique in distribution system loss minimization,
  Munyai, V., Chowdhury, S.P., Chowdhury, S.

- Design optimisation of bare conductors for overhead line applications,
  Munilall, A., Ijumba, N.M., Muftic, D.

- Random connection of new loads on a rural network and the effects on voltage unbalance,
  Moloko, T.S., Ijumba, N.M., Koch, R.

- Fuzzy modelling and performance analysis of PV array in embedded environment,
  Motale, O., Chowdhury, S., Chowdhury, S.P.

- A set of differential equations for modelling the temperature rise associated with the current from a lightning strike,
  Grant, M.D., Nixon, K.J., Dickson, A.S.

- Future trends in electricity generation, distribution, and control,
  Carroll, J.

- Boscia Albitrunca - A tree that is never struck by lightning?
  Trengoven, E., Jandrell, I.R.

- Overview of test design and setup for long air gap lightning performance evaluation of quasi-hemispherical air terminations vs a Franklin rod,
  Djurdjevic, I., West, N.J., Jandrell, I.R.

- Performance evaluation of a simplified integrated current transformer, for high frequency power converters *Pentz, D.C., Van der Merwe, F.H.*

Index